Space-Weathering on Primitive Asteroids. Coupling Infrared spectroscopy and electron microscopy

Stefano Rubino

université
PARIS-SACLAY

Space-Weathering on Primitive Asteroids Coupling Infrared spectroscopy and electron microscopy

Effets de l'altération spatiale sur les astéroïdes primitifs
Etude par spectroscopie Infrarouge et microscopie electronique

Thèse de doctorat de l'université Paris-Saclay

École doctorale n°127, Astronomie et Astrophysique d'Ile-de-France (AAIF)
Spécialité de doctorat : Astronomie et Astrophysique
Graduate School : Physique, Référent : Faculté des sciences d'Orsay

Thèse préparée dans les unités de recherche : **Institut d'Astrophysique Spatiale** (IAS, Université Paris-Saclay, CNRS), **Unite Matériaux et Transformations** (UMET, Université de Lille, CNRS) et **Synchrotron SOLEIL** (Université Paris-Saclay), sous la direction de **Rosario BRUNETTO**, chargé de recherche CNRS, la co-direction de **Hugues LEROUX**, professeur des univerités et le co-encadrement de **Ferenc BORONDICS**, responsable ligne de lumière.

Thèse soutenue à Paris-Saclay, le 30 Septembre 2022, par

Stefano RUBINO

Composition du jury

Membres du jury avec voix délibérative

Cyril SZOPA Professeur des universités, LATMOS (Université Paris-Saclay, CNRS)	Président du jury
Karine DEMYK Directrice de recherche, IRAP (Université de Toulouse, CNRS)	Rapportrice et Examinatrice
Michelle S. THOMPSON Assistant professor, Department of Earth, Atmospheric, and Planetary Sciences (Purdue University)	Rapportrice et Examinatrice
Takaaki NOGUCHI Professeur, Division of Earth and Planetary Sciences (Kyoto University)	Examinateur
Alessandra ROTUNDI Professeure, Dipartimento di Scienze e Tecnologie (Università Parthenope)	Examinatrice

THESE DE DOCTORAT
NNT : 2022UPASP089

université PARIS-SACLAY

ÉCOLE DOCTORALE
Astronomie
et Astrophysique
d'Île-de-France (AAIF)

Titre : Effets de l'altération spatiale sur les astéroïdes primitifs. Etude par spectroscopie Infrarouge et microscopie electronique.

Mots clés : Astéroïdes - Spectroscopie - Irradiation - Microscopie

Résumé :

L'étude des petits corps du système solaire est fondamentale pour la compréhension de sa jeunesse et de son évolution. Ces petits corps « primitifs » seraient « non-différenciés » (pas d'entrée en fusion et séparation des phases altérant la minéralogie). Ils n'auraient donc que très peu évolué depuis leur naissance, avec une composition étroitement liée à celle du disque proto-planétaire originel. Pourtant, d'autres processus, comme l'altération thermique, l'altération aqueuse, les chocs ou l'altération spatiale peuvent venir altérer la surface d'un corps primitif. Ceci est problématique, car les mesures acquises à distance de ces corps ont comme cible précisément leur surface. Si celle-ci est altérée, elle peut biaiser l'étude de la composition de ces petits corps. Il est donc important de comprendre les processus affectant la surface des astéroïdes primitifs, afin de pouvoir correctement interpréter leur composition.

Il y a plusieurs façons d'étudier la surface d'astéroïdes primitifs, tel que à distance, depuis la Terre ou un satellite orbitant le corps d'intérêt, en acquérant des données de spectroscopie (composition chimique et minéralogique de surface). Il est aussi possible d'étudier ces corps en laboratoire, en travaillant sur des matériaux analogues comme certaines classes de météorites « primitives » (les chondrites carbonées), sur des analogues terrestres (plus simples à étudier que les météorites, mais moins étroitement liés à la matière extraterrestre), ou enfin sur de la matière extraterrestre rapportée par les missions de retour d'échantillons.

Dans cette étude, nous nous sommes proposé d'étudier en laboratoire les effets de l'altération spatiale sur les surfaces d'astéroïdes primitifs. Plus précisément, cette étude est focalisée sur les effets du vent solaire, le processus dominant d'altération spatiale sur les surfaces « jeunes » du système solaire. Nous avons choisi trois minéraux terrestres analogues à une surface « primitive » – à savoir, trois minéraux hydratés (deux serpentines et une saponite) – dont nous avons produit des pastilles que nous avons bombardé avec des ions He et Ar, afin de simuler les effets de deux contributions différentes du vent solaire. Nous avons donc produit donc des analogues de surface primitive ayant subi de l'altération spatiale.

Ces analogues ont ensuite été caractérisés par spectroscopie infrarouge, du visible jusqu'à l'Infrarouge lointain, afin d'étudier l'évolution chimique après bombardement ionique de nos échantillons, en suivant les changements induit par le bombardement sur des bandes spectroscopiques caractéristiques des minéraux hydratés dans l'IR, ainsi que sur l'évolution du continuum dans le visible. Nous avons détecté plusieurs effets, tels que l'assombrissement des spectres visible, rougissement et bleuissement des pentes spectrales selon l'échantillon ainsi qu'un déplacement systématique vers les grandes longueurs d'ondes de plusieurs bandes spectrales.

Cette caractérisation spectroscopique a été suivie par une étude à plus petite échelle par microscopie électronique, dédiée à caractériser la surface de nos analogues altérés par microscopie électronique à balayage, et ensuite à étudier à l'échelle nanométrique les changements morphologiques et physico-chimiques ayant lieu dans la couche bombardée, par microscopie électronique à transmission. De forts effets de bullages de différents types ont été identifiés dans la couche amorphisée par bombardement ionique, ainsi que des changements de texture et certaines évolutions élémentaires (perte d'oxygène en surface, amorphisation préférentielle du magnésium, etc.).

Le couplage entre ces deux techniques, spectroscopie IR et microscopie électronique, agissant à différentes échelles, a permis une meilleure compréhension des effets d'altérations spatiale sur les corps primitifs, et pourra prêter support à l'étude de ce type de surface, qu'elle soit menée à distance ou en laboratoire sur des matériaux récoltés.

université PARIS-SACLAY
ÉCOLE DOCTORALE
Astronomie
et Astrophysique
d'Île-de-France (AAIF)

Title : Space-Weathering on Primitive Asteroids. Coupling Infrared spectroscopy and electron microscopy.
Keywords : Asteroids - Spectroscopy - Irradiation - Microscopy

Abstract :

The study of small bodies in our solar system is fundamental for understanding its youth and evolution. These small "primitive" bodies are "undifferentiated" (they did not undergo phase density-separation, irreversibly altering their mineralogy). They have evolved very little since their birth, spurring a composition relatively close to that of the primordial proto-planetary disk. However, other processes, such as thermal alteration, aqueous alteration, shocks, or space-weathering can affect these bodies' surfaces. This is an issue, since remote-sensed data acquired while studying these bodies target these very surfaces. If these surfaces have been altered, they can induce a certain bias in the study of the composition of these small bodies. Therefore, it is paramount to understand the processes affecting the surface of primitive asteroids to correctly assess their composition.

There are several ways to study the surface of primitive asteroids, such as remotely, from the Earth or from a satellite orbiting the body of interest, by acquiring spectroscopic data (gaining access to surface chemical and mineralogical composition). It is also possible to study these bodies in a laboratory environment, by working on analogous materials such as certain classes of "primitive" meteorites (carbonaceous chondrites), on terrestrial analogues (simpler to study than meteorites, but less closely related to extraterrestrial materials), or directly on extraterrestrial materials brought back by sample return missions.

In this work, we replicate in a laboratory environment the effects of space weathering (SpWe) on the surface of primitive asteroids. More specifically, we focus on the effects of solar wind, the dominant SpWe process on "young" surfaces of the solar system. We have chosen three terrestrial minerals analogous to a "primitive" surface - three hydrated minerals (two serpentines and one saponite) - of which we have produced several pellets which have been bombarded using He and Ar ions, to investigate the effects of two different solar wind. In doing so, we made analogous materials of weathered primitive surface matter.

These analogues were then characterized by infrared spectroscopy, from the visible to the far-infrared range, to study chemical changes prompted by ion bombardment. This was done by investigating how certain spectroscopic features – characteristic of hydrated silicates – changed upon ion-bombardment. We detected several effects, such as darkening in the visible range, visible slope reddening and bluing as well as a systematic shift towards longer wavelength affecting the position of several spectroscopic features.

This spectroscopic characterization was followed by a study at smaller scale, using electron microscopy. We first characterized the surface of our weathered analogues using scanning electron microscopy, and then investigated the morphological and physicochemical changes taking place in the bombarded layer, at a nanometer scale, using transmission electron microscopy. Strong vesiculation effects of various kinds were identified in the ion-bombarded amorphized layers, as well as textural changes and some elemental concentration evolution (such as the loss of oxygen in the utmost top surfaces, preferential amorphization of magnesium, etc.).

The coupling between these two techniques, IR spectroscopy and electron microscopy, acting at different scales, has allowed for a better understanding of SpWe effects on primitive bodies, and will be able to support current and future studies of primitive bodies, whether they are carried-out remotely or in a laboratory environment on returned samples.

L'étude des petits corps du système solaire est fondamentale pour la compréhension de sa jeunesse et de son évolution. Ces petits corps « primitifs » seraient « non-différenciés » (pas d'entrée en fusion et séparation des phases altérant la minéralogie). Ils n'auraient donc que très peu évolué depuis leur naissance, avec une composition étroitement liée à celle du disque proto-planétaire originel. Pourtant, d'autres processus, comme l'altération thermique, l'altération aqueuse, les chocs ou l'altération spatiale peuvent venir altérer la surface d'un corps primitif. Ceci est problématique, car les mesures acquises à distance de ces corps ont comme cible précisément leur surface. Si celle-ci est altérée, elle peut biaiser l'étude de la composition de ces petits corps. Il est donc important de comprendre les processus affectant la surface des astéroïdes primitifs, afin de pouvoir correctement interpréter la composition de ces « capsules temporelles » siderales.

Il y a plusieurs façons d'étudier la surface d'astéroïdes primitifs, tel que à distance, depuis la Terre ou un satellite orbitant le corps d'intérêt, en acquérant des données de spectroscopie (composition chimique et minéralogique de surface). Il est aussi possible d'étudier ces corps en laboratoire, en travaillant sur des matériaux analogues comme certaines classes de météorites « primitives » (les chondrites carbonées), sur des analogues terrestres (plus simples à étudier que les météorites, mais moins étroitement liés à la matière extraterrestre), ou enfin sur de la matière extraterrestre rapportée par les missions de retour d'échantillons.

Dans cette étude, nous nous sommes proposé d'étudier en laboratoire les effets de l'altération spatiale sur les surfaces d'astéroïdes primitifs. Plus précisément, cette étude est focalisée sur les effets du vent solaire, le processus dominant d'altération spatiale sur les surfaces « jeunes » du système solaire. Nous avons choisi trois minéraux terrestres analogues à une surface « primitive » – à savoir, trois minéraux hydratés (deux serpentines et une saponite) – dont nous avons produit des pastilles que nous avons bombardé avec des ions He et Ar, afin de simuler les effets de deux contributions différentes du vent solaire. Nous avons donc produit donc des analogues de surface primitive ayant subi de l'altération spatiale.

Ces analogues ont ensuite été caractérisés par spectroscopie infrarouge, du visible jusqu'à l'Infrarouge lointain, afin d'étudier l'évolution chimique après bombardement ionique de nos échantillons, en suivant les changements induit par le bombardement sur des bandes spectroscopiques caractéristiques des minéraux hydratés dans l'IR, ainsi que sur l'évolution du continuum dans le visible. Nous avons détecté plusieurs effets, tels que l'assombrissement des spectres visible, rougissement et bleuissement des pentes spectrales selon l'échantillon ainsi qu'un déplacement systématique vers les grandes longueurs d'ondes de plusieurs bandes spectrales.

Cette caractérisation spectroscopique a été suivie par une étude à plus petite échelle par microscopie électronique, dédiée à caractériser la surface de nos analogues altérés par microscopie électronique à balayage, et ensuite à étudier à l'échelle nanométrique les changements morphologiques et physico-chimiques ayant lieu dans la couche bombardée, par microscopie électronique à transmission. De forts effets de bullages de différents types ont été identifiés dans la couche amorphisée par bombardement ionique, ainsi que des changements de texture et certaines évolutions élémentaires (perte d'oxygène en surface, amorphisation préférentielle du magnésium, etc.).

Le couplage entre ces deux techniques, spectroscopie IR et microscopie électronique, agissant à différentes échelles, a permis une meilleure compréhension des effets d'altérations spatiale sur les corps primitifs, et pourra prêter support à l'étude de ce type de surface, qu'elle soit menée à distance ou en laboratoire sur des matériaux récoltés.

A mia sorella...

Acknowledgements

Three years is a weird extent of time. At the start of your Ph.D., it feels like comfortable - but daunting - amount of time... with so much to do, so much to learn, so much to see. It is only at the end the journey that a certain realization hits you : it all went by so fast. Even so, I personally feel like I would need three more years to thank all the wonderful people who have helped and supported me into becoming the scientist – and person - that I am today (and even if I actually spent three more years filling this "Acknowledgments" section, I would still end up forgetting somebody... So, bear with me for just this few pages).

I wish to start by thanking my wonderful supervisors, Rosario, Hugues and Ferenc.

Rosario, thank you for "keeping me around" 6 years ago - me, a young L3 student who apparently managed to impress you enough to think "let's keep an eye on this guy, we may need him soon enough...". Thank you for believing in my autonomy enough to let me spread my wings, but also for never being too far away to catch me in case I was too close to fall and needed some help - both professionally and personally. Some of the teachings you imparted to me, I will never forget as I hold them forever precious in my mind, as a scientist and as a person.

Hugues, thank you always for your time, your calm and your teachings. I was always looking forward to coming to Lille to work with you, and I do wish we would have been able to work together more often. I was able to learn so much under your guidance and discover new beautiful experimental techniques. It was often very sweet to see you gaze into the incredibly small details that electron microscopy can reveal, and I hope to one day be also able to appreciate the inner beauty of scientific data as you did.

Feri, where do I start. My shadow-director. Thank you for everything, for the endless talks about science but also about life in general (especially podcasts !). Working in SOLEIL was already a privilege but working alongside one of the nicest person I have ever met such as you was also extremely precious. I was always happy to come by at SMIS (not only for the cantine !). You have made a lot of long tomography session seem less long with your humor and good mood. I will miss hanging aournd the FPA while a measurement is being taken, talking about stuff. But also thank you for never doubting me, even when I was doubting myself.

To the members of my jury, thank you for your precious time and for having shared such an important moment of my professional (and personal !) life with me. Thank you to my reviewers, Karine Demyk and Michelle Thompson, for reading my manuscript, for their kind words regardng my work and their extremely precious insight on it. Thank you to Takaaki Noguchi and Alessandra Rotundi for their interest in my scientific work and their kind appreciation of it. Thank you finally to Cyril Szopa for accepting to preside my Ph.D. defense and for the kindness they showed to a very stressed-out Ph.D. student on the day of his Ph.D-defense !

I wish to thank the wonderful members (past and present !) of the Astrochemistry and Origin team at IAS – Alice, Cateline, Donia, Obadias, Riccardo, Zahia and Zélia – as well as my PhD comrades – Elsa, Romain, Tania and Yann, for these last three wonderful years spent working and living alongside you all. Special thanks must go to Yann, my PhD-brother, for being one of the kindest, funniest and most precious friends I made along this journey, and to Zélia, my wonderful mentor and friend, for always keeping an eye out for me and being always ready to listen and understand.

Thank you to the people I was able to interact with in Lille – Alexandre and Dan – for our precious discussion and friendliness between measurements.

Thank you to the rest of the SMIS team in SOLEIL (again, past and present !) – Anna, Christophe, Francesco and Stephane – for taking care of me and being always ready to help during my stays in SOLEIL.

Thank you to the members of the ISSI team 485, and especially to our team leader Francesca, for her help and support for the future of my career, and for her friendliness in general.

Thank you finally to the wonderful Ph.D students and Post-Doc community at IAS – Valentine, Pierre, Yann, Océane, Stefano, Axel and all of you wonderful people – for the extremely fun time we were able to share, despite the covid situation. I hope that we were all able to "jumpstart" something beautiful and precious among the youth in the lab that will hopefully carry-on once our job is done !

There are certain people in my personal life without whom all of this would not have been possible. I wish to thank my parents and my family in general, for their support, as well as my amazing group of friends in Paris and beyond, for their precious encouragements.

Finally, the most invaluable thank you to the three persons closest to me in my life : my best friend in the entire world, Max, for their boundless support and for all the wonderful times we have shared in these last six years since we met in L3 (you're next, little buddy !) ; my wonderful partner, Alice, for their precious help and priceless encouragement, especially during the final steps of this adventure, and for being the most amazing person I have ever met ; and finally, my little sister, Valentina, without whom I would quite literally be half the person I am today - your brother loves you.

And to you who are reading this acknowledgment section, thank you. I hope you will find what you seek in this manuscript, as well as in life.

"Here we stand, feet planted in the earth,
but might the cosmos be very near us,
only just above our heads ?"

TABLE OF CONTENTS

CHAPTER 1

Introduction : astrophysical context

Contents

1.1. On the early stages of our Solar System

The Solar System as we study and observe today has significantly evolved since its birth. This section is dedicated to describe the early phases of our Solar System, showcasing how we are able to investigate such stages and why it is relevant to do so.

1.1.1. Dusty beginnings

Molecular clouds, often associated with the more generic term of "nebulae", are the birthplace of stars. These vast volumes of gas (mostly molecular hydrogen and helium) and dust grains (in the form of silicates, hydrocarbons and ices) represent a stable structure which is constantly on the brink of gravitational collapse (Montmerle 2006). An example of molecular cloud is shown in Figure 1.1.

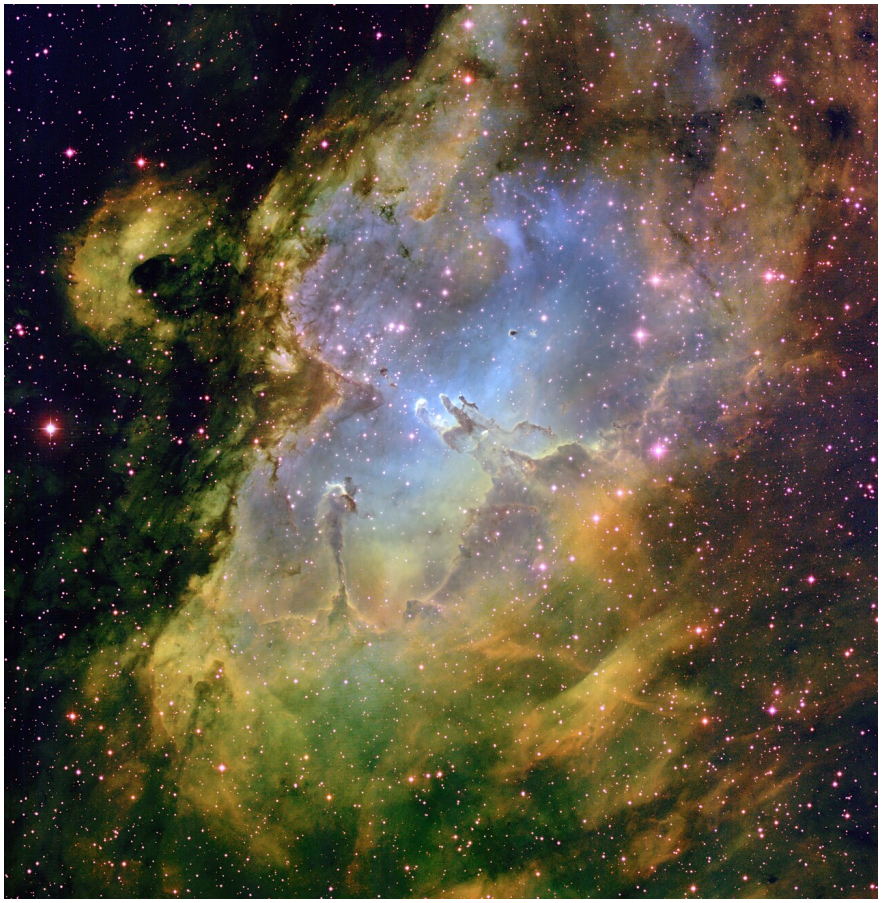

Figure 1.1: Wide-field image of the Eagle Nebula (M16). Credit: T. A. Rector B. A. Wolpa, NOAO, AURA.

A few billion years ago, approximately 4.56 billion (Bouvier 2010), one such nebula collapsed (Figure 1.2, panels a and b), possibly triggered by external perturbations such as traveling shock-waves. During the collapse, the averaging gas movements resulted in the creation of a gaseous flat disc, rotating around a central, heavier mass: a proto-star (Figure 1.2, panel c).

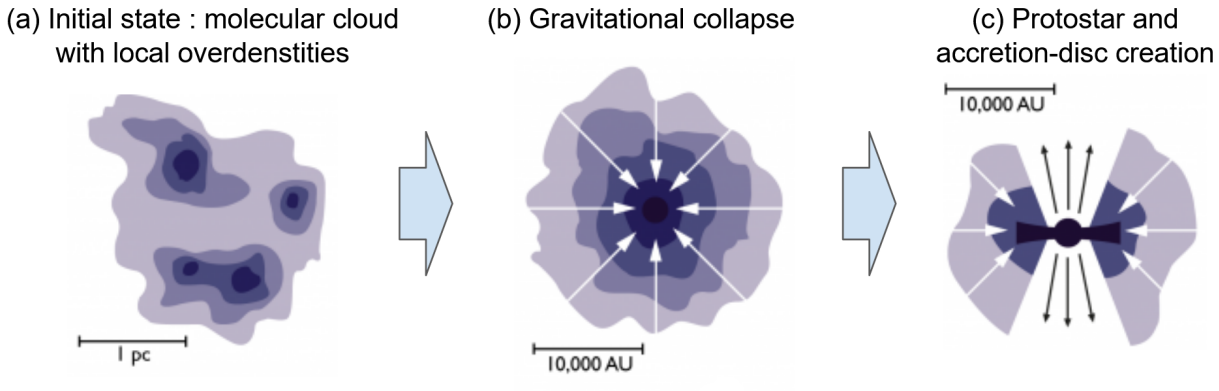

Figure 1.2: Gravitational collapse of a molecular cloud into an stellar system "embryo". Credit: Observatoire de Paris.

As this mass - which would one day become our Sun - kept growing, it established a certain temperature gradient along the accretion disc. This temperature gradient dictated the composition of our young stellar system (see Figure 1.3).

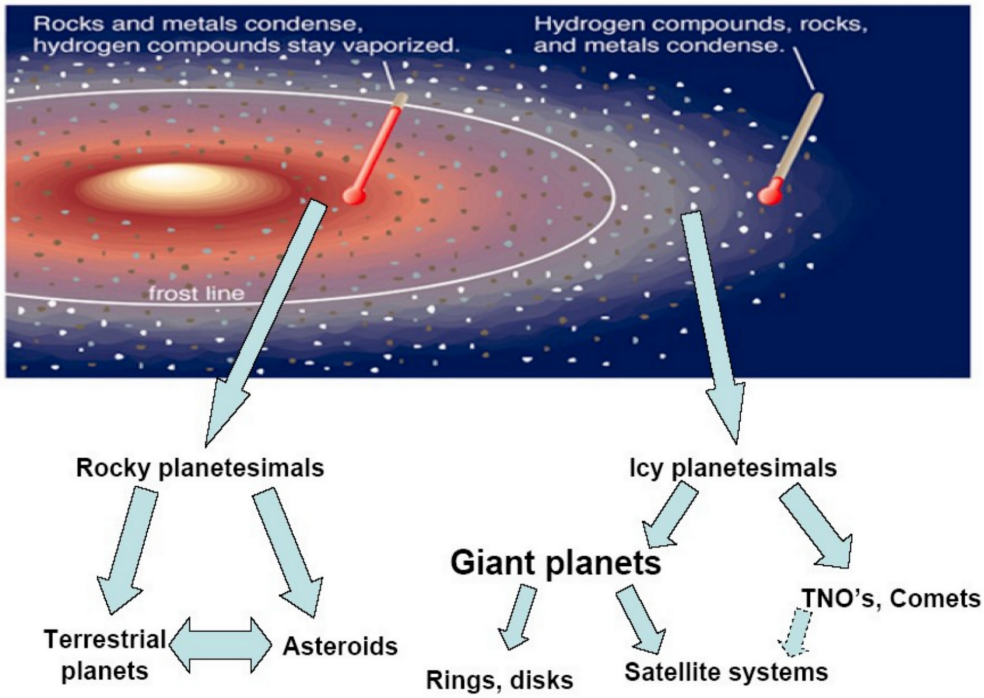

Figure 1.3: Schematic of a proto-planetary disk. credit : Prof. Sonia Fornasier, Laboratoire d'études spatiales et d'instrumentation en astrophysique (LESIA) - Observatoire de Paris-Meudon, "Planètes, satellites et petits corps du système solaire: cours d'introduction", 2019.

Close to the proto-star, the high temperatures would not allow for complex molecules to exist.

At a larger distance from the central mass, as the temperature dropped around 1400 K, refractory elements could condense, effectually giving birth to the first solid materials formed in the Solar System, known as CAIs (Calcium-Aluminum-rich Inclusions). Farther away from the star, as the temperature dropped further between 800 and 1400 K, anhydrous silicates such as olivines and pyroxenes were formed. Shocks, turbulence and impacts may have led to the melt (partial or complete) of these anhydrous silicates. Their re-condensation would lead to the birth of igneous spherules called chondrules, mineralogically dominated by olivine, pyroxene and Fe-rich minerals (Zolensky et al. 2018 and references therein). Both CAIs and chondrules would then aggregate with surviving interstellar grains. These materials can be found nowadays embedded in the matrix of some meteorites.

Lastly, beyond 5 Astronomical Units (AU) - the so-called "Ice/Frost Line" - the temperature drop allowed volatile elements to condensate, forming various ices (water, carbon dioxide, methane...). The "Ice Line" formed a natural split between two distinct regions of our young solar system: an internal "refractory" dust-rich region, and an external region, harboring silicate dust and volatile components in the form of icy dust. This dynamic is no longer what we can observe in the Solar System today. Indeed, as the proto-sun reached its final mass, various dust-aggregation processes at different scales started forming the larger observable constituents of our modern Solar System, effectually depleting the fine icy and silicate dust populations.

1.1.2. From dust to planetesimals

Submicron-sized dust particles began to assemble via low relative velocity collisions, forming dust aggregates, then pebbles and eventually large rocky bodies known as planetesimals. As loose dust started to condensate, the protoplanetary disc started to disappear (see Figure 1.4).

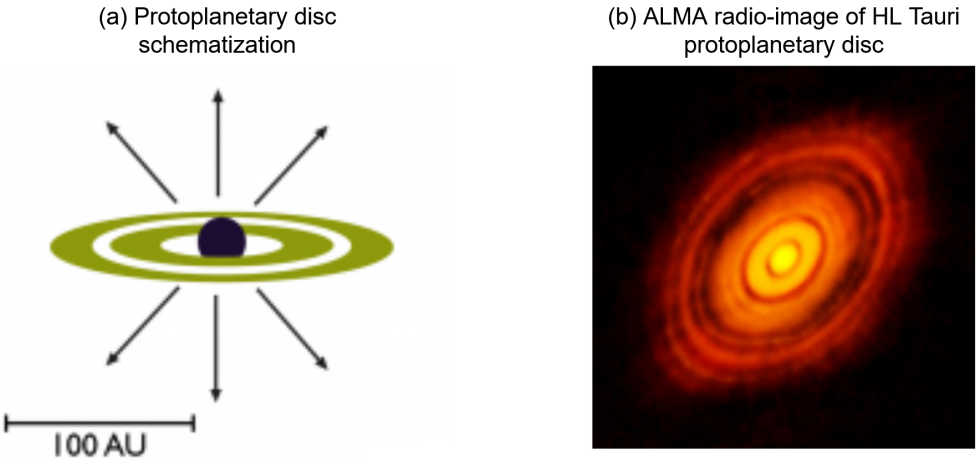

Figure 1.4: (a) Schematic of a proto-planetary disk. Credit: Observatoire de Paris. (b) Atacama Large Millimiter Array (ALMA) radio image of the protoplanetary disc observed in HL Tauri, approximately 450 light-years from Earth, in the Taurus Molecular Cloud (Stephens et al. 2014).

This process lasted for a few million years. As these dust aggregates reached centimeter-size, they started to sediment along the median plane of the disc. There, they would grow, up to kilometer-size. This step of planetesimal growth remains today the interest of scietific research. Collisional impact of bodies with such sizes, at the typical speed inside the proto-planetary disc (10 m/s in order of

magnitude), tend to be destructive instead of being beneficial to the body's growth (Chokshi et al. 1993). Eventually, as the population in the depleting gas disc started to be dominated by kilometer-size planetesimals, the accretion process shifted from occasional collision to gravitational attraction. This prompted the appearance of a divide among the planetesimal bodies, a divide related to their size.

1.1.3. Differentiated vs Primitive bodies

1.1.3.1 Large differentiated bodies

With gravitational attraction dominating the accretion regime, large planetesimals grew larger and faster than smaller ones, becoming the first planetary embryos. Due to their large size, these bodies underwent a physico-chemical process called "differentiation". Spurred by the joint effects of radioactive decay of heavy accreted elements, collisional impacts and gravitational pressure, these large bodies started to significantly heat up. As these bodies' constituents started to melt, denser metallic materials sank towards their centers, while lighter silicates rose to the surface. Collisional events were still able to locally mix materials with different densities, as well as prompting chemical reactions among them. However, the differentiation process is what dictated the mineralogical assembly and structure of these large bodies. These rocky bodies acquired a layered structure, and their mineral composition was irreversibly altered from their planetesimal stage. These planetary embryos had become the early versions of the planets, dwarf planets and large asteroids we are able to observe in our modern Solar System today.

1.1.3.2 Small primitive bodies and their composition

Some stragglers of ages past remained: smaller planetesimals did not undergo differentiation processes, being too small to trigger one. These small bodies were able to retain a composition quite similar to their original one, spurred from the dust-aggregation stage of their evolution. What remains of these small bodies after billion of years of gravitation evolution can still be observed today in the form of some classes of asteroids and comets. The scientific community refers to them as "Primitive Bodies". Our work focuses on this kind of body, since they act as some kind of "time-capsule" related to the early stages of our Solar System.

These bodies appear to be particularly carbon-rich, but their mineral composition is dominated by hydrated silicates, also known as phyllosilicates (Usui et al. 2018). The characteristic spectroscopic feature of these minerals, the 2.7 µm band - related to the stretching vibration of the (M)-OH bond, (M) being a metallic cation - has been detected on the surface of both C-type asteroid (162173) Ryugu (Kitazato et al. 2019) and B-type asteroid (101955) Bennu (Hamilton et al. 2019), two primitive bodies of particular interest in the current scientific context, since they are the targets of two sample-return type missions (Hayabusa2 from JAXA and OSIRIS-REx from NASA respectively - more on that in 1.2.3). The surface composition of Ryugu as also been better constrained thanks to the returned samples of the Hayabusa2 mission, indicating the presence of fine phyllosilicates grains - predominantly serpentine and saponite - and coarser grains including carbonates, magnetites and sulfides (Yokoyama et al. 2022).

Both serpentine and saponite correspond to two different classes of phyllosilicates, with two distinct crystal structures. Phyllosilicates are arranged in sheets of silicate tetrahedrons (each consisting of a central silicon atom linked to four oxygen atoms), interleaved with octahedron layers (metallic cation linked to eight oxygen atoms - Farmer 1974, see figure below). These are called T and O layers. All phyllosilicates are made of various arrangements of TO and TOT structures. Serpentines generally consists of an assembly of TO structures, weakly linked among themselves via hydrogen-binding. Saponites are made out of TOT structures, separated by an empty interlayer. This interlayer can harbour molecular H_2O water, as well as solvated metallic cations. More details regarding structural variations among phyllosilicates are discussed in 2.1.1.

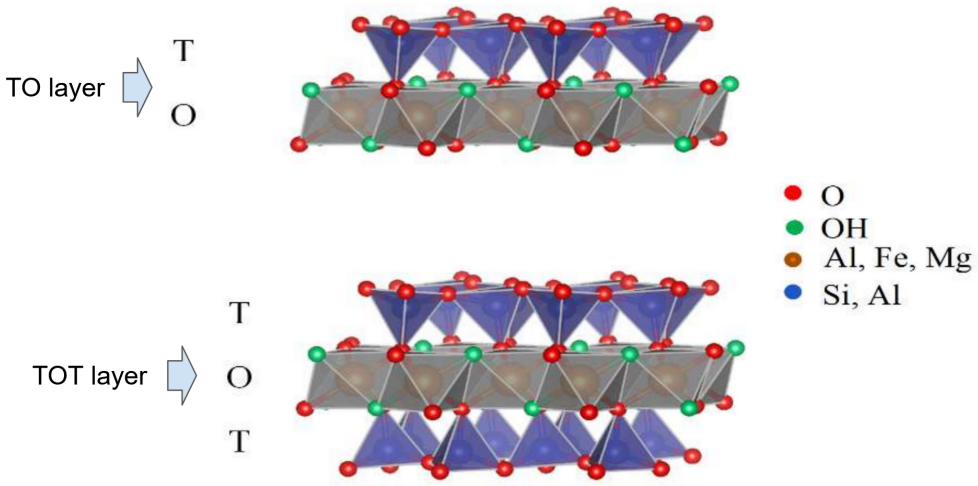

Figure 1.5: Structure of phyllosilicate sheets, highlighting the differences between TO and TOT structures. Adapted from Wang et al. 2020.

1.2. Ways of of studying asteroids

1.2.1. By far : remote sensing, photometric and spectral observations

The surface of outer bodies can be probed via on-Earth telescopes, orbiting observatories or nearby-probes, using various instruments. The two main techniques used are photometry and spectrometry.

Photometry is the study of the photon's flux from a celestial body in a narrow wavelength region, which is constrained using well-defined optical filters. Photometric measurements can provide unique insight such as the shape of a small body. Spectroscopy is the study of the distribution of the electromagnetic radiation emitted, reflected or transmitted from a body as a function of photon energy (often associated to the photon's wavelength). Applying these techniques via the use of telescopes or orbiting instruments is defined as acquiring "remote-sensed" data.

On-Earth telescopes and orbiting observatories were able to help our understanding of deep space and far away objects. On the other hand, space probes enabled us to greatly improve our understanding of our Solar System. Many bodies in our Solar System have been visited by space probes, un-piloted spacecrafts sent from Earth to gather scientific data. By orbiting around their target, space probes are able to fully characterize it by acquiring extensive data maps of multiple different

regions on each target, which helps in assessing compositional and morphological heterogeneities at the scale of the investigated body. Such a feat would not be possible directly from Earth. Space probes missions are often multi-target, meaning that they will spend a certain amount of time orbiting and studying a primary target, and then they will switch to one or more secondary targets. On their way to their targets, space probes can also engage in 'flyby' missions, where they will acquire quick reconnaissance data of a passing celestial object. Space probe missions require years of preparation, since the probe and its multiple detectors need to be engineered to resist a multiple year voyage in the vacuum of space without human intervention after departure from Earth. Because of the timescales involved, space probe missions often mobilize multiple generations of scientists. An example of such a mission is NASA's twin spacecrafts, Voyager 1 and Voyager 2, which were launched in 1977. Their primary mission was the study of Jupiter and Saturn. After a string of discoveries, their mission was extended : Voyager 2 was sent to explore Neptune and Uranus while the path of Voyager 1 was set to send it outside our Sun's heliosheath, leaving our solar system in 2012. Voyager 2 joined its twin on its interstellar journey in 2018. The two spacecrafts are still transmitting data to Earth after a 44 year long journey.

1.2.2. By proxy : laboratory studies on meteorites and analogue materials

The study of small bodies in our Solar System can also be conducted on Earth, which comes with some perks and drawbacks. The carrying capacity of space-probes and surface-landers is limited due to the inherent difficulties associated to this type of endeavour. Technological advances can only allow for certain types of instruments to be included, limiting the experimental techniques that can be used during these missions. A wide array of state-of-the-art techniques are, as of now, "grounded", only able to be performed in a laboratory environment. They may necessitate of a specific sample preparation (impossible to implement by semi-autonomous space-probes), or the machine associated to the technique is far to big for the carrying capacity of current-generation spacecrafts. However, applying these experimental techniques on extraterrestrial materials available on Earth can help the interpretation of remote-sensed data and can contribute to establishing a more complete view regarding small bodies and their history in our solar system.

Unfortunately, extraterrestrial materials that are directly linked to an identified celestial body (their "parent" body) are somewhat rare and, except for the Moon and a few other exceptions, fairly scarce. In the near future, the boom of sample-return type missions will mitigate this issue, but, as of today, by combining all of the materials ever recovered by sample-return missions - excluding Moon samples - we have less than 7 grams of available material directly linked to a certain small body ($\sim$ 1g of material from comet 81P/Wild, $<$ 1g from S-type asteroid Itokawa and 5.4g from C-type asteroid Ryugu).

Meteorites are the closest object available on Earth that can be used to study small bodies in our solar system from our laboratories. Meteorites are small rocky fragments originating from impacts between celestial bodies. Some of these debris get captured from the gravitational pull of our planet, and fall onto its surface, where they are collected and become available to the scientific community. There are four main types of meteorites (see Figure 1.6):

- Chondrites are stony-type meteorites, related to undifferentiated planetesimals. Their name comes from the presence of chondrules (see 1.1.1), silicate spherules embedded in their matrix. They represent the largest population of meteoritic material available on Earth (close to 85%). There are three main groups of chondrites: ordinary chondrites, carbonaceous chondrites and enstatite (E-type) chondrites (respectively approximately 80%, 4% and 2% of recorded falls - see Greenwood et al. 2020). This division is based on the mineralogy, bulk-chemical composition and oxygen isotope composition.

- Achondrites are also stony-type meteorites, originating in this case from differentiated bodies. They are characterized by the lack of chondrules, due to the melt and re-crystallization processes happening during the differentiation of their parent body. They represent approximately 6% of all recorded falls (Greenwood et al. 2020). Some examples of these type of meteorites include Lunar and Martian meteorites, as well as HED (Howardites, Eucrites and Diogenites, a specific type of achondrites originating from the V-type asteroid (4) Vesta - one of the rare exemption of meteorites with a clear, well-established link to a parent body).

- Pallasites are stony-iron meteorites, originating from the core-mantle boundary of differentiated asteroids (approximately 1% of all recorded falls - see Greenwood et al. 2020).

- Metallic (iron) meteorites are almost entirely made out of iron-nickel alloy. They originate from the metallic core of differentiated planetesimals (approximately 4% of all recorded falls - see Greenwood et al. 2020).

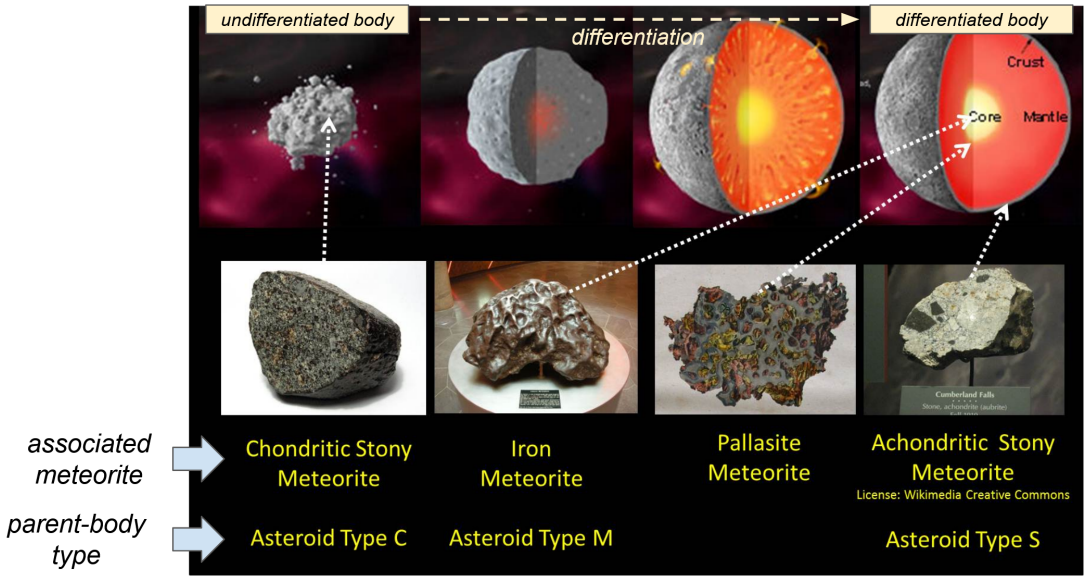

Figure 1.6: Meteorite classification by Examples of the four different families of meteorites, chondrites, achondrites, pallasites and metallic, and their associated parent body. Credit to Smithsonian Museum of Natural History (adaptation of original figure).

The study of primitive asteroids is associated with the carbonaceous chondrites sub-family. As the name entices, they are relatively rich in carbon (3 wt.%), which can be found in the form of graphite, carbonates or organic compounds. There are many groups of carbonaceous chondrites, divided according to their mineralogy and isotopic composition (Weisberg et al. 2006). All carbonaceous chondrites groups are named C plus the letter of a characteristic meteorite from that group (CI stands for "Ivuna"-type, CM for "Mighei'-type, etc. The CH-type, standing for "high iron content" is a notable exception. See figure 1.7 for full classification of carbonaceous-chondrites).

Type	Characteristic member	Place / Date of observed fall
CI	Ivuna	Tanzania / 1938
CM	Mighei	Ukraine / 1889
CV	Vigarano	Italy / 1910
CO	Ornans	France / 1868
CR	Renazzo	Italy / 1824
CK	Karoonda	Australia / 1930
CH	ALH85085	Antarctica (collected in 1985)

Figure 1.7: Carbonaceous chondrites classification.

Even though meteorites are "genetically" the closest material to outer-space bodies, the explicit link between meteorite families and their parent body is still one the most fundamental research topic of the scientific community. The spectral signatures of meteorites never seem to quite match that of potential parental asteroid families (McSween et al. 1991, Greenwood et al. 2020), with the notable exception of Martian meteorites being linked to the Red Planet and HED (Howardites, Eucrites, Diogenites) meteorites being related to the giant V-type asteroid Vesta (Consolmagno and Drake 1977). This spectral discrepancy highlights that some distinct composition-altering phenomena have affected either the meteorites, or their parent body (or both), creating a certain "distance" between the two. This difference, coupled with the lack of representation of all known asteroidal families among our on-Earth meteorite collection, limits what we can achieve by studying only meteoritic materials. Additionally, meteorites can be very heterogeneous. This heterogeneity can be a source of great insight, but can also hinder certain types of studies.

As an alternative, the choice can be made to work on pure terrestrial analogs. For instance, historically, research has focused on olivines and pyroxenes while investigating the properties of lunar materials (Hapke 2001 and reference therein). The perks and limitations of working with terrestrial samples will be detailed in 1.4.

1.2.3. Directly : sample-return missions

Sample-return type missions are focused on recovering materials from the surface of celestial bodies and bring then to Earth for further studying. In this instance, there is no ambiguity regarding the identity of the parent body. Having access to this information allows the scientific community to combine results from the remote-sensed data of the celestial body with the in-lab measurements of the recovered matter, acquiring unique scientific insight. Since the recovered samples are brought back via specially designed capsules, they are not affected by the harsh atmospheric entry, un-like meteorites. This pristine material can then be studied using state-of-the-art techniques in Earth laboratories.

The first sample-return mission to target a body other than our Moon was NASA's Stardust, which focused on collecting dust samples from the coma of the Wild 2 comet (Tsou et al. 2003), launched in 1999. In 2010, it's JAXA's turn, with the Hayabusa mission (formerly known as MUSES-C, Kawaguchi et al. 1999) returning to Earth with a few thousand grains from S-type asteroid Itokawa. The study of these samples, coupled with remote sensed-data from Itokawa's surface, contributed in establishing a link between S-type asteroids and LL-class meteorites, a sub-family of the ordinary chondrites group (Abe et al. 2006, Nakamura et al. 2011). Fourteen years later, the capsule from the Hayabusa2 mission (Watanabe et al. 2017) delivered 5.4g of surface materials from two distinct sites of C-type primitive asteroid Ryugu. Thousands of individual grains, varying in sizes, are currently being analyzed by laboratories all over the world, as part of a large international effort focused on characterizing this very precious material. In 2023, the OSIRIS-REx mission (NASA, Lauretta 2015) is expected to deliver large quantities of surface material from B-type primitive body Bennu. In the future, more sample return missions, targeting larger bodies such as the martian moon Phobos (MMX - JAXA) and the Red Planet itself (Mars Sample-Return Mission - NASA), are expected to enrich the stock of pristine, extraterrestrial material available on Earth.

During my PhD thesis, I was able to join the Hayabusa2 'STONE' preliminary analysis team, led by Prof. Tomoki Nakamura, as part of the team from the IAS Astro-Chemestry department. My contribution to the analysis of samples from Ryugu is discussed in section 3.2.3. To better apprehend

this part of my work, a dedicated section on the Hayabusa2 mission is presented here.

A focus on the Hayabusa2 (JAXA)

The Hayabusa2 mission (from the Japanese language, meaning "peregrine falcon") is an sample-return type mission operated by the Japanese space agency (JAXA), targeting C-type primitive asteroid (162173) Ryugu, shown in the figure below.

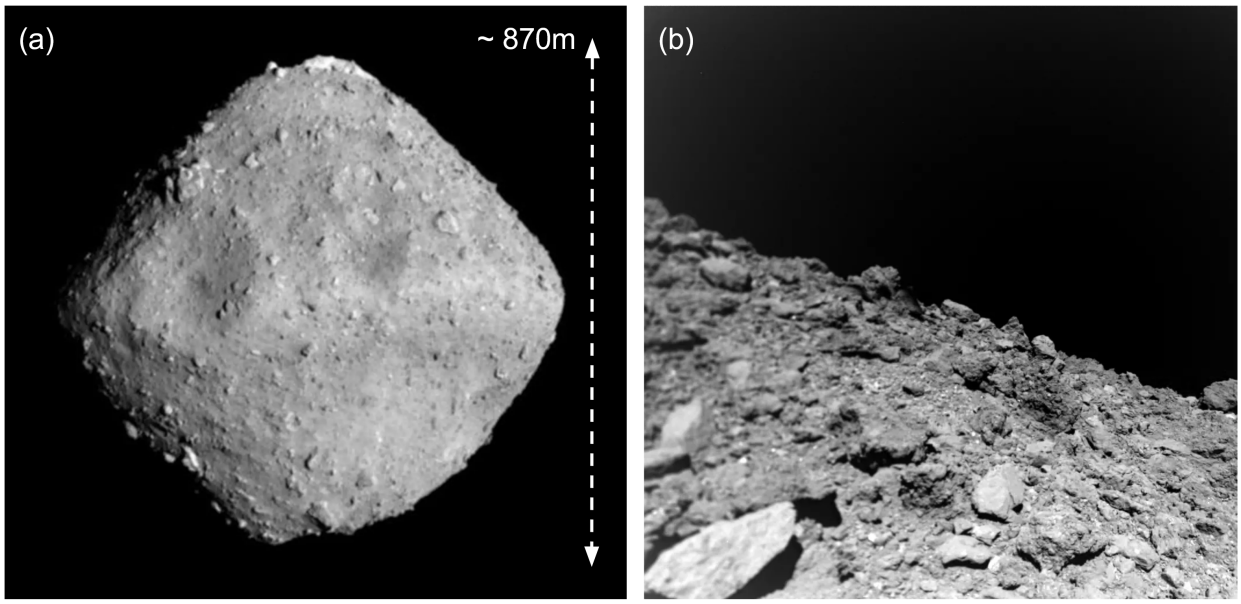

Figure 1.8: Optical Navigation Camera (ONC) images. (a) (162173) Ryugu. (b) Ryugu's surface. Credit : JAXA and Jaumann et al. 2019.

The goal of the mission was to visit a carbon-rich hydrated primitive body, such as C-type Ryugu, and return samples from the asteroid's surface. The science goals, summarized in Watanabe et al. 2017 were to:

1. Characterize material mixing and transport during the early history of our solar system around the frost/snow line, by characterizing the distribution of different materials (hydrated silicates, organic matter, etc.) on the surface of Ryugu.

2. Investigate mineral-water-organic reactions on planetesimals, by characterizing the distribution of organics and hydrated phases in remote-sensed data mapping the asteroid's surface

and in the returned samples.

3. Understand materials evolution in the early solar system by studying the history of Ryugu while looking for traces of alteration processes such as aqueous/thermal alteration and/or space-weathering (these alteration processes are defined 1.3.2).

4. Assess the dynamical processes to which planetesimals were subjected to during the early stages of our solar system, by reconstructing the collisional and impact-related history of Ryugu.

All these scientific goals are expected to shed light on fundamental questions such as the history of water and organics in the early solar-system, particularly in relation to our own planet. Furthermore, this investigation is expected to provide more insight on the relation between primitive C-type asteroids and carbonaceous chondrites.

The Hayabusa2 spacecraft departed Earth on 3 December 2014, with an important scientific payload (see Figure 1.9) including :

- remote sensing instruments : Optical Navigation Camera (ONC-T, ONC-W1, ONC-W2), Near-Infrared Camera (NIRS3), Thermal-Infared Camera (TIR), Light Detection And Ranging (LIDAR, a laser altimeter).

- surface sampling : Sampling device (SMP), Small Carry-on Impactor (SCI), Deployable Camera (DCAM3).

- deployable rovers : Mobile Ateroid Surface Scoult (MASCOT), MIcro-Nano Experimental Robot Vehicle for Asteroid (MINERVA-II).

In order to efficiently tackle the scientific goals described above, this large payload is essential in order to be able to combine observations at various scales (from in-situ remote-sensed global observations data, to local measurements done by rovers and eventually to microscopic measurements conducted on the returned material) and derive a comprehensive characterization of the investigated body.

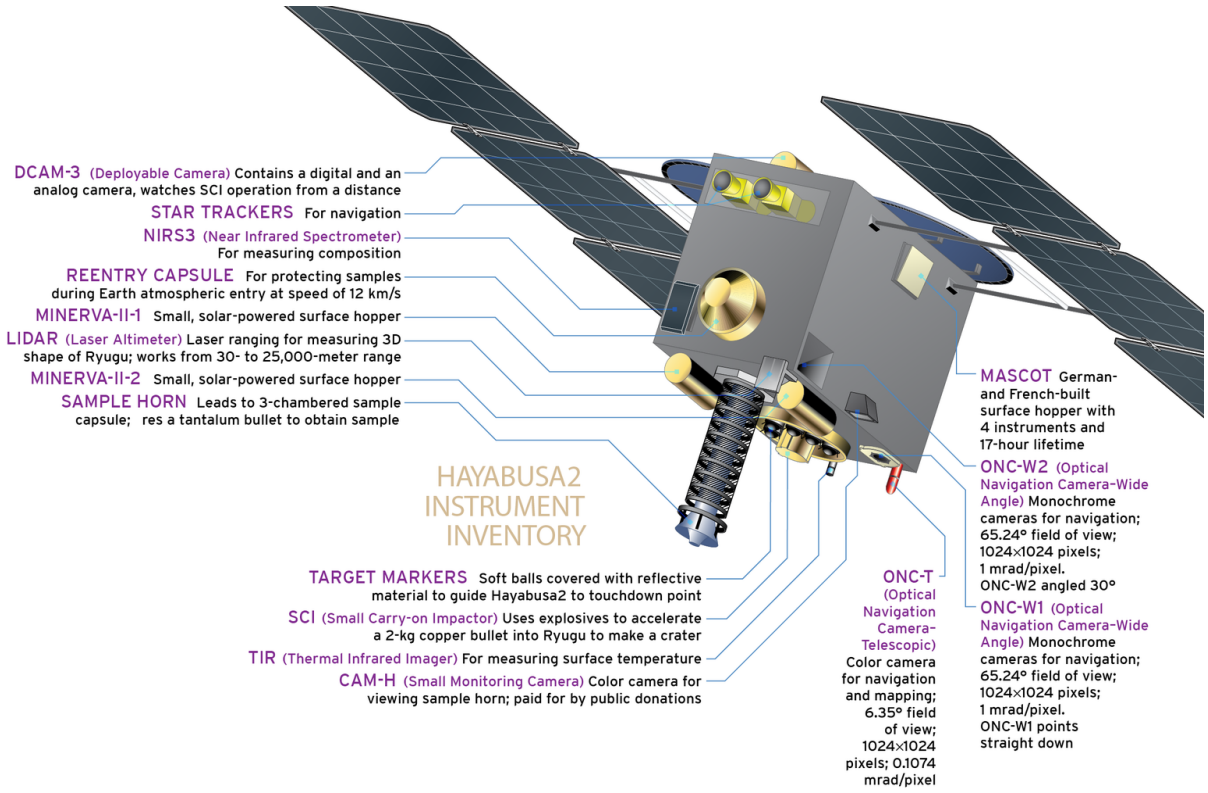

Figure 1.9: Hayabusa2 instrument inventory. Credit: Emily Lakdawalla, Charles H. Braden, and Loren A. Roberts for The Planetary Society.

Hayabusa2 arrived at rendez-vous point with asteroid Ryugu on 27 June 2018, where it began studying the body, leading spectroscopic surveys, lander observations and two instances of sample collection on two different sites on the asteroid's surface. One of the two sample collection sites was a region in proximity of an artificial crater, created by the Small Carry-on Impactor (SCI) experiment, in order to probe Ryugu's sub-surface (Arakawa et al. 2020). The spacecraft departed the asteroid on 13 November 2019, and approximately 5.4g of material from Ryugu arrived on Earth a year later, on 6 December 2020.

As of today, results from remote-sensing data and on-asteroid measurements have already been announced. Watanabe et al. 2019 were able to determine the shape, mass and geo-morphology of Ryugu and derive its - relatively low - density ($1.19 \pm 0.02 g/cm^3$), indicating the presence of highly porosity materials ($> 50\%$) on Ryugu. Kitazato et al. 2021 reported findings regarding the

surface reflectance spectra acquired with the Near-Infrared Spectrometer (NIRS3) instrument, which indicated the widespread presence of hydroxyl (OH)-bearing minerals all over the asteroid's surface, associated to the absorption feature detected at 2.7 µm - the OH band - which was observed over the entire asteroidal surface. Ryugu's OH-band intensity and low overall albedo appeared compatible with carbonaceous chondrites. The OH-band's positions was reported to be fairly homogeneous across the whole surface, with the exception of the region close to the SCI artificial crater, where the feature appeared slightly blue-shifted, possibly indicating the detection of less-altered materials, emerging from the sub-surface upon impact. Sugita et al. 2019 investigated the scenarios for Ryugu's formation and evolution, to provide context for the analysis of returned samples, highlighting that the remote-sensed data suggested episodes of partial dehydration of Ryugu's parent body due to internal heating. This indicates that Ryugu must have formed sufficiently early to contain high concentration of radioactive species responsible for heating (such as ^{26}Al), or formed near the Sun. Okada et al. 2020 investigated the particularly high porosity of Ryugu, indicating that both surface regolith and larger boulders appeared significantly porous, more so than carbonaceous chondrites, the closest material available on Earth to primitive bodies.

The analysis of returned samples from the preliminary analysis teams ended between May and June 2022. The scientific results from these laboratories studies and JAXA's sample-curation team are now starting to be published. Yada et al. 2022 and Pilorget et al. 2022 showcased the results of preliminary analysis on a large part of the recovered sample collection, confirming the low porosity detected from remote-sensed data as well as the presence of carbon-rich and hydrated minerals via the presence of weak absorption bands in the infrared range at 2.7 and 3.4 µm. The presence of carbonates and NH-rich compounds was also detected. No CAIs or chondrules were found in the recovered material, making Ryugu similar to CI chondrites, but with lower albedo and a higher porosity. The link with CI-type meteorites is further investigated by Yokoyama et al. 2022 by assessing the mineralogy, bulk chemical and isotopic composition of Ryugu samples, indicating that Ruygu's samples may be comparable to a "pristine", un-altered by Earth, CI-type meteorite.

1.3. Scientific framework and presentation of this work

1.3.1. Precious (but flawed) time capsules

As established previously, primitive bodies are akin to time capsules. Since they did not undergo differentiation processes, their composition is directly linked to that of the protoplanetary disc present at the formation of our Solar System. The study of their content can provide important insight regarding this distant era. Understanding their composition is key to gaining access the history of their contribution to the current state of our solar system. Their hydrated and carbon-rich nature spurs particular interest regarding scientific questions such as the distribution of water in our Solar System and eventually the emergence of life on our planet.

However, due to their long history, these bodies' surfaces have been affected by a number of altering processes, which may have modified their composition. Understanding the extent of these modifications is paramount in "de-biasing" studies focused on the composition of these bodies. These weathering effects are nonetheless difficult to identify. Remote-sensing surveys are often focused on the surface, which is subjected to these altering phenomena. This means that discerning original compositional variations from alteration processes is a significant endeavour. Furthermore, no additional insight can be gained by working directly with meteorites, since their passage through the Earth's atmosphere irreversibly alters their surface. This effectively overwrites all traces of surface alteration processes occurring on their parent body.

1.3.2. Alterations processes and Space-Weathering

Multiple processes may contribute in altering the surface composition of primitive bodies during their time in the Solar System. For instance, collisional impacts, thermal or aqueous alteration, and space-weathering may all alter these bodies' surface in various manners. This particular work focuses on the space-weathering contribution.

1.3.2.1 Collisional impacts

The history of our Solar System has been a very violent one. Collisions among planetesimals have been happening since before planetary formation and all throughout the young solar system era,

aided by at least two episodes of planetary migration (Bottke et al. 2002). Major destructive impacts among large bodies are at the origin of asteroidal families, which are observable today. Shocks from such catastrophic impacts may change the mineralogy of primitive bodies, though not as radically as differentiation processes.

1.3.2.2 Heating and Thermal/Aqueous alteration

Multiple sources of heating have been explored by the scientific community, and may have lead to different mineralogical and chemical changes of primordial bodies. Internal heating, due to radioactive decay of short lived elements such as ^{26}Al (McSween et al. 2002), probably enabled liquid water to flow on such primordial bodies. At low temperatures (<320 K), this flow of water produced hydrated minerals such as phyllosilicates, sulfates, oxides, carbonates and hydroxides (Fornasier et al. 2014). Local heating due to collisional events may have also led to total or partial localized melts at a microscopic level (Keil 2000).

At higher temperatures, volatiles were removed, and aqueous alteration was replaced with thermal metamorphism. Metamorphism is a process during which the mineral assemblage and texture of material can change, in the case of thermal metamorphism, driven by temperature changes. On primordial bodies, this thermal metamorphism resulted in the formation of new minerals via the melt and re-crystallization of previously distinct minerals, as well as changes in the material texture, such as the loss of the recognizable chondrules (Keil 2000).

Meteorites such as chondrites can keep a trace of aqueous and thermal alteration processes that may have happened on their parent body. This trace is indicated by their petrologic type (Van Schmus and Wood 1967), a scale from 1 to 6, indicating the degree of aqueous or thermal alteration associated to the meteorite's parent body. From type 3 to 1, aqueous alteration dominates with type 1 being the most altered. From type 3 to 6, thermal metamorphism dominates, with type 6 being the most altered state (see Figure 1.10).

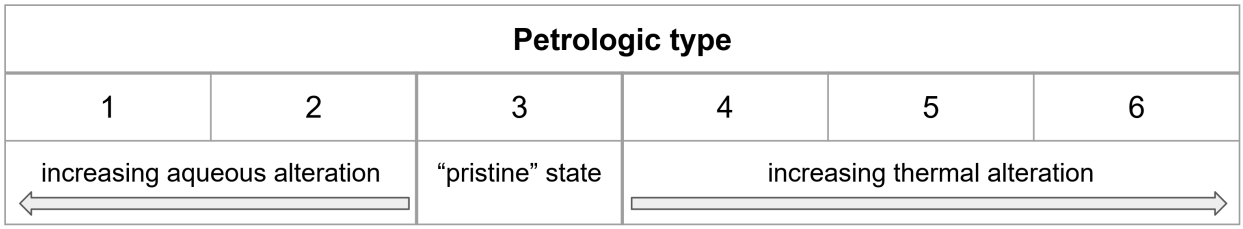

Figure 1.10: Petrologic types for chondrites.

1.3.2.3 Space-Weathering : a review of the current literature

Atmosphere-less bodies in our Solar System are known to be affected by Space Weathering (SpWe for short, see Figure 1.11). This phenomenon includes multiple processes, such as micrometeorite bombardment, high-energy particle bombardment (cosmic rays and and high energy solar ions) and low-energy particle bombardment (mainly from solar wind).

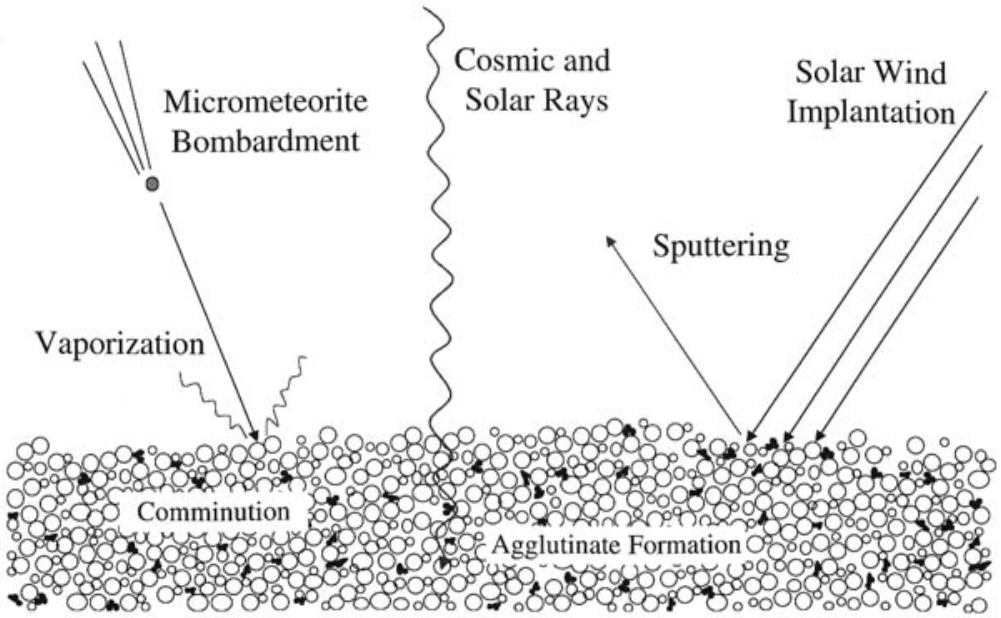

Figure 1.11: The different components of space weathering. Credit: Wikipedia Commons.

Fundamental reviews of SpWe on asteroids can be found in Brunetto et al. 2015 and Clark et al. 2002. The fundamentals of our understanding of Space Weathering comes from studying the Moon. It was first Gold 1955, while working on Lunar craters and mares, who suggested that solar radiation

may alter the surface composition of the Moon. The author hypothesized that surface darkening was a consequence of weathering. His prediction was confirmed when spectroscopic studies found the Apollo samples of Lunar regolith to be darker and redder in slope than pulverized Lunar rocks (the Lunar powder produced in laboratories would be a mix of pristine and weathered materials, but spectrally dominated by the pristine population). Early experiments on Lunar rocks erroneously linked the observed spectral effects to impact vitrification. However, by the end of the century, Keller and his associates (Keller and McKay 1993, Keller and McKay 1997, Keller et al. 1998), using transmission electron microscopy, showed that the effects were linked to a vapor-deposited coating present on regolith particles from mature soils. This coating was dotted with $npFe^0$ (or nanophase reduced Fe) varying in sizes. Both solar ion implantation sputtering and micro-meteorite bombardment can contribute to the creation of this thin layer. On Lunar soils, this tends to reduce the albedo (darkening), and induce reddening (Pieters et al. 2000, Hapke 2001). This surface rim also showed evidence of amophization, vesiculation and cation depletion (Keller and McKay 1997).

Understanding Lunar space-weathering would pave the way to the study of SpWe on asteroidal bodies. However, this first proved difficult, since the spectral trends associated with SpWe would be difficult to identify in remote sensed spectral data of asteroidal surfaces (lack of high albedo or strong spectral features). Sometimes, the identified spectral trend would differ from lunar-like SpWe and prove difficult to interpret (Clark et al. 2002, Pieters and Noble 2016). The study of Lunar SpWe relied greatly on experiments done on Lunar samples. The lack of asteroidal surface material to study in a laboratory environment would also hinder the understanding of asteroidal SpWe. However, in the last decade, the development of sample-return type missions has greatly contributed to a better understanding of this phenomenon. In particular, results from the Hayabusa mission (JAXA) first showed evidence of differently weathered regions on S-type asteroid (25143) Itokawa (Hiroi 2006). In this case, the more weathered regions appeared to be darker, redder and more $npFe^0$-rich. Electron-microscopy investigations conducted on the returned samples also highlighted the presence of a multilayered structure close to the surface of the grains, including amorphized silicates, $npFe^0$ and iron sulfide rich areas (Noguchi et al. 2011, Noguchi et al. 2014). The spectroscopic and microscopic studies of the Hayabusa mission (JAXA) also showed that solar

wind should be the main source of surface weathering in the inner Solar System, indicating that for short timescales (10E4-10E6 yr), solar wind is the main source of rapid weathering (Noguchi et al. 2011). Current generation sample-return mission are also contributing in providing great insight on SpWe processes on asteroids, specifically hydrated carbon-rich bodies such as B- and C-type asteroids Bennu and Ryugu. The Hayabusa2 mission (JAXA), targeting (162173) Ryugu, showed evidence of spectroscopic discrepancies between material near the center of the SCI artificial crater experiment (Arakawa et al. 2020) and its surrounding area. Kitazato et al. 2021 highlighted a decrease in intensity as well as a shift of the 2.7 µm hydration feature when comparing the material outside the crater to the fresher material excavated near the center of the artificial crater. One of the effects suggested to explain this phenomenon is SpWe. The study of the returned Ryugu grains by the preliminary analysis groups is ending, and we can expect upcoming works to show and describe SpWe models on primitive bodies. Complementary evidence may come with the investigations lead by the OSRIRIS-REx collaboration on returned Bennu grains from 2023.

As discussed previously, since asteroidal samples are quite rare, the scientific community has primarily carried out laboratory studies focusing on simulating SpWe on meteorites or asteroid surface analogs. As a complete in-lab simulation of SpWe is not feasible, it has spurred various branches of SpWe simulating experiments, each focusing on what are considered to be the driving processes of SpWe. Historically, solar wind and particle bombardment effects have been simulated using ion-accelerators (Demyk et al. 2001, Carrez et al. 2002, Loeffler et al. 2009), while micrometeorite impacts has been simulated by using nano-second pulsed laser (Moroz et al. 1996, Sasaki et al. 2002, Loeffler et al. 2008), and more recently by a more ballistic approach using dust accelerators (Cintala and Hörz 2008, Fiege et al. 2019). The target material for these laboratory experiments can change according to the scientific goal of the study. Its composition may vary with regards to the astronomical body which it is supposed to emulate. For some bodies, meteorites are the closest material we have available on Earth. A few examples may include HEDs for Vesta or carbonaceous-chondrites for hydrated carbon-rich bodies such as Bennu and Ryugu. Other studies, such as the one presented here, may focus on single component terrestrial rocks. For a long time, the main targets of these experiments have been anhydrous materials, such as olivine, pyroxene and ordinary

chondrites, since the scientific community has been focused on understanding Lunar SpWe and weathering on S-type asteroids. The interest for the S-type asteroid family came from their possible link with ordinary chondrites (Nakamura et al. 2011, Vernazza et al. 2014 DeMeo et al. 2022), the most abundant population of meteorites available on Earth. With two large sample-return missions, Hayabusa2 (JAXA) and OSISIS-REx (NASA) focused on carbon-rich hydrated bodies (Ryugu and Bennu respectively), there has been a gradual shift in target composition as well, as laboratory simulation focusing on carbonaceous chondrites and relevant minerals have started gaining momentum. Essential reviews of results from SpWe experiments on carbonaceous chondrites are shared in recent publications such as Laczniak et al. 2021 and Trang et al. 2021.

Multiple spectral trends related to different weathering mechanisms on carbonaceous chondrites have already been identified:

- *Changes in albedo and spectral slope.* Both pulsed-laser and ion bombardment experiments have caused darkening and brightening of the samples, coupled with spectral reddening and blueing. For some samples, these changes are exposure dependent (initial darkening switching to brightening at higher dosage, or reddening switching to blueing, and vice-versa), as well as wavelength dependency for reddening/blueing (Lantz et al. 2017, Thompson et al. 2019, Matsuoka et al. 2020). Ion bombardment experiments have shown coupling among these trends, such as darkening-reddening for some samples and brightening-blueing for others (Vernazza et al. 2013, Keller et al. 2015a, Lantz et al. 2017).

- *Changes in spectral feature intensity and position.* A general decrease in band intensity can be seen for both laser and ion-bombarded samples. Ion bombardment experiments also show a significant red-shift of the spectral features associated with (M)-OH stretching vibration at 2.7 µm and the Si-O stretching vibration at 10 µm in ion-bombarded hydrated silicates (Brunetto et al. 2014, Lantz et al. 2015, Vernazza et al. 2013, Lantz et al. 2017).

Further analysis investigating changes at smaller scales have also detected:

- *Surface texture changes.* Following pulsed-laser bombardment, surface melt and vapor deposits

have been identified (Thompson et al. 2019, Laczniak et al. 2021).

- *Volume morphology changes.* Vesiculation of the layers close to the surface has been seen in both laser-pulsed samples and ion-bombarded samples, as well as the general amorphization of the silicate matter (Thompson et al. 2019, Laczniak et al. 2021).

- *Compositional changes.* The formation of various Fe-based nanoparticles such as metallic Fe, Fe- and Fe-Ni-sulfides, Fe-oxides has been seen predominantly in laser bombarded samples (Thompson et al. 2020, Hallatt et al. 2022). Elemental changes such as the reduction of Fe^{3+} to Fe^{2+}, as well as the loss of O, possibly due de-hydroxylation, has also been detected in ion bombarded samples (Keller et al. 2015b, Keller et al. 2015c). The appearance of an Si-enriched/Mg-Fe-depleted thin layer close to the surface of the ion-bombarded samples has also been seen (Laczniak et al. 2021).

1.3.3. Context and outline for this work

As discussed before, having access to the composition of these primitive bodies is paramount in understanding the early history of our Solar System, and how it came to be what we are able to observe today. However, multiple effects can alter the surface composition of these bodies, which can hinder compositional studies. The work presented here is focused on understanding the effects of the solar-wind component of SpWe on primitive bodies. More specifically, the effects of in-lab replicas of solar wind ion-implantation on hydrated silicates will be studied by infrared spectroscopy and electron microscopy. While there are a certain number of studies coupling these two techniques for the study of the micro-meteorite contribution of SpWe, there are only a few focusing on ion-implantation. Moreover, most studies tackling alteration processes on primitive bodies have utilized carbonaceous chondrites as primitive bodies' surface analogs. This allows to experiment on matter from space, "genetically" close to that which is supposed to emulate. However, meteorites are often fairly heterogeneous, both in regards to composition and morphological texture: this heterogeneity can complicate the identification of weathering effects, effectively drowning them in local compositional or texture variations. Working on pure phase terrestrial hydrated silicates means working with more homogeneous materials, in which spectroscopic and morphological/elemental

changes can be more easily identified. The end-goal of this work is to investigate spectral and morphological/elemental changes upon solar-wind weathering conditions, in order to establish a significant link between these effects across the experimental techniques.

In order to fulfill this objective, we will be presenting in Chapter 2 the materials chosen as surface analogs of our "in-lab" carbon-rich hydrated body, our weathering experiment and the experimental techniques and instruments used in this investigation. In order to emulate the surface of a primitive body, three terrestrial hydrated silicates (two serpentines and one saponite) were chosen as surface analogs. Pellets made from these materials were then bombarded using 40 keV Helium and Argon cations, to emulate two different ion implantation regimes of the SpWe solar wind contribution.

Chapter 3 will be dedicated to pointing out the spectral trends identified upon weathering, from the Visible range to the Far-Infrared. We will also be discussing the significance of these results with respect to spectroscopic surveys and remote-sense acquisitions. Some complementary works in which I contributed during the PhD thesis, such as laboratory studies regarding the study of space-weathering on V-type asteroid Vesta, or my implication in the 'STONE' Hayabusa2 preliminary analysis team will also be presented.

Chapter 4 will focus on the morphological and compositional changes of the ion-bombarded layer, investigated both via scanning and transmission electron microscopy on thin sections extracted from the surface of our weathered pellets.

Finally, Chapter 5 will conclude the dissertation by summarizing the weathering-induced changes identified across the various techniques. We will explore their potential links and delve into the implications of this work for past, current and future studies focusing on primitive airless bodies.

CHAPTER 2

Materials and Methods

Contents

2.1. A laboratory replica of hydrated silicates in carbon-rich asteroids

2.1.1. Terrestrial analogs

Three phyllosilicate minerals were chosen to replicate the hydrated minerals at the surface of a carbon-rich, hydrated body: two serpentines and a saponite. For the rest of this work, they shall be referred as Serpentine Rawhide (from the Rawhide mines, in California, where it was excavated), Serpentine UB-N (a reference material from the "Service d'Analyse des Roches et des Mineraux" (SARM) institute, axtracted from Col-des-Bagenelles in France) and Saponite (extracted from caves in Griffith Park, in California). The Serpentine Rawhide and Saponite samples were purchased as rocks and were then reduced to powder following the sample preparation protocol described in 2.2. The Serpentine UB-N sample was bought in powder form. Since these are terrestrial rocks, they are bound to present some degree of terrestrial organic contamination. This does not affect the findings described here, since the primary objective of this work is focused on their mineral composition and their evolution. Additionally, the samples can't be expected to be perfectly mineralogically pure, but rather a mixture of minerals with a dominating phase and a few scarce contaminants.

To avoid misinterpretation and biases in our study, it is necessary to fully characterize the composition of our samples. That is why, prior to the space-weathering replica experiment, the samples were measured by energy dispersive X-ray spectroscopy (EDS) using a scanning electron microscope (SEM). This allowed us to learn in detail their chemical composition. The powders were also measured using X-ray Powder Diffraction (XRD), to identify the main phases present. Both measurements were performed at the Unité Matériaux et Transformation (UMET) lab in Lille. The main results from both these measurements are detailed in the following tables, each dedicated to one of our samples.

Formula Origin	$Mg_{2.8}Fe_{0.2}Al_{0.04}Si_{1.9}O_5(OH)_4$ Rawhide Mines (California)
SiO_2	45.81±0.32
Al_2O_3	0.89±0.10
MgO	45.78±0.19
$FeO - Fe_2O_3$	6.66±0.25
Cr_2O_3	0.86±0.15
Fe/(Fe+Mg)	0.07
Main mineral phase	chrysotile

Table 2.1: Serpentine Rawhide characteristics. Elemental composition is given in wt.%, obtained by SEM-EDS measurements

Formula Origin	$Ca_{0.05}Mg_{2.6}Fe_{0.4}Al_{0.1}Si_{1.8}O_5(OH)_4$ Col des Bagenelles (France)
SiO_2	45.46±0.33
Al_2O_3	3.32±0.17
MgO	40.59±0.4
FeO - Fe_2O_3	9.26±0.25
CaO	1.36±0.10
Fe/(Fe+Mg)	0.13
Main mineral phase	lizardite

Table 2.2: Serpentine UB-N characteristics. Elemental composition is given in wt.%, obtained by SEM-EDS measurements

Formula Origin	$Na_{0.5}Ca_{0.5}Mg_{1.0}Fe_{0.7}Al_{1.1}Si_{3.3}O_{10}(OH)_2$ Griffith Park (California)
SiO_2	48.98±0.31
Al_2O_3	14.77±0.17
MgO	9.90±0.15
$FeO - Fe_2O_3$	13.84±0.24
CaO	7.08±0.13
TiO_2	0.84±0.09
MnO	0.37±0.12
Na_2O	3.95±0.10
K_2O	0.25±0.04
Fe/(Fe+Mg)	0.46
Main mineral phase	griffithite

Table 2.3: Saponite characteristics. Elemental composition is given in wt.%, obtained by SEM-EDS measurements

The main identified phases, chrysotile, lizardite and griffithite greatly differ among themselves regarding their lattice structure. We shall explicit these differences.

All phyllosilicates at an atomic level are layered structures: these layers follow different arrangements of tetrahedral and octahedral units, T and O units respectively. Tetrahedral sheets are made of of SiO_4 and/or AlO_4 units. Octahedral layers harbour different cations such as Al, Mg, Fe, Ti, Li, etc.

One fundamental difference between serpentines and saponites is that serpentines are made out of TO layers, which are bound among each-other via hydrogen binding between the hydroxyl groups linked to the O unit and the oxygen atoms of the T units. Saponites, on the other hand, are made out of TOT layers, separated by an empty interlayer space, which can harbour water molecules and metallic cations.

Another fundamental difference resides in the difference between chrysotile and lizardite. The lizardite crystal lattice is made out of 'flat' TO sheets, spreading in 2 dimensions. On the other hand, chrysotile is made out of circular fibers, each made out of TO units.

The following figure recaps the different lattice structures associated to the main phase of each of our samples.

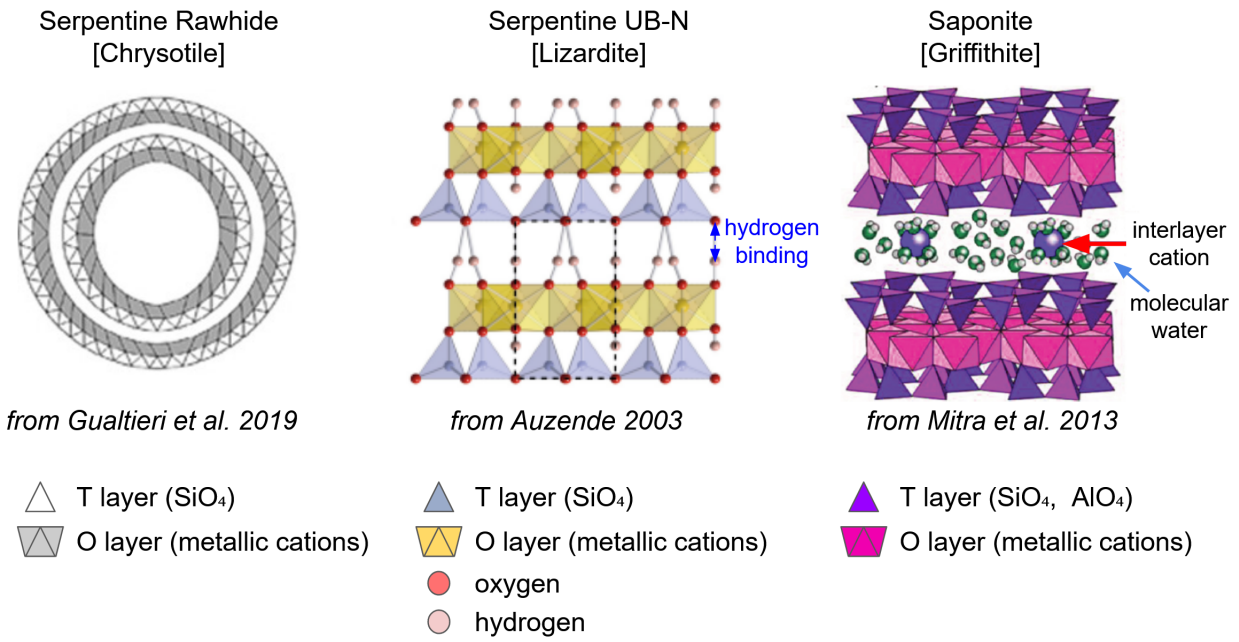

Figure 2.1: Crystal lattice of chrysotile, lizardite and griffithite, the main mineral phases of serpentine Rawhide, serpentine UB-N and our saponite sample respectively. Note that the name "griffithite" is only related to the geographical origin of this particular saponite sample, and the griffithite lattice shown here is actually common among members of the saponite family. For chrysotile and griffithite, the hydroxyl groups bound to the octahedral are shown. Images are taken from Gualtieri et al. 2019, Auzende 2003 and Mitra et al. 2013.

2.1.2. Sample preparation : from rock fragments to pellets and FIB sections

The sample preparation method used in this work is similar to that of previous ion bombardment studies which were focused on carbonaceous chondrites (see also Brunetto et al. 2014, Lantz et al. 2015, Lantz et al. 2017).

The rocky samples were crushed using an agate mortar and pestle. Although grain size was not constrained during the crushing process, the size range of each powdered sample was estimated using a scanning electron microscope (SEM, at UMET in Lille-France). The grain size was found to be in the range 1 - 100 µm for all samples. For each mineral sample, three pellets of 20 mm in diameter were prepared by pressing 240 mg of powdered sample onto a PEG substrate (powdered polyethylene glycol, average molecular mass of 8000 g/mol, from Fisher Scientific)) for a duration of 5 minutes, under a weight of 7 tons. For our samples, this corresponds to applying a pressure of

approximately 1750 bar. The following figures shows examples of the rock fragments used in order to produce the phyllosilicate powder, as well as a few examples of phyllosilicate pellets produced.

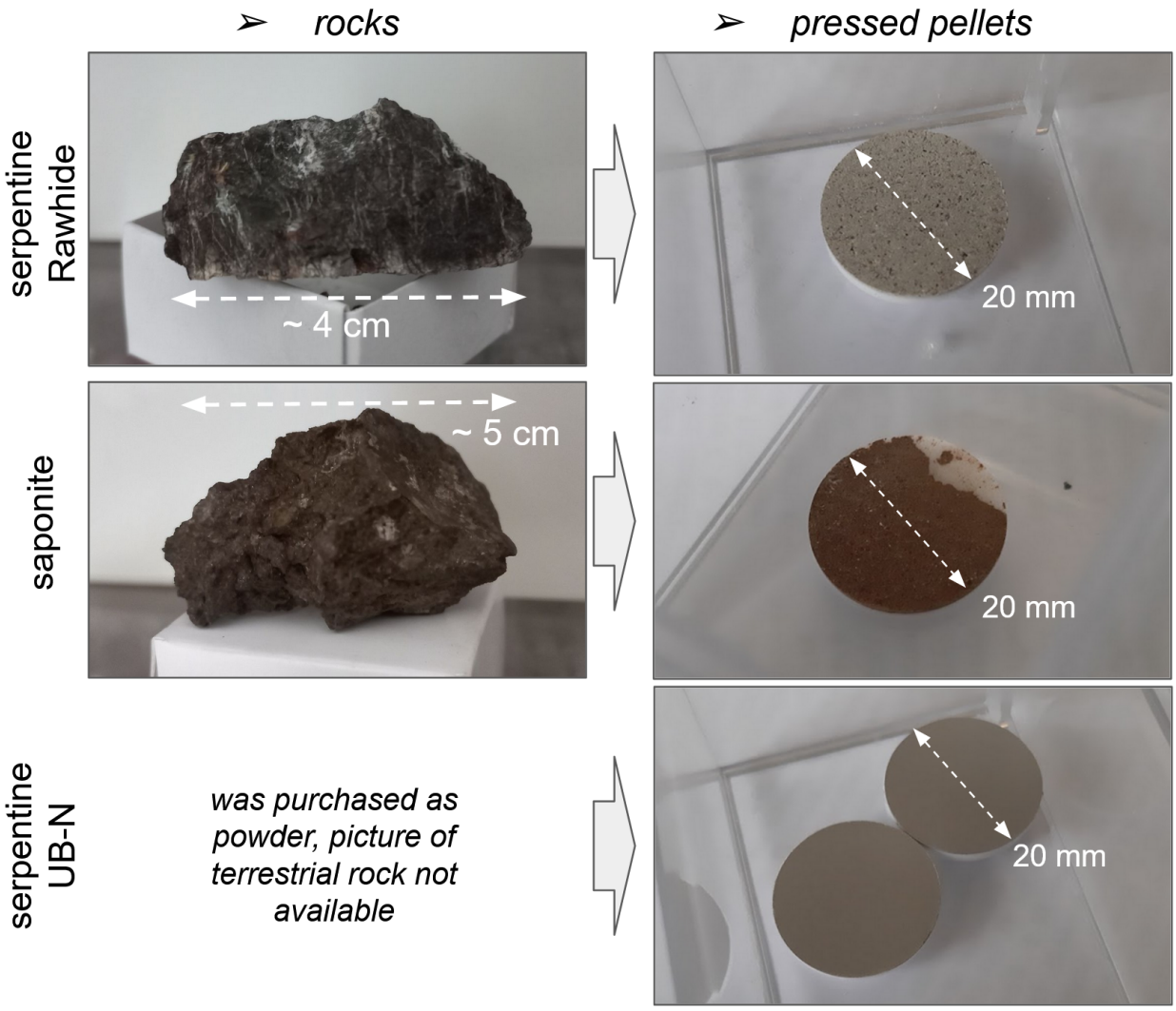

Figure 2.2: Rocky fragments of serpentine Rawhide and saponite, as well as a few examples of pressed-powder pellets produced from the phyllosilicate powder. The saponite pellet presented here is only shown for illustrative purpose and was not used in the experiment, since the phyllosilicate powder did not distribute evenly during the creation of the pellet, resulting in the surfacing of the PEG substrate on one side of the pellet.

The obtained pellets show a phyllosilicate layer which is fairly thick (>500 µm). This is preferable, since we want to avoid any ion (probing hundreds of nanometers - see SRIM results in section 2.3.3 for ion penetration depth) or photon (typically probing a few microns in materials as dense

as serpentines ; see Brunetto et al. 2020) from interacting with the PEG substrate. Six out of the nine pellets underwent ion bombardment. Three pellets were bombarded using He cations and three using Ar cations. The remaining three pellets were preserved as control samples, and were used to acquire data regarding the 'pristine' state of our samples.

Once the pellets were ion-bombarded, their surface underwent an extensive spectral characterization procedure (see Chapter 3), including under-vacuum Visible and Near-IR spectroscopy as well as a complete infrared characterization (from Near-IR to Far-IR) in ambient condition. A set of pellets was also measured using the SHADOWS spectro-gonio radiometer, to evaluate the bidirectional reflectance distribution function changing upon ion-bombardment.

Immediately after finishing the spectroscopic part of our analytical pipeline, our samples' surfaces were coated with a thin film of Carbon (30 minutes of deposition, 30°-50° rockening, 300 Å), to prepare for electron microscopy (see Chapter 4). This coating step is essential in order to evacuate the charges that can arise from the interaction of the electron flux with the sample, in order to achieve high quality and sharp images of the analysed surfaces. Topography changes upon ion-bombardment were investigated using scanning electron microscopy (SEM) imaging. The following figure shows two analyzed surfaces mounted on the SEM sample holder.

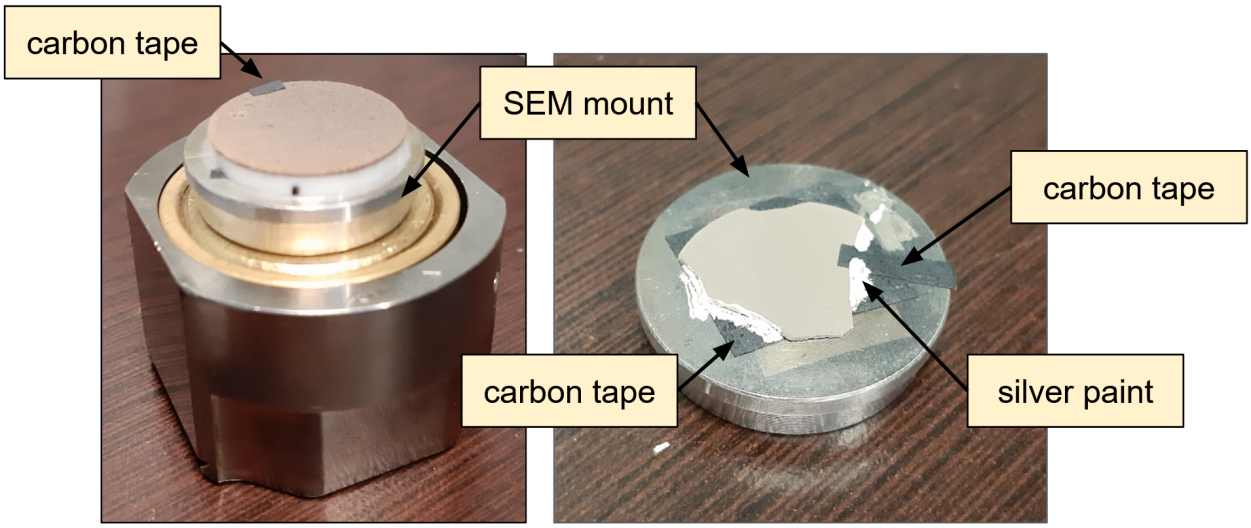

Figure 2.3: Saponite (left) and serpentine UB-N pellets, prepared for scanning electron microscopy analysis. The phyllosilicate layer of the serpentine UB-N pellet lost cohesion with the PEG during transportation, but fragments of its surface were still able to be measured. Carbon tape and silver paint were used, after carbon-coating the sample, in order to help evacuate charges during SEM analysis.

Following the SEM analysis, we proceeded with the extraction of six ultra-thin section (typically 100 nm thick) preparations by focused ion beam (FIB) technique, also called "FIB-sections". These sections were extracted from regions in the center of our weathered pellets. Due to the fibrous/layered nature of phyllosilicate, the extraction of these FIB-sections proved quite delicate, and required a second coating - this time using platinum - to solidify the surface of the samples and better protect the integrity of the FIB sections during extraction. These FIB-sections were extracted using a FEI Stata Dual-Beam 235 at the IEMN laboratory (Institut d'Electronique, Microelectronique et Nanotechnologies, Lille-France). A focused-ion beam is used to mill the surface of our sample in order to isolate and extract vertical sections, including surface ion-bombarded material as well as deeper, un-altered material. The following figure provides a few more details and example of an extracted FIB section.

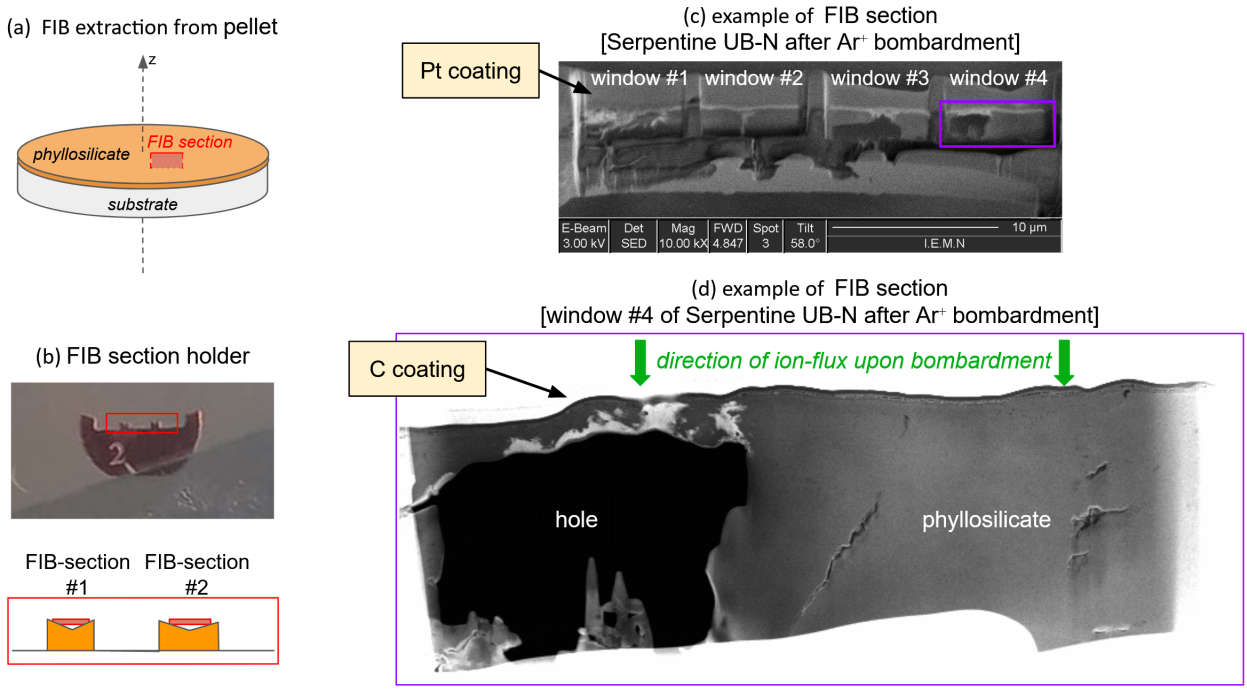

Figure 2.4: (a) Schematic of FIB-section extraction from pellet surface. (b) FIB-section holder. (c/d) Example of a FIB-section for Ar^+ bombarded serpentine UB-N.

These FIB-sections were then studied using a scanning transmission electron microscopy (see 2.4.3 for details).

2.2. Space-Weathering in a laboratory environment

We have described the materials chosen to emulate the surface of primitive hydrated asteroids used in this study. Now, we shall describe the effects of ion-bombardment in the context of solar-wind and Space Weathering. Firstly, we will explore the origin of this phenomenon, then describe the experimental setup we used to emulate it. Finally, we will end with the description of the experimental conditions used for this work and their limitations.

2.2.1. Solar-wind and ion bombardment

Solar-wind is one of the primary alteration processes on airless outer bodies in the inner Solar System. Fundamental reviews on solar wind are discussed in Gosling 2014 and references therein. Solar wind originates from the solar corona, the Sun's hot outer region. It consists of a moving

plasma, a flux of ions, accelerated by the high temperatures of the solar atmosphere. This accelerated plasma escapes the Sun's gravitational pull and permeates all interplanetary space.

Solar-wind consists primarily of electrons and protons (or H^+) with an energy of $\sim 1keV$. Alpha particles (He^{2+}) represent the second most abundant contribution to solar wind plasma. However, solar-wind also contains traces of heavier ions, following solar photospheric abundances (see Table below).

Element	Abundance Relative to Oxygen
H	1900 ± 400
He	75 ± 20
C	0.67 ± 0.10
N	0.15 ± 0.06
O	1.00
Ne	0.17 ± 0.02
Mg	0.15 ± 0.02
Si	0.19 ± 0.04
Ar	0.0040 ± 0.0010
Fe	$0.19 + 0.10 - 0.07$

Table 2.4: Average elemental abundances in the Solar Wind. Adapted from Gosling 2014.

The energy distribution of most ions in solar-wind follows the 1 keV/nucleon law (1 keV for $H+$, 4 keV for He^+, 36 keV for Ar^+, etc.). In accordance to the elemental abundances, most of solar wind is made out of low-energy particles (from 1 to 4 keV particles). However, there are some effects which can contribute to increase the energy of some ion populations in the solar wind, such as particle shock processes. Solar Energetic Particles (SEP), originating from solar active regions and solar flares can reach energies up to a few MeV. There are more high energy ion populations traveling in the interplanetary space which are not directly linked to a standard solar activity, such as cosmic rays, which can reach energies up to 10E8 keV.

Solar-wind ion populations contribute differently during ion implantation processes on airless bodies, depending on the ions impact parameters and mass (see discussion in Brunetto and Strazzulla 2005). The stopping power, which corresponds to the energy deposited per unit of path length in the implanted material, is also related to the ion energy and mass. There are two different regimes

of energy transfer: inelastic collision, related to the energy-loss of electrons, and elastic collision, related to the energy-loss of nuclei. The ratio of inelastic versus elastic energy loss can vary, with inelastic collision dominating for light ions and elastic collision dominating for heavy ions. Different ion populations can interact differently with the surface of airless bodies, according to their stopping power. Inelastic collisions tends to ionise the ion-implanted surface, while elastic collisions tend to dislodge atom from their lattice position (creating vacancies or replacements, as well as phonons). These different energy loss processes contribute to material alteration induced by Space Weathering, hence their relevance for this work.

2.2.2. The INGMAR-SIDONIE setup

The ion implantation setup used in this work is an experimental platform located at the CSNSM branch (Centre de Sciences Nucléaires et de Sciences de la Matière) of the IJCLab (Irène Joliot-Curie Laboratory) at the Paris-Saclay University. The setup allows for the in-situ measurements of ion-implanted samples under vacuum. The assembly is made out of two distinct parts, the INGMAR vacuum chamber and the SIDONIE accelerator.

The INGMAR (IrradiatioN de Glaces et Météorites Analysées par Réflectance VIs-IR) setup is the product of an IAS project led by Rosario Brunetto, in collaboration with the CSNSM. It consists of a vacuum chamber where the ion beam from SIDONIE interacts with the samples. Multiple samples can be loaded onto a racket (sample holder), allowing the ion-implantation and measurement of multiple samples without the need of breaking the vacuum seal. The lowest pressure attainable is 10E-8 mbar. A mixing chamber can also be used to inject gaseous mixtures into the main vacuum chamber. A closed-cycle He cryocooler (CTI, 14-300 K) is able to make the gaseous mix condensate on a given substrate, via a cold finger, which thus allows to ion-bombard frozen deposits. Spectroscopic survey upon ion-bombardment is possible in both transmission mode (for optically thin samples such as frozen deposits), and bidirectional reflectance mode (for optically thick samples, such as mineral pellets or rock slabs).

In transmission mode (INGMAR-T), the beam enters the chamber through a ZnSe window, hitting the sample with an angle of 10° with respect to the normal of the sample. It then goes through the

sample and is collected by a mercury-cadmium-telluride (MCT) detector.

In bidirectional reflectance mode (INGMAR-R), the sample is illuminated using two optic fibers, one for the visible light (illumination angle i = 15°) and a second for the near-infrared (i = 20°) but on a different plane. The illumination spot-sizes correspond to 20 mm and 12 mm in diameter for the visible and infrared sources respectively. A third optic fiber is used for collection, with a collection spot size of 3-4 mm in diameter and a fixed collection angle e = 15° (phase angle is 20° for visible and 15° for near-infrared, with regards to 3D-geometry). The outside end of the collecting optic fiber can be switched between a grating spectrometer in the visible and near-IR range (Maya2000Pro, Ocean Optic, 0.4-1.1 microns), and a Fourier Transform spectrometer in the near-IR and mid-IR range (Tensor 37, Bruker, 1-25 microns, depending on the chosen beamsplitter and detector) using an internal Globar source.

The INGMAR vacuum chamber is interfaced with the SIDONIE isotope separator (Chauvin et al. 2004), which provides the ion beam for ion-implantation experiments. A high-current ion source provides the ions, which are injected in a high dispersion analyzing magnet. The ion beam is then accelerated and focused on the samples inside the INGMAR chamber. The ion beam hits normal to the ion-bombarded sample.

2.2.3. Experimental conditions for this work

In my experiment, I used room temperature conditions, while the pressure in the INGMAR irradiation chamber was lowered down to $1 * 10^{-7}$ mbar. Regarding the solar-wind wind part of my experiment, due to obvious limitations in regards to time and resources, it is almost impossible to replicate in a laboratory environment all the spread in ion mass and energies included in solar-wind and affecting airless bodies. This entails that each study generally focuses on one or more individual components. In this work, we chose to use He^+ and Ar^+ with an energy of 40 keV. The choice for these ions at this energy is detailed further down below. The irradiation process was done step-by-step. This allowed us to acquire spectroscopic measurements at intermediary irradiation fluences, in order to follow the spectroscopic changes prompted by the ion-bombardment process. Spectroscopic data in the visible and infrared was acquired at fluences of 0, 1, 3 and 6 $*10^{16} ions/cm^2$ for He^+ and

0, 0.5, 1 and 2 $*10^{16} ions/cm^2$ for Ar^+. The ion flux for both ions was close to $10^{13} ions/(s.cm^2)$, which is relatively low and prevent the ion-bombarded surfaces from heat-related changes. The ion fluences were derived by direct measurement of the ion current, thanks to a brass ring placed before the entrance of the INGMAR chamber (Urso et al. 2020).

The "Stopping and range of ions in matter" (SRIM) code by Ziegler et al. 2010 was used to characterize the ion-implantation of 40 keV He^+ and Ar^+ in our samples. Unfortunately, the SRIM code is not able to take in account crystal lattice variations. Thus, we derived the relevant quantities for characterizing the ion implantation process only based on elemental composition and sample density (see Figure 2.5). The elemental composition given to SRIM is the one derived by the SEM-EDS, described in tables 2.1, 2.2 and 2.3. The density of all samples is set to $2.5 g/cm^3$ for the SRIM simulation, which is in the range of densities for serpentines and iron-rich saponites.

Sample	Ion	Energy [keV]	Stopping Power*		Penetration depth [nm]
			dE/dx (inelastic)	dE/dx (elastic)	
Serpentine Rawhide	He^+	40	$5{,}35 \times 10^{-1}$	2.29×10^{-2}	317.2
	Ar^+		$8{,}92 \times 10^{-1}$	2,765	40.6
Serpentine UB-N	He^+		$5{,}22 \times 10^{-1}$	$2{,}25 \times 10^{-2}$	322.1
	Ar^+		$8{,}66 \times 10^{-1}$	2,716	41.2
Saponite	He^+		$5{,}00 \times 10^{-1}$	$2{,}19 \times 10^{-2}$	334.1
	Ar^+		$8{,}10 \times 10^{-1}$	2,639	42.2

* Multiply by $2{,}4999 \times 10^2$ for units in keV/micron.

Figure 2.5: SRIM results for simulation of He^+ and Ar^+ implantation in our samples. The elemental composition given to SRIM is the one derived by the SEM-EDS, described in tables 2.1, 2.2 and 2.3. The density of all samples is $2.5 g/cm^3$ for the SRIM simulation.

The choice for He and Ar cations was made in order to investigate the two different energy loss regimes present in solar wind, described in 2.2.1 : inelastic (electronic) energy loss for (He^+), and elastic (nuclear) energy loss for (Ar^+). We see that, according to our SRIM simulation, there is approximately an order of magnitude between inelastic and elastic energy loss for 40 keV He^+,

with the inelastic regime dominating. On the other hand, there is also approximately an order of magnitude between elastic and inelastic energy loss for 40 keV Ar^+, but in this instance, the elastic regime is dominating.

While 40 keV is an energy close to the average energy of argon ions (36 keV) and other heavy ions present in the slow solar wind, it is ten times higher than the average energy for helium (4 keV). However, higher energy helium ions are also emitted from the Sun though active regions and solar flares (also discussed in 2.3.1), and they can also contribute to SpWe effects (Matsumoto et al. 2015).

The experimental conditions described above correspond to a certain weathering timescale. Brunetto et al. 2014 first, then Lantz et al. 2017 - who performed similar SpWe experiments on carbonaceous chondrites - derived the timescales related to these experimental conditions: the highest fluence obtained here, which is 6E16 $ions/cm^2$ for He^+, corresponds to timescales of about 10E3-10E4 years for an object in the inner solar system.

2.3. Visible and Infrared spectroscopy

2.3.1. A bit of History...

The origins of infrared spectroscopy can be traced to the beginning of the 19^{th} century, in 1800 to be precise. German-born British astronomer Wilhelm Herschel was testing different filters to direct sunlight through when he noticed that filters of different colors seemed to emanate different amounts of heat. To investigate this phenomenon, he had sunlight shine through a glass prism - a known dispersive since Isaac Newton's experiment on sunlight in 1666 - separating the different colors composing the sunlight. He then proceeded to measure the temperature as well as the relative brightness associated with each discernable color. His findings seemed to show that, while the maximum brightness was reached between green and yellow, the temperature associated to each spectral region seemed to steadily rise from violet to red (his results indicated a rise of +2°C in the violet region, +3.5°C in the green region and +7°C in the red region). This discrepancy in brightness and temperature distribution led him to investigate more, looking for the maximum of the heat curve. He found that the maximum rise in temperature, a +9°C raise, was found to appear

at 1.5 inches beyond the red end of the spectra, prompting the discovery of the invisible component of sunlight: infrared (or "heat rays" at the time).

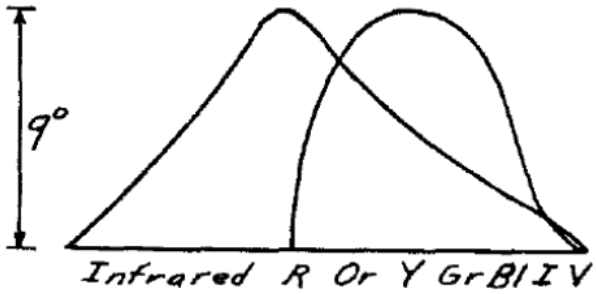

Figure 2.6: Herschel comparison of the heat and relative brightness distribution in the sun's spectrum. Spectrum obtained via a glass prism.

Having determined that these invisible infrared rays are analogous to visible light, the focus shifted on understanding what differentiates one from the other. Follow-up studies done by Herschel show that infrared light follows the sample refraction and reflection laws as visible light, but exhibits radically different behaviors regarding its transmission properties through various substances (some materials appearing opaque to visible light and transparent in the infrared, and vice-versa). Aside from these studies comparing optical properties between visible and infrared spectra, in 1802, another British scientist, Thomas Young, was able provide a structure to the visible and invisible colors of light, interpreting colors as a manifestation of light's wavelength. He then proceeded to measure the wavelength associated with the infrared and visible spectral ranges using his double-slit interferometer. Having then a reference scale to associate with light measurements, the first spectroscopic studies of light were conducted. From the discovery of infrared light, the idea of using infrared and visible light as a way to probe the chemical composition of matter starts to appear and be tested, leading to discoveries such as that of the Fraunhofer lines, a set of spectral absorption lines observed in the optical spectrum of the Sun. First identified by British chemist William Hyde Wollaston, in 1802, and then independently mapped by German physicist Joseph Von Fraunhofer in 1814, their origin will be discovered only in 1859, when German scientists Gustav Kirchhoff and Robert Bunsen noticed that the position of several Fraunhofer lines coincided with characteristic emission lines in the spectra of heated elements, deducing that the dark lines in the solar spec-

trum were caused by absorption of chemical elements in the Sun and the Earth's atmosphere. As a powerful and non-destructive analysis technique, infrared spectroscopy techniques are still being used and further developed to study all kind of matters in many different fields, from chemistry to geoscience, astronomy and fundamental physics.

2.3.2. Fundamentals of infrared spectroscopy

Infrared spectroscopy has multiple domains of application, from the study of biological samples to the characterization of mineral matter. It is particularly useful in the case of extraterrestrial materials for the following reasons:

- It is totally non-destructive, which is a big advantage when studying rare and precious samples.
- It can be sensible to both organics, hydration and mineral phases, making it a very powerful tool in assessing the general composition of the investigated matter.
- It is used in both laboratory environments and remote-sensing surveys, enabling the possibility of directly comparing laboratory results with observational data.

Infrared spectroscopy allows to probe chemical/molecular bonds. When an infrared photon is associated to a frequency close to that of the vibration mode of a particular functional group, it is absorbed by its associated chemical bond. This is highlighted by a lack of photons associated to that frequency, and the appearance of an "absorption band" instead. By plotting the energy distribution - also called spectrum - of light being scattered, emitted or transmitted by a given material, we are able to identify absorption bands, and relate their presence to the composition of the investigated matter. In IR spectroscopy, the photon energy is associated to its wavelength $\lambda[\mu m]$ or its wavenumber $\sigma[cm^{-1}] = 10000/\lambda[\mu m]$.

The infrared range can be divided into three parts. The limits of each division can vary slightly across application fields. In this work, we shall use the following limits:

- The Near-Infrared, from 0.8 to 5 μm (12500 - 4000 cm^{-1}).
- The Mid-Infrared, from 5 to 25 μm (4000 - 400 cm^{-1}).

- The Far-Infrared, from 25 to 1000 μm (400 - 10 cm^{-1}).

A chemical bond between two atoms can be approximated by an harmonic oscillator linking two masses, m_A and m_B. This model can lead to an analytical approximation of the bond's associated vibration mode ν:

$$\nu = (1/2\pi)\sqrt{k/\mu}$$

with $\mu = m_A m_B/(m_A + m_B)$ the reduced mass and k the force constant associated to the oscillator. For this approximation, k is related to the type of molecular bond. This approximation has its limits, since the actual vibration energy is dictated by quantum mechanics.

A chemical bond can vibrate following different modes, which can be regrouped into two families: stretching modes and bending modes. The following figure shows a few examples of stretching and bending vibrations.

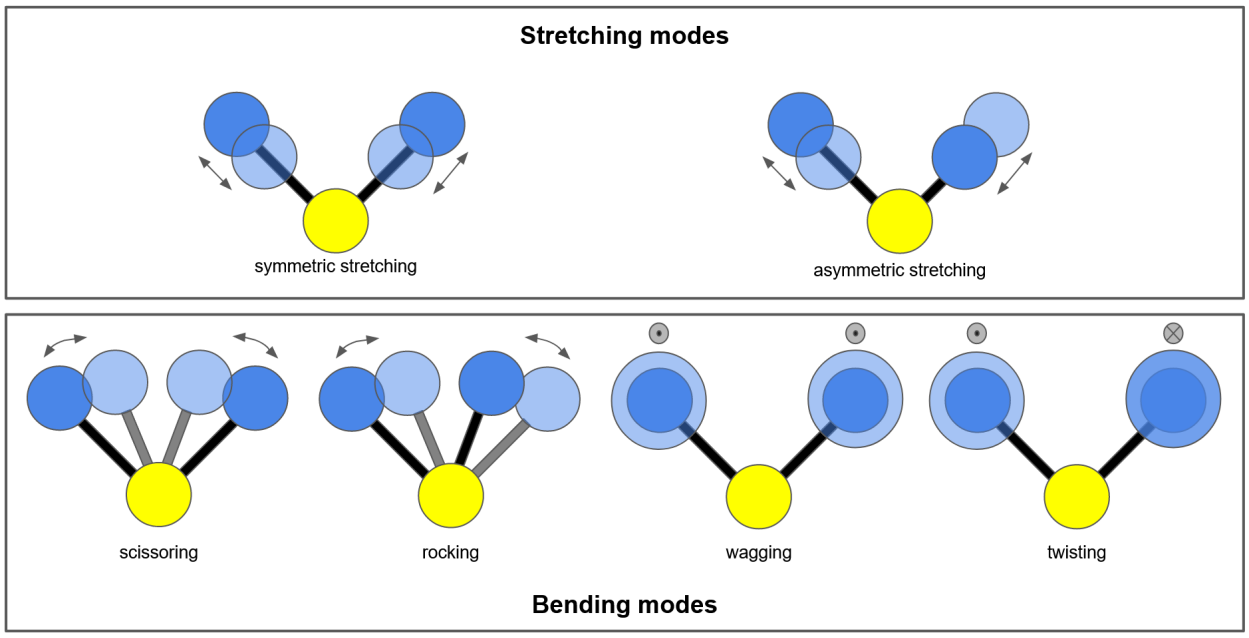

Figure 2.7: Various stretching and bending modes.

Our spectroscopic analysis will spun from the visible range to the far-infrared spectral range, in order to investigate the ion-bombardment effects on specific spectral features related to the chemical

composition of our hydrated samples. The spectroscopic features of interest are summarized in the following table. The given band position can vary slightly following the mineralogy of the investigated matter (Farmer 1974). No absorption bands will be analyzed in the visible range, where the study shall focus on slope and albedo ion-induced changes.

Band position (µm)	Band position ($cm^{-}1$)	Chemical bond	Related to...
2.7 - 2.8	3700 - 3600	(M)-OH stretching	hydration state
3 - 3.2	3300 - 3100	OH stretching	molecular H_2O water
10	1000	Si-O stretching	crystal lattice properties
15 - 16	650 - 600	(M)-OH bending	hydration state
18 - 25	550 - 400	Si-O bending	crystal lattice properties

Table 2.5: Spectroscopic features of hydrated minerals investigated in this work. (M) stands for metallic cation.

2.3.3. Spectroscopic setup used in this work

Upon ion-bombardment, the surface of the irradiated pellets underwent an extensive spectral characterization. The different setups and associated spectral ranges are presented in the following sections.

2.3.3.1 Visible and Near-IR: spectrometers at INGMAR

This setup has already been described in 2.2.2. The INGMAR-SIDONIE ion bombardment platform allows the acquisition of spectroscopic measurements in between the different steps of the ion-bombardment phase, directly inside the vacuum chamber. These in-situ measurements allows us to follow the evolution of spectroscopic bands upon ion-implantation while keeping the system under-vacuum ($P \sim 10^{-7} Pa$). The spectra are acquired through an optic fiber ($\sim 4mm$ collection spot size), which can be interfaced with a grating spectrometer in the Visible range (Maya2000Pro, Ocean Optics) and a Fourier Transform Infrared Spectrometer (Tensor37, Bruker) in the Near-IR range (see figure below).

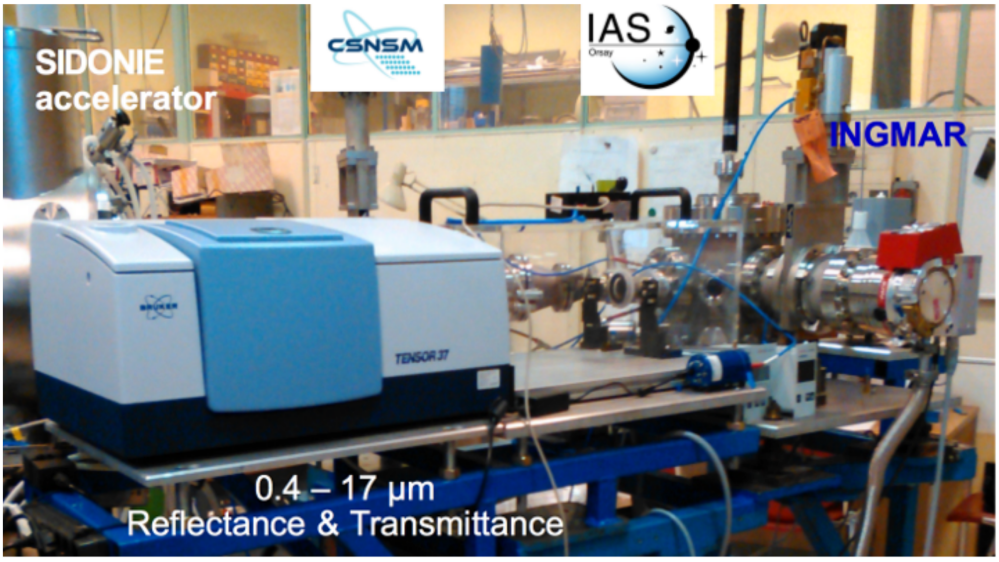

Figure 2.8: INGMAR-SIDONIE setup (IAS-CSNSM)

The spectra are ratioed to reference spectra acquired on Spectralon (99% reflectance, Labsphere) and on Infragold (Labsphere) reflectance standards. More details on the acquisition parameters are shown in the following table.

Instrument	Spectral range (µm)	Spectral resolution	N° of scans
Maya2000Pro	0.35 - 1.10	0.5 nm	200 (200 ms/scan)
Tensor37	1 - 4	16 cm-1	4096

Table 2.6: INGMAR-SIDONIE Vis-NIR: acquisition parameters

2.3.3.2 Mid-IR: FTIR hyperspectral imaging

The surface of the ion-bombarded pellets was also characterized in the mid-IR range, using an Agilent Cary 670/620 micro-spectrometer installed at the SOLEIL synchrotron on the SMIS beamline (see figure below).

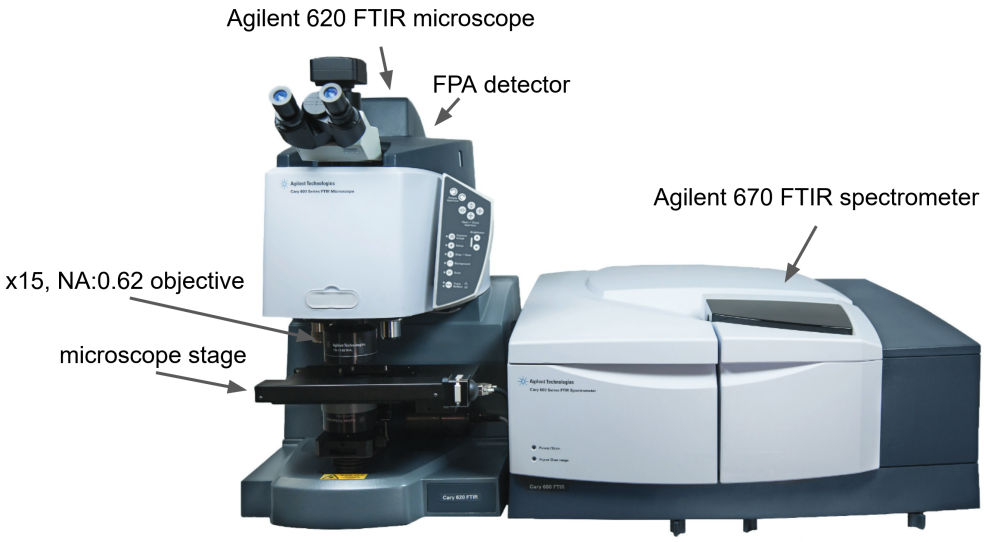

Figure 2.9: Agilent Cary 620 FTIR microscope coupled with an Agilent 670 FTIR spectrometer for FTIR microscopic imaging.

I used a x15 Schwarzschild objective with a numerical aperture (NA) of 0.62. The numerical aperture of an objective corresponds characterizes the range of angles over which the system can accept or reflect light (a large NA corresponds to a large range of angles). The Schwarzschild objective allows for confocal microscope reflectance measurements while minimizing the effects of back-scattered signal. The internal source of the instrument was used, which corresponds to a globar source. The detector used for these measurements is a focal plane array (FPA, see figure 2.10) with 128x128 pixels (each pixel is an MCT detector sizing about 40 microns). This detector allows the acquisition of hyper-spectral maps, which can be useful to quickly analyse heterogeneous samples. Each pixel of an hyperspectral maps is associated to an infrared spectrum, corresponding to the local reflected signal associated to the pixel's position.

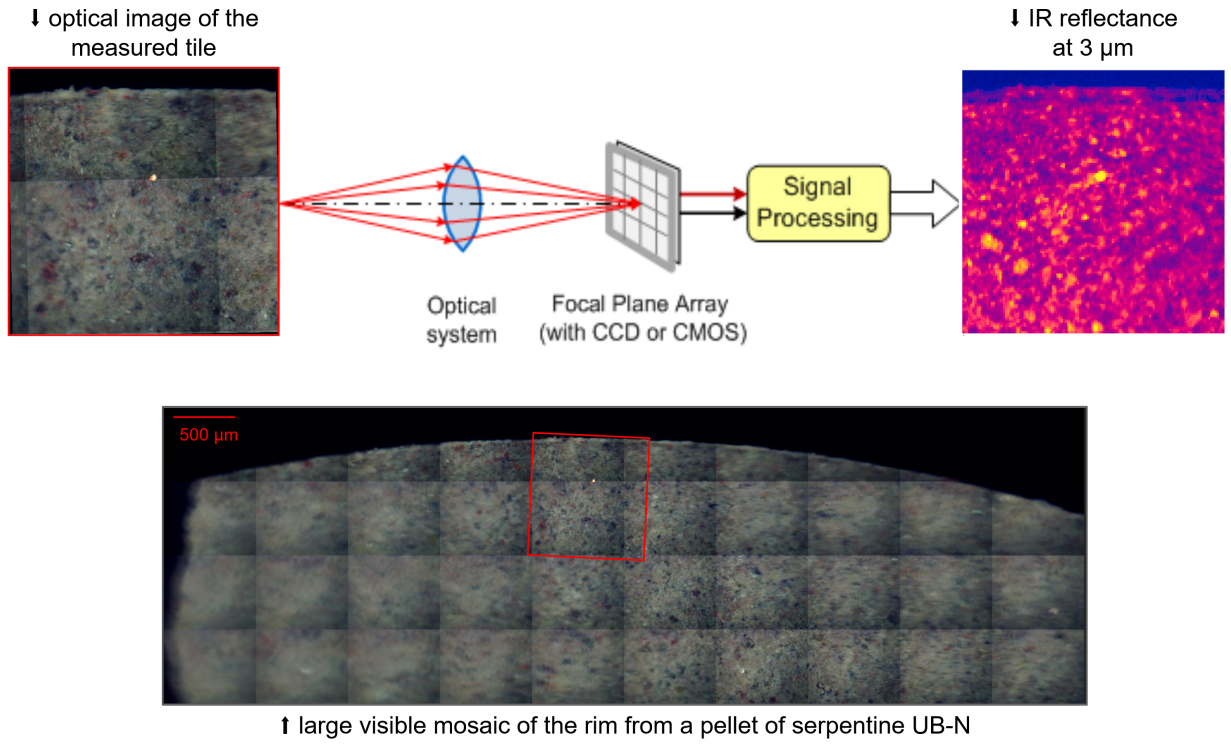

Figure 2.10: Working principle of hyperspectral imaging via focal plane array, showcased on an hyperspectral map acquired on the rim of a pellet made of serpentine UB-N pressed powder.

In the case of our pellets, the phyllosilicate layer is quite homogeneous; the FPA detector was used nonetheless, in order to extract an average spectrum of the pellet's surface by averaging the acquired hyper-spectral tile. The reflectance spectra were calculated with respect to a gold mirror, with a 12.5% attenuator placed in front. This is done to artificially improve spectral contrast on dark materials. The acquisition parameters associated to these measurements are summarized in the following table.

Objective	Spectral range (µm)	Spectral resolution	N° of scans
x15 (FOV: 704 x 704 µm)	2.5 - 12	4 cm^{-1}	256

Table 2.7: Agilent Mid-IR: acquisition parameters. FOV=field of view.

We acquired one hyperspectral map per sample, located at the center of our pellets, and then averaged the hyper-spectral maps to obtain 3 spectra per sample (for a total of 9 spectra) associated

to the various states of our ion-bombarded pellets: pristine, ion bombarded using 40 keV He^+ at $6E16 ions/cm^2$ and ion bombarded using 40 keV Ar^+ at $2E16 ions/cm^2$.

2.3.3.3 Far-IR: bolometer detector

The SMIS beamline at the SOLEIL synchrotron is also equipped with a NicPlan microscope with a IS50 FTIR spectrometer (Thermo Fisher), connected to a bolometer detector (boron doped silicon, 4.2K cooled, Infrared Laboratories) provided by IAS and a solid-state Si beamsplitter, allowing us to probe the far-IR range.

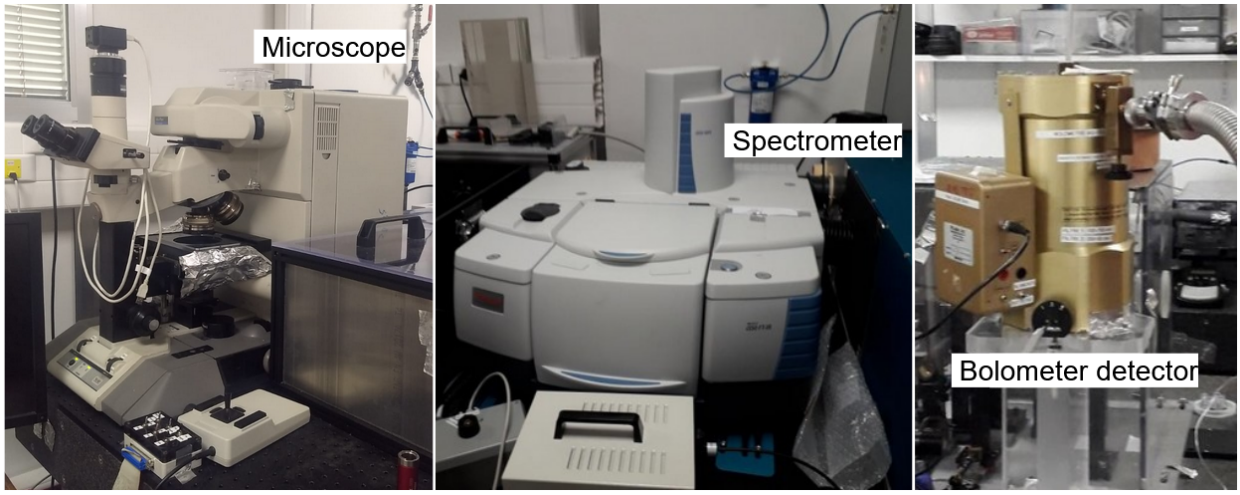

Figure 2.11: NicPlan microscope, IS50 FTIR spectrometer (Thermo Fisher) and bolometer detector (Infrared Laboratories).

The data was acquired in a confocal geometry. Since the hyperspectral data acquired in the mid-IR showed that the pellets were fairly homogeneous, for the Far-IR range I decided to acquire work on single acquisitions, located at the center of our pellets, acquired with the largest collection spot achievable with this instrument (a square region of 200x200 µm). The reflectance spectra associated to these 200x200 µm spots are calculated with respect to spectral measurements done on a gold mirror. The acquisition parameters for these measurements are summarized in the following table.

Objective	Spectral range (µm)	Spectral resolution	N° of scans
x32 (Spot: 200 x 200 µm)	15 - 50	4 cm-1	512

Table 2.8: Bolometer Far-IR: acquisition parameters

2.3.3.4 Reflectance Factors (REFF) with SHADOWS

In order to investigate the effects of ion-bombardment with respect to the observation geometry on spectroscopic data, the set of pellets made from the Serpentine Rawhide sample was measured using the SHADOWS spectro-gonio radiometer (Spectrophotometer with cHanging Angles for the Detection of Weak Signals, IPAG-Université de Grenoble, Potin et al. 2018, see following figure).

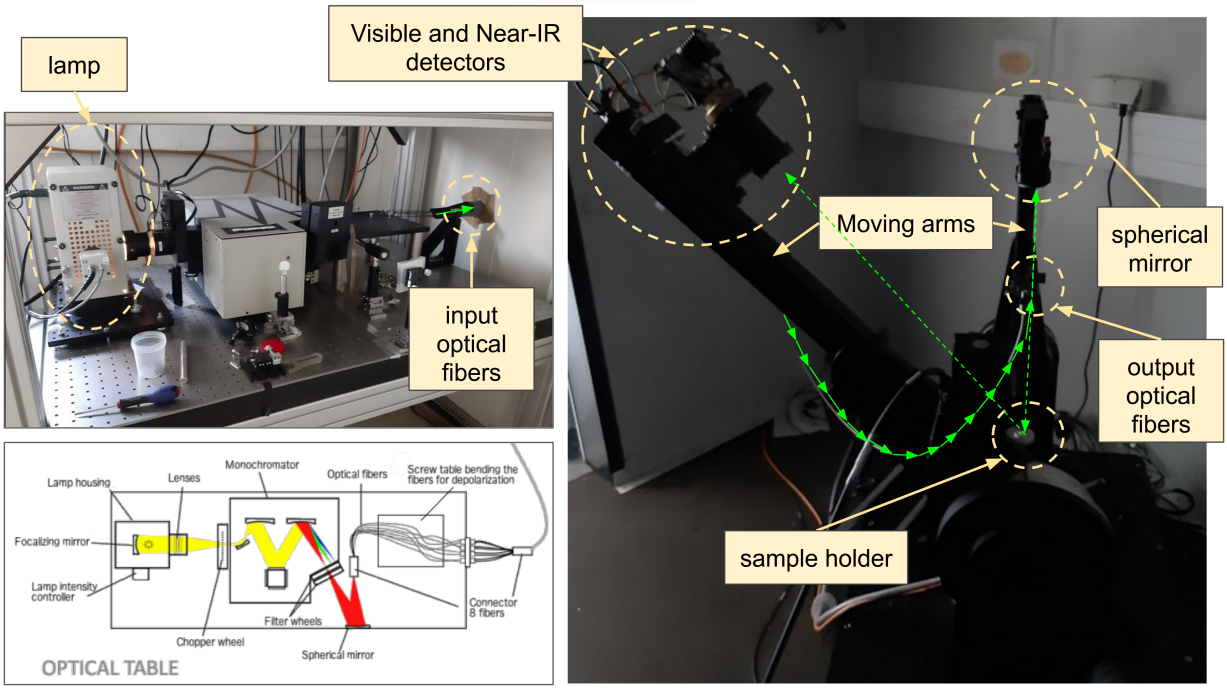

Figure 2.12: Schematization of the SHADOWS spectro-gonio radiometer.

This instrument acquires spectra in the near-IR spectral range at different observation geometries. A monochromatic beam is focused on the sample's surface (illumination spot : $\sim 5.2mm$ in diameter when normal to the surface). The reflected light is measured by two detectors, covering the visible and near-IR ranges, mounted on a rotating arm. The wavelenght associated to the monochromatic beam can be changed in order to probe the desired spectral range (the desired range spanning here from 400 nm to 4 microns). An optical system called "monochromator" is responsible for this step, which in the case of the SHADOWS instrument, uses a filter well to isolate and deliver the monochromatic beam. A single filter is not able to function over such a large spectral range,

and four filters were used for this experiment to achieve the desired spectral range. Each filter is associated to a certain spectral resolution, and we can detect the filter changes when plotting the evolution of this parameter (Figure 2.13, panel a).

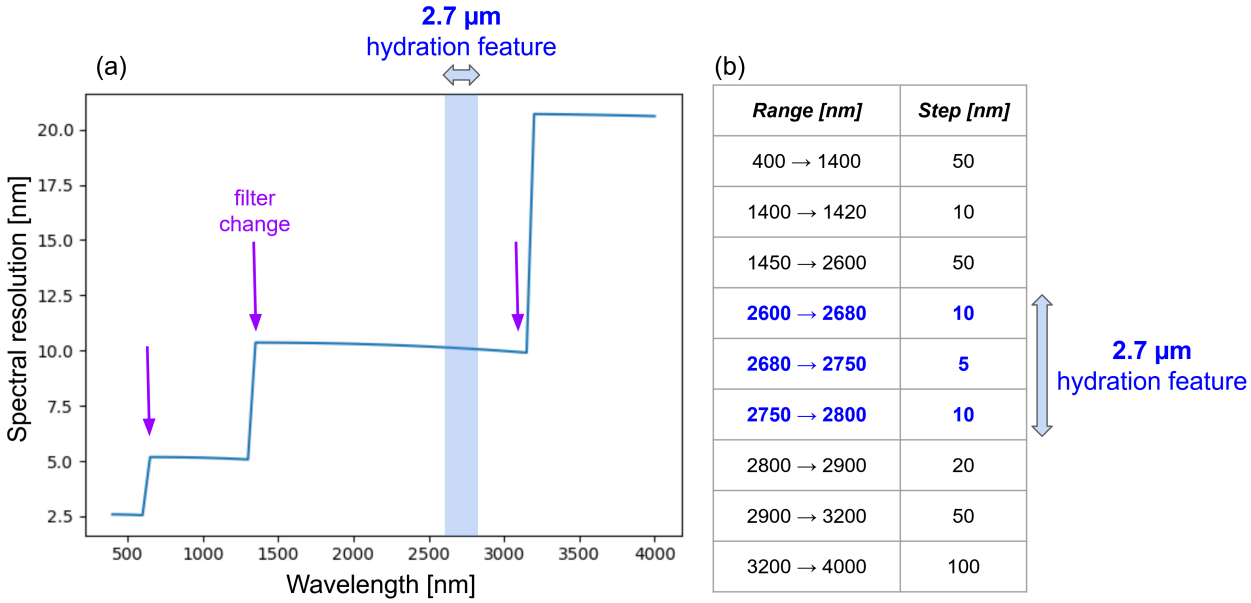

Figure 2.13: (a) Spectral resolution evolution. (b) Spectral step evolution.

The SHADOWS instrument allows us to set the spectral sampling associated to the measurements. Spectral sampling indicates the spectral distance between two adjacent spectral channels. For our data, the spectral sampling was set to be denser in the spectral region near the 2.7 µm hydration band, since it is the spectroscopic feature of interest for this study. The spectral sampling was "relaxed" in spectral regions which were expected to be flat and not showcase important absorption features. This allow us to significantly speed up the measurement process. The spectral sampling associated to our measurement is displayed in Figure 2.13 panel b.

The illumination and the observation angles, i and e, are defined with respect to the normal direction from the pellet surface (see Figure 2.14). These angles can be automatically changed, which allows us to acquire spectra for different observation geometries. We chose to acquire data at four different illumination angles ($i = 0, 20, 40 and 60$ degrees while having the observation angle e vary from -70 to 70 degrees with a 10 degree step. This gave us 56 possible geometrical configuration to explore.

The error associated to the measurement is of ±2.9° for the illumination angle and ±2.05° for the observation angle. Taking in account the spectral range and sampling chosen, this experimental configuration led to 13h of data-acquisition per sample.

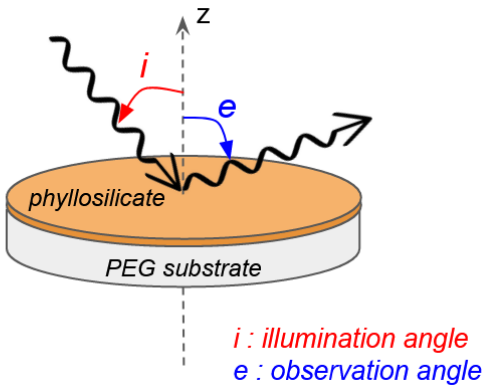

Figure 2.14: Definition of relevant angles for measurements with the SHADOWS instrument

The reflectance factor is calculated during the measurement by comparison with a Spectralon (99% reflectance, Labsphere) and Infragold (Labsphere) reflectance targets, taking into account the Reflectance Factors (REFF) of the references, meaning that the reference is measured at the same observation geometry of the sample. The reflectance of the samples is thus compared to a lambertian surface, by dividing the measured spectra by the reference spectra. In this configuration, reflectance values above 1 for specular configuration on very flat surfaces are to be expected.

2.4. Electron Microscopy

2.4.1. A bit of History...

The history of electron microscopy is much more recent than that of infrared spectroscopy, starting in 1928, when Hungarian nuclear physicist Leó Szilárd, former student of Albert Einstein, first conceptualized (and later patented) concepts for an electron microscope. However, the first practical demonstration of the principles of electron microscopy came in 1931, by physicist Ernst Ruska and electrical engineer Max Knoll in Germany. This first prototype was capable of a 400 power magnification, which was still lower than optical microscopes at the time (schematics of this first apparatus from Ruska can be seen in Figure 4.1 panel a). It was still a great proof of concept, which

attracted the attention of German electrical engineering company Siemens-Schuckert. Siemens financed further work from Ruska et al. to develop the first transmission electron microscope that could exceed the resolution attainable with optical microscopy in 1933 (Figure 4.1 panel b). The first commercial transmission electron microscope (TEM) came from Siemens in 1939. Ever since, technological improvements have led to machines capable of up to 2 000 000 magnification, but all remained based upon Ruska's prototype. In 1986, Ernst Ruska was awarded the Nobel Prize in Physics "for his fundamental work in electro optics, and for the design of the first electron microscope".

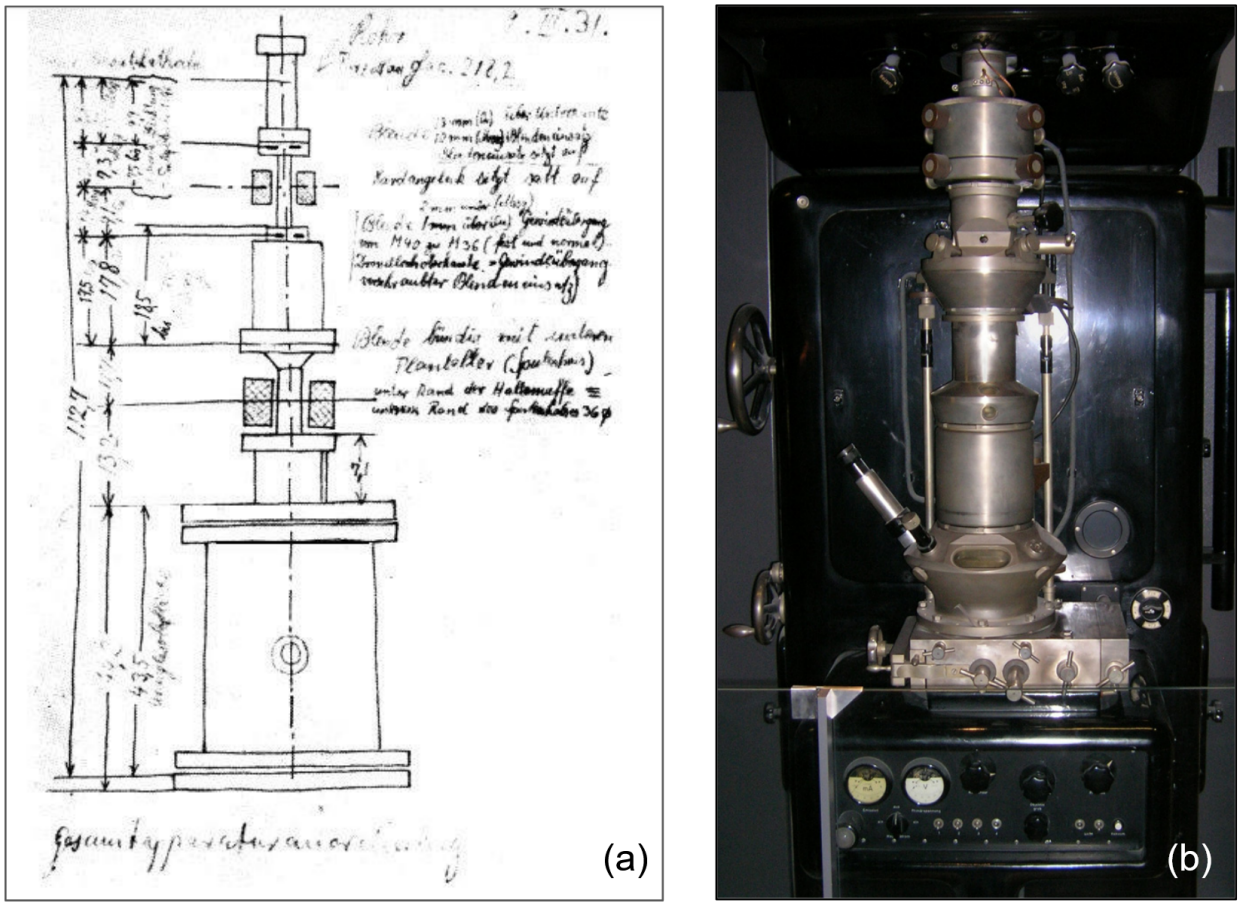

Figure 2.15: (a) Schematics of the 1931 prototype of an electron microscope by E. Ruska, and (b) the first electron microscope to achieve greater spatial resolutions than its optical rivals, in 1933, also by E. Ruska et al.

Scanning electron microscopy is a different electron microscopy technique with its own history. A

detailed record of the early development history of this technique can be found in McMullan (2006). From the development of television camera tubes, in 1935, the co-inventor of TEM Max Knoll published images using a scanning electron beam : this application came from the development of television camera tubes, to which Knoll contributed by working at the German Telefunken Company. But it was German physicist Manfred von Ardenne who in 1937 developed the first scanning electron microscope with a submicron probe. The necessity for this new imaging technique came from the need of addressing a few issues with TEM at the time (ex. chromatic aberrations on thick samples).

2.4.2. Fundamentals of electron microscopy

Electron microscopy uses an electron beam instead of photons as source of "illumination". The beam is redirected and focused using magnetic fields. Optical imaging instruments are often diffraction limited, meaning that the smallest feature they can resolve has a size of close to the wavelength associated to the illumination source. Since electrons have shorter wavelength than photons (up to 100 000 times shorter), electron microscope have a higher resolving power than light microscopes. In some configurations, even atomic resolution can be achieved. As the electron beam interacts with the investigated matter, multiple processes occur at different depths (see Figure below).

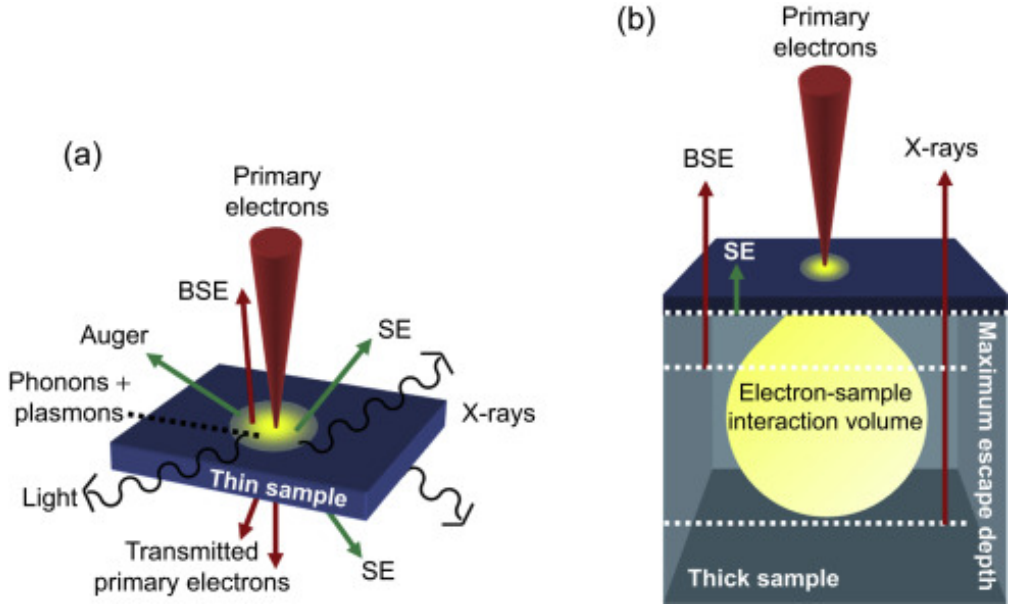

Figure 2.16: Signals detectable in electron microscopy for thin (a) and thick (b) samples, extracted from Inkson 2016.

Each process is related to the energy loss of the incident electrons, and translated to the emission of multiple signals. In thick samples, some of the signal we shall use in this work include low-energy secondary electrons (SE) and high-energy back-scattered electrons (BSE), emitted from the first hundreds of nanometers of the sample down to a few micron deep. X-Ray emission also occurs deeper in the interaction volume, down to a micron deep. The electronic signals provide topographical (SE) and compositional information (BSE allows for phase and atomic number contrast imaging, while energy dispersive X-ray spectroscopy provides the elemental composition of the probed matter). For thin samples, the transmitted electrons are used for imaging and diffraction in the TEM.

2.4.2.1 Scanning Electron Microscopy (SEM)

SEM imaging provides topographical and compositional information related to the surface of a sample. The focused electron beam is scanned across a rectangular area of the sample. SE, BSE and X-Ray spectroscopy can be used to quickly assess both the topography and the composition of an investigated area. SEM imaging is a relatively easy and quick technique to implement, since it requires less sample preparation than other electron microscopy technique. However, the image resolution of SEM images is generally lower than what can be achieved by techniques using transmitted electrons, such as STEM.

2.4.2.2 Scanning Transmission Electron Microscopy (STEM)

STEM is used on thinned samples, typically 100 nm thick. In the following work, high-angle annular dark field (HAADF) imaging was performed. HAADF imaging is an STEM technique relying on the detection of incoherently scattered electrons at an angle larger than 5 deg (also known as Rutherford scattered electrons). This techniques is particularly sensitive to variations in the atomic number of atoms in the probed material (Z-contrast images - larger Z is related to bright spots). The resolution of HAADF STEM images is dominated by the size of the electron beam. As for SEM, energy dispersive X-ray spectroscopy was also used during STEM analysis.

2.4.3. Electron microscopy setup used in this work

Once the extensive spectral characterization segment of our analytical pipeline was finished, it was time to visualize the effects of ion-bombardment at smaller scales using electron microscopy. The

scanning electron microscopy and scanning transmission electron microscopy setup used for this work are shown in the figure below and described in the following sections.

Figure 2.17: (a) JEOL JSM-7800F scanning electron microscope; (b) Thermo Fisher Scientific™ Titan Themis

2.4.3.1 Scanning Electron Microscopy (SEM)

The surface of the ion-bombarded pellets was imaged using JEOL JSM-7800F scanning electron microscope (see figure 2.17, panel a) with a working distance of 10 mm. Secondary electron imaging at 3 keV allowed us to visualize changes in the surface topography after the ion-bombardment. Low and high-magnification images (from a few hundreds down to x30 000 magnification) were taken to investigate changes at different scales.

2.4.3.2 Scanning Transmission Electron Microscopy (STEM)

The FIB sections were studied by scanning transmission electron microscope (STEM) using a Thermo Fisher Scientific™ Titan Themis operating at 300 kV. High-angle annular dark field (HAADF) STEM images, coupled with compositional data by EDS (Energy Dispersive X-Ray Spectroscopy) allowed us to investigate both the change in texture and chemical composition in the ion-implanted

layers. In order to minimise the beam damages (phyllosilicates are beam sensitive materials), we used a beam current of 60 pA for the HAADF imaging and 300 pA for the recording of hyperspectral EDS maps. EDS quantification was achieved using the Bruker software Esprit (version 1.9). The absorption and the k-factor corrections were applied assuming a thickness of 100 nm and using experimentally determined k-factors.

CHAPTER 3

Spectroscopic variations and detectability on asteroid surfaces

Contents

3.1. Spectroscopic results from our lab experiments

In this section, we shall present the results of the extensive spectroscopic characterization led on our ion-bombarded pellets. The goal of this section is to outline the various spectral changes and trends associated to ion-bombardment on spectral features relevant to phyllosilicates.

3.1.1. Vis-NIR measurements

3.1.1.1 In-situ, under vacuum (INGMAR-SIDONIE)

Both visible and near-infrared spectra were acquired upon ion-bombardment inside the INGMAR irradiation chamber, under vacuum (see 2.2.3 for more details about experimental conditions). For each pellet, multiple spectra were acquired.

- A spectrum prior the ion-bombardment, associated to the 'pristine' state of the target material.
- Two spectra from intermediate ion fluences: $1 * 10^{16}$ and $3 * 10^{16} ions/cm^2$ for He^+, $0.5 * 10^{16}$ and $1 * 10^{16} ions/cm^2$ for Ar^+.
- A final spectrum associated to the 'maximum fluence': $6 * 10^{16} ions/cm^2$ for He^+ and $2 * 10^{16} ions/cm^2$ for Ar^+.

Visible spectroscopy

Results

The complete data-set from the in-situ visible spectroscopy measurements is shown in the figure below (3.1). Note that the measurements associated to the pristine state of each sample (yellow for He^+ and light green for Ar^+) is somewhat different between the pellets chosen for He^+ bombardment and those chosen for Ar^+ bombardment. The overall spectral shape does not change much. However, the pristine spectra for the Ar^+ bombardment experiment have a higher reflectance than those associated to the He^+ experiment, appearing from 8% to 16% brighter. This is probably due to slight differences between the reference spectra acquired for the two experiments, perhaps coupled with the surface different state prior to ion-bombardment (the smallest difference in reflectance is

observed for the serpentine UB-N sample, the most homogeneous among our samples, since it is purchased as a reference material - see 2.1.1). This does not greatly affect the goal our our study, since we are more interested in the spectral changes upon ion-bombardment relative to the pristine material, rather than the absolute reflectance of our materials.

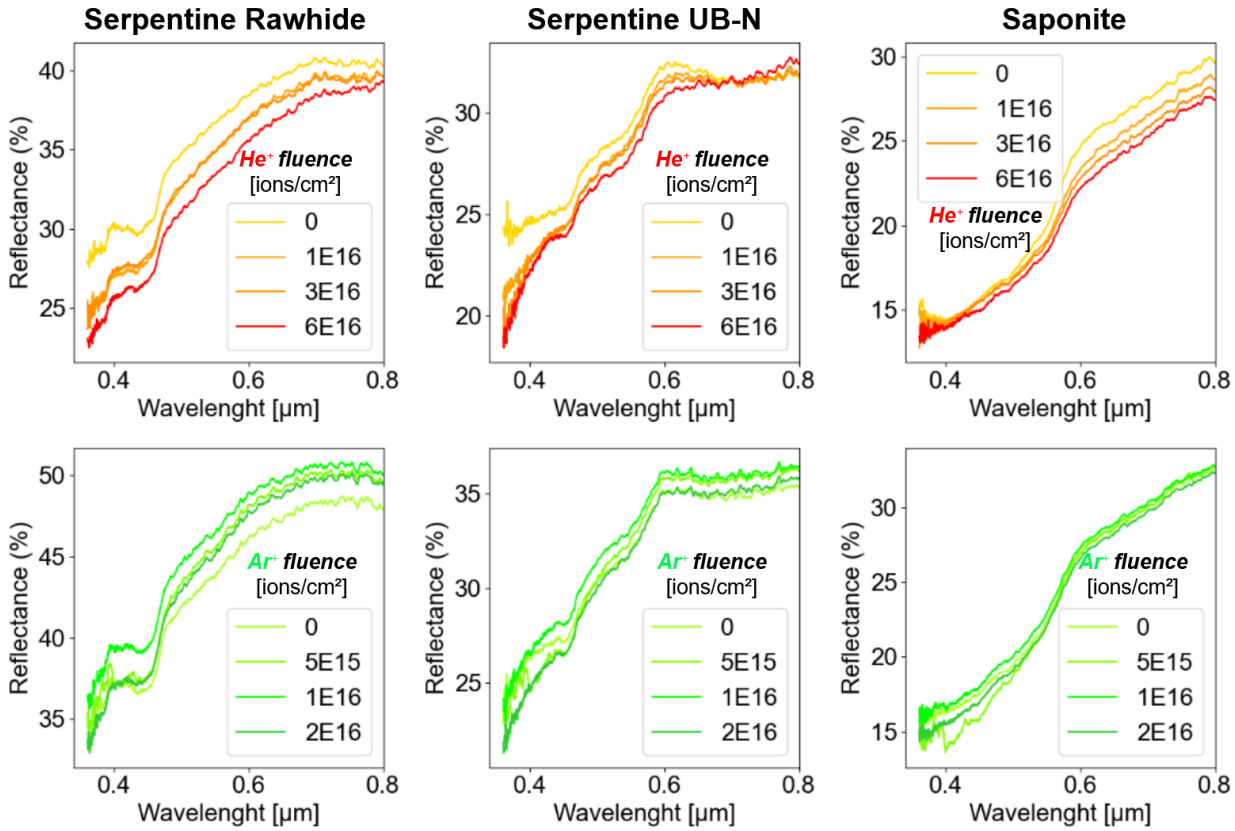

Figure 3.1: Complete visible spectroscopy data-set of three hydrated silicate pellets, ion-bombarded under vacuum using He^+ and Ar^+, at varying fluences.

The complete data-set shows us that spectral changes are more prominent in the case of He^+ bombardment. Spectral changes for the Ar^+ case either saturate much faster (for Serpentine Rawhide, the spectral shape does not change after the first bombardment step at 0.5E16 $ions/cm^2$), or do not seem to have much of an effect at all (the spectral shape for Serpentine UB-N and Saponite does not change significantly even after having achieved maximum fluence).

In order to better investigate and quantify the spectral changes upon bombardment, we extracted

two spectral parameters: the reflectance at 0.55 µm, and the visible spectral slope between 0.48 and 0.7 µm. The evolution of these parameters is shown in figure 3.2.

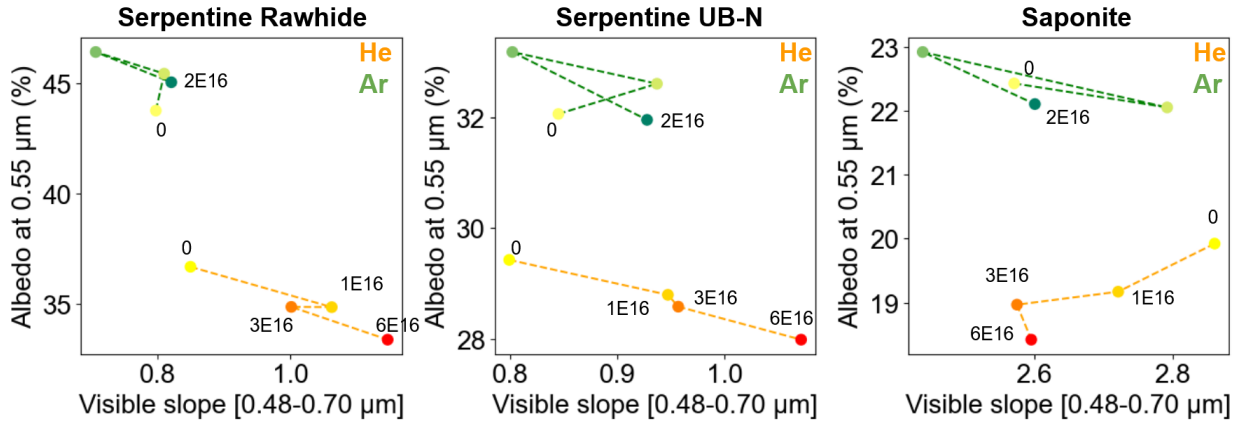

Figure 3.2: Evolution of the reflectance at 0.55 µm and of the visible slope between 0.48 and 0.7 µm (after normalisation at 0.55 µm) upon He-bombardment (in orange) and Ar-bombardment (in green), at various fluences. The intermediate fluences for the Ar case are removed for the sake of clarity (they are 5E16 ions/cm2 in light green and 1E16 ions/cm2 for green).

Focusing on the extracted spectral parameters, we notice that the absolute variations are not larger than 9% in reflectance (for the Serpentine Rawhide He-bombarded) and 0.3 µm-1 for the visible slope (for the Saponite). No clear trend seem to emerge for the Ar^+ bombarded samples once the final weathering state (corresponding to a fluence of 2E16 $ions/cm^2$) has been reached. For the He^+ case, we detect a clear reddening for both Serpentines (at maximum fluence, +35% increase in the visible slope for both Serpentines) and slight blueing (-9.3%) for the Saponite. All He-bombarded samples exhibit darkening. Upon having reached the maximum He^+ fluence, reflectance varies by -9% for Serpentine Rawhide, -4.9% for Serpentine UB-N and -7.5% for Saponite.

Discussion

The common darkening among the He-bombarded samples hints that there is some common weathering phenomenon which alters the optical properties of our sample. One such phenomenon could be changes in the porosity of the surface layers of our pellets. A potential increase in local porosity could contribute to trapping and dissipating incident photons more efficiently than a compact

structure would, lowering the overall brightness of the surface. If such scenario is correct, we would expect to find higher vesiculation in the Serpentine Rawhide sample (which exhibits the greatest dip in albedo), than in the Saponite and Serpentine UB-N samples. This is one the morphological changes that will be searched in the electron microscopy analysis (section 4.2).

The change of spectral slope upon He-bombardment seems to naturally separate the two phyllosilicate families: reddening for both serpentines and blueing for saponite. This would hint that the behaviour of the spectral slope is linked to changes affecting the different crystal lattices of these two families. Serpentines and saponites differ greatly regarding their lattices (as discussed in 2.1.1.), the main difference consisting in the presence of an inter-layer of molecular water separating each TOT units in saponites. Each TOT unit behaves almost as a separate entity, meaning that the lattice stress induced by the He-bombardment can be more easily dissipated at the scale of each TOT unit (compared to a more compact TO structure such as that of serpentines). This "lattice elasticity" could affect the efficiency of amorphization processes upon ion-bombardment. The precise link between these different lattice behaviours and the two distinct spectral slope changes seen in our two phyllosilicate families will be discussed further in the next chapters, where both IR spectroscopy in the mid-IR (focused on the SiO-stretching vibration band at 10 µm) and transmission electron microscopy will allow us to comment on possible differences in amorphization state of our He-bombarded samples.

It is difficult to comment on the behaviour of the Ar-bombarded samples: no clear spectral trend for either reflectance nor visible slope can be identified with clarity. This may be explained by a lack of significant changes upon Ar-bombardment, or rather a lack of sensible changes detected by visible spectroscopy, since visible photons penetrate much deeper than the Ar^+ penetration depth. The observed behaviour may also be the result of competing processes, where one contributing effect does not dominate the others.

Near-Infrared spectroscopy

Results

The near-IR spectroscopic range is of particular interest for hydrated minerals, since it allows to study water content and endogenous hydration of phyllosilicates. These studies are often conducted using the 2.7 µm feature as a spectral proxy, which is attributed to the stretching vibration of hydroxyl groups (O-H) covalently bonded to metallic atoms (M) of octahedral MO6 sites (more details discussed in 2.1.1). All data acquired in-situ with the INGMAR-SIDONIE setup showed this feature (see Figure 3.3). There appear to be certain differences in the overall band shape and peak position among our samples due to their different composition and crystal structure.

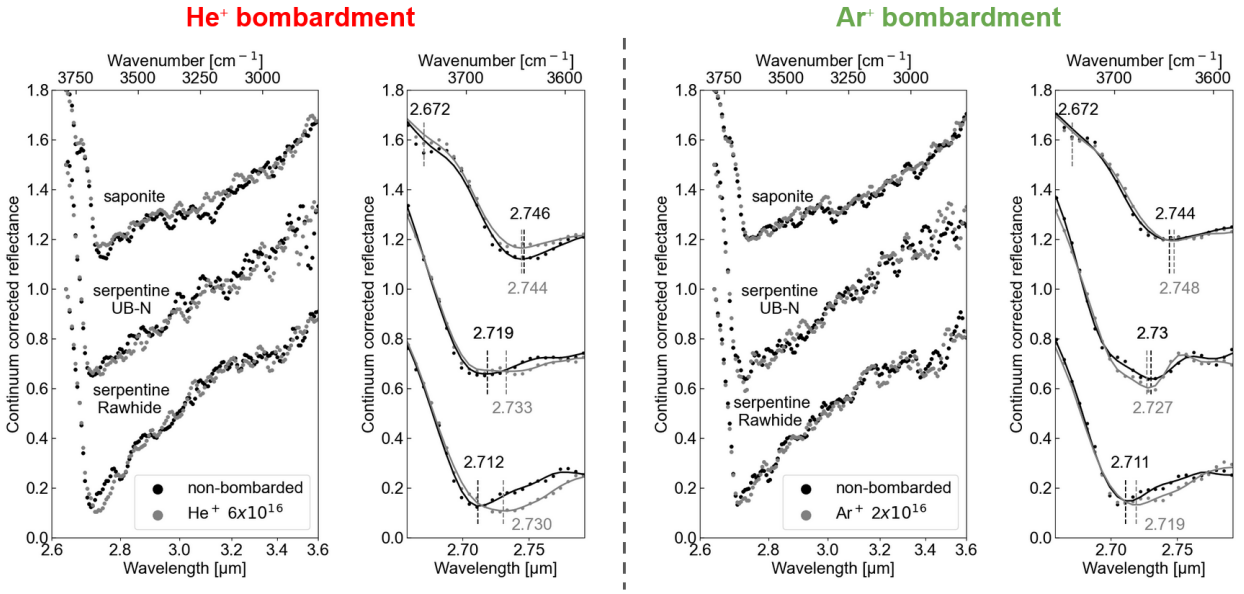

Figure 3.3: In-situ evolution of the 2.7 µm feature before (non-bombarded - black dots) and after maximum ion fluence ($6 * 10^{16} ions/cm^2$ for He^+ (left panel) and ($2 * 10^{16} ions/cm^2$ for Ar^+ (right panel) - grey dots). Spectra were shifted for clarity. A linear continuum correction from 2.64 µm to 4 µm was applied. Solid lines represent the Savitzky-Golay filter used for denoising the spectra. For plotting, the linear scale is used with respect to wavenumbers. The right sup-panel of each panel is a zoom on the region of the 2.7 µm bands.

Different trends seem to emerge upon ion-bombardment. In order to investigate these changes, we extracted two spectral parameters from the hydration band: its peak position and band depth. To account for noise in the collected spectra, spectral parameters of interest were estimated by applying different instances of a Savitzky-Golay filter to our spectra, then by determining the range of interest centered on the hydration feature. The peak position was obtained by computing the barycenter

associated to this range of interest (to account for the asymmetry of the spectral feature), and averaging the peak position of each Savitzky-Golay instance. The position of the feature computed on raw data (without denoising) was also included for the computation of the average position. The wavelength obtained by this algorithm was assimilated to the feature's position. This method allowed us to extract the band positions and their associated band depth before, upon and after ion-bombardment. The results are summarized in the following tables.

	Spectral parameters	Pristine state	He^+ bombarded ($6 * 10^{16} ions/cm^2$)	Relative and absolute variation
Serpentine Rawhide	Peak position (nm)	$2712 \pm 3nm$	$2730 \pm 4nm$	$+0.7\%$ / $+18nm$
	Band depth	0.846 ± 0.013	0.884 ± 0.004	$+4.3\%$ / $+0.038$
Serpentine UB-N	Peak position (nm)	$2719 \pm 5nm$	$2733 \pm 4nm$	$+0.5\%$ / $+14nm$
	Band depth	0.826 ± 0.013	0.828 ± 0.009	$+0.25\%$ / $+0.002$
Saponite	Peak position (nm)	$2746 \pm 3nm$	$2744 \pm 5nm$	-0.07% / $-2nm$
	Band depth	0.663 ± 0.006	0.620 ± 0.005	-6.5% / -0.043

Table 3.1: Hydration feature (2.7 µm) in-situ spectral parameters upon He^+ bombardment

	Spectral parameters	Pristine state	Ar^+ bombarded ($2 * 10^{16} ions/cm^2$)	Relative and absolute variation
Serpentine Rawhide	Peak position (nm)	$2711 \pm 4nm$	$2719 \pm 5nm$	$+0.3\%$ / $+8nm$
	Band depth	0.829 ± 0.016	0.850 ± 0.006	$+2.5\%$ / $+0.021$
Serpentine UB-N	Peak position (nm)	$2730 \pm 5nm$	$2727 \pm 3nm$	-0.1% / $-3nm$
	Band depth	0.842 ± 0.011	0.871 ± 0.019	$+3.4\%$ / $+0.029$
Saponite	Peak position (nm)	$2744 \pm 4nm$	$2747 \pm 3nm$	$+0.1\%$ / $+3nm$
	Band depth	0.590 ± 0.004	0.594 ± 0.004	$+0.7\%$ / $+0.004$

Table 3.2: Hydration feature (2.7 µm) in-situ spectral parameters upon Ar^+ bombardment

The peak position prior to ion-bombardment for the two serpentines is coherent with their composition: the feature of the serpentine Rawhide (slightly Mg-richer) is located at shorter wavelength compared to serpentine UB-N. All peak position values prior to ion-bombardment are coherent with the peak position associated with the hydroxyl stretching of hydrated silicates in the with reference spectra found in the literature (Vicente Rodriguez 1994 for the saponite ; Bishop et al. 2008, Takir et al. 2013 for serpentines), except for the peak position of Serpentine UB-N prior to Ar^+ bombardment, which appears to be significantly higher in wavelength. This may yet again be

an issue with the reflectance spectrum used as reference for the Ar^+ experiment, coupled with the overall noisiness of the sample.

For the He^+ bombarded samples, once the maximum ion fluence has been reached, the feature's position for the serpentines visibly changes, shifting towards longer wavelength, with band shifts of $+18nm$ for Serpentine Rawhide and $+14nm$ for Serpentine UB-N. On the other hand, for the saponite sample, the feature does not seem to move within our error bars. For the Ar^+ bombarded samples spectral changes are difficult to gauge (similar situation to that of visible spectroscopy). There appear to be again no significant changes with the Saponite sample. Behaviour for the Serpentine UB-N sample is particularly unclear, since the measured shift is within error-bars and towards shorter wavelength. Only the Serpentine Rawhide sample seems to exhibit a small band shift ($+6nm$). Band depth for all samples, He^+ and Ar^+ bombarded, does not seem to change within our error-bars, with the exception of the He^+ bombarded Saponite sample, which exhibits a slight band depth decrease upon having reached maximum ion fluence ($-7 \pm 2\%$). We also see some slight band broadening for the He^+ bombarded samples, but the measurement noise does not allow for the extraction of a trusty band width parameter.

Note that the saponite sample also displays a small peak around $2672nm$, associated with silanol groups (Si-OH) exposed in defects sites of the external layer surface (Trombetta et al. 2000). Ion bombardment does not seem to affect its position.

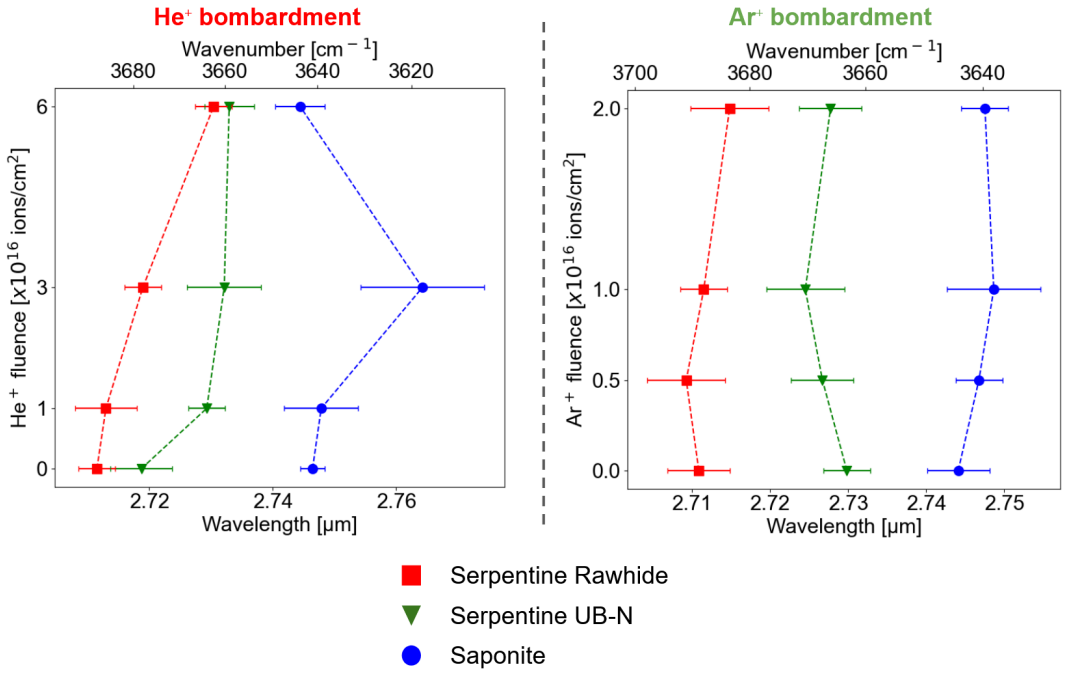

Figure 3.4: In-situ evolution of the 2.7 µm feature peak position of the studied phyllosilicates upon irradiation. Saponite in blue circles, serpentine UB-N in green triangles, and serpentine Rawhide in red squares. The irradiation fluence 0 refers to the samples before ion bombardment.

Looking at the evolution of the feature's position at intermediary fluences (see figure 3.4) provides further supports to the previous claims. Both He^+ bombarded serpentines end up having similar peak position upon reaching maximum fluence, but the evolution of their peak position does not follow the same trend (Serpentine UB-N changes far more rapidly than Serpentine Rawhide). The He^+ bombarded saponite sample feature's position is not sensibly affected, despite a particularly noisy spectra associated with the $3.10^{16} ions/cm^2$ fluence. For all Ar^+ bombarded samples, the feature's position never shifts significantly with respect to the associated error bars.

Discussion

Overall, ion bombardment processes induce little modifications of the intensity and shape of the hydration feature, but they induce detectable and significant modifications of the band peak position. The lack of significant changes in the Ar^+ bombarded samples may be explained by the depth of the associated ion-implanted layer ($40nm$ from SRIM simulations, see 2.2.3): the signal

from the pristine material below the ion-implanted layer dominates the collected signal, hence the difficulty in distinguishing clear spectral changes. For the He^+ bombarded samples, we see - similarly to the results from visible spectroscopy - different behaviors opposing the two serpentines and the saponite sample: a significant shift towards longer wavelength for the serpentine family and no changes in peak position for the saponite sample. Again, this opposition hints that the origin for these two different behaviors may lie in the crystal lattice differences (TO structure for serpentine and TOT + interlayer structure for saponite, see 2.1.1). For serpentines, any stress on a TO layer or the adjacent one will affect the hydrogen-bindings and will disturb the crystal lattice, affecting the immediate environment of the (M)-OH groups associated with the 2.7 µm feature. This will directly impact the position of the 2.7 µm band. On the contrary, since TOT units are separated by an empty inter-layer which can harbour molecular water, the lattice stress induced by He^+ bombardment can dissipate at the scale of the single TOT unit, resulting in a less disturbed environment surrounding hydroxyl groups. Other mechanisms, such as compositional-related processes (local variations of the Fe/(Mg+Fe) ratio or preferential amorphization of Mg-rich phyllosilicates (Hapke et al. 1975)), could also affect the position of the feature upon ion bombardment. The forthcoming electron microscopy analysis (Chapter 4) will present these changes being investigated at a nanometric scale.

3.1.1.2 Geometry-induced effects (SHADOWS)

We have seen that ion bombardment has certain effects on the 2.7 µm feature of hydrated silicates. Among these effects, we see a significant shift (tens of nanometers) of the peak position towards longer wavelength for members of the serpentine family. This effects was investigated on a setup with a fixed observation geometry (illumination angle $i = 15°$ for visible data and 20° for IR data, with a fixed collection angle $e = 15°$ for both, see 2.2.2 for more details). In this section, we shall investigate the potential dependency of this effect with respect to changes in the geometry of observation. Understanding the behaviours of spectral features of interest with changing geometry of observation is fundamental for remote sensing and lander spectroscopic observations, where same areas at the surface may be observed at varying geometries. Recent studies have already shown that the shape of the hydration feature in carbonaceous chondrites, often used as analog material

for hydrated carbon-rich asteroids surfaces, can be affected by the geometric configuration of an observation (Potin et al. 2019). Here, we shall investigate how the spectra of weathered materials change when measured at varying geometries.

We focus our analysis on a specific set of our samples: the trio of pellets made from the Serpentine Rawhide sample (the pristine sample plus the He^+ and Ar^+ bombarded ones). We chose this set of pellets since the Serpentine Rawhide samples are the one that exhibited the larger spectral shift in the in-situ measurements. We acquired laboratory Reflectance Factors (REFF) measurements on the set of pellets using the SHADOWS spectro-gonio radiometer at IPAG - Grenoble (France). The instrument itself and the experimental parameters used for this investigation are presented in section 2.3.3. We acquired infrared spectra focused on the 2.7 µm feature at different geometries. The measured spectra for illumination angles i values of 0°, 20°, 40° and 60°. At each illumination angle, we changed the observation angle from -70° to 70° with a 10° step. This resulted in 56 possible geometrical configuration being investigated, per pellet.

Results

Almost all the acquired spectra show the same absorption bands (see figure below):

- a deep 2.7 µm band associated as with the (M)-OH stretching vibration ;
- a broad 3 µm shoulder, which can be a combination of structural and adsorbed water bands (in this sample, minor amounts of structural water are expected, so this contribution is probably dominated by the contribution of adsorbed water) , as well as CH stretching bands around 3.4 µm ;
- overtones and combination mode peaks of water molecules at 1.4 and 1.9 µm (Ryskin 1974, Ockman 1958);
- two additional bands at 2.3 and 2.5 µm, originated from the stretching vibrations of Mg-OH and/or Fe-OH (Clark et al. 1990).

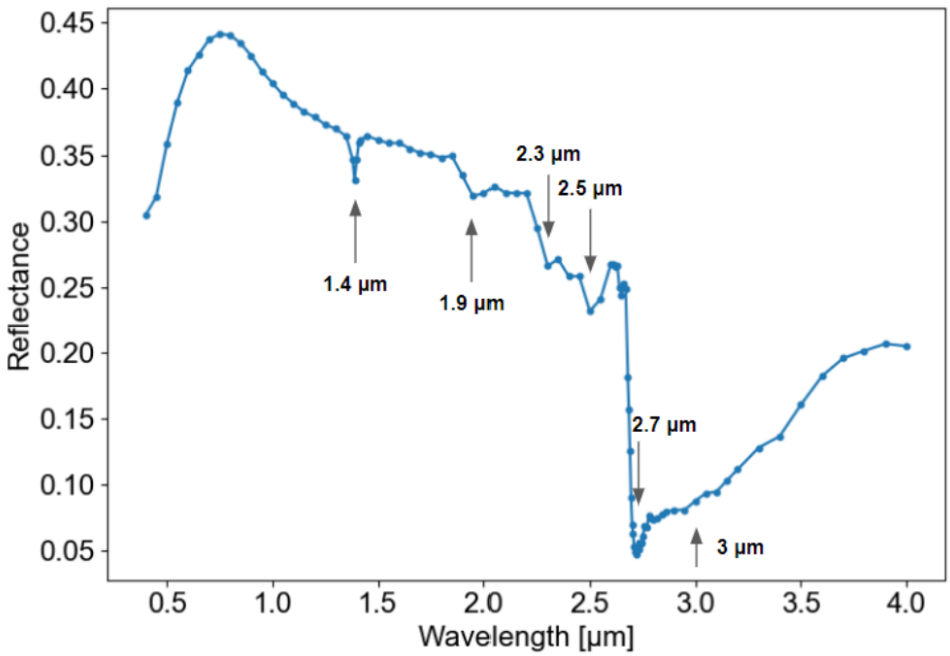

Figure 3.5: Example of acquired spectra - He^{+} bombarded serpentine Rawhide at illumination angle $i = 20°$ and $e = 40°$.

The water contribution at 3 µm is fairly distinct from the 2.7 µm (M)-OH stretching feature. In this sample, endogenous/structural water should not be present, indicating that the contribution seen here is mostly dominated by atmospheric water being adsorbed on the surface of the pellet. Its evolution is not relevant with respect to the remote-sensing implications of this particular work (a more in-depth study of this contribution is nonetheless discussed in Rubino et al. 2022).

The following figure shows the evolution of the hydration feature for all pellets at all the investigated configurations. The spectra were continuum removed and normalized. The unprocessed data-set can be seen in Rubino et al. 2022.

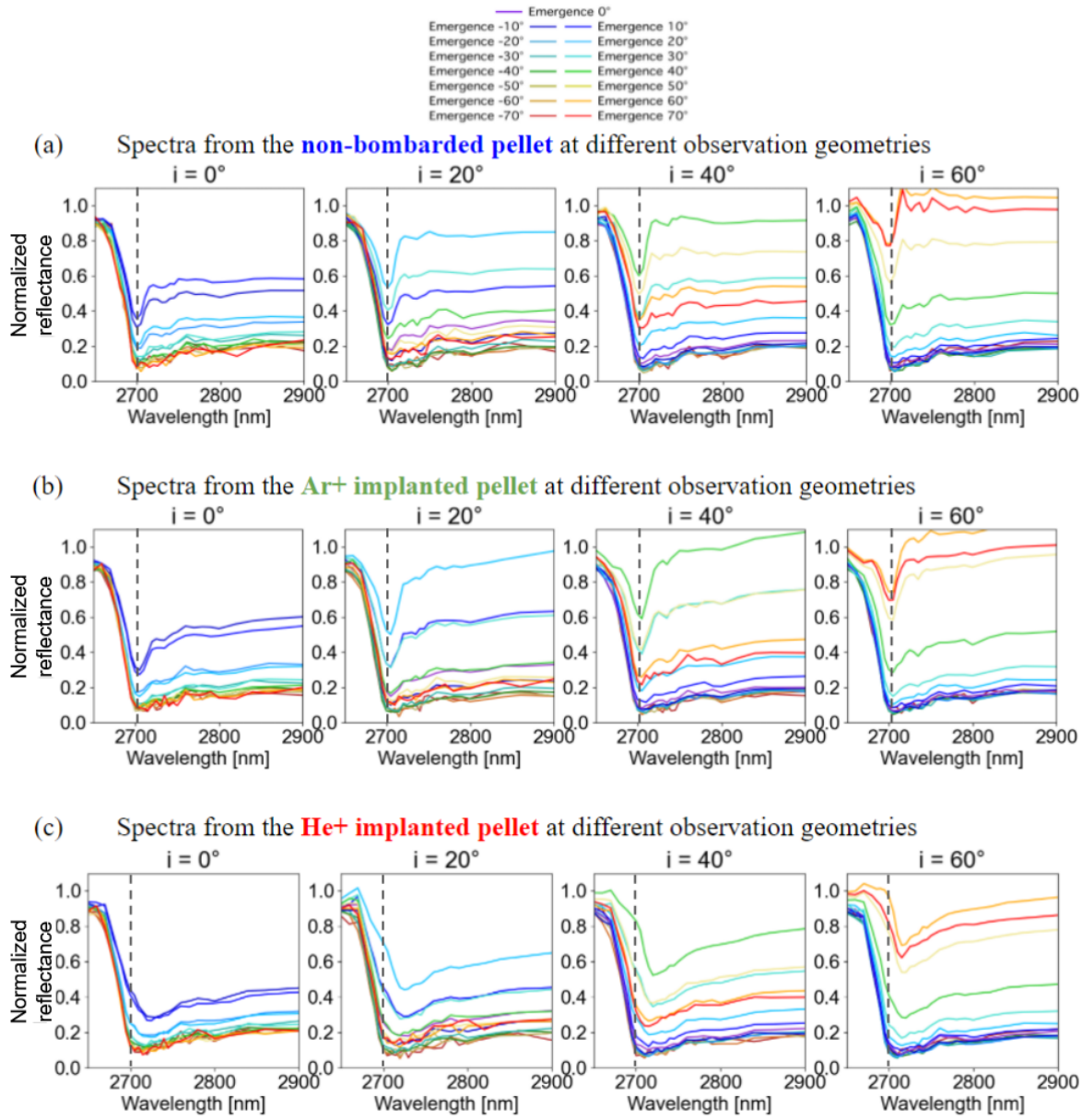

Figure 3.6: REFF spectra centered on the hydration feature, after continuum removal, for the considered trio of Serpentine Rawhide pellets (pristine pellet - panel (a), Ar^+ bombarded pellet - panel (b), He^+ bombarded pellet - panel (c))

All samples show a change in the shape of the hydration band: the feature gets sharper as we approach the near-specular reflection conditions ($i \sim e$). For some of these configurations, we note small peaks pointing up, just after the 2.7 µm feature (the most prominent is seen at approximately

2.715 µm in panel (a), for $i = 60$ and $e = 70$, the red spectrum). These are not artefacts due to the continuum-correction, but may be due to the increase of the specular reflection contribution at these configurations. These small peaks are signatures of the real part of the refractive index of the probed material. The presence of these small peaks can happen since the real part of the refractive index (n always oscillates like a derivative in the spectral region corresponding to an absorption band (see Kramers-Kronig relations). This oscillation is always lower before the band peak and higher after, meaning that the the specular contribution gets lower and then higher as we move towards longer wavelength past the spectral region of the absorption band. This induces two effects:

- a negative (or blue) shift of the 'apparent absorption' peak position when added with the multiple scattering contribution (such as the one seen in the red spectrum in panel (a) for $i = 60$.
- the appearance of a small positive bump after the absorption band (such as the one discussed just before.

For reference, the complex refractive index spectrum in serpentines to illustrate the optical constant's behavior can be found in Mooney and Knacke 1985.

As we look at our pellets individually, we see different behaviours:

- for the non-bombarded sample, the most prominent effect is the change in the shape of the hydration band. Approaching near-specular configuration, the feature gets sharper. Moreover, as the illumination angle i grows, for large phase angles, the apparent blue-shift due to the influence of the optical constants described above gets easier to notice.
- for the Ar^+ bombarded sample, the sharpening effect described above can also be seen in near-specular configurations. The slight shape change effect due to the influence of the optical constants is also noticeable for the $i = 60$, although less intense; there also seems to be a slight band position variability of the hydration feature.

- for the He^+ bombarded sample, the shape of the hydration band is not affected by observation geometry as strongly as in the cases described above (or even at all) ; however, we can see a clear global band red-shift in the position of the feature with respect to the other samples.

For all observations of the ion bombarded samples, in particular geometric configurations, the shape and position of the hydration feature are considerably altered with respect to the non-implanted pellet figure 3.5, panel a). Finally, we note that the curves for i = 0° in panel (a) of figure 3.5 are fairly asymmetric with respect to the emergence angle, which may appear surprising (one would expect in this configuration spectra associated to $e = \alpha$ and $e = -\alpha$ to be similar). This may be due to slight uncertainty in the position of the detector and slight differences on the observation spot position for symmetric emergence angles, possibly coupled to some lateral heterogeneity of the sample.

Having commented on the general observed trend, we shall now delve deeper into the evolution of the spectral parameters associated to the hydration band. More specifically, we shall investigate the evolution of peak position and band depth with the varying geometries. The spectral parameters were derived in a similar way to that of the in-situ INGMAR measurements. After removing a linear continuum between 2.6 to 4 µm, we applied different instances of a Savitzky-Golay filter, using different window size. This allows us to slightly smooth our data while taking in account different possible band shapes and degrees of noise correction. For each smoothed spectrum, we computed the barycenter associated to a spectral region of interested centered on the feature's position. We then averaged the wavelengths obtained for each Savitzky-Golay instance and associated this averaged value with the band position. Since the Savitzky-Golay filter acts as a data interpolation process, by taking in consideration multiple instances, the computed positional value is very precise, with an improved accuracy with respect to spectral sampling and resolution. These parameters still need to be taken in account when discussing the overall accuracy of the measurement. This method allowed us to extract the hydration band peak position associated to all geometries of observation. The band depth associated to the peak position is computed as $1 - R_{Feature}/R_{Continuum}$, considering a linear continuum between 2.6 and 4 µm.

We start with the evolution of the feature's position in the following figure (3.6).

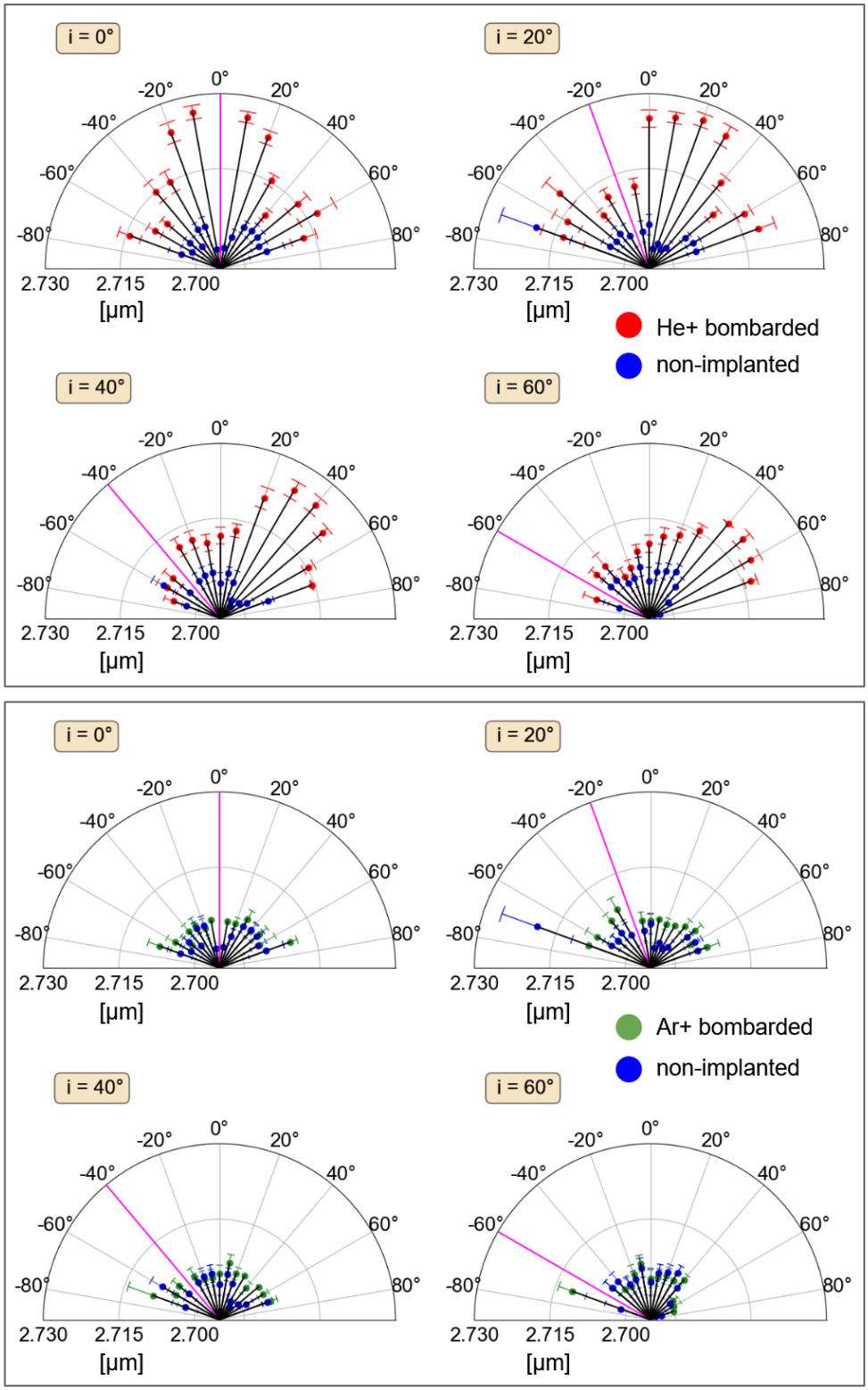

Figure 3.7: Evolution of the hydration feature position at different observation geometries. The position data from the ion bombarded pellets (in red for He^+ and in green for Ar^+) are compared with data from the pristine pellets (in blue). The magenta line indicates the illumination angle i. The polar plots show the evolution of the 2.7 µm peak position as a function of the observation angle e, for fixed illumination angles i. The observation angle e increases clockwise, while the illumination angle i increases counter-clockwise.

The three pellets behaves differently as the geometry of observation changes :

- The peak position for the He^+ bombarded pellet still exhibits a shift towards longer wavelength for virtually all the explored geometric configurations. However, the amplitude of this red-shift can be seen to vary significantly, from a few nanometers to a maximum of $28 \pm 2nm$ (for $i = 0$ and $e = -10$). The larger measured shifts are associated to near-specular configurations (i e, within an angular width of ± 20. Note that for large illumination angles ($\imath = 40°$) and ($\imath = 60°$) the spectral shift also for $i \pm -e$: this may be related to back-scattering effects.

- The effects of Ar^+ bombardment do not seem to affect the peak position significantly with respect to the pristine material, except for near-specular configurations, where a small red-shift can be measured (the larger one with an amplitude of approximately $6nm$. This may also be a limitation from the spectral resolution associated to these REFF measurements ($10nm$ in the hydration feature spectral region, see 2.3.3 for the evolution of the spectral resolution across the measured spectra).

- In the data-set associated to the non-bombarded pellet, we can spot the tiny blue-shift in peak position related to the contribution of the real-part of the refractive index (effect described above). This effect can be seen at near-specular configurations.

Next, the results on the band depth angular dependency are shown in the following figure (3.7). It is relevant to point out that for particularly flat and bright surfaces, band depth and apparent absorbance values can be correlated with albedo when derived from reflectance spectra (Milliken et al. 2007). This complicates the interpretation of band-depth values, especially when approaching specular configurations, due to the related increase in albedo.

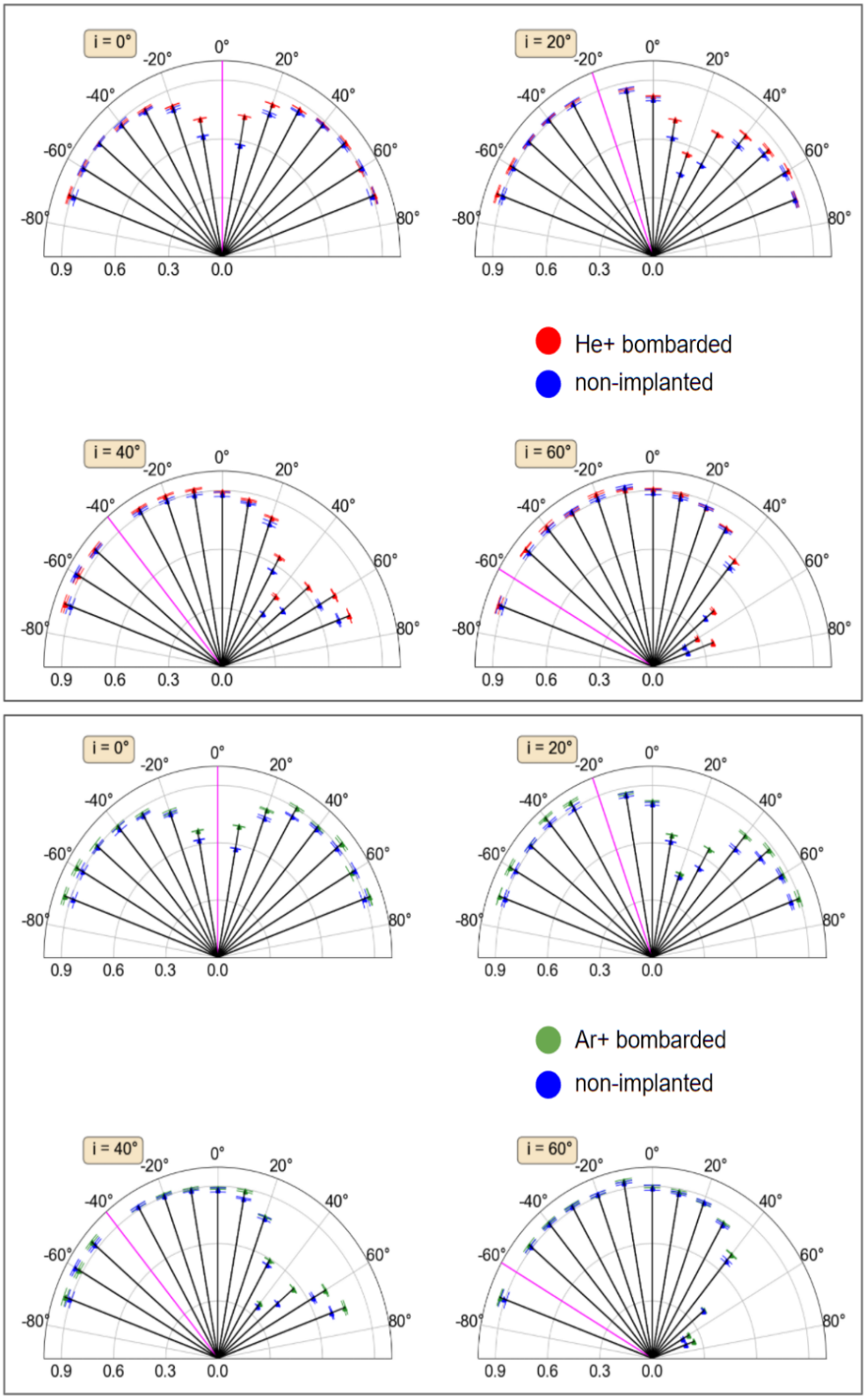

Figure 3.8: Evolution of the hydration feature band depth under different optical geometries for He^+ and Ar^+ bombarded pellets, with respect to the pristine pellet. The magenta line represents the direction of illumination which corresponds to the incidence angle i.

For all pellets, the hydration feature's band depth decreases in amplitude when approaching the specular configuration. For a fixed geometrical configuration, the hydration feature measured on both the bombarded pellets is deeper than for the pristine pellet: in near-specular configurations, the band depth in the He^+ bombarded is $\pm 30\%$ deeper than in the pristine pellet. For the Ar^+ bombarded pellet, the band depth is only $\pm 15\%$ deeper than in the pristine one. The cause of the apparent deepening of the feature upon ion-bombardment is unclear.

Note that these measurements are performed at ambient laboratory conditions $T \sim 300K$ and $P = 1bar$). This means that the shape of the phyllosilicate hydration feature at 2.7 µm may be affected by neighbouring absorption bands, especially by the 3 µm adsorbed water broad feature (corresponding to molecular H_2O water from ambient humidity resting on the sample's surface). However, Exponentially Modified Gaussian (EMG) fitting of our ion-bombarded serpentine Rawhide REFF data-set, presented in Rubino et al. 2022, shows that changes in the shape of the whole hydration band upon bombardment seem to be are dominated by the endogenous phyllosilicate hydration contribution, our absorption band of interest at 2.7 µm.

Discussion

The most prominent effect seen in our data-set is a significant red-shift of the feature's position upon He^+ bombardment. The spectral shift is related to chemical and physical changes induced by the ion bombardment in the first hundreds of nanometers of our pellet's surface. The ions are able to alter the material down to a certain depth, which has been estimated by the SRIM software (Ziegler et al. 2010) to be of approximately $310 \pm 90nm$ for He^+ in serpentines (see section 2.2.3). However, we see that the amplitude of the detected red-shift greatly varies with respect to the geometry of observation. Such diversity highlights that different effects are competing at each geometry, contributing to the apparent band shift. The scattering processes in a multi-layer compact structure are inherently complex, even for an supposedly homogeneous material such as our serpentine Rawhide pellet. Nonetheless, we can discuss the possible contributions of two main competing effects, which are volume (multiple) scattering and surface (specular) scattering.

- Photons undergoing multiple scattering events probe deeper layers of our sample, advancing deeper in the sample's volume. As the illumination angle i increases, these photons will likely probe less deep (as i varies from 0°, where the lights its the sample perpendicularly, to 60°, the photons' implantation depth does not change, but the vertical component of the vector associated to the implantation depth decreases). However, since the sample is observed at wavelengths of 2-3 µm, photons do not resolve layering at the scale of the implanted layer (approximately 300 nm as said above), thus mixing up both bombarded and pristine material.

- Specular scattering is particularly sensitive to the optical properties of the utmost top layers of our samples (surface scattering). In specular reflection, the photons' probing depth length would still mix ion-bombarded and pristine matter, but we can qualitatively expect here to have a more prominent contribution from the ion-bombarded one, compared to volume scattering. This means that the specular component of the measured signal carries more information about the very top layers of our sample, which corresponds to the ion-bombarded matter. This explains why near-specular geometries seem to better relay the effects of ion-bombardment (larger measured band shift). Note that the largest measured shift, corresponding to $i = 0$ at near-specular configuration can also count on back-scattered photons, which are also particularly sensitive the surface layers.

Overall, all the various patterns seen in our data may result from the combination of volume scattering, specular scattering and possibly back-scattering. The observations suggest that measurements at high illumination angles of ion-bombarded surfaces in near-specular configuration will be inherently slightly blue-shifted with respect to measurements done with a smaller illumination angle.

Looking at the Ar^+ bombarded data, we see yet again that the effects on the hydration feature are barely detectable, independently from the optical configuration. As discussed before, the ion-implantation depth associated to Ar^+ is significantly smaller than for He^+ (approximately 300 nm versus 40 nm). Stopping-power profiles for these two ions, shown in Brunetto et al. 2014, highlight the different energy-loss behavior, which explain the difference in the penetration depth of our ions. A smaller penetration depth means that there's less modified matter to probe: the photon's optical

path is dominated by pristine matter, since the thickness of the Ar^+ bombarded layer is much smaller than the wavelength of the probing photon, hence the difficulty in detecting any spectral changes related to the ion-bombardment. The altered layer remains poorly relevant even at specular geometry, where the detected red-shift in peak position is barely noticeable.

These laboratory REFF measurements highlights that there is an optimal geometric configuration to implement when conducting spectroscopic surveys of ion-bombarded, weathered materials. The spectral effects of ion-bombardment on hydrated surfaces can be better observed in near-specular configuration, with near-nadir illumination angle ($i \sim 0$). Incidence angles between 20 and 40° can also suffice, in case near-specular configuration is not achievable. This has consequences for space mission such as sample-return missions or orbiter missions, which shall be discussed in section 3.3.

3.1.2. Mid-IR measurements

We shall now focus on the results from our spectroscopic measurements in the mid-IR. The following measurements were acquired using an Agilent Cary 670/320 micro-spectrometer (the instrument itself and the experimental conditions for these analysis are described in section 2.3.3). The spectral range achieved with this instrument when using the FPA detector spans from 2.5 to 12 µm. This allowed us to probe the effects on ion-bombardment on two phyllosilicate spectroscopic features of interest: the hydration feature at 2.7 µm and the Si-O stretching vibration at $\sim 10m$, associated to the vibration of the Si-O bond in the crystal lattice. We have already discussed the ion-induced variations of the hydration feature above, using data more appropriate to do so (the in-situ data acquired using the INGMAR setup were acquired in vacuum, minimizing the contribution of the neighbouring adsorbed water band; the mid-IR spectra are acquired at ambient conditions). In this section, we shall discuss the effects of ion-bombardment on the 10 µm feature, comparing spectra associated to the pristine material and spectra from weathered material ($6.10^{16} ions/cm^2$ for He^+ and $2.10^{16} ions/cm^2$ for Ar^+). For technical constraints, we were not able to acquire mid-IR spectra from the pristine material, exposing it to ion-bombardment and then acquire spectra from the same region after bombardment for all pellets. More specifically, the pristine and He^+ bombarded spectra are associated to the same pellet and the same region of said pellet, while the

Ar^+ spectra are from another region of another pellets. This means that the He^+ and pristine spectra are directly comparable, while we need to exercise caution when comparing the Ar^+ spectra with the other two cases.

Results

The acquired mid-IR spectra, centered on the the 10 µm feature, are shown in the following figure (3.8). An horizontal continuum, extrapolated by drawing an horizontal line using the Christiansen Feature as an anchor point, has been removed from the spectra.

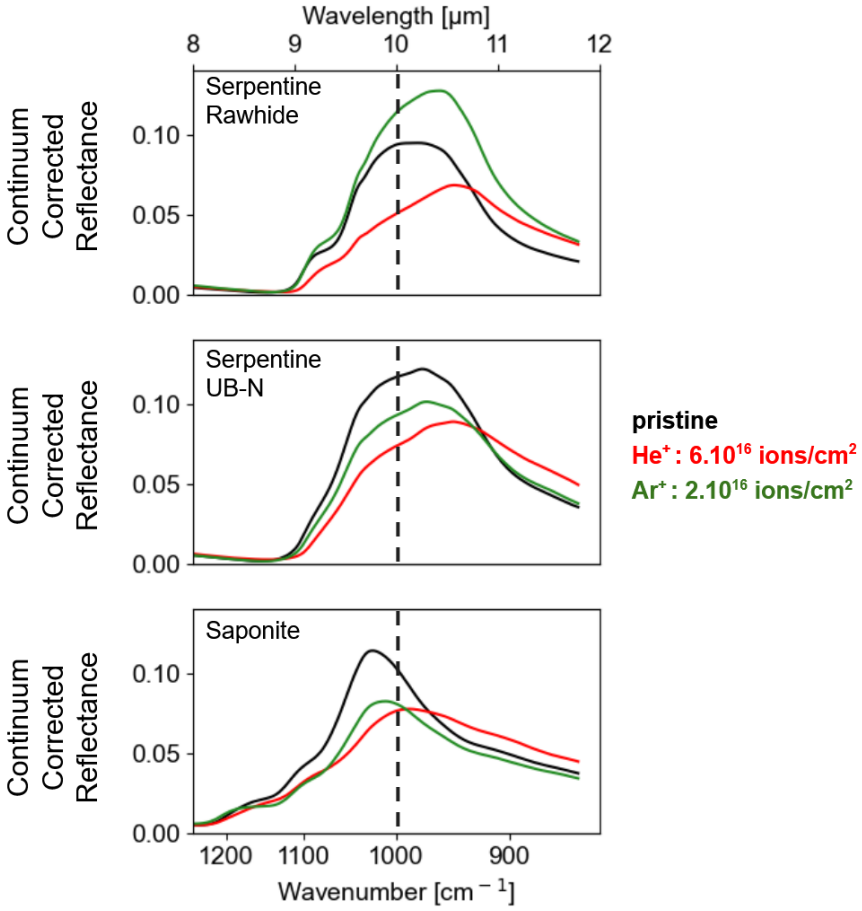

Figure 3.9: Mid-IR spectra centered on the 10 µm Si-O stretching feature of pristine, He^+ and Ar^+ bombarded pellets (in black, red and green respectively).

We see that there are clear changes in the shape of the 10 µm feature upon ion-bombardment, for

both the He^+ and the Ar^+ bombarded samples. The most prominent changes are detected for the He^+ bombarded samples. However, contrary to what we have seen in the previous sections in the near-IR range, where it was difficult to distinguish between data from pristine and Ar^+ bombarded material, the effects of Ar^+ bombardment are clearly noticeable here. This is probably due to the fact that, in the mid-IR range, from the Christiansen Feature and towards longer wavelength, the collected signal is dominated by surface scattering in our optical configuration. We are hence sensitive enough to the thin layer of Ar^+-bombarded material to be able to detect spectroscopic effects of the physico-chemical changes affecting these layers.

Different trends are seen among our ion-bombarded samples:

- One common trend is a noticeable red-shift towards longer wavelengths of the IR features. Note that this does not corresponds in reality to a band-shift "per se", but rather the consequence of a difference in the intensity of the 10 µm band contributions (Brunetto et al. 2020.

- We see a noticeable decrease in the overall reflectance of the 10 µm feature for all He^+ bombarded samples and for both the Ar^+ bombarded Serpentine UB-N and Saponite. The Ar^+ bombarded Serpentine Rawhide stands as an outlier, appearing brighter than the pristine material.

- All samples, except the Ar^+ bombarded Saponite sample, exhibit different degrees of band broadening.

In order to better discuss the difference in behaviour upon bombardment, we extracted relevant spectral parameters associated to the 10 µm feature: its peak position (associated to its maximum reflectance), the band area and the full-width at half of maximum (FWHM). The evolution of these parameters upon ion-bombardment is shown in the following figure (3.9).

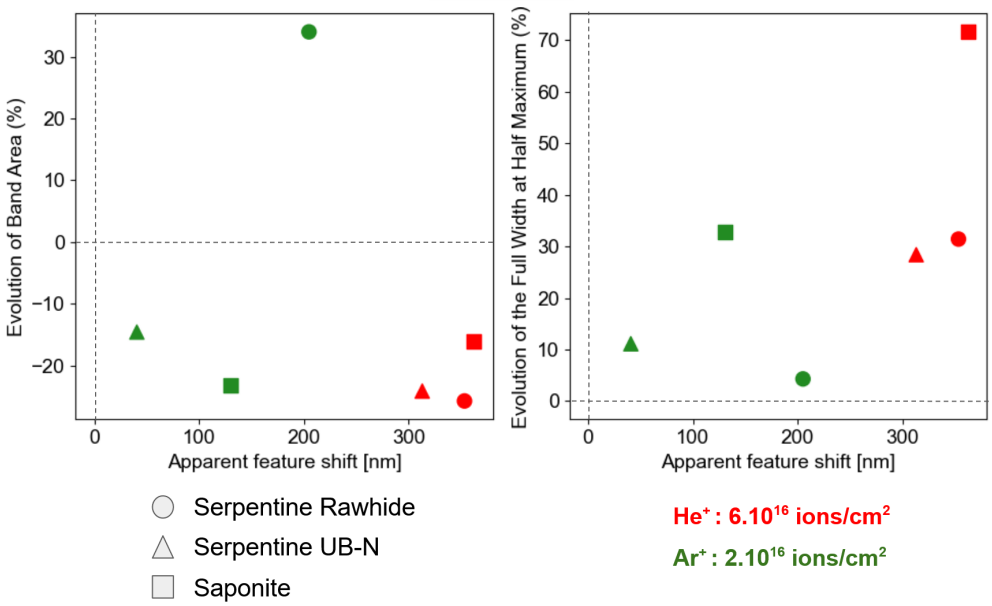

Figure 3.10: Evolution of the SiO-stretching band parameters at 10 µm upon He^+ and Ar^+ bombardment. In the left figure, the evolution of the band position and the band area are showed, while in the right panel, the evolution of the band position is plotted against the changes in the FWHM. The changes of these parameters are computed with respect to the parameters associated to the pristine material.

We see that the 10 µm feature for all He^+ bombarded samples undergoes a significant red-shift (shift $>$ 300 nm), as well as noticeable decrease in band area (up to -25% for He^+ bombarded Serpentine Rawhide). A greater discrepancy is seen for the evolution of the FWHM, used here to assess band broadening: for both serpentines, the 10 µm feature broadens up to +30% approximately, while for the saponite sample, upon He^+ bombardment, the feature broadens to more than 70% compared to the FWHM of the pristine material.

Changes on the Ar^+ bombarded Serpentine UB-N and Saponite peak position and band area are analogous to those of their He^+ bombarded "cousins", but less significant. The real outlier is the Ar^+ bombarded Serpentine Rawhide sample, exhibiting quite a significant band-shift (close to 200 nm), and a significant increase in band area (+33%). Broadening is less intense for the Ar^+ bombarded serpentines, and appear to be significant only for the Ar^+ bombarded saponite sample (+33%).

Discussion

The Ar^+ bombarded serpentine Rawhide sample appears as an outlier in our data-set: the significant increase in band area is puzzling. After closer inspection, it appears that the region of the pellet surface where I measured the Ar^+ spectra showcases many more 'flat' crystals, which would increase the overall reflectance by maximising the specular component of the incident photon beam (see figure below). This complicates the interpretation of comparison between reflectance values between the Ar^+ bombarded samples and the other, at least for the serpentine Rawhide.

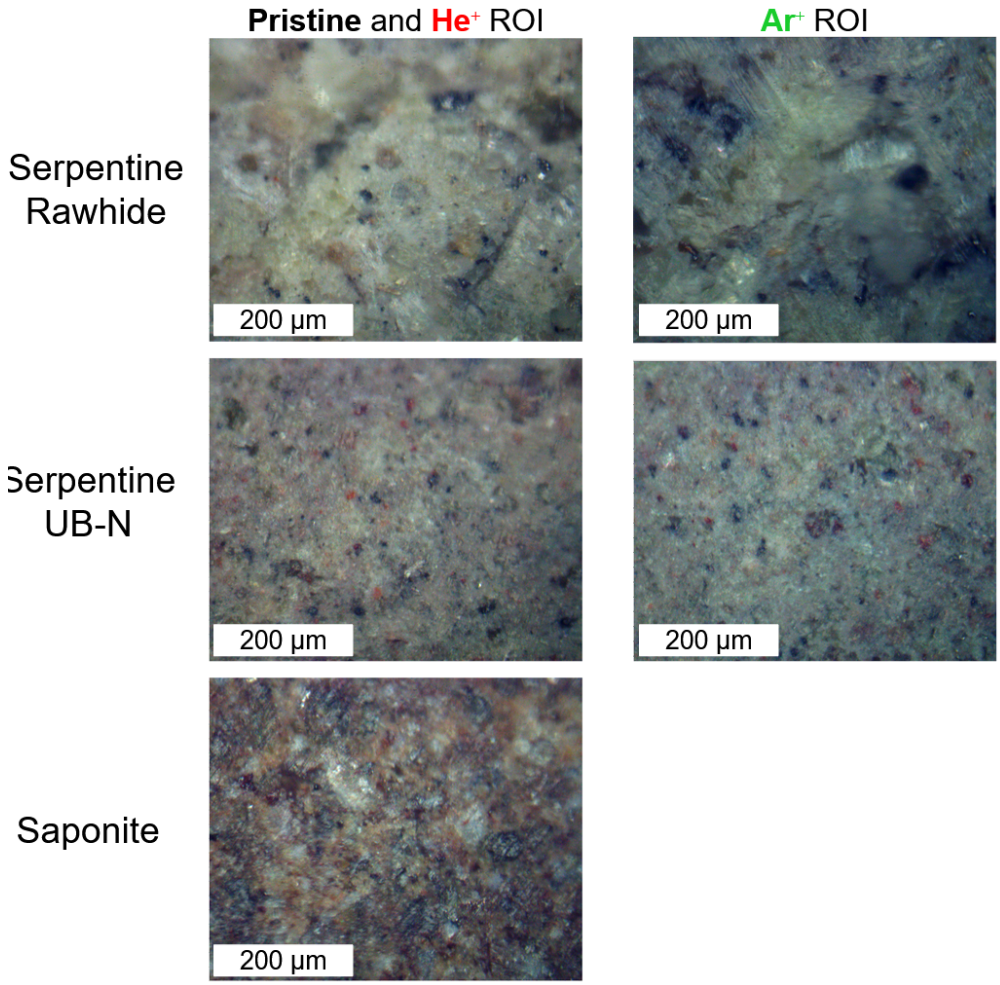

Figure 3.11: Regions of interest (ROIs) of the hyperspectral tiles for the pristine, He^+ and Ar^+ bombarded spectra. The Ar^+ bombarded saponite surface is missing because the optical image was not captured during the infrared acquisition.

The position of the Si-O stretching feature is tightly linked to its environment, and Si-O stretching modes with different environment contribute to the overall shape of the broad 10 µm band. An apparent band shift such as the one observed here upon ion-bombardment highlights the presence of significant chemical changes in the Si-O bond's environment. Generally speaking, Si-O stretching modes at longer wavelength are associated with Fe-rich phyllosilicates. The apparent red-shift of the 10 µm band may be interpreted by preferential amorphization of Mg upon ion-bombardment, causing a "virtual Fe enrichment" in the phyllosilicate structure. This "virtual Fe enrichment" seems to be present in both the He^+ and the Ar^+ bombarded samples.

Band broadening and band area decrease can generally be correlated to amorphization (disordering of the mineral crystal lattice, in this case due to damage sustained from the ion bombardment). We find significant broadening for all He^+ bombarded samples, associated to a consistent decrease in band area, compared to changes for the Ar^+ bombarded samples: this would suggest that, for a given volume probed by mid-IR photons, He^+ bombardment is a more efficient in amorphization process than Ar^+ bombardment. The larger implantation depth associated to He^+ is probably what gives He^+ its "edge" against Ar^+, as often seen in these spectroscopic measurements. This had already been discussed by Brunetto et al. 2014 on He^+ and Ar^+ bombarded olivine samples while also studying the 10 µm feature.

Band broadening upon ion-bombardment seems to be particularly sensitive to the crystal lattice of the bombarded matter, since for both bombarding ions we see a separation between the two serpentines and the saponite. For band broadening evolution, the two serpentines change in a similar way, and appear to be consistently less affected than the saponite sample. This would possibly suggest that the Si-O bond in saponite is more sensitive to amorphization than in serpentines. This contradicts one of the hypothesis made in the in-situ data analysis section, where we proposed that the separate TO layer of saponite would be able to better absorb and dissipate perturbations from ion-bombardment than the compact TOT structure of serpentines. The mid-IR results discussed here give more leeway to preferential amorphization of Mg as an explanation for the difference in behaviour observed for the 2.7 µm hydration feature. This subject shall be again discussed when

tackling the results from transmission electron microscopy (section 4.2).

Overall, the spectroscopic results in the mid-IR have shown that the 10 µm feature is more sensitive to ion bombardment than the 2.7 microns feature. The 10 µm feature is even able to efficiently relay the effects of Ar^+ bombardment, which remained difficult to quantify in the near-IR data. Being dominated by surface scattering means being much more sensible to the physico-chemical changes happening in the utmost top layers upon ion-bombardment, which translates into an apparent band-shift. The intensity of the various contributions of the 10 µm feature shift to facilitate the expression of more Fe-rich environments, with the He^+ bombarded Serpentine Rawhide presenting the larger observed shift. We also see significant band area decrease and band broadening, consistent with amorphization related to ion-bombardment, with the Saponite sample appearing to be more consistently sensitive to this process.

3.1.3. Far-IR measurements

In order to complete this extensive spectral characterization of our ion-bombarded pellets, we acquired spectra in the far-IR range, from 15 to 50 µm. The experimental setup and conditions associated to these measurements are described in section 2.3.3. As a reminder, the spectra showed below are collected on a 200x200 µm region, located at the pellets' center, at a spectral resolution of $4cm^{-1}$ (corresponding to approximately 0.16 µm in the 20 µm region and 0.98 µm in the 50 µm region), averaging 512 scans. Acquiring spectra in the far-IR range allows us to investigate the effects of ion-bombardment on spectroscopic features linked to the Si-O and (M)-OH bending vibrations in the crystal lattice (Schroeder 2002, Bishop 2018). For hydrated silicates the most common spectra features of interest include:

- A broad band associated to the Si-O bending modes, which occur between between 600 and 400 cm^{-1} (16.6 - 25 µm). This broad feature includes the spectral contributions of the Si-O-Si bending vibration centered near 470-485 cm^{-1} ($\sim$ 20.6-21.3 µm) and the Si-O-(M) bending vibration near 400-450 cm^{-1} ($\sim$ 22-24 µm), where (M) is an octahedral cation such as Al, Fe or Mg (Salisbury et al. 1987,Bishop 2018).

- Less intense bands which can be detected in the 833-600 cm^{-1} range (12 to 16.7 µm), associated to Si-O-Si, Si-O-Al or Si-O-Fe stretching vibrations (Salisbury et al. 1987).

- The (M)-OH bending bond, localized between 600 and 950 $cm - 1$ (10.5 - 16.6 µm) (Farmer 1974, Glotch et al. 2007, Bishop 2018).

Note that the (M)-OH bending feature is only visible for the serpentine samples. Its position, approximately 645 cm^{-1} corresponds to the Mg-OH bending vibration. Our saponite sample is particularly Fe- and Al-rich (3.7 and 5.8 At.% respectively, compared to 5.2 At.% for Mg - values derived by elemental composition given in 2.1.1 by SEM-EDS). It is possible that the (M)-OH bending mode for our saponite sample falls outside of the measured spectral range (Bishop et al. 2002 and reference therein reports positions for Al_2OH, $AlFe^{3+}OH$, Al_2MgOH, Fe^{3+}_2OH, $Fe^{3+}MgOH$ and Fe^{3+}_2OH in saponites to be all between 785 and $920cm^{-1}$) and that the small Mg-OH component is drowned in the noise of the data, since it should be located near the limit of the explored spectral range.

We shall first present the effects on the whole spectral range. Then, once having identified the spectral features most affected by weathering, we shall extract the spectral parameters associated to these features, in order to better quantify the changes upon bombardment. The overall spectral evolution of our bombarded pellets is shown in the following figure (3.10).

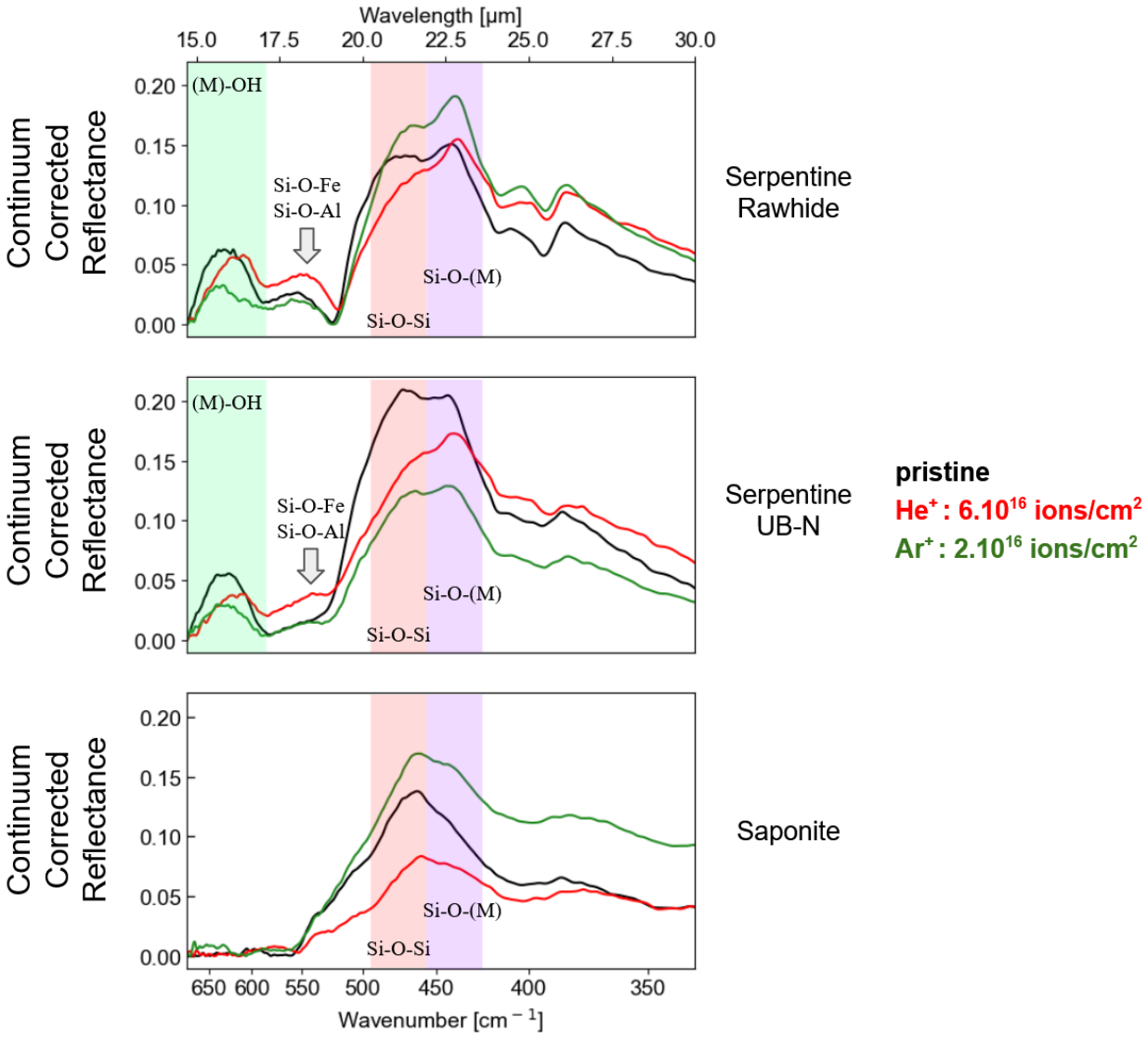

Figure 3.12: Far-IR spectra of the pristine, He^+ and Ar^+ bombarded pellets (in black, red and green respectively), showing the evolution upon ion-bombardment of multiples spectroscopic features.

Upon ion-bombardment, we can identify the following trends:

- For Serpentine Rawhide, upon He^+ bombardment, the whole spectrum up to 25 µm seems to shift towards longer wavelength. The relative intensity of the various spectral features also changes, especially for the broad 20 µm feature, as the Si-O-Si bending contribution seem to decrease, while the Si-O-(M) bending contribution increases and shifts towards longer wavelengths. The feature at 545 cm^{-1}, associated to the weak Si-O-(M) stretching bands,

seem to increase.

For the Ar^+ bombarded sample, the features do not seem to shift, with the exception of the left shoulder of the 20 µm feature (the Si-O-Si bending contribution), exhibiting a slight shift towards longer wavelength. We see great changes in the features' relative intensities: the (M)-OH feature greatly shrinks with respect to the pristine sample, while the 20 µm feature greatly increases.

- For Serpentine UB-N, we see similar changes than for Serpentine Rawhide. Upon He^+ bombardment, the whole spectrum up to 25 µm shifts towards longer wavelength, and the 20 µm feature's left shoulder (the Si-O4 bending contribution), leaving the Si-O-(M) contribution as the dominant one of the feature.

  For Ar^+ bombardment, we see no clear spectral shift, but radical changes in band intensity (decrease of the (M)-OH bending feature and of the broad 20 µm band). No noticeable change can be seen for the Si-O-(M) stretching feature at 545 cm^{-1}.

- In the case of Saponite, the main noticeable feature to discuss about is the Si-O-Si bending feature associated to the 20 µm band. The feature appears more peaked than for both serpentines, and does not exhibit clear spectral shift upon He^+ nor Ar^+ bombardment. However, for both cases, the band seems to get slightly broader.

To better assess the ion-induced changes, we extracted the following spectral parameters:

- The band maximum position and the band area of the (M)-OH bending feature (only for both serpentine samples).

- The band maximum position and of the broad 20 µm feature as well as the ratio between the area of the right shoulder and the left shoulder of the feature. This is done to probe the evolution of the two main contributions of the feature, Si-O-Si bending (left shoulder) and Si-O-(M) bending (right shoulder) with respect to one another.

These parameters were extracted from the continuum-corrected spectra, after applying Savitzky-

Golay filtering (windows size 35, order 2) in order to slightly smooth the spectra. The continuum is a "rubber-band" type continuum from 16.66 µm to 35.7 µm (from 600 to 280 cm^{-1}). The band position are associated to the feature's maxima. The area of the left and right shoulders of the 20 µm feature are computed between 523 - 456 cm^{-1} and 456 - 414 cm^{-1} respectively (approximately 19.1 - 21.9 µm and 21.9 - 24.1 µm). In the publication to come, which will be associated to these measurements, the same parameters will be derived using curve-fitting, and compared to those derived here.

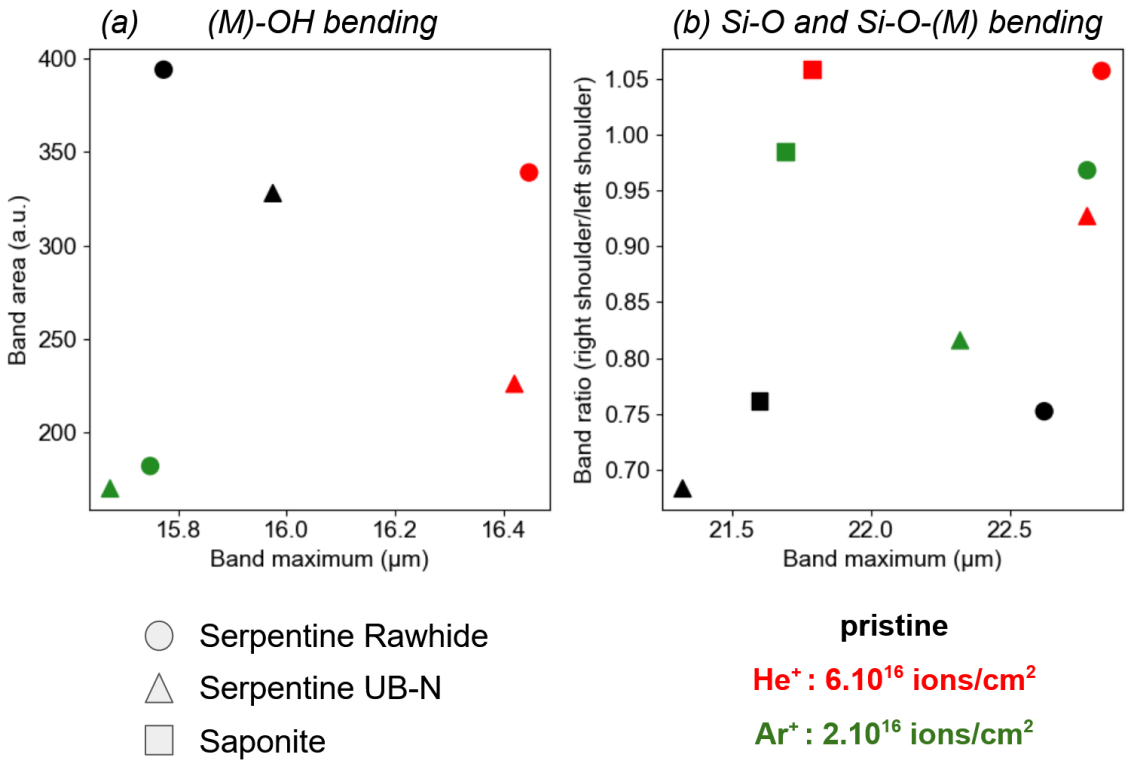

Figure 3.13: Evolution upon He^+ and Ar^+ bombardment of the spectral parameters associated with two features: the (M)-OH bending vibration feature (panel a) and the broad 20 µm feature, associated with Si-O and Si-O-(M) bending.

The (M)-OH bending feature, as seen before, is visible only for the serpentine samples. Upon He^+ bombardment, the feature's position greatly shifts towards longer wavelength, similarly to what happens for the (M)-OH stretching feature at 2.7 µm, but with a far greater shift (for Serpentine Rawhide we detect a shift of approximately 680 nm, while for Serpentine UB-N the shift is of

approximately 450 nm). For both serpentines, the position of the feature after He^+ bombardment is close to 16.4 µm (16.45 µm for Serpentine Rawhide and 16.42 µm for Serpentine UB-N). This shift towards longer wavelength is accompanied by a decrease in band area for both serpentines (approximately -14% for Serpentine Rawhide and -30% for Serpentine UB-N).

Upon Ar^+ bombardment, the (M)-OH feature's maximum shifts slightly towards shorter wavelengths (15.74 for Serpentine Rawhide and 15.67 µm for Serpentine UB-N), with a spectral shift of -30 nm for Serpentine Rawhide and -300 nm for Serpentine UB-N. The detected shift for Serpentine Rawhide is within the measurement error brackets, however we do see a change in shape of the feature which suggests a larger shift of the band center in figure 3.10: we are here witnessing the limits of assimilating band maxima with feature position.

The broad 20 µm shifts for all samples upon both He^+ and Ar bombardment, with the largest shift being associated to the He^+ bombarded serpentine UB-N (almost +1.5 µm). For all samples, the He^+ bombarded samples is more shifted than the Ar bombarded one by approximately 28%. The band area ratio increases upon bombardment for all samples, indicating that the Si-O-Si bending contribution gets less relevant upon bombardment compared to the Si-O-(M) bending.

Discussion

Changes in feature's position reflect what we have observed for the associated stretching band. The detected red-shift for the (M)-OH bending features in He^+ bombarded serpentines and for the broad 20 µm feature follows the previous discussions regarding preferential amorphization/sputtering of Mg for ion-bombarded samples, shifting the feature's position towards more Mg-poor/Fe-rich related positions. For the (M)-OH bending feature, this is further supported by the decrease in band area upon He^+ bombardment, and by its identification as the Mg-OH feature specifically. The Ar^+ bombarded (M)-OH exhibits a slight blue shift, accompanied by a harsh band area decrease. This would be correlated with an amorphization process which would not be biased by preferential sputtering of some elements, and would efficiently amorphize the whole ion-implanted structure.

The (M)-OH bending feature's position for pristine serpentine Rawhide and serpentine UB-N dif-

fers between the two samples (15.77 µm for Serpentine Rawhide and 15.97 for Serpentine UB-N), highlighting the slight compositional difference between them: Serpentine UB-N is more Fe- and Al- rich than Serpentine Rawhide, which shifts the position of the (M)-OH bending towards longer wavelength with respect to Serpentine Rawhide.

For serpentine Rawhide He^+, we have noticed the slight increase of the 545 cm^-1 feature, associated to the Si-O-(M) stretching feature. This would appear counter intuitive. However, in this spectral range there is a small band at 530$cm1$ which belongs to the perpendicular Mg-O vibrational mode. The feature's increase possibly highlights the creation/enrichment of the material in an Mg and O rich component, created upon ion-bombardment. If this is the case, this component should be identifiable during our STEM analysis (see Chapter 4).

The evolution of the broad 20 µm feature indicates changes at scale of the structural layers of the minerals' crystal lattice. Upon both He^+ and Ar^+ bombardment, the feature's maximum shifts towards longer wavelength, indicating changes in the relative contributions of its two spectral constituents (the Si-O-Si bending vibration - left shoulder - and the Si-O-(M) bending vibration - right shoulder). A shift towards longer wavelength indicates that the change upon ion-bombardment is in favour of the Si-O-(M) feature. This is also highlighted by the increase of the band area ratio upon bombardment: for all samples, upon ion-bombardment, the band area ratio increases, from approximately 0.7-0.75 for the pristine samples to larger values (from 0.81 for Ar^+ bombardment Serpentine UB-N to 1.06 for Serpentine Rawhide). This change means that the Si-O-(M) contribution gets more relevant than the Si-O-Si in the crystal lattice of our samples, i.e., effects of ion-induced amorphization are more prominent on the tetrahedral layer than on the octohedral layer of our samples' crystal lattice. The larger effect observed for the He^+ bombarded samples may be explained again by its larger implantation depth with respect to Ar^+.

The interpretation of the spectral changes observed here shall be compared with direct electron microscopy measurements, at a smaller scale, in Chapter 4.

3.1.4. Summary : spectral changes on hydrated silicates upon ion-bombardment

For the sake of clarity, prior to discussing the spectral changes induced by these ion-bombardment experiments with respect to remote-sensing and laboratory analysis of primitive material, we shall recap the observed trends in the following tables.

			He^+, 40 keV, 6E16 ions/cm²		
			Serpentine Rawhide	Serpentine UB-N	Saponite
Visible	Albedo at 0,55 µm		Darkening	Darkening	Darkening
	Slope from 0,48 - 0,7 µm		Reddening	Reddening	Blueing
Near-IR	Hydration feature (M)-OHs at 2,7 µm	Position	Red-shift	Red-shift	-
		Intensity	↗	-	↘
Mid-IR	Silicate feature Si-Ob 10 µm	Position	Red-shift	Red-shift	Red-shift
		Band area	↘	↘	↘
		Band asymmetry	↗	↗	↗
Far-IR	Hydration feature (M)-OHb at 16 µm	Position	Red-shift	Red-shift	*not-detected*
		Band area	↘	↘	
	Silicate feature Si-O and Si-O-(M) at 20 µm	Position	Red-shift	Red-shift	Red-shift
		Si-O contribution wrt. Si-O-(M)	↘	↘	↘

Figure 3.14: Summary table of ion-induced spectroscopic changes among hydrated silicates for 40 keV He^+ at a fluence of $6 * 10^{16} ions/cm^2$.

			Ar⁺, 40 keV, 2E16 ions/cm²		
			Serpentine Rawhide	Serpentine UB-N	Saponite
Visible	Albedo at 0,55 µm		Brightening	Brightening, then Darkening	Brightening, then Darkening
	Slope from 0,48 - 0,7 µm		*no clear trend*	*no clear trend*	*no clear trend*
Near-IR	Hydration feature (M)-OHs at 2,7 µm	Position	Red-shift	-	-
		Intensity	↗	↗	-
Mid-IR	Silicate feature Si-Ob 10 µm	Position	Red-shift	Red-shift	Red-shift
		Band area	↘	↗	↘
		Band asymmetry	↗	↗	↗
Far-IR	Hydration feature (M)-OHb at 16 µm	Position	Blue-shift	Blue-shift	*not-detected*
		Band area	↘	↘	
	Silicate feature Si-O and Si-O-(M) at 20 µm	Position	Red-shift	Red-shift	Red-shift
		Si-O contribution wrt. Si-O-(M)	↘	↘	↘

Figure 3.15: Summary table of ion-induced spectroscopic changes among hydrated silicates for 40 keV Ar^+ at a fluence of $2 * 10^{16} ions/cm^2$.

3.2. Implications for space missions

3.2.1. Remote sensing data of hydrated carbon-rich bodies

In the previous sections, we have seen the effects of ion-induced weathering on the spectral signatures of hydrated silicates, from the visible range to the far-infrared. One of the scopes of this work is to determine possible biases in the spectroscopic identification of weathered materials by remote sensing. However, not all the spectral trends described above can be valid proxies for assessing material weathering through remote sensing. In this section, we shall summarize the most prominent changes we observed in our laboratory data and discuss their detectability in the context of space missions. Prior to this discussion, we shall recap the most prominent spectral changes identified in our laboratory data.

- In the visible range, weathering appears to be dominated by inelastic energy loss, since the only clear detectable spectroscopic trend is associated to the He^+ bombarded samples. We see clear darkening among all samples, coupled with slope reddening for serpentines and blueing

for saponite.

- In the near-IR range, the (M)-OH stretching band (2.7 µm) changes in both shape and position upon bombardment. The most prominent effect is a slight shift of the band's center towards longer wavelength (+19 nm for the largest detected shift in He^+ bombarded Serpentine Rawhide for the in-situ measurements). Note that our REFF measurements indicates that this shifts amplitude is dependent of the geometry of observation, with the shift's amplitude getting larger for measurements more sensitive to the surface layers (near-specular configurations).

- In the mid-IR range, clear spectroscopic trends can be identified for both He^+ and Ar^+ weathering: we see for all samples a clear shift of the band-center towards longer wavelength (from +40 nm up to +360 nm shift for Ar^+ Serpentine UB-N and He^+ bombarded Saponite respectively). We also detect some degree of band broadening, particularly intense for the He^+ bombarded samples.

- In the far-IR range, two features of interest, the (M)-OH bending at 16 µm and the broad Si-O bending 20 µm show changes upon ion-bombardment. The (M)-OH bending feature shifts towards longer wavelength upon He^+ bombardment, while we see either a slight blue-shift or no shift at all upon Ar^+ bombardment. In both cases, the band area shrinks. The 20 µm feature's band maximum also shifts towards longer wavelength, as the contribution of the Si-O-Si bending contribution diminishes with respect to the Si-O-(M) one.

Regarding weathering-induced changes with respect to reflectance and slope in the visible range, as tackled in the introduction, a number of laboratory studies have identified clear trends in anhydrous bodies. Darkening coupled with reddening has been seen on both terrestrial silicates and ordinary chondrites as well as lunar material (see Clark et al. 2002 and references therein). Remote-sensing data acquired of the surface of the Moon has also contributed in re-affirming that fresher, younger surfaces appeared brighter and bluer than more weathered, older regions (Pieters and Noble 2016). On carbonaceous and hydrated materials, a number of effects such as darkening, brightening, red-

dening and bluing has been observed across multiples laboratory studies focusing on carbonaceous chondrites and in one other case pure phyllosilicates (Lantz et al. 2017, Thompson et al. 2019, Matsuoka et al. 2020, Laczniak et al. 2021, Nakauchi et al. 2021), indicating that changes in the visible range my be a proxy for SpWe on these type of matters more difficult to interpret that for anhydrous materials. In our work, we detect slight darkening coupled with reddening for our Mg-rich serpentines and blueing for our Fe-rich saponite. The analysis at smaller scale lead with electron microscopy may help (in Chapter 4) in assessing if this difference in behaviour is related to the differences in crystal lattice among these phyllosilicate families or related to the samples' iron content. However, slight darkening and slope changes seen upon ion-bombardment of the laboratory data do not suffice on their own to assess weathering state of surface materials, since other effects may dominates for real-case surfaces, such as photo-metric effect from the surface topography or changes in the surface's grain size (our results are nonetheless put in perspective with remote sensing data on carbonaceous asteroids Ryugu and Bennu in a dedicated paragraph further down).

Direct band area measurement would not act as a good proxy of weathering for similar reasons. However, a common change seen at every spectral range is a shift towards longer wavelength of band centers associated to spectroscopic features linked to metallic cations in the phyllosilicate lattice, mainly the (M)-OH and Si-O-(M) stretching and bending modes. The amplitude of this spectral shift does depend on the geometry of observation (our results indicates so at least for the (M)-OH stretching feature), but this dependency implies that there exists an optimal geometry to observe space-weathered surfaces, where the spectroscopic changes induced by ion-bombardment are more prominent. Spectral changes on hydrated surfaces in the near-IR can be better observed near specular configuration with near-nadir illumination angle (although small incidence angles between 20° and 40° can also suffice, in case near-specular configuration is not achievable). For remote-sensing data, the optimal observational configuration would correspond to spectroscopic surveys done in nadir configuration (the detector onboard the orbiting craft is observing perpendicularly to the surface of the studied body) with a small phase angle.

However, we have to precise that the laboratory results on angle dependency were derived on par-

ticularly flat surfaces, while real object often exhibits a more complex topography. Moreover, many atmosphere-less bodies are covered in regolith, which weakens the specular components contribution of the overall collected signal. However, both the Hayabusa2 and OSIRIS-REx mission are helping re-defining the idea that regolith covers the entirety of a small body's surface (light regolith may escape the gravitational pull of small bodies, or flow and accumulate in certain regions). Some geographical region, with less regolith, or with fractured boulders (exposing flat surfaces) could exhibit a stronger specular component, which would possibly be significant enough to carry sensible information for surface composition studies. The detected spectral shift gets larger and larger with the increase of wavelength, from tenth of nanometers for the (M)-OH stretching feature at 2.7 µm, to hundreds of nanometers for the Si-O stretching feature at 10 µm, up to a few microns for (M)-OH and Si-O bending features in the far-IR. This means that similar amplitude shifts could be detectable by current generation space instruments, such as those on both the Hayabusa2 and the OSIRIS-REx crafts (spectral sampling of $\sim$ 18 nm for NIRS3 on-board Hayabusa2 - Iwata et al. 2017 -, $\sim$ 10 nm and $\sim$ 80 nm for OVIRS and OTES respectively on-board OSIRIS-REx - Reuters et al. 2018 and Christensen et al. 2018). This would suggest that focusing on spectral shift would serve as a good proxy to distinguish between pristine and weathered material.

However, the band center position also does not suffice on its own to asses material weathering. Band centers are related to the chemical composition of the analysed material. If we take the case of Ryugu and Bennu, the phyllosilicate peak position observed at the surface of these two bodies is about 2.72 µm and 2.74 µm respectively (Kitazato et al. 2019, Hamilton et al. 2019), and appears to be quite homogeneous across the bodies' surface. These peak positions are compatible with both weathered materials and phyllosilicates with different compositions. It is not possible to discriminate on the two scenarios based on the peak band center only. Nonetheless, since band center shifts are such a prominent effect, discussing the results of spectroscopic surveys with respect to geographical and topographical context could allow us to acquire sufficient information to infer from band position the weathered state of the analysed material (this is discussed in Riu et al. 2021, where the analysis of natural Ryugu craters highlights that for younger surfaces, the hydration feature appears slightly blue-shifted - indicating the presence of less altered material). For young

surfaces ($< 10^7$ years in the inner solar system), where surface processing is dominated by space-weathering (Vernazza et al. 2009, Noguchi et al. 2014, Bonal et al. 2015), less weathered terrains should exhibits band centers at shorter wavelengths than the older, more weathered materials. By surveying specific geographical regions, such as impact craters, one would expect to see spectroscopic variations driven by space-weathering, in line with the spectroscopic changes described above (band position changes, albedo and slope evolution). All these trends are also in line with studies led on non-hydrated S-type asteroids, for which laboratory studies have also identified characteristic spectral trends associated to weathering, such as darkening and reddening of the visible slope (Brunetto et al. 2015 and references therein).

Regarding hydrated primitive bodies, the SCI crater experiment onboard Hayabusa2 (Arakawa et al. 2020) provided an excellent test to investigate surface properties changes between weathered and more pristine sub-surface material. An artificial crater on the surface of Ryugu was produced by launching a 2 kg copper projectile at a velocity of $2km/s$. The goal of this experiment was to expose the asteroid sub-surface for remote-sensing and sample-collection. Kitazato et al. 2021 investigate the spectral differences between the surface and sub-surface of the SCI-crater region, by comparing the spectra from far away regions from the impact site with spectra near the crater region. The investigation was conducted by normalizing the spectra associated to the crater region with a surface "standard" of Ryugu (chose to be representative of Ryugu). The results from Kitazato et al. 2021 are shown in the figure below.

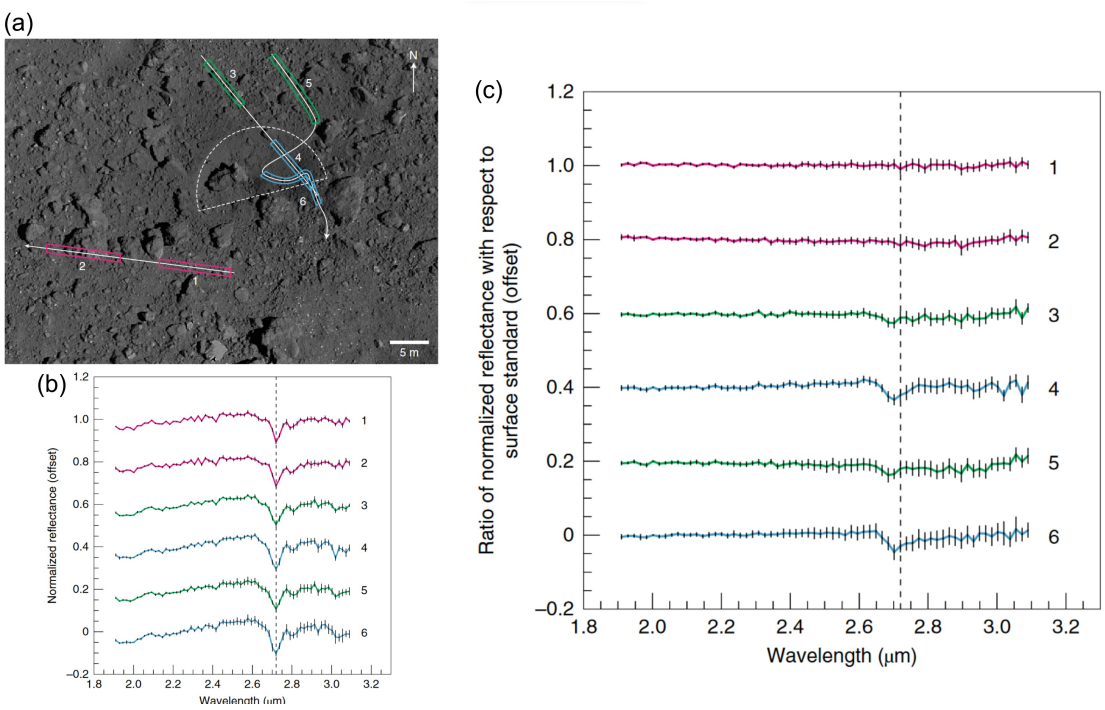

Figure 3.16: From Kitazato et al. 2021: NIRS3 observations of the SCI crater region. (a) Context image taken by the ONC-T camera. The dashed semi-circle represents the rim of the SCI crater. The arrows indicate the motion of NIRS3 footprints during three descent operations. (b) NIRS3 spectra averaged over regions corresponding to the coloured boxes shown in a. The colour of each site represents its surface characteristics: magenta, green and cyan are the ejecta-free region, ejecta-rich region outside the crater and ejecta-rich region inside the crater, respectively. Error bars are 1 within the boxes. (c) Ratios of the normalized spectra shown in b to the ones of the surface standard for Ryugu. The spectra are normalized and vertically shifted for clarity. The dashed vertical lines at 2.72 m denote the peak wavelength of the OH absorption of the spectra in b.

Ratio-ed spectra from far away regions appear almost flat, while those associated to regions closer to the crater show the presence the OH feature, getting stronger and more shifted towards shorter wavelenght for the ejecta regions from the impact (associated to more primitive material from the subsurface). The OH feature in this sub-surface rich regions peaks at 2.7 µm, exhibiting a shift of $20nm$ compared to the "standard" position of 2.72 µm detected across Ryugu's surface. The amplitude of the detected spectral shift is compatible with our ion-bombardment experiments (considering the scarse spectral sampling of NIRS3), indicating a possible origin related to SpWe.

SpWe effects are also being investigated for B-type Bennu asteroids. Bennu's visible spectra ap-

pears spectrally blue (Clark et al. 2011, Hamilton et al. 2019, Simon, A. A. et al. 2020). Moreover, younger material investigated near the Nightingale sample collect site appear darker and redder than the rest of Bennu's surface Lauretta et al. 2022. Spectral blueing and surface brightening are not described by classical "lunar-type" SpWe. However, both processes are not uncommon in SpWe laboratory experiments on carbonaceous chondrites (Lantz et al. 2017,Thompson et al. 2019, Matsuoka et al. 2020, Laczniak et al. 2021). Trang et al. 2021 derived via modeling that the presence of nanophase magnetite is what causes carbonaceous asteroid to become blue-er with weathering, with nanophase magnetite being a product of SpWe on some CM-chondrites such as Murchison (Thompson et al. 2020). The creation of magnetite is related to the presence of Fe-bearing hydrated silicates. Our ion-bombardment results appear partially in-line with these findings, since our Fe-rich saponite is the only sample exhibiting blueing (and darkening, not brightening) upon weathering. The STEM measurements in chapter 4 shall investigate for the presence of nanophase magnetite in this sample.

The OTES instruments onboard OSIRIS-REx is able to detect possible SpWe effects on the 10 µm silicate feature in the Mid-IR. Lantz et al. 2020 investigated such effects by studying the distribution of the 10 µm feature from the Detailed Survey EQ3 OTES data, highlighting the presence of two end-member peaks, at ~ 835 (11.97 µm) and $965 cm^{-1}$ (10.36 µm), plus a third population, peaking at $\sim 915 cm^{-1}$ (10.93 µm) (see following Figure).

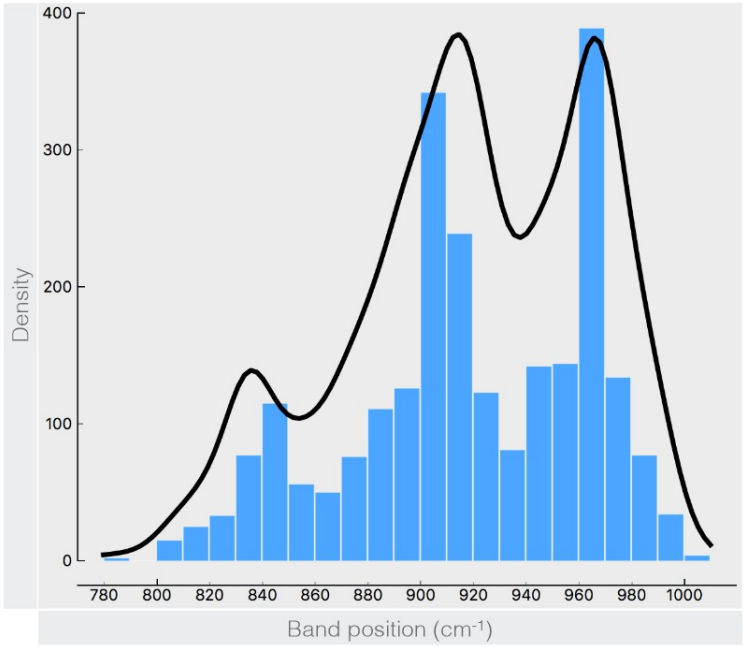

Figure 3.17: From Lantz et al. 2020 : distribution of MIR band position (simple minimum estimation) from Detailed Survey EQ3 OTES data. Data have been smoothed using a Savitzky-Golay filter. End-member peaks at 835 and 965 cm-1 come with a third population around 915 cm-1 consistent with SpWe effects. The black line is a density model to guide the eyes. The same kind of distribution with three populations is obtained when analysis is performed on unprocessed data.

The peak position associated to the third population, peaking at $\sim 915 cm^{-1}$ (10.93 µm), could be compatible with SpWe effects measured on carbonaceous chondrites (Lantz et al. 2017, Thompson et al. 2019). The detected spectral shift would be of approximately 570 nm, which far larger than what we have observed for our ion-bombarded phyllosilicates in the mid-IR (larger shift detected of approximately 350 nm). However, Brunetto et al. 2020 have also shown that Bennu's OTES spectrum is compatible with an average spectrum of He^+ bombarded Tagish Lake (C-ungrouped type) and Mighei (CM-type) meteorites, which shows sensible position red-shift of the 10 and 20 µm features.

3.2.2. Comparison with results on carbonaceous chondrites under the same experimental conditions

As introduced in the first chapter, most laboratories studies investigating the effects of SpWe on primitive surfaces chose to work on meteorites - more specifically carbonaceous chondrites. The number of studies, such as the one presented here, focusing on pure hydrated terrestrial mineral

phases, remains fairly limited (one can cite the work presented in Hallatt et al. 2022 on pulse-laser irradiation experiment or Nakauchi et al. 2021 H^+ bombardment experiments on phyllosilicates). It is relevant to ask ourselves how do terrestrial analogues compare to meteorites when subjected to the same experimental conditions associated to this work. In this case, this can be done by comparing our spectroscopic results with those discussed in Brunetto et al. 2014, Lantz et al. 2015, Lantz et al. 2017 and Brunetto et al. 2020, where multiple carbonaceous chondrites underwent ion-bombardment weathering at fluences comparable to those described in this work, using the same experimental setup at the INGMAR-SIDONIE ion-bombardment platform. When comparing these two different type of sample-dataset, we detect similar trends, but acting with different amplitudes.

For instance, if we take the example of He^+ bombarded CM chondrite Mighei at $6{*}10^{16} ions/cm^2$ we detect a shift of the hydration feature close to 90 nm (Lantz et al. 2017), far smaller than the 14 nm shift detected on our classic lizardite serpentine UB-N sample). On the other hand, if we compare the behaviour of Ar^+ bombarded CM Murchison at $6 * 10^{15} ions/cm^2$ (a fluence almost 3 times weaker than we have reached in this work), there appears to be a weak red-shift of approximately 10 nm Lantz et al. 2015, while no noticeable shift had been seen in our work for the Ar^+ bombarded serpentine UB-N. The He^+ bombarded CM Murchison sample from Lantz et al. 2015, bombarded up to $3 * 10^{16} ions/cm^2$ (half of the maximum fluence reached in this work), also exhibits quite noticeable shift of 30 nm. Similarly, the silicate feature at 10 µm for CM Mighei also exhibits a noticeable red-shift of 600 nm (Brunetto et al. 2020), again, larger that what was detected for our serpentine UB-N sample (350 nm). It appears as if the phyllosilicate-rich matrix of carbonaceous-chondrites is more sensible to ion-bombardment effects than pure terrestrial phyllosilicate. This may be due to the different nature and intrinsic heterogeneity of meteorite material compared to terrestrial silicates, but a more thorough investigation is needed and will be conducted in an upcoming publication.

3.2.3. Remote sensing data of other bodies: the case of Vesta

Coupling the study of spectroscopic trends with topographical and geological information can also help understand space-weathering on other bodies. During my Ph.D., I had the opportunity to join

one of the International Space Science Institute teams, ISSI Team 485 "Deciphering Compositional Processes in Inner Airless Bodies of our Solar System", selected in the framework of the ISSI-call for proposal 2019, led by Dr. Francesca Zambon. The goal of this project was to investigate the different surface processing effects affecting Vesta, Mercury and the Moon, while understanding their differences and similarities. For the scope of this project, I conducted ion-bombardment experiments similar to those I applied to my phyllosilicate pellets, bombarding pellets made from four HED meteorites (NWA-4968, NWA-6232, NWA-6909 and NWA-7234) with He^{+} cations at 40 keV with different fluences (1E16 $ions/cm^2$, 3E16 $ions/cm^2$ and 6E16 $ions/cm^2$) in order to reproduce and investigate the effects of space-weathering on Vesta. HEDs (howardite-eucrite-diogenite) meteorites are a subgroup of the achondrite meteorites family. HEDs originates from V-type Vesta asteroids (Kelley et al. 2003, McSween Jr. et al. 2013), and are thus tightly related to it, being the closest material we can use as surface analog of Vesta. They are mainly made our of low-Ca pyroxene and plagioclase feldspar, with minor olivine phases. My contribution to the ISSI project was dedicated to studying the evolution upon ion-bombardment of the visible slope (0.4 - 0.7 µm), the near-IR slope (0.7 - 1.4 µm) and the global slope (0.7 - 2.4 µm, approximately) in the Vis-Near range, as well as the study of two spectroscopic features at 1 µm and 2 µm approximately (referred to Band I and Band II). These features are associated to the electronic transitions of Fe^{2+} in pyroxenes crystal lattice (Moriarty III and Pieters 2016).

The ion-bombarded pellets underwent a similar spectral characterization to those of my phyllosilicate pellets. The end-goal is to compare the laboratory findings with the spectroscopic surveys of Vesta, acquired during the DAWN mission (NASA). The DAWN mission launched in 2007, with the mission of studying two of the largest bodies in the asteroids belt: V-type asteroid Vesta and the dwarf planet Ceres.

Analysis of the mid-IR range measurements is still ongoing. However we found identified consistent spectral trends in the visible and the near-IR range, such as:

- Slight shift of bands at I and I µm features (associated to Fe^{+2} electronic transitions in pyroxenes).

- A increase in band area ratio (Band II / Band I).
- Significant slope reddening in both the Visible and the Near-IR range, as well as reddening of the global slope.

The changes described above are shown in the following figure.

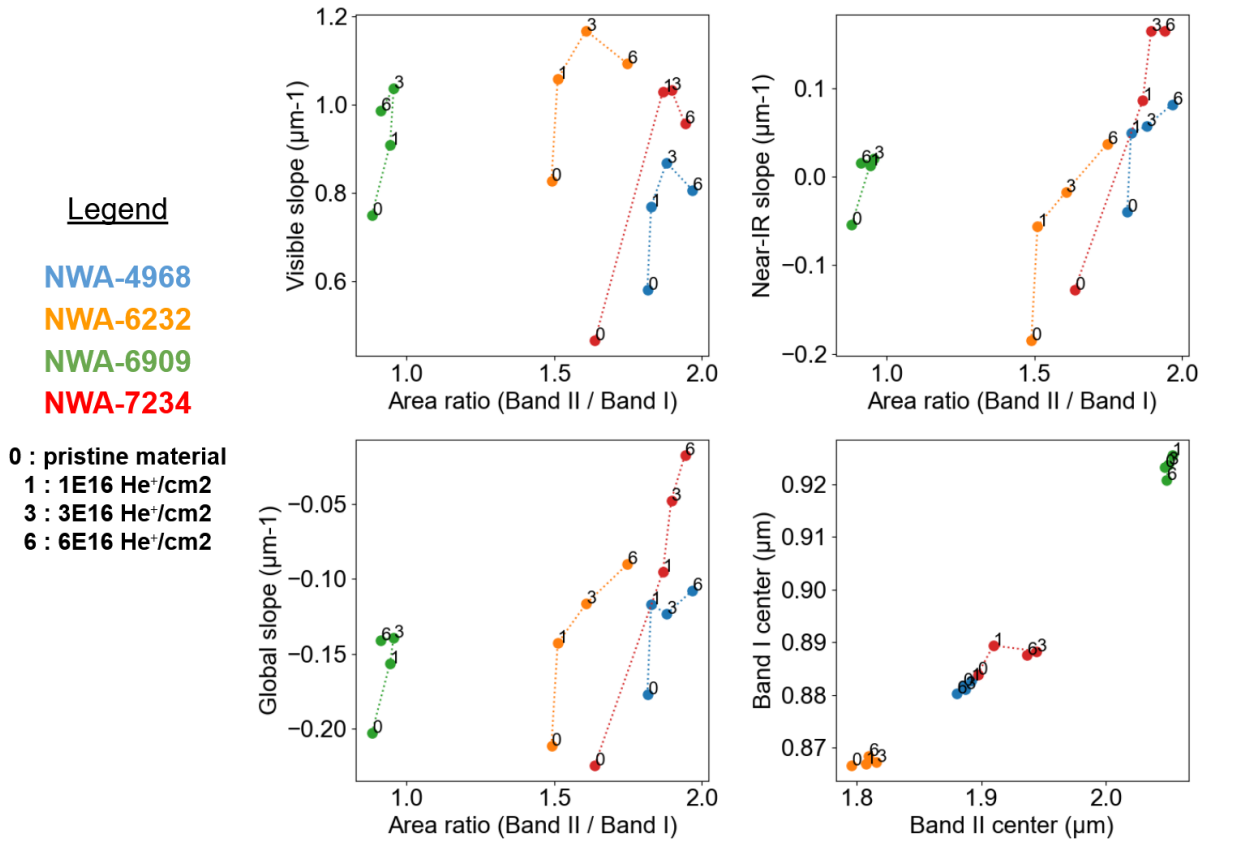

Figure 3.18: Evolution upon 40 keV He^+ bombardment of various spectral parameters at different fluences (0 : pristine material, 1 : 1E16 $ions/cm^2$, 3 : 3E16 $ions/cm^2$, 6 : 6E16 $ions/cm^2$) of four pellets made from HEDs meteorites (NWA-4968 in blue, NWA-6232 in orange, NWA-6909 in green and NWA-7234 in red). The spectral parameters were selected in order to maximise the dispersion of the points associated to each weathering fluence while minimizing the number of parameters. The chosen parameters are: the visible slope (0.4 - 0.7 µm), the near-IR slope (0.7 - 1.4 µm), the global slope and the band centers for the 1 µm and the 2 µm features (Band I and Band II), as well as the band area ratio between Band II and Band I.

The spectral shift, contrary to our results on hydrated silicates, is difficult to use here as a proxy for

space-weathering, since it is very variable while being very slight, and seems to mostly affect Band II (the feature at 2 µm). However, slope and band area ratio variations coupled with geographical data can help understand space-weathering effects in specific region of interests on the surface of Vesta. These results and their discussion in the context of remote sensing data from Vesta and other basaltic asteroids will be published in the following months, including a paper focusing on the laboratory experiments, which I will lead as first author.

3.2.4. The case of returned samples: a focus on the Hayabusa2 preliminary analysis and my contribution to the 'STONE' team.

Investigating the spectral trends due to ion-bombardment on hydrated silicates was done to provide support to remote sensing analysis and de-bias compositional analysis of space-weathered surfaces. Naturally, these results can also be used to support laboratory analysis on returned materials from sample-return mission. In the case of the Hayabusa2 mission, this could be particularly relevant, since there were two collection sites: one associated with "standard" Ryugu surface (chamber A) and a second one near the artificial SCI crater (chamber C). Material from chamber C could contain grains from both the weathered surfaces and the excavated, more pristine material, from the ejecta of the artificial crater. Possible heterogeneity in the (M)-OH and Si-O stretching and bending feature's position among grains from Chamber A and Chamber C could be explained by space-weathering effects.

Le Pivert-Jolivet and al. 2022 delves on this matter, focusing on the (M)-OH stretching feature measured by the MicrOmega instrument at ISAS-JAXA. The MicrOmega instrument is a visible near-infrared hyperspectral microscope, originally designed to characterize the texture and composition of martian samples. The ExoMars rover from the ESA mission with the same name, dedicated to investigate the surface of Mars for possible signs of past biosignatures (and currently awaiting confirmation for launch), is equipped with this instrument. Two other copies of this instrument exist, one at the Institut d'Astrophysique Spatiale d'Orsay, and a second one at the ISAS-JAXA facility, where the first analysis and curation of Ryugu samples is done. The MicrOmega instrument at ISAS-JAXA is used to establish a catalog of all the samples which were brought back from

Ryugu, by proceeding to a first characterization in the near-IR range. This allows to have access to the preliminary mineral composition, hydration and possible organic content of all samples in a totally non-destructive way (one of the perks of infrared spectroscopy).

As discussed by Le Pivert-Jolivet and al. 2022, other processes can also contribute in the spectral difference between samples from Chamber A and Chamber C, such as a different Saponite/Serpentine compositions in the two collection sites. Moreover, other phenomena, such as the destruction of the weathered surface layer during the collection or transportation of the samples, or the alteration of the sample surface when exposed to the Earth atmosphere, could hinder the identification of weathered samples among the collection. Coupling spectroscopic analysis with other experimental techniques, such as electron microscopy imaging, would help identify grains or grain-regions which would show evidence of space-weathering Noguchi and al. 2021.

During my PhD thesis, I was able to join the Hayabusa2 'STONE' initial analysis team, led by Prof. Tomoki Nakamura, as part of the team from the IAS Astro-chemistry group. Initial analysis teams are international collaborations led by principal investigators (PI) of the Hayabusa2 mission. For the Hayabusa2 mission, there are six initial analysis teams, each associated to a specific topic and with its own perspective on Ryugu's samples. The 'STONE' team was dedicated to study of the mineralogy and petrology of coarse grains from Ryugu.

As a member of the IAS/Astro-chemistry group, my contribution to the analysis of Ryugu samples first consisted in participating in the rehearsal analysis which were led on materials considered analogs to Ryugu in order to prepare the analytical pipeline which would be used once we received the samples from Ryugu. The first rehearsals were focused on applying our analytical techniques to individual grains of the CM-type meteorite Murchison. My contribution consisted in acquiring, processing and interpreting data from infrared computed tomography (IR-CT) analysis of microscopic Murchison fragments, from 30 to 80 µm in size (see Brunetto et al. 2020). Murchison was chosen because at that time it was not clear which class between CMs or CIs was the best analogue of Ryugu.

IR-CT is an analytical technique developed by Mike Martin at ALS synchrotron (Martin et al. 2013) and implemented at SMIS/SOLEIL by Dr. Zélia Dionnet (Dionnet 2018), which allows the non-destructive three-dimensional characterization of mineral, hydrated and organic phases in a microscopic sample (tenths of microns) in a totally non-destructive way (see the following figure for an example of a reconstructed IR-CT data-set). This allows us to be able to access the heterogeneity and co-localization of all these phases inside the studied sample.

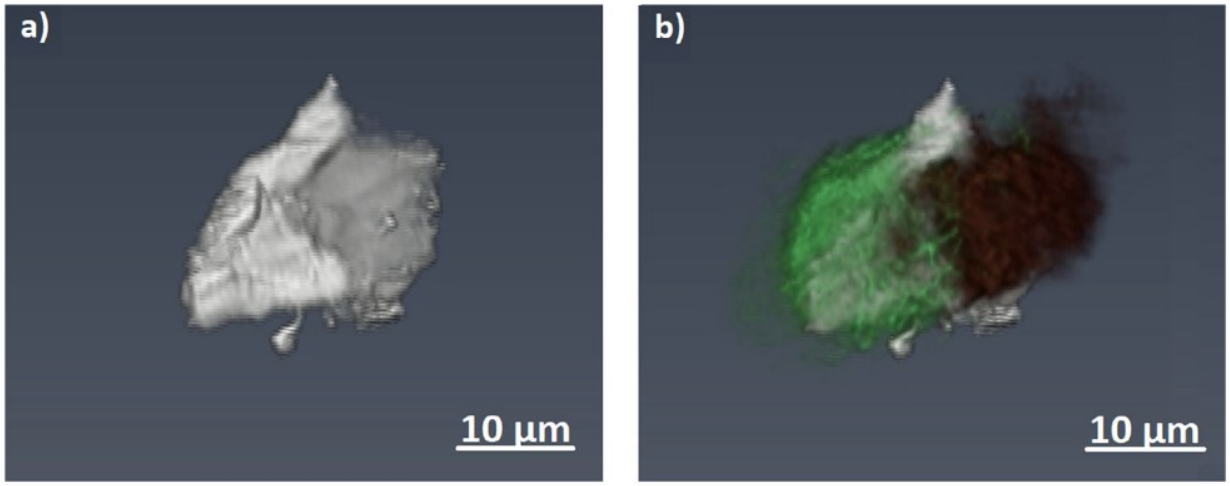

Figure 3.19: From Dionnet et al. 2020: Detection and separation of olivine and pyroxene minerals in 3-D for a particle from Itokawa (RA-QD02-0214). a) X-ray data where only the particle (and not the glue) is represented and the two levels of grays, proportional to the different LAC at 8 keV, show the olivine (light gray) and the Ca-rich pyroxene (dark gray). b) IR data superimposed onto X-ray data, with IR reconstruction of olivine in green and Ca-rich pyroxene in brown

For the scope of the rehearsal, I acquired and processed a dozen of IR-CT data-set of various Murchison grains unheated and or at different temperatures, in order to emulate the effects of thermal heating on a hydrated carbon-rich primitive body. The number of spectra for a single IR-CT data-set can vary from approximately 400 000 spectra to 1 500 000 spectra, depending on the size of the measured sample. In order to efficiently and quickly process this large quantity of data, I took the code originally written by Dr. Dionnet for IR-CT during her Ph.D. thesis and built upon it to create a fully fleshed python routine called 'Nebulia', which facilitates the data reduction and processing of IR-CT data and it has been used on all IR-CT data collected at IAS since its creation, including data from Ryugu's sample. The 'Nebulia' software will be the subject of a future method

article, which will lead to its release for OpenSource use for IR-CT data reduction.

IR-CT is a powerful technique, but the size of the sample which can be measured is limited, since it is based on transmission spectroscopy: signals transmitted from samples larger than 100 µm are difficult to exploit for 3D reconstruction (the IR absorption saturates). In order to mitigate this issue, during my PhD thesis, I contributed to the development of a second technique: Infrared Surface Imaging (IR-SI) (Dionnet et al. 2022). IR-SI is based on reflectance spectroscopy, and is thus free from sample size-limits. The idea is to map the surface of a microscopic sample using infrared hyperspectral imaging, and project the data on a 3D shape-model of the measured particle. This is not dissimilar from what is done on larger bodies with remote-sensed data mapped on an asteroid shape model, but applying it to microscopic samples has its own challenges. The technique is still under development, but we were able to also apply it to the received Ryugu samples. An example of results which can be obtained via IR-SI, to which I contributed, is shown in the following figure for the case of CM chondrite Aguas Zarcas.

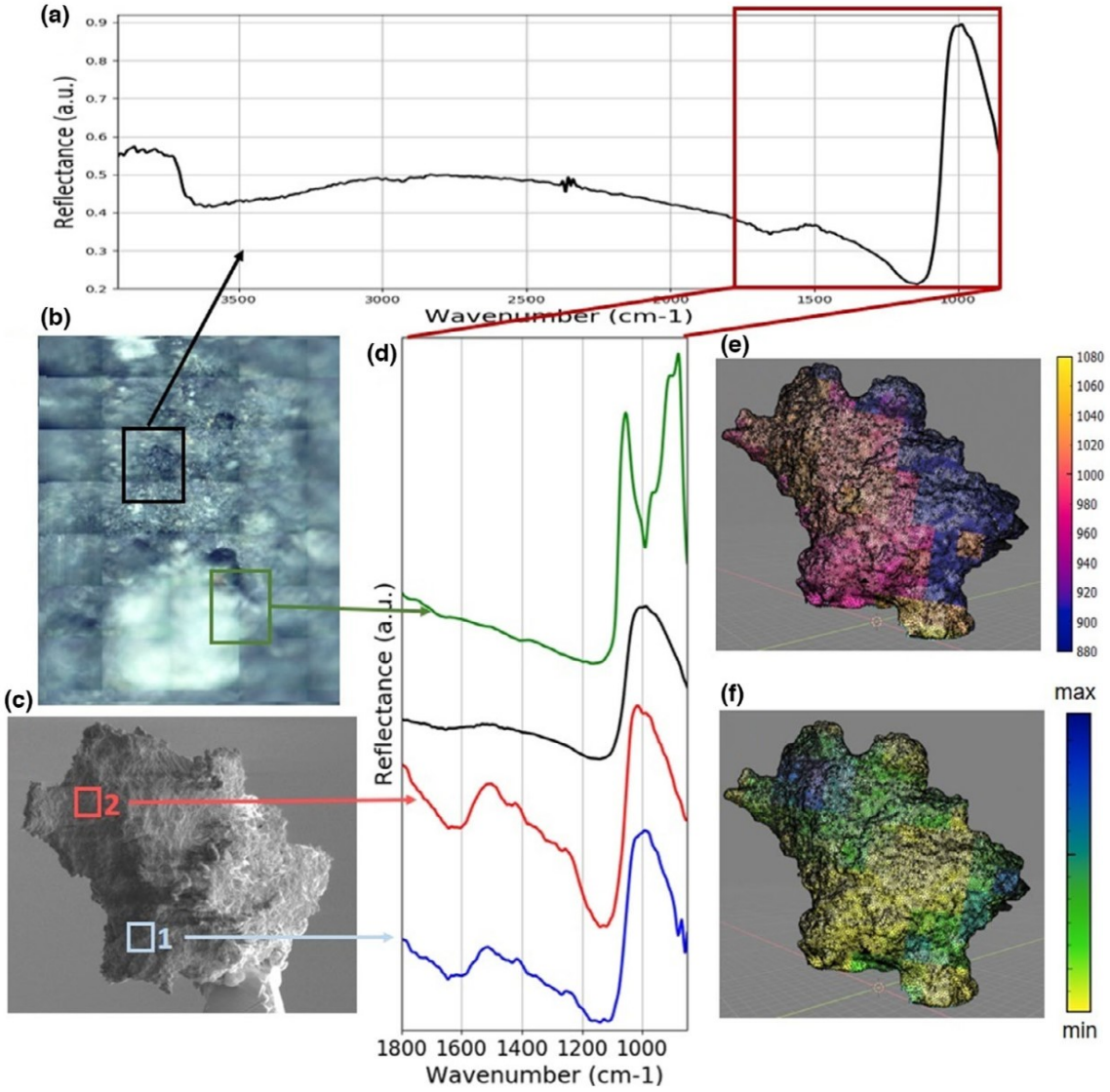

Figure 3.20: From Dionnet et al. 2022: a) Average IR spectrum from a chip of CM-type meteorite Aguas Zarcas. b) Visible image of the Aguas Zarcas chip. c) Scanning electron microscopy image of a 3D small fragment of Aguas Zarcas. d) Zoom of reflectance spectra in the range 1800–850 cm^{-1} for the average spectrum in black, inside a chondrule in green and for areas 1 and 2 of panel (c) in red and blue. e) Projection of the SiO band position on the 3D volume: regions in pink and yellow correspond, respectively, to a maximum of the SiO band around 980 and 1010 cm1. A part of the fragment was slightly out of focus for this angle and produced a noisier spectrum (blue region in panel [e]). f) Intensity of the H_2O band at 1614 cm^{-1} distribution projected on the 3D volume: more hydrated areas appear in blue and less hydrated ones in yellow.

I also participated in establishing and testing the analytical pipeline which would be applied to the

analysis of microscopic grains from Ryugu. In June 2021 we received 30 microscopic grains, from 20 to 150 µm in size. The analytical pipeline used in order to characterize these precious samples was presented during the Hayabusa Symposium in Novemeber 2021 by me, and is described in Rubino et al 2022b (submitted). It had previously been tested by our team on a microscopic fragment of CK-chondrites NWA-5515 (Aléon-Toppani et al. 2021. My contribution consisted in processing and interpreting the IR-CT 3D reconstruction with respect to the other experimental techniques used. The goal of the chosen analytical pipeline is to maximise the scientific output of a multi-instrument/multi-scale analysis and to minimize the sample loss and alteration. To do so, a sequence of experimental techniques, from non-destructive to more destructive is established. An example of this analytical pipeline is showed in the following figure.

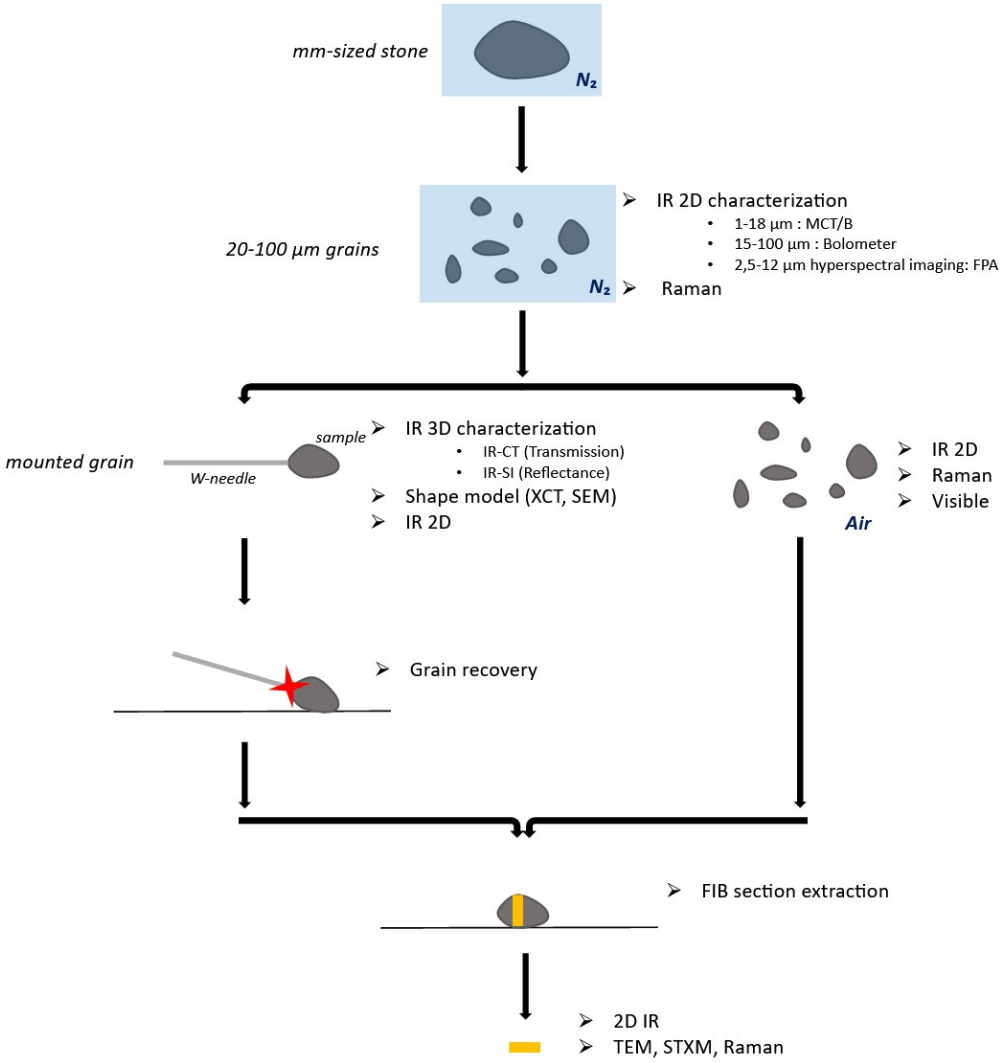

Figure 3.21: From Rubino et al. 2022b (submitted): Cartoon summarizing the analytical pipeline used for Ryugu's particles. Note that everything is stored under a dry N atmosphere when not in this pipeline.

From June 2021 to June 2022 we successfully applied this pipeline to Ryugu grains. Results are under analysis and papers will be published in the next months. Some of the work our team did on Ryugu grains will contribute to the large initial paper associated the results from the whole "STONE" analysis team (Nakamura et al. 2022, Science, *in press*), publication of which I am a co-author.

CHAPTER 4

Morphological and physicochemical changes of weathered hydrated silicates

Contents

The spectroscopic characterization led on our ion-bombarded pellets brought out certain spectral trends visible upon weathering. However, there is still some ambiguity regarding the physico-chemical and morphological changes that can produce the observed trends. To study these changes, we shall now investigate the weathering effects at a smaller scale - down to the nanometer scale - by using techniques associated to electron microscopy such as:

- Secondary electron imaging via scanning electron microscopy (SEM).
- High-angle annular dark field (HAADF) STEM imaging.
- Compositional mapping by Energy Dispersive X-Ray Spectroscopy (EDS).

The SEM imaging survey was performed on the ion-bombarded pellets, as well as on the control pellets, while STEM-HAADF and STEM-EDS data were acquired from FIB sections extracted from the surface of the ion-bombarded samples. A focused beam of gallium ions was used to extract the FIB sections. The following table shows a recap of the samples described above.

	SEM analysis	STEM-EDS analysis
number of samples	9	6
type	pellet	FIB-section
details	3 pellets per phyllosilicate: •pristine •He^+ at 40 keV ($6 * 10^{16} ions/cm^2$) •Ar^+ at 40 keV ($2 * 10^{16} ions/cm^2$)	2 FIB-sections per phyllosilicate: •He^+ at 40 keV ($6 * 10^{16} ions/cm^2$) •Ar^+ at 40 keV ($2 * 10^{16} ions/cm^2$)

Table 4.1: Samples for electron microscopy analysis.

4.1. Surface topography upon ion-bombardment by SEM

I have used Scanning electron microscopy (SEM) imaging in order to investigate the state of our samples' surfaces before and after ion-bombardment. Secondary electron images of the center of our pellets were acquired using a relatively low acceleration voltage of 3 kV (see 2.4.3 for more information about the setup used), after having coated the surface with a 300 Å thick carbon layer. The coating of the surface is necessary for the correct evacuation of charges under the electron beam, which is paramount in acquiring high quality and detailed images.

We started the imaging survey with a quick scan at low magnification of the surface of our pellets. For all pellets, we saw a slight morphology heterogeneity. In order to illustrate this heterogeneity, we shall focus on the surface of the serpentine Rawhide pristine pellet (keeping in mind that all pellets have shown approximately the same surface features). A low-magnification image of the pristine pellet made from serpentine Rawhide powder is shown in the following figure.

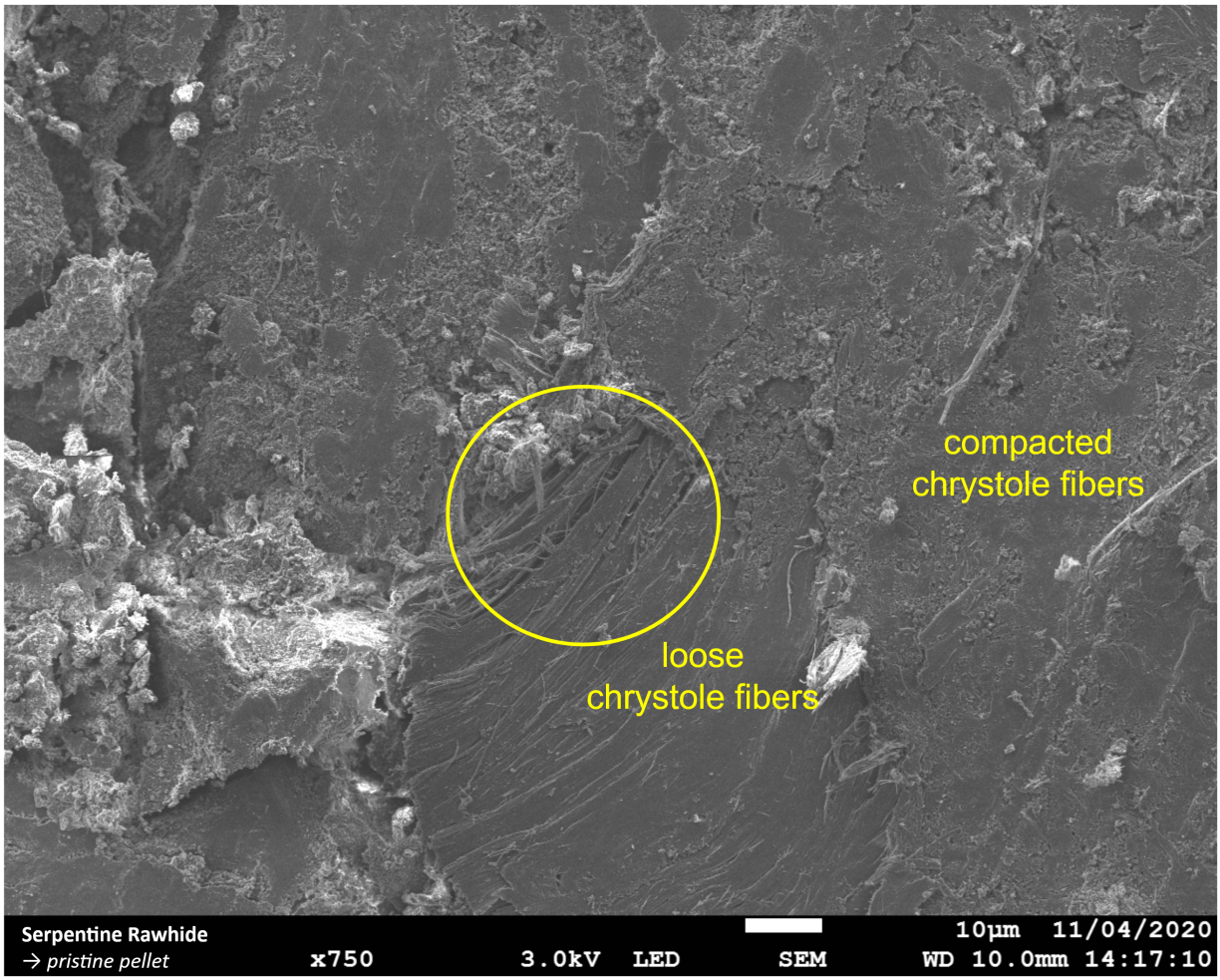

Figure 4.1: Secondary electron image of the pristine Serpentine Rawhide pellet, acquired at 3 keV with x750 magnification power.

Most of the surface appears to be made of flat, fine compacted powder. Since these are pressed-powder pellets, we can see large fractures where the powder has locally become more loose. Overall, the whole surface appears quite rough, which can complicate the interpretation of the sample micro-

structure. However, this is intrinsic to our sample preparation (from loose powder to compressed-powder pellets), and was expected. For the scope of this study, we chose to avoid the region showing large fractures for the high magnification acquisitions. Large individual grains can also be seen occasionally. In some flat regions, the pressed powder appears a bit more loose, and we can identify individuals phyllosilicate grains (for Serpentine UB-N and Saponite) or fibers (Serpentine Rawhide). To investigate the effects of ion bombardment on these distinct phyllosilicate structures, secondary electron images were taken at high magnification (Figure 4.2).

Secondary electron images of these structures taken at high magnification are shown in the following figure. For each pellet, pristine or ion-bombardment, we have looked for similar morphological features to compare.

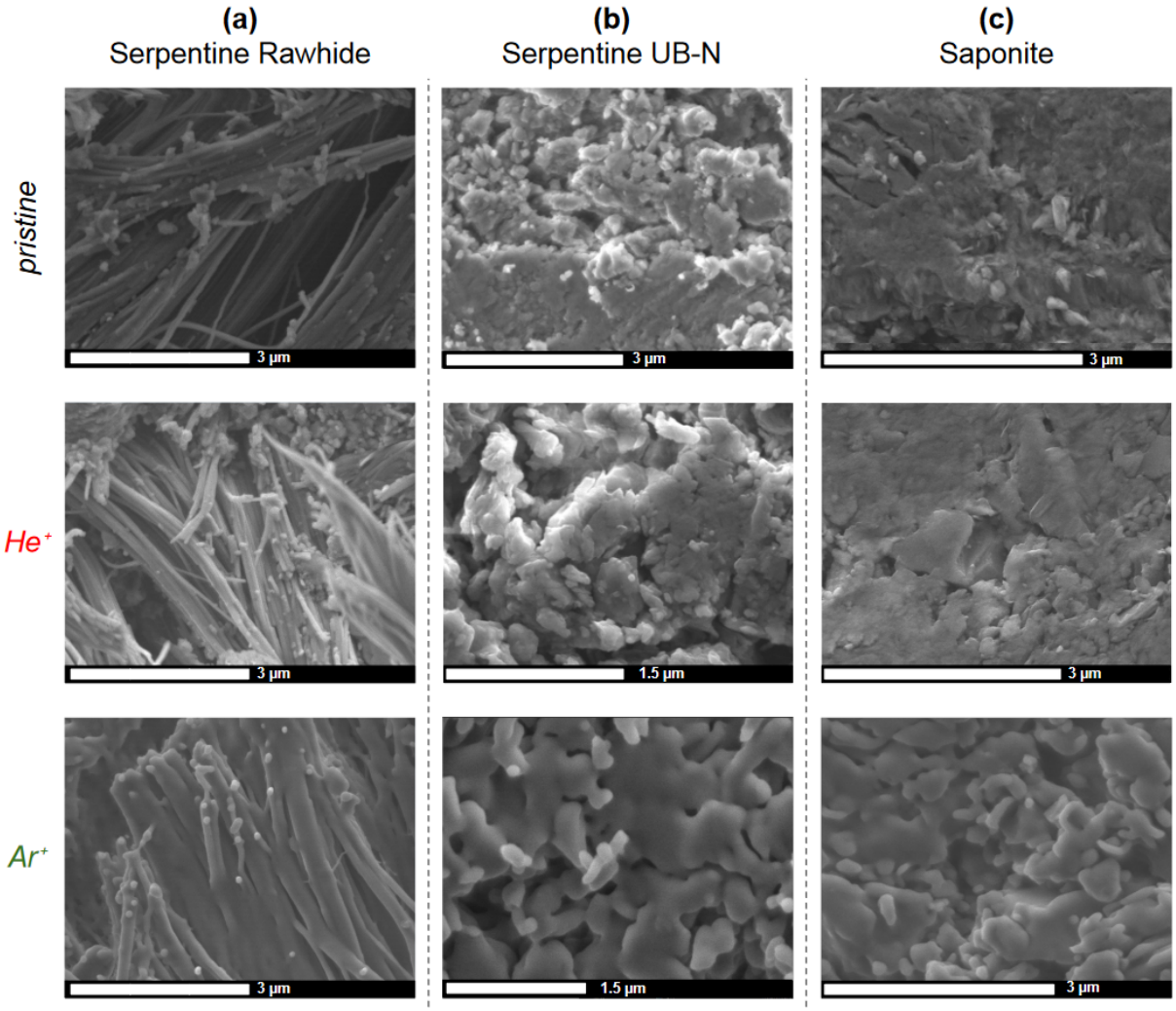

Figure 4.2: Secondary electron images of the central region of our pellets. The center of the pristine pellet is compared to the center of the He^+ and Ar^+ bombarded pellets. This is done for all our samples: Serpentine Rawhide (a), Serpentine UB-N (b) and Saponite (c). The images acquired with an acceleration voltage of 3 kV at various magnifications, from x20 000 to x40 000.

The He^+ bombarded surfaces do not appear to greatly differ from the pristine ones: no significant morphological change can help distinguish the He^+ bombarded samples from the pristine ones. On the other hand, the Ar^+ bombarded surfaces show clear changes. The He^+ bombarded samples retain a grainy, frothy texture similar to that of the pristine samples, while Ar^+ bombardment dulls and soften harsh angles and structures. The borders of individual grains and fibers appear to be blurred out by the heavy ion bombardment. Every feature smaller than 10 nm in size seemed to

be removed. Overall, the most prominent morphological change observed among our pellets, is a "polishing effect" seen on the Ar^+ bombarded surfaces, with respect to the pristine surfaces.

The secondary electron images acquired with SEM have shown that Ar^+ greatly alters the surface topography of our samples, while He^+ bombarded surfaces are not distinguishable from pristine surfaces. The smoothing-effects associated to the Ar^+ bombarded samples is related to larger energy deposited by elastic collisions from the Ar^+ ions compared to He^+. According to SRIM simulations in serpentine and saponite, the energy deposited by unit of length from elastic collision by Ar^+ is almost 100 times larger than for He^+, $\sim 6.5 * 10^2$ keV/µm versus ~ 5.4) keV/µm respectively. The larger deposited energy is responsible for the alteration of nanometric-size features observed on Ar^+ bombarded surfaces.

4.2. Compositional and microstructural modifications by STEM

The FIB sections extracted from the surface of our samples allow us to access the ion-implanted layers, in order to characterize their texture, morphology and composition by HAADF-STEM imaging and EDS compositional mapping (see 2.4.3 for experimental conditions). All FIB sections were extracted from flat surface regions of our bombarded pellets. The following figure shows an example of two FIB sections.

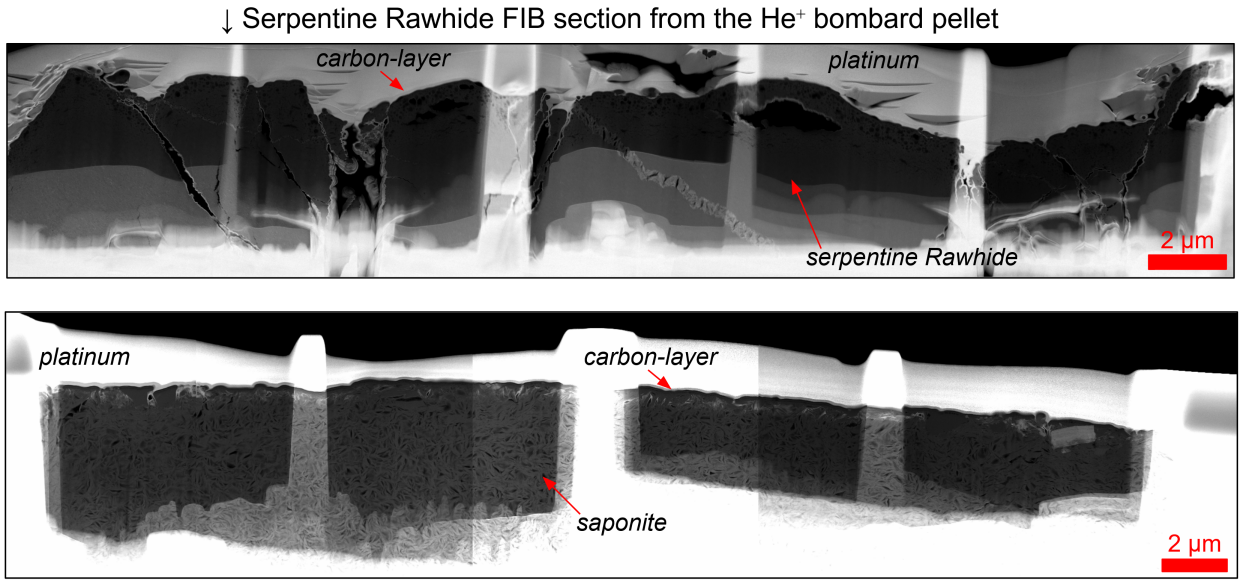

Figure 4.3: HAADF images of FIB sections, one extracted from the He^+ bombarded serpentine Rawhide pellet (top) and the other extracted from the Ar^+ bombarded Saponite pellet.

4.2.1. Serpentine Rawhide

For this sample, the FIB sections were taken perpendicular to the chrysotile fibers. The fibers' cylindrical sections can be seen in the following figure, with a size of 30 nm in diameter and exhibiting a central hole with a typical size of 5 nm. Porosity is also present between the fibers.

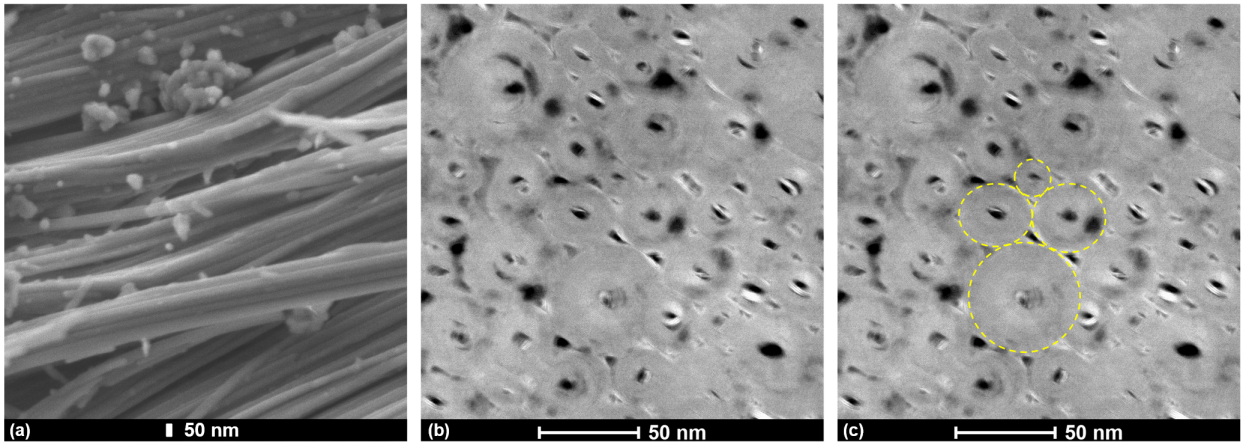

Figure 4.4: Serpentine Rawhide fibrous morphology, as seen in their pristine state. (a) SEM image of chrysotile fibers on the surface of the pristine serpentine Rawhide pellet, (b) HAADF image of of chrysotile fibers sections, as seen in the FIB sections, (c) circular shape of the chrysotile fibers with various sizes, highlighted with dashed-line yellow circles to help the reader.

4.2.1.1 (a) He^+ bombarded

This sample is the one undergoing the most prominent and observable changes among our collection of FIB sections observed here. A global view of this sample can be seen in the following figure.

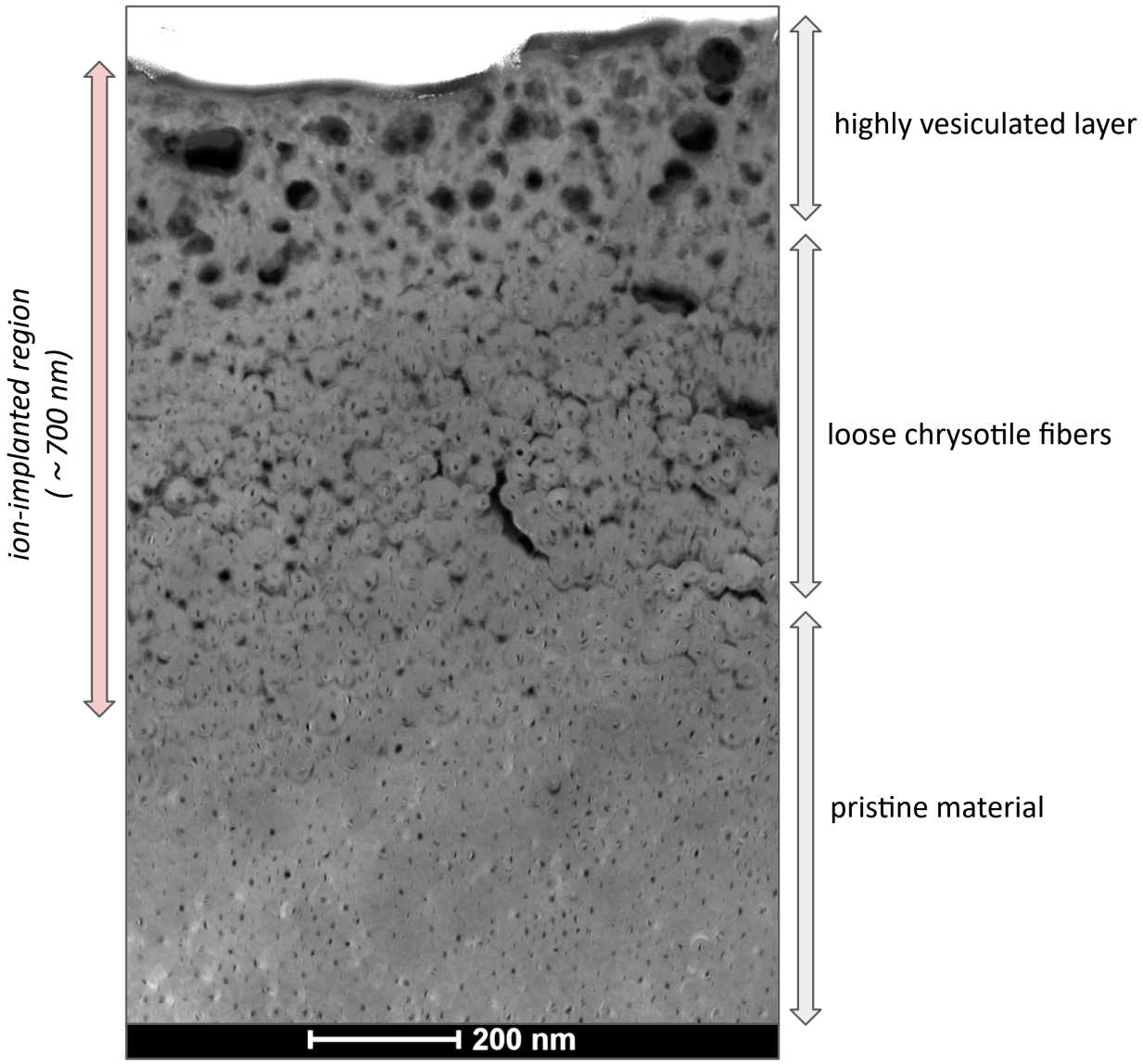

Figure 4.5: HAADF image global view of He^+ bombarded serpentine Rawhide.

Three different regions with varying textures can be seen (Figure 4.5).

- Below 700 nm in depth, we find the chrysotile fibres in what we identify to be their pristine state, with no evidence of interaction with the bombarding ions (Figure 4.6, panel a).
- Closer to the surface of the sample, with a smooth transition, the cohesion among the chrysotile fibres appears diminished, as seen by the presence of larger gaps among them. This region

extends from the 300 to approximately 700 nm (Figure 4.6, panel b).

- The area close to the surface is highly vesiculated with bubbles up to several hundreds of nm. Its depth varies from approximately 250 nm to 400 nm. The chrysotile fibers do not survive in this region (Figure 4.6, panel a).

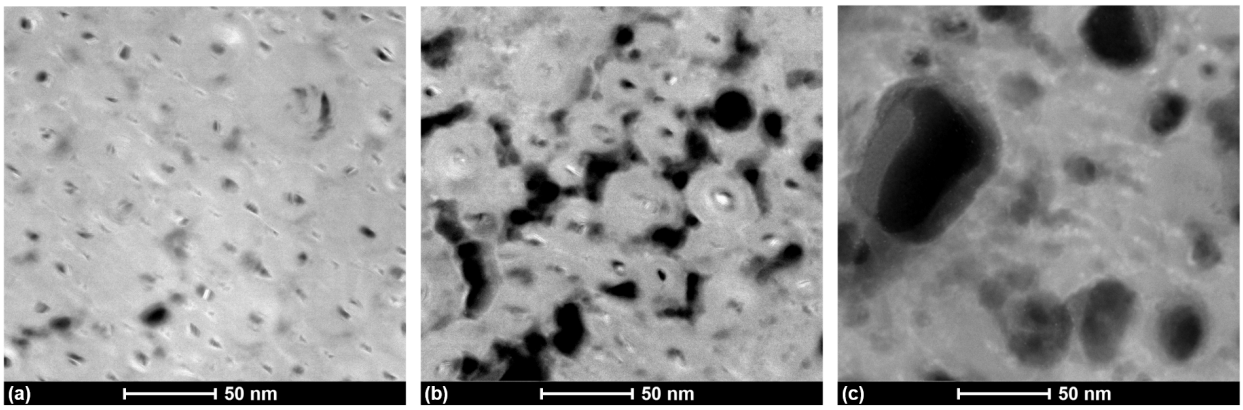

Figure 4.6: High resolution HAADF images highlighting three different textures seen in He^+ bombarded serpentine Rawhide. (a) compacted chrysotile fibers in the pristine region, below 700 nm from the surface. (b) intermediate region between 700 and 400 nm from the surface, with more loose fibers. (c) Surface implanted layer, above 400 nm from the surface, highly vesiculated, exhibiting no chrysotile fibers.

Voids appear to be present all across the sample. The deepest, pristine regions show small voids associated to the juxtaposition of chrysotile fibers. The intermediate regions also shows these voids, accompanied by larger cracks, as there appear to be less cohesion among the fibers, making the fiber interspace larger. The surface regions have lost the fiber texture and exhibits large bubbles. We can trace the evolution of void-size and sample porosity as a function of depth in our FIB section (see figure 4.7), to better assess the existence of these three regions in our sample. The ImageJ software was used to detect the porosity in the selected ROI (figure 4.7, panel a) using intensity thresholding: each pixel of the grey-scale image below a certain value was considered to be voids. This thresholding step provided us with a binary mask highlighting voids in the ROI (figure 4.7, panel b). The porosity was computed along the profile axis by segmenting the threshold-ed image into a number of bins (bin-size of 5 nm) and by dividing the number of pixels associated to porosity (black pixels) with the total number of pixels in a segment, for each segment along the profile axis

(figure 4.7, panel c). The voids Feret's diameter was computed directly using ImageJ particle finder protocol on the binary mask (figure 4.7, panel d). Feret's diameter is a measure of an object size along a specified direction, and is used in this case to discuss the size of voids (since they not perfectly circular).

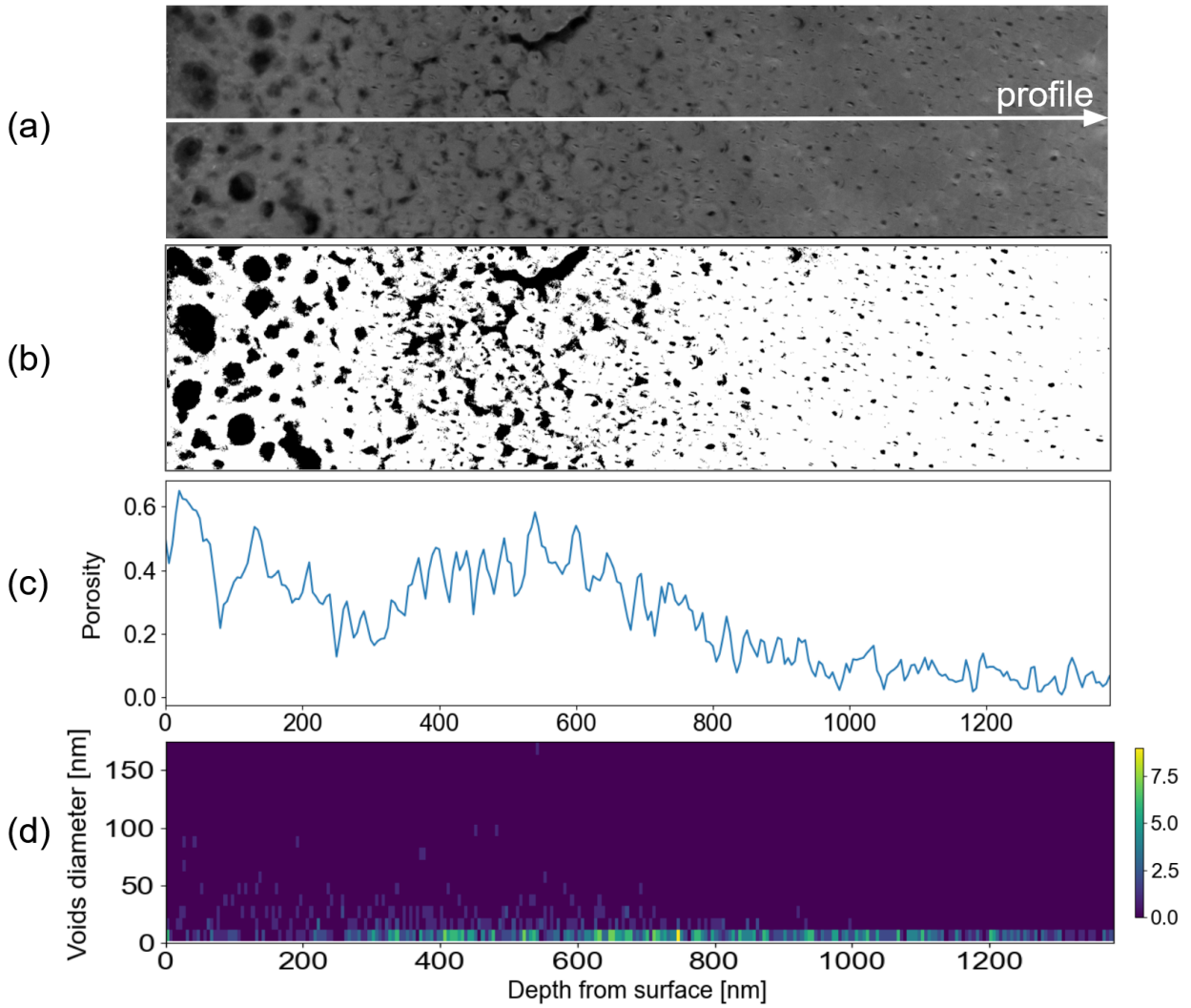

Figure 4.7: (a) HAADF global image of He^{+} bombarded serpentine Rawhide. (b) Threshold-ed image highlighting the porosity inside the sample (bubbles, fractures and voids). (c) Evolution of the porosity as a function of depth (binned along the x-axis for bin-size of 5 nm). (d) Distribution of the Feret's diameter of 881 voids (identified by thresholding) as a function of depth (x-axis bin-size of 5 nm, y-axis bin-size of 10 nm).

Several hyperspectral EDS maps were acquired in multiple regions of the FIB section. On figure 4.8,

we show a large composition profile including the entire modified layer and the pristine phyllosilicate below.

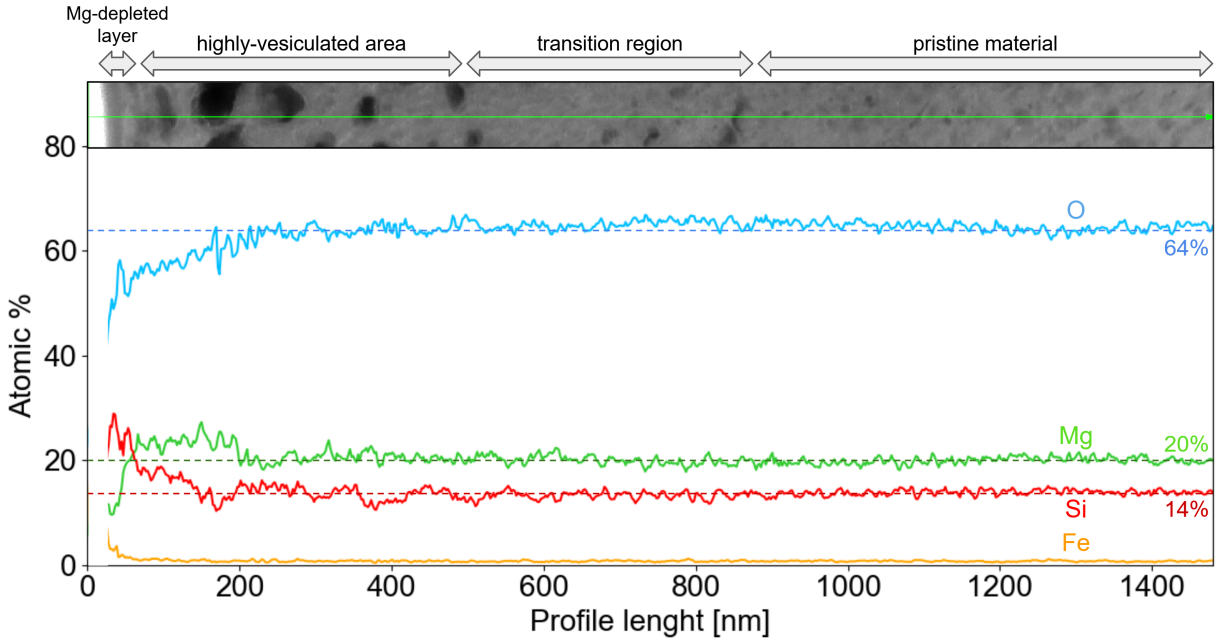

Figure 4.8: Compositional profile in He^+ bombarded serpentine Rawhide.

Global profiles allows us to better appreciate and quantify compositional changes over large regions.

- The average oxygen concentration diminishes in the ion-bombarded layer: from $\sim 64at\%$ in the pristine material, down to $\sim 50at\%$ at the utmost surface. This depletion is localized in the highly vesiculated region, the one exhibiting large bubbles (20 to 120 nm thick). By integrating the area under the oxygen-curve in the oxygen-depleted region, and by comparing it with the area associated to a pristine region with the same length, we are able to derive the oxygen-loss affecting the ion-bombarded sample. We measure that, in this surface region approximately 200 nm thick, there is a 8% depletion in overall oxygen content with respect to the pristine material.

- A thin surface layer, approximately 20 nm thick, appears to be strongly depleted in magnesium (see also Figure 4.9 for a zoomed-in compositional profile on this surface layer). Magnesium content in this thin layer 20 nm thick decreases of total Mg content by $\sim 20\%$ relative to the

pristine material. This depletion is followed by an increase in magnesium content in top part of the highly vesiculated layer, over a thickness of approximately 180 nm (increase of total Mg content by $\sim$ 17% relative to the pristine material), mainly localized in the area closest to the surface of this region.

- Fe content is particularly low (which is in line with the elemental composition derived by SEM-EDX presented in the previous chapters) and does not seem to change in the ion-bombarded layer.

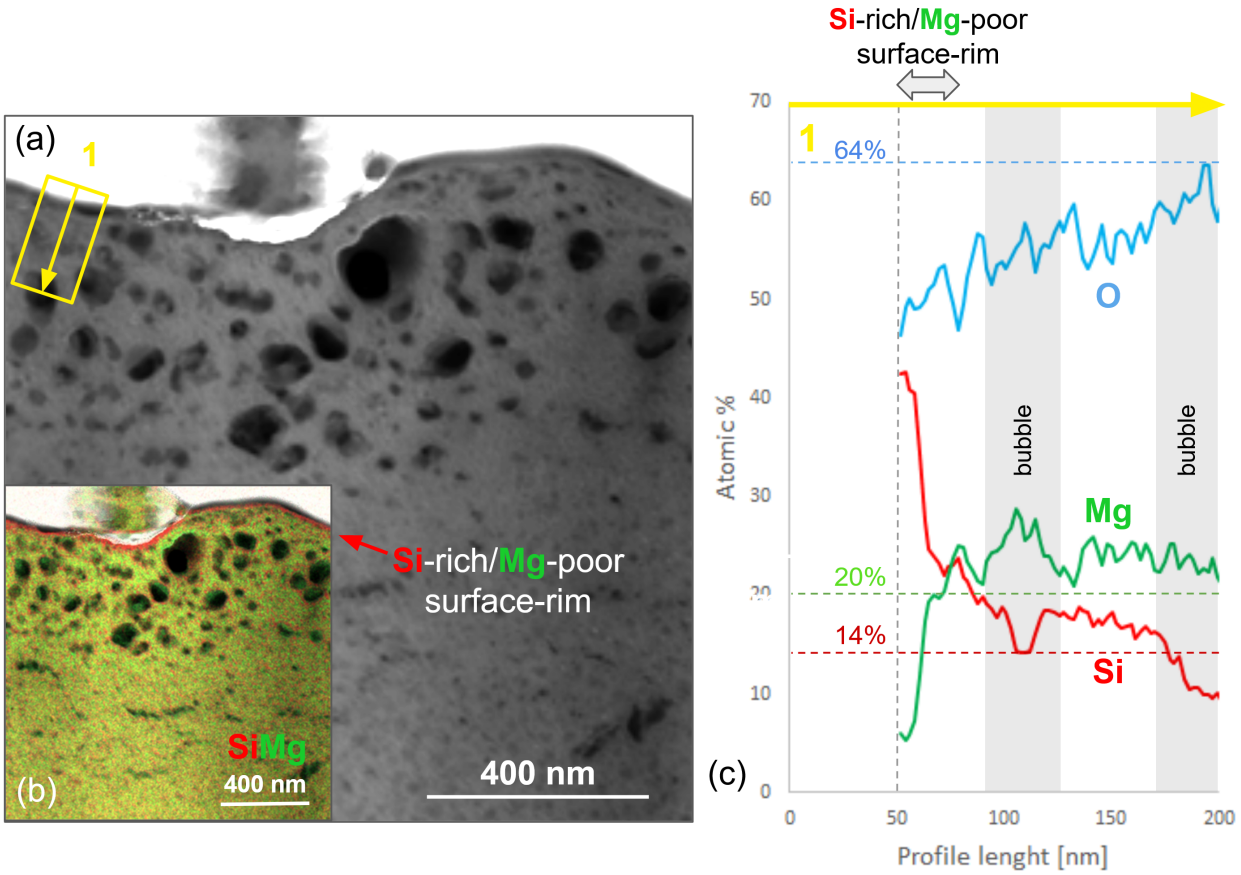

Figure 4.9: (a) HAADF image of serpentine Rawhide He^+ bombarded and the ROI associated to the zoomed-in compositional profile. (b) RG/SiMg composite image from intensity STEM-EDX. (c) Zoomed-in compositional profile localized on the thin Mg-depleted layer close to the surface.

The EDS maps also showed that some of the larger bubbles do not appear to be empty (figure 4.10). They are partially filled with a MgO-rich material. The area surrounding these large bubbles seems

to be depleted in Mg (presence of a red Si-rich thin rim surrounding the bubbles).

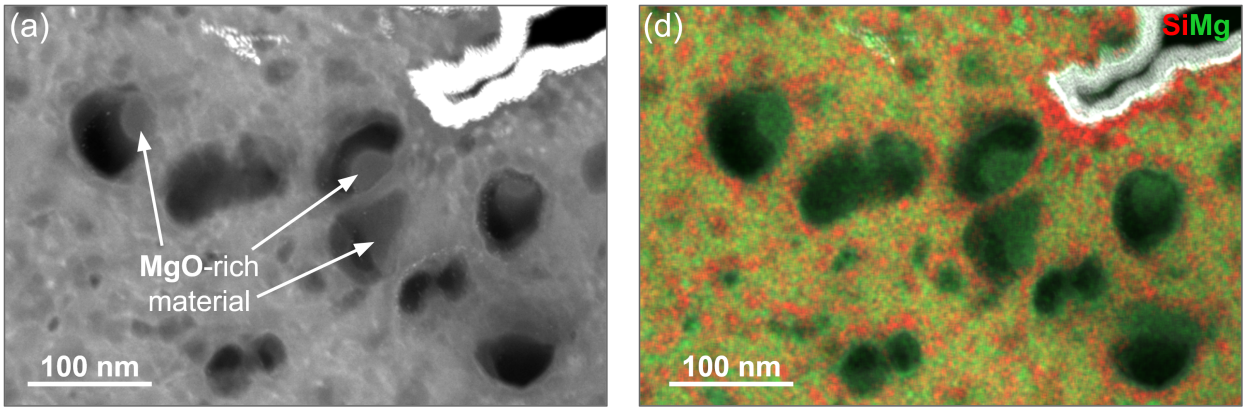

Figure 4.10: (a) HAADF image of multiple bubbles. (b) RG/SiMg composite image from intensity STEM-EDX of multiple bubbles (note the green Mg rich agglomerate inside the bubble, as well as the thin red Si-rich surrounding some bubbles).

Some HAADF images also show the presence of large surface bubbles/blisters in some areas, as well as very large regions of coalesced bubbles cracking the mineral's structure.

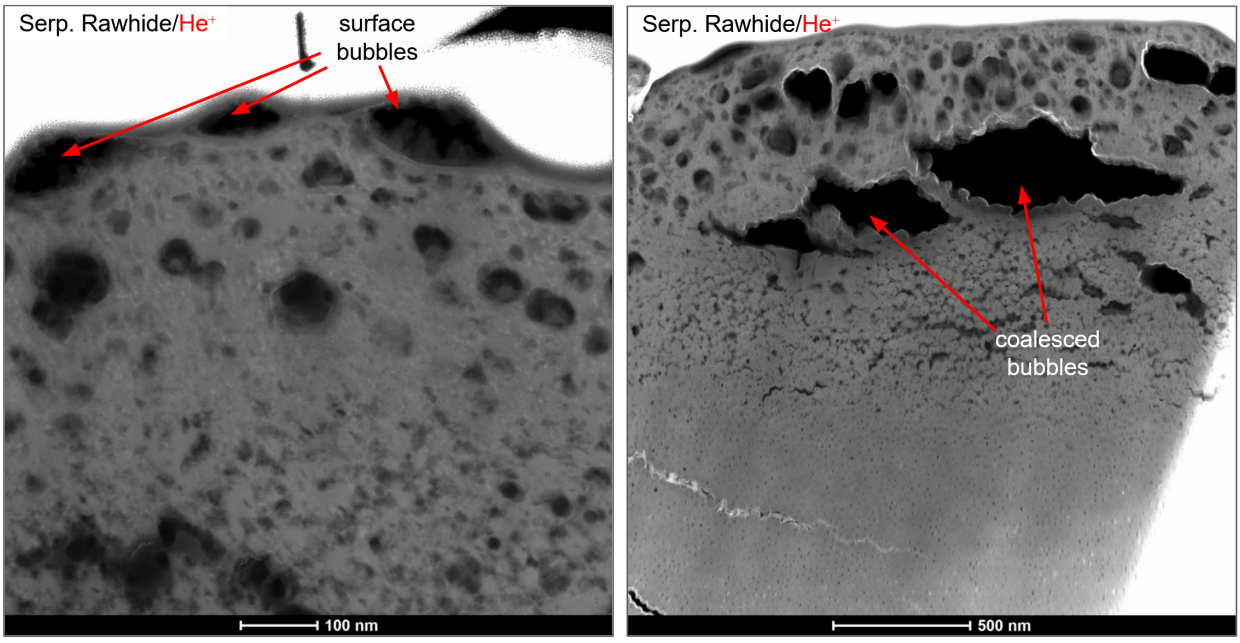

Figure 4.11: Surface bubbles and coalesced bubbles in serpentine Rawhide He^{+} bombarded.

4.2.1.2 (b) Ar^+ bombarded

In the Serpentine Rawhide Ar bombarded sample, we see only two different regions (Figure 4.11):

- A somewhat pristine region, made out of the arrangement of chrysotile fibers, below 400 nm depth, showing less or no evidence of ion bombardment.
- A highly vesiculated region with large bubbles (from 20 to 120 nm in diamater), 350-400 nm deep from the surface. Most of the observed bubbles appear to be filled with a less dense material. In this region, the texture of arranged chrysotile fibers has disappeared.
- A thin surface-rim (approximately 30 nm thick), with a different texture from the rest of the sample. The darker hue of the matter hints that it is less dense that the rest of the sample, similar to the agglomerate in the observed bubbles.

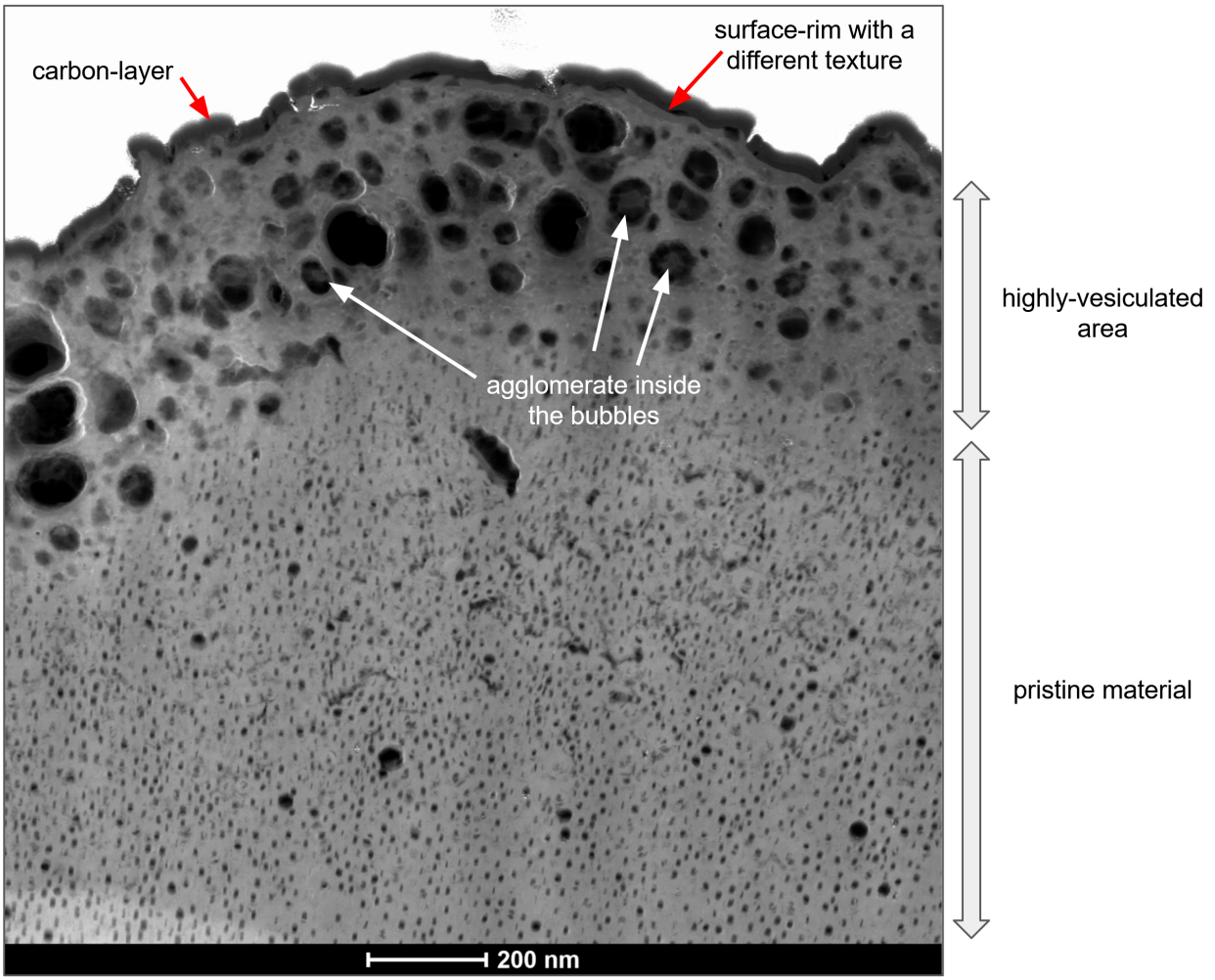

Figure 4.12: HAADF image global view of Ar^+ bombarded serpentine Rawhide. The ion-bombarded highly vesiculated layer is seen above the more pristine arrangement of chrysotile fibers, with a separation seen between 350-400 nm from the surface. A surface rim with another texture from the rest of the sample is seen at the utmost surface.

Porosity and void diameter evolution confirms the presence of two distinct regions (see figure 4.13). There appears to be a highly porous thin layer separating the two ion-bombarded layer from the pristine material.

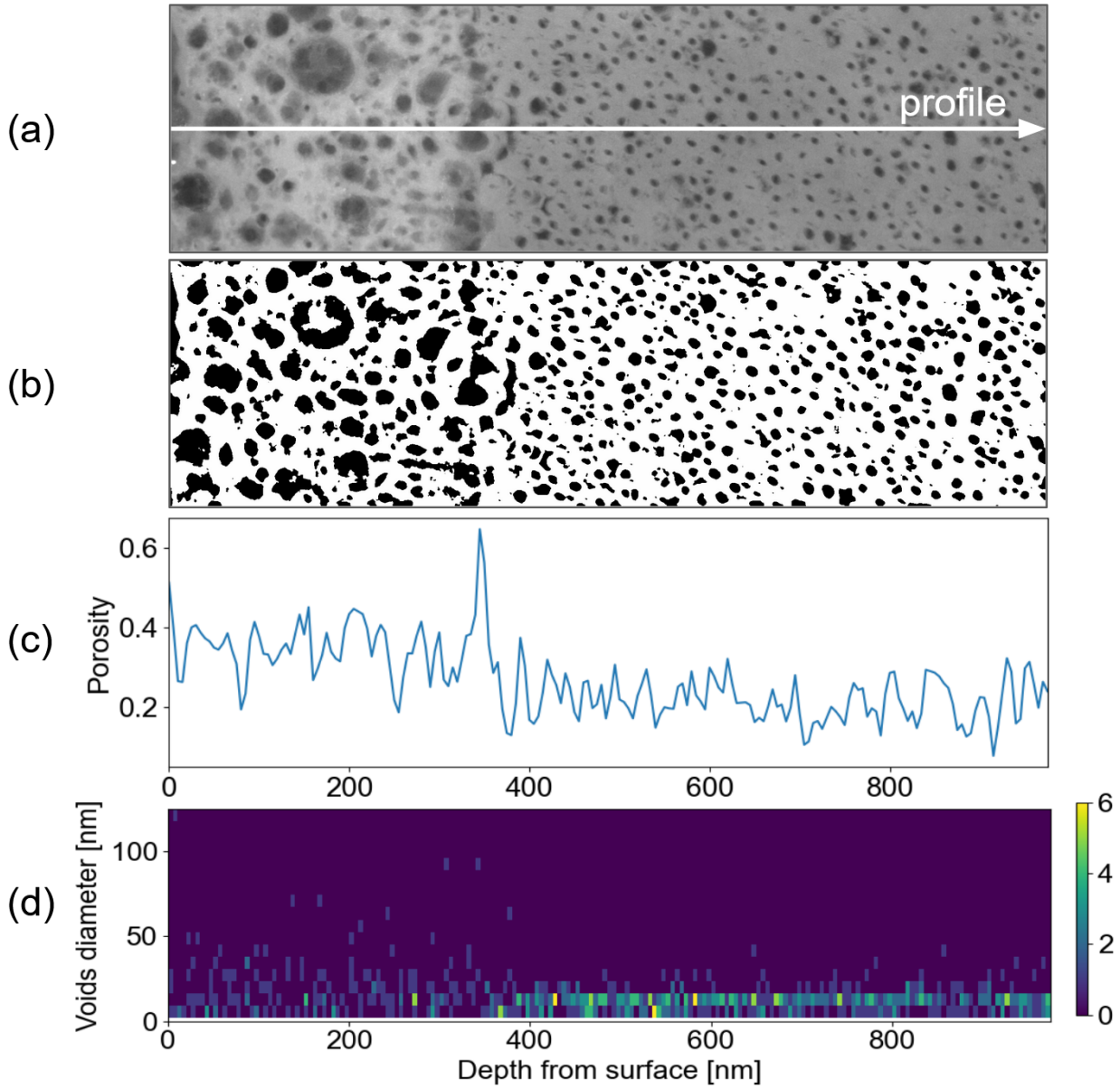

Figure 4.13: (a) HAADF global image of Ar^+ bombarded serpentine Rawhide. (b) Threshold-ed image highlighting the porosity inside the sample (bubbles, fractures and voids). (c) Evolution of the porosity as a function of depth (binned along the x-axis for bin-size of 5 nm). (d) Distribution of the Feret's diameter of 653 voids (identified by thresholding) as a function of depth (x-axis bin-size of 5 nm, y-axis bin-size of 10 nm).

The global composition (figure 4.14) show a decrease in oxygen at%, similarly to the He^+ case. The decrease is less prominent (from $\sim 66at\%$ to $\sim 57at\%$), and appears to be localized in the upper part of the highly-vesiculated area. We measure a decrease in overall quantity of oxygen of $\sim 4\%$.

Similarly to the He^+ case, we also detect the presence of a thin Mg-depleted rim near the surface (-31% with respect to the pristine material), followed by an Mg-enriched area ($+18\%$ with respect to the pristine material).

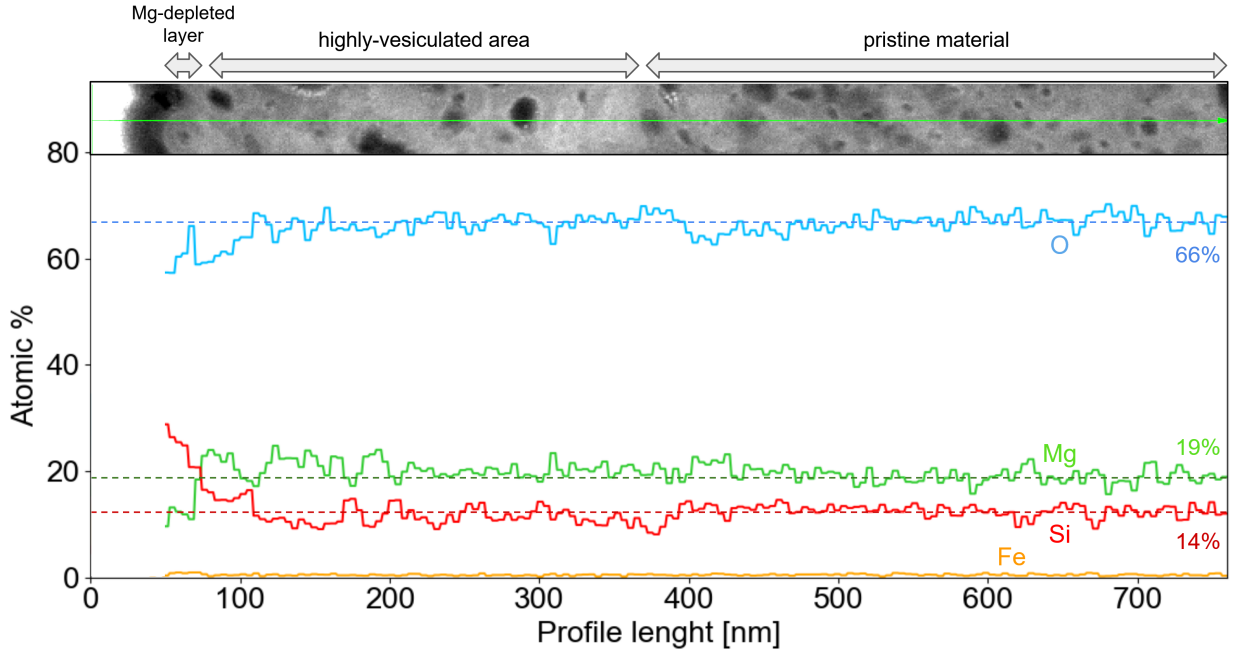

Figure 4.14: Compositional profile in Ar^+ bombarded serpentine Rawhide.

Similarly to the He^+ case, EDS maps revealed MgO rich material inside of some of the larger bubbles and an SiO-righ/Mg-depleted thin rim at the utmost top surface as well as surrounding the filled bubbles (see Figure below). No Ar was detected in the bubbles. No noticeable changes in the very low Fe content.

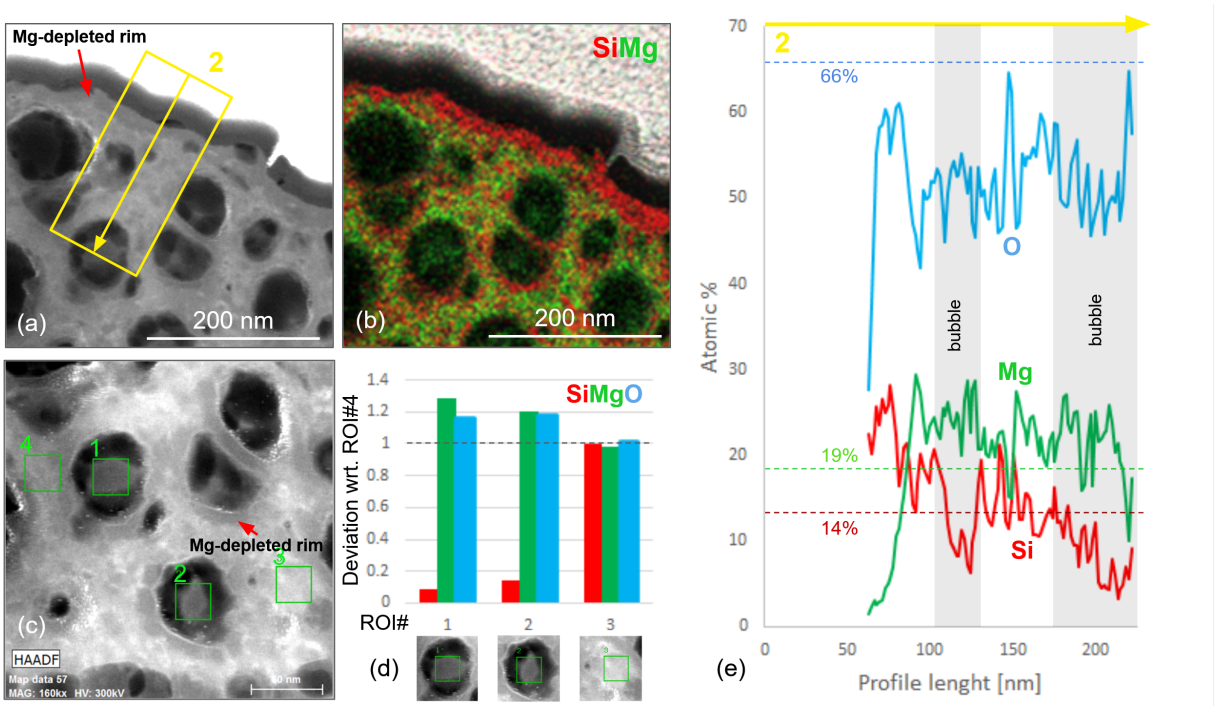

Figure 4.15: Serpentine Rawhide Ar^+ bombarded. (a) zoomed-in HAADF image focused on the thin Mg-depleted rim at the surface. (b) RG/SiMg composite image from intensity STEM-EDX, (c) HAADF image of two bubbles, (d) compositional variations of selected ROIs (2 ROIs inside the bubbles and 1 ROI in the surrounding material), (e) compositional profile of the utmost top surface (raw profile).

Finally, in this sample we also see coalesced bubbles localized at the bottom of the ion-bombarded layer, but we find no evidence of surface bubbles. These localized coalesced regions are responsible for the increase in porosity in the layer separating the ion-bombarded region from the pristine one (figure 4.16).

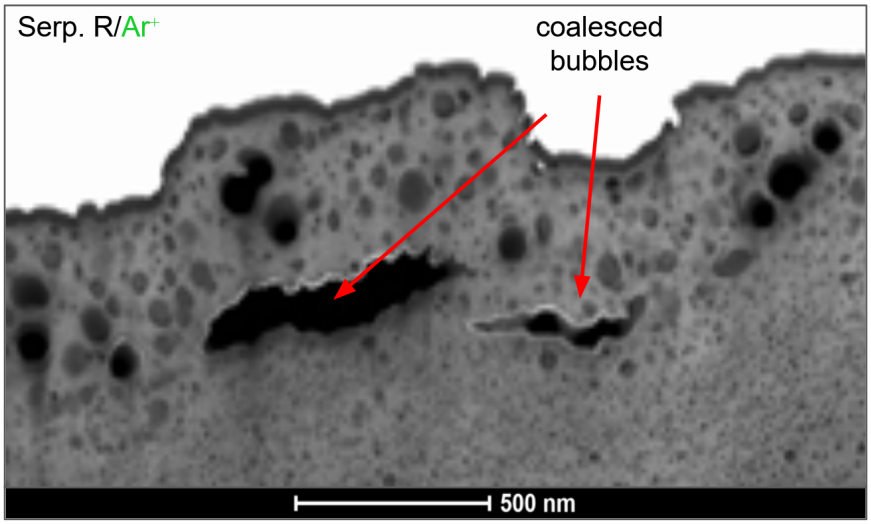

Figure 4.16: Coalesced bubbles in Ar^+ bombarded serpentine Rawhide.

4.2.2. Serpentine UB-N

The serpentine UB-N sample was difficult to analyse, since it appeared to be particularly fragile under the electron beam. As a consequence, the overall quality of the HAADF images is lower that what has been shown for serpentine Rawhide.

4.2.2.1 (a) He^+ bombarded

In the case of the Serpentine UB-N He^+ bombarded sample, the modified layer is about 300 nm thick, in agreement with the SRIM simulation (see chapter 2, paragraph 2.2.3). There are two populations of bubbles (see figure 4.17):

- There are large elongated bubbles, which are tenth of nanometers up to a hundred nanometers in diameter. The direction of elongation is globally parallel to the basal plane of the serpentine. These larger bubbles seem to be present all across the ion-bombarded layer, down to approximately 300 nm.

- A large population of tiny bubbles dotting the material, of only a few nanometers in diameter, is also visible. These population is localized deeper in the sample, from approximately 100 nm down to 300 nm.

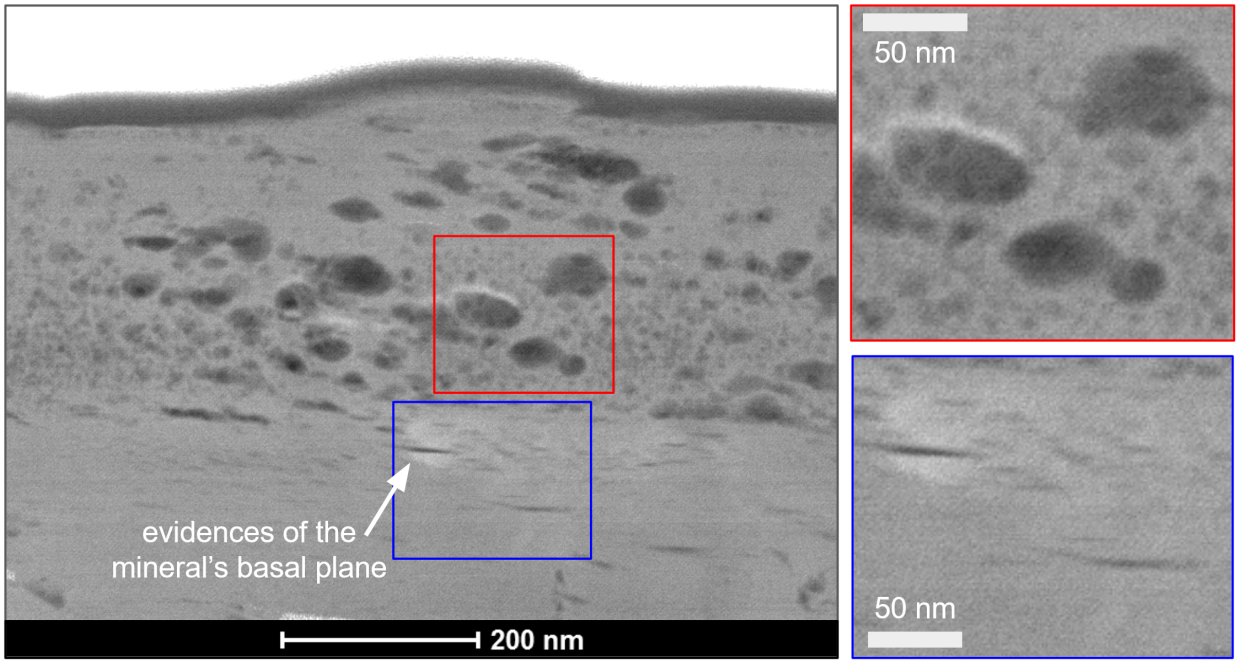

Figure 4.17: Global view of He^+ bombarded serpentine UB-N. Zoomed-in HAADF images of the detected bubbles (red selection) and of the pristine material (yellow selection).

The composition profile across the irradiated layer shows that the utmost top surface region appears to be significantly depleted in O (figure 4.18), from $65at\%$ down to $46.5at\%$. The compositional gradient extend on about 150 nm. In the affected area, overall quantity of O diminishes by 7%. No noticeable changes in Fe content.

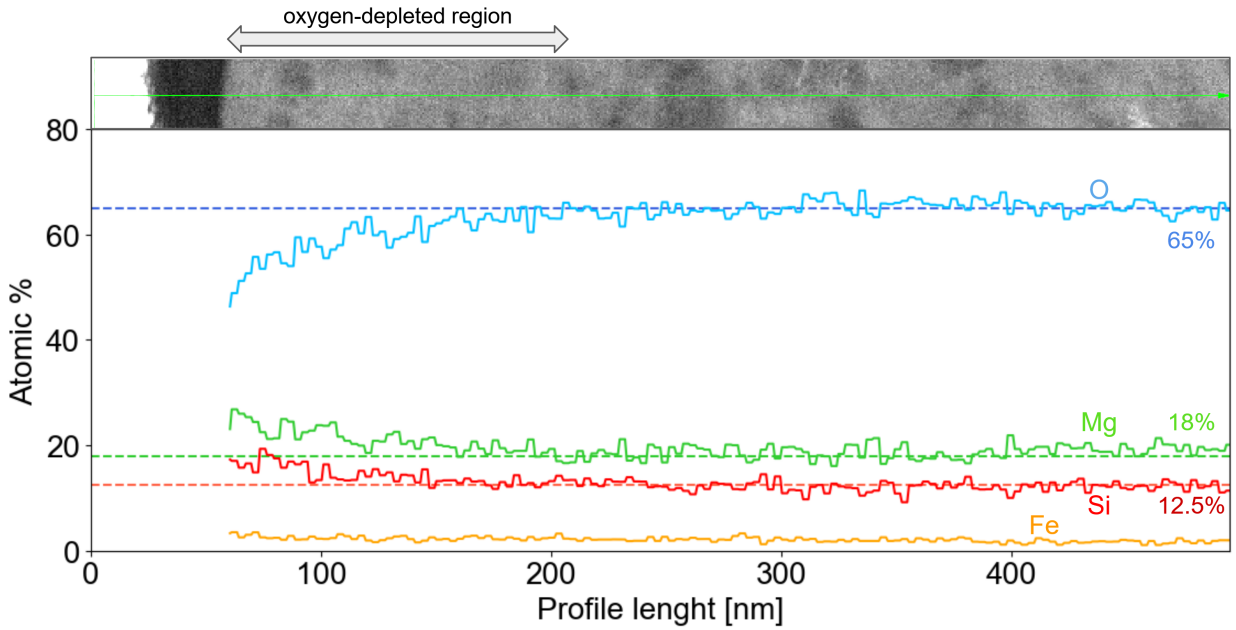

Figure 4.18: Global profile He^+ bombarded serpentine UB-N.

EDS mapping shows that the detected bubbles appear to be empty. No sensible compositional variation was detected in the vesiculated region, except for oxygen (figure 4.19). No Si-rich/Mg-poor surface layer is detected in this sample, contrary to the Rawhide sample.

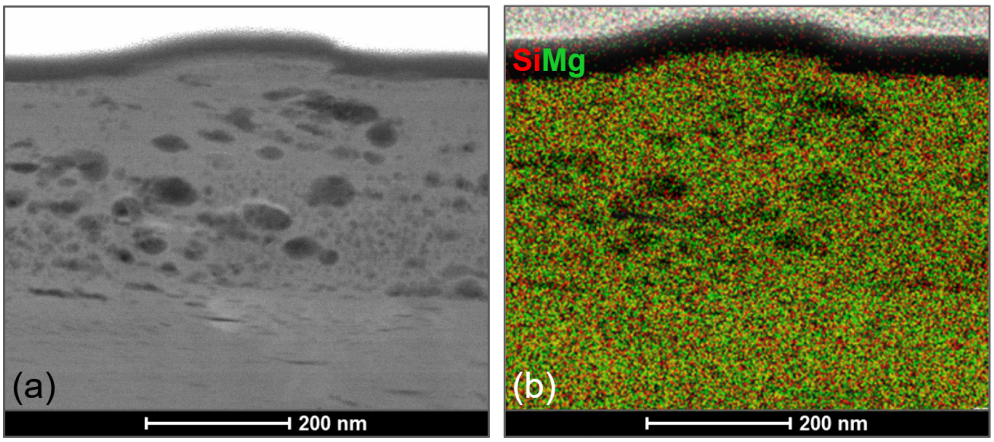

Figure 4.19: Serpentine UB-N He^+ bombarded. (a) HAADF image of the sample, (b) RG/SiMg composite image from intensity STEM-EDX.

4.2.2.2 (b) Ar^+ bombarded

The effects of Ar^+ bombardment on the serpentine UB-N sample appear to be localized on the utmost top surface, over a layer approximately 70 nm thick (figure 4.20). The ion-bombarded layer appears darker than the pristine material, and exhibits a almost continuous empty structure, centered at a depth around 40 nm. This empty structure appears to be a continuous layer of coalesced bubbles. The bubbles are dotted with bright spots that the EDS quantification identified as being Pt and Ga contamination from re-deposition during the FIB section extraction process. We also see a very thin bright layer, only a few nanometers thick, which separates the ion-bombarded matter from the pristine one.

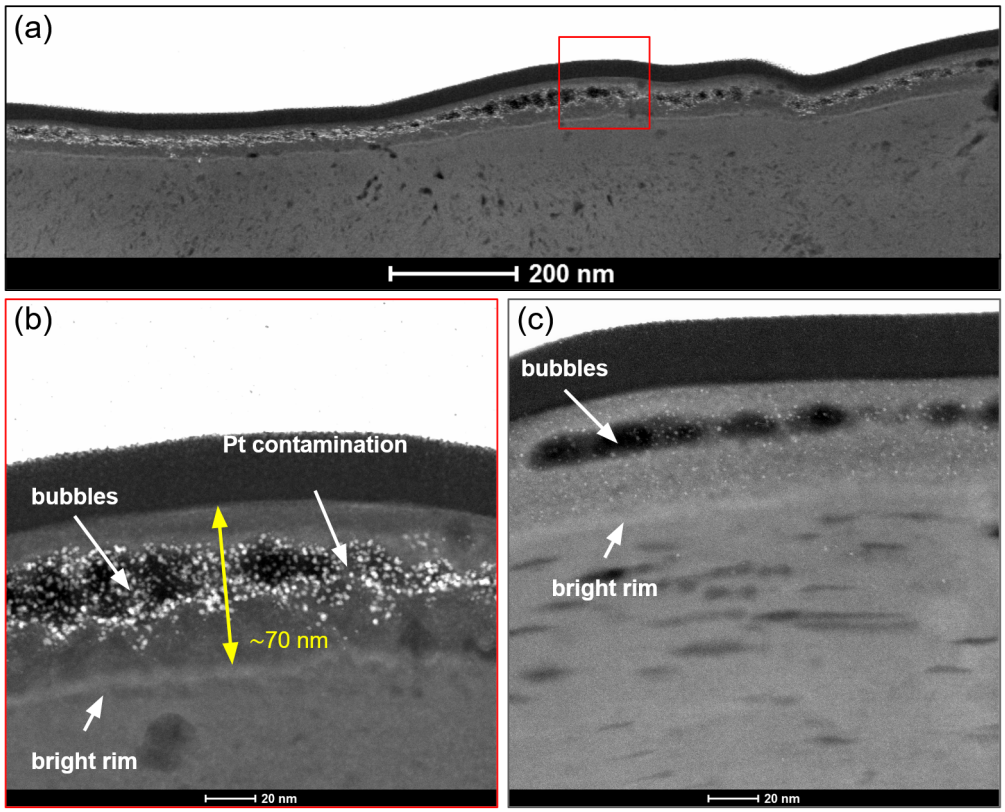

Figure 4.20: (a) Global view of Ar^+ bombarded serpentine UB-N. (b) Zoomed-in HAADF images on the ion-bombarded layer (red selection). (c) Zoomed-in HAAD on another ion-bombarded layer, less contaminated.

The compositional profile across the sample revealed that the ion-bombarded layer appears to be

particularly depleted in both oxygen and magnesium, from approximately 58$at\%$ to an average value of 45$at\%$ for oxygen, and from 19$at\%$ down to approximately 10$at\%$ for magnesium (figure 4.21). No noticeable changes in Fe content.

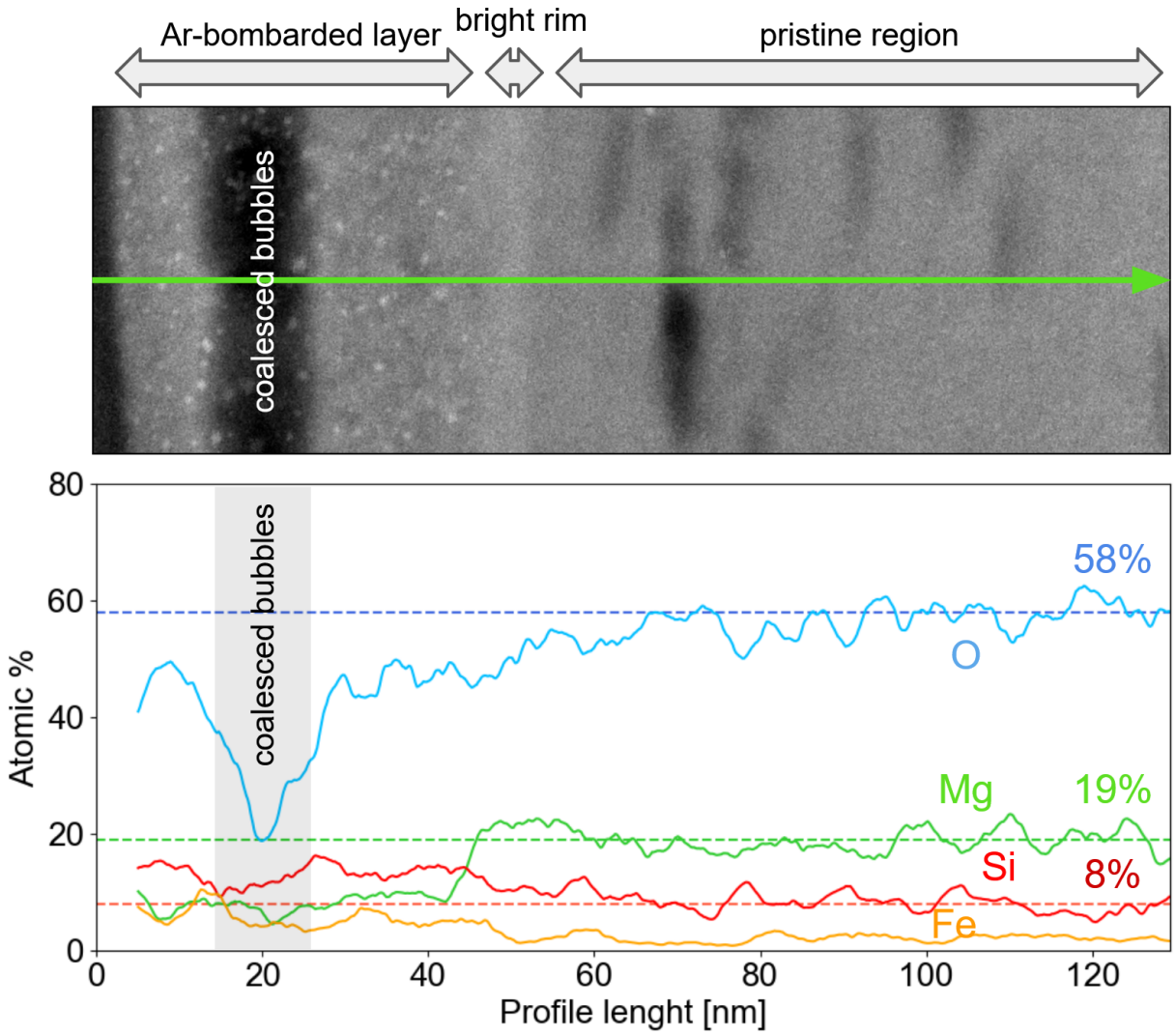

Figure 4.21: Global profile across the Ar-bombarded serpentine UB-N sample. Due to noisy data, the elemental profiles have been smoothed using a mobile average (window size of 20 data points). Note that there is a normalization issue with the global profile here, possibly to data processing malfunctions. The origin of this discrepancy is still being investigated. However, this does not hinder us from discussing relative elemental variations across the profile.

EDS mapping further highlights the difference in elemental composition between the ion-bombarded layer and the pristine material (figure 4.22). Unfortunately, elemental mapping on the bright very

thin rim separating the two regions did not give exploitable results, and due to the delicate nature of the sample, further mapping proved unsuccessful.

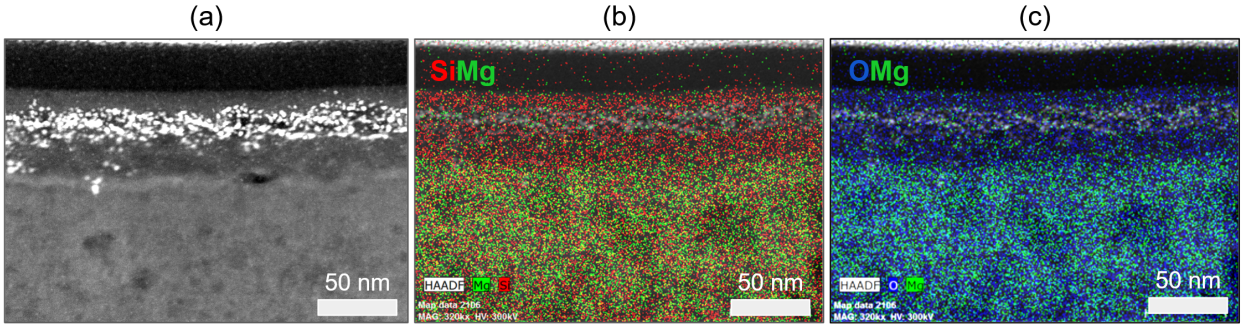

Figure 4.22: (a) HAADF image of the Ar-bombarded layer in serpentine UB-N. (b) RG/SiMg composite image from intensity. (c) BG/OMg composite image from intensity.

4.2.3. Saponite

4.2.3.1 (a) He^+ bombarded

For the He^+ bombarded saponite, the modified layer is about 350 nm deep. This layer contains elongated bubbles with various sizes, up to approximately 150 nm (figure 4.23). These bubbles are found down to 350 nm deep from the surface. Their elongation appears parallel to the basal plane, similar to the He^+ bombarded serpentine UB-N sample. The fibrous texture of the saponite sample, visible below 350 nm in the pristine matter, seem to disappear in the ion-bombarded material surrounding the bubbles.

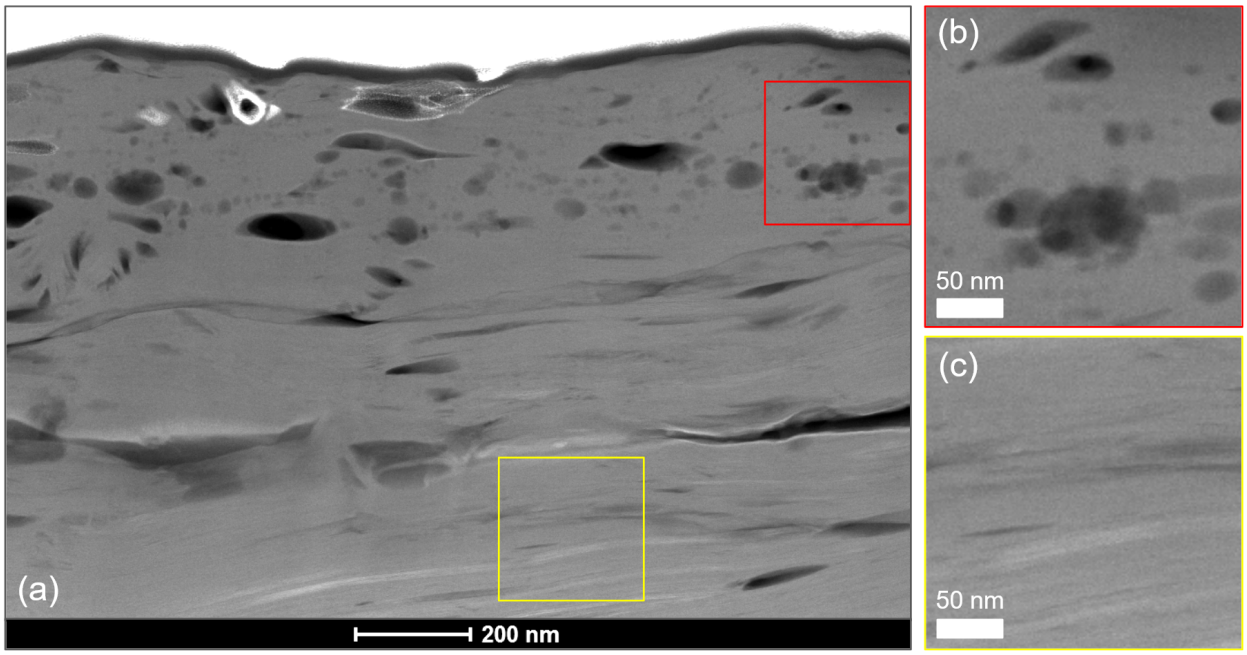

Figure 4.23: (a) Global view of He^+ bombarded saponite. (b) Zoomed-in HAADF images on bubbles (red selection). (c) Zoomed-in HAAD image on the pristine material (yellow selection).

The global compositional profiles highlights oxygen depletion near the sample's surface (again, similar result to the He^+ serpentine case), from approximately $65at\%$ to $46.5at\%$ (figure 4.24). Overall, the utmost surface appears be 9.5% depleted in oxygen, with respect to the pristine material. Again, no noticeable changes in Fe content (this is confirmed when looking at raw signal data from the EDS maps).

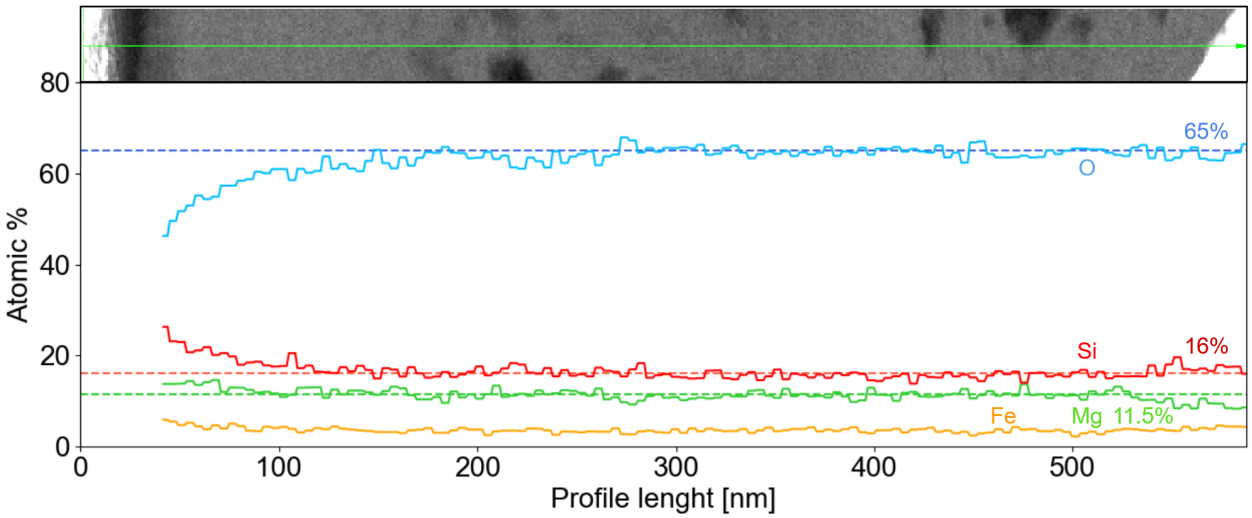

Figure 4.24: Global profile He^+ bombarded saponite.

EDS mapping finds no difference in composition between the bubbles, the surrounding ion-bombarded material and the pristine matter below (figure 4.25).

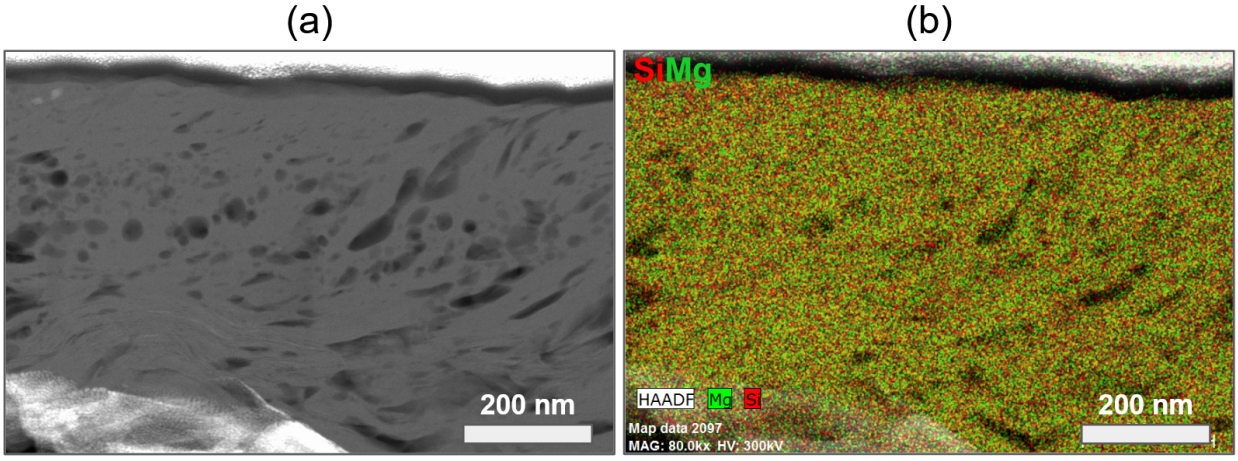

Figure 4.25: Saponite He^+ bombarded. (a) HAADF image of the sample, (b) RG/SiMg composite image from intensity STEM-EDX.

4.2.3.2 (b) Ar^+ bombarded

For the Ar^+ bombarded saponite sample, we observe similar effects to that of the Ar^+ bombarded serpentine UB-N sample (figure 4.26).

- The un-altered fibrous material, located below 80 nm in depth.
- The ion-implanted rim, approximately 80 nm thin, crossed by a layer of coalesced bubbles, approximately 40 nm deep from the surface. All traces of the fibrous structure have disappeared.

However, we see no trace of a brighter rim separating the two regions. The division between these two regions is by a change in texture.

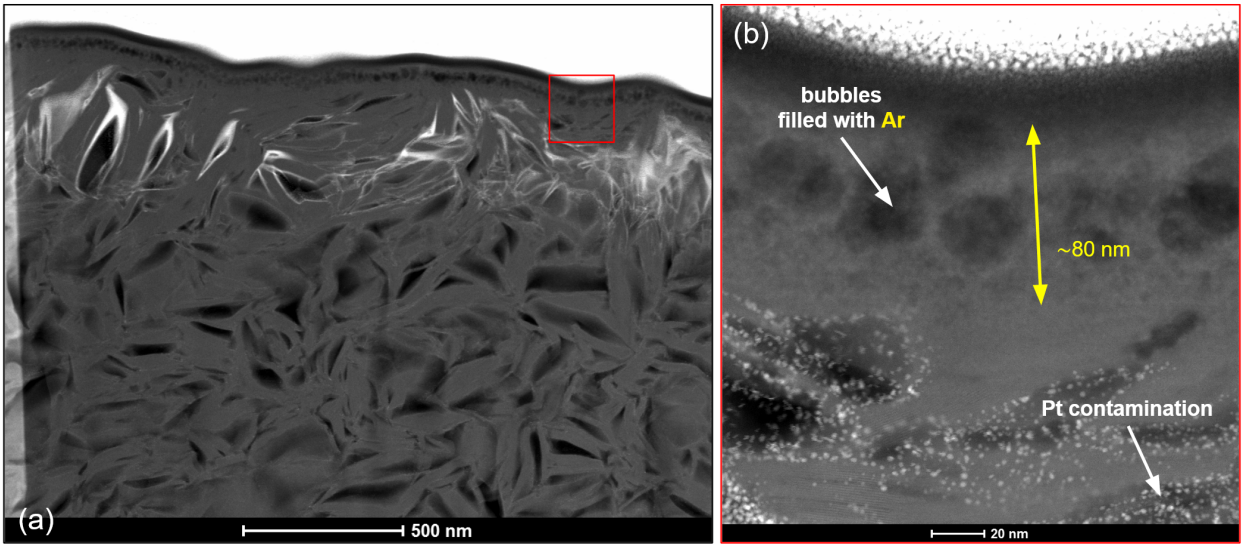

Figure 4.26: Saponite Ar^+ bombarded. (a) HAADF image of the sample, (b) Zoomed-in HAADF image of the ion-bombarded layer. Note that the Pt contamination from FIB-sectioning does not seem to affect the bubbles created by ion-bombardment.

The global profile highlights only a slight oxygen depletion in the ion-bombarded layer (figure 4.27). No noticeable changes in Fe content.

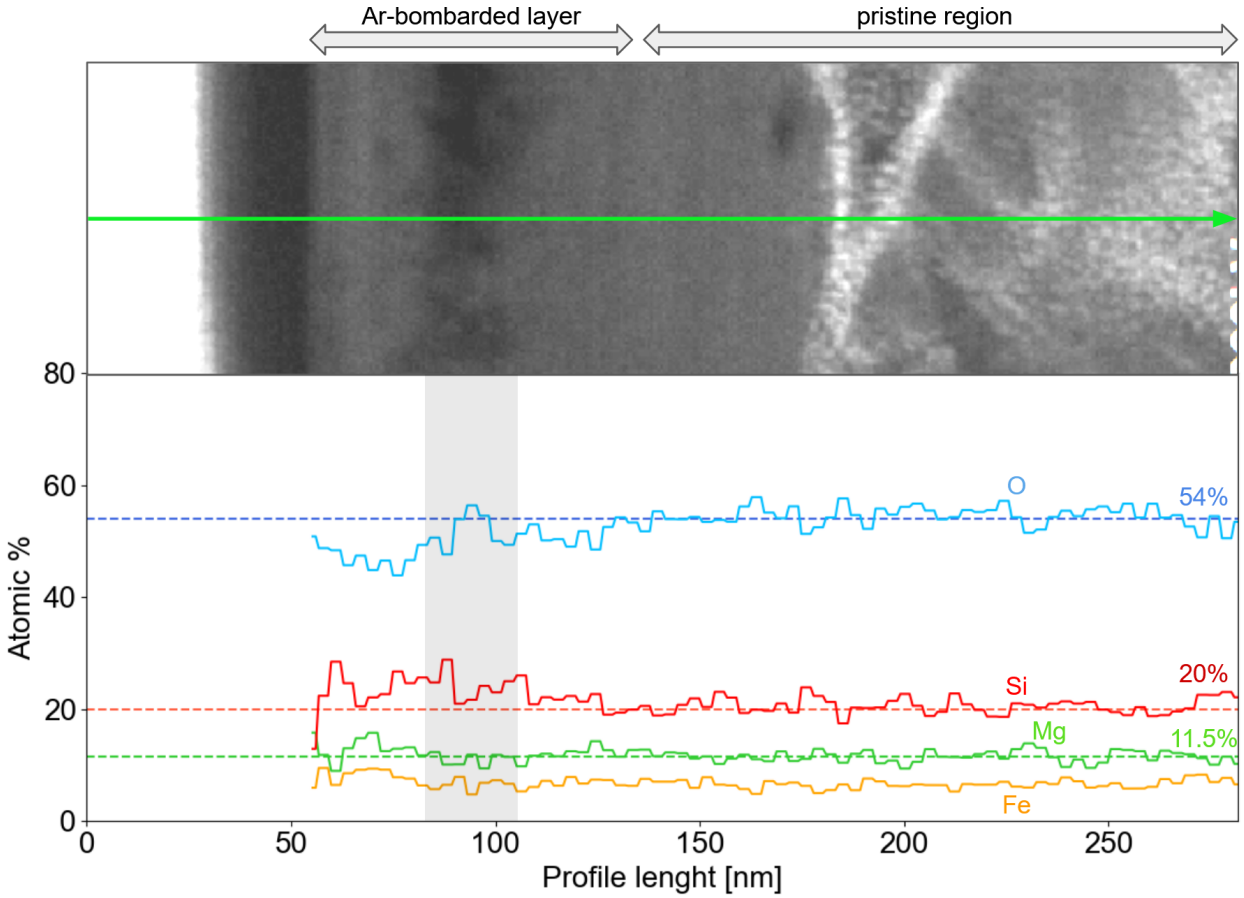

Figure 4.27: Global profile Ar^+ bombarded saponite. Similar to Ar^+ bombarded serpentine UB-N, here too it seems that there is a normalization issue with the global profile. Again, this should not hinder us from discussing relative elemental variations across the profile.

EDS mapping confirm the evolution seen via the elemental profile, and highlight that Ar has remained captured in some of the bubbles (figure 4.28 and figure 4.29).

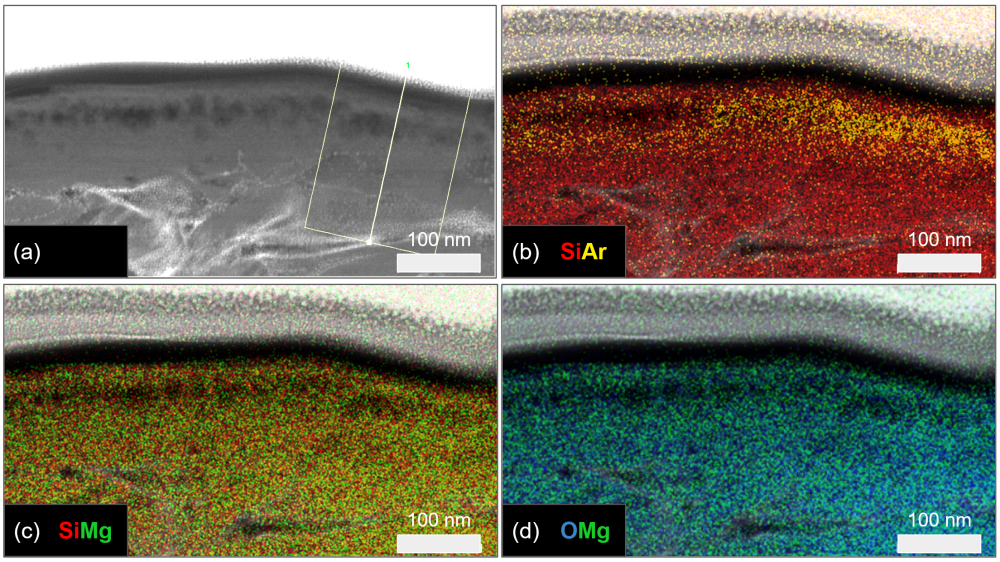

Figure 4.28: Saponite Ar^+ bombarded. (a) HAADF image of the sample, (b) RY/SiAr composite image from intensity STEM-EDX. (b) RG/SiMg composite image from intensity STEM-EDX. (d) BG/OMg composite image from intensity STEM-EDX.

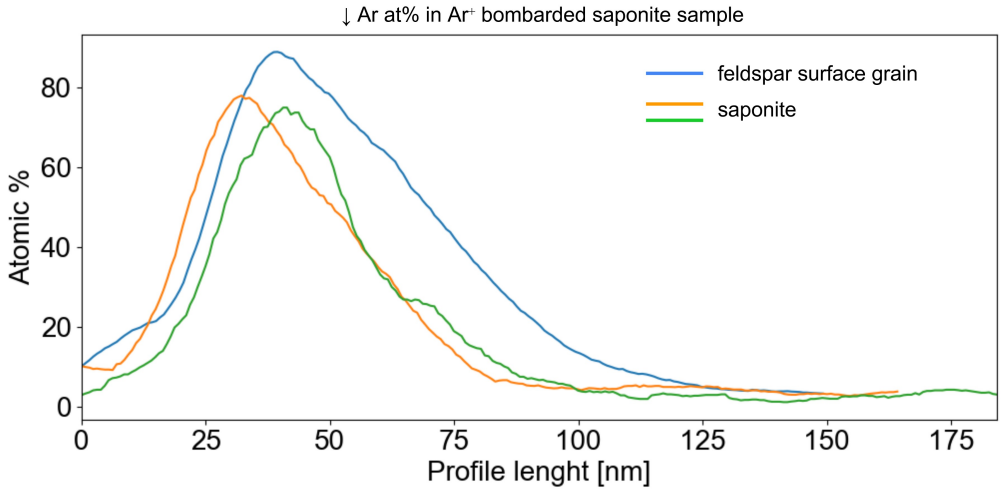

Figure 4.29: Composition profile highlighting the evolution of Ar at% along surface profiles extracted from the Ar^+ bombarded saponite FIB section. The blue curve is associated to an Ar^+ bombarded feldspar grain, identified in the saponite FIB section, which also underwent Ar^+ bombardment. The effects of Ar^+ bombardment on this isolated feldspar grain are discussed in the following section.

4.3. Interpretation of microstructural changes upon weathering

The following tables summarise the main changes upon ion-bombardment observed by STEM-EDS measurements.

			He^+ , 40 keV, 6E16 ions/cm²		
			Serpentine Rawhide	Serpentine UB-N	Saponite
Morphological changes	*Ion implantation depth [nm]*	*SRIM*	317.2	322.1	334.1
		Measured	700	330	350
	Loss of micro-structure		Total	Partial	Partial
	Vesiculation		High (round bubbles)	Low (elongated bubbles)	Low (elongated bubbles)
	Void/Bubble composition		Mg- and O-rich agglutinate (+ gas?)	Empty (or gas?)	Empty (or gas?)
Chemical changes			❑ de-hydroxylation ❑ Mg-poor/Si-rich surface layer ❑ Mg-rich area below the Mg-poor/Si-rich layer	❑ de-hydroxylation	❑ de-hydroxylation

Table 4.2: Observed changes by STEM on FIB section of He^+ bombarded samples.

			Ar^+ , 40 keV, 2E16 ions/cm²		
			Serpentine Rawhide	Serpentine UB-N	Saponite
Morphological changes	*Ion implantation depth [nm]*	*SRIM*	40.6	41.2	42.2
		Measured	300	70	80
	Loss of micro-structure		Total	Total	Total
	Vesiculation		High (round bubbles)	High (coalesced bubble rim)	High (coalesced bubble rim)
	Void/Bubble composition		Mg- and O-rich agglutinate (+ gas?)	Empty (or gas?)	Ar + other gas?
Chemical changes			❑ de-hydroxylation ❑ Mg-poor/Si-rich surface layer ❑ Mg-rich area below the Mg-poor/Si-rich layer	❑ de-hydroxylation ❑ Mg-poor/Si-rich surface layer	❑ de-hydroxylation

Table 4.3: Observed changes by STEM on FIB section of Ar^+ bombarded samples.

We see a certain number of ion-bombardment induced trends which are common among all our

samples.

- For all samples, the original fibrous/layered structure characteristic of phyllosilicate is changed in the ion-affected region. For all Ar^+ bombarded samples and for the He^+ bombarded serpentine Rawhide, it does not survive ion-bombardment, while for He^+ bombarded serpentine UB-N and saponite, it is only partially destroyed.

- In all ion-bombarded regions, we see various instances of vesiculation with bubbles varying in shape and sizes across the samples: round MgO-rich bubbles for He^+ and Ar^+ bombarded serpentine Rawhide, elongated bubbles for He^+ bombarded serpentine UB-N and saponite, and finally a layer of coalesced bubbles for Ar^+ bombarded serpentine UB-N and saponite.

- All samples exhibit some degree of oxygen loss, probably related to de-hydroxylation, mainly localized in the surface regions of the ion-bombarded areas. This oxygen loss appears to be more prominent for the He^+ bombarded samples.

- Multiple samples show changes in the concentration and localisation of magnesium in the ion-bombarded layer (Mg-poor surface layer and MgO-rich bubbles for serpentine Rawhide, as well as heavy Mg-depletion in the Ar^+-bombarded layer of serpentine UB-N).

The STEM-EDS analysis of our ion-bombarded samples has shown that all sample are not affected equally by ion-related weathering processes: serpentine Rawhide made of fibers appears to be the most affected sample, with significant texture and compositional changes in the ion-bombarded layer, followed by the serpentine UB-N, for which He^+ bombardment is only able to locally affect oxygen content and local texture, while Ar^+ bombardment changes Mg/O content and texture in the whole ion-bombarded layer. Finally, the saponite sample appears to be much more resilient than both serpentines, with weathering-changes related mostly to the oxygen content of the ion-implanted region.

Implantation depth: SRIM vs observation

For all (or almost all) the samples, the length of ion-implantation derived by SRIM simulation is

smaller than the actual implantation depth observed. The measured ion-implantation depth for He implanted serpentine Rawhide is close to 700 nm, while the SRIM simulation predicted an ion-implantation depth of approximately 300 nm. Similarly, all Ar^+ bombarded samples show an ion-implantation which double (for serpentine UB-N and saponite) or even septuple (for serpentine Rawhide) from the SRIM derived depth. This is explained by multiple factors. First, SRIM simulations do not account for the initial porosity of the sample, as is seen clearly for the serpentine Rawhide sample. For this sample, the arrangement of chrysotile fibers is already a somewhat porous structure (core of the fiber cylinder and interspace between fibers). As a consequence, ions can implant far deeper in the sample, since they encounter less matter to stop them than in a more compact sample such as serpentine UB-N. Moreover, SRIM simulations also do not take into account the evolution of porosity in the ion-bombarded sample. As bubbles start to appear and grow, the porosity into the ion-bombarded layer increases, and arriving ions encounter even less solid material, probing even deeper in the sample. The three regions observed for the serpentine Rawhide are a testimony of this mechanism. At the start of the He^+ implantation, the first hundreds of nanometers of matter are affected. As the fibrous texture of chrysotile starts to disappear and larger bubble begin to appear, ions are able to traverse this region more easily due to the increased porosity, probing deeper into the sample, creating the second ion-implantation layer, made of loose chrysotile fibers which have lost cohesion due to He^+ implantation. A similar mechanism may have happened also for the Ar^+ bombarded serpentine Rawhide sample, however with no visible transition region visible due to the shorter initial traveling distance of Ar^+. The two bubble population observed for the He^+ bombarded serpentine UB-N may also originates from porosity evolution in the sample.
For the Ar^+ implanted serpentine UB-N and saponite sample, a different mechanism may have taken place (see figure 4.31): both these samples show a coalesced bubble rim located at a depth of approximately 40 nm, which corresponds to the ion-implantation depth derived by SRIM simulation. It is possible that, at the start of the Ar^+ implantation experiment, only the first 40 nm of matter were affected by Ar^+ (figure 4.31, panel 1). At this depth, bubbles started to form by gas injection in the mineral system (figure 4.31, panel 2). At some point, the size of these bubbles passed a certain threshold, making the bubbles coalesce in an almost continuous empty bubble rim

(figure 4.31, panel 3-4). This prompted the appearance of a new and secondary sputtering surface inside the sample. Arriving Ar^+ ions more easily traverse the now amorphized first 40 nm of matter, encounter the coalesced bubble rim and then encounter a new surface to implant, effectively almost doubling their probing depth (figure 4.31, panel 5).

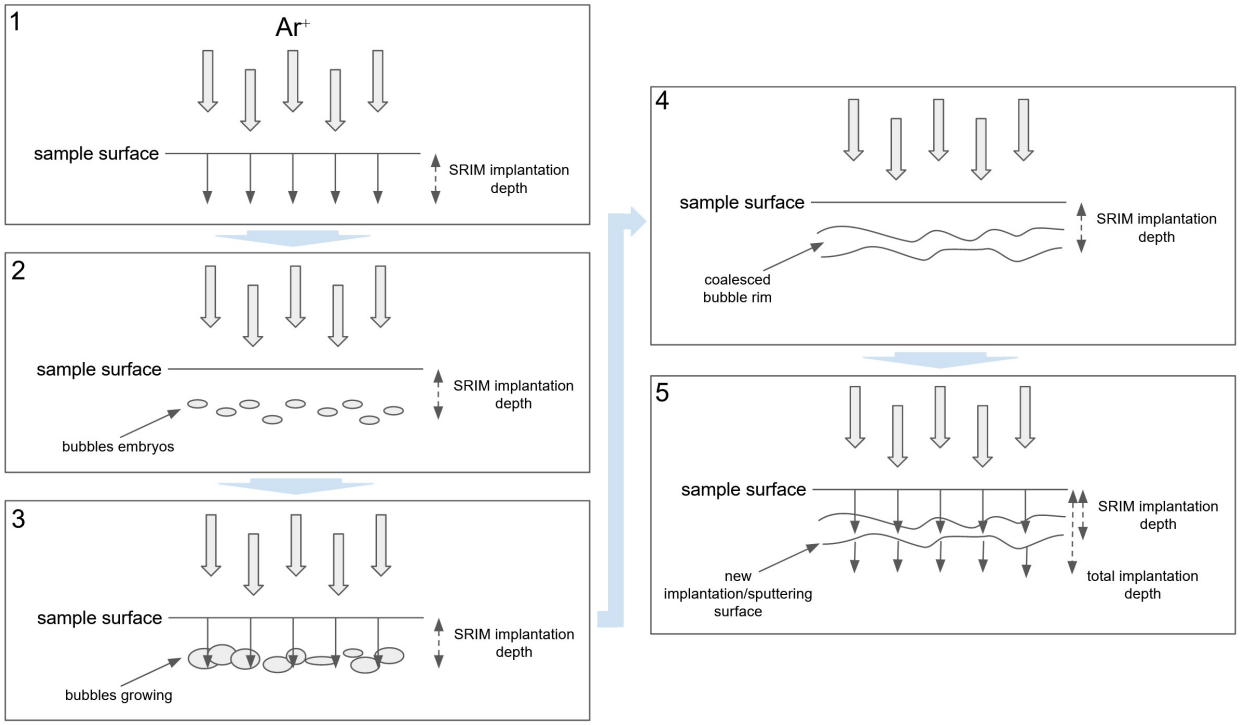

Figure 4.30: Proposed mechanism for Ar^+ implantation in serpentine UB-N and saponite, to explain the larger observed ion-implantation depth.

Bubbles and vesiculation

Vesiculation and the creation of bubbles plays an important role in the ion-implantation process of our samples. Vesiculation of the material close to the surface is not uncommon in experiment tackling SpWe. Vesiculation has been seen in pulsed-laser irradiation (Thompson et al. 2019) and ion-bombarded carbonaceous chondrites (Laczniak et al. 2021). Bubbles and vesiculation has also been detected on lunar samples (Gu et al. 2022, Noble et al. 2005), on Itokawa samples (Noguchi et al. 2014, Thompson et al. 2014) and by experiment reproducing lunar-type SpWe on anhydrous phases such as olivines (Carrez et al. 2002, Demyk et al. 2001). In figure 4.32, examples of bubbles and

vesiculation extracted from the literature cited before are shown for illustrative purpose. Note that the shape, localization and nature of the observed vesiculated rim is different among the shown examples (bubble shape, coalesced rim of individual bubbles) but it is always localized near the surface of the sample. Our vesiculated layers show a number of similar features to the examples taken from literature, such as the presence of surface bubbles/vesicles or blisters similar to those observed for Itokawa's samples or highly vesiculated/coalesced regions similar to those observed for He^+ bombarded Murchison and lunar grains (a more in-depth comparison with the results from Laczniak et al. 2021 is presented in this section further down below).

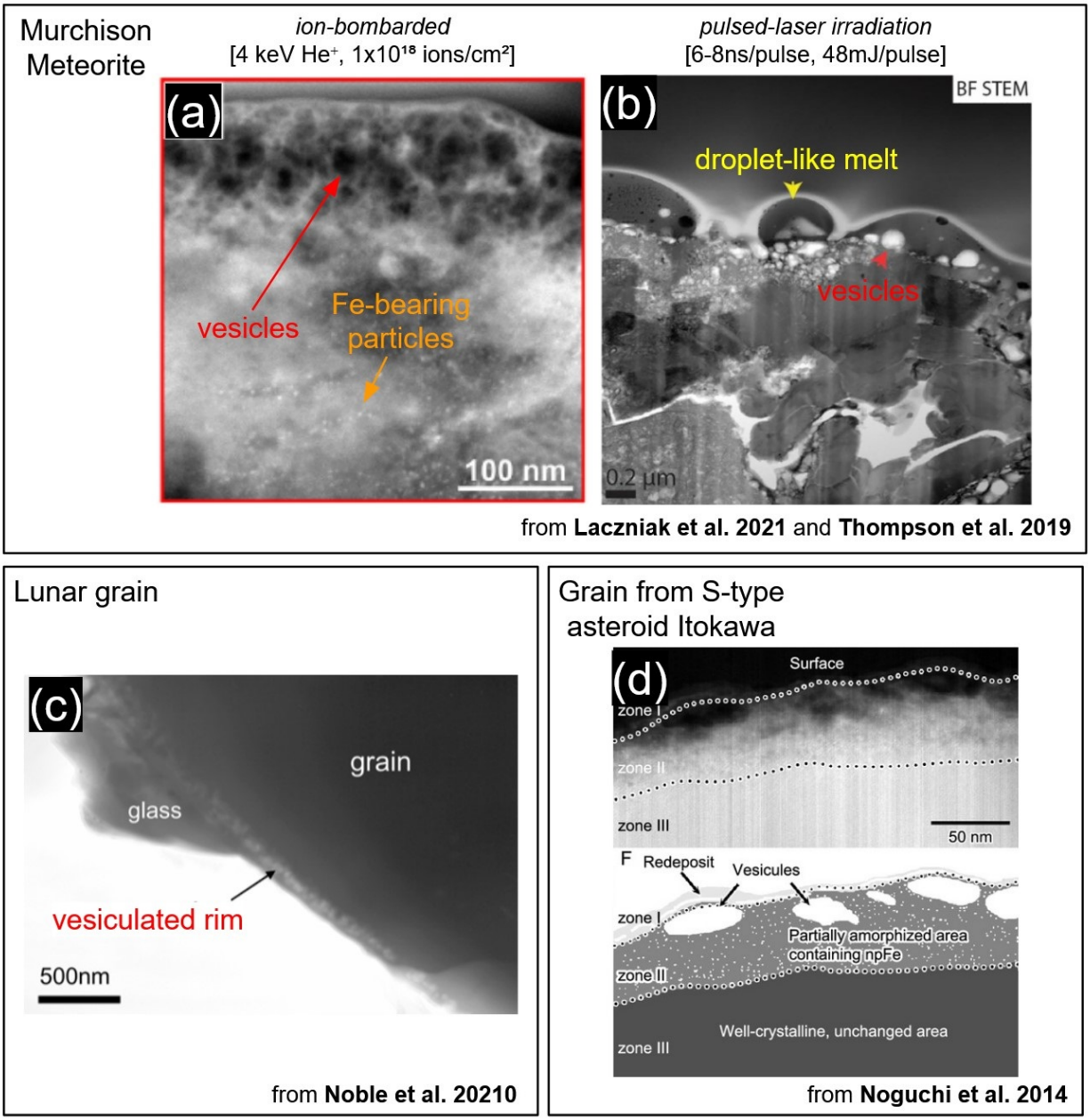

Figure 4.31: Examples of vesiculation and bubbles in the scientific literature. (a) From Laczniak et al. 2021: HAADF STEM image of a highly vesiculated area (approximately 105 nm thick) of 4 keV He^+ bombarded Murchison chip. (b) From Thompson et al. 2019: Bright-field STEM imaging and microanalysis of the laser-pulsed irradiated Murchison meteorite chip. (c) From Noble et al. 2005: a continuous vesicular rim from Lunar regolith particle 79035. (d) From Noguchi et al. 2014: Surface features observed on ferromagnesian silicates in the Itokawa particles investigated in this study and corresponding schematic diagrams with interpretation of their textures (np(Fe,Mg)S, nanophase (Fe,Mg)S; npFe, nanophase Fe).

Vesicles and bubbles are born in upon ion-bombardment via gas implantation in the mineral, in this instance He_g and Ar_g. EDS mapping is unable to identify captured He_ginside the bubbles, but we did manage to detect Ar_g in some isolated bubbles in saponite. These isolated bubbles, not having coalesced, managed to trap Ar_g, contrary to the serpentine UB-N case, where the coalesced bubble-rim may have led to the escape of Ar_g.

The vesiculated layers highlight that the creation of elongated bubbles (become more round as they increase in size) and vesiculation tends to be an an-isotropic process, as the growth of bubble's embryo seem to be "guided" by the mineral structure of the ion-bombarded material. This is especially visible for the serpentine UB-N and saponite He^+ bombarded samples, for which small bubbles appear elongated, following the mineral basal plane. The area surrounding these vesiculated region appear to systematically loose the original mineral structure, as we see no traces of the fibrous structure for serpentine Rawhide and of the layered structure for serpentine UB-N and saponite near the bubbles. The loss of the fibrous/layered texture upon bombardment highlights various degrees of change in the silicate lattice of the ion-bombarded regions. We can't talk about degree of amorphization since STEM-HAADF and EDS are not sensible to it (in the near future, electron diffraction data using transmission electron microscopy will be acquired to investigate amorphization in ion-implanted regions). However, loss of texture in STEM images is often a symptom of amorphization. As bubbles grow and their surrounding environment gets more and more amorphized, we note that they tend to take on a more spherical shape. The creation of bubbles in all samples denotes a certain atomic mobility upon ion-bombardment (more on that in the following paragraphs).

Looking at our results, one would wish to be able to assess how different our vesiculation process are compared to similar experiments on anhydrous phases for a comparison with "lunar"-style SpWe experiment. Comparing our results with other studies is difficult because of the many varying parameters which can change among SpWe-focused studies. During my PhD, I was able to replicate my ion-bombardment experiment of four HED meteorites. Analyzing the micro-structure of these anhydrous material who would have been subjected to the same experimental conditions of my hydrated silicates would allow us to establish a more direct comparison between our vesiculation

processes observed on phyllosilicate and the one which would be observable on pyroxene and olivine phases present in these ion-bombarded HEDs pellets. Unfortunately, this has not been done as of today for lack of time. However, in a twist of luck, we were able to ion-bombard a feldspar grain, emerging on the surface of the Ar^+ bombarded saponite sample (our samples being terrestrial rocks are not free of mineral contamination, and this feldspar grain was one of them). The complete data processing of Ar^+ bombardment on this feldspar grain has not been done yet, however we note that HAADF STEM images show no difference in the size of the vesiculation rim between the feldspar grain and saponite (see figure 4.33), nor in the ion-implantation depth in both samples. This suggests that vesiculation for the Ar bombarded samples is mainly caused by ion implantation, and not by possible degassing of species upon the phyllosilicate de-hydroxilation, such as H_2O, H_2 or O_2. De-hydroxilation and the possible creation of the species cited here is discussed in the following paragraph.

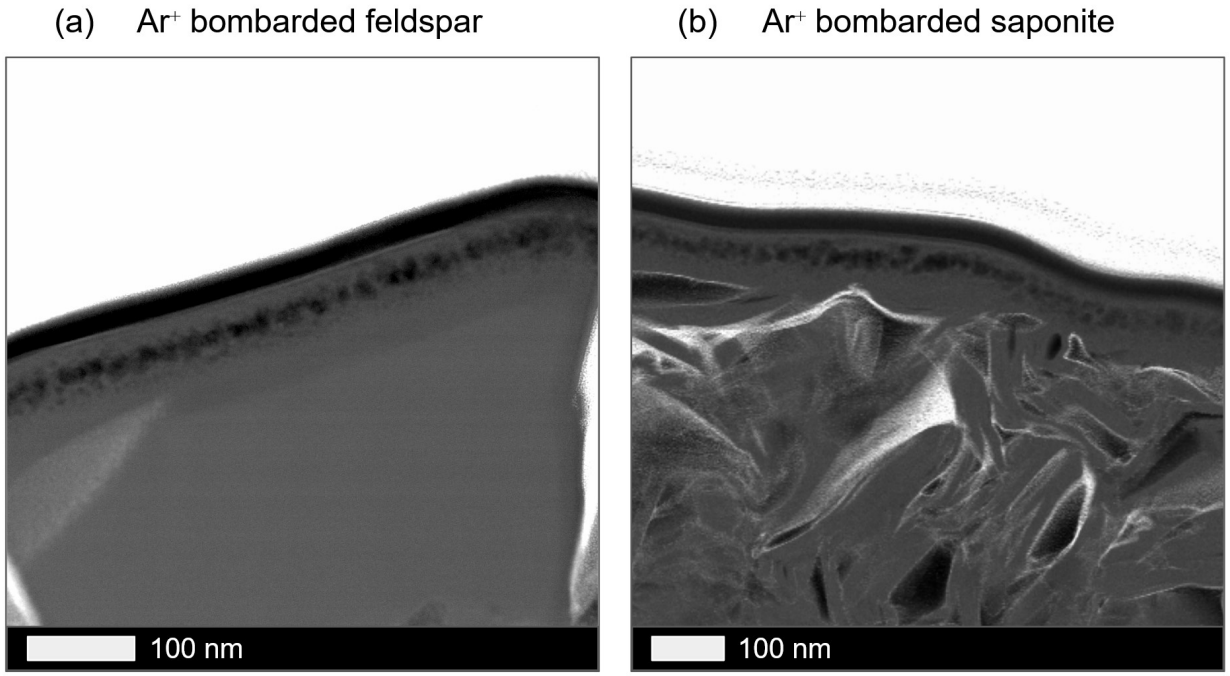

Figure 4.32: HAADF STEM image of a feldspar grain localized on the surface of the saponite Ar^+ bombarded pellet (a), and of Ar^+ bombarded saponite. No notable differences can be seen regarding the ion-bombarded layer structure or width.

This vesiculation and amorphization process seems particularly efficient for the serpentine Rawhide

sample, independently from the ion considered. This is probably related to the fiber textured nature of this sample. The arrangement of fibers in chrysotile exposes much more surface than a more classical compact-layered phyllosilicate structure. More exposed surface leads to more regions where sputtering effects from ion-bombardment may occur, amplifying ion-bombardment effects on these fibrous, more porous regions.

It is relevant to reaffirm that the results presented here originate from an experiment performed with an ion-flux of approximately $10^{13} ions/cm^2/s$, which is low enough to prevent collisional heating of the sample upon bombardment but relatively high when compared to natural solar-wind. Laczniak et al. 2022 have performed low-flux experiments on Murchison matrix at fluxes much closer to the natural solar wind ($10^{11} ions/cm^2/s$) and see the development of only minor vesiculation. All the ion-bombarded samples presented here showcase some degree of vesiculation, but it is generally fairly developed across all samples. This, coupled with the results from Laczniak et al. 2021 indicates that there is some dependency of vesiculation effects upon ion-flux, with a faster "gas-injection-rate" in the ion-bombarded material resulting in the development of more vesicles. This may be due the coupling of two effects, the difference in the gas volume which are being injected per unit of time between low- and high-flux experiments, as well as the different energy deposition rate associated to low- and high-flux bombardment conditions. Further studies comparing the effect of ion-flux, coupled with SRIM simulation comparing voids creation and atomic displacement associated to each varying fluxes are needed to better understand ion-flux effects overall.

De-hydroxylation

A common trend seen in all samples is the oxygen depletion in the utmost surface layers observed via EDS mapping. Oxygen loss upon weathering has been observed on ion-bombarded carbonaceous chondrites (Keller et al. 2015b) and olivine (Demyk et al. 2001). All our samples changes in surface chemistry seem to point out a certain oxygen mobility upon ion-bombardment. This would suggest that there is preferential loss of oxygen in the crystal lattice of phyllosilicates upon irradiation. Since phyllosilicates are hydrated species, harbouring hydroxyls (-OH) bonds and molecular water, we can expect the oxygen loss to be correlated with de-hydroxylation. The values associated to

oxygen depletion in the ion-bombarded layers are compatible with preferential destruction of the (M)-OH bond and subsequent loss of oxygen. De-hydroxylation can spur the creation of gaseous species, such H_2O, O_2 and H_2, which may have contributed to the creation of vesicles and bubbles in the ion-implanted material before escaping or remaining trapped in the created bubbles (EDS mapping is unable to identify if these species remained captured inside the bubbles or were evacuated at some point). However, since we have seen that there are no significant differences between the vesiculated layer of an hydrous sample (saponite) and an anhydrous one (the feldspar grain shown in the paragraph before, which can't undergo de-hydroxilation), we conclude that the contribution of these gaseous species to the growth of bubbles is very weak or non-existent.

We note that the depth associated to the oxygen depletion varies greatly when comparing He^+ and Ar^+ bombarded samples (see the following table).

sample	serpentine Rawhide	serpentine UB-N	saponite
40 keV He^+	200 nm	120 nm	140 nm
40 keV Ar^+	100 nm	70 nm	80 nm

Table 4.4: Estimate of the depth associated to oxygen depletion in the ion-bombarded samples.

This difference, similarly to the total ion-penetration depth, is related to the different collisional regimes dominating for He^+ and Ar^+ bombardment. In 2.2.3, via SRIM simulations we have seen that, for Ar bombarded samples, elastic collision dominate the implantation regime, while inelastic collisions dominates for He^+ bombarded samples. Elastic collisions dominated regimes deposit more energy per unit of length than inelastic dominated regimes (in our case, Ar^+ deposits almost 100 times more energy than He^+ for the same traversed distance). As a consequence, for a same material, Ar^+ will travel less far than He^+ prior to depositing all its energy, overall affecting a shorter distance than He^+, hence the observed difference in distance.

Finally, we note that the overall shape of the oxygen depletion curve for most of the samples resembles an erf function:

$$erf(x) = \frac{2}{\sqrt{\pi}} \int_0^x e^{-t^2} dt$$

The erf function, also known as the Gauss error function, can be used to describe two materials

separated by a planar interface (as well as its complementary function, $erfc(x) \sim 1 - erf(x)$). This function is used to quantify the phenomena of absorption and desorption through a free surface (see figure below for illustrative purposes).

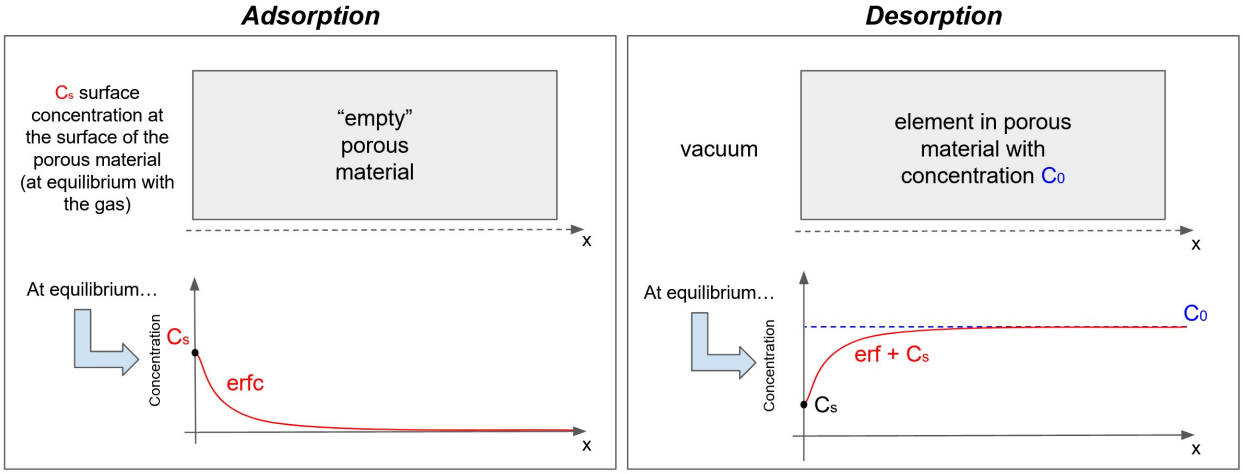

Figure 4.33: Example of use of erf and erfc functions to quantify the equilibrium state of two systems: a gaseous species in contact with a material having a zero initial composition (adsorption, left), and a species diluted in a system with initial composition C_0 in contact with vacuum (desorption, right). These are just examples to illustrate the shape of the erf function.

The oxygen depletion curves we measured seem to describe a desorption case, in which the de-hydroxylation process has given a certain mobility to oxygen in the samples via preferential destruction of the (M)-OH bond. The mobile oxygen has then left the utmost surface towards the vacuum. We plan to apply erf fitting to the oxygen depletion curves in order to better quantify this desorption processes. These results will be shown in a future publication tackling the results of this entire chapter.

Magnesium mobility upon irradiation

For some samples, de-hydroxylation is accompanied by certain changes in magnesium concentration and localization in the ion-implanted layer. Preferential Mg-mobility has been seen in He^+-bombarded Mg-rich olivine grains embedded in the matrix of Murchison (Laczniak et al. 2021) and on terrestrials olivine samples (Demyk et al. 2001, Carrez et al. 2002). For the serpentine Rawhide sample, in both He^+ and Ar^+ case, we see the appearance of a surface rim, approximately 30-40 nm

thick, which appears to be particularly depleted in Mg. Intensity STEM-EDX mapping shows that this layer has about the same amount of Si as the un-irradiated material but the amount of magnesium is much lower. The harsh depletion of Mg in this surface layer suggest that Mg is preferentially sputtered upon ion-bombardment during the amorphization process, indicating a certain mobility of Mg in the crystal lattice. This is coherent with Mg^{2+} in octahedral sites being more mobile than Si^{4+} in tetrahedral sites (Davoisne et al. 2008). Since the ion-bombardment experiments are done under vacuum, sputtered Mg has possibly left the surface ion-bombarded surface, drawn by the vacuum. However, some of the sputtered Mg may have instead moved deeper in the sample by virtue of the electric field present during the ion-bombardment procedure. This process has already been hypothesized by Davoisne et al. 2008. Forward scattering may have also contributed to pushing from the utmost surface to deeper in the sample. This would explain the slight Mg-enrichment seen just below the Mg-depleted/Si-rich surface layer in both He^+ and Ar^+ bombarded serpentine Rawhide (for the He^+ case, the Mg-depleted rim is depleted by approximately 20% in Mg with respect to the Mg concentration of deeper pristine material over short distance of 40 nm, and is followed by a Mg-enrichment of approximately 17%, distributed over 180 nm - the proximity in depletion and enrichment value suggest an link between the two).

Similar Mg-depleted/Si-rich rims are detected in the inferior part of the large bubbles identified in the serpentine Rawhide He^+) and Ar^+ bombarded cases. As these bubbles grow larger, they act as a supplementary sputtering surface (similarly to the phenomenon we discussed when comparing SRIM ion penetration values and observed penetration depth for Ar^+ serpentine UB-N and saponite samples), hence why we see a 'replica' of the surface effects on the inferior outline of these bubbles. The sputtered Mg in this instance does not escape the sample due to the vacuum, but remains trapped inside the bubble, precipitating as an Mg-rich phase (likely MgO). EDS chemical mapping shows that these agglomerates are also O-rich. This further supports the idea of preferential Mg and O mobility in the phyllosilicate lattice upon ion-bombardment. An MgO enrichment had been previously observed by Carrez et al. 2002 and Davoisne et al. 2008 on the surface of a 4 keV He^+ bombarded olivine. In our case, this precipitate could be both magnesium oxide or magnesium hydroxide agglutinate (possibly brucite - $Mg(OH)_2$), since both can be created upon the destruction

of the -Mg-OH system (EDS mapping does not distinguish between the two).

The Ar^+ bombarded serpentine UB-N sample also shows heavy signs of Mg-depletion in the ion-bombarded layer, which is approximately 40 nm thick (similar thickness of the Mg-depleted/Si-rich rim detected for the serpentine Rawhide sample), indicating that preferential sputtering of Mg happened in this sample too. No MgO-rich agglutinate nor Mg-enrichment past the ion-bombarded sample has been detected by EDS mapping. It is possible that most of the sputtered Mg in serpentine UB-N may have left the sample. This hypothesis shall be tested in future SRIM simulations. Note also that the Ar^+ bombarded saponite does not show any evidence of Mg-depletion and/or mobility. This may possibly due to the relatively high Fe-content of the saponite with respect to the serpentine samples ($Fe/(Fe + Mg)$ value equal to 0.46 for saponite against 0.07 and 0.13 for serpentine Rawhide and UB-N respectively). Again, this too shall be further investigated via more SRIM simulations.

Comparison with ion-bombarded carbonaceous chondrites

Recent studies have been focusing on simulating SpWe on hydrated carbon-rich surfaces by working on carbonaceous chondrites as surface analogs, such as Laczniak et al. 2021. In this paragraph, I wish to compare the various results derived by my study and the one led by Laczniak et al. 2021, to identify possible differences arising by our different samples (terrestrial hydrated minerals VS carbonaceous chondrites). In Laczniak et al. 2021, the authors led 1 keV H^+ and 4 keV He^+ irradiation experiments on a slab of Murchison CM2 meteorite to mimic the effects of solar wind irradiation on primitive bodies. The fluence achieved were $8.1 * 10^{17} ion/cm^2$ for H^+ and $1 * 10^{18} ions/cm^2$ for H^+ and He^+ respectively. The authors led an extensive characterization of the irradiated samples, including scanning transmission electron microscopy (STEM) on FIB sections extracted from the irradiated samples and detailed composition analysis by EDS. Since they were working on a carbonaceous chondrite, they were able to probe the effects of ion-irradiation not only on the hydrated phyllosilicate matrix of the meteorite, but also on other phases, such as Mg-rich and Fe-rich olivines embedded in the meteorite matrix. For the sake of simplicity, we shall only compare the results on the He^+ bombarded matrix sample with the results from our He^+

bombarded samples. The following tables sums up the differences and similarities between our results.

		Samples			
		Slab	Pellet		
		4 keV He^+ - 1x10^{18} ions/cm²	40 keV He^+ - 6x10^{16} ions/cm²		
		Murchison matrix (Laczniak et al. 2021)	**Serpentine Rawhide**	**Serpentine UB-N**	**Saponite**
Vesiculation rim	Degree	High	High	Moderate	Low
	Thickness	100 – 130 nm	250 - 400 nm	200 - 250 nm	200 nm
	Bubbles/ Vesicles	Spherical and oblong up to 130 nm in length	Spherical up to 100 nm in length filled with MgO-rich material	Spherical and oblong Up to 70 nm in length	Spherical and oblong Up to 150 nm in length
Amorphization*		Complete down to 150-175 nm deep	Complete down to 400 nm deep	Partial	Partial
Chemical changes		No clear change reported	❑ de-hydroxylation ❑ Mg-poor/Si-rich surface layer (40 nm thick) ❑ Mg-rich area below the Mg-poor/Si-rich layer	❑ de-hydroxylation	❑ de-hydroxylation
Presence of Fe-bearing nanoparticles?		Yes	No	No	No

* as discussed previously, while waiting for electron diffraction measurement, the assessment of amorphization for the samples included in this work is based only on the change/loss of the typical phyllosilicate texture, and as to be considered with caution.

Table 4.5: Comparing ion-irradiation induced changes between the samples of this study and 4 keV He^+ bombarded Murchison slab from Laczniak et al. 2021.

The effects of ion-bombardment on the hydrated matrix of Murchison appear to be dominated by vesiculation and amorphization. No clear chemical change seem to affect the ion-bombarded layer, which is surprising when looking at the degree of amorphization in the Murchison samples and when looking at our samples, which all exhibits various degrees of texture loss accompanied by de-hydroxylation. It is possible that the low energy used in Laczniak et al. 2021 does not displace atoms in the phyllosilicate efficiently enough to engage noticeable chemical changes. For our experiment, we worked using 40 keV He^+, for which the electronic interactions are higher than for 4 keV He^+. Our results, coupled with the the lack of chemical changes seen at 4 keV by Laczniak et al. 2021 on the Murchison matrix seem to suggest that sputtering is more closely related to electronic scattering rather than nuclear one. However, Keller et al. 2015b is able to detect a loss of oxygen in similar irradiated Murchison samples (4 keV He^+) via electron energy-loss spectroscopy (EELS). This could either showcase a detectability issue of slight compositional changes with EDS-mapping, or a

possible ion-flux difference between Laczniak et al. 2021 and Keller et al. 2015b.

Another noticeable difference between our experiment is the detection of nanophase Fe-bearing particles in the ion-bombarded Murchison sample, and the lack of detection in our samples. This may be due by the elemental composition of our samples, since most of our samples sensibly poorer in Fe content ($Fe/(Fe+Mg)$ between 0.4 and 0.5 approximately for Murchison matrix (Fuchs et al. 1973)). Our saponite sample is the exception, sporting a $Fe/(Fe+Mg) \sim 0.46$, but again, no npFe0 was detected in this sample as well (the other samples had $Fe/(Fe+Mg)$ equal to 0.07 for serpentine Rawhide and 0.13 for serpentine UB-N - see chapter 2).

Comparison with space-weathered Itokawa samples

Our ion-bombarded sample are to be compared also with extraterrestrial samples for which we have evidences of SpWe. For instance, SpWe effects have been detected on a number of particles from S-type asteroid Itokawa. The main trends which were found are summarized here. These are only the effects seen at a microscopic scale.

- Multiple regions associated to SpWe have been detected near the surface of multiple Itokawa grains (Noguchi et al. 2011, Noguchi et al. 2014, Thompson et al. 2014). For many particles, the surface layer appeared to be made out of layered zone. Zone I, which corresponds to the utmost surface, consists in a Si-rich thin redeposition rim (a few nanometers thick), completely amorphous but we no vesiculation, composed of sputter deposits and/or impact vapor deposits. This thin rims shows a composition different from the material below, indicating that it originated from surrounding materials. Zone II, located below Zone I and from 30 to 60 nm thick, is a composite rim, partially amorphized, which includes varying degrees of vesiculation and abundant nanophase Fe-bearing particles. Finally, Zone III, located below Zone II, is of a more crystalline nature, exhibiting fractures and dislocations. Beside this 3-zoned layers, there are multi-layer composite rims, which can harbour layers particularly Si-enriched and Mg/Fe depleted, compared to the surrounding materials (Thompson et al. 2014).

- In Hicks et al. 2020, one of the effects of SpWe on the ion-bombarded layers of Itokawa is the

reduction of Fe (by interaction upon H^+ bombardment with FeO, which creates $Fe_{(0)}$ and water vapor as a byproduct).

Other effects, such as vesiculation and the presence of nanophase Fe, are showcased in the following table, in order to easily visualize the differences and similarities between our samples and the weathered Itokawa grains.

		Samples			
		Itokawa dust particle	Pellet		
			40 keV He^+ - $6x10^{16}$ ions/cm^2		
			Serpentine Rawhide	Serpentine UB-N	Saponite
Vesiculation rim	Degree	Low (mostly surface blisters)	High	Moderate	Low
	Thickness	30 – 60 nm	250 - 400 nm	200 - 250 nm	200 nm
	Bubbles/ Vesicles	Oblong Up to 50 nm in length	Spherical up to 100 nm in length filled with MgO-rich material	Spherical and oblong Up to 70 nm in length	Spherical and oblong Up to 150 nm in length
Amorphization*		Complete (near the surface), partial (deeper), or mixed	Complete down to 400 nm deep	Partial	Partial
Chemical changes		❑ Si-rich redeposition rims extremely thin (2-3 nm thick) ❑ In some instance, Si-rich and MgFe-poor rim slightly deeper in the sample ❑ Fe reduction	❑ de-hydroxylation ❑ Mg-poor/Si-rich surface layer (40 nm thick) ❑ Mg-rich area below the Mg-poor/Si-rich layer	❑ de-hydroxylation	❑ de-hydroxylation
Presence of Fe-bearing nanoparticles?		Yes	No	No	No

* as discussed previously, while waiting for electron diffraction measurement, the assessment of amorphization for the samples included in this work is based only on the change/loss of the typical phyllosilicate texture, and as to be considered with caution.

Table 4.6: Comparing ion-irradiation induced changes between the samples of this study and the traces of SpWe detected on Itokawa dust grains.

We are not expecting to see similar mineralogical changes among the two analysis, since we are looking here at radically different samples (anhydrous silicates VS hydrated minerals). However, some similarities do emerge, such as the presence of a thin surface rim with a different composition than the subsurface material (although the surface rim for Itokawa is a few nanometers thick and for our serpentine samples it extends down to 40 nm deep). It is interesting to note that this surface rims have similar composition even if they have possibly different origins: both appear Si-enriched/Mg-depleted, even though the Itokawa rim is a product of the redeposition of sputtered Si, while for serpentine Rawhide it is a product of preferential sputtering of Mg, and not a re-deposition.

Surface bubbles and blisters are also a common point between the two analysis, even though the low, isolated vesiculation for Itokawa grains is not comparable with the vesiculation for the serpentine Rawhide sample for which we have identified blisters. Note also that the size of the blisters is sensibly different (up to 50 nm for Itokawa and up to 150 nm for serpentine Rawhide). These blisters are derived from solar-wind implantation in Itokawa samples, as discussed in Noguchi et al. 2014, however their growth may be affected by the redeposition layer, absent for our hydrated silicates, which would possibly hinder the growth of large blisters on Itokawa particles.
Overall, the effects of SpWe on anhydrous extraterrestrial materials have similarities with SpWe on hydrated terrestrial minerals regarding morphological changes such as vesiculation and amorphization, but appear far less chemically altered than our samples.

Preliminary discussion regarding Ryugu recovered grains

The effects of SpWe on recovered particles from Ryugu will be soon published (Noguchi et al. 2022, in preparation). However, there are a certain number of effects which can be summarized from the various conference abstracts published in the last months.

Some recovered particles stood out for their different surface morphology, exhibiting large open bubbles abundant on their surface (Noguchi et al. 2021). Preliminary analysis indicated that the rim associated to this vesiculated region appeared particularly Fe-rich. Follow-up analysis (Matsumoto et al. 2021, Noguchi et al. 2022, Thompson et al. 2022), identified the presence of impact craters, melted drops, splashes and glassy spherules on the surface of SpWe Ruygu particles, all effects which studies on Lunar regolith suggests originates from micro-meteorites impacts. However, it is relevant to note that the thickness of the amorphous surface layer identified on carbonates grains, at the surface of these Ryugu particles, is compatible with 1 keV H^+ bombardment, indicating that solar wind may have also affected the surface of Ryugu.
The amorphous surface silicate rim was found to vary in thickness, from tenths of nanometers up to 300-500 nm thick (Thompson et al. 2022, Matsumoto et al. 2022), showing rare nanophase inclusions. What's particularly interesting with respect to our work presented here, is that the utmost surface layer of this amorphized, which is just 7 to 13 nm thick, appears to be significantly different

in elemental composition with respect to the rest of the amorphous layer and with respect to the more pristine material located deep below. This chemical composition seems to be related to the presence of nanophases with high Z-contrast.

Even though most of the effects detected at the surface of Ryugu particles seem to be linked to meteorite bombardment, some of our ion-bombarded samples do reproduce similar trends, such as the high large bubbles vesiculation (serpentine Rawhide), the presence of a very thin surface rim with a different composition (serpentine Rawhide and Ar^+ bombarded serpentine UB-N) and finally the creation of a very thin rim made out of high Z-contrast nanophases (Ar^+ bombarded serpentine UB-N). More similarities or differences may appear once more publications start to appear.

CHAPTER 5

Conclusion and Perspectives

Contents

5.1. Linking spectroscopic trends and electron microscopy changes

In this work, we have probed the effects of ion-bombardment on hydrated silicates in order to emulate SpWe on the surface of hydrated carbon-rich primitive bodies. One of the few perks of this work was to study these changes both via infrared spectroscopy and electron microscopy. The final goal of this study shall be to probe the link between the spectral changes observed via spectroscopy and the chemical and morphological changes detected via electron microscopy. There are a number of changes seen at small scale, via electron microscopy, which do relate to spectroscopic changes seen at larger scale. These linked are summarized in the following figure and further developed individually in the following paragraphs.

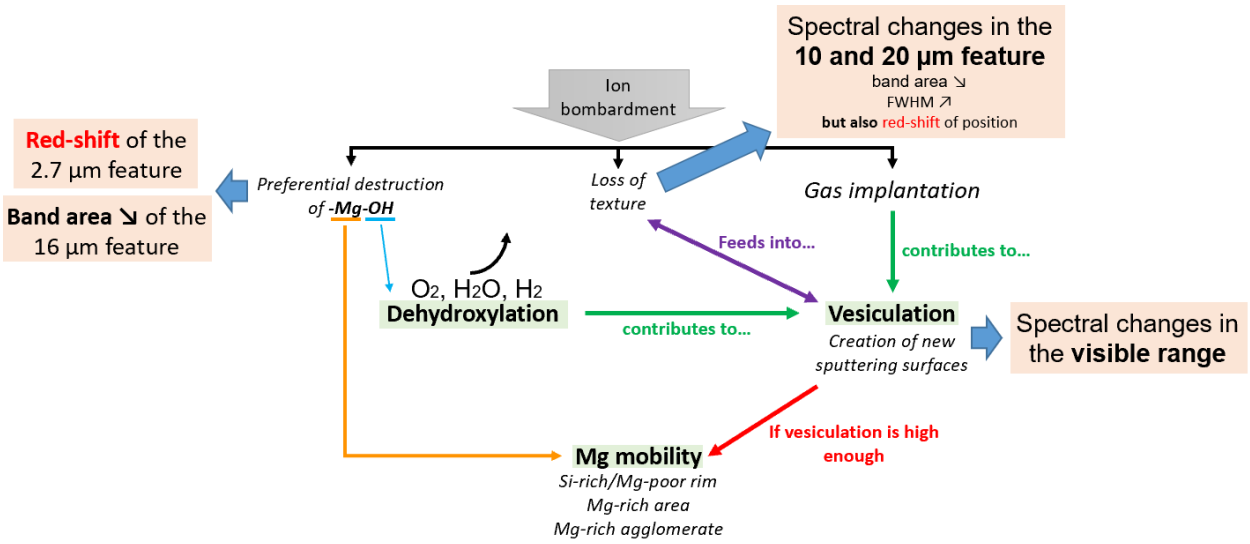

Figure 5.1: Recap of ion-bombardment processes seen in our phyllosilicates.

5.1.1. De-hydroxylation: changes of the hydration features and oxygen-loss

Loss of oxygen content in the ion-bombarded layers is observed at different intensities across all samples. We have already discussed in the previous chapter that this oxygen loss is to be put in perspective with the possible loss of hydration of these minerals via de-hydroxylation. This can be investigated by comparing the oxygen loss with changes of the spectroscopic hydration features at 2.7 and 16 µm, associated to the (M)-OH stretching mode (with M a metallic cation) and the Mg-OH bending mode. This comparison is done in the following table.

[H]

		He^+			Ar^+		
		Serpentine Rawhide	*Serpentine UB-N*	*Saponite*	*Serpentine Rawhide*	*Serpentine UB-N*	*Saponite*
Hydration feature at 2.7 µm	*Peak position shift [nm]*	+ 19	+ 14	not observed	+ 8	not observed	not observed
	Band depth evolution	+ 4.3%	not observed	- 6.5%	+ 2.5%	+ 3.4%	not observed
Hydration feature at 16 µm	*Peak position shift [nm]*	+ 680	+ 450	feature not present	- 30	- 300	feature not present
	Band area evolution	- 13%	-30%		- 53%	- 48%	
Chemical changes	*Oxygen loss after bombardment (estimate)*	- 8% over 200 nm	- 7% over 120 nm	- 9.5% over 140 nm	- 4% over 100 nm	observed* over 70 nm	observed* over 80 nm
	Mg content in bombarded layer	depleted (sputtered and precipitate in bubbles)	-	-	depleted (sputtered and precipitate in bubbles)	depleted (sputtered)	-

* these values were not computed since the presence of the coalesced bubble rim complicated the interpretation of elemental profiles.

As a consequence of de-hydroxilation, the number of -OH bonds in the ion-bombarded material decreases, which should affects the band area and the band intensity of -OH related features, such as the hydration features described above. We have seen that band depth and band intensities for the 2.7 µm feature in our data-set were difficult to compute due to noise in the data-set, so it is difficult to relate the changes of these parameters to the detected oxygen loss (although we have seen that the band depth is indeed affected by ion-bombardment while we were discussing the effects of the geometry of observation on ion-bombarded surfaces - chapter 3, section 3.1.1.3 -, indicating that upon weathering, the band depth seemed to slightly increase at least for the serpentine Rawhide sample. The cause of this apparent increase is still now unclear). Moreover, we have seen the oxygen-depleted layers in our samples vary in thickness, from 70 to 200 nm approximately, which is far smaller than the photon's probing depth in the near-IR (a few microns), and so the oxygen-depleted layer overall remains poorly relevant in the collected signal in the near-IR, which could explain the weak/non-existent changes seen in the 2.7 µm band-depth.

The most apparent effect we were able to quantify for the 2.7 µm feature, has been its peak position shift. De-hydroxylation can affect the position of the hydration feature, since we know that the position of the 2.7 µm peak is derived by the different (M)-OH contributions. Our results on the

serpentine Rawhide sample show that de-hydroxylation affecting preferentially Mg-OH bonds may have contributed to the observed long-ward shift, since this shift could be related to the diminishing contribution of the Mg-OH bonds to the 2.7 µm feature, creating an 'apparent' shift towards longer wavelength, where the Fe-OH stretching feature resides. However, the two other He^+ bombarded samples stand as outliers regarding this explanation, for different reasons.

The He^+ bombarded serpentine UB-N sports a large peak-shift of the 2.7 µm feature and oxygen loss over the utmost top layer. No sensible variation of the Mg/Fe ratio, which would justify the detected shift, is observed. However, we see that the ion-bombarded layer appears to be partially amorphized, indicating that lattice stress and changes induced by ion-implantation can also red-shift the position of the 2.7 µm feature (which make sense, since the position of all chemical bonds is influenced by their environment, and de-hydroxilation changes the phyllosilicate environment).

The saponite sports the largest oxygen loss detected, and is associated to no hydration feature peak-shift and only partial lattice amorphization. Its behaviour could be related to the fact that the saponite sample is particularly Fe-rich. It is possible that the contribution of the Mg-OH bond was already weak prior to ion-bombardment, and its small decreasing contribution (which remains undetected in the EDS measurements) upon weathering is not noticeable due to the already red-shifted position associated to the high Fe-rich content.

For Ar^+ serpentine UB-N and saponite sample we confirm that, due to the difference in probing depth of near-IR photons VS the implantation depth of Ar^+ (a few microns vs 40 nm), the oxygen loss associated to de-hydroxylation seen by STEM-EDS has no detectable effects on the 2.7 µm hydration feature.

In the near future, I wish to use an alternative method described in Le-Pivert et al. 2022 (in preparation), which consists in Gaussian fitting the hydration feature using only on half of the data-points, more specifically the left shoulder of the feature before 2.7 µm, which is the less noisy part of the feature. This method should allow us to derive more convincing measurements of the band intensity, band area and band width, for a more direct comparison with oxygen loss and amorphization seen by STEM. This will also allow us to more easily compare our extracted band intensity measurements with the weak 2.7 µm feature seen on Ryugu surface and better constraint

the weakness of this feature to SpWe effects.

The other hydration feature we want to relate to the chemical and morphological changes seen in our work is the Mg-OH bending mode at 16 µm, detectable for both serpentines (but undetectable for the Fe-rich saponite). The band area of the Mg-OH bending feature does decrease upon ion-bombardment for all samples, which is in-line with preferential destruction of the Mg-OH bond. We are able to observe this band decrease since in this wavelength range, and with our geometry, we are dominated by surface scattering (probing depth is less than 1 µm - Brunetto et al. 2020) and thus the collected signal is much more sensible to the irradiated surface layers of the sample than for the near-IR measurements. Our results suggest that oxygen sputtering is more easily probed in the Mid-IR with the OH bending modes than by the OH stretching mode at 2.7 µm.
Note that the Mid- and Far-Ir range were not able to be investigate for Ryugu in remote-sensed data by the Hayabusa2 mission (no spectroscopic instrument was sensible in the mid- and far-IR), but we do have these ranges for Bennu. In the average OTES spectrum of Bennu shown by Hamilton et al. 2019, we see a very weak feature at approximately 555 $cm^{-}1$ (see figure below), which the authors associate to magnetite. However, this very weak feature is compatible with a heavily weathered Mg-OH bending feature. It is relevant to note that the intensity of the feature could be associated also to Bennu's phyllosilicate composition, which is thought to be more Fe-rich (Simon, A. A. et al. 2020), and thus more similar to our saponite sample (which also exhibits a very weak/non-existent Mg-OH bending feature). The compositional explanation is also supported by the broad rich shoulder of the Si-O stretching feature, between 700 and 800 cm^{-1}, which could be associated to Fe-OH bending modes (Farmer 1974, Glotch et al. 2007, Bishop et al. 2008).

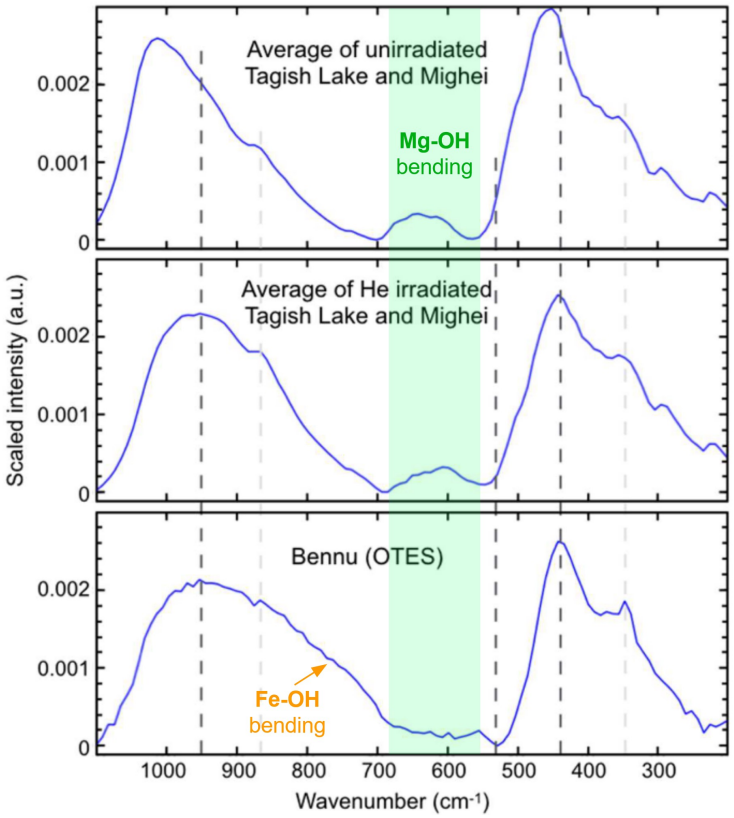

Figure 5.2: From Brunetto et al. 2020: the spectrum of Bennu compared with unirradiated and irradiated carbonaceous chondrites. A linear combination of irradiated CM Mighei and irradiated C2 Tagish Lake meteorites (middle panel) provides a better qualitative match of the average spectrum of Bennu (bottom (Hamilton et al. 2019)) than the combination of the unirradiated samples (top). The average of the two meteorites is chosen here simply as an example to illustrate the effect of irradiation on the specific features of their hydrated minerals, rather than attempting to find the best analog of Bennu. The peak positions of the main features of Bennu are highlighted by vertical dashed lines. Each spectrum has been normalized to its total intensity. The identification of Mg-OH and Fe-OH features has been added from the original image for the purpose of this work.

Overall, regarding the SpWe effects on the hydration features of phyllosilicates (peak-shift for the 2.7 µm and peak-shift + band area decrease for the 16 µm feature), the results from our work suggest that both chemical effects (de-hydroxylation, Mg-depletion) and physical effects (amorphization, lattice stress upon ion-bombardment) contribute to varying degrees to the spectral changes observed for the 2.7 µm and the 16 µm features.

5.1.2. Amorphization: silicate infrared feature and loss of microscopic phyllosilicate texture

The loss of texture in the ion-bombarded layers seen via STEM is probably accompanied by a degree of lattice amorphization, as discussed in CH4. Future measurements of electron diffraction via TEM will allow us to better constrain the degree of amorphization in our samples. In the meantime, we have assimilated this amorphization with a certain loss of microscopic texture, observed via STEM-HAADF imaging. These crystal lattice modifications should reflect in the associated silicate spectral features, such as the Si-O stretching feature at 10 µm and the broad silicate feature at 20 µm, which includes two contributions: the Si-O bending bond (20.6 - 21.3 µm) from the T layer of phyllosilicate and the Si-O-(M) bond (22 - 24 µm), linking T and O layers (Salisbury et al. 1987, Bishop 2018) .The following table relates the observed texture loss with the spectral changes associated to the spectroscopic features described above.

		He^+			Ar^+		
		Serpentine Rawhide	*Serpentine UB-N*	*Saponite*	*Serpentine Rawhide*	*Serpentine UB-N*	*Saponite*
Silicate feature at 10 µm	*Peak position shift [nm]*	+ 352	+ 312	+ 363	+ 205	+ 40	+ 130
	Band area evolution	- 25.7%	- 24.2%	- 16%	+ 34.2%	- 15.5%	- 23.1%
	FWHM evolution	+ 32%	+ 28.5%	+ 72%	+ 4.7%	+ 11%	+ 32.8%
Silicate feature at 20 µm	*Peak position [µm]*	22.83 (pristine: 22.62)	22.77 (pristine: 21.32)	21.78 (pristine: 21.59)	22.78 (pristine: 22.62)	22.32 (pristine: 21.32)	21.69 (pristine: 21.59)
	Band area ratio Si-O-(M) / Si-O	1.05 (pristine: 0.75)	0.93 (pristine: 0.68)	1.06 (pristine: 0.76)	0.96 (pristine: 0.75)	0.81 (pristine: 0.68)	0.98 (pristine: 0.76)
Texture loss in the ion-implanted layer		total	partial	partial	total	total	total
Chemical changes	*O content in bombarded layer*	depleted (de-hydroxylation)	depleted (de-hydroxylation)	depleted (de-hydroxylation)	depleted (de-hydroxylation)	depleted (de-hydroxylation)	depleted (de-hydroxylation)
	Mg content in bombarded layer	depleted (sputtered and precipitate in bubbles)	-	-	depleted (sputtered and precipitate in bubbles)	depleted (sputtered)	-

Table 5.1: Probing amorphization in our ion-bombarded samples by comparing the evolution of the silicate features at 10 and 20 µm with structural and chemical modifications of the ion-bombarded layer observed by STEM-EDS. For the 10 µm feature, the change on the position is given by the position-shift of the peak, while for the 20 µm feature, the feature's position is reported. This is done to better visualize the two composition of the 20 µm feature (Si-O bending bond (20.6 - 21.3 µm) and Si-O-(M) bond (22 - 24 µm)) and better visualize which contribution dominates prior to ion-bombardment.

The load of data in the table above can appear rough and puzzling. It is inherently complicated to derive trends among all the various parameters and effects. However, there are some considerations emerging from it.

For instance, it appears that the spectral changes observed for the 10 µm feature can't be explained only via the Mg/Fe chemical changes seen STEM-EDS mapping. More specifically, we have detected a large red-shift of the Si-O stretching feature for all samples, but the only samples for which we have detected abundant Mg-mobility and/or loss in the ion-bombarded layers are the serpentine Rawhide sample and the Ar^+ bombarded serpentine UB-N. On the other hand, the larger detected shift of the 10 µm feature is associated to the He^+ bombarded saponite, for which we detected the largest oxygen-depletion as well as the largest band broadening. Physical modifications, such as

lattice stress and vesiculation also do not correlate alone with spectral variations seen. It appears that, for the 10 µm feature, peak position-shift can't be associated exclusively to chemical changes, but must also be related to structural and physical changes upon ion-bombardment (changes due to lattice stress in the phyllosilicate lattice alter the Si-O stretching bond environment and generate/contribute to the observed shift), even more so than the 2.7 µm hydration feature (larger detected shift, from approximately 20 nm for the hydration feature up to hundreds of nanometers for the Si-O stretching band). All samples exhibits some degree of lattice stress, which is related in the mid-IR to the broadening of the Si-O stretching feature, seen across all samples (the individual values of FWHM evolution may vary with respect to the ratio of implanted vs pristine matter).

The 20 µm feature seems to follow a similar behaviour. This is particularly clear when comparing the band area ratio of He^+ bombarded serpentine Rawhide and saponite. We know that for serpentine Rawhide, Mg is preferentially sputtered across the ion-implanted layer. We would expect that these change would be reflected in the band area ratio of the 20 µm feature (the band area ratio represent the ratio between the area of the right shoulder of the feature - the Si-O-(M) bending contribution - divided by the area of the left shoulder - the Si-O contribution). Preferential sputtering of Mg would decrease the intensity of the Si-O-(M) contribution, and consequentially decrease the value of the band area ratio. However, we see that upon weathering the most affected feature is the left shoulder, the Si-O feature, as as such, we see that the band ratio increases. This suggests that this feature is more sensible to lattice stress of the T layer induced by amorphization processes upon ion-bombardment than to chemical modification such Mg-loss.

Overall, the spectral changes observed in the Mid- and Far-IR seems to be more heavily affected by lattice stress than elemental changes.

5.1.3. Porosity evolution and changes observed in the visible range (darkening and slope evolution).

Upon ion-bombardment, we have seen our sample exhibits various trends in the visible range. Previous studies have shown that the changes in the visible range are often linked to the creation of new species upon bombardment, such as npFe0 causing reddening or magnetite nanophase causing

blueing (Trang et al. 2021, Noble et al. 2007). Among our samples, we detect both trends, all coupled with darkening, but the STEM-EDS analysis has not detected the clear creation of metallic nano-phases in the ion-bombarded samples, indicating that physical changes of the crystal lattice may also contribute to darkening/brightening and reddening/blueing. Studies have shown that porosity and grain size can affect brightness and spectral slope (see discussion in Sultana et al. 2021), and we have seen vesiculation appearing with various degrees of intensities among all our samples. In the following figure, we relate the trends observed in the visible range with loss of texture and vesiculation observed via HAADF imaging.

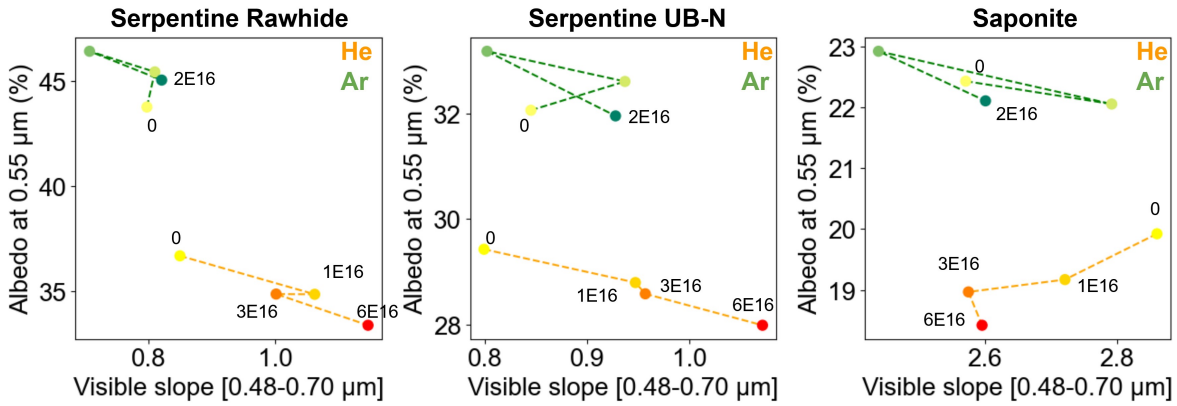

	He^+			Ar^+		
	Serpentine Rawhide	*Serpentine UB-N*	*Saponite*	*Serpentine Rawhide*	*Serpentine UB-N*	*Saponite*
Vesiculation	high (round bubbles)	low (elongated bubbles)	low (elongated bubbles)	high (round bubbles)	high (coalesced bubble rim)	high (coalesced bubble rim)

Figure 5.3: Visible results upon ion-bombardment and degree of vesiculation observed in the ion-bombarded layer via STEM-HAADF imaging.

Clear trends can be identified for the He^+ bombardment case, such as darkening across all samples, coupled with reddening for the serpentines and blueing for the saponite. A common trend for all these samples seen via HAADF imaging is vesiculation, the creation of small and large bubbles (from 20 nm to 200 nm) in the ion-bombarded layers. This bubbling, coupled with the loss of texture due to amorphization, increases the porosity of the bombarded layer, ass seen in chapter 4, creating several internal surfaces on which photons can behaves differently than in the rest of

the sample (for instance, they can be more easily trapped or dissipated). This could justify the various instances of darkening seen across our He^+ bombarded samples, from the most vesiculated one, serpentine Rawhide, which darkened the most, to the less vesiculated one, the saponite sample, which darkened the less. The changes in slope are less easy to interpret. Reddening is associated with Mg-rich serpentines, while blueing is associated to an Fe-rich saponite. These effects could be linked to either the Mg/Fe ratio, or the difference in structure among our samples (or both). Our current results do not allow us to clearly establish a dominant process here.

Regarding the Ar^+ bombarded samples, a clear trend cannot be established. This may be due to effects such as elemental and lattice changes competing over a very short depth (from 40 nm to 200 nm), far smaller than the penetrating depth of visible photons (approximately 40 µm for serpentine, see discussion in Brunetto et al. 2020). The results of Ar^+ bombarded serpentine Rawhide sample on the vesiculation and amorphization of the ion-bombarded sample are very similar to those of the He+ bombarded sample, but on a shorter distance (150-200 nm VS 700 nm). One would expect to detect similar changes in the visible range, if the photons probing the matter were sensible enough to account for these changes. However, that is not the case, as the Ar^+ bombarded serpentine Rawhide final irradiation stage only exhibits very slight brightening. The explanation for this phenomenon is unclear.

The remaining Ar^+ bombarded samples have a particular thing in common: the creation during bombardment of a coalesced bubble rim. This bubble rim has possibly started out as a layer of isolated small bubbles, which grew as the experiment proceeded. At some points, all these individual bubbles coalesced, creating an extended empty (or gaz filled) layer, separating two silicate regions. This brutal change, from isolated bubbles to the creation of effectively a "natural" dioptre in our samples, may be reflected in the visible data. My current hypothesis is that the coalescence of these bubble rims has happened after reaching the 0.5E16 $ions/cm^2$ fluence and prior to reaching the 1E16 $ions/cm^2$ fluence. This hypothesis derives by the fact that we see a clear brutal change in the observed trend for the data segment between these two fluences. For serpentine UB-N, the samples brighten and slightly reddens up to 0.5E16 $ions/cm^2$, then between 0.5 and 1E16 $ions/cm^2$, the sample has continued to brighten but the slope as undergone significant blueing, and from 1E16

$ions/cm^2$ to 2E16 $ions/cm^2$ the sample darkens and reddens. A similar behaviour is observed for the saponite sample, except that during the first irradiation step, the sample darkens instead of brightening. The "gear-shift" observed between the 0.5 and the 1E16 $ions/cm^2$ fluences may be due to the gaz bubbles reaching some sort of critical size, coalescing into a thin empty/gaseous rim close to the surface, acting as some sort of dioptre parallel to the sample surface, possibly changing the properties of the material from a compact material to a segmented/layered material.

The difference in the first step of irradiation between the two samples (brightening for serpentine UB-N and darkening for saponite), may be related to the presence in the serpentine UB-N sample of a thin brighter rim located at the limit between the ion-bombarded region and the pristine material. The elemental analysis of this thin rim was unsuccessful, but their relative brightness in the HAADF images compared to the rest of the ion-bombarded material suggest that this is a heavier material (high Z in Z-contrast images). Looking at the chemical composition of our sample derived by SEM-EDS (see chapter 2 section 2.1.1), we know that the serpentine UB-N sample also contains Fe, as well as traces of Al and Cr. These brighter particles could be associated to some sort of nanophase derived from these elements and could be responsible for the observed initial brightening prior to the coalescence of the bubble rim at higher fluences. For now, this is just one proposed scenario that shall need to be further investigated, for instance by re-trying to determine the elemental composition of this bright rim in serpentine UB-N.

The scenarios associated to the discussion led here on Ar-bombarded serpentine UB-N and saponite are schematized in the following figure.

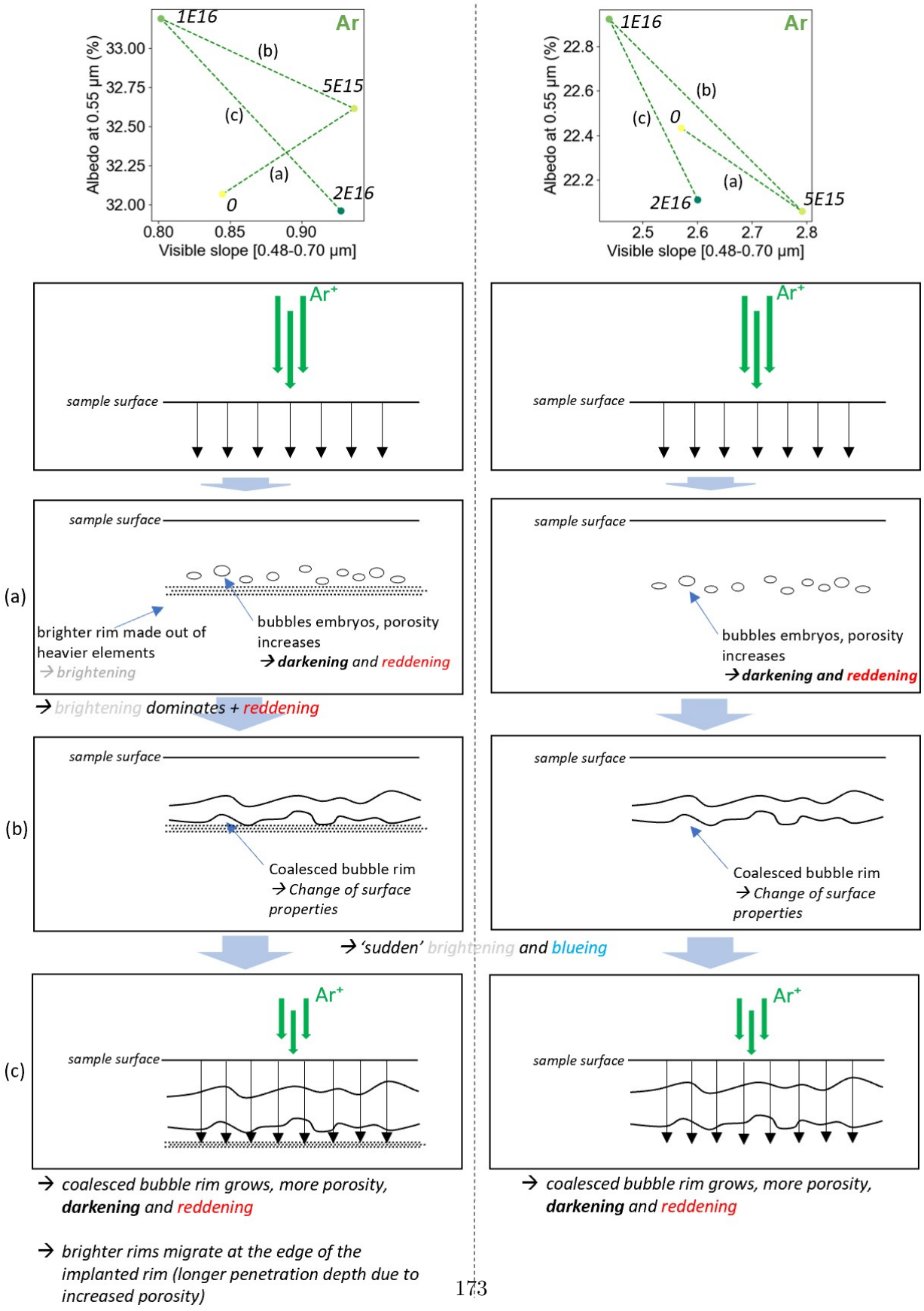

Figure 5.4: Cartoon showing the Ar^+ bombardment effects on serpentine UB-N and saponite, related to the spectral changes seen in the visible range.

5.2. Final considerations, future works and perspectives

As this work comes to an end, we have derived a certain number of changes induced by ion-bombardment on hydrated silicates. While this work hopefully contributes to the understanding of solar-wind irradiation on hydrated silicates of primitive bodies, there are multiple ways in which future experiments and analysis could expand and build upon the results discussed here.

One aspect which shall be further investigated and quantified in an upcoming publication (focusing on the results from the mid- and far-IR, as well as the transmission electron microscopy results), is the dependency of the various spectroscopic, chemical and morphological changes seen in this work with respect to the inelastic and elastic energy loss regime. Exploring this dependency is what prompted the used in this study of He^+ and Ar^+ at 40 keV. As discussed in Chapter 2, these experimental conditions do not are not fully representative of actual solar wind (which, as a reminder, is mainly dominated by low-energy H^+ and He^+ particles - 1 to 4 keV, and for which Ar^+ is a sensibly minor component). However, working with 40 keV He^+ and Ar^+ allows us to clearly investigate the effects of inelastic and elastic energy loss separately, since they each dominate for one of the used ions (as seen by SRIM simulations, see figure below).

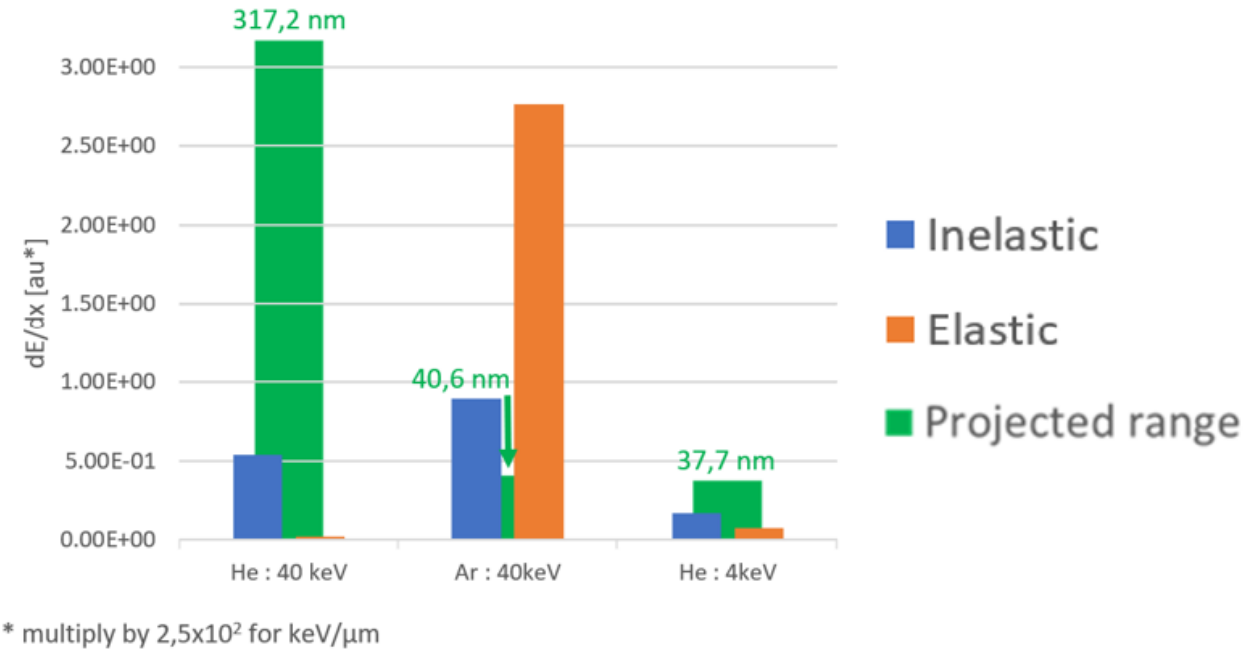

Figure 5.5: Ion-implantation parameters derived by SRIM on serpentine Rawhide.

This approach, even if it does not suffice to replicate actual solar wind conditions, allows to investigate effects linked to two distinct energy loss regimes, effects which can than be compared and interpreted with respect to real case observations. In our work, a few trends - which will be further developed in the upcoming publications - start to emerge, such that dehydroxylation seems to be more tightly connected with the inelastic regime, while loss of texture and vesiculation seem to be more prominent under elastic regime (see figure below).

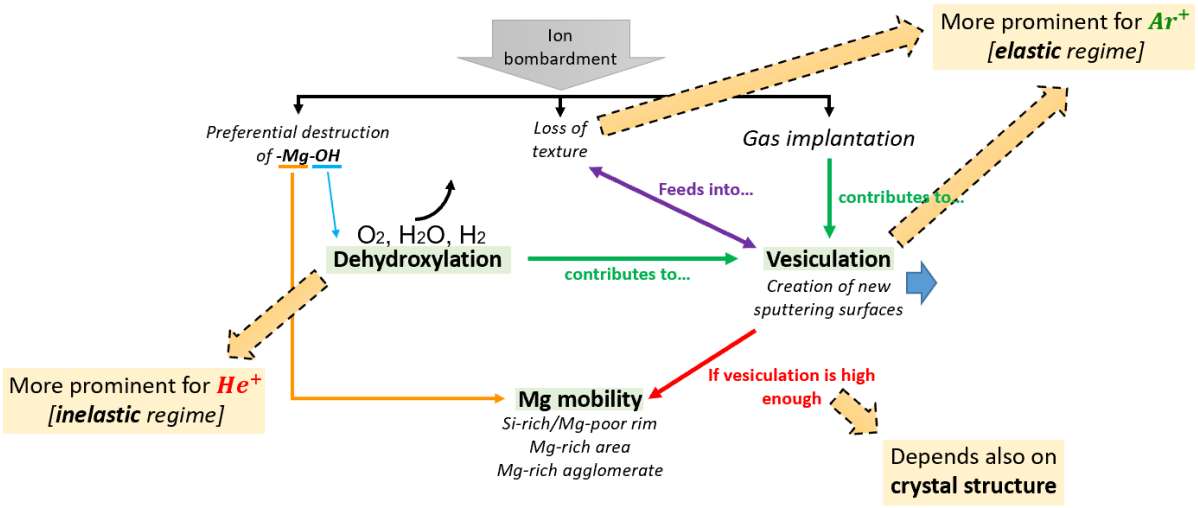

Figure 5.6: Recap of ion-bombardment processes seen in our phyllosilicate samples with respect to energy loss regime.

Some of these effects are comparable to solar-wind induced changes which have been seen on real case objects (a few examples may include the hydration feature red-shift observed on the SCI crater - related to the He^+ bombardment experiments, or the creation of smooth surface layers on solar-wind weathered particles (Noguchi et al., in press) - related to the surface smoothing seen for the Ar^+ case. In becomes apparent than, even if our experimental conditions do not replicate closely actual solar-wind conditions, the produced effects are still comparable and to real case observations.

Other ways to improve our expand the implication of this work is delving on the matter of the material chosen as surface analog for our experiment. For instance, we have seen that the study

of terrestrial rocks presents some advantages, such as working with more homogeneous material than meteorites, while still showing results which are coherent with studies focuses on meteorites. However, in order to widen our current understanding of ion-implantation on phyllosilicates, more pure phases samples should be subjected to similar experiment, to explore more endmembers.

Compositional-wise, in our case, we were missing a Fe-rich serpentine and a Mg-rich saponite sample among our chosen samples. The Mg-rich saponite sample is relatively easy to find. For instance, conducting ion-bombardment experiments on a talc ($Mg_3Si_4O_{10}(OH)_2$) pellet could be relatively easy to do. However, particularly Fe-rich serpentines such as cronstedtite ($Fe_2^{2+}Fe^{3+}((Si, Fe^{3+})_2O_5)(OH)_4$) are quite rare, and often available in very low quantities, which complicates the experiment. Regarding sample mineral structure, in our experiment we were able to explore the effects if ion-bombardment on fibrous and layered structures (both TO and TOT layers). It would be interesting to experiment on pellets made out of mixture with varying ratios of different texture phyllosilicates, to emulate the varying ratios of saponite and serpentines in the hydrated matrix of meteorites and returned samples. This would allow the study of well constrained heterogeneous material.

Other SpWe conditions could be explored such as different ions and different energies, to better explore other contributions of solar-wind to SpWe (1 keV H^+ or 4 keV He^+ for instance). Another interesting investigation would be to use the exact same terrestrial phyllosilicates presented in this work for an experiment focused on replicating the effects of micro-meteorites impacts using pulsed-laser irradiation, to have a more direct comparison between ion-bombardment and micro-meteorite impact on the exact same hydrated terrestrial phyllosilicates. This is currently the work of Ph.D student and colleague Dan Hallat (working under the supervision of Prof. Hugues Leroux, Hallatt et al. 2022).

Finally, a more direct approach could be taken in order to have a more direct comparison with returned grains from Ryugu and Bennu, by producing weathered individual isolated particle with a size range similar to that of the returned samples (20 to 100 µm length particle for instance). This could be done by ion-bombarding isolated grains instead of pellets. This isolated ion-bombarded grains would be measured via 3D-dimensional infrared characterization techniques (described in chapter 3) such as IR-CT and IR-SI, the same techniques we applied at IAS on Ryugu particles.

The same analytical pipeline applied to Ryugu could be then applied on this weathered grains, such as FIB-sectioning and infrared microscopy, in order to characterize the ion-implanted matter at the scale of a whole ion-bombarded microscopic grain. Ion-bombarded pressed powder pellets are thought to represent good surface analogs for remote-sensing data, since they emulate the regolith texture present at the surface of an asteroid (note that this concept has starting to evolve recently, since both Ryugu and Bennu surfaces are not dominated with fine-grained regolith (Okada et al. 2020, Lauretta et al. 2019), hence dissimilar to lunar surfaces (Papike et al. 1982)). These weathered individual grains could represent good analogs of returned samples.

This work has highlighted a number of spectroscopic effects on hydrated space-weathered surfaces, from the visible range to the far-IR. Effects of SpWe were identified for almost all samples at varying degree on intensity among the multiple spectral range.

The visible range proved sensible to ion bombardment effects for almost all our samples, with noticeable changes such darkening, reddening and blueing. We have shown that investigation on the visible range are not only correlated with the creation of nanophases upon weathering, but also on physical evolution such as porosity changes and vesiculation, which hints that the interpretation of spectral changes on real remote-sensed data is more complicated than what was imagined. Overall, the visible range good proxy for investigating weathering effects on space-weathered hydrated bodies.

In the near-IR range, the hydration feature at 2.7 µm revealed to be particularly sensible to weathering mainly regarding its position, and mainly for the serpentine samples. For possible hydrated bodies sporting larger quantities of saponite with respect to serpentine, the 2.7 µm feature appears to not be a good proxy of solar wind weathering. Note that for the serpentine samples, the amplitude of the largest detected shift is approximately of 20 nm, which is just about detectable for current generation sample return missions (spectral sampling of $\sim$ 18 nm for the NIRS3 instrument for Hayabusa2 and $\sim$ 10 for the OVIRS instrument for OSIRIS-REx). As discussed in chapter 3, a shift of the hydration feature possibly related to SpWe was detected near the SCI-artificial crater on Ryugu by Kitazato et al. 2021), indicating that the largest spectral sampling available was sufficient. However, improving the spectral sampling over the hydration feature (by doubling

the number of spectral channels around 2.7 µm, at least) could allow the detection of smaller spectral shift linked to possibly less weathered surfaces associated to less exposed regions. The mid- and far-IR proved to be particularly sensible to both physical and chemical changes induced upon solar wind bombardment. Beside the large (hundreds of nanometers) spectral shift detected for the 10 µm feature, particular interest should be given to the (M)-OH bending modes, in particular to the Mg-OH bending mode at 16 µm, which appears to be a good proxy of de-hydroxilation upon ion-implantation. The asymmetry of the 20 µm feature appears also of particular interest for future (and current studies for which the data is available, such as Bennu), since our work highlights that it is directly related to physical changes in the phyllosilicate mineral upon weathering.

Overall, this work was set to reproduce the effects of the solar wind contribution of SpWe on hydrated surfaces in order to provide support to current and future space missions targeting primitive bodies. The comparison between what we have observed in this work and data from the Hayabusa2 mission has started and will hopefully continue as more results start to be published. There is still work to do when comparing our work with remote sensed data from Bennu while we wait for the approximately 250 g of material recovered from its surface (Lauretta et al. 2022). Our experiments highlighted spectral trends and changes which are not all directly comparable to what has been observed on Ryugu and Bennu as of now. It is possible that some of our ion-bombarded samples are emulating SpWe effects on primitive bodies of a different type from Bennu and Ryugu, or other bodies all-together such as G-type giant carbonaceous asteroid Ceres, hence the importance of increasing sample-return type missions in order to widen our understanding of SpWe effects across our solar system.

Bibliography

M. Abe, Y. Takagi, K. Kitazato, S. Abe, T. Hiroi, F. Vilas, B. E. Clark, P. A. Abell, S. M. Lederer, K. S. Jarvis, T. Nimura, Y. Ueda, and A. Fujiwara. Near-infrared spectral results of asteroid itokawa from the hayabusa spacecraft. *Science*, 312(5778):1334–1338, 2006. doi: 10.1126/science.1125718. URL https://www.science.org/doi/abs/10.1126/science.1125718.

A. Aléon-Toppani, R. Brunetto, J. Aléon, Z. Dionnet, S. Rubino, D. Levy, D. Troadec, F. Brisset, F. Borondics, and A. King. A preparation sequence for multi-analysis of µm-sized extraterrestrial and geological samples. *Meteoritics & Planetary Science*, 56(6):1151–1172, 2021. doi: https://doi.org/10.1111/maps.13696. URL https://onlinelibrary.wiley.com/doi/abs/10.1111/maps.13696.

M. Arakawa, T. Saiki, K. Wada, K. Ogawa, T. Kadono, K. Shirai, H. Sawada, K. Ishibashi, R. Honda, N. Sakatani, Y. Iijima, C. Okamoto, H. Yano, Y. Takagi, M. Hayakawa, P. Michel, M. Jutzi, Y. Shimaki, S. Kimura, Y. Mimasu, T. Toda, H. Imamura, S. Nakazawa, H. Hayakawa, S. Sugita, T. Morota, S. Kameda, E. Tatsumi, Y. Cho, K. Yoshioka, Y. Yokota, M. Matsuoka, M. Yamada, T. Kouyama, C. Honda, Y. Tsuda, S. Watanabe, M. Yoshikawa, S. Tanaka, F. Terui, S. Kikuchi, T. Yamaguchi, N. Ogawa, G. Ono, K. Yoshikawa, T. Takahashi, Y. Takei, A. Fujii, H. Takeuchi, Y. Yamamoto, T. Okada, C. Hirose, S. Hosoda, O. Mori, T. Shimada, S. Soldini, R. Tsukizaki, T. Iwata, M. Ozaki, M. Abe, N. Namiki, K. Kitazato, S. Tachibana, H. Ikeda, N. Hirata, N. Hirata, R. Noguchi, and A. Miura. An artificial impact on the asteroid (162173) ryugu formed a crater in the gravity-dominated regime. *Science*, 368(6486):67–71, 2020. doi: 10.1126/science.aaz1701. URL https://www.science.org/doi/abs/10.1126/science.aaz1701.

A. L. Auzende. *Evolution des microstructures des serpentinites en contexte convergent : effet du degré de métamorphisme et de la déformation.* PhD thesis, Clermont-Ferrand 2, 2003.

J. Bishop, J. Madeová, P. Komadel, and H. Fröschl. The influence of structural fe, al and mg on the infrared oh bands in spectra of dioctahedral smectites. *Clay Minerals - CLAY MINER*, 37, 12 2002. doi: 10.1180/0009855023740063.

J. Bishop, M. Dyar, E. Sklute, and A. Drief. Physical alteration of antigorite: A mössbauer spectroscopy, reflectance spectroscopy and tem study with applications to mars. *Clay Minerals - CLAY MINER*, 43, 03 2008. doi: 10.1180/claymin.2008.043.1.04.

J. L. Bishop. Chapter 3 - remote detection of phyllosilicates on mars and implications for climate and habitability. In N. A. Cabrol and E. A. Grin, editors, *From Habitability to Life on Mars*, pages 37–75. Elsevier, 2018. ISBN 978-0-12-809935-3. doi: https://doi.org/10.1016/B978-0-12-809935-3.00003-7. URL https://www.sciencedirect.com/science/article/pii/B9780128099353000037.

L. Bonal, R. Brunetto, P. Beck, E. Dartois, Z. Dionnet, Z. Djouadi, J. Duprat, E. Füri, Y. Kakazu, G. Montagnac, P. Oudayer, E. Quirico, and C. Engrand. Visible-ir and raman microspectroscopic investigation of three itokawa particles collected by hayabusa: Mineralogy and degree of space weathering based on nondestructive analyses. *Meteoritics & Planetary Science*, 50(9):1562–1576, 2015. doi: https://doi.org/10.1111/maps.12496. URL https://onlinelibrary.wiley.com/doi/abs/10.1111/maps.12496.

W. F. Bottke, A. Morbidelli, R. Jedicke, J.-M. Petit, H. F. Levison, P. Michel, and T. S. Metcalfe. Debiased orbital and absolute magnitude distribution of the near-earth objects. *Icarus*, 156 (2):399–433, 2002. ISSN 0019-1035. doi: https://doi.org/10.1006/icar.2001.6788. URL https://www.sciencedirect.com/science/article/pii/S0019103501967880.

A. e. a. Bouvier. The age of the Solar System redefined by the oldest Pb–Pb age of a meteoritic inclusion. *Nature Geoscience*, 2010. doi: 10.1038/ngeo941.

R. Brunetto and G. Strazzulla. Elastic collisions in ion irradiation experiments: A mechanism

for space weathering of silicates. *Icarus*, 179(1):265–273, 2005. ISSN 0019-1035. doi: https://doi.org/10.1016/j.icarus.2005.07.001. URL https://www.sciencedirect.com/science/article/pii/S0019103505002356.

R. Brunetto, C. Lantz, D. Ledu, D. Baklouti, M. Barucci, P. Beck, L. Delauche, Z. Dionnet, P. Dumas, J. Duprat, C. Engrand, F. Jamme, P. Oudayer, E. Quirico, C. Sandt, and E. Dartois. Ion irradiation of allende meteorite probed by visible, ir, and raman spectroscopies. *Icarus*, 237:278–292, 2014. ISSN 0019-1035. doi: https://doi.org/10.1016/j.icarus.2014.04.047. URL https://www.sciencedirect.com/science/article/pii/S0019103514002395.

R. Brunetto, M. Loeffler, D. Nesvorný, S. Sasaki, and G. Strazzulla. *Asteroid Surface Alteration by Space Weathering Processes*. 01 2015. ISBN 9780816532131. doi: 10.2458/azu_uapress_9780816532131-ch031.

R. Brunetto, A. Aléon-Toppani, S. Rubino, D. Baklouti, F. Borondics, Z. Dionnet, Z. Djouadi, C. Lantz, T. Nakamura, M. Takahashi, D. Troadec, and A. Tsuchiyama. IR Micro-Spectroscopy and Micro-Tomography of Isolated Murchison Grains in Preparation of the Hayabusa2 Sample Return. In *51st Annual Lunar and Planetary Science Conference*, Lunar and Planetary Science Conference, page 1135, Mar. 2020.

R. Brunetto, C. Lantz, T. Nakamura, D. Baklouti, T. Le Pivert-Jolivet, S. Kobayashi, and F. Borondics. Characterizing irradiated surfaces using ir spectroscopy. *Icarus*, 345:113722, 2020. ISSN 0019-1035. doi: https://doi.org/10.1016/j.icarus.2020.113722. URL https://www.sciencedirect.com/science/article/pii/S0019103520301135.

P. Carrez, K. DEMYK, P. CORDIER, L. GENGEMBRE, J. GRIMBLOT, L. D'HENDECOURT, A. P. JONES, and H. LEROUX. Low-energy helium ion irradiation-induced amorphization and chemical changes in olivine: Insights for silicate dust evolution in the interstellar medium. *Meteoritics & Planetary Science*, 37(11):1599–1614, 2002. doi: https://doi.org/10.1111/j.1945-5100.2002.tb00814.x. URL https://onlinelibrary.wiley.com/doi/abs/10.1111/j.1945-5100.2002.tb00814.x.

N. Chauvin, F. Dayras, D. Le Du, and R. Meunier. Sidonie: an electromagnetic isotope separator for preparation of high purity thin targets. *Nuclear Instruments and Methods in Physics Research Section A: Accelerators, Spectrometers, Detectors and Associated Equipment*, 521(1):149–155, 2004. ISSN 0168-9002. doi: https://doi.org/10.1016/j.nima.2003.11.417. URL https://www.sciencedirect.com/science/article/pii/S0168900203030778. Accelerator Target Technology for the 21st Century. Proceedings of the 21st World Conference of the International Nuclear Target Society.

A. Chokshi, A. G. G. M. Tielens, and D. Hollenbach. Dust coagulation. *Astrophysical Journal*, 1993.

P. R. Christensen, V. E. Hamilton, and al. The osiris-rex thermal emission spectrometer (otes) instrument. *Space Science Reviews*, 214, 2018.

M. J. Cintala and F. Hörz. Experimental impacts into chondritic targets, part i: Disruption of an l6 chondrite by multiple impacts. *Meteoritics & Planetary Science*, 43, 2008.

B. Clark, B. Hapke, C. Pieters, and D. Britt. Asteroid space weathering and regolith evolution. *Asteroids III*, 2002.

B. E. Clark, R. P. Binzel, E. S. Howell, E. A. Cloutis, M. Ockert-Bell, P. Christensen, M. A. Barucci, F. DeMeo, D. S. Lauretta, H. Connolly, A. Soderberg, C. Hergenrother, L. Lim, J. Emery, and M. Mueller. Asteroid (101955) 1999 rq36: Spectroscopy from 0.4 to 2.4m and meteorite analogs. *Icarus*, 216(2):462–475, 2011. ISSN 0019-1035. doi: https://doi.org/10.1016/j.icarus.2011.08.021. URL https://www.sciencedirect.com/science/article/pii/S0019103511003381.

R. N. Clark, T. V. V. King, M. Klejwa, G. A. Swayze, and N. Vergo. High spectral resolution reflectance spectroscopy of minerals. *Journal of Geophysical Research: Solid Earth*, 95(B8):1617–1637, 1990. doi: https://doi.org/10.1029/JB095iB08p12653.

G. J. Consolmagno and M. J. Drake. Composition and evolution of the eucrite parent body: evidence from rare earth elements. *Geochimica et Cosmochimica Acta*, 41(9):1271–1282, 1977. ISSN 0016-

7037. doi: https://doi.org/10.1016/0016-7037(77)90072-2. URL https://www.sciencedirect.com/science/article/pii/0016703777900722.

Davoisne, Leroux, H., Frère, M., Gimblot, J., Gengembre, L., Djouadi, Z., Ferreiro, V., d'Hendecourt, L., and Jones, A. Chemical and morphological evolution of a silicate surface under low-energy ion irradiation. *A&A*, 482(2):541–548, 2008. doi: 10.1051/0004-6361:20078964. URL https://doi.org/10.1051/0004-6361:20078964.

F. E. DeMeo, B. J. Burt, M. Marsset, D. Polishook, T. H. Burbine, B. Carry, R. P. Binzel, P. Vernazza, V. Reddy, M. Tang, C. A. Thomas, A. S. Rivkin, N. A. Moskovitz, S. M. Slivan, and S. J. Bus. Connecting asteroids and meteorites with visible and near-infrared spectroscopy. *Icarus*, 380:114971, 2022. ISSN 0019-1035. doi: https://doi.org/10.1016/j.icarus.2022.114971. URL https://www.sciencedirect.com/science/article/pii/S0019103522000896.

K. Demyk, P. Carrez, H. Leroux, P. Cordier, A. Jones, J. Borg, E. Quirico, P.-I. Raynal, and L. Dhendecourt. Structural and chemical alteration of crystalline olivine under low energy he^+ irradiation. *http://dx.doi.org/10.1051/0004-6361:20010208*, 368, 03 2001. doi: 10.1051/0004-6361:20010208.

Z. Dionnet. *Infrared Micro-tomography for the characterization of extra-terrestrial materials*. PhD thesis, 2018. URL http://www.theses.fr/2018SACLS291. Thèse de doctorat dirigée par Brunetto, Rosario Astronomie et Astrophysique Université Paris-Saclay (ComUE) 2018.

Z. Dionnet, R. Brunetto, A. Aléon-Toppani, S. Rubino, D. Baklouti, F. Borondics, A.-C. Buellet, Z. Djouadi, A. King, T. Nakamura, A. Rotundi, C. Sandt, D. Troadec, and A. Tsuchiyama. Combining ir and x-ray microtomography data sets: Application to itokawa particles and to paris meteorite. *Meteoritics & Planetary Science*, 55(7):1645–1664, 2020. doi: https://doi.org/10.1111/maps.13538. URL https://onlinelibrary.wiley.com/doi/abs/10.1111/maps.13538.

Z. Dionnet, A. Aléon-Toppani, R. Brunetto, S. Rubino, M. D. Suttle, C. Lantz, C. Avdellidou, D. Baklouti, F. Borondics, Z. Djouadi, F. Grieco, E. Héripré, T. Nakamura, A. Rotundi, and M. Scheel. Multiscale correlated analysis of the aguas zarcas cm chondrite. *Meteorit-*

ics & Planetary Science, 57(5):965–988, 2022. doi: https://doi.org/10.1111/maps.13807. URL https://onlinelibrary.wiley.com/doi/abs/10.1111/maps.13807.

V. C. Farmer. The Layer Silicates. In *The Infrared Spectra of Minerals*. Mineralogical Society of Great Britain and Ireland, 01 1974. ISBN 9780903056052. doi: 10.1180/mono-4.15. URL https://doi.org/10.1180/mono-4.15.

K. Fiege, M. Guglielmino, N. Altobelli, M. Trieloff, R. Srama, and T. M. Orlando. Space weathering induced via microparticle impacts: 2. dust impact simulation and meteorite target analysis. *Journal of Geophysical Research: Planets*, 124(4):1084–1099, 2019. doi: https://doi.org/10.1029/2018JE005564. URL https://agupubs.onlinelibrary.wiley.com/doi/abs/10.1029/2018JE005564.

S. Fornasier, C. Lantz, M. Barucci, and M. Lazzarin. Aqueous alteration on main belt primitive asteroids: Results from visible spectroscopy. *Icarus*, 233:163–178, 2014. ISSN 0019-1035. doi: https://doi.org/10.1016/j.icarus.2014.01.040. URL https://www.sciencedirect.com/science/article/pii/S0019103514000712.

L. H. Fuchs, E. J. Olsen, and K. J. Jensen. Mineralogy, mineral-chemistry, and composition of the murchison (c2) meteorite. 1973.

T. D. Glotch, G. R. Rossman, and O. Aharonson. Mid-infrared (5–100 m) reflectance spectra and optical constants of ten phyllosilicate minerals. *Icarus*, 192(2):605–622, 2007. ISSN 0019-1035. doi: https://doi.org/10.1016/j.icarus.2007.07.002. URL https://www.sciencedirect.com/science/article/pii/S0019103507003016.

T. Gold. The Lunar Surface. *Monthly Notices of the Royal Astronomical Society*, 115(6):585–604, 12 1955. ISSN 0035-8711. doi: 10.1093/mnras/115.6.585. URL https://doi.org/10.1093/mnras/115.6.585.

J. Gosling. Chapter 12 - the solar wind. In T. Spohn, D. Breuer, and T. V. Johnson, editors, *Encyclopedia of the Solar System (Third Edition)*, pages 261–279. Elsevier, Boston, third edition edition,

2014. ISBN 978-0-12-415845-0. doi: https://doi.org/10.1016/B978-0-12-415845-0.00012-8. URL https://www.sciencedirect.com/science/article/pii/B9780124158450000128.

R. C. Greenwood, T. H. Burbine, and I. A. Franchi. Linking asteroids and meteorites to the primordial planetesimal population. *Geochimica et Cosmochimica Acta*, 277:377–406, 2020. ISSN 0016-7037. doi: https://doi.org/10.1016/j.gca.2020.02.004. URL https://www.sciencedirect.com/science/article/pii/S0016703720301058.

L. Gu, Y. Chen, Y. Xu, X. Tang, Y. Lin, T. Noguchi, and J. Li. Space weathering of the chang'e-5 lunar sample from a mid-high latitude region on the moon. *Geophysical Research Letters*, 49 (7):e2022GL097875, 2022. doi: https://doi.org/10.1029/2022GL097875. URL https://agupubs.onlinelibrary.wiley.com/doi/abs/10.1029/2022GL097875. e2022GL097875 2022GL097875.

A. F. Gualtieri, G. Lusvardi, A. Zoboli, D. Di Giuseppe, and M. Lassinantti Gualtieri. Biodurability and release of metals during the dissolution of chrysotile, crocidolite and fibrous erionite. *Environmental Research*, 171:550–557, 2019. ISSN 0013-9351. doi: https://doi.org/10.1016/j.envres.2019.01.011. URL https://www.sciencedirect.com/science/article/pii/S0013935119300131.

D. Hallatt, H. Leroux, E. Dubois, and F. Braud. EXPLORING THE RESPONSE OF RYUGU-INSPIRED PHYLLOSILICATES TO A PULSED LASER. In *53rd Lunar and Planetary Science Conference*, Texas, United States, Mar. 2022. URL https://hal.archives-ouvertes.fr/hal-03664443.

V. E. Hamilton, A. A. Simon, P. R. Christensen, D. C. Reuter, B. E. Clark, M. A. Barucci, N. E. Bowles, W. V. Boynton, J. R. Brucato, E. A. Cloutis, H. C. Connolly, K. L. Donaldson Hanna, J. P. Emery, H. L. Enos, S. Fornasier, C. W. Haberle, R. D. Hanna, E. S. Howell, H. H. Kaplan, L. P. Keller, C. Lantz, J.-Y. Li, L. F. Lim, T. J. McCoy, F. Merlin, M. C. Nolan, A. Praet, B. Rozitis, S. A. Sandford, D. L. Schrader, C. A. Thomas, X.-D. Zou, D. S. Lauretta, D. E. Highsmith, J. Small, D. Vokrouhlický, E. Brown, T. Warren, C. Brunet, R. A. Chicoine, S. Desjardins, D. Gaudreau, T. Haltigin, S. Millington-Veloza, A. Rubi, J. Aponte, N. Gorius, A. Lunsford, B. Allen, J. Grindlay, D. Guevel, D. Hoak, J. Hong, J. Bayron, O. Golubov, P. Sánchez, J. Stromberg, M. Hirabayashi, C. M. Hartzell, S. Oliver, M. Rascon, A. Harch,

J. Joseph, S. Squyres, D. Richardson, L. McGraw, R. Ghent, R. P. Binzel, M. M. A. Asad, C. L. Johnson, L. Philpott, H. C. M. Susorney, F. Ciceri, A. R. Hildebrand, E.-M. Ibrahim, L. Breitenfeld, T. Glotch, A. D. Rogers, S. Ferrone, H. Campins, Y. Fernandez, W. Chang, A. Cheuvront, D. Trang, S. Tachibana, H. Yurimoto, G. Poggiali, M. Pajola, E. Dotto, E. Mazzotta Epifani, M. K. Crombie, M. R. M. Izawa, J. de Leon, J. Licandro, J. L. R. Garcia, S. Clemett, K. Thomas-Keprta, S. Van wal, M. Yoshikawa, J. Bellerose, S. Bhaskaran, C. Boyles, S. R. Chesley, C. M. Elder, D. Farnocchia, A. Harbison, B. Kennedy, A. Knight, N. Martinez-Vlasoff, N. Mastrodemos, T. McElrath, W. Owen, R. Park, B. Rush, L. Swanson, Y. Takahashi, D. Velez, K. Yetter, C. Thayer, C. Adam, P. Antreasian, J. Bauman, C. Bryan, B. Carcich, M. Corvin, J. Geeraert, J. Hoffman, J. M. Leonard, E. Lessac-Chenen, A. Levine, J. McAdams, L. McCarthy, D. Nelson, B. Page, J. Pelgrift, E. Sahr, K. Stakkestad, D. Stanbridge, D. Wibben, B. Williams, K. Williams, P. Wolff, P. Hayne, D. Kubitschek, J. D. P. Deshapriya, M. Fulchignoni, P. Hasselmann, E. B. Bierhaus, O. Billett, A. Boggs, B. Buck, S. Carlson-Kelly, J. Cerna, K. Chaffin, E. Church, M. Coltrin, J. Daly, A. Deguzman, R. Dubisher, D. Eckart, D. Ellis, P. Falkenstern, A. Fisher, M. E. Fisher, P. Fleming, K. Fortney, S. Francis, S. Freund, S. Gonzales, P. Haas, A. Hasten, D. Hauf, A. Hilbert, D. Howell, F. Jaen, N. Jayakody, M. Jenkins, K. Johnson, M. Lefevre, H. Ma, C. Mario, K. Martin, C. May, M. McGee, B. Miller, C. Miller, G. Miller, A. Mirfakhrai, E. Muhle, C. Norman, R. Olds, C. Parish, M. Ryle, M. Schmitzer, P. Sherman, M. Skeen, M. Susak, B. Sutter, Q. Tran, C. Welch, R. Witherspoon, J. Wood, J. Zareski, M. Arvizu-Jakubicki, E. Asphaug, E. Audi, R.-L. Ballouz, R. Bandrowski, K. J. Becker, T. L. Becker, S. Bendall, C. A. Bennett, H. Bloomenthal, D. Blum, J. Brodbeck, K. N. Burke, M. Chojnacki, A. Colpo, J. Contreras, J. Cutts, C. Y. Drouet d'Aubigny, D. Dean, D. N. DellaGiustina, B. Diallo, D. Drinnon, K. Drozd, R. Enos, C. Fellows, T. Ferro, M. R. Fisher, G. Fitzgibbon, M. Fitzgibbon, J. Forelli, T. Forrester, I. Galinsky, R. Garcia, A. Gardner, D. R. Golish, N. Habib, D. Hamara, D. Hammond, K. Hanley, K. Harshman, C. W. Hergenrother, K. Herzog, D. Hill, C. Hoekenga, S. Hooven, E. Huettner, A. Janakus, J. Jones, T. R. Kareta, J. Kidd, K. Kingsbury, S. S. Balram-Knutson, L. Koelbel, J. Kreiner, D. Lambert, C. Lewin, B. Lovelace, M. Loveridge, M. Lujan, C. K. Maleszewski, R. Malhotra, K. Marchese, E. McDonough, N. Mogk, V. Morrison, E. Morton, R. Munoz, J. Nel-

son, J. Padilla, R. Pennington, A. Polit, N. Ramos, V. Reddy, M. Riehl, B. Rizk, H. L. Roper, and the OSIRIS-REx Team. Evidence for widespread hydrated minerals on asteroid (101955) bennu. *Nature Astronomy*, 3(4):332–340, Apr 2019. ISSN 2397-3366. doi: 10.1038/s41550-019-0722-2. URL https://doi.org/10.1038/s41550-019-0722-2.

Hapke, C. William, and W. Edward. Effects of vapor-phase deposition processes on the optical, chemical, and magnetic properties oe the lunar regolith. *The moon*, 13, 1975. doi: https://doi.org/10.1007/BF00567525. URL https://doi.org/10.1007/BF00567525.

B. Hapke. Space weathering from mercury to the asteroid belt. *Journal of Geophysical Research*, 106:10039–10074, 05 2001. doi: 10.1029/2000JE001338.

Hicks, J. C. Bridges, T. Noguchi, A. Miyake, J. D. Piercy, and S. H. Baker. Fe-redox changes in itokawa space-weathered rims. *Meteoritics & Planetary Science*, 55(12):2599–2618, 2020. doi: https://doi.org/10.1111/maps.13611. URL https://onlinelibrary.wiley.com/doi/abs/10.1111/maps.13611.

T. e. a. Hiroi. Developing space weathering on the asteroid 25143 itokawa. *Nature*, 2006.

B. Inkson. 2 - scanning electron microscopy (sem) and transmission electron microscopy (tem) for materials characterization. In G. Hübschen, I. Altpeter, R. Tschuncky, and H.-G. Herrmann, editors, *Materials Characterization Using Nondestructive Evaluation (NDE) Methods*, pages 17–43. Woodhead Publishing, 2016. ISBN 978-0-08-100040-3. doi: https://doi.org/10.1016/B978-0-08-100040-3.00002-X. URL https://www.sciencedirect.com/science/article/pii/B978008100040300002X.

T. Iwata, K. Kitazato, and al. Nirs3: The near infrared spectrometer on hayabusa2. *Space Science Reviews*, 208, 2017.

R. Jaumann, N. Schmitz, T.-M. Ho, S. E. Schröder, K. A. Otto, K. Stephan, S. Elgner, K. Krohn, F. Preusker, F. Scholten, J. Biele, S. Ulamec, C. Krause, S. Sugita, K.-D. Matz, T. Roatsch, R. Parekh, S. Mottola, M. Grott, P. Michel, F. Trauthan, A. Koncz, H. Michaelis, C. Lange, J. T.

Grundmann, M. Maibaum, K. Sasaki, F. Wolff, J. Reill, A. Moussi-Soffys, L. Lorda, W. Neumann, J.-B. Vincent, R. Wagner, J.-P. Bibring, S. Kameda, H. Yano, S. Watanabe, M. Yoshikawa, Y. Tsuda, T. Okada, T. Yoshimitsu, Y. Mimasu, T. Saiki, H. Yabuta, H. Rauer, R. Honda, T. Morota, Y. Yokota, and T. Kouyama. Images from the surface of asteroid ryugu show rocks similar to carbonaceous chondrite meteorites. *Science*, 365(6455):817–820, 2019. doi: 10.1126/science.aaw8627. URL https://www.science.org/doi/abs/10.1126/science.aaw8627.

J. Kawaguchi, K. T. Uesugi, A. Fujiwara, and H. Saitoh. The muses-c, mission description and its status. *Acta Astronautica*, 45(4):397–405, 1999. ISSN 0094-5765. doi: https://doi.org/10.1016/S0094-5765(99)00159-9. URL https://www.sciencedirect.com/science/article/pii/S0094576599001599. Third IAA International Conference on Low-Cost Planetary Missions.

K. Keil. Thermal alteration of asteroids: evidence from meteorites. *Planetary and Space Science*, 48(10):887–903, 2000. ISSN 0032-0633. doi: https://doi.org/10.1016/S0032-0633(00)00054-4. URL https://www.sciencedirect.com/science/article/pii/S0032063300000544. Asteroids, Comets, Meteors (ACM) Conference.

L. Keller and D. McKay. Discovery of vapor deposits in the lunar regolith. *Science*, 09 1993. doi: 10.1126/science.261.5126.1305.

L. P. Keller and D. S. McKay. The nature and origin of rims on lunar soil grains. *Geochimica et Cosmochimica Acta*, 61(11):2331–2341, 1997. ISSN 0016-7037. doi: https://doi.org/10.1016/S0016-7037(97)00085-9. URL https://www.sciencedirect.com/science/article/pii/S0016703797000859.

L. P. Keller, S. J. Wentworth, and D. S. McKay. Surface-Correlated Nanophase Iron Metal in Lunar Soils: Petrography and Space Weathering Effects. In *New Views of the Moon: Integrated Remotely Sensed, Geophysical, and Sample Datasets*, page 44, Jan. 1998.

L. P. Keller, R. Christoffersen, C. A. Dukes, R. Baragiola, and Z. Rahman. Ion Irradiation Experiments on the Murchison CM2 Carbonaceous Chondrite: Simulating Space Weathering of

Primitive Asteroids. In *46th Annual Lunar and Planetary Science Conference*, Lunar and Planetary Science Conference, page 1913, Mar. 2015a.

L. P. Keller, R. Christoffersen, C. A. Dukes, R. A. Baragiola, and Z. Rahman. Fe and O EELS Studies of Ion Irradiated Murchison CM2 Carbonaceous Chondrite Matrix. In *78th Annual Meeting of the Meteoritical Society*, volume 78 of *LPI Contributions*, page 5354, July 2015b.

L. P. Keller, R. Christoffersen, C. A. Dukes, R. A. Baragiola, and Z. Rahman. Experimental Space Weathering of Carbonaceous Chondrite Matrix. In *Space Weathering of Airless Bodies: An Integration of Remote Sensing Data, Laboratory Experiments and Sample Analysis Workshop*, volume 1878 of *LPI Contributions*, page 2010, Nov. 2015c.

M. S. Kelley, F. Vilas, M. J. Gaffey, and P. A. Abell. Quantified mineralogical evidence for a common origin of 1929 kollaa with 4 vesta and the hed meteorites. *Icarus*, 165(1):215–218, 2003. ISSN 0019-1035. doi: https://doi.org/10.1016/S0019-1035(03)00149-0. URL https://www.sciencedirect.com/science/article/pii/S0019103503001490.

K. Kitazato, R. E. Milliken, T. Iwata, M. Abe, M. Ohtake, S. Matsuura, T. Arai, Y. Nakauchi, T. Nakamura, M. Matsuoka, H. Senshu, N. Hirata, T. Hiroi, C. Pilorget, R. Brunetto, F. Poulet, L. Riu, J.-P. Bibring, D. Takir, D. L. Domingue, F. Vilas, M. A. Barucci, D. Perna, E. Palomba, A. Galiano, K. Tsumura, T. Osawa, M. Komatsu, A. Nakato, T. Arai, N. Takato, T. Matsunaga, Y. Takagi, K. Matsumoto, T. Kouyama, Y. Yokota, E. Tatsumi, N. Sakatani, Y. Yamamoto, T. Okada, S. Sugita, R. Honda, T. Morota, S. Kameda, H. Sawada, C. Honda, M. Yamada, H. Suzuki, K. Yoshioka, M. Hayakawa, K. Ogawa, Y. Cho, K. Shirai, Y. Shimaki, N. Hirata, A. Yamaguchi, N. Ogawa, F. Terui, T. Yamaguchi, Y. Takei, T. Saiki, S. Nakazawa, S. Tanaka, M. Yoshikawa, S. Watanabe, and Y. Tsuda. The surface composition of asteroid 162173 ryugu from hayabusa2 near-infrared spectroscopy. *Science*, 364(6437):272–275, 2019. doi: 10.1126/science.aav7432. URL https://www.science.org/doi/abs/10.1126/science.aav7432.

K. Kitazato, R. E. Milliken, T. Iwata, M. Abe, M. Ohtake, S. Matsuura, Y. Takagi, T. Nakamura, T. Hiroi, M. Matsuoka, L. Riu, Y. Nakauchi, K. Tsumura, T. Arai, H. Senshu, N. Hirata,

M. A. Barucci, R. Brunetto, C. Pilorget, F. Poulet, J.-P. Bibring, D. L. Domingue, F. Vilas, D. Takir, E. Palomba, A. Galiano, D. Perna, T. Osawa, M. Komatsu, A. Nakato, N. Takato, T. Matsunaga, M. Arakawa, T. Saiki, K. Wada, T. Kadono, H. Imamura, H. Yano, K. Shirai, M. Hayakawa, C. Okamoto, H. Sawada, K. Ogawa, Y. Iijima, S. Sugita, R. Honda, T. Morota, S. Kameda, E. Tatsumi, Y. Cho, K. Yoshioka, Y. Yokota, N. Sakatani, M. Yamada, T. Kouyama, H. Suzuki, C. Honda, N. Namiki, T. Mizuno, K. Matsumoto, H. Noda, Y. Ishihara, R. Yamada, K. Yamamoto, F. Yoshida, S. Abe, A. Higuchi, Y. Yamamoto, T. Okada, Y. Shimaki, R. Noguchi, A. Miura, S. Tachibana, H. Yabuta, M. Ishiguro, H. Ikeda, H. Takeuchi, T. Shimada, O. Mori, S. Hosoda, R. Tsukizaki, S. Soldini, M. Ozaki, F. Terui, N. Ogawa, Y. Mimasu, G. Ono, K. Yoshikawa, C. Hirose, A. Fujii, T. Takahashi, S. Kikuchi, Y. Takei, T. Yamaguchi, S. Nakazawa, S. Tanaka, M. Yoshikawa, S. Watanabe, and Y. Tsuda. Thermally altered subsurface material of asteroid (162173) ryugu. *Nature Astronomy*, 5(3):246–250, Mar 2021. ISSN 2397-3366. doi: 10.1038/s41550-020-01271-2. URL https://doi.org/10.1038/s41550-020-01271-2.

Laczniak et al. UNRAVELING SOLAR WIND SPACE WEATHERING OF CARBON-RICH ASTERODS: LOW-FLUX VS. HIGH-FLUX ION IRRADIATION OF MURCHISON. MetSoc 2022, Aug. 2022.

D. Laczniak, M. Thompson, R. Christoffersen, C. Dukes, S. Clemett, R. Morris, and L. Keller. Characterizing the spectral, microstructural, and chemical effects of solar wind irradiation on the murchison carbonaceous chondrite through coordinated analyses. *Icarus*, 364:114479, 2021. ISSN 0019-1035. doi: https://doi.org/10.1016/j.icarus.2021.114479. URL https://www.sciencedirect.com/science/article/pii/S0019103521001597.

Lantz, Brunetto, R., Barucci, M. A., Dartois, E., Duprat, J., Engrand, C., Godard, M., Ledu, D., and Quirico, E. Ion irradiation of the murchison meteorite: Visible to mid-infrared spectroscopic results. *A&A*, 577:A41, 2015. doi: 10.1051/0004-6361/201425398. URL https://doi.org/10.1051/0004-6361/201425398.

C. Lantz, R. Brunetto, M. Barucci, S. Fornasier, D. Baklouti, J. Bourçois, and M. Godard. Ion

irradiation of carbonaceous chondrites: A new view of space weathering on primitive asteroids. *Icarus*, 285:43–57, 2017. ISSN 0019-1035. doi: https://doi.org/10.1016/j.icarus.2016.12.019. URL https://www.sciencedirect.com/science/article/pii/S0019103516300252.

C. Lantz, V. E. Hamilton, R. Brunetto, R. D. Hanna, P. R. Christensen, and D. S. Lauretta. Can We Detect Space Weathering on Bennu Using OTES Data? In *51st Annual Lunar and Planetary Science Conference*, Lunar and Planetary Science Conference, page 1850, Mar. 2020.

Lauretta, D. N. DellaGiustina, C. A. Bennett, D. R. Golish, K. J. Becker, S. S. Balram-Knutson, O. S. Barnouin, T. L. Becker, W. F. Bottke, W. V. Boynton, H. Campins, B. E. Clark, H. C. Connolly, C. Y. Drouet d'Aubigny, J. P. Dworkin, J. P. Emery, H. L. Enos, V. E. Hamilton, C. W. Hergenrother, E. S. Howell, M. R. M. Izawa, H. H. Kaplan, M. C. Nolan, B. Rizk, H. L. Roper, D. J. Scheeres, P. H. Smith, K. J. Walsh, C. W. V. Wolner, D. E. Highsmith, J. Small, D. Vokrouhlický, N. E. Bowles, E. Brown, K. L. Donaldson Hanna, T. Warren, C. Brunet, R. A. Chicoine, S. Desjardins, D. Gaudreau, T. Haltigin, S. Millington-Veloza, A. Rubi, J. Aponte, N. Gorius, A. Lunsford, B. Allen, J. Grindlay, D. Guevel, D. Hoak, J. Hong, D. L. Schrader, J. Bayron, O. Golubov, P. Sánchez, J. Stromberg, M. Hirabayashi, C. M. Hartzell, S. Oliver, M. Rascon, A. Harch, J. Joseph, S. Squyres, D. Richardson, L. McGraw, R. Ghent, R. P. Binzel, M. M. A. Asad, C. L. Johnson, L. Philpott, H. C. M. Susorney, E. A. Cloutis, R. D. Hanna, F. Ciceri, A. R. Hildebrand, E.-M. Ibrahim, L. Breitenfeld, T. Glotch, A. D. Rogers, S. Ferrone, C. A. Thomas, Y. Fernandez, W. Chang, A. Cheuvront, D. Trang, S. Tachibana, H. Yurimoto, J. R. Brucato, G. Poggiali, M. Pajola, E. Dotto, E. M. Epifani, M. K. Crombie, C. Lantz, J. de Leon, J. Licandro, J. L. R. Garcia, S. Clemett, K. Thomas-Keprta, S. Van wal, M. Yoshikawa, J. Bellerose, S. Bhaskaran, C. Boyles, S. R. Chesley, C. M. Elder, D. Farnocchia, A. Harbison, B. Kennedy, A. Knight, N. Martinez-Vlasoff, N. Mastrodemos, T. McElrath, W. Owen, R. Park, B. Rush, L. Swanson, Y. Takahashi, D. Velez, K. Yetter, C. Thayer, C. Adam, P. Antreasian, J. Bauman, C. Bryan, B. Carcich, M. Corvin, J. Geeraert, J. Hoffman, J. M. Leonard, E. Lessac-Chenen, A. Levine, J. McAdams, L. McCarthy, D. Nelson, B. Page, J. Pelgrift, E. Sahr, K. Stakkestad, D. Stanbridge, D. Wibben, B. Williams, K. Williams, P. Wolff, P. Hayne, D. Kubitschek, M. A.

Barucci, J. D. P. Deshapriya, S. Fornasier, M. Fulchignoni, P. Hasselmann, F. Merlin, A. Praet, E. B. Bierhaus, O. Billett, A. Boggs, B. Buck, S. Carlson-Kelly, J. Cerna, K. Chaffin, E. Church, M. Coltrin, J. Daly, A. Deguzman, R. Dubisher, D. Eckart, D. Ellis, P. Falkenstern, A. Fisher, M. E. Fisher, P. Fleming, K. Fortney, S. Francis, S. Freund, S. Gonzales, P. Haas, A. Hasten, D. Hauf, A. Hilbert, D. Howell, F. Jaen, N. Jayakody, M. Jenkins, K. Johnson, M. Lefevre, H. Ma, C. Mario, K. Martin, C. May, M. McGee, B. Miller, C. Miller, G. Miller, A. Mirfakhrai, E. Muhle, C. Norman, R. Olds, C. Parish, M. Ryle, M. Schmitzer, P. Sherman, M. Skeen, M. Susak, B. Sutter, Q. Tran, C. Welch, R. Witherspoon, J. Wood, J. Zareski, M. Arvizu-Jakubicki, E. Asphaug, E. Audi, R.-L. Ballouz, R. Bandrowski, S. Bendall, H. Bloomenthal, D. Blum, J. Brodbeck, K. N. Burke, M. Chojnacki, A. Colpo, J. Contreras, J. Cutts, D. Dean, B. Diallo, D. Drinnon, K. Drozd, R. Enos, C. Fellows, T. Ferro, M. R. Fisher, G. Fitzgibbon, M. Fitzgibbon, J. Forelli, T. Forrester, I. Galinsky, R. Garcia, A. Gardner, N. Habib, D. Hamara, D. Hammond, K. Hanley, K. Harshman, K. Herzog, D. Hill, C. Hoekenga, S. Hooven, E. Huettner, A. Janakus, J. Jones, T. R. Kareta, J. Kidd, K. Kingsbury, L. Koelbel, J. Kreiner, D. Lambert, C. Lewin, B. Lovelace, M. Loveridge, M. Lujan, C. K. Maleszewski, R. Malhotra, K. Marchese, E. McDonough, N. Mogk, V. Morrison, E. Morton, R. Munoz, J. Nelson, J. Padilla, R. Pennington, A. Polit, N. Ramos, V. Reddy, M. Riehl, S. Salazar, S. R. Schwartz, S. Selznick, N. Shultz, and T. O.-R. Team. The unexpected surface of asteroid (101955) bennu. *Nature*, 568(7750):55–60, Apr 2019. ISSN 1476-4687. doi: 10.1038/s41586-019-1033-6. URL https://doi.org/10.1038/s41586-019-1033-6.

D. S. Lauretta. *OSIRIS-REx Asteroid Sample-Return Mission*, pages 543–567. Springer International Publishing, Cham, 2015. ISBN 978-3-319-03952-7. doi: 10.1007/978-3-319-03952-7_44. URL https://doi.org/10.1007/978-3-319-03952-7_44.

D. S. Lauretta, C. D. Adam, A. J. Allen, R.-L. Ballouz, O. S. Barnouin, K. J. Becker, T. Becker, C. A. Bennett, E. B. Bierhaus, B. J. Bos, R. D. Burns, H. Campins, Y. Cho, P. R. Christensen, E. C. A. Church, B. E. Clark, H. C. Connolly, M. G. Daly, D. N. DellaGiustina, C. Y. D. d'Aubigny, J. P. Emery, H. L. Enos, S. F. Kasper, J. B. Garvin, K. Getzandanner, D. R. Golish, V. E. Hamilton, C. W. Hergenrother, H. H. Kaplan, L. P. Keller, E. J. Lessac-Chenen, A. J. Liounis, H. Ma,

L. K. McCarthy, B. D. Miller, M. C. Moreau, T. Morota, D. S. Nelson, J. O. Nolau, R. Olds, M. Pajola, J. Y. Pelgrift, A. T. Polit, M. A. Ravine, D. C. Reuter, B. Rizk, B. Rozitis, A. J. Ryan, E. M. Sahr, N. Sakatani, J. A. Seabrook, S. H. Selznick, M. A. Skeen, A. A. Simon, S. Sugita, K. J. Walsh, M. M. Westermann, C. W. V. Wolner, and K. Yumoto. Spacecraft sample collection and subsurface excavation of asteroid (101955) bennu. *Science*, 377(6603):285–291, 2022. doi: 10.1126/science.abm1018. URL https://www.science.org/doi/abs/10.1126/science.abm1018.

T. Le Pivert-Jolivet and al. *(in preparation)*, 2022.

M. Loeffler, R. Baragiola, and M. Murayama. Laboratory simulations of redeposition of impact ejecta on mineral surfaces. *Icarus*, 196:285–292, 07 2008. doi: 10.1016/j.icarus.2008.02.021.

M. J. Loeffler, C. A. Dukes, and R. A. Baragiola. Irradiation of olivine by 4 kev he+: Simulation of space weathering by the solar wind. *Journal of Geophysical Research: Planets*, 114(E3), 2009. doi: https://doi.org/10.1029/2008JE003249. URL https://agupubs.onlinelibrary.wiley.com/doi/abs/10.1029/2008JE003249.

M. C. Martin, C. Dabat-Blondeau, M. Unger, J. Sedlmair, D. Y. Parkinson, H. A. Bechtel, B. Illman, J. M. Castro, M. Keiluweit, D. Buschke, B. Ogle, M. J. Nasse, and C. J. Hirschmugl. 3d spectral imaging with synchrotron fourier transform infrared spectro-microtomography. *Nature Methods*, 10(9):861–864, Sep 2013. ISSN 1548-7105. doi: 10.1038/nmeth.2596. URL https://doi.org/10.1038/nmeth.2596.

Matsumoto et al. Surface morphologies and space weathering features of Ryugu samples. Hayabusa Symposium, Nov. 2021.

Matsumoto et al. NANO-PHASE OPAQUE MINERALS IN VAPOR DEPOSITED RIMS FOUND ON SAMPLES FROM C-TYPE ASTEROID RYUGU. In *85th Annual Meeting of The Meteoritical Society 2022*, Meteorite Society Conference, Aug. 2022.

T. Matsumoto, A. Tsuchiyama, A. Miyake, T. Noguchi, M. Nakamura, K. Uesugi, A. Takeuchi, Y. Suzuki, and T. Nakano. Surface and internal structures of a space-weathered rim of an itokawa

regolith particle. *Icarus*, 257:230–238, 2015. ISSN 0019-1035. doi: https://doi.org/10.1016/j.icarus.2015.05.001. URL https://www.sciencedirect.com/science/article/pii/S0019103515002031.

M. Matsuoka, T. Nakamura, T. Hiroi, S. Okumura, and S. Sasaki. Space weathering simulation with low-energy laser irradiation of murchison CM chondrite for reproducing micrometeoroid bombardments on c-type asteroids. *The Astrophysical Journal*, 890(2):L23, feb 2020. doi: 10.3847/2041-8213/ab72a4. URL https://doi.org/10.3847/2041-8213/ab72a4.

H. McSween, A. Ghosh, R. Grimm, L. Wilson, and E. Young. Thermal evolution models of asteroids. *Asteroids III*, 01 2002.

H. Y. McSween, M. E. Bennett, and E. Jarosewich. The mineralogy of ordinary chondrites and implications for asteroid spectrophotometry. *Icarus*, 90(1):107–116, 1991. ISSN 0019-1035. doi: https://doi.org/10.1016/0019-1035(91)90072-2. URL https://www.sciencedirect.com/science/article/pii/0019103591900722.

H. Y. McSween Jr., R. P. Binzel, M. C. De Sanctis, E. Ammannito, T. H. Prettyman, A. W. Beck, V. Reddy, L. Le Corre, M. J. Gaffey, T. B. McCord, C. A. Raymond, C. T. Russell, and the Dawn Science Team. Dawn; the vesta–hed connection; and the geologic context for eucrites, diogenites, and howardites. *Meteoritics & Planetary Science*, 48(11):2090–2104, 2013. doi: https://doi.org/10.1111/maps.12108. URL https://onlinelibrary.wiley.com/doi/abs/10.1111/maps.12108.

R. E. Milliken, J. F. Mustard, F. Poulet, D. Jouglet, J.-P. Bibring, B. Gondet, and Y. Langevin. Hydration state of the martian surface as seen by mars express omega: 2. h2o content of the surface. *Journal of Geophysical Research: Planets*, 112(E8), 2007. doi: https://doi.org/10.1029/2006JE002853. URL https://agupubs.onlinelibrary.wiley.com/doi/abs/10.1029/2006JE002853.

S. Mitra, S. A. Prabhudesai, D. Chakrabarty, V. K. Sharma, M. A. Vicente, J. P. Embs, and R. Mukhopadhyay. Dynamics of water in synthetic saponite clays: Effect of trivalent ion substitution. *Phys. Rev. E*, 87:062317, Jun 2013. doi: 10.1103/PhysRevE.87.062317. URL https://link.aps.org/doi/10.1103/PhysRevE.87.062317.

T. e. a. Montmerle. Solar System Formation and Early Evolution: the First 100 Million Years. *Earth, Moon, and Planets*, 2006. doi: 10.1007/s11038-006-9087-5.

T. Mooney and R. Knacke. Optical constants of chlorite and serpentine between 2.5 and 50 m. *Icarus*, 64(3):493–502, 1985. ISSN 0019-1035. doi: https://doi.org/10.1016/0019-1035(85)90070-3. URL https://www.sciencedirect.com/science/article/pii/0019103585900703.

D. P. Moriarty III and C. M. Pieters. Complexities in pyroxene compositions derived from absorption band centers: Examples from apollo samples, hed meteorites, synthetic pure pyroxenes, and remote sensing data. *Meteoritics & Planetary Science*, 51(2):207–234, 2016. doi: https://doi.org/10.1111/maps.12588. URL https://onlinelibrary.wiley.com/doi/abs/10.1111/maps.12588.

L. Moroz, A. Fisenko, L. Semjonova, C. Pieters, and N. Korotaeva. Optical effects of regolith processes on s-asteroids as simulated by laser shots on ordinary chondrite and other mafic materials. *Icarus*, 122(2):366–382, 1996. ISSN 0019-1035. doi: https://doi.org/10.1006/icar.1996.0130. URL https://www.sciencedirect.com/science/article/pii/S001910359690130X.

T. Nakamura, T. Noguchi, M. Tanaka, M. E. Zolensky, M. Kimura, A. Tsuchiyama, A. Nakato, T. Ogami, H. Ishida, M. Uesugi, T. Yada, K. Shirai, A. Fujimura, R. Okazaki, S. A. Sandford, Y. Ishibashi, M. Abe, T. Okada, M. Ueno, T. Mukai, M. Yoshikawa, and J. Kawaguchi. Itokawa dust particles: A direct link between s-type asteroids and ordinary chondrites. *Science*, 333(6046): 1113–1116, 2011. doi: 10.1126/science.1207758. URL https://www.science.org/doi/abs/10.1126/science.1207758.

Y. Nakauchi, M. Abe, M. Ohtake, T. Matsumoto, A. Tsuchiyama, K. Kitazato, K. Yasuda, K. Suzuki, and Y. Nakata. The formation of h 2 o and si-oh by h 2 + irradiation in major minerals of carbonaceous chondrites. *Icarus*, 355:114140, 02 2021. doi: 10.1016/j.icarus.2020.114140.

S. K. Noble, L. P. Keller, and C. M. Pieters. Evidence of space weathering in regolith breccias i: Lunar regolith breccias. *Meteoritics & Planetary Science*, 40(3):397–408, 2005. doi: https:

//doi.org/10.1111/j.1945-5100.2005.tb00390.x. URL https://onlinelibrary.wiley.com/doi/abs/10.1111/j.1945-5100.2005.tb00390.x.

S. K. Noble, C. M. Pieters, and L. P. Keller. An experimental approach to understanding the optical effects of space weathering. *Icarus*, 192(2):629–642, 2007. ISSN 0019-1035. doi: https://doi.org/10.1016/j.icarus.2007.07.021. URL https://www.sciencedirect.com/science/article/pii/S0019103507003569.

Noguchi et al. Mineralogy and surface modification of small grains recovered from the asteroid 162173 Ryugu. Hayabusa Symposium, Nov. 2021.

Noguchi et al. MINERALOGY AND SPACE WEATHERING OF FINE FRACTION RECOVERED FROM ASTEROID (162173) RYUGU. In *53rd Lunar and Planetary Science Conference (2022*, Lunar and Planetary Science Conference, mar 2022.

T. Noguchi and al. Mineralogy and surface modification of small grains recovered from the asteroid 162173 Ryugu. In *Hayabusa Symposium 2021*, Nov. 2021.

T. Noguchi, T. Nakamura, M. Kimura, M. Zolensky, M. Tanaka, T. Hashimoto, M. Konno, A. Nakato, T. Ogami, A. Fujimura, M. Abe, T. Yada, T. Mukai, M. Ueno, T. Okada, K. Shirai, Y. Ishibashi, and R. Okazaki. Incipient space weathering observed on the surface of itokawa dust particles. *Science (New York, N.Y.)*, 333:1121–5, 08 2011. doi: 10.1126/science.1207794.

T. Noguchi, M. Kimura, T. Hashimoto, M. Konno, T. Nakamura, M. E. Zolensky, R. Okazaki, M. Tanaka, A. Tsuchiyama, A. Nakato, T. Ogami, H. Ishida, R. Sagae, S. Tsujimoto, T. Matsumoto, J. Matsuno, A. Fujimura, M. Abe, T. Yada, T. Mukai, M. Ueno, T. Okada, K. Shirai, and Y. Ishibashi. Space weathered rims found on the surfaces of the itokawa dust particles. *Meteoritics & Planetary Science*, 49(2):188–214, 2014. doi: https://doi.org/10.1111/maps.12111. URL https://onlinelibrary.wiley.com/doi/abs/10.1111/maps.12111.

N. Ockman. The infra-red and raman spectra of ice. *Advances in Physics*, 7(26):199–220, 1958. doi: 10.1080/00018735800101227.

T. Okada, T. Fukuhara, S. Tanaka, M. Taguchi, T. Arai, H. Senshu, N. Sakatani, Y. Shimaki, H. Demura, Y. Ogawa, K. Suko, T. Sekiguchi, T. Kouyama, J. Takita, T. Matsunaga, T. Imamura, T. Wada, S. Hasegawa, J. Helbert, T. G. Müller, A. Hagermann, J. Biele, M. Grott, M. Hamm, M. Delbo, N. Hirata, N. Hirata, Y. Yamamoto, S. Sugita, N. Namiki, K. Kitazato, M. Arakawa, S. Tachibana, H. Ikeda, M. Ishiguro, K. Wada, C. Honda, R. Honda, Y. Ishihara, K. Matsumoto, M. Matsuoka, T. Michikami, A. Miura, T. Morota, H. Noda, R. Noguchi, K. Ogawa, K. Shirai, E. Tatsumi, H. Yabuta, Y. Yokota, M. Yamada, M. Abe, M. Hayakawa, T. Iwata, M. Ozaki, H. Yano, S. Hosoda, O. Mori, H. Sawada, T. Shimada, H. Takeuchi, R. Tsukizaki, A. Fujii, C. Hirose, S. Kikuchi, Y. Mimasu, N. Ogawa, G. Ono, T. Takahashi, Y. Takei, T. Yamaguchi, K. Yoshikawa, F. Terui, T. Saiki, S. Nakazawa, M. Yoshikawa, S. Watanabe, and Y. Tsuda. Highly porous nature of a primitive asteroid revealed by thermal imaging. *Nature*, 579(7800): 518–522, Mar 2020. ISSN 1476-4687. doi: 10.1038/s41586-020-2102-6. URL https://doi.org/10.1038/s41586-020-2102-6.

J. J. Papike, S. B. Simon, and J. C. Laul. The lunar regolith: Chemistry, mineralogy, and petrology. *Reviews of Geophysics*, 20(4):761–826, 1982. doi: https://doi.org/10.1029/RG020i004p00761. URL https://agupubs.onlinelibrary.wiley.com/doi/abs/10.1029/RG020i004p00761.

C. M. Pieters and S. K. Noble. Space weathering on airless bodies. *Journal of Geophysical Research: Planets*, 121(10):1865–1884, 2016. doi: https://doi.org/10.1002/2016JE005128. URL https://agupubs.onlinelibrary.wiley.com/doi/abs/10.1002/2016JE005128.

C. M. Pieters, L. A. TAYLOR, S. K. NOBLE, L. P. KELLER, B. HAPKE, R. V. MORRIS, C. C. ALLEN, D. S. McKAY, and S. WENTWORTH. Space weathering on airless bodies: Resolving a mystery with lunar samples. *Meteoritics & Planetary Science*, 35(5):1101–1107, 2000. doi: https://doi.org/10.1111/j.1945-5100.2000.tb01496.x. URL https://onlinelibrary.wiley.com/doi/abs/10.1111/j.1945-5100.2000.tb01496.x.

C. Pilorget, T. Okada, V. Hamm, R. Brunetto, T. Yada, D. Loizeau, L. Riu, T. Usui, A. Moussi-Soffys, K. Hatakeda, A. Nakato, K. Yogata, M. Abe, A. Aléon-Toppani, J. Carter, M. Chaigneau,

B. Crane, B. Gondet, K. Kumagai, Y. Langevin, C. Lantz, T. Le Pivert-Jolivet, G. Lequertier, L. Lourit, A. Miyazaki, M. Nishimura, F. Poulet, M. Arakawa, N. Hirata, K. Kitazato, S. Nakazawa, N. Namiki, T. Saiki, S. Sugita, S. Tachibana, S. Tanaka, M. Yoshikawa, Y. Tsuda, S. Watanabe, and J.-P. Bibring. First compositional analysis of ryugu samples by the micromega hyperspectral microscope. *Nature Astronomy*, 6(2):221–225, Feb 2022. ISSN 2397-3366. doi: 10.1038/s41550-021-01549-z. URL https://doi.org/10.1038/s41550-021-01549-z.

S. Potin, O. Brissaud, P. Beck, B. Schmitt, Y. Magnard, J.-J. Correia, P. Rabou, and L. Jocou. Shadows: a spectro-gonio radiometer for bidirectional reflectance studies of dark meteorites and terrestrial analogs: design, calibrations, and performances on challenging surfaces. *Appl. Opt.*, 57 (28):8279–8296, Oct 2018. doi: 10.1364/AO.57.008279. URL http://opg.optica.org/ao/abstract.cfm?URI=ao-57-28-8279.

S. Potin, P. Beck, B. Schmitt, and F. Moynier. Some things special about neas: Geometric and environmental effects on the optical signatures of hydration. *Icarus*, 333:415–428, 2019. ISSN 0019-1035. doi: https://doi.org/10.1016/j.icarus.2019.06.026. URL https://www.sciencedirect.com/science/article/pii/S0019103519301162.

D. C. Reuters, A. A. Simon, and al. The osiris-rex visible and infrared spectrometer (ovirs): Spectral maps of the asteroid bennu. *Space Science Reviews*, 214, 2018.

L. Riu, C. Pilorget, R. Milliken, K. Kitazato, T. Nakamura, Y. Cho, M. Matsuoka, S. Sugita, M. Abe, S. Matsuura, M. Ohtake, S. Kameda, N. Sakatani, E. Tatsumi, Y. Yokota, and T. Iwata. Spectral characterization of the craters of ryugu as observed by the nirs3 instrument on-board hayabusa2. *Icarus*, 357:114253, 2021. ISSN 0019-1035. doi: https://doi.org/10.1016/j.icarus.2020.114253. URL https://www.sciencedirect.com/science/article/pii/S0019103520305789.

S. Rubino, S. Potin, C. Lantz, D. Baklouti, P. Beck, O. Brissaud, H. Leroux, E. Quirico, B. Schmitt, F. Borondics, and R. Brunetto. Geometry induced bias in the remote near-ir identification of phyllosilicates on space weathered bodies. *Icarus*, 376:114887, 2022. ISSN 0019-1035. doi: https://

doi.org/10.1016/j.icarus.2022.114887. URL https://www.sciencedirect.com/science/article/pii/S0019103522000094.

Y. I. Ryskin. The vibrations of protons in minerals: hydroxyl, water and ammonium. In *The Infrared Spectra of Minerals*. Mineralogical Society of Great Britain and Ireland, 1974. ISBN 9780903056052. doi: 10.1180/mono-4.9.

J. W. Salisbury, L. S. Walter, and N. Vergo. Mid-infrared (2.1-25 um) spectra of minerals; first edition. Technical report, 1987. URL http://pubs.er.usgs.gov/publication/ofr87263. Report.

S. Sasaki, T. Hiroi, K. Nakamura, Y. Hamabe, E. Kurahashi, and M. Yamada. Simulation of space weathering by nanosecond pulse laser heating: dependence on mineral composition, weathering trend of asteroids and discovery of nanophase iron particles. *Advances in Space Research*, 29 (5):783–788, 2002. ISSN 0273-1177. doi: https://doi.org/10.1016/S0273-1177(02)00012-1. URL https://www.sciencedirect.com/science/article/pii/S0273117702000121.

P. Schroeder. Infrared spectroscopy in clay science. *Teaching Clay Science*, 11, 01 2002.

Simon, A. A., Kaplan, H. H., Cloutis, E., Hamilton, V. E., Lantz, C., Reuter, D. C., Trang, D., Fornasier, S., Clark, B. E., and Lauretta, D. S. Weak spectral features on (101995) bennu from the osiris-rex visible and infrared spectrometer. *A&A*, 644:A148, 2020. doi: 10.1051/0004-6361/202039688. URL https://doi.org/10.1051/0004-6361/202039688.

I. W. Stephens, L. W. Looney, W. Kwon, M. Fernández-López, A. M. Hughes, L. G. Mundy, R. M. Crutcher, Z.-Y. Li, and R. Rao. Spatially resolved magnetic field structure in the disk of a t tauri star. *Nature*, 514(7524):597–599, Oct 2014. ISSN 1476-4687. doi: 10.1038/nature13850. URL https://doi.org/10.1038/nature13850.

S. Sugita, R. Honda, T. Morota, S. Kameda, H. Sawada, E. Tatsumi, M. Yamada, C. Honda, Y. Yokota, T. Kouyama, N. Sakatani, K. Ogawa, H. Suzuki, T. Okada, N. Namiki, S. Tanaka, Y. Iijima, K. Yoshioka, M. Hayakawa, Y. Cho, M. Matsuoka, N. Hirata, N. Hirata, H. Miyamoto, D. Domingue, M. Hirabayashi, T. Nakamura, T. Hiroi, T. Michikami, P. Michel, R.-L. Ballouz,

O. S. Barnouin, C. M. Ernst, S. E. Schröder, H. Kikuchi, R. Hemmi, G. Komatsu, T. Fukuhara, M. Taguchi, T. Arai, H. Senshu, H. Demura, Y. Ogawa, Y. Shimaki, T. Sekiguchi, T. G. Müller, A. Hagermann, T. Mizuno, H. Noda, K. Matsumoto, R. Yamada, Y. Ishihara, H. Ikeda, H. Araki, K. Yamamoto, S. Abe, F. Yoshida, A. Higuchi, S. Sasaki, S. Oshigami, S. Tsuruta, K. Asari, S. Tazawa, M. Shizugami, J. Kimura, T. Otsubo, H. Yabuta, S. Hasegawa, M. Ishiguro, S. Tachibana, E. Palmer, R. Gaskell, L. L. Corre, R. Jaumann, K. Otto, N. Schmitz, P. A. Abell, M. A. Barucci, M. E. Zolensky, F. Vilas, F. Thuillet, C. Sugimoto, N. Takaki, Y. Suzuki, H. Kamiyoshihara, M. Okada, K. Nagata, M. Fujimoto, M. Yoshikawa, Y. Yamamoto, K. Shirai, R. Noguchi, N. Ogawa, F. Terui, S. Kikuchi, T. Yamaguchi, Y. Oki, Y. Takao, H. Takeuchi, G. Ono, Y. Mimasu, K. Yoshikawa, T. Takahashi, Y. Takei, A. Fujii, C. Hirose, S. Nakazawa, S. Hosoda, O. Mori, T. Shimada, S. Soldini, T. Iwata, M. Abe, H. Yano, R. Tsukizaki, M. Ozaki, K. Nishiyama, T. Saiki, S. Watanabe, and Y. Tsuda. The geomorphology, color, and thermal properties of ryugu: Implications for parent-body processes. *Science*, 364(6437):eaaw0422, 2019. doi: 10.1126/science.aaw0422. URL https://www.science.org/doi/abs/10.1126/science.aaw0422.

R. Sultana, O. Poch, P. Beck, B. Schmitt, and E. Quirico. Visible and near-infrared reflectance of hyperfine and hyperporous particulate surfaces. *Icarus*, 357:114141, 2021. ISSN 0019-1035. doi: https://doi.org/10.1016/j.icarus.2020.114141. URL https://www.sciencedirect.com/science/article/pii/S0019103520304814.

D. Takir, J. P. Emery, H. Y. Mcsween Jr., C. A. Hibbitts, R. N. Clark, N. Pearson, and A. Wang. Nature and degree of aqueous alteration in cm and ci carbonaceous chondrites. *Meteoritics & Planetary Science*, 48(9):1618–1637, 2013. doi: https://doi.org/10.1111/maps.12171. URL https://onlinelibrary.wiley.com/doi/abs/10.1111/maps.12171.

Thompson et al. EVIDENCE FOR MICROMETEOROID BOMBARDMENT ON THE SURFACE OF ASTEROID RYUG. In *53rd Lunar and Planetary Science Conference (2022*, Lunar and Planetary Science Conference, mar 2022.

M. Thompson, M. Loeffler, R. Morris, L. Keller, and R. Christoffersen. Spectral and chemical

effects of simulated space weathering of the murchison cm2 carbonaceous chondrite. *Icarus*, 319:499–511, 2019. ISSN 0019-1035. doi: https://doi.org/10.1016/j.icarus.2018.09.022. URL https://www.sciencedirect.com/science/article/pii/S0019103518302276.

M. Thompson, R. Morris, S. Clemett, M. Loeffler, D. Trang, L. Keller, R. Christoffersen, and D. Agresti. The effect of progressive space weathering on the organic and inorganic components of a carbonaceous chondrite. *Icarus*, 346:113775, 2020. ISSN 0019-1035. doi: https://doi.org/10.1016/j.icarus.2020.113775. URL https://www.sciencedirect.com/science/article/pii/S0019103520301627.

M. S. Thompson, R. Christoffersen, T. J. Zega, and L. P. Keller. Microchemical and structural evidence for space weathering in soils from asteroid itokawa. *Earth, Planets and Space*, 66(1): 89, Aug 2014. ISSN 1880-5981. doi: 10.1186/1880-5981-66-89. URL https://doi.org/10.1186/1880-5981-66-89.

D. Trang, M. S. Thompson, B. E. Clark, H. H. Kaplan, X.-D. Zou, J.-Y. Li, S. M. Ferrone, V. E. Hamilton, A. A. Simon, D. C. Reuter, L. P. Keller, M. A. Barucci, H. Campins, C. Lantz, D. N. DellaGiustina, R.-L. Ballouz, E. R. Jawin, H. C. Connolly, K. J. Walsh, and D. S. Lauretta. The role of hydrated minerals and space weathering products in the bluing of carbonaceous asteroids. *The Planetary Science Journal*, 2(2):68, apr 2021. doi: 10.3847/psj/abe76f. URL https://doi.org/10.3847/psj/abe76f.

M. Trombetta, G. Busca, M. Lenarda, L. Storaro, R. Ganzerla, L. Piovesan, A. Jimenez Lopez, M. Alcantara-Rodrıguez, and E. Rodrıguez-Castellón. Solid acid catalysts from clays: Evaluation of surface acidity of mono- and bi-pillared smectites by ft-ir spectroscopy measurements, nh3-tpd and catalytic tests. *Applied Catalysis A: General*, 193(1):55–69, 2000. ISSN 0926-860X. doi: https://doi.org/10.1016/S0926-860X(99)00413-5. URL https://www.sciencedirect.com/science/article/pii/S0926860X99004135.

P. Tsou, D. E. Brownlee, S. A. Sandford, F. Hörz, and M. E. Zolensky. Wild 2 and interstellar sample collection and earth return. *Journal of Geophysical Research: Planets*, 108(E10), 2003.

doi: https://doi.org/10.1029/2003JE002109. URL https://agupubs.onlinelibrary.wiley.com/doi/abs/10.1029/2003JE002109.

R. Urso, V. Vuitton, G. Danger, L. Dhendecourt, L. Flandinet, Z. Djouadi, O. Mivumbi, F.-R. Orthous-Daunay, A. Ruf, V. Vinogradoff, C. Wolters, and R. Brunetto. Irradiation dose affects the composition of organic refractory materials in space: Results from laboratory analogues. *Astronomy and Astrophysics*, 644, 11 2020. doi: 10.1051/0004-6361/202039528.

F. Usui, S. Hasegawa, T. Ootsubo, and T. Onaka. AKARI/IRC near-infrared asteroid spectroscopic survey: AcuA-spec. *Publications of the Astronomical Society of Japan*, 71(1), 12 2018. ISSN 0004-6264. doi: 10.1093/pasj/psy125. URL https://doi.org/10.1093/pasj/psy125. 1.

W. Van Schmus and J. Wood. A chemical-petrologic classification for the chondritic meteorites. *Geochimica et Cosmochimica Acta*, 31(5):747–765, 1967. ISSN 0016-7037. doi: https://doi.org/10.1016/S0016-7037(67)80030-9. URL https://www.sciencedirect.com/science/article/pii/S0016703767800309.

P. Vernazza, R. P. Binzel, A. Rossi, M. Fulchignoni, and M. Birlan. Solar wind as the origin of rapid reddening of asteroid surfaces. *Nature*, 458(7241):993–995, Apr 2009. ISSN 1476-4687. doi: 10.1038/nature07956. URL https://doi.org/10.1038/nature07956.

P. Vernazza, D. Fulvio, R. Brunetto, J. Emery, C. Dukes, F. Cipriani, O. Witasse, M. Schaible, B. Zanda, G. Strazzulla, and R. Baragiola. Paucity of tagish lake-like parent bodies in the asteroid belt and among jupiter trojans. *Icarus*, 225(1):517–525, 2013. ISSN 0019-1035. doi: https://doi.org/10.1016/j.icarus.2013.04.019. URL https://www.sciencedirect.com/science/article/pii/S001910351300184X.

P. Vernazza, B. Zanda, R. P. Binzel, T. Hiroi, F. E. DeMeo, M. Birlan, R. Hewins, L. Ricci, P. Barge, and M. Lockhart. MULTIPLE AND FAST: THE ACCRETION OF ORDINARY CHONDRITE PARENT BODIES. *The Astrophysical Journal*, 791(2):120, aug 2014. doi: 10.1088/0004-637x/791/2/120. URL https://doi.org/10.1088/0004-637x/791/2/120.

L. G. B. M. Vicente Rodriguez, Suarez Barrios. Acid activation of a ferrous saponite (griffithite): Physicochemical characterization and surface area of the products obtained. *Clays and Clay Minerals - CLAYS CLAY MINER*, 42:724–730, 12 1994. doi: 10.1346/CCMN.1994.0420608.

X. Wang, Y. Li, and H. Wang. Structural characterization of octahedral sheet in dioctahedral smectites by thermal analysis. *Minerals*, 10(4), 2020. ISSN 2075-163X. doi: 10.3390/min10040347. URL https://www.mdpi.com/2075-163X/10/4/347.

S. Watanabe, M. Hirabayashi, N. Hirata, N. Hirata, R. Noguchi, Y. Shimaki, H. Ikeda, E. Tatsumi, M. Yoshikawa, S. Kikuchi, H. Yabuta, T. Nakamura, S. Tachibana, Y. Ishihara, T. Morota, K. Kitazato, N. Sakatani, K. Matsumoto, K. Wada, H. Senshu, C. Honda, T. Michikami, H. Takeuchi, T. Kouyama, R. Honda, S. Kameda, T. Fuse, H. Miyamoto, G. Komatsu, S. Sugita, T. Okada, N. Namiki, M. Arakawa, M. Ishiguro, M. Abe, R. Gaskell, E. Palmer, O. S. Barnouin, P. Michel, A. S. French, J. W. McMahon, D. J. Scheeres, P. A. Abell, Y. Yamamoto, S. Tanaka, K. Shirai, M. Matsuoka, M. Yamada, Y. Yokota, H. Suzuki, K. Yoshioka, Y. Cho, S. Tanaka, N. Nishikawa, T. Sugiyama, H. Kikuchi, R. Hemmi, T. Yamaguchi, N. Ogawa, G. Ono, Y. Mimasu, K. Yoshikawa, T. Takahashi, Y. Takei, A. Fujii, C. Hirose, T. Iwata, M. Hayakawa, S. Hosoda, O. Mori, H. Sawada, T. Shimada, S. Soldini, H. Yano, R. Tsukizaki, M. Ozaki, Y. Iijima, K. Ogawa, M. Fujimoto, T.-M. Ho, A. Moussi, R. Jaumann, J.-P. Bibring, C. Krause, F. Terui, T. Saiki, S. Nakazawa, and Y. Tsuda. Hayabusa2 arrives at the carbonaceous asteroid 162173 ryugu—a spinning top–shaped rubble pile. *Science*, 364(6437):268–272, 2019. doi: 10.1126/science.aav8032. URL https://www.science.org/doi/abs/10.1126/science.aav8032.

S.-i. Watanabe, Y. Tsuda, M. Yoshikawa, S. Tanaka, T. Saiki, and S. Nakazawa. Hayabusa2 mission overview. *Space Science Reviews*, 208(1):3–16, Jul 2017. ISSN 1572-9672. doi: 10.1007/s11214-017-0377-1. URL https://doi.org/10.1007/s11214-017-0377-1.

M. K. Weisberg, T. J. McCoy, and A. N. Krot. Systematics and Evaluation of Meteorite Classification. In D. S. Lauretta and H. Y. McSween, editors, *Meteorites and the Early Solar System II*, page 19. 2006.

T. Yada, M. Abe, T. Okada, A. Nakato, K. Yogata, A. Miyazaki, K. Hatakeda, K. Kumagai, M. Nishimura, Y. Hitomi, H. Soejima, M. Yoshitake, A. Iwamae, S. Furuya, M. Uesugi, Y. Karouji, T. Usui, T. Hayashi, D. Yamamoto, R. Fukai, S. Sugita, Y. Cho, K. Yumoto, Y. Yabe, J.-P. Bibring, C. Pilorget, V. Hamm, R. Brunetto, L. Riu, L. Lourit, D. Loizeau, G. Lequertier, A. Moussi-Soffys, S. Tachibana, H. Sawada, R. Okazaki, Y. Takano, K. Sakamoto, Y. N. Miura, H. Yano, T. R. Ireland, T. Yamada, M. Fujimoto, K. Kitazato, N. Namiki, M. Arakawa, N. Hirata, H. Yurimoto, T. Nakamura, T. Noguchi, H. Yabuta, H. Naraoka, M. Ito, E. Nakamura, K. Uesugi, K. Kobayashi, T. Michikami, H. Kikuchi, N. Hirata, Y. Ishihara, K. Matsumoto, H. Noda, R. Noguchi, Y. Shimaki, K. Shirai, K. Ogawa, K. Wada, H. Senshu, Y. Yamamoto, T. Morota, R. Honda, C. Honda, Y. Yokota, M. Matsuoka, N. Sakatani, E. Tatsumi, A. Miura, M. Yamada, A. Fujii, C. Hirose, S. Hosoda, H. Ikeda, T. Iwata, S. Kikuchi, Y. Mimasu, O. Mori, N. Ogawa, G. Ono, T. Shimada, S. Soldini, T. Takahashi, Y. Takei, H. Takeuchi, R. Tsukizaki, K. Yoshikawa, F. Terui, S. Nakazawa, S. Tanaka, T. Saiki, M. Yoshikawa, S.-i. Watanabe, and Y. Tsuda. Preliminary analysis of the hayabusa2 samples returned from c-type asteroid ryugu. *Nature Astronomy*, 6(2):214–220, Feb 2022. ISSN 2397-3366. doi: 10.1038/s41550-021-01550-6. URL https://doi.org/10.1038/s41550-021-01550-6.

T. Yokoyama, K. Nagashima, I. Nakai, E. D. Young, Y. Abe, J. Aléon, C. M. O. Alexander, S. Amari, Y. Amelin, K. ichi Bajo, M. Bizzarro, A. Bouvier, R. W. Carlson, M. Chaussidon, B.-G. Choi, N. Dauphas, A. M. Davis, T. D. Rocco, W. Fujiya, R. Fukai, I. Gautam, M. K. Haba, Y. Hibiya, H. Hidaka, H. Homma, P. Hoppe, G. R. Huss, K. Ichida, T. Iizuka, T. R. Ireland, A. Ishikawa, M. Ito, S. Itoh, N. Kawasaki, N. T. Kita, K. Kitajima, T. Kleine, S. Komatani, A. N. Krot, M.-C. Liu, Y. Masuda, K. D. McKeegan, M. Morita, K. Motomura, F. Moynier, A. Nguyen, L. Nittler, M. Onose, A. Pack, C. Park, L. Piani, L. Qin, S. S. Russell, N. Sakamoto, M. Schönbächler, L. Tafla, H. Tang, K. Terada, Y. Terada, T. Usui, S. Wada, M. Wadhwa, R. J. Walker, K. Yamashita, Q.-Z. Yin, S. Yoneda, H. Yui, A.-C. Zhang, H. C. Connolly, D. S. Lauretta, T. Nakamura, H. Naraoka, T. Noguchi, R. Okazaki, K. Sakamoto, H. Yabuta, M. Abe, M. Arakawa, A. Fujii, M. Hayakawa, N. Hirata, N. Hirata, R. Honda, C. Honda, S. Hosoda, Y. ichi Iijima, H. Ikeda, M. Ishiguro, Y. Ishihara, T. Iwata, K. Kawahara,

S. Kikuchi, K. Kitazato, K. Matsumoto, M. Matsuoka, T. Michikami, Y. Mimasu, A. Miura, T. Morota, S. Nakazawa, N. Namiki, H. Noda, R. Noguchi, N. Ogawa, K. Ogawa, T. Okada, C. Okamoto, G. Ono, M. Ozaki, T. Saiki, N. Sakatani, H. Sawada, H. Senshu, Y. Shimaki, K. Shirai, S. Sugita, Y. Takei, H. Takeuchi, S. Tanaka, E. Tatsumi, F. Terui, Y. Tsuda, R. Tsukizaki, K. Wada, S. ichiro Watanabe, M. Yamada, T. Yamada, Y. Yamamoto, H. Yano, Y. Yokota, K. Yoshihara, M. Yoshikawa, K. Yoshikawa, S. Furuya, K. Hatakeda, T. Hayashi, Y. Hitomi, K. Kumagai, A. Miyazaki, A. Nakato, M. Nishimura, H. Soejima, A. Suzuki, T. Yada, D. Yamamoto, K. Yogata, M. Yoshitake, S. Tachibana, and H. Yurimoto. Samples returned from the asteroid ryugu are similar to ivuna-type carbonaceous meteorites. *Science*, 0(0):eabn7850, 2022. doi: 10.1126/science.abn7850. URL https://www.science.org/doi/abs/10.1126/science.abn7850.

J. F. Ziegler, M. Ziegler, and J. Biersack. Srim – the stopping and range of ions in matter (2010). *Nuclear Instruments and Methods in Physics Research Section B: Beam Interactions with Materials and Atoms*, 268(11):1818–1823, 2010. ISSN 0168-583X. doi: https://doi.org/10.1016/j.nimb.2010.02.091. URL https://www.sciencedirect.com/science/article/pii/S0168583X10001862. 19th International Conference on Ion Beam Analysis.

M. E. Zolensky, N. M. Abreu, M. A. Velbel, A. Rubin, N. Chaumard, T. Noguchi, and T. Michikami. Chapter 2 - physical, chemical, and petrological characteristics of chondritic materials and their relationships to small solar system bodies. In N. Abreu, editor, *Primitive Meteorites and Asteroids*, pages 59–204. Elsevier, 2018. ISBN 978-0-12-813325-5. doi: https://doi.org/10.1016/B978-0-12-813325-5.00002-1. URL https://www.sciencedirect.com/science/article/pii/B9780128133255000021.

APPENDIX

Raw spectroscopic data

In this section, the raw data of most of the spectroscopic data present in this work are showcased. In figure A.1, the visible and near-IR range are shown, while in figure A.2, the reader can look at the the mid- and far-IR raw data.

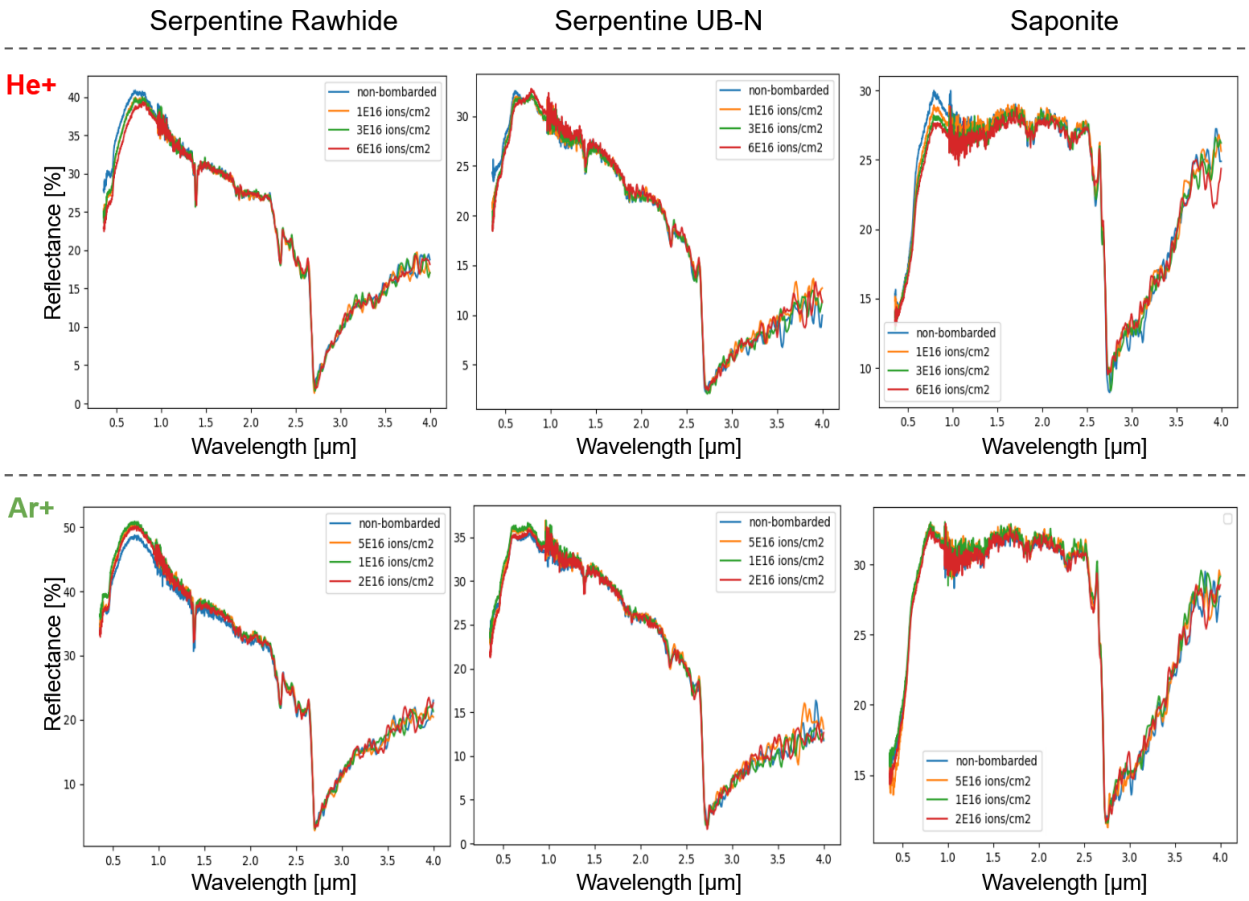

Figure A.1: Raw data in the visible and near-IR range of the ion-bombarded phyllosilicate pellet studied in this work. The data was acquired under vacuum with the INGMAR-SIDONIE setup (see Chapter 2 for more informations about the setup.)

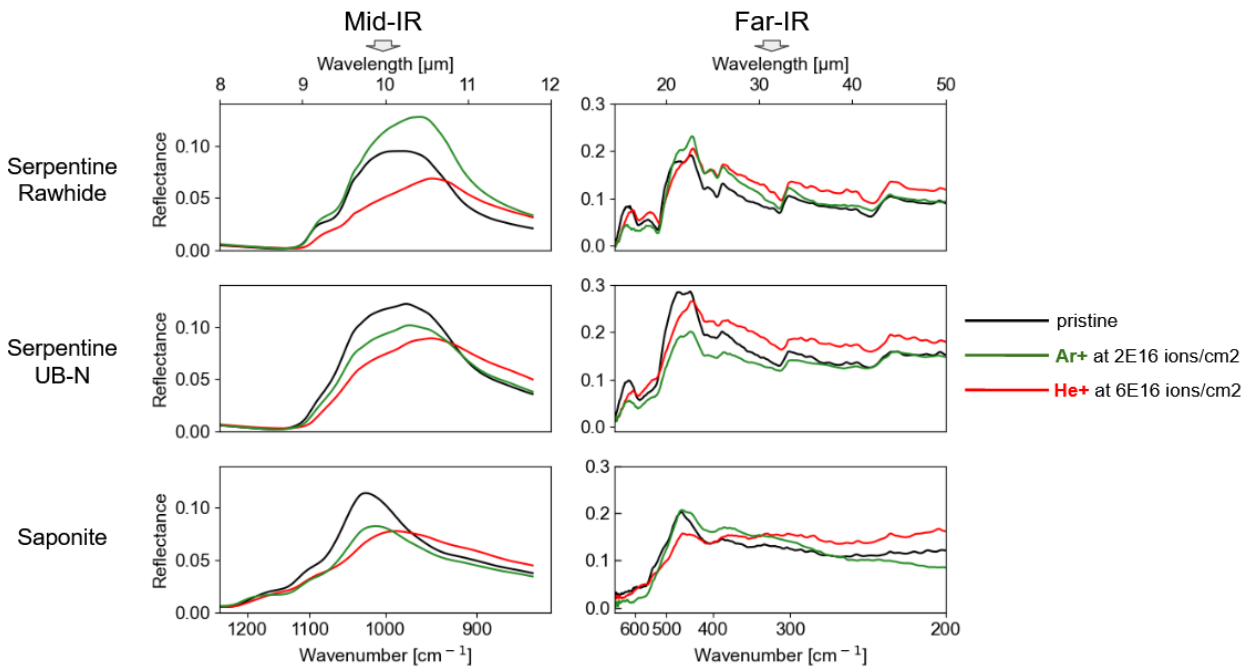

Figure A.2: Raw data in the mid- and far-IR range of the ion-bombarded phyllosilicate pellet studied in this work. For informations about the experimental setups used, see Chapter 2.

Making published data easily available to the scientific community grants interesting ways to collaborate and better compare studies across researchers and research domains. The entirity of the spectroscopic data which has been presented here can be found at the Solid Spectroscopy Hosting Architecture of Databases and Expertise (SSHADE) archive in the Database for AstrochemistrY and SpectroscopY at IAS-Orsay (DAYSY) sub-archive. The spectra available in the archive have had very little to none post-processing (no contrinuum-removal, for instance).

The visible and near-IR data acquired in-situ with the INGMAR setup can be found at the following links : serpentine Rawhide, serpentine UB-N and saponite. For the Ar^+ case, all spectra can be found here. The near-IR data associated to the bidirectional reflectance measurements acquired with the SHADOWS instrument can be found here. The mid- and far-IR data are currently being added to the database.

APPENDIX

Publications during Ph.D. years

In the following pages, the reader can find three publications related to my work done during the Ph.D years, for which I am first author: the first one deals with the effects of SpWe on the hydration feature of pure phyllosilicate pellets, the second one explores the geometry dependency of remote-sensing data on solar wind ion-bombarded surface analogs and the third one showcases the analytical pipeline used to measure Ryugu particles at IAS. Two other articles, for which I was heavily involved regarding data acquisition and data processing, are also presented here: the first one deals with the analysis of CM2 chondrite Aguas Zarcas (first author : Zélia Dionnet) and the second one showcases an example of preparation sequence for multi-analysis of µm-sized extraterrestrial samples (first auhtor: Alice Aléon-Toppani).

The Planetary Science Journal, 1:61 (7pp), 2020 December https://doi.org/10.3847/PSJ/abb94c

Space Weathering Affects the Remote Near-IR Identification of Phyllosilicates

Stefano Rubino[1], Cateline Lantz[1], Donia Baklouti[1], Hugues Leroux[2], Ferenc Borondics[3], and Rosario Brunetto[1]
[1] Institut d'Astrophysique Spatiale, Université Paris-Saclay, CNRS, F-91405, Orsay, France; stefano.rubino@ias.u-psud.fr
[2] Univ. Lille, CNRS, INRAE, ENSCL, Centrale Lille, UMR 8207—Unité Matériaux et Transformations, F-59000 Lille, France
[3] SMIS Beamline, SOLEIL Synchrotron, BP48, L'Orme des Merisiers, F-91192 Gif sur Yvette Cedex, France
Received 2020 June 1; revised 2020 September 2; accepted 2020 September 15; published 2020 November 6

Abstract

Near-infrared (NIR) spectrometers on board current sample return missions Hayabusa2 and the Origins-Spectral Interpretation-Resource Identification-Security-Regolith Explorer (OSIRIS-REx) from primitive bodies detected the presence of hydrated silicates on the surface of asteroids Ryugu and Bennu, respectively. These detections relied upon the study of the 2.7 μm OH-stretching spectral feature, whose peak position is related to the composition and structure of minerals. However, space weathering might alter the band profile, depth and position, thus complicating the interpretation of remote sensing data. In order to better understand these processes and provide support to space missions, we performed ion bombardment experiments on serpentine and saponite analogs. These two phyllosilicates are among the dominant mineral phases found in hydrated carbonaceous chondrites, which are possible analogs to surface materials observed on these primitive asteroids. We studied the behavior of the 2.7 μm band as a function of ion fluence and found that the evolution of the phyllosilicate depends on its nature. For the saponite sample, the band is only slightly affected by ion bombardment, while for both serpentine samples it shifts toward longer wavelengths. For both samples, peak intensity and width is not strongly affected. The band shift for serpentine indicates that space weathering introduces a bias in the interpretation of NIR remote sensing observations of phyllosilicates. The shift observed in our experiments can be detected by instruments on board Hayabusa2 and OSIRIS-REx, depending on the geometry of observation. Our findings provide support to the interpretation of such data.

Unified Astronomy Thesaurus concepts: Space weather (2037); Spectroscopy (1558); Near infrared astronomy (1093); Infrared astronomy (786); Laboratory astrophysics (2004); Small solar system bodies (1469); Surface composition (2115); Surface processes (2116)

1. Introduction

The study of hydrated silicates in small bodies, as tracers of aqueous alteration, is of utmost importance for understanding the evolution of primitive materials in the early solar system. Two sample return missions have been launched to study asteroids expected to have undergone aqueous alteration: the Hayabusa2 mission Japan Aerospace Exploration Agency (JAXA) targeting C-type asteroid 162173 Ryugu (Watanabe et al. 2017) and the Origins-Spectral Interpretation-Resource Identification-Security-Regolith Explorer (OSIRIS-REx) mission (NASA) targeting B-type asteroid 101955 Bennu (Lauretta et al. 2017). The detection of hydration on the asteroids' surfaces can be achieved by remote sensing in the near-infrared (NIR) spectral range, using the 2.7 μm band of phyllosilicates. This feature is attributed to the stretching vibration of hydroxyl groups (O-H) covalently bonded to metallic atoms (M) of octahedral MO6 sites. Its position and shape are sensitive to the mineral's composition and structure (Madejová et al. 2017). In particular, the peak position has been well studied in terrestrial phyllosilicates as a function of the Mg/Fe ratio, with wavelengths shorter for Mg-rich than for Fe-rich compositions (Farmer 1974; Besson & Drits 1997; Bishop et al. 2008). The 2.7 μm band has been measured in aqueously altered carbonaceous chondrites (Zolensky & McSween 1988; Miyamoto & Zolensky 1994), and also detected on asteroids despite telluric absorption (Lebofsky 1978; Rivkin et al. 2002). More recently, this feature has been observed by the Dawn mission on the dwarf planet Ceres (de Sanctis et al. 2015) and by Hayabusa2 and OSIRIS-REx on Ryugu and Bennu (Hamilton et al. 2019; Kitazato et al. 2019).

Atmosphere-less bodies in our solar system are known to be affected by space weathering (SpWe). This phenomenon includes multiple processes, such as micrometeorite bombardment, high-energy cosmic and solar ion bombardment, and low-energy solar wind bombardment (Beth Ellen Clark et al. 2002; Brunetto et al. 2015). Understanding the relative rates of all SpWe processes and their optical effects has been challenging for quite awhile (Clark et al. 2002). The spectroscopic and microscopic studies of the Hayabusa mission (JAXA) showed that solar wind should be the main source of surface weathering in the inner solar system (Noguchi et al. 2014). At this short distance from the Sun, solar wind is the main source of rapid (10^4–10^6 yr) weathering, while the effects caused by micrometeorite bombardment act on a longer timescale (10^8 yr; Brunetto et al. 2015). Heating processes are also known to affect the surface properties of asteroids. Marchi et al. (2009) discussed how episodes of strong solar heating could have partly removed volatiles components from near-Earth orbits (NEOs) asteroids surfaces. Regarding primitive NEOs in particular, like C-type asteroids, the effects on the hydration features are expected to be more severe. However, Marchi et al. also point out that data collected until now is not unambiguous enough to explain the difference of the NEOs hydration features solely on solar heating. Thermal fatigue caused by solar heating can also affect the surface properties of asteroids, governing regolith generation on small asteroids, thus contributing to the surface rejuvenation processes (Delbo et al. 2014). Overall, SpWe induces variations of the spectral properties of surface materials, including spectral reddening/blueing in the visible (Vis)–NIR range (Clark et al. 2001; Binzel et al. 2001; Hiroi et al. 2006; Lantz et al. 2013).

SpWe can be replicated on Earth through the use of ion irradiation and/or laser pulse experiments. Previous studies on carbonaceous chondrites (CCs) reported variations of IR bands upon ion bombardment, in both the NIR and MIR ranges (Vernazza et al. 2013; Lantz et al. 2015). In particular, in the experiment carried out by Lantz et al. (2017), the 2.7 μm band of CCs had been observed to change in shape as well as shift in position toward longer wavelengths after ion bombardment. However, Lantz et al. (2017) used spectral measurements acquired at atmospheric pressure. Thus, the presence of atmospheric water adsorbed on the surface of the studied samples might have affected the band shape above 2.8 μm, and its potential contribution to the reported global change cannot be excluded. In this paper we report new experimental results of ion bombardment on terrestrial phyllosilicates as a simulation of SpWe of atmosphere-less bodies rich in hydrated silicates. These experiments were performed in a vacuum chamber to simulate space conditions. We monitored the 2.7 μm feature before and after ion bombardment.

Table 1
Composition of the Samples Used in This Study

	Serpentine UB-N SARM[a]	Serpentine UB-N	Serpentine Rawhide	Saponite
SiO_2	45.25 ± 0.18	45.46 ± 0.33	45.81 ± 0.32	48.98 ± 0.31
Al_2O_3	3.33 ± 0.09	3.32 ± 0.17	0.89 ± 0.10	14.77 ± 0.17
MgO	40.41 ± 0.22	40.59 ± 0.40	45.78 ± 0.19	9.90 ± 0.15
FeO−Fe_2O_3	9.22 ± 0.35	9.26 ± 0.25	6.66 ± 0.25	13.84 ± 0.24
CaO	1.37 ± 0.04	1.36 ± 0.10	nd	7.08 ± 0.13
TiO_2	0.13 ± 0.01	nd	nd	0.84 ± 0.09
Cr_2O_3	nd	nd	0.86 ± 0.15	nd
MnO	0.12 ± 0.01	nd	nd	0.37 ± 0.12
Na_2O	0.11 ± 0.04	nd	nd	3.95 ± 0.10
K_2O	0.02 ± 0.01	nd	nd	0.25 ± 0.04

Note. Compositions were obtained by the Scanning Electron Microscope–Energy-Dispersive X-ray Spectroscopy (SEM–EDX) measurements performed at the UMET lab, University of Lille.
[a] The first column is the composition of the serpentine UB-N provided by the SARM. Uncertainties are given at 1σ. nd = not detected.

2. Samples and Methods

2.1. Sample Description and Preparation

The irradiation experiments were performed on serpentines and saponite. These minerals correspond to the major hydrated silicate phases found in CI- and CM-type chondrites (Brearley 2006; King et al. 2015) and may probably dominate at the surface of Ryugu and Bennu (Hamilton et al. 2019; Kitazato et al. 2019). The saponite sample is a griffithite (Fe-rich saponite), coming from Griffith Park in California. Two serpentine samples were used, labeled serpentine Rawhide and serpentine UB-N. Serpentine Rawhide is mostly antigorite with chrysotile veins and comes from the Rawhide mines in California. Serpentine UB-N comes from the Col des Bagenelles in France, structurally dominated by lizardite (Gayk & Kleinschrodt 2000). Chemical compositions of the samples were measured by energy dispersive X-ray spectroscopy (EDX; at 15 keV) on a scanning electron microscopy (SEM). The structural formulae were found as following: $Na_{0.5}Ca_{0.5}Mg_{1.0}Fe_{0.7}Al_{1.1}Si_{3.3}O_{10}(OH)_2$ for saponite, $Mg_{2.8}Fe_{0.2}Al_{0.04}Si_{1.9}O_5(OH)_4$ for serpentine Rawhide, and $Ca_{0.05}Mg_{2.6}Fe_{0.4}Al_{0.1}Si_{1.8}O_5(OH)_4$ for serpentine UB-N. We summarize elemental composition information of our samples in Table 1. The two serpentine samples differ in their atomic ratio Fe/(Fe+Mg) content. The ratio is equal to 0.07 for serpentine Rawhide and to 0.13 for serpentine UB-N.

The sample preparation method and the experimental protocol were similar to previous ion bombardment studies, which were focused on carbonaceous chondrites (Brunetto et al. 2014; Lantz et al. 2015, 2017). The samples were crushed using an agate mortar. Since terrestrial rocks were used, the resulting powders cannot be considered perfectly pure. A low fraction of terrestrial organics together with some minor mineral phases are expected to be present (such as clinochlore in the saponite/griffithite and calcite in the serpentine UB-N). However, these impurities should not interfere with the 2.7 μm phyllosilicate feature. Although grain size was not constrained during the crushing process, the size range of each powdered sample was estimated using an SEM (at Unité Matériaux et Transformation, Université de Lille (UMET), France). The grain size of the powders is found in the range 1–100 μm for all samples. For each mineral sample, two pellets of 20 mm in diameter were prepared by pressing ∼240 mg of powdered sample onto a PEG substrate (powdered polyethylene glycol with an average molecular mass of 8000 g/mol, from Fisher Scientific) for a duration of 5 minutes, under a weight of 7 tons. The phyllosilicate layer is thick enough (>500 μm) to avoid any ion (see the Stopping and Range of Ions in Matter (SRIM) results in Section 2.2) or photon (typically probing a layer of 2 μm in the 2–3 μm wavelength region for serpentines; see Brunetto et al. 2020) from interacting with the PEG substrate. Out of the six pellets, three underwent ion bombardment, while the remaining pellets were preserved as control samples, in case we needed more data regarding the "non-bombarded" state of our samples and to check for potential contamination/evolution over time.

2.2. Experimental Setup

We performed ion bombardment at room temperature in the IrradiatioN de Glaces et Météorites Analysées par Réflectance (IMGMAR, Vis–Institut d'Astrophysique Spatiale (IAS)–Centre de Sciences Nucléaires et de Sciences de la Matière (CSNSM), Orsay) vacuum chamber ($P \sim 10^{-7}$ mBar) interfaced to the SIDONIE implanter (CSNSM, Orsay) using He^+ at

40 keV and ion fluences of 1×10^{16}, 3×10^{16}, and 6×10^{16} ions cm^{-2}. The ion flux was of $\sim 10^{13}$ions/($s\,cm^2$). The ion fluence was derived by a direct measurement of the ion current, thanks to a brass ring placed before the entrance of the vacuum chamber (Urso et al. 2020). The implantation depth in our samples was estimated by the SRIM code (Ziegler et al. 2010; see Brunetto et al. 2014 for details) to be of 360 ± 110 nm for the saponite and 310 ± 90 nm for the two serpentine samples. SRIM simulation results were obtained using composition results from our SEM–EDX measurements and densities from Skinner (1963) and Roberts et al. (1990).

The applicability of He^+ irradiation at 40 keV as a simulation of solar ion irradiation and its limitations are discussed by Brunetto et al. (2014) and Lantz et al. (2017). We summarize here the main points for the sake of clarity. Due to obvious limitations in time and resources, it is almost impossible to reproduce in the laboratory all the range of ion mass and energies affecting asteroid surfaces, so each study typically focuses on one particular component. Following previous studies (Brunetto et al. 2014; Lantz et al. 2015), we chose He+ in order to simulate an important fraction of the ions in the solar wind. The particles emitted with the slow solar wind have energies ∼1 keV/u and their flux decreases with the square of distance from the Sun. Hydrogen is the main component (∼95%, average energy ∼1 keV), and helium is the second most abundant species (∼4.6%) with an average energy of ∼4 keV. While the energy of 40 keV is close to the average energy for heavier ions present in the slow solar wind (such as Ar^+), it is also about 10 times higher than the average energy for He. However, higher-energy helium ions are also emitted from the Sun through active regions and solar flares. Their contribution to SpWe effects on airless bodies should not be neglected. For instance, Matsumoto et al. (2015) proposed that high-energy He^+ ions might have played a role in the formation of a thick space-weathered layer detected on an Itokawa particle. Using the energy spectra of ions from active regions and solar flares (e.g., Johnson 1990), Brunetto et al. (2014) estimated that the weathering timescales of asteroids by 40 keV He+ are about 10 times longer than 4 keV He+. Of course, many more ion species and energies are involved in the weathering processes, so the 40 keV He+ irradiations studied here are certainly not an exhaustive reproduction of asteroid SpWe.

The whole surface of each pellet was subjected to ion bombardment, with the exception of a small external corona (∼500 μm in width), which is an area masked by the sample holder used to mount the samples vertically in the vacuum chamber. We acquired reflectance spectroscopy measurements in the NIR (0.96–4 μm) before and after each bombardment step, directly in the vacuum chamber. We used a Fourier Transform InfraRed spectrometer (Tensor37, Bruker) and a Vis–NIR optic fiber to collect light from the sample with an angle $e = 15°$, while the illumination angle was $i = 20°$ and the phase angle was 15° (because the incident and emission angles and the surface normal are not in the same plane; see Lantz et al. 2017). The illumination spot was about 12 mm in diameter while the collection spot size is ∼4 mm.

To calibrate the absolute reflectance of our measurements, we acquired reference spectra in the vacuum chamber using a Spectralon standard (99% Lambertian reflectance, Labsphere). An additional reference measurement was performed on InfraGold (Labsphere), which allowed the correction of minor NIR features present in the Spectralon spectrum. The spectral resolution was 16 cm^{-1}, the spectral sampling was 8 cm^{-1}, and we accumulated 4096 scans per spectrum.

In addition to the vacuum spectra (referred to as in situ), we performed measurements under ambient conditions (ex situ) using two different setups. We acquired spectra on virgin pellets (the control samples) and on the ion bombarded ones with the highest fluence. They are reported in the Appendix. The Fourier transform infrared spectroscopy (FTIR) measurements reported in Figure A1 (right) were acquired with an Agilent Cary 670/620 microspectrometer installed at the SMIS beamline of the SOLEIL synchrotron (France). IR spectra were measured using the internal Globar source, with respect to gold references. More details can be found in Brunetto et al. (2018). The FTIR spectra shown in Figure A1 (left) were acquired with a PerkinElmer point spectrometer, installed at the Institut d'Astrophysique Spatiale (France). An internal Globar source was used, with respect to both the Spectralon and the InfraGold standard cited above. It is relevant to point out that the ex situ setups described above have different optical geometries: the Agilent microspectrometer uses an IR microscope (15x objective, N.A. = 0.62), while the PerkinElmer measures biconical reflectance.

3. Results

All spectra acquired before ion bombardment showed the 2.7 μm feature. We were able to distinguish certain differences in band shape and peak position among our samples due to their different composition and crystal structure (Figure 1).

The peak position of the 2.7 μm feature was estimated by applying different instances of a Savitzky–Golay filter to our spectra, then by determining the region of interest centered on our feature, computing the barycenter associated to this region of interest (ROI) (to account for the asymmetry of the spectral feature), and averaging the peak position of each Savitzky–Golay instance. The position of the feature computed on raw data (without denoising) was also included for the computation of the average position. The wavelength obtained by this algorithm was assimilated to the feature's position. This method allowed us to extract the following band positions: 2746 ± 3 nm for the saponite, 2719 ± 5 nm for the serpentine UB-N, and 2711 ± 3 nm for the serpentine Rawhide. The peak position for the two serpentines is coherent with their composition: the feature of the serpentine Rawhide (slightly Mg-richer) is located at shorter wavelength compared to serpentine UB-N. All values are coherent with the peak position associated with the hydroxyl stretching of hydrated silicates in the reference spectra found in the literature for each sample (Rodriguez 1994 for the saponite; Bishop et al. 2008; Takir et al. 2013 for the serpentines).

It is important to address that the MO-H stretching band can incorporate multiple contributions depending on the complexity of the phyllosilicate sample. For instance, in saponite, interlayer H_2O molecules are expected to contribute to the general shape of the feature. This can be seen in our in situ spectra (Figure 1), where the general shape of the virgin saponite spectrum around 3–3.3 μm is deeper than for both virgin serpentines. Additionally, spectra acquired ex situ with the PerkinElmer point spectrometer and with the Agilent microscope (Figure A1) show the contribution of adsorbed atmospheric water at the surface of our samples; contribution that we were able to minimize in our in situ measurements on INGMAR since the samples were left in the vacuum chamber at $P \sim 10^{-7} mBar$ for 8 hours before ion bombardment and remained there for the whole duration of the experiment.

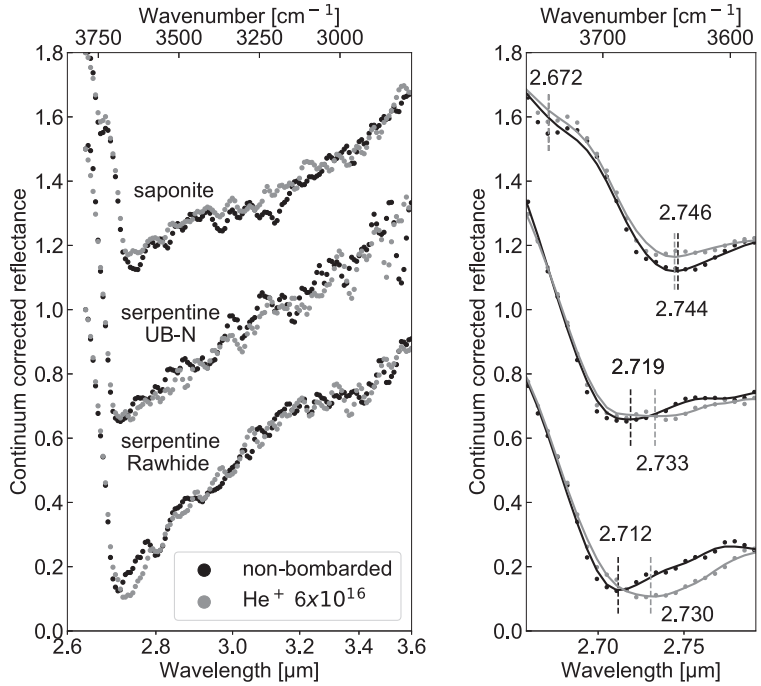

Figure 1. In situ evolution of the 2.7 μm feature before (non-bombarded; black dots) and after maximum ion fluence (6×10^{16}ions/cm^2; gray dots). Spectra were shifted for clarity. A linear continuum correction from 2.64 μm to 4 μm was applied. Solid lines represent the Savitzky–Golay filter used for denoising the spectra. For plotting, the linear scale is used with respect to wavenumbers. The right panel is a zoomed in on the region of the 2.7 μm bands.

After exposure to the maximum fluence (6×10^{16}ions/cm^2), the feature's position for the serpentines changes as follows: 2733 ± 4 nm for the serpentine UB-N and 2730 ± 4 nm for the serpentine Rawhide. The newly measured position for the saponite feature is 2744 ± 5 nm, which hints that the peak's position for the saponite does not change after bombardment within our error bars. The saponite sample also displays a small peak around 2672 nm (best visible in the zoomed-in panel of Figure 1), which originated from the Si-OH vibration mode (Trombetta et al. 2000). Ion bombardment does not affect its position. Finally, we notice that the band depth for both serpentines does not change within our error bars, while the saponite feature's depth decreases (−7 ± 2%) and broadens slightly. Overall, ion bombardment processes do not seem to significantly alter the intensity and shape of the 2.7 μm feature in phyllosilicates, and its effects can mostly be found in the evolution of the feature's position.

The evolution of the phyllosilicate band position as a function of ion fluence is reported in Figure 2. Serpentine Rawhide shows clear evidence of a MO-H band position gradual shift toward longer wavelengths with increasing bombardment fluence (small error bars due to the narrow shape of the feature). At the end of the experiment, the measured shift was 19 ± 3 nm for serpentine Rawhide and 14 ± 3 nm for serpentine UB-N. The evolution with increasing fluence amount for the serpentine UB-N and the saponite is more difficult to assert due to the broader shape of the feature for these samples, which affects the error associated with the computed position. Nonetheless, two different behaviors emerge clearly: the MO-H feature for both serpentines shifts toward longer wavelengths, while the peak position of the saponite does not change within our error bars, except for the measurement acquired in medium ion fluence (3×10^{16}ions/cm^2), which was a particularly noisy acquisition compared to all other experiments.

The effects upon ion bombardment have been also measured ex situ, for samples irradiated at 6×10^{16}ions/cm^2 with two other instruments (see Section 2). The spectral shifts, measured ex and in situ, are compared in Figure 3.

The ex situ spectral shifts are different from the ones measured in situ (INGMAR). We interpret these differences as an effect of the different optical geometries for the three measurements (see Section 4). Nonetheless, these ex situ results are coherent with the two tendencies identified in the in situ spectra, since in both serpentines, a spectral shift can be identified, contrary to the saponite sample.

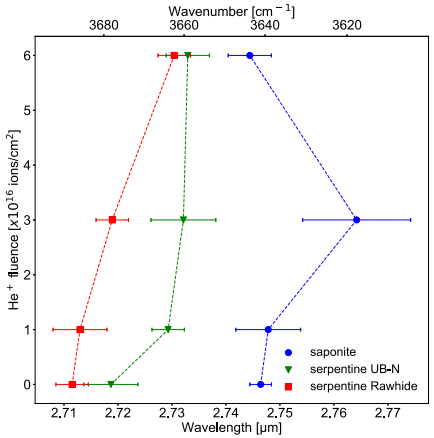

Figure 2. In situ evolution of the 2.7 μm feature peak position of the studied phyllosilicates upon irradiation. Saponite is in blue circles, serpentine UB-N is in green triangles, and serpentine Rawhide is in red squares. The irradiation fluence 0 refers to the samples before ion bombardment.

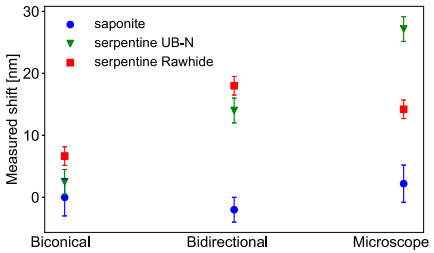

Figure 3. Comparing the bombardment-induced spectral shift of the MO-H feature measured with different optical geometries (associated to different instruments): biconical reflection (PerkinElmer point spectrometer), bidirectional reflection (INGMAR setup), and microscope reflection (Agilent IR microscope). Same color/symbol code as in Figure 2.

4. Discussion

Contrary to other IR bands of phyllosilicates that are coupled to other vibrations of the structure, the O-H stretching band is completely separated and is only affected by the immediate vicinity of the hydroxyl group (Farmer 1974). The samples we chose for this study belong to two different classes of phyllosilicates that correspond to two distinct types of crystal structure. In the saponite subgroup the octahedral layer containing metals bonded to hydroxyl groups (O-H) is covalently bonded to the oxygens of the tetrahedral Si-O layers that are both above and below it. The different layers are arranged to form a tetrahedral-octahedral-tetrahedral (TOT) unit separated from the following by an interlayer of water molecules (and possibly cations; Mitra et al. 2013). That way, each TOT unit almost behaves as a separate entity, the lattice stress induced by He^+ bombardment is relaxed at the scale of the TOT unit, and the immediate environment of each hydroxyl group cannot be disturbed easily. In serpentines, the octahedral layer containing metals bonded to O-H is covalently bonded to a single Si-O layer, creating an TO structure, while hydrogen bindings provide cohesion with the Si-O layer of the adjacent TO layer (Auzende 2003). No water interlayer separates each TO layer. Any stress on the TO layer or the adjacent one will affect the hydrogen bindings and will disturb the crystal lattice of the serpentine (similarly to what observed by Leroux et al. 2019 in olivines), affecting the immediate environment of the MO-H groups, which in turn, will impact the position of the 2.7 μm band. This crystal structure difference may explain why the 2.7 μm band position of the serpentine samples is more affected than the saponite sample in our experiments. Compositional-related processes, such as local variations of the Fe/(Mg+Fe) ratio, preferential amorphization of Mg-rich phyllosilicates, or preferential sputtering of Mg (Hapke et al. 1975), could also affect the position of the feature upon bombardment. Scanning electron microscopy (SEM) and transmission electron microscopy (TEM) measurements will be performed in a forthcoming study on all our samples to investigate the effects of ion bombardment at a nanometric scale.

Ion bombardment does not seem to greatly affect the shape or intensity of the 2.7 μm feature. In our case, both serpentines' hydration peaks retained the same shape and intensity, despite the spectral shift. For the saponite sample, a slight decrease in intensity ($-7 \pm 2\%$) as well as a light broadening of the feature seems to occur. No particular tendency regarding the intensity or shape emerges in the in situ measurements at intermediate fluences, but the in situ changes between non-bombarded samples and samples bombarded at maximum fluence are consistent with the changes observed in the ex situ spectra (Figure A1). In particular, the measurements acquired with biconical reflectance (PerkinElmer point spectrometer, as seen in left panel in Figure A1) clearly show the decrease in intensity for the saponite sample, while no changes can be observed for the serpentine samples.

We measured the shift after ion bombardment with three instruments, each with a different optical geometry (Figure 3). The PerkinElmer point spectrometer measures biconical reflectance, and an off-axis mount greatly decreases the contribution of specular reflectance in the associated measurements. The INGMAR setup measures bidirectional reflectance (with a phase angle of $\varphi = 15°$), similarly to how the OVIRS (OSIRIS-REx Visible and InfraRed Spectrometer) and NIRS3 (Near Infrared Spectrometer) instruments operate on board OSIRIS-REx and Hayabusa2. Finally, the Agilent spectrometer is interfaced with an IR microscope. We notice that there is a sort of "inversion" between the two serpentines when comparing the measured shifts with the INGMAR setup and the Agilent microscope. Overall, the effect of spectral band shift is more easily detected at certain geometries probably because photons penetrate less and thus better probe the upper irradiated layers. Indeed, previous studies have shown that as the phase angle increases, the mean path of photons probing the sample surface also increases (Adams & Filice 1967), which hints that the contribution of volume scattering with respect to surface scattering gets more important. In the case of remote sensing of asteroid surfaces, this implies that the spectral shift would be more easily detected in observations performed at small phase angles. This scenario can be verified in data collected by Hayabusa2 and OSIRIS-REx, when a given terrain is observed at different geometries during the mission.

In this new study, the in situ spectra were acquired in a vacuum chamber. This, and the fact that our detection relies on bidirectional reflection, allowed us to acquire measurements in conditions comparable to the remote sensing measurements acquired by Hayabusa2 and OSIRIS-REx orbiting Ryugu and Bennu respectively. Thus our spectra may provide support to the interpretation of remote sensing data of these two missions. Our results imply that SpWe may induce a bias in the interpretation of NIR remote sensing observations of phyllosilicates on planetary surfaces. The 2.7 μm feature is generally used as a remote sensing proxy to determine the Mg-to-Fe ratio of phyllosilicates (Sabins 1999; Bishop et al. 2008). Since ion bombardment induces for certain minerals a shift of the 2.70–2.72 μm feature toward longer wavelengths, the estimation of the composition of hydrated minerals will be biased on space-weathered surfaces.

The maximum spectral shift observed in our measurements in the vacuum chamber is 19 ± 3 nm for the serpentine Rawhide (Mg-rich serpentine), which is a value that can be detected in the data acquired by the NIRS3/Hayabusa2 (spectral sampling of $\sim$18 nm; Iwata et al. 2017) and the OVIRS/OSIRIS-REx (spectral sampling of $\sim$10 nm; Christensen et al. 2018) instruments. The phyllosilicate peak position observed on Ryugu and Bennu is about 2.72 μm and 2.74 μm, respectively, and its position is quite homogeneous all across the asteroids' surface (Kitazato et al. 2019; Hamilton et al. 2020). The peak positions of the two asteroids are compatible both with irradiated or unirradiated phyllosilicates of different composition, and it is not possible to discriminate the two scenarios based on the average peak position only. However, our laboratory results definitely support the idea that, if solar wind is the dominant SpWe process for young ($<10^7$ years) surfaces in the inner solar system, as suggested by many authors (e.g., Vernazza et al. 2009; Noguchi et al. 2014; Bonal et al. 2015), the least altered terrains on Ryugu and Bennu may be characterized by positions of the 2.7 μm feature peaking at shorter wavelengths than the oldest (more altered) terrains (Lantz et al. 2017). The Small Carry-on Impactor (SCI) crater experiment on board Hayabusa2 (Arakawa et al. 2020) has provided an excellent test of this hypothesis (Kitazato et al. 2020), as it has produced a fresh crater at the surface of Ryugu. In the case of older surfaces ($>10^8$ years), the effect of solar wind irradiation would tend to saturate, and spectral differences among different terrains would be limited, while other competitive processes such as micrometeorite bombardments or heating processes would contribute significantly.

5. Conclusions

The laboratory reproduction of solar wind irradiation provides the community with relevant data for the interpretation of SpWe effects on the surface of primitive asteroids. The irradiation-induced changes of the 2.7–2.8 μm phyllosilicate feature depend on the phyllosilicate nature. Serpentines have their 2.7 μm feature modified by ion irradiation, both in the profile and peak position, whereas saponite bands do not significantly change position after irradiation and only show a limited reduction of the band intensity. Our experiments suggest that SpWe may induce a bias in the spectral interpretation of NIR remote sensing observations of asteroids, which is an effect that is within the reach of detection by both Hayabusa2 and OSIRIS-REx at their respective targets. We anticipate this bias to be stronger for observations performed at smaller phase angles.

The serpentine UB-N sample was provided by the Service d'Analyse des Roches et des Minéraux (SARM) in Nancy, France. We thank J. Carter for providing us with the serpentine Rawhide and the saponite samples, which were purchased from Minerals Unlimited in Ridgecrest, California. We thank two anonymous reviewers for their useful remarks and suggestions. We are grateful to K. Kitazato, T. Nakamura, A. Aléon-Toppani, Z. Djouadi, Y. Arribard, and R. Urso for helpful and useful discussions. We thank O. Mivumbi, D. Ledu, C.O. Bacri, and P. Benoit-Lamaitrie for help and technical support with SIDONIE and INGMAR. INGMAR is a joint IAS-CSNSM (Orsay, France) facility funded by the P2IO LabEx (ANR-10-LABX-0038) in the framework Investissements d'Avenir (ANR-11-IDEX-0003-01). The ex situ microspectroscopy measurements were supported by grants from Region Ile-de-France (DIM-ACAV) and SOLEIL. This work has been funded by the Centre National d'Etudes Spatiales (CNES-France) and by the ANR project CLASSY (Grant ANR-17-CE31-0004-02) of the French Agence Nationale de la Recherche.

Appendix

In addition to the in situ INGMAR measurements, we acquired additional ex situ measurements with two other instruments (spectra are shown in Figure A1): a PerkinElmer point spectrometer (left) and an Agilent microspectrometer (right). Both data sets were acquired with a Globar source, with a spectral resolution of 4 cm^{-1}. Differences in the shape of the 2.7 μm feature compared to the INGMAR measurements are due to the influence of the different optical geometries, which characterize each instrument, and the different contributions of adsorbed water.

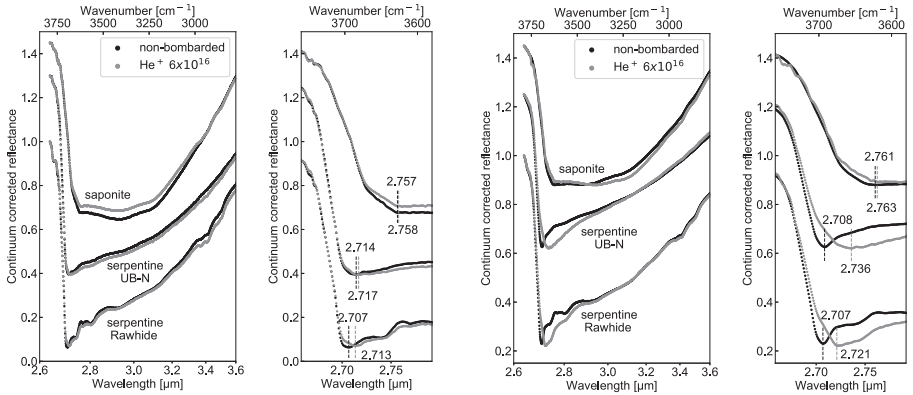

Figure A1. Ex situ evolution of the 2.7 μm feature before (virgin; black dots) and after maximum ion fluence (gray). Spectra were acquired at ambient pressure with two different setups: the PerkinElmer point spectrometer (left) and the Agilent IR microscope (right). For plotting, a linear scale is used with respect to wavenumbers. A linear continuum correction from 2.64 μm to 4 μm was applied. Right panels for each pair are zoomed in around the center of the bands plotted in the left panel.

ORCID iDs

Stefano Rubino https://orcid.org/0000-0003-3198-1123
Cateline Lantz https://orcid.org/0000-0003-0974-4770
Donia Baklouti https://orcid.org/0000-0002-2754-7829
Hugues Leroux https://orcid.org/0000-0002-8806-8434
Rosario Brunetto https://orcid.org/0000-0003-3001-9362

References

Adams, J. B., & Filice, A. L. 1967, JGR, 72, 5705
Arakawa, M., Saiki, T., Wada, K., et al. 2020, Sci, 368, 67
Auzende, A.-L. 2003, PhD thesis, Laboratoire Magmas et Volcans, https://hal.univ-grenoble-alpes.fr/LMV/tel-00825144
Besson, G., & Drits, V. A. 1997, CCM, 45, 158
Binzel, R. P., Rivkin, A. S., & Bus, S. J. 2001, M&PS, 36, 36
Bishop, J. L., Lane, M. D., Dyar, M. D., & Brown, A. J. 2008, ClMin, 43, 35
Bonal, L., Brunetto, R., Beck, P., et al. 2015, M&PS, 50, 1562
Brearley, A. J. 2006, in Meteorites and the Early Solar System II, ed. D. S. Lauretta & H. Y. McSween, Jr. (Tucson, AZ: Univ. Arizona Press), 585
Brunetto, R., Lantz, C., Dionnet, Z., et al. 2018, P&SS, 158, 38
Brunetto, R., Lantz, C., Ledu, D., et al. 2014, Icar, 237, 278
Brunetto, R., Lantz, C., Nakamura, T., et al. 2020, Icar, 345, 113722
Brunetto, R., Loeffler, M. J., Nesvorný, D., Sasaki, S., & Strazzulla, G. 2015, in Asteroids IV, ed. P. Michel, F. E. DeMeo, & W. F. Bottke (Tucson, AZ: Univ. Arizona Press), 597
Christensen, P. R., Hamilton, V. E., Mehall, G. L., et al. 2018, SSRv, 214, 87
Clark, B. E., Hapke, B., Pieters, C., & Britt, D. 2002, in Asteroids III, ed. W. F. Bottke, Jr. et al. (Tucson, AZ: Univ. Arizona Press), 585
Clark, B. E., Lucey, P., Helfenstein, P., et al. 2001, M&PS, 36, 1617
de Sanctis, M. C., Ammannito, E., Raponi, A., et al. 2015, Natur, 528, 241
Delbo, M., Guy, L., Justin, W., et al. 2014, Natur, 508, 233
Farmer, V. C. 1974, The Infrared Spectra of Minerals, Vol. 4 (London: Mineralogical Society of Great Britain and Ireland)
Gayk, T., & Kleinschrodt, R. 2000, JMetG, 18, 293
Hamilton, V. E., Simon, A. A., Christensen, P. R., et al. 2019, NatAs, 3, 332
Hamilton, V. E., Simon, A. A., Kaplan, H. H., et al. 2020, in 51st Lunar and Planetary Science Conf. (The Woodlands, TX), 1049
Hapke, B., Cassidy, W., & Wells, E. 1975, Moon, 13, 339
Hiroi, T., Masanao, A., Kohei, K., et al. 2006, Natur, 443, 56
Iwata, T., Kohei, K., Masanao, A., et al. 2017, SSRv, 208, 317
Johnson, R. E. 1990, in Energetic charged–Particle Interactions with Atmospheres and Surfaces, Physics and Chemistry in Space Planetology, Vol. 19, ed. L. J. Lanzerotti, M. Hill, & D. Stoffler Munster (Berlin: Springer), 232
King, A. J., Schofield, P. F., Howard, K. T., & Russell, S. S. 2015, GeCoA, 165, 148
Kitazato, K., Milliken, R. E., Iwata, T., et al. 2019, Sci, 364, 272
Kitazato, K., Milliken, R. E., Iwata, T., et al. 2020, NatAs, submitted
Lantz, C., Brunetto, R., Barucci, M. A., et al. 2015, A&A, 577, A41
Lantz, C., Brunetto, R., Barucci, M. A., et al. 2017, Icar, 285, 43
Lantz, C., Clark, B. E., Barucci, M. A., & Lauretta, D. S. 2013, A&AS, 554, A138
Lauretta, D. S., Balram-Knutson, S. S., Beshore, E., et al. 2017, SSRv, 212, 925
Lebofsky, L. A. 1978, MNRAS, 182, 17P
Madejová, J., Gates, W. P., & Petit, S. 2017, Developments in Clay Science, Vol. 8 (Amsterdam: Elsevier), 107
Marchi, S., Delbo, M., Morbidelli, A., Paolicchi, P., & Lazzarin, M. 2009, MNRAS, 400, 147
Matsumoto, T., Akira, T., Akira, M., et al. 2015, Icar, 257, 230
Mitra, S., Prabhudesai, S. A., Chakrabarty, D., et al. 2013, PhRvE, 87, 062317
Miyamoto, M., & Zolensky, M. E. 1994, Metic, 29, 849
Noguchi, T., Makoto, K., Takahito, H., et al. 2014, M&PS, 49, 188
Rivkin, A. S., Howell, E. S., Vilas, F., & Lebofsky, L. A. 2002, in Asteroids III, ed. W. F. Bottke, Jr. et al. (Tucson, AZ: Univ. Arizona Press), 235
Roberts, W. L., Thomas, J. C., George, R. R., et al. 1990, Encyclopedia of Minerals (New York: Van Nostrand Reinhold)
Rodriguez, M. A. V. 1994, CCM, 42, 724
Sabins, F. F. 1999, Ore Geology Reviews, 14, 157
Skinner, B. J. 1963, Sci, 139, 821
Takir, D., Joshua, P. E., Harry, Y. M., et al. 2013, M&PS, 48, 1618
Trombetta, M., Guido, B., Maurizio, L., et al. 2000, Applied Catalysis A: General, 193, 9
Urso, R. G., Donia, B., Zahia, D., Noemí, P.-A., & Rosario, B. 2020, ApJL, 894, L3
Vernazza, P., Binzel, R. P., Rossi, A., Fulchignoni, M., & Birlan, M. 2009, Natur, 458, 993
Vernazza, P., Fulvio, D., Brunetto, R., et al. 2013, Icar, 225, 517
Watanabe, S.-I., Yuichi, T., Makoto, Y., et al. 2017, SSRv, 208, 3
Ziegler, J. F., Ziegler, M. D., & Biersack, J. P. 2010, NIMPB, 268, 1818
Zolensky, M., & McSween, H. Y., Jr. 1988, In Meteorites and the Early Solar System, Vol. 14 (Tucson, AZ: Univ. Arizona Press), 114

Icarus 376 (2022) 114887

Contents lists available at ScienceDirect

Icarus

journal homepage: www.elsevier.com/locate/icarus

Geometry induced bias in the remote near-IR identification of phyllosilicates on space weathered bodies

Stefano Rubino [a,*], Sandra Potin [b], Cateline Lantz [a], Donia Baklouti [a], Pierre Beck [c], Olivier Brissaud [c], Hugues Leroux [d], Eric Quirico [c], Bernard Schmitt [c], Ferenc Borondics [e], Rosario Brunetto [a]

[a] Institut d'Astrophysique Spatiale, Université Paris-Saclay, CNRS, F-91405 Orsay, France
[b] Laboratoire d'Etudes Spatiales et d'Instrumentation en Astrophysique (LESIA), Observatoire de Paris, Université PSL, CNRS, Sorbonne Université, Université de Paris, 5 place Jules Janssen, 92195 Meudon, France
[c] Université Grenoble Alpes, CNRS, IPAG, 414 rue de la Piscine, 38400 Saint-Martin d'Hères, France
[d] Univ. Lille, CNRS, INRAE, Centrale Lille, UMR 8207—Unité Matériaux et Transformations, F-59000 Lille, France
[e] SMIS Beamline, SOLEIL Synchrotron, Gif sur Yvette Cedex, France

ARTICLE INFO

Keywords:
Space weather
Small solar system bodies
Spectroscopy
Near infrared astronomy
Laboratory astrophysics

ABSTRACT

Sample return missions Hayabusa2 (JAXA) and OSIRIS-REx (NASA) found evidence of hydrated silicates on the surface of C and B-type asteroids Ryugu and Bennu. This detection relied on the study of the 2.7 μm OH-stretching spectral feature revealed from remote sensing observations of the asteroids' surfaces. Laboratory studies simulating the effects of space weathering (SpWe) on primitive bodies have shown that the feature's position, considered as the wavelength of the band minimum, can vary under ion implantation, shifting towards longer wavelengths for implanted surfaces. Since SpWe is a surface process, we investigated how the geometry of observation can affect the hydration feature on space weathered surfaces. Here, we report new laboratory Reflectance Factors (REFF) measurements on pristine and ion-bombarded phyllosilicate pellets, to monitor the evolution of the 2.7 μm feature with varying observation geometry. We found that, as we approach specular reflection, the feature's position for He+ bombarded surfaces shifts towards longer wavelengths. We interpret that the spectral shift is due to chemical and physical changes induced by ion implantation in the first hundreds of nanometers of our phyllosilicate pellets. The diversity in the observed amplitude of the shift means that different competing effects are dominating at different optical configurations, mainly volume and surface scattering. The effects of the ion-implanted matter are especially visible when measuring in near-specular conditions, where the specular component (more sensible to the very top surface (implanted layer) of the sample)dominates - hence the larger shift measured. Our results indicate that the geometry of observation can induce a certain bias in the interpretation of remote sensing data from space-weathered bodies.

1. Introduction

A correct interpretation of the hydration features on small bodies is paramount in understanding the evolution of primitive materials in the early Solar System. It is particularly relevant in the context of the two sample-return missions Hayabusa2 (JAXA) and OSIRIS-REx (NASA), targeting the C-type asteroid (162173) Ryugu (Watanabe et al., 2017) and the B-type asteroid (101955) Bennu (Lauretta et al., 2017), respectively. Hayabusa2 successfully collected material from the surface of its target first in February 2019, then in July 2019, and brought back several grams of Ryugu grains to the Earth, on Dec. 62,020. OSIRIS-REx has also performed sample collection from its target's surface in October 2020, and the spacecraft is now in the next phase of the mission, Earth Return Cruise, starting in March 2021. Besides sample collection, both missions performed extensive spectroscopic surveys in both the visible and the near-IR of their target's surfaces, using the NIRS3 (Near Infrared Spectrometer, (Iwata et al., 2017) and OVIRS (OSIRIS-REx Visible and InfraRed Spectrometer, (Christensen et al., 2018) instruments, respectively. They detected a band at *2.72 μm* on Ryugu (Kitazato et al., 2019) and at *2.74 μm* on Bennu (Hamilton et al., 2019), associated with the stretching vibration of hydroxyl groups (-OH) covalently bonded to metallic atoms (M) in phyllosilicates. The position and the shape of this hydration feature can vary with mineral composition and structure (Madejová et al., 2017). The *2.7 μm* feature has been studied in carbonaceous chondrites (Takir et al., 2013), but it has also been detected on outer space bodies, such as the dwarf planet Ceres (De Sanctis et al., 2015) and some other low-albedo objects (such as C-class and related asteroids - (Jones et al., 1990; Usui et al., 2018; Rivkin et al., 2002). On Bennu, the feature appears to be deep and broad, similar in shape to laboratory spectra of some carbonaceous chondrites. However, Ryugu's feature is significantly weaker and narrower, indicating a different degree of surface hydration and/or a different thermal history (Kitazato et al., 2021). Hayabusa2 also conducted an impact experiment using the Small Carry-on Impactor (SCI). Results are described by (Arakawa et al., 2020) and the subsurface material NIRS3 observations are presented by (Kitazato et al., 2021). The excavated material exhibits a *2.7 μm* feature that appears stronger and slightly blueshifted in comparison to the one observed for the surface. Space weathering (SpWe) could explain these observations: SpWe affects atmosphere-less bodies in our solar system by multiple processes, such as micrometeorite bombardment, high-energy cosmic irradiation and solar wind bombardment, with both high and low energy ions (Clark et al., 2002; Brunetto et al., 2015). SpWe can alter the physical and chemical structure of surface materials on asteroidal bodies, inducing variations of their spectral properties (Clark et al., 2001; Ishiguro et al., 2007). Recent attempts to reproduce solar wind SpWe in the laboratory, both on carbonaceous chondrites (CCs) (Lantz et al., 2015, 2017; Brunetto et al., 2020) and on hydrated terrestrial silicates (Rubino et al., 2020), have shown that the *2.7 μm* feature in native hydrated silicates appears at shorter wavelengths than in ion-bombarded samples, similarly to the observation by NIRS3 on the SCI crater on Ryugu. However, recent studies have shown that the geometrical configuration of an observation can affect the shape of the hydration feature in carbonaceous chondrites (Potin et al., 2019). Remote sensing instruments onboard space missions often observe objects at different times and angles, in a way that the same area is measured at various geometries. Thus, it is important to investigate and understand how the geometry of the observation can affect the hydration feature on space weathered surfaces. To address this question, we report new experimental Reflectance Factor (REFF) measurements on pristine and ion-bombarded phyllosilicate pellets, aimed at monitoring the evolution of the *2.7 μm* feature with varying observation geometry.

2. Samples and methods

2.1. Samples description and preparation

The new REFF measurements were done on the phyllosilicate pellets used by Rubino et al. (2020), which underwent He^+ and Ar^+ ion bombardment at *40 keV*, at room temperature and $P \sim 10^{-7}$mBar, with an ion fluence of $6 \cdot 10^{16}$ ions/cm^2 for He^+ and $2 \cdot 10^{16}$ ions/cm^2 for Ar^+. The relevance and the limitations of He^+ and Ar^+ ion-bombardment at *40 keV* as a simulation of solar wind irradiation are presented in the paper preceding this work, Rubino et al. (2020), and further discussed by Brunetto et al. (2014) and Lantz et al. (2017).

The measurements presented in this work were performed on a serpentine sample. Serpentines are among the major hydrated silicates phases found in CI- and CM-type chondrites (King et al., 2015) and can be used as analogs for the surface of primitive hydrated bodies such as Ryugu and Bennu (Kitazato et al., 2019; Hamilton et al., 2019). Our serpentine was extracted from the Rawhide mines, in California. It will thus be referred to as Serpentine Rawhide. This sample is mostly antigorite with chrysotile veins, with a $Fe/(Fe + Mg)$ ratio equal to *0.07*.

The sample was crushed using an agate mortar. The grain size of the resulting powder was estimated by scanning electron microscopy (SEM), and was found in the range *1–100 μm*. Three pellets were made by pressing *~240 mg* of powdered sample onto a PEG substrate (powdered polyethylene glycol with an average molecular mass of *8000 g/mol*, from Fisher Scientific), for a duration of *5* min, using a *7*-tons press. We made three pellets, two of them underwent ion-bombardment, while the third/last pellet was preserved as a control sample. The pellets have a somewhat flat surface, which is expected to produce strong specular effects. Additional details about the samples and sample preparation can be found in Rubino et al., 2020.

It is relevant to note that meteorites are generally used as analogue materials for asteroidal surfaces. And in fact, ion-implantation experiments have already been conducted on meteorites (see Brunetto et al., 2014, Lantz et al., 2015–2017). However, meteorites can also be very heterogeneous materials, especially at the scale we are working here (mm to fractions of microns). This heterogeneity may introduce other effects in our measurements, which may not be well constrained. This may hinder the efforts in deriving a sort of "general behavior" of hydrated silicates under ion-bombardment, hence the choice in this work of focusing on pure (or almost pure) phyllosilicate phases.

2.2. Experimental setup

2.2.1. Reflectance factor (REFF)

We performed the REFF measurements with the SHADOWS (Spectrophotometer with cHanging Angles for the Detection Of Weak Signals) spectro-gonio radiometer at the Université of Grenoble Alpes (Potin et al., 2018). This instrument allows the aquisition of spectra in the visible and near infrared range (*350–5000 nm*) at different observation geometries. A monochromatic beam is focused on the sample's surface, with beam-size of approximately *5.2 mm* in diameter for a nadir illumination (normal to the surface). The reflected light is measured by two detectors, covering the visible and near-infrared ranges, mounted on a rotating arm. The illumination and the observation angles are defined with respect to the normal to the surface and can be changed, which allows us to automatically acquire spectra for different observation geometries. For our measurements, we set four illumination angles: *0°*, *20°*, *40°* and *60°*, with an angular resolution of *±2.9°*. For each illumination angle, we acquired a series of spectra by varying the observation angle, from *−70°* to *70°*, with a *10°* step and an angular resolution of *±2.05°*, exploring all geometrical configurations except opposition geometry. For each sample, using these parameters, a total of 56 geometrical configurations were explored. The spectral sampling and the evolution of the spectral resolution in our spectra are shown in Appendix A. This parameter set configuration resulted in approximately 13 h of acquisition per sample. The reflectance factor is calculated during the measurement by comparison with a Spectralon (99% reflectance, Labsphere) and Infragold (Labsphere) reflectance targets, taking into account the Reflectance Factors (REFF) of the references, meaning that the reference is measured at the same observation geometry of the sample. The reflectance of the samples is thus compared to a lambertian surface, by dividing the measured spectra with the reference spectra. In this configuration, reflectance values above 1 for specular configuration on very flat surfaces are to be expected.

2.2.2. Scanning Electron Microscopy imaging

After spectroscopic measurements, Scanning Electron Microscopy SEM studies were conducted at the University of Lille, France. A thin coating of carbon was deposited over the pellet surface to perform high resolution secondary electron imaging at 3 keV, using a JEOL JSM-7800F at a working distance of 10 *mm*. High magnification images of the pellets' surfaces were acquired to visualize changes in the surface topography due to ion implantation.

3. Results

3.1. Main spectral features

Almost all the acquired spectra show the same absorption bands

* Corresponding author.
E-mail address: stefano.rubino@ias.u-psud.fr (S. Rubino).

https://doi.org/10.1016/j.icarus.2022.114887
Received 3 June 2021; Received in revised form 11 January 2022; Accepted 11 January 2022
Available online 19 January 2022

(shown in Fig. 1):

- a deep 2.7 μm band associated as with the (M)-OH stretching vibration;
- a broad 3 μm shoulder, which can be a combination of structural and adsorbed water bands (in this sample, minor amounts of structural water are expected, so this contribution is probably dominated by the contribution of adsorbed water), as well as CH stretching bands around 3.4 μm;
- overtones and combination mode peaks of water molecules at 1.4 and 1.9 μm (Ryskin, 1974; Ockman, 1958);
- two additional bands at 2.3 and 2.5 μm, originated from the stretching vibrations of Mg-OH and/or Fe-OH (Clark et al., 1990).

Generally speaking, the first effect we notice is a change in the shape of the hydration band at *2.7 μm*, which gets sharper as we approach the specular reflection geometry (see Fig. 2). For some configurations, when looking at the whole dataset (see Appendix B, Fig. B1), approaching specular geometry, strong features seem to sharpen while less intense ones seem to shrink.

We also note that due to a possible increase of the contribution from specular reflection, spectra from these configurations also could exhibit the spectral signature of the real refractive index from the top layer. This can happen because the real part of the refractive index *n* always oscillates like a derivative around a band (see Kramers-Kronig relations -) and is always lower before the band peak and higher after: thus the specular contribution is lower and then higher. This induces a negative (or blue) shift of the 'apparent absorption' peak position when added with the multiple scattering contribution. This signature would corresponds to the slight bump after the 2.7 μm feature (at approximately 2.715 μm), and the tiny blue-shift of the 2.7 μm band, visible in the non-bombarded sample (the position of the feature shifts from 2.705 μm for [$i = 60°$, $e = 0°$] to 2.700 for [$i = 60°$, $e = 60°$] - note that the spectral sampling here corresponds to 5 *mm*). For reference, the complex refractive index spectrum in serpentines to illustrate the optical constant's behavior can be found in Mooney and Knacke (1985).

Delving a bit deeper, while focusing on the hydration band, different behavior can be seen for the different cases:

- For the non-bombarded sample, the most prominent effect is the change in the shape of the hydration band. Approaching near-specular configuration, the feature gets sharper. Moreover, as the incidence angle *i* grows, for large phase angles, the apparent blue-shift due to the influence of the optical constants described above get more notable;

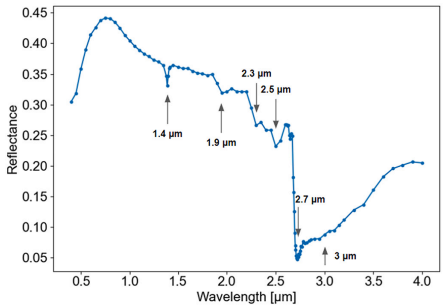

Fig. 1. Example of acquired spectra – He^+ implanted pellet at *(i, e)* =20 °, 40 °).

- For the Ar^+ bombarded sample, the sharpening effect described above can also be seen in near-specular configurations. The slight shape change effect due to the influence of the optical constants is also noticeable for the $i = 60°$ case, although less intense; there also seems to be a slight band position variability of the hydration feature (see Section 3.2 for a detailed explanation);
- For the He^+ bombarded sample, the shape of the hydration band isn't affected by observation geometry as strongly as in the cases described above (or even at all); however, we can see a clear global band red-shift in the position of this band with respect to the other samples. The extent and evolution of this shift is further discussed in Section 3.2.

These effects are better seen in the complete dataset, shown in Appendix B. We note that for all observations of the ion implanted samples in particular geometric configurations, the shape and position of the hydration feature can be considerably altered (Fig. 2, panel c) with respect to the non-implanted pellet (Fig. 2, panel a).

Finally, we note that the curves in panel (a) of Fig. 2 are fairly asymmetric with respect to the emergence angle. This may be due to slight uncertainty in the position of the detector and slight differences on the observation spot position for symmetric emergence angles, possibly coupled to some lateral heterogeneity of the sample.

3.2. REFF dataset results

We quantified the changes of the hydration feature at *2.7 μm* with varying optical geometries. To determine the two spectral parameters of interest, the peak position and the band depth, we applied the same method as in our previous work (Rubino et al., 2020). We first removed a linear continuum from *2.6* to *4 μm*. The continuum-removed spectra, centered on the hydration feature, are shown in the Appendix B, Fig. B2. We then applied different instances of a Savitzky-Golay filter, using different windows-size values, to slightly smooth our data while taking in account different band shapes and degrees of noise correction. For each smoothed spectrum, we defined a region of interest (ROI) centered on the band and computed the barycenter associated to this spectral ROI to account for the asymmetry of the spectral feature. Finally, we averaged the wavelength obtained on each Savitzky-Golay instance and associated this value with the band position. Since the Savitzky-Golay filter acts as a sort of data interpolation process, by taking in consideration multiple instances of it, the computed positional value is very precise, with an improved accuracy with respect to spectral sampling and resolution (which still need to be taken in account when discussing the overall accuracy of the measurement). This method allowed us to extract the band position for all observation geometries. The band depth is calculated as $1 - R_{Band}/R_{Continuum}$, at the wavelength corresponding to the center of the band, and considering a linear continuum between the two inflection points of the band. The position values are shown in the polar plots of Fig. 3.

For the He^+ implanted pellets, the irradiation-induced spectral shift at longer wavelengths can be seen in all optical configurations. The amplitude of this shift can vary from a few nanometers to a maximum of *28 ± 2 nm*. The maximum is reached when observing in a specular configuration, with an angular width of about ±20° (i.e., $e \sim i \pm 20°$). It is interesting to observe that for the large illumination angles, $i \sim 40°$ and $60°$, the spectral shifts increase also when $i \sim -e$: this might possibly be suggestive of backscattering effects. For the Ar^+-implanted pellets, the spectral shift at longer wavelengths with respect to the non-bombarded sample is less pronounced and can only be observed in specular configurations, where its amplitude is close to *6 nm*. Overall, the spectral resolution of our dataset does not allow us to efficiently distinguish between an Ar + implanted pellet and a pristine one in most non-specular optical configurations. Looking at the positional data from the non-bombarded pellet, we can also spot the effect described in 3.1, where for specular geometries the specular component start to dominate

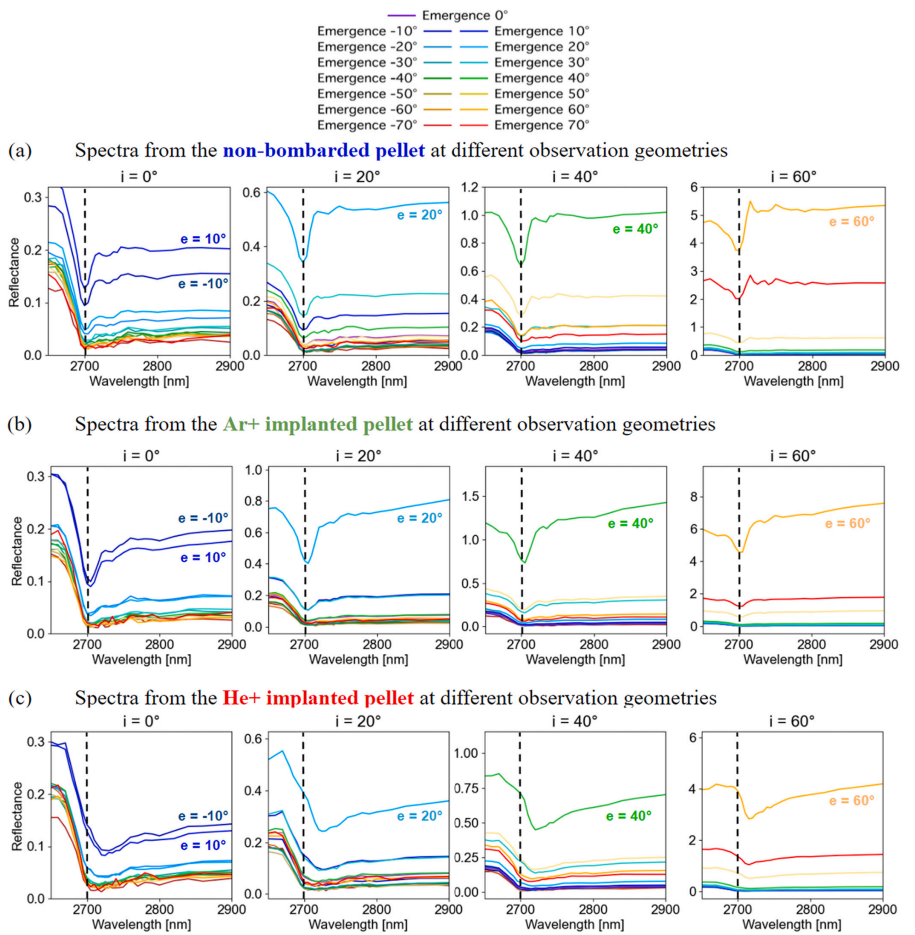

Fig. 2. Detail of the REFF measurements centered around the hydration band (complete dataset but restricted to *2.65–2.9 μm*). The dashed line is precisely at 2.7 μm, and is used to gauge the evolution of the 2.7 μm feature's position.

the spectra, and the spectral signature from the real refractive index can be seen affecting the peak position, slightly blue-shifting it in these configurations. The evolution of the *2.7 μm* band depth (Fig. 4) was also measured in a similar manner to the band position. It is relevant to note that commenting band-depth value in reflectance spectra on particularly bright surfaces can be quite delicate. As discussed by Milliken et al. (2007), band depth and apparent absorbance values can be correlated to albedo when derived from reflectance spectra. In the case of our study, the direct measure of band depth can be biased, especially approaching specular configurations, due to the measured albedo. This complicates the interpretation of this spectral parameter. However, this study highly focuses on the position of the hydration feature and its evolution upon ion-implantation. Results on band-depth are still reported here.

For all pellets, the *2.7 μm* band depth decreases in amplitude when approaching the specular configuration. For a fixed geometrical configuration, the hydration feature measured on both the implanted pellets is deeper than for the pristine pellet. In specular configurations (or approaching specular-like, for $i = 0$), the *2.7 μm* band depth in the He^+ implanted pellets is ~*30%* deeper than in the pristine pellet. In the Ar^+ implanted pellets, the band intensity is only ~15% deeper than in the pristine pellet.

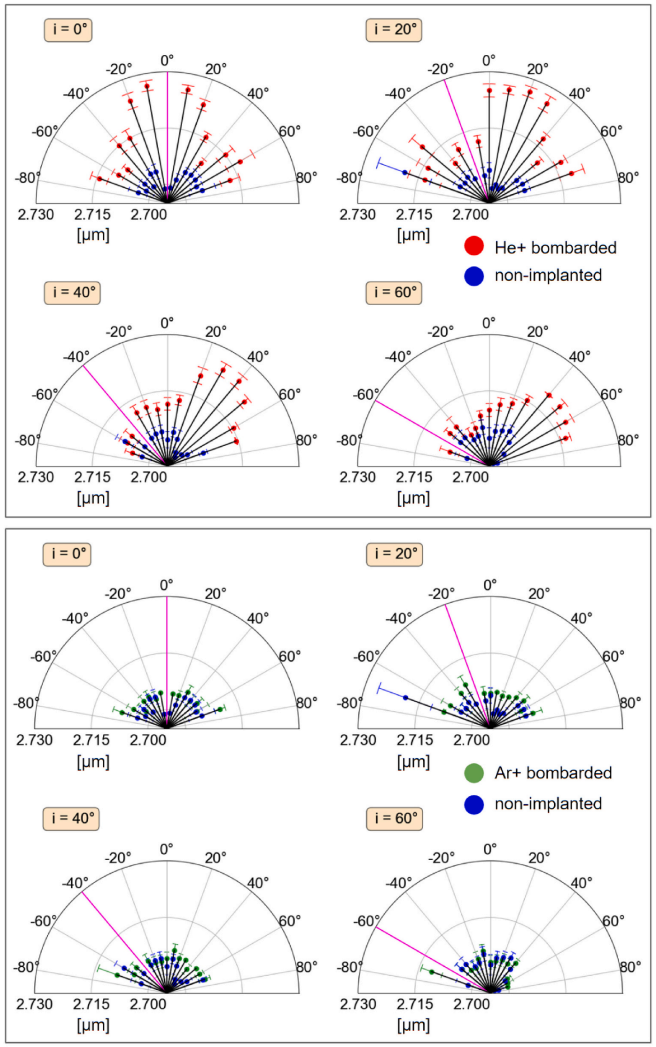

Fig. 3. Evolution of the *2.7 μm* hydration feature position under different optical geometries for He^+ and Ar^+ implanted pellets, with respect to the non-implanted pellet. The magenta line represents the direction of the illumination angle *i*. The plot shows the evolution of the *2.7 μm* peak position as a function of the observation angle *e*, for fixed illumination angles *i*. In the polar plots, the observation angle *e* increases clockwise, while the illumination angle *i* increases counter-clockwise (scale not reported). The data from the ion implanted pellets (red for He^+ and green for Ar^+) are compared with data from the pristine pellets (in blue).

3.3. EMG modeling findings

It is important to address that the hydration feature in phyllosilicates can incorporate multiple contributions depending on the complexity of the phyllosilicate sample. Structural and adsorbed water can also have a spectral signature near *3 μm*, which can contribute to the broad spectral band at *3 μm*. The quantification of these contributions and their evolution can be accessed by Exponentially Modified Gaussian (EMG) modeling (Grushka, 1972; Potin et al., 2020). In Fig. 5, we show the modeling of the various components of the broad spectral feature at *3 μm*, before and after bombardment by He^+. This EMG modeling is first applied to spectra from Rubino et al. (2020), that we acquired with an Agilent Cary 670/620 micro-spectrometer installed at the SMIS beamline of the SOLEIL synchrotron (France), using a Schwarzschild objective

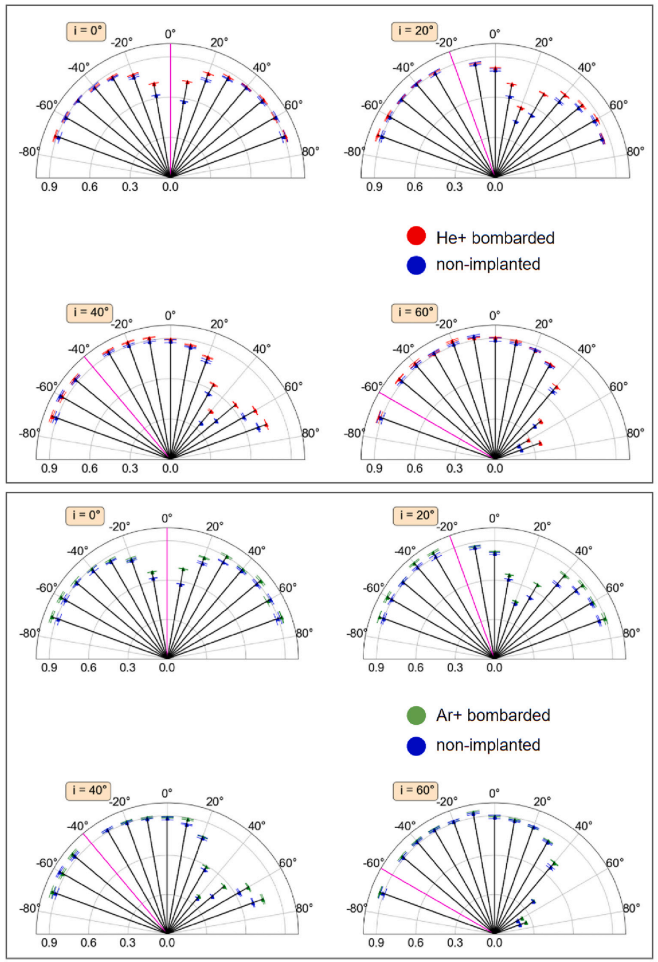

Fig. 4. Evolution of the 2.7 μm hydration feature depth under different optical geometries for He^+ and Ar^+ implanted pellets, with respect to the non-implanted pellet.The magenta line represents the direction of illumination which corresponds to the incidence angle.

with a numerical aperture of 0.81. We measured IR spectra using the internal Globar source, with respect to gold references, following the same procedure described by (Brunetto et al., 2018). Spectra were baseline-corrected and normalized using a linear continuum between *2.6* and *4 μm*.

The high spectral resolution (*4* cm^{-1}) and dense spectral sampling of these measurements allow the precise detection of various components in the band. The large absorption band at *3 μm* is a combination of several features, each tracing the presence of a -OH group bearer, plus the nearby features around *3.4 μm* due to -CH_2 and -CH_3 aliphatic groups. The various detected components could be due to a metal-OH group in a hydrated mineral, or water molecules. Variations in band depth, position of the minimum and FWHM are the results of modifications in the number of hydroxyl groups, as well as in the crystal structure of the minerals, as shown by previous investigations (Bishop et al., 1994, Frost et al., 2000, Potin et al., 2020b). A shift upon ion-bombardment in the position of the minimum and/or broadening of the band with respect to the non-bombarded sample may indicate a distortion of the crystal lattice, bringing the -OH groups closer or further, so modifying their oscillation frequency. Band depth, position of

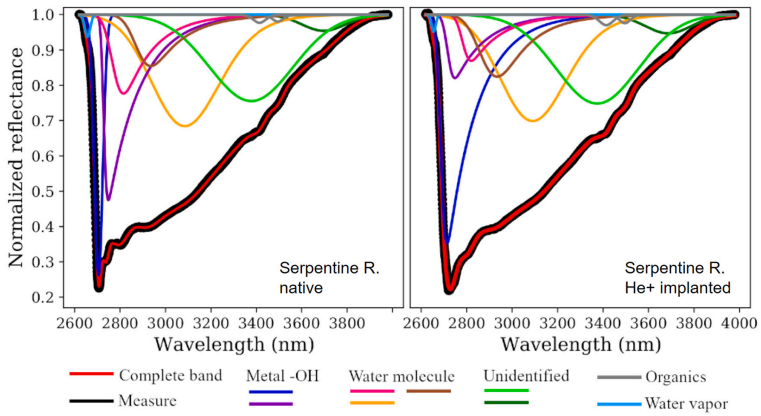

Fig. 5. Comparison of the components forming the band at 3 μm before and after ion implantation on a pellet of Serpentine Rawhide, measured on an IR microspectrometer using Schwarzschild objective with a numerical aperture of 0.81. The values are normalized considering a linear continuum around the absorption band. Fitting values from EMG modeling and their associated errors are shown in Table C1 in Appendix C.

reflectance minimum, and Full-Width at Half Maximum (FWHM), for the complete band and each component before and after bombardment, can be found in Appendix C.

It is important to note that the profile of the global band observed on both measurements is still recognizable between the two measurements, with the band depth only augmented by 0.8%, a band position shift of 20 nm towards the longer wavelengths and a decrease of the FWHM of 8 nm upon ion-bombardment. However, the various components of the spectral feature can be highly altered, such as the metal-OH component at 2.715 μm, losing 9% of depth, shifting of 105 nm towards the longer wavelengths and thinning of 17 nm. It is relevant to keep in mind that the components identification in the case of the ion-bombarded sample can be complicated by the disordering induced by the ion-implantation and the fact that the spectra associated to the bombarded sample is probably a mix of both bombarded and non-bombarded sample.

Based on the results of the EMG algorithm on the microspectrometer data, we applied EMG modeling to the REFF measurements. However, since REFF measurements have a lower spectral sampling and resolution than the spectra acquired with the microspectrometer, the algorithm is able to separate and quantify only four components, some being the combination of the previous detected components too close to each other to be accurately separated with this spectral resolution and sampling. The components are:

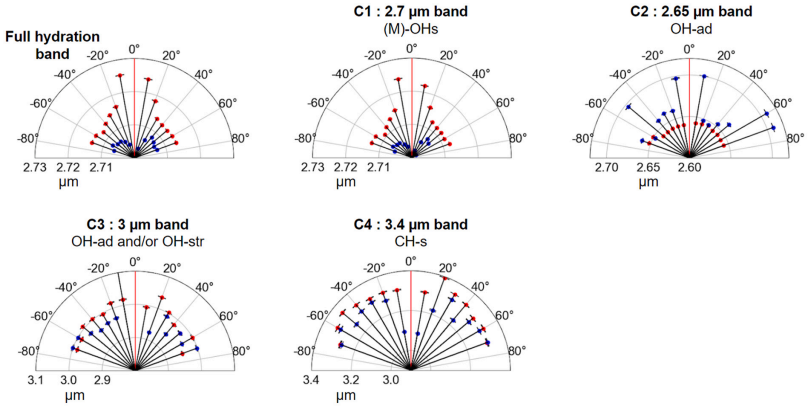

Fig. 6. EMG fitting results on the He^+ implanted pellet in red and for the native pellet in blue, for the illumination angle i =0°: evolution of the position of the hydration band and of the four components found by the model. C1 = (M)-OH; C2 = adsorbed-water (OH-as); C3 = adsorbed- and structural-water (OH-ad and OH-str); C4 = organics (CH-stretching).

- C1: the 2.7 μm peak due to the (M)-OH stretching;
- C2: a small peak at 2.65 μm due to adsorbed water;
- C3: a 3 μm band associated with adsorbed water;
- C4: a band at 3.4 μm due to CH-stretching of organics.

The results for the He^+ implanted pellet for illumination angle i =0° are shown in Fig. 6. We decided to show only the results from the He^+-implanted pellet, since we already saw that the Ar^+ case show little to no spectral changes upon ion bombardment. As a reminder, we are focusing on the changes in position of the hydration feature since the primary focus of this study is to determine possible compositional biases in the interpretation of the hydration feature's position. This value is representative of the type of hydrated silicate, while other parameters - such as band-depth of FWHD - instruct us about ion-implantation effects, such as amorphization.

We observe that each component is somehow impacted by the irradiation and shows different bidirectional behaviors with respect to the non-bombarded sample. However, the changes in the position of the hydration band as a whole are dominated by the shift in position the 2.7 *μm* peak, as this component represents the major contribution to this spectral feature. The position of each component shown here are not computed with the barycenter method described in Section 3.2, but are instead a result of the EMG modeling. Note that, since our measurements were performed under air, the components related to the adsorbed water molecules detected at longer wavelengths are not relevant for the remote sensing implication of this work.

3.4. SEM imaging results

To further investigate the difference among the He^+ and Ar^+ implantation effects, we analyzed the state of the pellet's surface after bombardment with Scanning Electron Microscope (SEM) imaging. The acquired images are presented in Fig. 7.

No notable difference can be seen between the He^+ bombarded surface and the unirradiated one. However, there is a significant difference between these two and the Ar^+ bombarded surface. It appears that, even though the spectroscopic effects of the Ar^+ are difficult to detect, the heavy ion bombardment significantly alters the surface morphology, acting as a smoothing process, contrary to our He^+ bombarded pellet, which retains its grainy and frothy texture. The Ar^+ dulls and sometimes removes grainy morphological features that characterize the two other pellets. The removed features appear to be smaller than *10 nm* in size. The smoothing resulting from the Ar^+ bombardment has significantly altered the morphology of the pellet's surface, somewhat reducing the granularity of it.

4. Discussion

Measurements on the He^+ bombarded pellet showed a clear shift in the position of the *2.7 μm* feature with respect to the non-implanted pellets as well as some slight broadening (see Fig. B.2), consistent with ion-bombardment induced disordering, can also be seen. The spectral shift is due to chemical and physical changes induced by the ion implantation in the first hundreds of nanometers from the surface. The implantation depth in our samples was estimated by the SRIM software

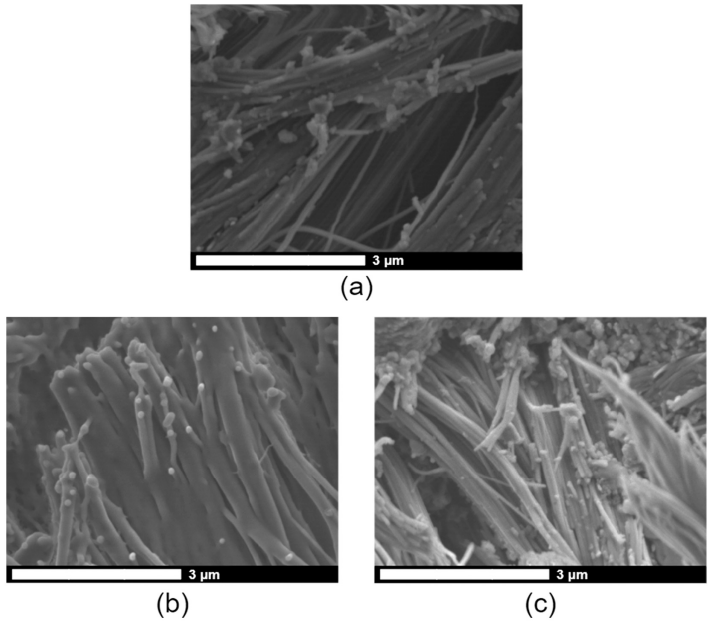

Fig. 7. Scanning Electron Microscopy (SEM) images of the centers from the native Serpentine Rawhide pellet (a), the Ar^+ bombarded pellet (b) and the He^+ bombarded one (c).Images are acquired at 3 kV with ×20 000 magnification.

(Ziegler et al., 2010) to be 0.310 ± 0.090 μm for He^+. However, we have seen that the amplitude of this spectral shift depends on the optical configuration of each measurement. Such diversity means that different effects are competing at the same time at different geometries. The scattering processes in a multi-layer compact structure are inherently complex. Two possible contributions and/or competing effects are volume (multiple) scattering and surface (specular) scattering.

Photons undergoing multiple scattering events in the volume of our sample are more sensible to the deeper layers of our sample. As the illumination angle increases, these photons will likely probe less deep. However, since the sample is observed at wavelengths of 2–3 μm, photons do not resolve layering at the scale of the implanted layer (approximately 0.3 μm as said above), thus mixing up both implanted and non-implanted material. The second contribution is related to specular scattering, which is sensitive to the optical properties of the utmost top layers of our samples. In specular reflection, the probing depth length would still mix ion-implanted and non-implanted matter, but we can qualitatively expect here to have a more prominent contribution from the ion-implanted one, compared to volume scattering. Hence, the specular component carries more information about the very top layer. This explains why specular geometrie in our dataset seem to better relay the effects of the ion-implantation, via the larger measured band-shift. The larger shift measured for $i = 0°$ at near-specular configuration compared to the other near-specular configurations could be explained taking in account the contribution of backscattered photons, which are also particularly sensitive to the surface layers of our samples.

All the patterns seen in our data may result from the combination of volume scattering, specular scattering and possibly backscattering. Overall, the observations suggest that measurements at high illumination angles of ion-implanted surfaces in near-specular configuration will be inherently slightly blue-shifted with respect to measurements done with a smaller illumination angle.

As we compare the effects of He^+ and Ar^+ implantation, we see that for the latter the effects on the hydration feature's position are barely detectable, independently from the optical configuration. The relative thickness of the layers altered by the two ions is noticeably distinct, as there is an order of magnitude difference between the penetration depth of He^+ and Ar^+ in serpentine (from SRIM code simulation: ∼ 0.310 μm for He^+ and ∼ 0.040 μm for Ar^+). Stopping-power profiles for these two ions, shown in (Brunetto et al., 2014), highlight the different energy-loss behavior, which explain the difference in the penetration depth of our ions. The SEM images in Fig. 7 also highlight that the effects of Ar^+ are more prominent on the pellet's surface. A smaller penetration depth means that there's less implanted/modified matter to probe. The photon's optical path is dominated by native matter, the thickness of the Ar^+-implanted layer is much smaller than the wavelength of the probing photon, hence the difficulty in seeing the spectral effects of implanted matter. The altered layer is poorly relevant even at specular geometry. The light loss of surface granularity, due to Ar^+ sputtering, doesn't seem to play a particular role here.

Our study highlights that there is an optimal way to remotely detect ion implantation effects on Solar System surfaces: the spectral effects on hydrated surfaces can be better observed near specular configuration with near-nadir illumination angle. Incidence angles between 20 and 40° can also suffice, in case near-specular configuration is not achievable. These results can be put in the context of the Near-IR spectroscopic surveys carried out on the primitive hydrated bodies Ryugu and Bennu. In terms of remote sensing observation, the configuration that would maximize the spectral effects of space weathering on a primitive hydrated body would correspond to a measurement performed in nadir configuration (the detector onboard the orbiting craft is observing perpendicularly to the surface of the studied body) with a small phase angle φ associated with the measurement. However, it is relevant to point out that for this to work, the asteroidal surface to be analyzed would need to be particularly flat, which is not necessarily the case. For real case objects, surfaces are randomly distributed in orientation within the orbiter's observation footprint and in many cases are covered by regolith, which means that the specular components can be weaker and more dispersed than for our flat pellets: its contribution would be less easy to quantify. This sentence however has to be nuanced, since recent sample return missions, both Hayabusa missions and OSIRIS-REx, have shown that the idea of regolith covering the entirety of the surface of small airless bodies is a notion that needs to be revisited. Light regolith may escape the gravitational pull of small bodies, or flow and accumulate in certain regions. This means that, in the light of our study, for some geographical region, the specular component (which would always be present) would possibly be significant enough to carry sensible information for surface composition studies. Moreover, the spectral shift would probably be also more easily detected in spectroscopic surveys with a tighter field of view, dedicated to some particularly regular feature of interest. This would be the case for example for measurements conducted on fresh impact craters, boulders or fragments of boulders (which could be fractured due to temperature variations, hence exposing flat surfaces) or for rover/lander based measurements, where the chances of having the detector pixel filled with a smooth-enough surface would be larger. For now, these effects may be still hidden in the already acquired datasets, since the current trend consist of comparing different facets of a boulder at the same geometry of observation (see the study of the Otohime Saxon on Ryugu by Tatsumi et al. (2021)), instead of focusing on one facet at different geometries.

In the case of Ryugu and Bennu, their spectroscopic surveys were performed at varying geometric configurations on various regions. In Bennu's case, Deshapriya et al. (2021) show that crater regions on Bennu display a slightly blue-shifted hydration feature with respect to the average position of 2.74 μm (±0.01) (Hamilton et al., 2019). This effect may point to the presence of less-weathered regions on the surface of Bennu, but in the light of this study, it would prove relevant to put in perspective these results with information regarding the measurament's geometry used for crater survey. Furthermore, this also means that the average position of the hydration feature on Bennu, 2.74 μm (±0.01) (Hamilton et al., 2019), may be slightly blue-shifted due to the contribution of these blue-shifted regions. Taking into account this blue-shift in the OVIRS band centre would bring its attribution closer to the CI-CM group 2 type spectra described by (Takir et al., 2013), further supporting the CM2.1–2.2 petrologic-type attribution done by Hamilton et al.

In the case of Ryugu, the hydration feature has been extensively studied around the artificial SCI crater (Tatsumi et al., 2019; Arakawa et al., 2020). Near-nadir configuration with phase angle φ=31.1° to 35.7° was kept during the various descent operations made to image the crater (Kitazato et al., 2021). Since phase angle was kept almost constant, the data acquired during the spectroscopic surveys of the SCI crater is, according to our findings, inherently less biased and easier to interpret, meaning that the slight peak variations of the hydration feature when comparing old and excavated terrains were indeed caused by chemical alterations at the surface, due to space weathering and/or thermal effects.

5. Conclusion

In order to better understand how the geometry of observation can affect remote sensing observations of space weathered primitive bodies, we measured the REFF function of He^+ and Ar^+ bombarded serpentine pellets, at varying illumination angles. We found that in the case of the He^+ bombarded, the position of the *2.7 μm* hydration band, due to the stretching of hydroxyl groups connected to a metallic cation ((M)-OHs), shifts towards longer wavelengths as we approach specular configuration. This is due to chemical and physical changes induced by ion implantation effects in the first hundreds of nanometers, such as preferential amorphization of Mg-rich phyllosilicates or preferential sputtering of Mg (Hapke et al., 1975). The larger band-shift is measured at specular configuration, suggesting that the spectral signature of the

implanted layer is carried by specular reflection. The diversity in the observed amplitude of the shift means that the main driver of this effect is the amount of specular reflection in the collected signal. Additional scattering effects will concur to the final result, but their contribution is more difficult to assess. Using a spectral deconvolution based on EMG profiles, we showed that the irradiation affects the various components of the hydration band independently. One can suggest that the variation of the band observed on the REFF measurements before and after irradiation are due to the alterations of the components themselves. Since the *2.7 μm* hydration band's position is characteristic of the composition of hydrated silicates, it is relevant to highlight its dependency with the angle of measurement, in order to avoid possible detection and interpretation biases.

A future work, currently in preparation, will focus on delving deeper in our sample, in order to study the chemical and physical changes induced by ion bombardment, using Transmission Electron Microscopy (TEM) imaging and Energy Dispersive X-Ray Spectroscopy (TEM-EDX) to investigate the structural and chemical changes of the ion implanted samples.

Declaration of Competing Interest

None.

Acknowledgments

We thank O. Mivumbi, D. Ledu, C.O. Bacri, and P. Benoit-Lamaitrie for help and technical support with SIDONIE and INGMAR. INGMAR is a joint IAS-CSNSM (Orsay, France) facility funded by the P2IO LabEx (ANR-10-LABX-0038) in the framework Investissements d'Avenir (ANR-11-IDEX-0003-01). We would also like to thank A. Fadel for help and technical support with the SEM acquisitions. Finally, we thank both reviewers from the journal for their precious comments and questions. This work has been funded by the ANR project CLASSY (Grant ANR-17-CE31-0004-02) of the French Agence Nationale de la Recherche and by the Centre National d'Etudes Spatiales (CNES-France). The instrument SHADOWS was funded by the OSUG@2020 Labex (Grant ANR10 LABX56), by 'Europlanet 2020 RI', within the European Union's Horizon2020 research and innovation program (Grant N°654208) and by the Centre National d'Etudes Spatiales (CNES). HL thanks I-SITE ULNE and the MEL for funding. The electron microscopy works at the University of Lille were performed with the support of the Chevreul Institute, the European FEDER and Région Hauts-de-France.

Appendix A. Spectral parameters

The spectral sampling for the acquired spectra was adjusted to be denser around the 2.7 μm band and looser where there were no bands of interest, to achieve a good compromise between quality of the measurement and time of acquisition. The spectral resolution was also adjusted with the same intent. In Fig. A1, both these spectral parameters and their variations along the spectra are shown.

(a)

Range [nm]	*Step [nm]*
400 → 1400	50
1400 → 1420	10
1450 → 2600	50
2600 → 2680	10
2680 → 2750	5
2750 → 2800	10
2800 → 2900	20
2900 → 3200	50
3200 → 4000	100

(b)

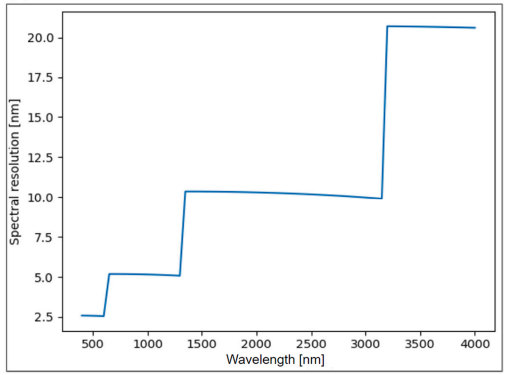

Fig. A1. (a) Evolution of the spectral step and (b) Evolution of the spectral resolution

Appendix B. Complete REFF dataset

In Fig. B1, the complete spectra of the entire REFF dataset for this experiment are shown. For high illumination angles *i*, when approaching specular configuration, spectral effects due to the domination of the specular components (explained under Fig. 1) result in the alteration of the continuum shape, the reduction of weak features and the accentuation of the 1.4 and the 2.7 μm bands.

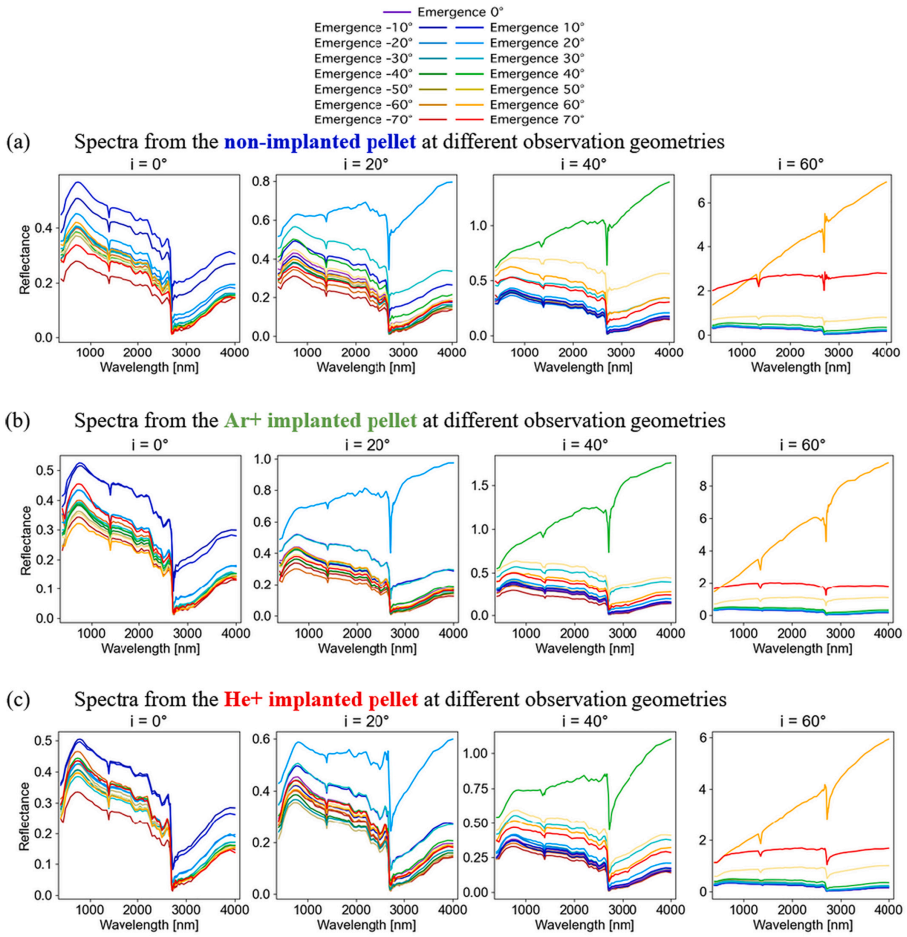

Fig. B1. Complete REFF dataset

In Fig. B2, the spectra centered on the hydration feature, after continuum removal, are shown. We can see that the band tends to shrink as we approach specular configuration. We are also able to appreciate the change in band-shape and observe the feature broadening upon ion-implantation, being much wider for the He^{+} bombarded sample.

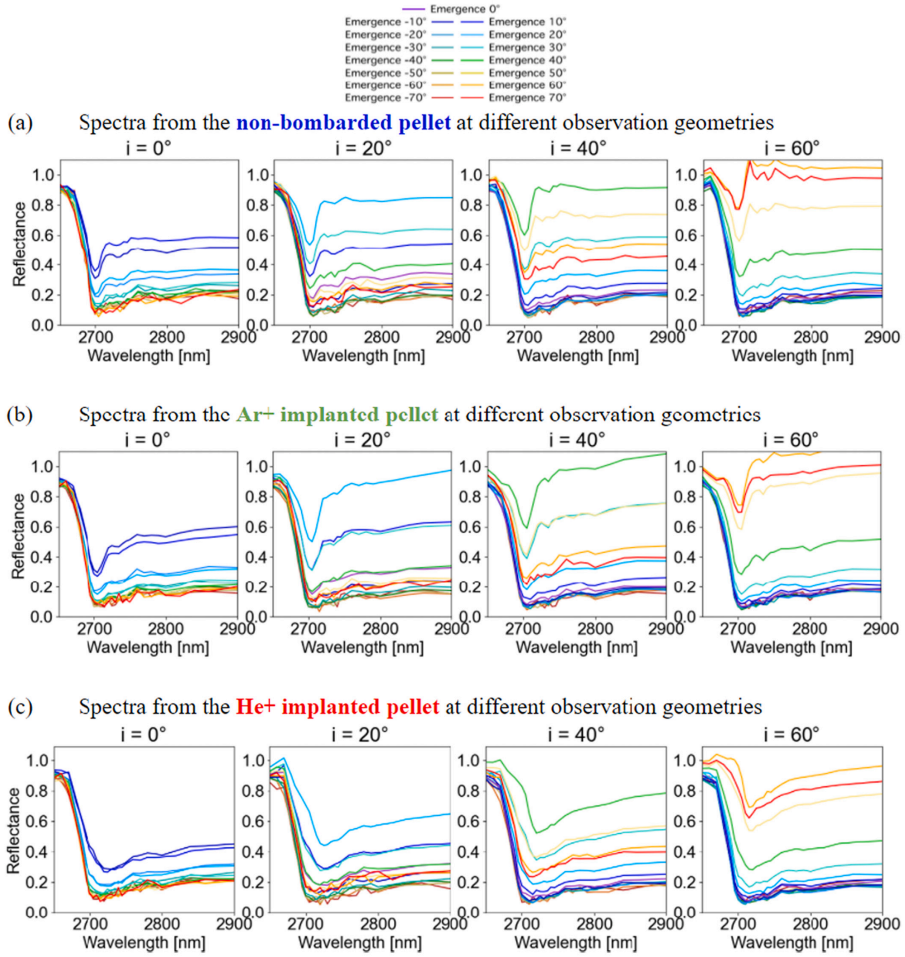

Fig. B2. REFF dataset (complete dataset but restricted to 2.65–2.9 μm, after continuum removal)

Appendix C. Exponentially modified Gaussian (EMG) modeling: complete band parameters table

Table C1 presents the band parameters of the complete band and components derived from Fig. 5. The position of the band is considered as the wavelength at which the reflectance is at its minimum value inside the band. The band depth is calculated as $1 - R_{Band}/R_{Continuum}$, at the wavelength corresponding to the center of the band, and considering a linear continuum between the two inflection points of the band, R_{Band} being the measured reflectance at the position of minimum and $R_{Continuum}$ the reflectance of a linear continuum at the same wavelength. The errors are calculated following the procedure described in Potin et al. (2020a), considering 0.001 error bars and 500 simulated spectra. The errors are calculated, as described in Potin et al. (2020), based on the bootstrap statistical method. In this case, the fits are reproduced 500 times on the original data where a random fluctuation of 0.001 has been added. This method resulted in a large number of spectral parameters for each component, whose distribution is centered on the most probable value, considered here as the modeled band parameter, and with a FWHM corresponding to the error.

Table C1
Band parameters of the complete 3 μm band and components derived from the modelization shown on Fig. 5. The colors to represent the components are similar to those in Fig. 5.

Component	Identification		Band depth (%)	Min. Position (nm)	FWHM (nm)	Effect on BD	Effect on Position	Effect on FWHM
Complete band		Virgin	76.943 ± 0.020	2707.554 ± 0.028	617.362 ± 0.246	0.801	20.467	−8.366
		He implanted	77.744 ± 0.016	2728.021 ± 0.086	608.960 ± 0.220			
1 (light blue)	Water vapor	Virgin	6.264 ± 0.019	2656.891 ± 0.136	58.211 ± 0.756	−1.458	−1.885	−1.42
		He implanted	4.806 ± 0.043	2655.006 ± 0.117	56.791 ± 1.336			
2 (blue)	Metal-OH	Virgin	73.736 ± 0.046	2705.483 ± 0.029	43.838 ± 0.083	−9.497	8.712	91.087
		He implanted	64.239 ± 1.688	2714.195 ± 0.405	134.925 ± 0.581			
3 (purple)	Metal-OH	Virgin	22.422 ± 0.133	2715.049 ± 0.214	168.194 ± 0.293	−9.472	105.478	−17.549
		He implanted	12.950 ± 0.322	2820.527 ± 0.277	150.645 ± 1.011			
4 (pink)	Water molecule	Virgin	52.393 ± 0.203	2748.566 ± 0.088	126.128 ± 0.079	−34.077	−0.241	14.938
		He implanted	18.316 ± 1.583	2748.325 ± 0.839	141.066 ± 2.083			
5 (brown)	Water molecule	Virgin	14.578 ± 0.064	2935.286 ± 0.111	205.608 ± 0.299	2.992	−0.702	17.29
		He implanted	17.570 ± 0.234	2834.584 ± 0.418	222.898 ± 1.576			
6 (orange)	Water molecule	Virgin	31.580 ± 0.058	3084.526 ± 0.202	357.631 ± 0.234	−1.248	7.464	−10.357
		He implanted	30.332 ± 0.257	3091.990 ± 1.197	347.274 ± 2.112			
7 (green)		Virgin	24.513 ± 0.029	3377.774 ± 0.236	435.971 ± 0.447	0.482	0.337	−10.667
		He implanted	24.995 ± 0.167	3378.111 ± 2.989	425.304 ± 1.535			
8 (grey)	Organics	Virgin	2.352 ± 0.026	3414.209 ± 0.553	66.581 ± 0.781	0.576	−0.091	6.317
		He implanted	2.928 ± 0.055	3414.118 ± 0.268	72.898 ± 0.707			
9 (grey)	Organics	Virgin	2.002 ± 0.018	3494.997 ± 0.254	58.211 ± 0.756	0.36	0.786	−1.42
		He implanted	2.362 ± 0.058	3495.763 ± 0.330	56.791 ± 1.336			
10 (dark green)		Virgin	4.625 ± 0.019	3697.060 ± 0.133	225.406 ± 0.133	0.568	−7.957	12.27
		He implanted	5.193 ± 0.093	3689.103 ± 1.740	237.676 ± 2.332			

References

Arakawa, M., Saiki, T., Wada, K., Ogawa, K., Kadono, T., Shirai, K., Sawada, H., et al., 2020. An artificial impact on the asteroid (162173) Ryugu formed a crater in the gravity-dominated regime. Science 368 (6486), 67–71.

Brunetto, R., Lantz, C., Ledu, D., Baklouti, D., Barucci, M.A., Beck, P., Delauche, L., et al., 2014. Ion irradiation of Allende meteorite probed by visible, IR, and Raman spectroscopies. Icarus 237 (July), 278–292.

Brunetto, R., Loeffler, M.J., Nesvorný, D., Sasaki, S., Strazzulla, G., 2015. Asteroid surface alteration by space weathering processes. Asteroids IV. https://doi.org/10.2458/azu_uapress_9780816532131-ch031.

Bishop, J.L., Pieters, C.M., Edwards, J.O., 1994. Infrared spectroscopic analyses on the nature of water in montmorillonite. Clay Clay Miner 42, 702–716. https://doi.org/10.1346/CCMN.1994.0420606.

Brunetto, R., Lantz, C., Dionnet, Z., Borondics, F., Aléon-Toppani, A., Baklouti, D., Barucci, M.A., et al., 2018. Hyperspectral FTIR imaging of irradiated carbonaceous meteorites. Planetary and Space Science 158 (September), 38–45.

Brunetto, R., Lantz, C., Nakamura, T., Baklouti, D., Le Pivert-Jolivet, T., Kobayashi, S., Borondics, F., 2020. Characterizing irradiated surfaces using IR spectroscopy. Icarus 345 (July), 113722.

Christensen, P.R., Hamilton, V.E., Mehall, G.L., Pelham, D., O'Donnell, W., Anwar, S., Bowles, H., et al., 2018. The OSIRIS-REx thermal emission spectrometer (OTES) instrument. Space Sci. Rev. 214 (5), 87.

Clark, Roger N., King, Trude V.V., Klejwa, Matthew, Swayze, Gregg A., Vergo, Norma, 1990. High spectral resolution reflectance spectroscopy of minerals. J. Geophys. Res. 95 (B8), 12653.

Clark, B.E., Lucey, P., Helfenstein, P., Bell Iii, J.F., Peterson, C., Veverka, J., Mcconnochie, T., et al., 2001. Space weathering on Eros: constraints from albedo and spectral measurements of psyche crater. Meteorit. Planet. Sci. 36 (12), 1617–1637.

Clark, Beth Ellen, Hapke, Bruce, Pieters, Carlé, Britt, Daniel, 2002. Asteroid space weathering and regolith evolution. Asteroids III 585 (90086–90082).

De Sanctis, M.C., Ammannito, E., Raponi, A., Marchi, S., McCord, T.B., McSween, H.Y., Capaccioni, F., et al., 2015. Ammoniated phyllosilicates with a likely outer solar system origin on (1) Ceres. Nature 528 (7581), 241–244.

Deshapriya, J.D.P., Barucci, M.A., Bierhaus, E.B., Fornasier, S., Hasselmann, P.H., Merlin, F., Clark, B.E., et al., 2021. Spectral analysis of craters on (101955) Bennu. Icarus 357 (March), 114252.

Frost, R.L., Ruan, H., Kloprogge, TheoJ., Gates, W., 2000. Dehydration and dehydroxylation of nontronites and ferruginous smectite. Thermochim. Acta 346, 63–72. https://doi.org/10.1016/s0040-6031(99)00366-4.

Grushka, E., 1972. Characterization of Exponentially modified Gaussian peaks in chromatography. Anal. Chem. 44 (11), 1733–1738.

Hamilton, V.E., Simon, A.A., Christensen, P.R., Reuter, D.C., Clark, B.E., Barucci, M.A., Bowles, N.E., et al., 2019. Evidence for widespread hydrated minerals on asteroid (101955) Bennu. Nature Astronomy 3 (4), 332–340.

Hapke, B., Cassidy, W., Wells, E., 1975. Effects of vapor-phase deposition processes on the optical, chemical, and magnetic properties OE the lunar regolith. The Moon. 13, 339–353. https://link.springer.com/article/10.1007/BF00567525.

Ishiguro, Masateru, Hiroi, Takahiro, Tholen, David J., Sasaki, Sho, Ueda, Yuji, Nimura, Tokuhiro, Abe, Masanao, et al., 2007. Global mapping of the degree of space weathering on asteroid 25143 Itokawa by Hayabusa/AMICA observations. Meteorit. Planet. Sci. 42 (10), 1791–1800.

Iwata, Takahiro, Kitazato, Kohei, Abe, Masanao, Ohtake, Makiko, Arai, Takehiko, Arai, Tomoko, Hirata, Naru, et al., 2017. NIRS3: the near infrared spectrometer on Hayabusa2. Space Sci. Rev. 208 (1), 317–337.

Jones, Thomas D., Lebofsky, Larry A., Lewis, John S., Marley, Mark S., 1990. The composition and origin of the C, P, and D asteroids: water as a tracer of thermal evolution in the Outer Belt. Icarus 88 (1), 172–192.

King, A.J., Schofield, P.F., Howard, K.T., Russell, S.S., 2015. Modal mineralogy of CI and CI-like chondrites by X-ray diffraction. Geochim. Cosmochim. Acta 165 (September), 148–160.

Kitazato, K., Milliken, R.E., Iwata, T., Abe, M., Ohtake, M., Matsuura, S., Arai, T., et al., 2019. The surface composition of asteroid 162173 Ryugu from Hayabusa2 near-infrared spectroscopy. Science 364 (6437), 272–275.

Kitazato, K., Milliken, R.E., Iwata, T., Abe, M., Ohtake, M., Matsuura, S., Takagi, Y., et al., 2021. Thermally altered subsurface material of asteroid (162173) Ryugu. Nature Astronomy. https://doi.org/10.1038/s41550-020-01271-2. January.

Lantz, C., Brunetto, R., Barucci, M.A., Dartois, E., Duprat, J., Engrand, C., Godard, M., Ledu, D., Quirico, E., 2015. Ion irradiation of the Murchison meteorite: visible to mid-infrared spectroscopic results. Astronomy & Astrophysics. https://doi.org/10.1051/0004-6361/201425398.

Lantz, C., Brunetto, R., Barucci, M.A., Fornasier, S., Baklouti, D., Bourçois, J., Godard, M., 2017. Ion irradiation of carbonaceous chondrites: a new view of space weathering on primitive asteroids. Icarus 285 (March), 43–57.

Lauretta, D.S., Balram-Knutson, S.S., Beshore, E., Boynton, W.V., Drouet d'Aubigny, C., DellaGiustina, D.N., Enos, H.L., et al., 2017. OSIRIS-REx: sample return from asteroid (101955) Bennu. Space Sci. Rev. 212 (1), 925–984.

Madejová, J., Gates, W.P., Petit, S., 2017. IR spectra of clay minerals. Developments in Clay Science. https://doi.org/10.1016/b978-0-08-100355-8.00005-9.

Milliken, Ralph E., Mustard, John F., Poulet, François, Jouglet, Denis, Bibring, Jean-Pierre, Gondet, Brigitte, Langevin, Yves, 2007. Hydration state of the Martian surface as seen by Mars express OMEGA: 2. H2O content of the surface. J. Geophys. Res. 112 (E8) https://doi.org/10.1029/2006je002853.

Mooney, T., Knacke, R.F., 1985. Optical constants of chlorite and serpentine between 2.5 and 50 μm. Icarus 64 (3), 493–502.

Ockman, Nathan, 1958. The infra-red and Raman spectra of ice. Adv. Phys. 7 (26), 199–220.

Potin, Sandra, Brissaud, Olivier, Beck, Pierre, Schmitt, Bernard, Magnard, Yves, Correia, Jean-Jacques, Rabou, Patrick, Jocou, Laurent, 2018. SHADOWS: a Spectro-Gonio radiometer for bidirectional reflectance studies of dark meteorites and terrestrial analogs: design, calibrations, and performances on challenging surfaces. Appl. Opt. 57 (28), 8279–8296.

Potin, S., Beck, P., Bonal, L., Schmitt, B., Garenne, A., Moynier, F., Agranier, A., Schmitt-Kopplin, P., Malik, A.K., 2020b. Mineralogy, Chemistry, and Composition of Organic Compounds in the Fresh Carbonaceous Chondrite Mukundpura: CM1 or CM2? Meteoritics & Planetary Science 557, 1681–1696.

Potin, S., Beck, P., Schmitt, B., Moynier, F., 2019. Some things special about NEAs: geometric and environmental effects on the optical signatures of hydration. Icarus 333 (November), 415–428.

Potin, S., Manigand, S., Beck, P., Wolters, C., Schmitt, B., 2020. A model of the 3-μm hydration band with Exponentially modified Gaussian (EMG) profiles: application to hydrated chondrites and asteroids. Icarus 343 (June), 113686.

Rivkin, A.S., Howell, E.S., Vilas, F., Lebofsky, L.A., 2002. Hydrated minerals on asteroids: the astronomical record. Asteroids III 1, 235–253.

Rubino, S., Lantz, C., Baklouti, D., Leroux, H., Borondics, F., Brunetto, R., 2020. Space weathering affects the remote near-IR identification of phyllosilicates. The Planetary Report. https://doi.org/10.3847/PSJ/abb94c.

Ryskin, Y.I., 1974. The vibrations of protons in minerals:hydroxyl, water and ammonium. The Infrared Spectra of Minerals 137–182.

Takir, Driss, Emery, Joshua P., Mcsween, Harry Y., Hibbitts, Charles A., Clark, Roger N., Pearson, Neil, Wang, Alian, 2013. Nature and degree of aqueous alteration in CM and CI carbonaceous chondrites. Meteorit. Planet. Sci. https://doi.org/10.1111/maps.12171.

Tatsumi, Eri, Kouyama, Toru, Suzuki, Hidehiko, Yamada, Manabu, Sakatani, Naoya, Kameda, Shingo, Yokota, Yasuhiro, et al., 2019. Updated inflight calibration of Hayabusa2's optical navigation camera (ONC) for scientific observations during the cruise phase. Icarus 325 (June), 153–195.

Tatsumi, E., Sugimoto, C., Riu, L., Sugita, S., Nakamura, T., Hiroi, T., Morota, T., et al., 2021. Collisional history of Ryugu's parent body from bright surface boulders. Nature Astronomy 5 (1), 39–45.

Usui, Fumihiko, Hasegawa, Sunao, Ootsubo, Takafumi, Onaka, Takashi, 2018. AKARI/IRC Near-Infrared Asteroid Spectroscopic Survey: AcuA-Spec. Publ. Astron. Soc. Jpn 71 (1). https://doi.org/10.1093/pasj/psy125.

Watanabe, Sei-Ichiro, Tsuda, Yuichi, Yoshikawa, Makoto, Tanaka, Satoshi, Saiki, Takanao, Nakazawa, Satoru, 2017. Hayabusa2 Mission overview. Space Sci. Rev. 208 (1), 3–16.

Ziegler, James F., Ziegler, M.D., Biersack, J.P., 2010. SRIM – the stopping and range of ions in matter (2010). Nucl. Instrum. Methods Phys. Res., Sect. B. https://doi.org/10.1016/j.nimb.2010.02.091.

Small grains from Ryugu: handling and analysis pipeline for Infrared Synchrotron Microspectroscopy

Stefano Rubino (stefano.rubino@universite-paris-saclay.fr)
Institut d'Astrophysique Spatiale https://orcid.org/0000-0003-3198-1123
Zélia Dionnet
Institut d'Astrophysique Spatiale
Alice Aléon-Toppani
Institut d'Astrophysique Spatiale
Rosario Brunetto
Institut d'Astrophysique Spatiale
Tomoki Nakamura
Tohoku University: Tohoku Daigaku
Donia Baklouti
Institut d'Astrophysique Spatiale
Zahia Djouadi
Institut d'Astrophysique Spatiale
Cateline Lantz
Institut d'Astrophysique Spatiale
Obadias Mivumbi
Institut d'Astrophysique Spatiale
Ferenc Borondics
Synchrotron SOLEIL
Stephane Lefrançois
Synchrotron SOLEIL
Christophe Sandt
Synchrotron SOLEIL
Francesco Capitani
Synchrotron SOLEIL
Eva Héripré
Laboratoire MSSMat: Laboratoire Mecanique des Sols Structures et Materiaux
David Troadec
IEMN: Institut d'Electronique de Microelectronique et de Nanotechnologie
Megumi Matsumoto
Tohoku University: Tohoku Daigaku
Kana Amano
Tohoku University: Tohoku Daigaku
Tomoyo Morita
Tohoku University: Tohoku Daigaku
Hisayoshi Yurimoto
Hokkaido University: Hokkaido Daigaku
Takaaki Noguchi
Kyushu University: Kyushu Daigaku
Ryuji Okazaki
Kyushu University: Kyushu Daigaku
Hikaru Yabuta
Hiroshima University: Hiroshima Daigaku
Hiroshi Naraoka
Kyushu University: Kyushu Daigaku
Kanako Sakamoto
JAXA ISAS: Uchu Koku Kenkyu Kaihatsu Kiko Uchu Kagaku Kenkyujo
Shogo Tachibana
Tokyo Daigaku
Seiichiro Watanabe
Nagoya University: Nagoya Daigaku
Yuichi Tsuda
JAXA ISAS: Uchu Koku Kenkyu Kaihatsu Kiko Uchu Kagaku Kenkyujo

Research Article

Keywords: sample-return mission, Hayabusa2, IR spectroscopy, precious samples, non-destructive analysis, analytical pipeline

Posted Date: May 13th, 2022

DOI: https://doi.org/10.21203/rs.3.rs-1622610/v1

Title : Small grains from Ryugu: handling and analysis pipeline for Infrared Synchrotron Microspectroscopy

Author #1 : Stefano Rubino, IAS - Université Paris-Saclay (CNRS) - France, stefano.rubino@universite-paris-saclay.fr
Author #2 : Zélia Dionnet, IAS - Université Paris-Saclay (CNRS) - France, zelia.dionnet@universite-paris-saclay.fr
Author #3 : Alice Aléon-Toppani, IAS - Université Paris-Saclay (CNRS) - France, alice.aleon@universite-paris-saclay.fr
Author #4 : Rosario Brunetto, IAS - Université Paris-Saclay (CNRS) - France, rosario.brunetto@universite-paris-saclay.fr
Author #5 : Tomoki Nakamura, Tohoku University - Japan, tomoki.nakamura.a8@tohoku.ac.jp
Author #6 : Donia Baklouti, IAS - Université Paris-Saclay (CNRS) - France, donia.baklouti@universite-paris-saclay.fr
Author #7 : Zahia Djouadi, IAS - Université Paris-Saclay (CNRS) - France, zahia.djouadi@universite-paris-saclay.fr
Author #8 : Cateline Lantz, IAS - Université Paris-Saclay (CNRS) - France, cateline.lantz@universite-paris-saclay.fr
Author #9 : Obadias Mivumbi, IAS - Université Paris-Saclay (CNRS) - France, obadias.mivumbi@universite-paris-saclay.fr
Author #10 : Ferenc Borondics, SMIS/SOLEIL – France, ferenc.borondics@synchrotron-soleil.fr
Author #11 : Stephane Lefrançois, SMIS/SOLEIL – France, stephane.lefrancois@synchrotron-soleil.fr
Author #12 : Christophe Sandt, SMIS/SOLEIL – France, christophe.sandt@synchrotron-soleil.fr
Author #13 : Francesco Capitani, SMIS/SOLEIL – France, francesco.capitani@synchrotron-soleil.fr
Author #14 : Eva Héripré, Laboratoire MSSMat – CentraleSupélec - Université Paris-Saclay (CNRS) – France, eva.heripre@centralesupelec.fr
Author #15 : David Troadec, IEMN - Université de Lille – France, david.troadec@univ-lille.fr
Author #16 : Megumi Matsumoto, Tohoku University – Japan, m_matsumoto@tohoku.ac.jp
Author #17 : Kana Amano, Tohoku University – Japan, amakana@dc.tohoku.ac.jp
Author #18 : Tomoyo Morita, Tohoku University – Japan, tomoyo.morita.q1@dc.tohoku.ac.jp
Author #19 : Hisayoshi Yurimoto, Hokkaido University – Japan, yuri@ep.sci.hokudai.ac.jp
Author #20 : Takaaki Noguchi, Kyushu University – Japan, noguchi.takaaki.906@m.kyushu-u.ac.jp
Author #21 : Ryuji Okazaki, Kyushu University – Japan, okazaki.ryuji.703@m.kyushu-u.ac.jp
Author #22 : Hikaru Yabuta, Hiroshima University – Japan, hyabuta@hiroshima-u.ac.jp
Author #23 : Hiroshi Naraoka, Kyushu University – Japan, naraoka@geo.kyushu-u.ac.jp
Author #24 : Kanako Sakamoto, ISAS/JAXA – Japan, sakamoto.kanako@jaxa.jp
Author #25 : Shogo Tachibana, University of Tokyo – Japan, tachi@eps.s.u-tokyo.ac.jp
Author #26 : Seiichiro Watanabe, Nagoya University – Japan, seicoro@eps.nagoya-u.ac.jp
Author #27 : Yuichi Tsuda, ISAS/JAXA – Japan, tsuda.yuichi@jaxa.jp
and the Hayabusa2-initial-analysis team

Abstract

Sample-return missions allow the study of materials collected directly from celestial bodies, unbiased by atmospheric entry effects and/or Earth alteration and contamination phenomena, using state-of-the-art techniques - but only if the collected material stays pristine. The scarcity of outer-space unaltered material recovered until now makes this material extremely precious. To maximize the scientific output of current and future sample-return missions, the scientific community needs to plan for ways of storing, handling, and measuring this precious material while preserving their pristine state for as long as the 'invasiveness' of measurements allows. In July 2021, as part of the Hayabusa2 (JAXA) "Stone" preliminary examination team, we received several microscopic particles from the asteroid Ryugu, with the goal of performing IR hyper-spectral imaging and IR micro-tomography studies. Here we describe the sample transfer, handling methods and analytical pipeline we implemented to study this very precious material while minimizing and surveilling their alteration history on Earth.

Keywords

sample-return mission – Hayabusa2 – IR spectroscopy – precious samples – non-destructive analysis – analytical pipeline

I. Introduction

The study of materials from outer space is paramount in understanding how our solar system evolved from its beginning. Their chemical composition helps us trace both the origin and the history of processes affecting an astronomical body. This investigation can be performed by different means :

- from afar, using on-Earth telescopes or orbiting observatories (such as the recently launched James Webb Space Telescope) to study the surface composition of far-away bodies;
- close-by, using space-probes and sample-return mission, working with spacecrafts to map outer-bodies and possibly collect materials from their surface;
- by proxy, conducting measurements while simulating space conditions on materials available on Earth, from terrestrial rocks to samples more closely related to outer bodies, such as meteorites or collected samples from sample-return missions.

The last item is of particular interest in the current context, since the scientific community all around the world has been preparing itself to welcome precious samples from C-type primitive asteroid (162173) Ryugu, collected by the Hayabusa2 mission from JAXA (Watanabe et al. 2017). In December 2020, the Hayabusa2 mission brought back to Earth 5.4 g of matter from

two different collect sites at the surface of Ryugu. In the near future, more samples collected from outer space bodies are expected to arrive on Earth, such as samples from another primitive asteroid, B-type (101955) Bennu, collected by the OSIRIS-REx mission from NASA (Lauretta et al. 2017). Studying these precious materials with state-of-the-art techniques in laboratories on Earth grants us unique opportunities to study materials unaltered by Earth, providing us great scientific insight on the early stages of our solar system that would not be obtainable otherwise (Vernazza et al. 2021). However, the scarcity of such materials calls for a certain degree of caution when transferring, handling and measuring these samples, in order to minimize sample loss and sample alteration post-arrival on Earth. Sample loss may occur due to manipulation, preparation or during destructive analyses, while exposure to the Earth atmosphere may significantly alter the chemical composition of such delicate samples. It follows that there is a need to accurately plan for the arrival of such samples, to maximize the scientific output achievable before possible sample loss. In this work, we shall describe the sample transfer methods and the analytical pipeline we applied to perform an extensive infrared characterization of several Ryugu particles in July 2021.

II. Sample preparation and sample transfer

On the 1st of June, four samples consisting of mm-sized stones - A0055, A0064, C0002 and C0046 - arrived in Tohoku University at Sendai. All samples were stored in an N_2-filed glove box with oxygen concentration < ~5 ppm and dew points < -50C. In this glove box, via a high-resolution optical microscope, approximately 30 particles were transferred to our custom made sample-holders, using a very thin fiber and electrostatic force (no adhesive bond). Size range varied from 20 to 90 µm, with a particularly large particle of 150 µm. These samples had to travel from Tohoku University (Sendai, Japan), where the allocated particles were handled to the SOLEIL synchrotron in France while :

- under N_2 atmosphere, to avoid irreversible chemical alteration (example : Na sulfates growth on the particle surface (Nakamura et al. 2022));
- retaining their 3D structure during the trip for us to perform 3D IR characterization techniques;
- remain measurable by IR reflectance spectroscopy while sealed inside the sample-holder, under N_2 atmosphere.

These constraints led to the use of an appropriate sample holder, which would not only be used for transportation, but also for performing our preliminary infrared characterization while keeping the samples under N_2 atmosphere. No pre-made commercial solution was found adequate. Instead, we designed and assembled a custom-made sample-holder.

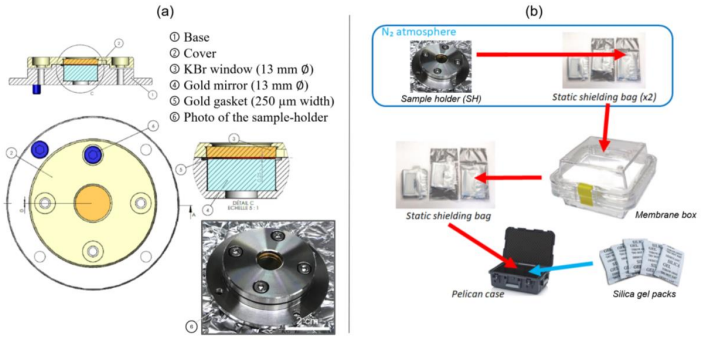

Figure 1. (a) Schematics of our custom-made sample holder for the transfer of microscopic grains under N_2 atmosphere ; (b) Sample transfer setup.

The sample-holder is made of five parts (see Figure 1.a) : a base, a cover, a gold mirror, a gold gasket and a KBr window. The base and the cover are made from non-magnetic stainless steel. The gold mirror is inserted into the base and fixed using a lateral screw. Particles from Ruygu are deposited on this gold mirror for their transfer and preliminary analysis. The KBr window is glued to the cover using an epoxy glue (3M™ Scotch-Weld™ *Epoxy* Adhesive *2216*, used for ultra-vacuum applications). The KBr window allows us to acquire measurements through the cover, keeping the sample-holder seal intact. The gold gasket sits on the mirror and keeps the particles from being crushed. To some degree, it also acts as a seal, isolating the samples. To avoid contamination, the base and the cover underwent a heavy cleaning process : the pieces were first degreased, then were put in a bath of fluorocitric acid, followed by heated ultrasonic cleaning (80°C max at 27 kHz) with an alkaline cleaning agent and finally a heated ultrasonic cleaning (80°C max at 27 kHz) with deionized water. After the cleaning procedure, all the pieces were put inside cleanroom-ready static shielding bags. The whole system was then assembled inside a glovebox under N_2 atmosphere (P ~ 6 mBar, H_2O = 1.0 ppm, O_2 = 1.2 ppm). Each sample-holder was then put inside two cleanroom static shielding bags, while still being inside the glovebox. This double protection would be able to keep the dry N_2 atmosphere sealed inside the bags. The bags holding the sample-holders were then

removed from the glovebox and each one was put inside a membrane box, to reduce the damage from shocks and vibration during sample transfer. These membrane boxes were also put inside larger cleanroom static shielding bags, which were heat-sealed, to further isolate the sample-holders. Finally, all sample-holders traveled from France to Japan in a pelican case padded with foam and silica gel packs (Figure 1.b).

Once arrived in Sendai, the empty sample holders were opened in another glovebox, and were loaded with microscopical particles from Ryugu. Following a similar protocol to that of the outward journey, 32 particles were sent to France under a dry N_2 atmosphere, distributed among four sample-holders (14 particles from the 1st touchdown-site (particles labeled starting with A) in SH2 and SH3, and 18 particles from the 2nd touchdown-site (particles labeled starting with C) in SH1 and SH4). In order to monitor the atmosphere's changes surrounding our sample-holders, a few contingency measures were taken. During the whole trip, the sample-holders were accompanied by a "control"-holder : this one would carry a few control samples that would easily react to changes in the atmosphere, such as iron dust (Iron powder, -200 mesh, 99+% (metals basis), Thermo Scientific™ Alfa Aesar 000737.A1) to monitor oxidation processes. A second "control"-holder, loaded with drierite (calcium sulfate) and some Fe dust, was kept in France, to monitor hydration and oxidation when not under dry N_2 conditions.

III. Sample reception and characterization

III.a Measurements inside the sample-holder (N_2 atmosphere)

The samples arrived at SOLEIL (France) in early July. The sample-holders were first inspected using an optical microscope through the KBr window (Figure 2). We successfully identified 28 out of 32 of the original Ryugu particles by their morphological correspondence with the grains prepared at Tohoku University and/or thanks to their IR "Ryugu-like" spectral signature (mainly the 2.7 µm feature).

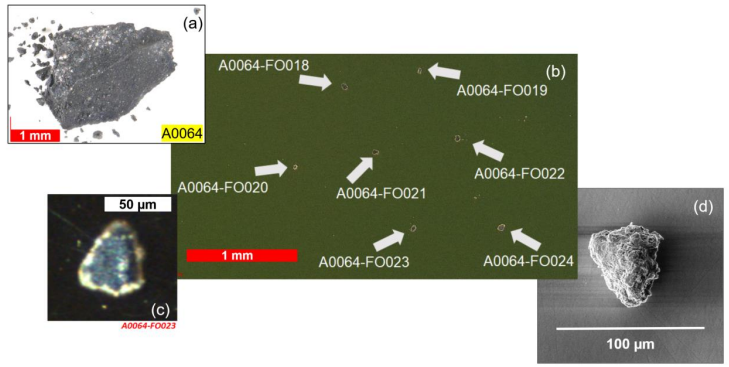

Figure 2. (a) Ryugu mm-size grain A0064, (b) seven microscopic grains picked from A0064 stone, resting on the gold mirror of sample holder #3, (c) visible image of one of the picked grains, A0064-FO023, (d) SEM image of A0064-FO023 (HV 2 kV - 50 pA - ICE detector)

Once the samples were identified, the analytical pipeline began with a full spectral characterization using IR synchrotron beam, from 1 to 50 µm, while keeping the sample-holder sealed to minimize exposure to air. The goal of this first step in our analytical pipeline was threefold :

- ❖ Identify interesting spectral features in each Ryugu grain.
- ❖ Select grains to be mounted on needle for 3D characterization.
- ❖ Have a trace of the 'unaltered' state of the grains, prior to the opening of sample-holder, to follow grain alteration.

Our sample-holder design allowed us to easily acquire measurements using multiple instruments without the risk of compromising the samples. In order to cover the above-mentioned spectral range, we used three different FTIR microscopes (see Figure 3):

1) a Continuum microscope with a FTIR spectrometer equipped with an MCT/B detector, synchrotron-radiation-fed, allowing us to probe both the Near and Mid-IR spectral ranges (from 1 to 18 µm);

2) a NicPlan microscope with a IS50 FTIR spectrometer (Thermo Fisher), equipped with a bolometer detector (boron doped silicon, 4.2 K cooled, Infrared Laboratories) and a solid-state Si beamsplitter, allowing us to probe the Far-IR range (from 15 to 50 µm);
3) an Agilent Cary 670/620 micro-spectrometer using the internal Globar source, equipped with a focal plane array (FPA) detector, allowing us to acquire spectral maps and hyperspectral images in the Mid-IR range (from 2.5 to 12 µm).

The large spectral coverage obtained by coupling all these instruments allowed us to detect carbonates (around 7 µm), organics (around 3.4 and 6.2 µm), and phyllosilicates minerals (around 2.7 µm for the Metal-OH stretching vibration and 10 µm for the SiO stretching vibration). Hyperspectral imaging in the mid-IR allowed us to start probing the composition heterogeneity of isolated grains.

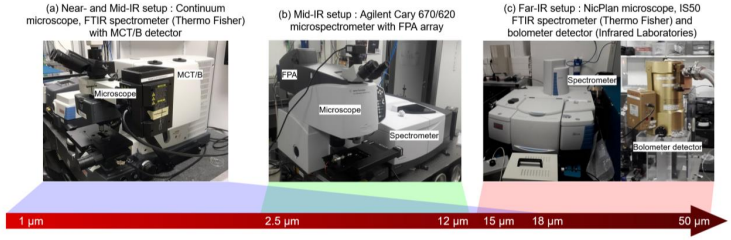

Figure 3. The different systems used and their respective spectral ranges

Raman spectra and maps were also acquired to investigate the characteristics of the endemic aromatic organics in Ryugu's grain, as well as to complement mineral identification data. These measurements were done on isolated small fragments detached from the main grains, to avoid alteration from the Raman laser.

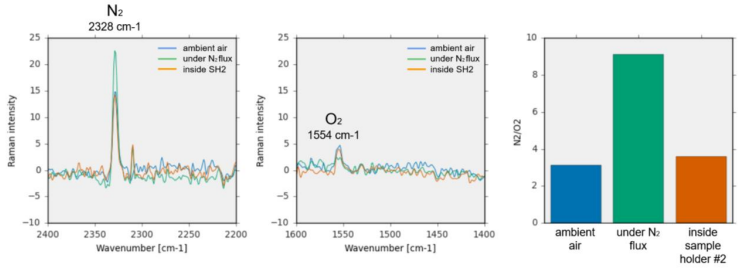

Figure 4 . Raman spectra on SH2, detecting presence of both N_2 and O_2 inside, with an N_2/O_2 ratio similar to that of ambient atmosphere

Raman was also used to detect molecular oxygen inside one of the sample holders (SH2, see Figure 4), indicating that the holders had lost their air-shut condition at some point, probably in flight from Japan to France. Upon reception, we realized that the small static-shielding bags holding the sample-holders were torn open, possibly due to the pressure difference between the inside and the outside of the bags during the flight. This had probably led to the air from the larger static-shielding bag entering the sample-holders. The grains may have been exposed to air for about 72-96 hours during transportation, before putting them again in a dry N_2 atmosphere. However, we did not observe any modification on the sample holder's KBr window (a control KBr window we exposed to air for 24h showed clear modifications). We inferred that Ryugu grains remained in a relatively dry environment in spite of the presence of O_2, probably thanks to the presence of numerous desiccant packs in the traveling case, which prevented an increase of humidity.

To easily acquire spectroscopic measurements through the KBr window, the grains were arranged onto a gold mirror. This fact had unforeseen consequences on the spectroscopic measurements of all small particles, with the collected spectra showing some peculiarities affecting the surface scattering spectral region (from approximately 9 µm and above). In standard conditions, the IR beam would shine onto the particle surface, be reflected by the grain's surface and be then collected for analysis. This is what we observed for the largest particle in our set of grains, which had a size of approximately 150 µm (Figure 5, left panel). However, for smaller particles (size < 100 µm), the IR beam is able to go through the grain, similar to what happens in transmission measurements. The transmitted beam would then hit the gold mirror where the particle would rest, shining back inside and through the measured

grain, to be collected for spectral analysis (Figure 5, right panel). This means that the collected beam would be a mix of reflected signal and double-transmitted signal. Their respective contributions may be difficult to gauge, but for small grains one would think that this double-transmitted signal would dominate. The consequences of this effect on the spectra measured in these conditions are the following :

- Inversion of the spectral bands in the surface scattering region (above 9 µm) ;
- Interpretation of band intensity is not straightforward.

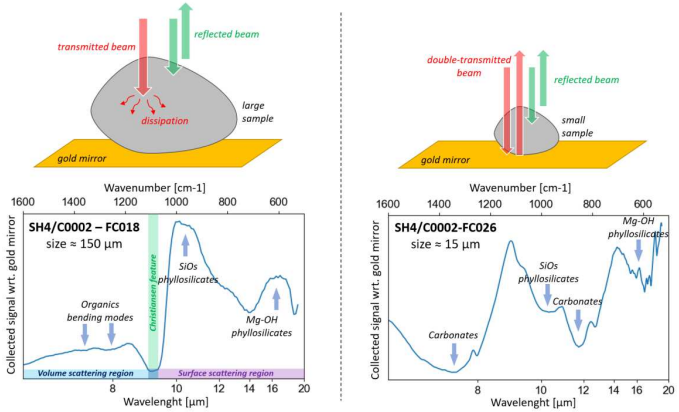

Figure 5. [left panel] cartoon modeling large grain behavior for infrared measurements on gold ; in the bottom panel, the collected signal with respect to a gold background from C0002-FC018, the largest grain in our set (size of approximately 150 µm). The collected signal behaves as expected from a standard reflectance measurement (spectral bands point downward before the Christiansen feature and upward after). [right panel] cartoon modeling large grain behavior for infrared measurements on gold, highlighting the contribution of a double-transmitted beam going through the sample and shining back towards the detector ; in the bottom panel, the collected signal with respect to a gold background from C0002-FC026, one the the smaller grains in our set (size of approximately 15 µm). The collected signal behaves erratically, with all the bands pointing downwards. The collected signal behaves like a transmission spectrum, even though it has been acquired in a reflectance configuration.

This quirk makes the interpretation of the collected signal from small grains more delicate but does not invalidate the usefulness of the measured spectra.

III.b Measurements out of the sample-holder (ambient air)

Based on the spectral properties obtained with the first step of our analytical pipeline, we selected 9 grains to be mounted on W and Al needle for 3D characterization. The sample holders were opened, and the grains were mounted on W or Al needles using Pt-weld at two different FIB-SEM microscopes in Saclay and in Lille (Aléon-Toppani et al. 2021). These mounted grains underwent then 3D characterization in both transmission and reflectance, using Infrared Computed Tomography (IR-CT) and Infrared Surface Imaging (IR-SI) respectively (see Figure 6). IR-CT allows us to assess the compositional heterogeneity of small particles in a 3D space (Zelia Dionnet et al. 2020), while IR-SI allows us to assess the surface composition for larger particles, treating the grain as a planetary surface by projecting the 2D IR hyper-spectral maps on a 3D shape model (Zélia Dionnet et al. 2022). From mounted grains, FIB sections are extracted to perform TEM analysis, following similar procedures to what are described in Aléon-Toppani et al. (2021).

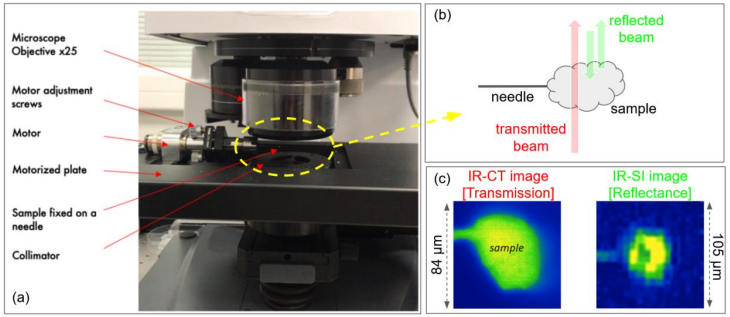

Figure 6. IR-CT and IR-SI principle of measurement. (a) description of 3D measurements setup pieces, (b) schematization of beam path for IR-CT measurements (transmitted beam) and IR-SI (reflected beam), (c) example of 1 hyperspectral image from IR-CT and IR-SI imaging techniques. For IR-CT, 90 images are acquired, one every 2°, rotating the sample from 0° to 180° : the final dataset consists of 128x128x90 spectels. For IR-SI, 18 images are acquired, one every 20°, rotating the sample from 0° to 360° : the final dataset consists of 32x32x18 spectels.

The grains that have not yet been mounted remained in their respective sample-holder. Some of these grains underwent complementary measurements, such as Raman and visible near IR (Vis-NIR) micro-spectroscopy (Maupin et al. 2020). All grains are kept in a N_2 atmosphere when they are not being measured.

IV. Conclusion

We received in July 2021 several particles from the asteroid Ryugu as part of the "STONE" preliminary analysis team. The samples traveled in a custom-made sample holder which allowed spectroscopic measurements while preserving the samples from weathering phenomena due to their exposure to the atmosphere. The sample-holders lost their air-shut condition during the trip but were exposed only to dry air for less than 96 hours, as the control samples which traveled alongside Ryugu's samples showed. Upon arrival, the N_2 atmosphere was restored and the samples were subjected to a precise analytical pipeline, presented in Figure 7, with the goal of maximizing the scientific output achievable before possible sample loss.

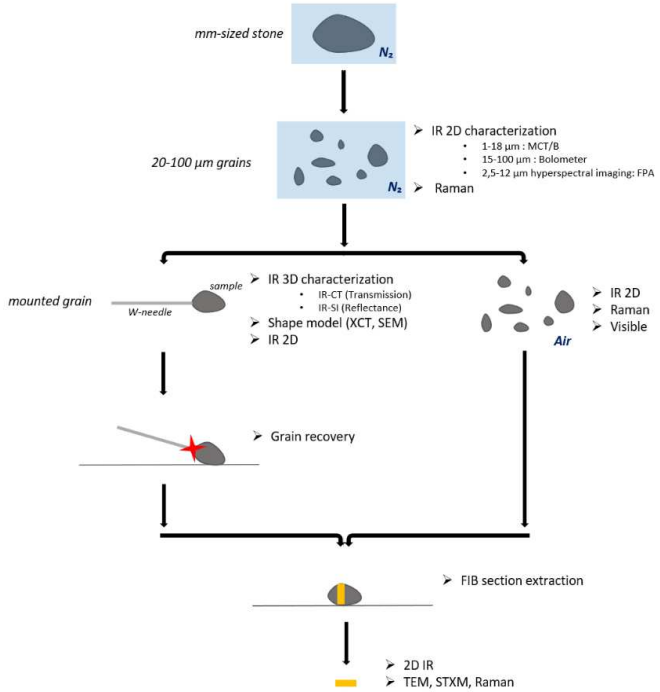

Figure 7. Cartoon summarizing the analytical pipeline used for Ryugu's particles. Note that everything is stored under a dry N_2 atmosphere when not in this pipeline.

Beside the loss of the air-shut condition of the sample-holders due to the pressure difference between the first layer of static shielding bags and the air inside the airplane cabin (issue which could be dealt with by replacing the first layer of static shielding bags with a hard-shell vessel, such as a flange), the analytical pipeline summarized here allowed to fully characterize the spectral response of multiple grains in the IR range (from 1 to 50 µm), in both 2D and 3D, coupled with Raman and visible spectroscopy, prior to subjecting the samples to smaller scale and more destructive electron microscopy measurements. The entire process granted us complementary results providing great insight on this very precious material.

Declarations

Availability of data and materials

The data that support the findings of this study are available from the corresponding author, Stefano Rubino (stefano.rubino@universite-paris-saclay.fr) upon reasonable request.

Competing interests

The authors declare no competing interests.

Funding

This work has been funded by the CNES-France (Hayabusa2 mission) and by the ANR project CLASSY (Grant ANR-17-CE31-0004-02). The micro-spectroscopy measurements were supported by grants from Region Ile-de-France (DIM-ACAV) and SOLEIL.

Authors' contributions

This work is part of the multi-analytical sequence of the Hayabusa2 "Stone" MIN-PET group, led by Tomoki Nakamura. Authors from Tohoku University selected and prepared the samples in the custom-made sample holders. The IAS/Soleil team handled the conception of these sample-holders. Their transportation from Soleil to Tohoku University (and back) was possible thanks to a joint effort from both two teams. The IAS/Soleil team also conducted the measurements in Soleil. Eva Héripré and David Troadec are responsible for mounting the microscopic samples on the metal needles for IR-CT and IR-SI.

Acknowledgments

We thank Moe Matsuoka for her precious help in preparing and sending Ryugu's particles from Sendai-Japan all the way to Orsay-France.

References

Aléon-Toppani, Alice, Rosario Brunetto, Jérôme Aléon, Zelia Dionnet, Stefano Rubino, Dan Levy, David Troadec, et al. 2021. "A Preparation Sequence for Multi-analysis of µm-sized Extraterrestrial and Geological Samples." *Meteoritics & Planetary Science* 56 (6): 1151–72.

Dionnet, Zélia, Alice Aléon-Toppani, Rosario Brunetto, Stefano Rubino, Martin D. Suttle, Cateline Lantz, Chrysa Avdellidou, et al. 2022. "Multiscale Correlated Analysis of the Aguas Zarcas CM Chondrite." *Meteoritics & Planetary Science*, March. https://doi.org/10.1111/maps.13807.

Dionnet, Zelia, Rosario Brunetto, Alice Aléon-Toppani, Stefano Rubino, Donia Baklouti, Ferenc Borondics, Anne-Cécile Buellet, et al. 2020. "Combining IR and X-ray Microtomography Data Sets: Application to Itokawa Particles and to Paris Meteorite." *Meteoritics & Planetary Science* 55 (7): 1645–64.

Lauretta, D. S., S. S. Balram-Knutson, E. Beshore, W. V. Boynton, C. Drouet d'Aubigny, D. N. DellaGiustina, H. L. Enos, et al. 2017. "OSIRIS-REx: Sample Return from Asteroid (101955) Bennu." *Space Science Reviews* 212 (1): 925–84.

Maupin, Romain, Zahia Djouadi, Rosario Brunetto, Cateline Lantz, Alice Aléon-Toppani, and Pierre Vernazza. 2020. "Vis–NIR Reflectance Microspectroscopy of IDPs." *The Planetary Science Journal* 1 (3): 62.

Nakamura, T. et al. 2022. "Formation and evolution of Cb-type asteroid Ryugu: direct evidence from returned samples" *Science* (submitted)

Vernazza, P., P. Beck, O. Ruesch, A. Bischoff, L. Bonal, G. Brennecka, R. Brunetto, et al. 2021. "Sample Return of Primitive Matter from the Outer Solar System." *Experimental Astronomy*, October. https://doi.org/10.1007/s10686-021-09811-y.

Watanabe, Sei-Ichiro, Yuichi Tsuda, Makoto Yoshikawa, Satoshi Tanaka, Takanao Saiki, and Satoru Nakazawa. 2017. "Hayabusa2 Mission Overview." *Space Science Reviews* 208 (1): 3–16

The Meteoritical Society

Meteoritics & Planetary Science 57, Nr 5, 965–988 (2022)
doi: 10.1111/maps.13807

Multiscale correlated analysis of the Aguas Zarcas CM chondrite

Zélia DIONNET[1,2,3]*, Alice ALÉON-TOPPANI[1], Rosario BRUNETTO[1], Stefano RUBINO[1], Martin D. SUTTLE[4], Cateline LANTZ[1], Chrysa AVDELLIDOU[5], Donia BAKLOUTI[1], Ferenc BORONDICS[6], Zahia DJOUADI[1], Francesco GRIECO[7], Eva HÉRIPRÉ[8], Tomoki NAKAMURA[9], Alessandra ROTUNDI[2,3], and Mario SCHEEL[6]

[1]Institut d'Astrophysique Spatiale, CNRS, Université Paris-Saclay, Orsay 91405, France
[2]Dip. Di Scienze Applicate, Università di Napoli Parthenope, Centro Direzionale di Napoli, Isola C4, Naples 80143, Italy
[3]Istituto di Astrofisica e Planetologia Spaziali—INAF, Rome, Italy
[4]School of Physical Sciences, The Open University, Walton Hall, Milton Keynes MK7 6AA, UK
[5]Observatoire de la Côte d'Azur, Laboratoire Lagrange, CNRS, Université Côte d'Azur, Blvd de l'Observatoire, Nice Cedex 4 06304, France
[6]SOLEIL Synchrotron, Gif-sur-Yvette, France
[7]Department of Physics and Astronomy, University of Ghent, Ghent, Belgium
[8]CentraleSupélec, CNRS, Laboratoire de Mécanique des Sols, Université Paris-Saclay, Structures et Matériaux, Gif-sur-Yvette 91190, France
[9]Division of Earth and Planetary Materials Science, Laboratory for Early Solar System Evolution, Tohoku University, Sendai, Japan
*Corresponding author: E-mail: zelia.dionnet@universite-paris-saclay.fr

(Received 09 October 2021; revision accepted 21 February 2022)

Abstract–In this paper, we report the results of a campaign of measurements on four fragments of the CM Aguas Zarcas (AZ) meteorite, combining X-ray computed tomography analysis and Fourier-transform infrared (FT-IR) spectroscopy. We estimated a petrologic type for our sampled CM lithology using the two independent techniques, and obtained a type CM2.5, in agreement with previous estimations. By comparing the Si-O 10-μm signature of the AZ average FT-IR spectra with other well-studied CMs, we place AZ in the context of aqueous alteration of CM parent bodies. Morphological characterization reveals that AZ has heterogeneous distribution of pores and a global porosity of 4.5 ± 0.5 vol %. We show that chondrules have a porosity of 6.3 ± 1 vol%. This larger porosity could be inherited due to various processes such as temperature variation during the chondrule formation and shocks or dissolution during aqueous alteration. Finally, we observed a correlation between 3D distributions of organic matter and mineral at micrometric scales, revealing a link between the abundance of organic matter and the presence of hydrated minerals. This supports the idea that aqueous alteration in AZ's parent body played a major role in the evolution of the organic matter.

INTRODUCTION

CM chondrites are the most abundant samples among carbonaceous chondrites and hydrated meteorite (Suttle et al., 2021). There is significant diversity among CM chondrites as they exhibit evidence of varying degrees of aqueous alteration and brecciation (Brearley, 2013; Brearley & Jones, 1998; Chizmadia & Brearley, 2008; Metzler et al., 1992). Thus, they represent very valuable sources to understand the mechanisms involved in aqueous alteration and the nature of alteration products (e.g., Hanowski & Brearley, 2001; Hewins et al., 2014). Aguas Zarcas (AZ) is a recent CM fall recovered from Costa Rica in 2019. Thanks to a rapid recovery, hundreds of fragments were collected before local rainfall. This makes the samples from this carbonaceous chondrite very valuable because terrestrial alteration is highly limited, as proven by a fresh fusion crust (Martin & Lee, 2020) and the absence of common weathering products. This chondrite is classified as a CM2 breccia in the Meteoritical Bulletin (Gattacceca et al., 2019). In 2020, several groups presented the results of preliminary characterizations and analyses of several fragments of AZ (Davidson et al., 2020; Hicks & Bridges, 2020; Kebukawa et al., 2020; Kouvatsis & Cartwright, 2020; Pizzarello et al., 2020; Takir et al., 2020; Tunney et al., 2020; Villalon et al., 2020) describing at least three main lithologies: one rich in metal and two CM lithologies, including a chondrule-rich and a chondrule-poor variety.

More recently, Kerraouch et al. (2021) described five different lithologies, reflecting the petrographic diversity of materials preserved in the AZ meteorite. They distinguished a brecciated CM lithology, a C1/2 lithology, a C1 lithology, and two distinct metal-rich lithologies. According to them, the presence of multiple lithologies and their intricacy at millimetric scale as well as the presence of unique and rare lithologies in AZ indicates a complex history in a "highly dynamic environment." Thus the history of AZ could be comparable to the history of the rubble-pile asteroids Ryugu and Bennu, which are interpreted as second-generation parent bodies, formed by disruption and reaccretion (Michel et al., 2020; Okada et al., 2020; Walsh et al., 2020). The recent discovery of pyroxene brecciated boulders on the surface of Bennu has confirmed this hypothesis (DellaGiustina et al., 2021). Kerraouch et al. (2021) concluded that "the different lithologies of the fresh AZ breccia, which represent different levels of hydration and heating, are good analogs for the types of materials that will be returned from asteroids Bennu and Ryugu." More recently, analyses of Ryugu grains have shown that their spectra are different from the ones of CM meteorites and more similar to the ones of CI chondrites (Pilorget et al., 2021; Yada et al., 2021). However, the remote sensing spectrum of asteroid Bennu measured by the OTES instrument onboard OSIRIS-REx (Hamilton et al., 2021) has shown that Bennu is closer to CM chondrites. This makes the AZ meteorite, and more generally fresh CM chondrites, high priority samples for further investigation.

The mineralogy of AZ has been described in several abstracts (see Hicks & Bridges, 2020; Takir et al., 2020). They have described abundant phyllosilicate (mainly serpentine) mixed with olivine and pyroxene grains and FeNi sulfides. Some groups have also shown that the organic matter contained in AZ is also intriguing (Pizzarello et al., 2020; Tunney et al., 2020). According to Kebukawa et al. (2020), the organic compounds present inside the metal-rich lithologies are unique with high aliphatic concentrations, indicating a more primitive nature relative to the organic matter found in a "typical" CM lithology. However, they described this CM-like lithology as very comparable to that measured from Murchison. Likewise, Glavin et al. (2021) studied the amino acids and found similar properties to those measured in Murchison. The heterogeneity of the organic matter, resulting from very different postaccretional histories, inside a single meteorite reinforces the idea of a complex history with reagglomeration, as presented by Kerarouch et al. (2021) inside AZ, and inside other carbonaceous chondrites (Changela et al., 2018; Le Guillou et al., 2014, Vinogradoff et al., 2017). Therefore, multiscale correlated analysis of the different lithologies within the AZ meteorite has the potential to unlock new insights into the interaction between silicate rock and organics on primitive C-type asteroids.

In this paper, we report the results of a multianalytical campaign on four fragments of different sizes from the AZ meteorite. In the first section, we present the results of a synchrotron-based X-ray computed tomography (XCT) characterization on a millimetric fragment of AZ to explore the structural diversity of this meteorite. The XCT data also allowed us to calculate the microporosity of AZ. We then describe Fourier-transform infrared (FT-IR) reflection measurements on a millimetric fragment of AZ to get a large-scale first look at its molecular composition and to obtain the average AZ spectrum, which can be compared to remote sensing observation of asteroid surfaces (Hamilton et al., 2021; Kitazato et al., 2019). Finally, we performed complementary measurements on two small fragments of AZ by FT-IR hyperspectral imaging, to study organic matter and characterize the mineral phases at a higher spatial resolution (1–100 μm). In the Discussion section, we combined information obtained from FT-IR and X-ray imaging over a wide range of length scales from the millimeter scale down to the micron scale, and used these to discuss different stages of AZ's history.

MATERIALS AND METHODS

Sample Description and Analytical Plan

At the Institut d'Astrophysique Spatiale (IAS), we obtained a mm-sized fragment of AZ with a mass of approximately 0.15 g. Four fragments of different sizes were extracted from this large fragment and analyzed by different analytical methods requiring different preparation. Table 1 summarizes the characteristics of the four studied fragments, while a more complete description of each fragment and the associated analysis is given below. Note that AZ-3 sections are focused ion beam (FIB) sections that were extracted from fragment AZ_3.

[Correction added on 26 Apr 2022, after first online publication: The spelling of the 11th author "Francesco Greco" was changed to "Francesco Grieco".]

Table 1. Inventory of AZ fragments studied in this work, including details of the different analytical methods and fragment preparation procedures used.

Name	Size	Applied measurement	Sample preparation
AZ_1	Surface: 300 × 300 μm	FT-IR–reflection	Raw fragment
AZ_2	1160 × 920 × 400 μm	X-CT	Raw fragment
AZ_3	20 × 15 × 30 μm	FT-IR–reflection + IR-CT	Welded on W needle
AZ_3_sections	2 μm thin	FT-IR–2D transmission + Raman + EDS	FIB sections of AZ_3
AZ_4	200 × 200 × 11 μm	FT-IR–2D transmission	Crushed inside diamond cell

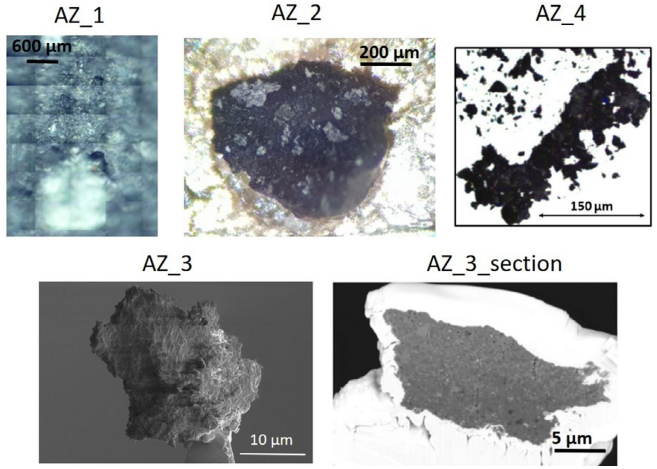

Fig. 1. Optical images (for AZ_1, AZ_2, and AZ_4) and SEM images (for AZ_3 and AZ_3_section) of the fragments of the AZ meteorite studied in this paper. (Color figure can be viewed at wileyonlinelibrary.com.)

First of all, FT-IR imaging analysis in reflection mode was performed on a small part of the surface of the largest fragment (AZ_1) (Fig. 1). The AZ_1 fragment was later subsampled using a scalpel, generating a smaller chip (AZ_2: 1160 μm × 920 μm × 400 μm size), which was then analyzed by XCT.

A first micrometric fragment AZ_3 (20 × 15 × 30 μm^3) was then analyzed using 3D FT-IR hyperspectral imaging to study the 3D distribution of the different phases. This fragment was naturally detached from the bulk (neither selection nor preparation). It was welded onto the tip of a tungsten needle by platinum ion beam-induced deposition (as in Aléon-Toppani et al., 2021). Measurements in reflection at different angles were first acquired on the small fragment AZ_3 to obtain data on the fragment's surface composition. We then performed FT-IR tomography (see Dionnet, Brunetto, et al. [2020] for a description of the method) to analyze the abundance and 3D distribution of mineral phases and organic matter inside the fragment while preserving its physical integrity. Thanks to this 3D characterization, we were able to visualize the compositional heterogeneity inside the fragment and subsequently select specific areas to study at higher resolution. We then extracted three FIB sections (3 μm thickness) from the AZ_3 fragment by using FIB preparation, and performed FT-IR and Raman microspectroscopy on them (see Aléon-Toppani et al. [2021] for the description of the full protocol on a 3D fragment to FIB sections).

The FIB sections were later analyzed by energy-dispersive X-ray spectroscopy (EDS) in a scanning electron microscope (SEM) to retrieve the structure and elemental composition. These analyses at smaller scales are well adapted for studying the carbonaceous component and its mineral host, down to the micrometer scale (Aléon-Toppani et al., 2021).

Finally, another micrometric fragment AZ_4 was analyzed using a more invasive and classical preparation: fragment AZ_4 was crushed inside a diamond compression cell (as in Merouane et al. [2012] and in Dionnet et al. [2018]), forming a flattened sample with a thickness of ~11 μm and a surface area below 200 × 200 μm. In such preparation, we lose information about the 3D structure but we maximize the IR response of the organic and mineral signatures in transmission by reducing scattering effects.

XCT Analyses: Measurement and Data Treatment

XCT measurements were performed at the synchrotron SOLEIL (France) on the ANATOMIX beamline (Weitkamp et al., 2017) for fragment AZ_2, with a monochromatic beam at 16.87 keV and a voxel size of 0.325 μm for a field of view of 0.65 mm^2. Thanks to X-ray 2D detectors, we measured 2000 projections that were normalized using corresponding flat- and dark-field images. The filtered projections allow reconstruction of a 3D volume using ring filters (Paganin et al., 2002) by means of the academic software PyHST2 (Mirone et al., 2014). The voxel value in the 3D volume corresponds to the linear attenuation coefficient (LAC) of the material.

The LAC gives indications about the average atomic number of the probed matter, meaning that features with high-density contrast, such as pores, can be quickly resolved. First, we segmented our data using a LAC threshold that discriminates two components: pores versus silicate phases. A more detailed description of this method is presented by Dionnet, Suttle, et al. (2020). After data segmentation, we measured the porosity by counting the number of empty voxels inside the fragment divided by the number of voxels composing the fragment. These data also allowed us to study the size and the shape distributions of the different populations of voids with a resolution around 1 μm. The study of pore anisotropy employed the Quant3D software (Ketcham, 2005; Ketcham & Ryan, 2004).

We then performed a more complex segmentation. As suggested by Griffin et al. (2012), features inside a CM chondrite can be identified using segmentation based on the surrounding voxels' average value. In this study, for each silicate-voxel, we generated the histogram of the LAC value for a square of 20 × 20 voxels around the voxel of interest. We then estimated the mean and the standard deviation of this distribution and used these values to classify the voxel. Finally, based on knowledge of CM chondrites (Howard et al., 2015) and previous studies of AZ, we are able to identify regions with different LAC values as common components inside CM chondrites. For instance, chondrules correspond to darker areas with a quite large standard deviation, by contrast, tochilinite-cronstedtite intergrowths (TCIs) can be identified as bright areas with a very small dispersion of the LAC distribution. Thanks to this second segmentation, we have estimated volume proportions of the chondrules and the TCIs within the matrix.

A manual inspection helped us to determine specific parameters on a few chondrules. First, we extracted their size and morphological properties. We then performed 3D analyses of small regions around some representative chondrules. We obtained the chondrule's volume, a description of its shape, and the values of their porosities. All the 3D models presented in this article have been produced thanks to the software Tomviz (tomviz.org).

FT-IR Spectroscopy

FT-IR hyperspectral imaging was performed on the surface of AZ_1, on the two smaller fragments AZ_3 and AZ_4, and on the AZ_3 sections with an Agilent Cary 670/620 microspectrometer coupled to a focal plane array (FPA) detector of 128 × 128 pixels, installed at the SMIS beamline of the SOLEIL synchrotron. Each pixel collects a whole spectrum in the range 850–3950 cm^{-1} (~2.5 to 11.8 μm). Before each analysis, we collected a background using either a gold standard for the reflectance measurements, or a close empty point inside the diamond compression cell for the flattened fragment, or an empty field of view for the transmittance measurements on the needle-mounted fragment. We used the internal Globar source for all the analyses presented in this paper, while in all measurements, the spatial resolution was diffraction-limited (for details, see Dionnet et al., 2018; Sandt et al., 2019).

Representative areas on the surface of the grain AZ_1 were analyzed in reflectance with a ×15 objective at standard magnification (which provides a 5.5 μm projected pixel size) with a spectral resolution of 4 cm^{-1}.

For the fragment AZ_3, we acquired a collection of hyperspectral maps in 2D for the fragment mounted at the tip of the tungsten needle. When rotating the fragment, a 2D hyperspectral map in reflectance was acquired every 20° with a pixel size of 3.3 μm (×25 objective in standard magnification mode) and a spectral resolution of 8 cm^{-1}. These 2D hyperspectral reflectance maps can be projected on a 3D shape model obtained from the high resolution images collected in the SEM at different angles, providing a novel technique of combining FT-IR and SEM images in 3D,

never used before on an extraterrestrial material. This task is done by comparing and aligning the projections of the SEM 3D model with the infrared reflectance maps. Prominent localized topological or spectral features are used to strengthen the spatial correlation.

The AZ_4 fragment flattened in the compression cell was analyzed in transmittance with the same objective lens (×25) but also employing additional high magnification optics, i.e., with an additional ×5 magnification placed in front of the FPA detector. This gives a 0.66 µm projected pixel size. Here our spectral resolution was 4 cm^{-1}. A similar configuration was used to analyze the FIB sections extracted from the second micrometric grain (AZ_3).

Finally, for the infrared computed tomography (IR-CT) measurements (Yesiltas et al., 2016), we collected 180 2D hyperspectral maps (projections) in transmission with a pixel size of 0.66 µm (×25 objective in high magnification mode) and a spectral resolution of 4 cm^{-1} (for further details, see the method described by Dionnet, Brunetto, et al., 2020).

Raman Microspectroscopy

We acquired Raman spectra on the three FIB sections extracted from the fragment AZ_3, in order to characterize the aromatic component of their organic matter and to determine AZ's organic heterogeneity. The Raman spectrometer used was a Thermo Fisher with a 532 nm exciting laser radiation. Maps on the FIB sections were recorded with a laser spot through an Olympus UIS2 100X/0.90 NA LWD objective providing a spot size of about 1 µm. The laser power was less than 0.3 mW, similar to previous studies on the Paris meteorite (Dionnet et al., 2018) in order to avoid any laser-induced damage to the samples.

SEM-EDS Analysis

In addition to secondary electron images, some quantitative analyses were also performed on AZ_3 FIB sections with EDS on a SEM. SEM-EDS acquisitions were done at 20 keV on a Thermo Fisher HELIOS Nanolab 660 dual beam microscope fitted with an EDAX Octane super 30 mm^2 EDS analytical system. These analyses were used to extract the ratio Mg/Fe on few locations inside FIB sections. SE images have been analyzed to extract porosity with a resolution of 0.1 µm thanks to the threshold method using ImageJ. The choice of the threshold and saturation of the sample due to charging effects are the main errors sources. The estimation of the porosity is thus obtained with a relative error of 15%.

RESULTS

XCT Analyses: Morphological Description at the Large Scale

Global Description of the Morphological Properties

Fragment AZ_2 is very heterogeneous, showing a complex assembly of minerals with different LAC and thus various compositions. The main structures are identified in Fig. 2. We can distinguish two main distinct components, which most likely correspond to different lithologies:

(i) Most of the fragment has a texture similar to the one described in the CM-lithology of AZ (Kerrouach et al., 2021). Based on this previous study and expected composition of CM chondrites (Howard et al., 2015), we have inferred the identification of the different components visible in XCT images. Indeed, Fig. 2 reveals the presence of many structures embedded inside a fine-grained matrix (Howard et al., 2015; Kerrouach et al., 2021; Leroux et al., 2015).

The fragment AZ_2 contains a lot of bright rounded regions. These regions have a higher LAC than the matrix, as they contain more iron. They are interpreted as TCIs, which are common features in CM chondrites that have experienced mild to moderate degrees of aqueous alteration (Rubin et al., 2007). Previously, Martin and Lee (2020) also noticed the presence of numerous TCIs in the matrix of AZ. Using the segmentation procedure, we determine that TCIs represent 26 vol% of the CM-like lithology in this fragment. This value is consistent with the expected values for CM chondrites (i.e., between 15 and 40 vol%; Rubin et al., 2007).

Few chondrules are present in this fine-grained matrix. Thanks to the second segmentation protocol, we calculate the relative chondrule abundance as 17 ± 2 vol% in the CM-like lithology. This value with its error bar fits with the estimation presented in Kouvatsis and Cartwright (2020) that chondrules represent around 16 vol% in the chondrule-poor CM lithology. This indicates that the majority of our large fragment comes from the chondrule-poor CM lithology as defined in Kouvatsis and Cartwright (2020).

In addition, we noticed a few multiphase regions, with irregular shapes, enclosed in fine-grained rims. We identified them as possible CAIs. We detected only a few metallic Fe-Ni bearing phases, which is consistent with the SEM-EDS observations performed by Martin and Lee (2020) for lithologies present inside our fragment. Material related to the two metal-rich lithologies identified by Kerraouch et al. (2021) is absent in this fragment.

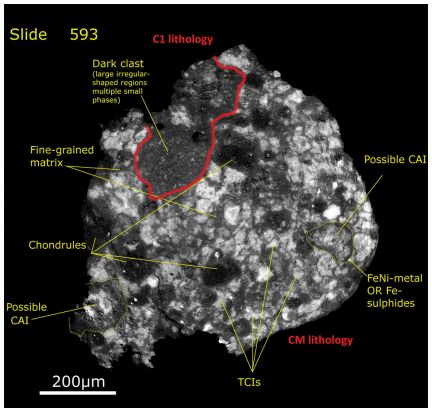

Fig. 2. XCT slice inside the fragment AZ_2 with identification of different components. (Color figure can be viewed at wileyonlinelibrary.com.)

(ii) The second lithology is present in AZ_2 as a small region, visible in the top left of Fig. 2. This lithology has a relatively homogeneous texture at the µm scale and contains some bright inclusions. Its texture is somewhat similar to that of chondrule fine-grained rims. By comparing our data and XCT data published in Kerraouch et al. (2021), we identify this part of the fragment as a clast coming from the C1 lithology, representing 6.5 vol% of the fragment AZ_2. This lithology is composed of matrix phyllosilicates, magnetite, sulfides, and some carbonates (Kerraouch et al., 2021).

Study of Porosity

Our estimation of the porosity inside AZ_2 gave a value of 4.5 ± 0.5 vol% at a voxel size of 0.325 µm. This is similar to porosity values estimated for CMs with image analysis methods (Corrigan et al., 1997). A striking feature of our fragment is that pores are not equally distributed, as illustrated in Fig. 3, where the pores are colored in red. We can distinguish areas with many pores (as for instance the lower left of the fragment presented in Fig. 3) and in contrast, we can also find regions with almost no pores (mainly matrix far from any chondrules or fractures). In the fragment AZ_2, a large proportion of pores (44 vol%) are located near/in chondrules, but only represent 6.5 vol% of the whole fragment.

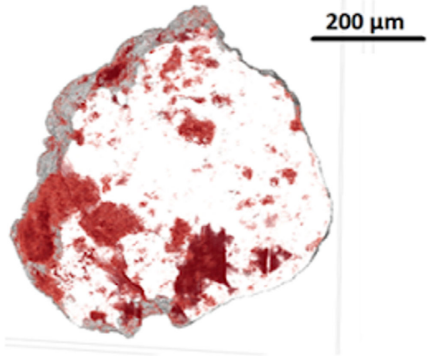

Fig. 3. 3D visualization of half the fragment of AZ_2 (sliced in the middle), with the pores emphasized in red and the edges in gray. The figure allows the visualization of all the pores present in the half fragment. (Color figure can be viewed at wileyonlinelibrary.com.)

Study of Chondrules

A manual identification of 12 porphyritic/granular chondrules was performed to more precisely characterize physical parameters such as chondrule shape, size, and anisotropy. These chondrules have diameters between 40 and 400 µm, which is consistent with the observation of Kouvatsis and Cartwright (2020). Moreover, collection of 3D data facilitated the accurate study of their shape. We observed that chondrules generally have a moderate elongated shape: average anisotropic index $A = 4.25$ (an anisotropic coefficient of 1 means spherical shape and the larger is the value of A, the more elongated are the studied components). However, we did not observe any preferred orientation of the elongation direction.

Finally, we determined an average porosity of 6.3 ± 1 vol% inside the chondrules, which varies among individual chondrules: with low values inside smaller chondrules (as the one shown in Fig. 4b) and higher values inside chondrules that are located near fractured regions (see Fig. 4a). Some chondrules present internal elongated pores as in Fig. 4c, not associated with fractures inside the whole fragment. The pores inside chondrules are elongated with an anisotropic coefficient of $A = 6.25$. Notably, pores inside elongated chondrules often follow the direction of the elongation of their respective chondrule. As a point of comparison, we also estimated the anisotropy coefficient of pores

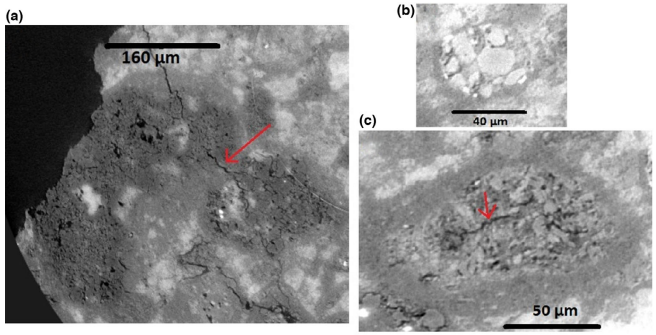

Fig. 4. XCT images of representative chondrules inside CM's lithology inside the fragment AZ_2. The arrows indicate elongated fractures inside or near chondrules. (Color figure can be viewed at wileyonlinelibrary.com.)

present inside the matrix (A = 11.3). This very high value means that pores detected in this study (at the micrometric scale) are mainly present in the form of long cracks inside the matrix.

FT-IR Spectroscopy in Reflection: Mineral Components and Their Heterogeneity

We conducted two multiscale campaigns using FT-IR hyperspectral imaging. The following section presents the results we obtained in reflectance at the surface of the large fragment (AZ_1) and on the small 3D fragment (AZ_3). We have performed this study to characterize the mineral components and their heterogeneity. Moreover, spectra obtained in reflectance are valuable as they are comparable to remote sensing data.

Average Mid-Infrared Spectra at Large Scale

The large chip (grain AZ_1) was analyzed in reflection with a ×15 objective in order to obtain FT-IR spectra representative of the whole fragment. The average spectrum of the matrix was obtained by averaging 16,384 spectra, corresponding to an area of 700 µm × 700 µm. Moreover, another area was analyzed at the edge of a chondrule to obtain the spectra of a large chondrule (this chondrule has a diameter around 800 µm) and this time, we averaged the 76 spectra corresponding to the big chondrule. Both spectra are presented in Fig. 5.

The mid-infrared (MIR) spectra (Fig. 5a) can be divided into two parts, affected by different scattering regimes. The Christiansen feature, around 1100 cm^{-1} (~9.1 µm), marks the boundary between the surface scattering regime for higher wavelengths and the volume scattering regime for lower wavelengths. The main retstrahlen band is centered around 1000 cm^{-1} (10 µm) and is related to the Si-O stretching modes of silicates. In the average spectra of the matrix, we observed a broad band centered around 1000 cm^{-1} (10 µm). At high wave numbers, we observe a large band due to water stretching mode between 3000 and 3700 cm^{-1} with a small shoulder due to OH at 3660 cm^{-1} (~2.7 µm). Measurements were performed under ambient air and a part of the detected water is due to adsorbed water. This contribution is an issue for quantitative study of water but does not affect quantitative comparison of various regions inside a single sample as discussed below.

In hydrated carbonaceous chondrites, the OH band is typical of phyllosilicates (Beck et al., 2014). Water bending modes are responsible for a weak band at 1640 cm^{-1} (~6.1 µm). As described in Beck et al. (2014), the 10 µm profile in our average spectra is similar to a saponite profile, whereas the main expected component of CM carbonaceous chondrites is serpentine as discussed by Howard et al. (2015). Beck et al. (2014) hypothesized that the saponite-like profile for serpentine in CM could be due to (i) serpentine having especially low crystallinity, which impacts the infrared spectra; or (ii) it could be due to the effect of cation substitutions in the serpentines. Thus, we also conclude that in our spectra the large broad band is attributed to serpentine.

On the contrary, the spectra from the chondrule reveal a multipeaked band, with a main peak at

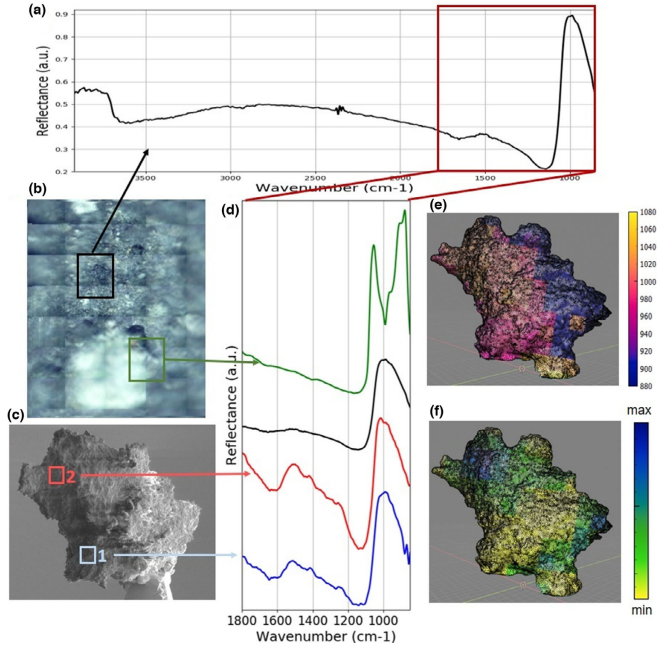

Fig. 5. a) Average FT-IR spectrum of the measured chip surface AZ_1. b) Visible image of the fragment AZ_1. c) SEM images of the 3D small fragment AZ_3. d) Zoom of reflectance spectra in the range 1800–850 cm^{-1} for the average spectrum in black, inside a chondrule in green and for areas 1 and 2 of panel (c) in red and blue. e) Projection of the SiO band position on the 3D volume: regions in pink and yellow correspond, respectively, to a maximum of the SiO band around 980 and 1010 cm^{-1}. A part of the fragment was slightly out of focus for this angle and produced a noisier spectrum (blue region in panel [e]). f) Intensity of the H_2O bands at 1614 cm^{-1} distribution projected on the 3D volume: more hydrated areas appear in blue and less hydrated ones in yellow. (Color figure can be viewed at wileyonlinelibrary.com.)

1056 cm^{-1} (~9.5 µm), a smaller shoulder at 965 cm^{-1} (~10.4 µm), and a strong contribution at 874 cm^{-1} (~11.4 µm), which corresponds to a composition dominated by anhydrous olivine (Hamilton, 2010).

In addition, on the matrix spectra, we also observed very weak contributions of CH features around 2900 and 3000 cm^{-1} (~3.4 to 3.3 µm) for the stretching modes and between 1200 and 1400 cm^{-1} (~8.3 to 7.1 µm) for CH bending vibrations and aromatic C = C stretching vibrations. Organic matter is more visible in IR transmission and thus a more precise characterization will follow in FT-IR hyperspectral imaging in transmission: organic component and its heterogeneity. Even if aliphatic organic matter is expected to be present in the AZ's spectra, terrestrial contamination cannot be totally excluded. Indeed, a study on powders has shown that CH features in reflectance could also be attributed to contamination by volatile hydrocarbons induced by exposure to air in the laboratory (Salisbury et al., 1991). It is difficult to conclude based only on the average spectra presented in Fig. 5. Hyperspectral imaging in transmission discussed later will help to remove this ambiguity about the indigenous or exogenous origin of aliphatic matter.

3D Studies in Reflection on Preserved Fragments

Reflectance spectra were also collected on the 3D, topographically complex surfaces of the small fragment AZ_3 (as shown in Fig. 5c in a SEM image of the

fragment). These spectra show large bands of Si-O, typical of phyllosilicate. Their band centers vary between 980 cm^{-1} (~10.2 μm) and 1010 cm^{-1} (~9.9 μm) in different areas of the fragments (see Fig. 5e). Figure 5f shows the heterogeneity in terms of hydration at the surface of the fragment AZ_3. We notice the presence of a more hydrated area at the top of the fragment, which correlates with a small shift of the silicate band position toward larger wavelengths (see area 2 in Fig. 5c).

FT-IR Hyperspectral Imaging in Transmission: Organic Component and Its Heterogeneity

Reflectance measurements are quite sensitive to inorganic silicate phases and therefore provide information on the identity and diversity of mineral phases. Here, using transmission IR spectroscopy, we are able to collect complementary information on the organic phases and their relationship to the mineralogy in two of the smaller fragments (AZ_3 and AZ_4) extracted from the CM-like lithology.

3D Studies in Transmission on Preserved Fragments

We performed IR-CT on the small fragment AZ_3. This technique allows us to analyze the fragment's internal composition. Figures 6b–d show the reconstructed area under different bands in the FT-IR spectra, which are proportional to the volume concentration of different components (for more details on IR-CT, see Dionnet, Brunetto, et al. 2020). The continuum represents the distribution of the matter and brings constraints about the shape of the sample. It is represented in panels b–d in light pink to help the reader to recognize the different components inside the whole sample.

The two bands representative of the distribution of H_2O (around 1620 cm^{-1} [~6.2 μm] and 3700 cm^{-1} [~2.7 μm] for the bending and stretching mode, respectively) are shown in blue. The OH band at 3660 cm^{-1} due to the hydroxyl is visible as a shoulder on the spectra (especially in the blue spectra of Fig. 6). As in reflection, we found a region at the top of the fragment that is more hydrated. The same area is also enriched in aliphatic organic matter, as shown by the orange distribution presented in panel (c) of Fig. 6. The heterogeneity and more clearly the detection of aliphatic organic matter inside the sample by IR-CT (and not only on the surface) are pieces of evidence of the endogenous origin of the majority of organic matter detected in our analyses. This analysis has emphasized a compositional heterogeneity inside the small fragment AZ_3 and thus we decided to further explore this heterogeneity as described in the following section.

Analysis of the FIB Sections

The IR-CT 3D measurements have the advantage of being totally nondestructive and noninvasive; however, they are time-consuming (typically 1/2 days per sample) and because of complex scattering issues, the quality of the spectral data in 3D is not as good as equivalent measurements collected in 2D on a flat surface. To overcome this problem, we applied one more step in the sample preparation (see also Aléon-Toppani et al. [2021] for further technical information). The AZ_3 fragment was serially sectioned using FIB technologies to generate a series of three FIB sections (see Fig. 7a). The orientation of the particle prior to sectioning was carefully selected to ensure that regions of interest were subsampled as required. Thickness of the FIB sections allowed us to perform FT-IR characterization in transmission with a pixel size of 0.66 μm (without being limited by the scattering effect due to the volume) and also to subsequently measure these same sections with Raman spectroscopy, EDS analysis (see Fig. 7 for an example of the results of the analysis performed on the second sections, located in the middle of the fragment AZ_3).

The 2D spectra of the FIB sections show bands that are similar to the ones measured in 3D in the whole fragment AZ_3, but their peak position and their relative band area show small variations between the three sections and between different spots within a single section. In particular, organic matter bands are more important on sections 1 and 2 and located on half of the sections (near areas 2 and 3) as predicted by our 3D characterization. Moreover, we observed a shift of the maximum of the silicate band between 980 cm^{-1} (~10.2 μm) and 1010 cm^{-1} (~9.9 μm), both visible in the spectra presented in Fig. 6 and in panel c of Fig. 7. Local variations in Mg/Fe ratio may explain this band shift, as confirmed by the EDS analysis shown in Fig. 7. We have estimated a Mg/Fe ratio of 0.58 for area 1, 1.61 for area 2, and 0.84 for area 3 (both compatible with a serpentine composition). The region enriched in Mg (area 2) corresponds to the region with a maximum of the SiO band around 1010 cm^{-1} (~9.9 μm). Thus the 10 μm band detected in our samples shifts toward a higher wave number when the Mg/Fe ratio increases, as previously shown in other solid solution series minerals by Tarantino et al. (2003), Hofmeister and Pitman (2007), Hamilton (2010), and Bates et al. (2020).

Variations in the abundance of organic matter (up to a factor of 3 compared to the average abundance in the whole fragment AZ_3) or degree of hydration are also visible within the sections (as shown in panels d and e of Fig. 7), i.e., at a scale below 10 μm. The relationship

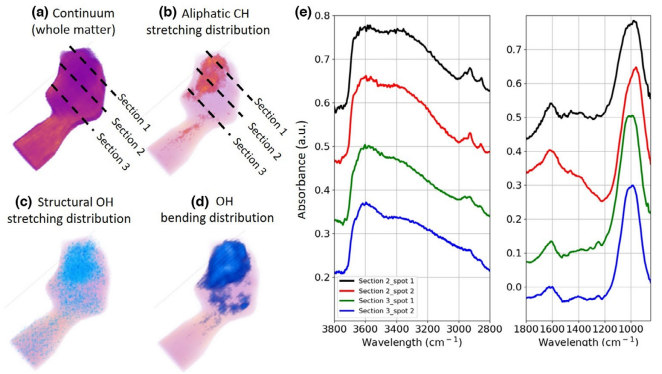

Fig. 6. a–d) 3D distribution of the whole matter (a), of the aliphatic CH stretching band (b), of the OH stretching bands (c), and bending band (d). On panels (a)–(d) are indicated the relative position of the three FIB sections taken from the AZ_3 fragment. e) Spectra in transmission between 2600 and 3720 cm^{-1} and between 850 and 1250 cm^{-1} for different regions inside FIB sections 2 and 3. (Color figure can be viewed at wileyonlinelibrary.com.)

between organic matter and surrounding silicates will be discussed for several fragments in the following section.

Moreover, we looked for structural heterogeneity of the organic matter inside this small fragment (AZ_3 sections 1–3) both by studying the shape of the aliphatic stretching band with FT-IR and by analyzing the shape of Raman D and G bands. Focusing on the area rich in aliphatic CH bonds, we estimated the ratio CH_2/CH_3 for spectra obtained by performing a spatial binning of nine pixels (close neighbors, a filter of 10% was applied to neglect pixels with low aliphatic CH band intensity). The fit was performed with the five Gaussians model described by Merouane et al. (2012). We obtained a value of 1.2 ± 0.2 without any significant local difference within the sections. This value is of the same order of magnitude as previous values estimated on different CM (see for example Kebukawa et al., 2011). Raman spectroscopy was performed on the three sections from AZ_3 to study the G and D bands (Busemann et al., 2007). These bands are sensitive to the structure and degree of order of the polyaromatic component in complex carbonaceous phases in meteorites (Quirico et al., 2014). The G band of AZ exhibits classical parameters for a CM chondrite: a maximum peak position around 1595 ± 5 cm^{-1} and a full width half maximum (FWHM) around 90–100 cm^{-1}. We found that the aromatic C = C was present in all the spectra measured inside the three sections. Still, we did not detect significant variations in intensity, in the position, or in the FWHM of the G and D bands inside this small fragment (see Fig. 7c).

From SE images (Fig. 7a), we can estimate the porosity inside the three FIB sections. To cover a larger area of AZ and ensure a more representative perspective, we averaged the porosity estimated on the three sections, which gave a value of $3.9 \pm 0.5\%$ inside the small fragment.

Fragment Crushed Inside the Diamond Compression Cell

Finally, we present results obtained in transmission on the fragment AZ_4 crushed inside the diamond compression cell. With this configuration, spectra show only upward absorption bands (absorbance y scale). The main feature is the silicate band at ~1000 cm^{-1} (10 μm), that is typical of hydrated phyllosilicate minerals, the main component of the CM chondrite matrix (see Fig. 8 for different spectra inside AZ_4). The shape and position of this peak are still consistent with the observation in reflection described above and correspond to a serpentine-rich sample. Another relevant absorption band is the large one due to H_2O stretching centered at 3500 cm^{-1} (~2.9 μm). The water bending mode (located at 1640 cm^{-1} [~6.1 μm]) is well separated from the rest of the 1500 cm^{-1} (~6.7 μm) multipeaks which are due to organic components: C = C aromatic stretching and the C-H bending. Carbonates can also contribute to this band.

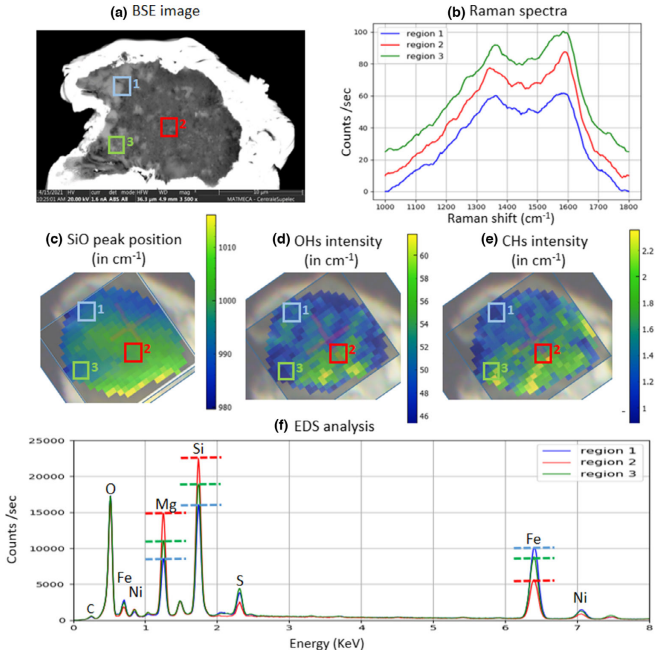

Fig. 7. a) Back scattering electron (BSE) image of section 3 and (b) Raman spectra for the three areas defined in panel (a). c–e) Spatial distribution inside section 2 obtained by FT-IR spectroscopy of the position of the maximum of the 10 μm band, of the intensity of the OH stretching band, and of the intensity of the aliphatic CH stretching band. f) Average EDS spectra in the three regions defined in panel (a). (Color figure can be viewed at wileyonlinelibrary.com.)

We used five clusters (*k*-means clustering analysis) to analyze the spatial distribution of the different components in this part of the fragment. The result of this clustering is presented in Fig. 8. Clustering helps to rapidly identify regions with different spectral signatures. The carbonate-rich area stands out (cluster 1—orange spectra in Fig. 8b); we noticed a very strong band at 1457 cm^{-1} (~6.9 μm) and its overtones at 2510 cm^{-1} (~4.0 μm) and 880 cm^{-1} (~11.4 μm) (Bruckman & Wriessnig, 2013). Complementary Raman analyses confirmed the presence of carbonates and allowed us to identify these as calcite. As in other CM chondrites (see De Leuw et al. [2010]; Dionnet et al. [2018]; Lee et al. [2014] for the case of the Paris meteorite), calcite spots are present as globules with a size of around 30–40 μm. Clusters 2–5 represent areas in the matrix with differences in intensity of the Si-O and water bands. We observed a small shift in the position of the silicate band maxima between 990 cm^{-1} (~10.1 μm; cluster 2) and 1010 cm^{-1} (~9.9 μm; cluster 5). This gradual shift is correlated with water intensity variation from a weak water band (cluster 2) to a stronger one (cluster 5).

The aliphatic CH bands at 2800–3000 cm^{-1} (~3.6–3.3 μm) also change in intensity between the different clusters and seem correlated with the strength of the water stretching bands, suggesting a link between the presence of aliphatic organic matter and hydration extent. Using the five Gaussians fit described in Merouane et al. (2012), we have estimated the CH_2/CH_3 ratio for the different clusters. We found the same value 1.3 ± 0.3 for all clusters. We observed a quantitative heterogeneity for the distribution of the organic matter but no structural difference at the scale of the fragment.

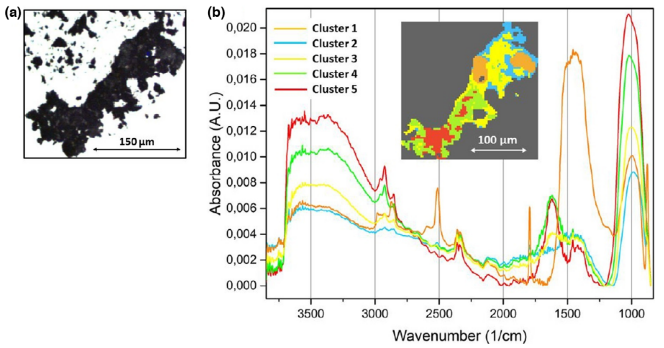

Fig. 8. a) Visible image of the first fragment after crushing. b) *k*-means clustering and average spectra for each cluster with associated colors. (Color figure can be viewed at wileyonlinelibrary.com.)

Homogeneous aromatic components were also observed in the Raman spectra of this fragment as in fragment AZ_3.

Comparison of the Results Obtained on the Different Fragments

The study of different fragments at various scales and with different setups has revealed a complex structure. Focusing on the CM lithology, we have shown that it is composed of CAIs, Fe-Ni sulfides, elongated chondrules, and TCIs embedded in a fine-grained matrix, all visible in fragment AZ_2 by XCT (see Fig. 2). IR spectroscopy (on fragments AZ_1, AZ_3, and AZ_4) revealed that the matrix is mainly composed of serpentine with an internal variation of Mg/Fe ratio, visible in the shift of the 10 μm band. This heterogeneity is spatially correlated with various degrees of hydration: the regions enriched in Mg (with spectra showing a SiO band with a maximum around 1010 cm^{-1} [~9.9 μm]) correspond to the most hydrated areas. The correlation between an increase in Mg and hydration is a trend already observed in CC meteorites by Tomeoka et al. (1989), Browning et al. (1996), and Hanna et al. (2020). The aliphatic CH band intensity is also correlated with the strength of the water stretching bands. We did not detect any structural heterogeneity of the aliphatic matter inside single fragments or, at a larger scale, between two fragments originating from different locations inside the matrix of the CM-like lithology (similar CH_2/CH_3 ratio of 1.3 ± 0.3 for fragments AZ_3 and AZ_4). Thus we observed a quantitative heterogeneity for the distribution of the organic matter but no structural differences. A study of Raman spectra also shows that the distribution of the aromatic C = C is quite homogeneous at the scale of micrometric fragments. The distribution of polyaromatic carbon compounds appears unrelated to the distribution of aliphatics. In addition, we have estimated a porosity around 4.5 vol% in fragment AZ_2, mainly due to elongated pores/fractures. Within error bars, the value of porosity estimated on AZ_3 sections is consistent with the value estimated for the larger fragment AZ_2.

DISCUSSION

Matrix Properties and Comparison with Other CMs

To compare the average composition detected by FT-IR, we have plotted the reflectance spectra of AZ and other CM chondrites. The comparison data set was collected during the past few years using the same experimental setup at SOLEIL, and most of the samples were prepared at Tohoku University in the framework of a rehearsal campaign for Hayabusa2, although some of the samples were prepared previously as powders compressed into pellets (see Lantz et al., 2017). In Fig. 9a, we show the average reflectance spectra of our different meteorite samples obtained at large scale (mm-sized spot), focusing on the structure of the 10 μm band (1000 cm^{-1}). The spectra were scaled to unity at the main peak position, in order to stress how the position and profile of the 10 μm band change moving from the meteorites with a matrix dominated by phyllosilicates (left panel, main peak position typically above

1000 cm^{-1}), to primitive CM2 meteorites such as Paris or Murchison showing the presence of partly amorphous hydrated silicates in the matrix as well as abundant anhydrous phases in chondrules (central panel), down to meteorites dominated by anhydrous phases both in the matrix and chondrules (right panel, main peak position below 1000 cm^{-1} [10 μm], usually determined by olivines). In other words, the average large-scale spectra of the considered meteorites carry information about their matrix mineralogy and relative phase abundances and its relative abundance with respect to other phases such as those in chondrules or inclusions (Cloutis et al., 2011; Noun et al., 2019; Potin et al., 2020.

In order to build a convenient graph that would allow a quick comparison among the analyzed samples, we report the peak position of the main Si-O band with respect to the minimum of the first derivative after the 10 μm band. This last parameter corresponds to an inflection point of the spectrum and to the point with a minimum slope on the left part of the SiO band (e.g., between 1000 and 1100 cm^{-1} for AZ). These parameters are diagnostic of the composition and structure of the main minerals of the meteorites. In Fig. 9b we can clearly separate the region of meteorites with a phyllosilicate-rich matrix (e.g., Orgueil) on the right, the most primitive meteorites (e.g., CM2 Paris) at the center of the graph, and the most heated meteorites (e.g., Allende) whose matrix is rich in anhydrous phases. This kind of representation could be useful to estimate the approximate degree of aqueous alteration and the relative amount of heating undergone by a meteorite based on the spectral parameters (Beck et al., 2018; Cloutis et al., 2011; Hanna et al., 2020). AZ is between the region with phyllosilicate-rich matrix and the region corresponding to the primitive meteorites. This confirms a moderate degree of aqueous alteration as concluded by previous research (Davidson et al., 2020). Moreover, the presence of more than one distinct lithology confirms its description as a brecciated meteorite given in the Meteoritical Bulletin.

The spectrum of Bennu obtained with OTES (Hamilton et al., 2021) was added in Fig. 9 for comparison; its characteristics are close to the one of CM primitive meteorites as predicted in the literature. In 2021, the James Webb Space Telescope was launched with the instrument MIRI onboard. This instrument can focus on the 10 μm band of an asteroid's spectrum with a spectral resolving power $R \sim 3000$ (Wells et al., 2015), which is large enough to distinguish spectra from different areas defined in Fig. 9b. However, the signal-to-noise ratio has to be really good to precisely extract the 10 μm band's parameters and could be the limiting factor.

Aqueous Alteration Inside AZ

From our data, we can estimate with two independent methods the petrologic subtype of the CM-like lithology inside AZ and discuss the degree of hydration experienced by our fragments. The first method uses the FT-IR data in reflectance. Hanna et al. (2020) defined a mathematical expression to correlate the degree of aqueous alteration and Si-O stretching spectral features in CMs. They showed that a high degree of alteration is directly proportional to a decrease of the difference, in wave numbers, between the Christiansen feature and the Si-O stretching band center. Since an increase in aqueous alteration extent among CMs corresponds to a lower petrologic subtype, by assessing the position of these two spectral features, a further classification and comparison of the meteorites can be achieved. The mathematical correlation is petrologic subtype = $(y + 105.2)/122.2$, where y represents the difference in wave numbers between the Christiansen feature and Si-O stretching band.

We analyzed the reflectance spectra shown in Fig. 10 in a similar way. Reflectance spectra were treated by extracting relevant spectral parameters. Similar to the results found in Hanna et al. (2020), the difference between the Christiansen feature and the maximum of the Si-O peak position seems to be a reliable parameter for predicting the subpetrologic type of CM chondrite samples ($r = 0.82$). In our case, we found the relation with the petrologic type = $(y + 256.7)/184.4$, where y represents the difference in wave numbers between the Christiansen feature and Si-O. The trend observed in Hanna et al. (2020) was confirmed in this study by using the same method on a different set of samples (which can explain the variation between the coefficient of linear regression). Using the interpolation obtained based on the difference between the Christiansen feature and the maximum of the Si-O peak position, we found a petrologic type between 2.4 and 2.5 using our data in reflectance (see Fig. 10).

The second method is based on the quantification of TCIs. The quantity of TCIs estimated inside our large fragment is around 26 ± 2 vol%. Rubin et al. (2007) predicted between 20% and 40% of TCIs for a CM depending on aqueous alteration. They proposed a relationship between the petrologic type of carbonaceous chondrites to the percent of TCIs present in the fragment. The 26 vol% estimated by XCT analyses of the CM-like lithology corresponds to a petrographic type of 2.4 ± 0.2. The two methods (obtained from XCT and FT-IR) give compatible values for the extent of aqueous alteration. Furthermore, they are largely in agreement with previous literature

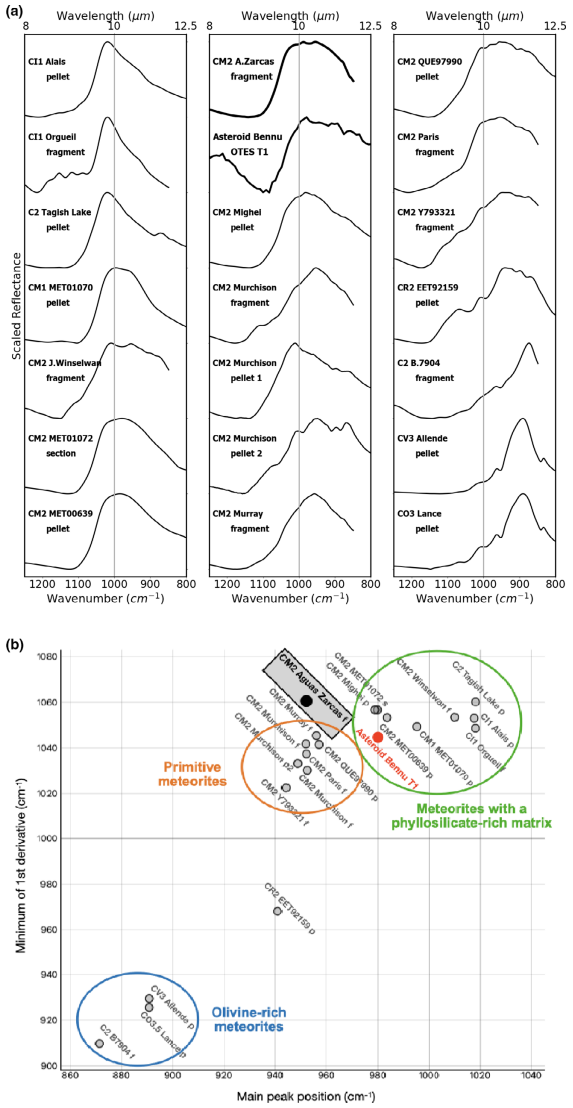

Fig. 9. a) The average large-scale (mm-sized spot) MIR reflectance spectra of the meteorites selected in this study. The spectral range is restricted to the values corresponding to the surface scattering regime (Christiansen features and main reststrahlen bands), with particular emphasis on the Si-O stretching bands. All the spectra were scaled to unity at the position of their main Si-O stretching band, but without performing a continuum removal. Pellet refers to compressed meteorite powders; fragments refer to the surface of 3D samples. The spectra of Tagish Lake, Mighei, Alais, Allende, and Lancé come from Lantz et al. (2017). The spectra of Murchison pellets come from Lantz et al. (2015). The spectrum of Paris comes from Noun et al. (2019). The spectrum of Bennu comes from Hamilton et al. (2021). b) The minimum of the first derivative versus the peak position of the main Si-O band, for the average large-scale spectra of the considered meteorites. (Color figure can be viewed at wileyonlinelibrary.com.)

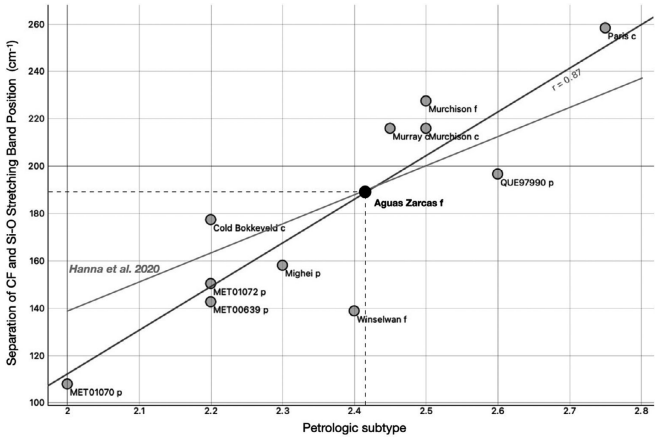

Fig. 10. Difference between the Christiansen feature and the position of the maximum of the main Si-O peak obtained on reflectance spectral parameters according to the petrological type. The dark line represents the fit obtained with our data and the gray line represents the fit obtained by Hanna et al. (2020). This last fit has been obtained by a similar method but with a different set of meteorites.

assessments: three clasts with petrological type 2.6 (for the two first clasts) and 2.8 (for the third clast) were observed in the CM-like lithology by Kerrouach et al. (2021), while Davidson et al. (2020) described a fragment with a petrological subtype between 2.2 and 2.4.

Organic Matter Description and Heterogeneity in the Mineral Context

In this section, we focus on the relation between the organic and minerals phases. Figure 11 shows the distribution of three parameters (the position of the maximum of the silicate band, the intensity of aliphatic organic matter, and the degree of hydration) as a function of each other for each pixel of the two fragments studied in transmission, i.e., the fragment crushed inside a diamond compression cell (AZ_4) and the sections from the 3D small fragment (AZ_3). Our data reveal a positive correlation between aliphatic organic matter abundance and hydration extent (H_2O abundance), and by inference the degree of aqueous alteration. In both fragments, pixels enriched in organic matter have correspondingly stronger OH signatures. The same pixels also show a maximum of the silicate band between 990 and 1010 cm^{-1} (~10.1 to 9.9 μm), which corresponds to silicate enriched in magnesium compared to the rest of the fragment. The two fragments have different sizes. Thus, the heterogeneity in two areas separated by more than 150 μm (in the case of the crushed fragment) is also observable over a comparable range inside a single fragment, between two locations separated by less than 20 μm.

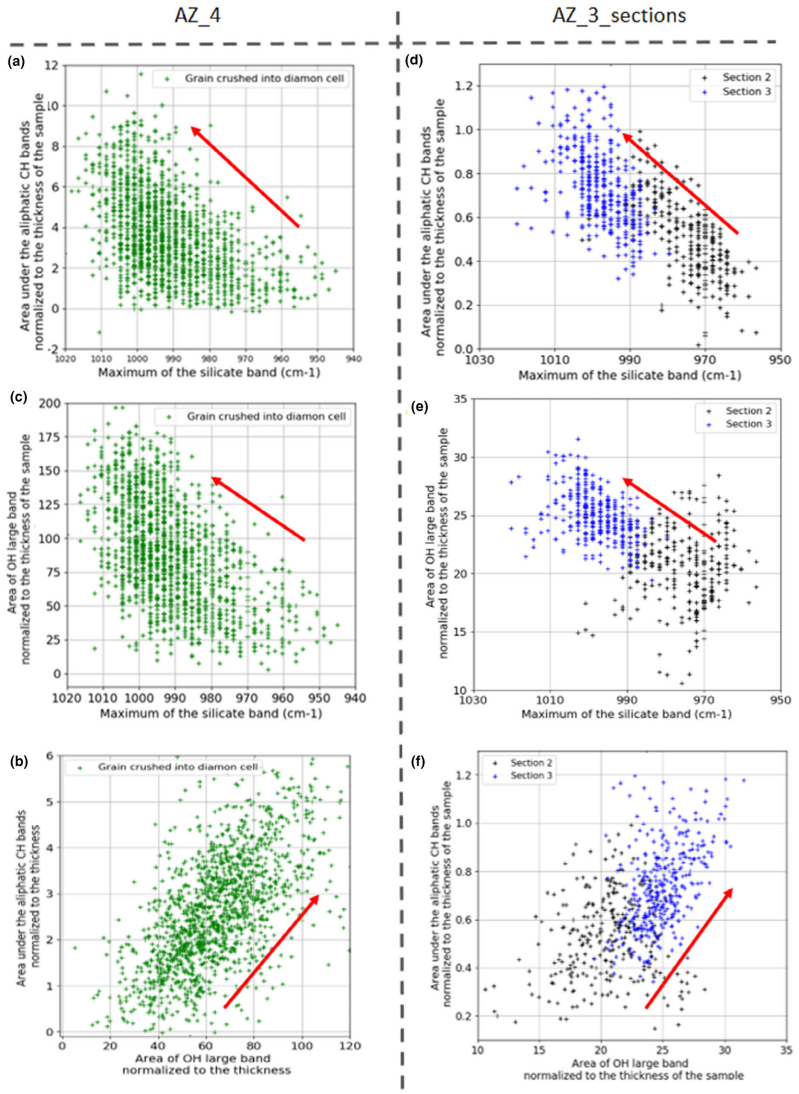

Fig. 11. Correlation diagrams for the fragment AZ_4 crushed into the diamond compression cell (panels [a]–[c]) and for the sections AZ_3_sections (panels [d]–[f]). a and d) Position of the silicate band maxima versus intensity of the aliphatic organic matter. b and e) Position of the silicate band maxima versus the degree of hydration. c and f) Intensity of the aliphatic organic matter versus the degree of hydration. The intensity of the aliphatic organic matter and the degree of hydration are estimated by calculating the area, respectively, under the CH aliphatic features (integration after a baseline correction between 2826 and 3007 cm^{-1}) and the OH stretching feature (after a baseline correction between 3015 and 3631 cm^{-1}). A normalization by the thickness of the sample (i.e., 3 μm) is moreover performed to obtain the degree of hydration. (Color figure can be viewed at wileyonlinelibrary.com.)

Organic matter is not homogeneously distributed inside the studied CM chondrite. We detected hotspots of organic aliphatic matter that are correlated with more hydrated regions within the fragment (those enriched in Mg-bearing silicates). This suggests that aqueous alteration in the AZ parent body played a major role in the evolution of the organic matter in agreement with previous studies on other CM chondrites, such as Le Guillou et al. (2014), Vinogradoff et al. (2017), and Noun et al. (2019). On the contrary, the aromatic compounds detected using Raman spectroscopy appear to be homogeneously distributed at the μm-scale and unaffected by variations in the extent of aqueous alteration. Variations in the CH_2/CH_3 ratios in AZ at the micrometer scale were not detected. This implies no changes in the aliphatic organic matter branching degree in the fragment. Vinogradoff et al. (2017) emphasized a correlation between water alteration and the heterogeneity of the organic matter. Dionnet et al. (2018) demonstrated a heterogeneous CH_2/CH_3 ratio inside a single fragment of the Paris meteorite. The petrologic subtype of AZ is lower than that of Paris (reflecting more advanced alteration in the AZ fragment) and this might explain the homogeneity of the aliphatics observed here (Isa et al., 2021). An extensive aqueous alteration process may cause a further homogenization of organic matter and it can be the reason why no variation of the CH_2/CH_3 ratios in different hydration zones has been observed in this work. Concerning the aromatic signature, neither variation of intensity nor various band profiles were observed in our fragment (we observed the same D and G bands everywhere inside our fragments). The G band exhibits its main peak position around 1590 ± 5 cm^{-1} and the FWHM is between 90 and 100 cm^{-1}, which is typical for CM chondrites (Busemann et al., 2007). The absence of modification of the Raman signature in the more altered regions suggests that the aqueous alteration leaves the polyaromatic compounds unaffected. At the same time, a higher concentration of aliphatic organic compounds in the same regions suggests that aqueous alteration may have been responsible for the generation of new aliphatic molecules.

Scale of the Porosity

We performed two independent estimates of porosity applied at different scales and using distinct analytical approaches. First, the XCT data gave a value of 4.5 vol% ± 0.5 by counting voxels with a low LAC. The LAC is not sensitive to low-Z materials (Z being the average atomic number); thus, some voxels, considered as empty voxels by XCT, may contain low-Z material, such as organic matter. Matrajt et al. (2012) as well as De Gregorio et al. (2013), Changela et al. (2018), Le Guillou et al. (2014), Floss et al. (2014), and Nakamura-Messenger et al. (2006) have observed different types of organic matter in extraterrestrial material using transmission electron microscopy. They observed organic globules with a size from 30 to 500 nm. Similar features may be contained inside the pore distribution observed in our fragments. The largest ones have sizes similar to the voxel in our study. The second value of porosity, estimated using image analysis of the SEM images of the FIB sections of the smallest fragment of AZ, can help resolve this issue, as in the case of SE images, black pixels could only be voids. Moreover, the resolution is better with SE images and we should be able to see pores as small as 0.1 μm (versus a resolution of 1 μm for XCT analyses). This method gives us a porosity of 3.9 ± 0.5 vol%. The fact that the second estimation gives a slightly lower value confirms that "pores" voxels counted as pores by XCT are mainly empty and not full of low-density matter. There is only a small difference between the two values, meaning that the majority of pores described in this paper are bigger than 0.1 μm.

However, the values of porosity found here are small compared to expected values for CM chondrites as estimated in Consolmagno et al. (2008). Various values of porosity can be found for CM fragments depending on the method of measurement and the size of the fragment studied. Consolmagno et al. (2008) found values around 20–25 vol% for porosity in CM chondrites by using pycnometry while the point-counting method finds 3–4 vol% porosity (Corrigan et al., 1997). As explained in Consolmagno et al. (2008), this could be due to the scale of porosity: "The difference between point-counting and He/bead porosity measurements most likely indicate that the porosity in carbonaceous chondrites is found on a scale either too large or too small to be seen easily in thin section." This means that in the measurement of small fragment volumes we necessarily miss porosity whose scales are larger than the size of the fragment or smaller than 0.1 μm.

With our measurements, we are sensitive only to the microporosity. The magnitude of our measurement is consistent with values obtained by image treatment (Corrigan et al., 1997; Hezel et al., 2013). According to Friedrich et al. (2017), XCT measurement is comparable to ideal gas pycnometry for ordinary chondrites when measuring with a resolution below 2.6 μm. The resolution in our data is much better than the one used by Friedrich et al. (2017), but working with carbonaceous chondrites, we notice that the difference is important. We also observed anisotropy in the distribution of pores, with different values for pores inside the matrix versus pores inside the chondrules. The anisotropy is more significant for pores inside the matrix. Pores are primarily due to the presence of large-scale cracks and most likely originate due to shock effects such as thermal shocks and impacts. Smaller pores present inside the "compact" matrix should be present as nanometric pores but are not visible at our scale. This observation fits well with the description of the porosity at fine scales inside the primitive carbonaceous chondrite Paris observed by Zanetta et al. (2021). In addition, the difference between our values and the 25 vol% measured by Consolmagno et al. (2008) is probably due to pores at millimetric scales, not visible in our fragments because of their sizes. Such big pores would have weakened the fragments too much and they would have broken.

To sum up, pore size distribution is a continuum in carbonaceous chondrites between the nanoscale, mainly contained in the matrix of amorphous silicates (Zanetta et al., 2021), the micron-scale features seen in XCT and to larger mm-to-cm-scale. The different size regimes observed during studies is inherent in the techniques used but various papers also suggest that these three scales could be representative of different processes that happened at different times in the history of carbonaceous chondrite: Nanoscale porosity present in fine-grained rims could be characteristic of the nebula processes before matrix accretion (Zanetta et al., 2021) or could be residual porosity of the accretional phases, such as voids left after the melting of water-ice (Matsumoto et al., 2019; Trigo-Rodriguez et al., 2006), while bigger pores (micron to cm scales) could be the result of secondary processes such as circulation of fluids, shock, thermal fracture, or dehydration (DeCarli et al., 2001). In addition to these scales, a population of much larger voids (occasionally termed macroporosity) are expected to exist on second-generation rubble-pile asteroids (such as Ryugu and Bennu). These large meter-scale voids are necessary to account for the anomalously low densities of some asteroids (Britt et al., 2002). For instance, Cambioni et al. (2021) have estimated that the porosity of the meter-sized bounders on the surface of Bennu can reach up to 50%–60%. At this large scale, pores are mainly due to impacts (Avdellidou et al., 2020) and thermal fatigue (Delbo et al., 2014).

Petrofabrics and Porosity of AZ Chondrules: Origin and Evolution

The size of the chondrules is in agreement with literature data: the mean average size of chondrules is around 300 μm for CM chondrites (Weisberg et al., 2006) but Kouvatsis and Cartwright (2020) observed chondrules up to 1500 μm in a chondrule-rich CM lithology of AZ.

Chondrules also have elongated shapes. The size of the chondrules is in agreement with literature data: the mean average size of chondrules is around 300 μm for CM chondrites (Weisberg et al., 2006). The elongate shape of chondrules was also reported by Yang et al. (2021) inside a compact lithology present in AZ and could be due to hypervelocity impacts. Indeed, they have proposed a formation model for AZ involving a "series of ejection and reaccretion of sub-cm-sized fragments produced by ejection events" to explain the presence of various lithologies including those that show evidence of strong impacts.

We measured a porosity value of 6.3 ± 1 vol%. Lewis et al. (2018) and Macke et al. (2011) performed similar measurements with XCT and both concluded that porosity is significantly higher in the matrix than in the chondrules. Quantitative measurements of the porosity inside chondrules has been performed in only a few papers and they predict very low values: around 1–2 vol% (Lewis et al., 2018) in L4 ordinary meteorites and 0.1–0.6% of porosity in the chondrules of Allende (Ebel & Rivers, 2007). Regions of high porosity are either close to fractures inside the fragment, which could have facilitated water passage, in or around chondrules. However, both meteorites studied in these papers are metamorphosed with clear evidence of growth of new minerals that will likely reduce porosity. On the contrary, Hanowski and Brearley (2001) characterized 35 chondrules inside a single CM and have shown that the effect of aqueous alteration is very different according to the type of chondrules: the dissolution of primary phases could explain high porosity especially in the case of

clinoenstatite-rich chondrules. Measurements for porosity inside chondrules in CM chondrites are currently absent and our study brings a first order of magnitude value for chondrule porosity in CM chondrites.

In the following discussion, we outline how chondrule porosity may be expected to evolve over the geological history of a chondrite parent body:

(i) Due to heating effects during chondrule formation: Inside unaltered chondrules, since they have igneous origins, any internal void space is most likely to be irregular interstitial space between crystals and is formed by volume contraction. The molten droplet will take less volume than the cooled solid and cooling from the outside inwards will create void space, probably near the center as observed in I-type cosmic spherules described by Feng et al. (2005) and Genge et al. (2017). The location of the voids inside chondrules will discriminate against this hypothesis. In our case, the voids are equally spread inside the chondrules, thus the heating effect cannot explain the high value of porosity found in chondrules inside our sample.

(ii) Accretional porosity present inside fine-grained rims: A small part of the porosity could be present in the edge of the chondrules in their inner fine-grained rim. Trigo-Rodriguez et al. (2006) argued that fine-grained rims around some chondrules in CM meteorites preserve their original accretionary porosity. By contrast, much of the remaining fine-grained matrix is instead affected by impact-induced compaction and therefore exhibits lower porosity values. The matrix could have been compacted with strain accommodated by primarily deformation of the matrix, leaving the chondrules unaltered (Bland et al., 2014, Davison et al., 2016; Forman et al., 2017). Zanetta et al. (2021) have also observed a higher porosity at the edge of chondrules in Paris fine-grained rims. In our case, a manual check confirms the presence of slightly more porous regions around the chondrules, but it does not explain the high porosity detected for chondrules in this study. Chondrule porosity is unlikely to be accretional residual porosity.

(iii) Aqueous alteration progressively replaces the primary accretionary phases in carbonaceous chondrites with secondary minerals. In chondrules, the glass and Fe-Ni-metal are highly susceptible to fluids and alter first while more resistant anhydrous silicates (olivine and pyroxene) alter later. Secondary mineralization processes typically operate by direct replacement, producing pseudomorphic forms that preserve the habit and texture of their former primary phases (Hanowski & Brearley, 2001; Velbel et al., 2012, 2015). This explains why pseudomorphic chondrule outlines are observed in heavily altered CM2s and CM1 chondrites (Grady et al., 1987; Zolensky et al., 1997). However, not all primary minerals experience isovolumetric replacement. For example, Lee and Lindgren (2016) documented the presence of void spaces (pores) in partially altered forsterite and clinoenstatite grains. These void spaces are crystallographically controlled, being oriented parallel to the (010) and (001) axes in forsterite and the (001) axis in clinoenstatite. They are interpreted as having formed by congruent dissolution. As alteration advanced, these voids were subsequently infilled by a later generation of polyhedral serpentine. Dissolution during aqueous alteration is therefore a potential explanation for the origin of chondrule voids. However, the chondrules identified in this study contain both chondrule metal and bright Fe-rich anhydrous silicates. The retention of these fluid-susceptible phases implies chondrules have suffered a low degree of alteration. Dissolution could be only partially responsible for the high chondrule porosity values that we have observed.

(iv) Due to shocks: Impact compaction and brittle failure will create secondary porosity in the form of fractures. The fractures will be linear and branched so that they can be easily discriminated. We have estimated the value of anisotropy of voids inside chondrules to discriminate this hypothesis and it gives a value of 6.25, meaning elongated pores inside chondrules. The chondrules are elongated and this seems to corroborate the shock scenario (cf. Hanna et al., 2015). Lindgren et al. (2015) have also studied the effect of flattening of chondrules due to shock inside CM chondrites, and argued that chondrule flattening occurred after alteration, and thus changed the shape of pores produced by aqueous alteration. It makes the effect of alteration hard to distinguish from the effect of shock when speaking of the shape of pores inside chondrules. It is likely that the elongated void pattern visible in our sample is the result of a moderate aqueous alteration followed by a shock episode.

We conclude that porosity inside chondrules examined in this paper is then primarily due to shocks and, to a lesser extent, to dissolution during aqueous alteration. In a CM 2.5 chondrite, aqueous alteration could dissolve anhydrous silicates (Velbel et al., 2015). However, more data on other CM chondrite chondrule porosity would be very useful to better understand the phenomena which produce porous chondrules.

CONCLUSION

This study focused on the CM chondrite AZ, investigated with both FT-IR spectroscopy and XCT analyses. Analyses were performed at different scales to better understand its complex history and specifically to clarify the following points:

(a) We obtained a global description of our different fragments. We observed two lithologies inside our biggest fragment AZ_1: one similar to the C1 lithology described by Kerraouch et al. (2021), and a CM-like lithology. Comparing this last one with other CM carbonaceous chondrites, we can describe AZ's CM lithology as an intermediate between carbonaceous chondrites with phyllosilicate-rich matrix and the least altered carbonaceous chondrites.

(b) Concerning the extent of aqueous alteration, both techniques used in this paper have converged to classify our CM-like fragment as a CM2.5. Moreover, we have confirmed the conclusion of Hanna et al. (2020): the difference between the maximum of the Si-O band and the Christiansen feature extracted from measurement in reflection is a suitable parameter to predict the petrological subtype of a new CM chondrite.

(c) In addition, a study of porosity, pore distribution, and pore shape allowed us to evaluate the extent to which secondary processes have affected AZ: in addition to a moderate degree of aqueous alteration, this meteorite has also undergone shock processing.

(d) Concerning the organic component, we found spatial heterogeneity in abundance: a higher concentration of aliphatic organic compounds correlated with more hydrated regions enriched in Mg-bearing silicates. Our results revealed a positive correlation between more advanced aqueous alteration and higher aliphatic matter abundances. This suggests that aqueous alteration may have been responsible for the generation of new (biologically important) aliphatic molecules while apparently leaving larger polyaromatic compounds unaffected.

This paper was also an opportunity to discuss new tools useful to describe the diversity of carbonaceous chondrites. Spectral parameters of FT-IR measurement in reflection were extracted and placed in a diagram that allows a quick comparison of any new sample measured in the same condition with other carbonaceous chondrites. The projection of hyperspectral imaging measurements in reflectance onto a 3D volume has been performed using the 3D model obtained with a reconstruction based on SEM images, which is also a novel method at the scale of the individual grain. Such nondestructive measurement could be rapidly performed at the surface of any new sample thanks to IR-SI and will be particularly useful in the near future, with the return of precious extraterrestrial material by sample return missions. It will be helpful to reveal trends that could be sought at a scale in remote sensing data sets. It will help to build a bridge between the remote sensing observations of asteroid surfaces and the chemical and physical processes operating between the milliscale and the nanoscale characterized in the laboratory.

Estimations of porosity for the whole fragment and inside the chondrules were performed and showed that (i) porosity measurements on meteorites should always come with a caveat of the size range over which they are valid; (ii) different ranges of pore sizes could be representative of different stages of the sample's history; and (iii) chondrules can also contain pores, especially those created by secondary processes on the parent bodies, as in our case. More 3D studies focusing on the size distribution and spatial distribution of pores inside CMs are needed to understand the complex structural properties of primitive bodies.

Acknowledgments—Z. Dionnet was supported by a CNES postdoctoral allocation and by the Italian Space Agency within the ASI-INAF agreements I/032/05/0 and I/024/12/0. C. Avdellidou acknowledges funding support from the National Research Agency (ANR), project ORIGINS (ANR-18-CE31-0014). We acknowledge SOLEIL for provision of synchrotron radiation on ANATOMIX facilities through the proposal 20191248. ANATOMIX is an Equipment of Excellence (EQUIPEX) funded by the Investments for the Future program of the French National Research Agency (ANR), project NanoimagesX, grant no. ANR-11-EQPX-0031. The microspectroscopy measurements were supported by grants from Region Ile-de-France (DIM-ACAV) and SOLEIL. FIB sectioning and SEM images were acquired from a dual-beam microscope which is part of the MATMECA platform, supported by the "Investissement d'avenir" program (n°ANR-10-EQPX-37). This work was also supported by the Centre National d'Etudes Spatiales (CNES-France, Hayabusa2 mission). We thank J. Aleon, T. Hiroi, E. Quirico, P. Beck, and M. Zolensky for providing us with meteorite samples, and V.E. Hamilton and A. Brearley for their constructive comments on the manuscript during review.

Data Availability Statement—The data that support the findings of this study are available from the corresponding author upon reasonable request.

Editorial Handling—Dr. Daniel Glavin

REFERENCES

Aléon-Toppani, A., Brunetto, R., Aléon, J., Dionnet, Z., Levy, D., Troadec, D., Rubino, S., Brisset, F., Borondics, F., and King, A. 2021. A Preparation Sequence for Multi-Analysis of µm-Sized Extraterrestrial and Geological Samples. *Meteoritics & Planetary Science* 56: 1151–72.

Avdellidou, C., Di Donna, A., Schultz, C., Harthong, B., Price, M. C., Peyroux, R., Britt, D., Cole, D., and Delbo, M. 2020. Very Weak Carbonaceous Asteroid Simulants I: Mechanical Properties and Response to Hypervelocity Impacts. *Icarus* 341: 113648.

Bates, H. C., King, A. J., Donaldson Hanna, K. L., Bowles, N. E., and Russell, S. S. 2020. Linking Mineralogy and Spectroscopy of Highly Aqueously Altered CM and CI Carbonaceous Chondrites in Preparation for Primitive Asteroid Sample Return. *Meteoritics & Planetary Science* 55: 77–101.

Beck, P., Garenne, A., Quirico, E., Bonal, L., Montes-Hernandez, G., Moynier, F., and Schmitt, B. 2014. Transmission Infrared Spectra (2–25 lm) of Carbonaceous Chondrites (CI, CM, CV–CK, CR, C2 Ungrouped): Mineralogy, Water, and Asteroidal Processes. *Icarus* 229: 263–77.

Beck, P., Maturilli, A., Garenne, A., Vernazza, P., Helbert, J., Quirico, E., and Schmitt, B. 2018. What Is Controlling the Reflectance Spectra (0.35–150 µm) of Hydrated (and Dehydrated) Carbonaceous Chondrites? *Icarus* 313: 124–38.

Bland, P. A., Collins, G. S., Davison, T. M., Abreu, N. M., Ciesla, F. J., Muxworthy, A. R., and Moore, J. 2014. Pressure-Temperature Evolution of Primordial Solar System Solids During Impact-Induced Compaction. *Nature Communications* 5: 1–13.

Brearley, A. J. 2013. Nebular vs Parent Body Processing of Chondritic Meteorites. In *Meteorites, Comets and Planets*, 2nd ed., edited by A. M. Davis, 309–34. Cambridge: Elsevier.

Brearley, A. J., and Jones, R. H. 1998. Chondritic Meteorites. In *Planetary Materials, Reviews in Mineralogy*, edited by J. J. Papike, vol. 36, 3-001–3-398. Chantilly, Virginia: Mineralogical Society of America.

Britt, D. T., Yeomans, D., Housen, K., and Consolmagno, G. 2002. Asteroid Density, Porosity, and Structure. In *Asteroids III*, edited by W. F. Bottke Jr., A. Cellino, P. Paolicchi, and R. P. Binzel, 485–500. Tucson, Arizona: University of Arizona Press.

Browning, L. B., McSween Jr., H. Y., and Zolensky, M. E. 1996. Correlated Alteration Effects in CM Carbonaceous Chondrites. *Geochimica et Cosmochimica Acta* 60: 2621–33.

Bruckman, V. J. and Wriessnig, K. 2013. Improved Soil Carbonate Determination by FT-IR and X-Ray Analysis. *Environmental Chemistry Letters* 11: 65–70.

Busemann, H., Alexander, M. O., and Nittler, L. R. 2007. Characterization of Insoluble Organic Matter in Primitive Meteorites by MicroRaman Spectroscopy. *Meteoritics & Planetary Science* 42: 1387.

Cambioni, S., Delbo, M., Poggiali, G., Avdellidou, C., Ryan, A. J., Deshapriya, J. D. P., Asphaug, E. et al. 2021. Fine-Regolith Production on Asteroids Controlled by Rock Porosity. *Nature* 598: 49–52.

Changela, H. G., Le Guillou, C., Bernard, S., and Brearley, A. J. 2018. Hydrothermal Evolution of the Morphology, Molecular Composition, and Distribution of Organic Matter in CR (Renazzo-Type) Chondrites. *Meteoritics & Planetary Science* 53: 1006–29.

Chizmadia, L. J. and Brearley, A. J. 2008. Mineralogy, Aqueous Alteration, and Primitive Textural Characteristics of Fine-Grained Rims in the Y-791198 CM2 Carbonaceous Chondrite: TEM Observations and Comparison to ALHA81002. *Geochimica et Cosmochimica Acta* 72: 602–25.

Cloutis, E. A., Hudon, P., Hiroi, T., Gaffey, M. J., and Mann, P. 2011. Spectral Reflectance Properties of Carbonaceous Chondrites: 2. CM Chondrites. *Icarus* 216: 309–46.

Consolmagno, G. J., Britt, D. T., and Macke, R. J. 2008. The Significance of Meteorite Density and Porosity. *Chemie der Erde* 68: 1.

Corrigan, C. M., Zolensky, M. E., Dahl, J., Long, M., Weir, J., Sapp, C., and Burkett, P. J. 1997. The Porosity and Permeability of Chondritic Meteorites and Interplanetary Dust Particles. *Meteoritics* 32: 509–16.

Davidson, J., Alexander, C. M. O'D., Bates, H. C., King, A. J., Foustoukos, D. I., Schrader, D. L., Bullock, E. S. et al. 2020. Coordinated Studies of Samples Relevant for Carbonaceous Asteroid Sample Return: CM Chondrites AZ and Meteorite Hills 00639 (Abstract #1623). 51st Lunar and Planetary Science Conference. CD-ROM

Davison, T. M., Collins, G. S., and Bland, P. A. 2016. Mesoscale Modeling of Impact Compaction of Primitive Solar System Solids. *The Astrophysical Journal* 821: 68.

De Gregorio, B. T., Stroud, R. M., Nittler, L. R., Alexander, C. M. O'D., Bassim, N. D., Cody, G. D., Kilcoyne, A. L. D. et al. 2013. Isotopic and Chemical Variation of Organic Nanoglobules in Primitive Meteorites. *Meteoritics & Planetary Science* 48: 904–28.

De Leuw, S., Rubin, A. E., and Wasson, J. T. 2010. Carbonates in CM Chondrites: Complex Formational Histories and Comparison to Carbonates in CI Chondrites. *Meteoritics & Planetary Science* 45: 513–30.

DeCarli, P. S., Bowden, E., and Seaman, L. 2001. Shock Induced Compaction and Porosity in Meteorites (Abstract). *Meteoritics & Planetary Science* 36: A47.

Delbo, M., Libourel, G., Wilkerson, J., Murdoch, N., Michel, P., Ramesh, K. T., Ganino, C., Verati, C., and Marchi, S. 2014. Thermal Fatigue as the Origin of Regolith on Small Asteroids. *Nature* 508: 233–6.

DellaGiustina, D. N., Kaplan, H. H., Simon, A. A., Bottke, W. F., Avdellidou, C., Delbo, M., Ballouz, R.-L. et al. 2021. Exogenic Basalt on Asteroid (101955) Bennu. *Nature Astronomy* 5: 31–8.

Dionnet, Z., Aléon-Toppani, A., Baklouti, D., Borondics, F., Brisset, F., Djouadi, Z., Sandt, C., and Brunetto, R. 2018. Organic and Mineralogic Heterogeneity of the Paris Meteorite Followed by FTIR Hyperspectral Imaging. *Meteoritics & Planetary Science* 53: 2608–23.

Dionnet, Z., Brunetto, R., Aléon-Toppani, A., Rubino, S., Baklouti, D., Borondics, F., Buellet, A. C. et al. 2020. Combining IR and X-Ray Micro-Tomography Data Sets: Application to Itokawa Particles and to Paris Meteorite. *Meteoritics & Planetary Science* 55: 1645–64.

Dionnet, Z., Suttle, M., Longobardo, A., Folco, L., Rotundi, A., Della, C. V., and King, A. 2020. X-Ray Computed Tomography: Morphological and Porosity Characterization of Giant Antarctic Micrometeorites. *Meteoritics & Planetary Science* 55: 1581–99.

Ebel, D. S. and Rivers, M. L. 2007. Meteorite 3-D Synchrotron Microtomography: Methods and Applications. *Meteoritics & Planetary Science* 42: 1627.

Feng, H., Jones, K. W., Tomov, S., Stewart, B., Herzog, G. F., Schnabel, C., and Brownlee, D. E. 2005. Internal Structure of Type I Deep-Sea Spherules by X-Ray Computed Microtomography. *Meteoritics & Planetary Science* 40: 195–206.

Floss, C., Le Guillou, C., and Brearley, A. J. 2014. Coordinated NanoSIMS and FIB-TEM Analyses of Organic Matter and Associated Matrix Materials in CR3 Chondrites. *Geochimica et Cosmochimica Acta* 139: 1–25.

Forman, L. V., Bland, P. A., Timms, N. E., Daly, L., Benedix, G. K., Trimby, P. W., Collins, G. S., and Davison, T. M. 2017. Defining the Mechanism for Compaction of the CV Chondrite Parent Body. *Geology* 45: 559–62.

Friedrich, J. M., Ruzicka, A., Macke, R. J., Thostenson, J. O., Rudolph, R. A., Rivers, M. L., and Ebel, D. S. 2017. Relationships Among Physical Properties as Indicators of High Temperature Deformation or Post-Shock Thermal Annealing in Ordinary Chondrites. *Geochimica et Cosmochimica Acta* 203: 157–74.

Gattacceca, J., McCubbin, F. M., Bouvier, A., and Grossman, J. N. 2019. The Meteoritical Bulletin, No. 108. *Meteoritics & Planetary Science* 55: 1146–50.

Genge, M. J., Suttle, M., and Van Ginneken, M. 2017. Thermal Shock Fragmentation of Mg Silicates Within Scoriaceous Micrometeorites Reveal Hydrated Asteroidal Sources. *Geology* 45: 891–4.

Glavin, D. P., Elsila, J. E., McLain, H. L., Aponte, J. C., Parker, E. T., Dworkin, J. P., Hill, D. H., Connolly, H. C., and Lauretta, D. S. 2021. Extraterrestrial Amino Acids and L-Enantiomeric Excesses in the CM2 Carbonaceous Chondrites AZ and Murchison. *Meteoritics & Planetary Science* 56: 148–73.

Grady, M. M., Graham, A. L., Barber, D. J., Aylmer, D., Kurat, G., Ntaflos, T., Ott, U., Palme, H., and Spettel, B. 1987. Yamato-82042: An Unusual Carbonaceous Chondrite with CM Affinities. *Memoirs of the National Institute of Polar Research (Tokyo)* 46: 162–78.

Griffin, L. D., Elangovan, P., Mundell, A., and Hezel, D. C. 2012. Improved Segmentation of Meteorite Micro-CT Images Using Local Histograms. *Computers & Geosciences* 39: 129–34.

Hamilton, V. E. 2010. Thermal Infrared (Vibrational) Spectroscopy of Mg-Fe Olivines: A Review and Applications to Determining the Composition of Planetary Surfaces. *Chemie der Erde—Geochemistry* 70: 7–33.

Hamilton, V. E., Christensen, P. R., Kaplan, H. H., Haberle, C. W., Rogers, A. D., Glotch, T. D., Breitenfeld, L. B. et al. 2021. Evidence for Limited Compositional and Particle Size Variation on Asteroid (101955) Bennu from Thermal Infrared Spectroscopy. *Astronomy & Astrophysics* 650: A120.

Hamilton, V. E., Simon, A. A., Christensen, P. R., Reuter, D. C., Clark, B. E., Barucci, M. A., Bowles, N. E. et al., OSIRIS-REx Team. 2019. Evidence for Widespread Hydrated Minerals on Asteroid (101955) Bennu. *Nature Astronomy* 3: 332–40. https://doi.org/10.1038/s41550-019-0722-2.

Hanna, R. D., Hamilton, V. E., Haberle, C. W., King, A. J., Abreu, N. M., and Friedrich, J. M. 2020. Distinguishing Relative Aqueous Alteration and Heating Among CM Chondrites with IR Spectroscopy. *Icarus* 346: 113760. https://doi.org/10.1016/j.icarus.2020.113760.

Hanna, R. D., Ketcham, R. A., Zolensky, M., and Behr, W. M. 2015. Impact-Induced Brittle Deformation, Porosity Loss, and Aqueous Alteration in the Murchison CM Chondrite. *Geochimica et Cosmochimica Acta* 171: 256–82.

Hanowski, N. P. and Brearley, A. J. 2001. Aqueous Alteration of Chondrules in the CM Carbonaceous Chondrite, Allan Hills 81002: Implications for Parent Body Alteration. *Geochimica et Cosmochimica Acta* 65: 495–518.

Hewins, R. H., Bourot-Denise, M., Zanda, B., Leroux, H., Barrat, J.-A., Humayun, M., Göpel, C. et al. 2014. The Paris Meteorite, the Least Altered CM Chondrite So Far. *Geochimica et Cosmochimica Acta* 124: 190–222.

Hezel, D. C., Elangovan, P., Viehmann, S., Howard, L., Abel, R. L., and Armstrong, R. 2013. Visualisation and Quantification of CV Chondrite Petrography Using Micro-tomography. *Geochimica et Cosmochimica Acta* 116: 33–40.

Hicks, L. J. and Bridges, J. C. 2020. Aqueous Alteration in the CM2 AZ Meteorite (Abstract #2869). 51st Lunar and Planetary Science Conference. CD-ROM.

Hofmeister, A. M. and Pitman, K. M. 2007. Evidence for Kinks in Structural and Thermodynamic Properties Across the Forsterite-Fayalite Binary from Thin-film IR Absorption Spectra. *Physics and Chemistry of Minerals* 34: 319–33.

Howard, K. T., Alexander, C., Schrader, D. L., and Dyl, K. A. 2015. Classification of Hydrous Meteorites (CR, CM and C2 Ungrouped) by Phyllosilicate Fraction: PSD-XRD Modal Mineralogy and Planetesimal Environments. *Geochimica et Cosmochimica Acta* 149: 206–22.

Isa, J., Orthous-Daunay, F. R., Beck, P., Herd, C. D., Vuitton, V., and Flandinet, L. 2021. Aqueous Alteration on Asteroids Simplifies Soluble Organic Matter Mixtures. *The Astrophysical Journal Letters* 920: 39.

Kebukawa, Y., Alexander, C. M. O'D., and Cody G. D. 2011. Compositional Diversity in Insoluble Organic Matter in Type 1, 2 and 3 Chondrites as Detected by Infrared Spectroscopy. *Geochimica et Cosmochimica Acta* 75: 3530–41.

Kebukawa, Y., Zolensky, M. E., Mathurin, J., Dartois, E., Engrand, C., Duprat, J., Deniset-Besseau, A. et al. 2020. Organic Matter in the AZ (CM2) Meteorite: High Abundance of Aliphatic Carbon in Metal-Rich Lithology (Abstract #1349). 51st Lunar and Planetary Science Conference. CD-ROM.

Kerraouch, I., Bischoff, A., Zolensky, M. E., Pack, A., Patzek, M., Hanna, R. D., Fries, M. D. et al. 2021. The Polymict Carbonaceous Breccia AZ: A Potential Analog to Samples Being Returned by the OSIRIS REx and Hayabusa2 Missions. *Meteoritics & Planetary Science* 56: 277–310.

Ketcham, R. A. 2005. Three-Dimensional Grain Fabric Measurements Using High-Resolution X-Ray Computed Tomography. *Journal of Structural Geology* 27: 1217–28.

Ketcham, R. A. and Ryan, T. 2004. Quantification and Visualization of Anisotropy in Trabecular Bone. *Journal of Microscopy* 213: 158–71.

Kitazato, K., Milliken, R. E., Iwata, T., Abe, M., Ohtake, M., Matsuura, S., Arai, T. et al. 2019. The Surface Composition of Asteroid 162173 Ryugu from Hayabusa 2 Near-Infrared Spectroscopy. *Science* 364: 272–5.

Kouvatsis, I. and Cartwright, J. A. 2020. The AZ Meteorite: A Review of Chondrules and Fine-Grained Rims Observed Within a New Carbonaceous Chondrite (CM2). *Fall* 51: 2512.

Lantz, C., Brunetto, R., Barucci, M. A., Dartois, E., Duprat, J., Engrand, C., Godard, M., Ledu, D., and Quirico, E. 2015. Ion Irradiation of the Murchison Meteorite: Visible to Mid-Infrared Spectroscopic Results. *Astronomy & Astrophysics* 577: 1–9.

Lantz, C., Brunetto, R., Barucci, M. A., Fornasier, S., Baklouti, D., Bourçois, J., and Godard, M. 2017. Ion Irradiation of Carbonaceous Chondrites: A New View of Space Weathering on Primitive Asteroids. *Icarus* 285: 43–57.

Le Guillou, C., Bernard, S., Brearley, A. J., and Remusat, L. 2014. Evolution of Organic Matter in Orgueil, Murchison and Renazzo During Parent Body Aqueous Alteration: In Situ Investigations. *Geochimica et Cosmochimica Acta* 131: 368–92.

Lee, M. R. and Lindgren, P. 2016. Aqueous Alteration of Chondrules from the Murchison CM Carbonaceous Chondrite: Replacement, Pore Filling, and the Genesis of Polyhedral Serpentine. *Meteoritics & Planetary Science* 51: 1003–21.

Lee, M. R., Lindgren, P., and Sofe, M. R. 2014. Aragonite, Breunnerite, Calcite and Dolomite in the CM Carbonaceous Chondrites: High Fidelity Recorders of Progressive Parent Body Aqueous Alteration. *Geochimica et Cosmochimica Acta* 144: 126–56.

Leroux, H., Marinova, M., Jacob, D., Hewins, R., Zanda, B., Humayun, M., and Lorand, J. P. 2015. A TEM Study of the Fine-Grained Material of the NWA 7533 Martian Regolith Breccia (Abstract #7533). 46th Lunar and Planetary Science Conference. CD-ROM.

Lewis, J. A., Jones, R. H., and Garcea, S. C. 2018. Chondrule Porosity in the L4 Chondrite Saratov: Dissolution, Chemical Transport, and Fluid Flow. *Geochimica et Cosmochimica Acta* 240: 293–313.

Lindgren, P., Hanna, R. D., Dobson, K. J., Tomkinson, T., and Lee, M. R. 2015. The Paradox Between Low Shock-Stage and Evidence for Compaction in CM Carbonaceous Chondrites Explained by Multiple Low-Intensity Impacts. *Geochimica et Cosmochimica Acta* 148: 159–78.

Macke, R. J., Consolmagno, G. J., and Britt, D. T. 2011. Density, Porosity, and Magnetic Susceptibility of Carbonaceous Chondrites. *Meteoritics & Planetary Science* 46: 1842–62.

Martin, P. M. C. and Lee, M. R. 2020. Degree of Aqueous Alteration of the CM Carbonaceous Chondrite AZ: Implications for Understanding Ryugu and Bennu (Abstract #1375). 51st Lunar and Planetary Science Conference. CD-ROM.

Matrajt, G., Messenger, S., Brownlee, D., and Joswiak, D. 2012. Diverse Forms of Primordial Organic Matter Identified in Interplanetary Dust Particles. *Meteoritics & Planetary Science* 47: 525–49.

Matsumoto, M., Tsuchiyama, A., Nakato, A., Matsuno, J., Miyake, A., Kataoka, A., Ito, M. et al. 2019. Discovery of Fossil Asteroidal Ice in Primitive Meteorite Acfer 094. *Science Advances* 5: 5078.

Merouane, S., Djouadi, Z., Le Sergeant d'Hendecourt, L., Zanda, B., and Borg, J. 2012. Hydrocarbon Materials of Likely Interstellar Origin from the Paris Meteorite. *The Astrophysical Journal* 756: 154.

Metzler, K., Bischoff, A., and Stöffler, D. 1992. Accretionary Dust Mantles in CM Chondrites: Evidence for Solar Nebula Processes. *Geochimica et Cosmochimica Acta* 56: 2873–97.

Michel, P., Ballouz, R. L., Barnouin, O. S., Jutzi, M., Walsh, K. J., May, B. H., Manzoni, C. et al. 2020. Collisional Formation of Top-Shaped Asteroids and Implications for the Origins of Ryugu and Bennu. *Nature* 11: 2655.

Mirone, A., Brun, E., Gouillart, E., Tafforeau, P., and Kieffer, J. 2014. The PyHST2 Hybrid Distributed Code for High Speed Tomographic Reconstruction with Iterative Reconstruction and A Priori Knowledge Capabilities. *Nuclear Instrument Methods Physical Research, Section B* 324: 41.

Nakamura-Messenger, K., Messenger, S., Keller, L. P., Clemett, S. J., and Zolensky, M. E. 2006. Organic Globules in the Tagish Lake Meteorite: Remnants of the Protosolar Disk. *Science* 5804: 1439–42.

Noun, M., Baklouti, D., Brunetto, R., Borondics, F., Calligaro, T., Dionnet, Z., Le Sergeant d'Hendecourt, L. et al. 2019. A Mineralogical Context for the Organic Matter in the Paris Meteorite Determined by a Multi-Technique Analysis. *Life* 9: 44.

Okada, T., Fukuhara, T., Tanaka, S., Taguchi, M., Arai, T., Senshu, H., Sakatani, N. et al. 2020. Highly Porous Nature of a Primitive Asteroid Revealed by Thermal Imaging. *Nature* 579: 518–22.

Paganin, D., Mayo, S. C., Gureyev, T. E., Miller, P. R., and Wilkins, S. W. 2002. Simultaneous Phase and Amplitude Extraction from a Single Defocused Image of a Homogeneous Object. *Journal of Microscopy* 206: 33.

Pilorget, C., Okada, T., Hamm, V., Brunetto, R., Yada, T., Loizeau, D., Riu, L. et al. 2021. First Compositional Analysis of Ryugu Samples by the MicrOmega Hyperspectral Microscope. *Nature Astronomy* 6: 221–5. https://doi.org/10.1038/s41550-021-01549-z.

Pizzarello, S., Yarnes, C. T., and Cooper, G. 2020. The AZ (CM2) Meteorite: New Insights into Early Solar System Organic Chemistry. *Meteoritics & Planetary Science* 55: 1525–38.

Potin, S., Beck, P., Bonal, L., Schmitt, B., Garenne, A., Moynier, F., Agranier, A., Schmitt-Kopplin, P., Malik, A. K., and Quirico, E. 2020. Mineralogy, Chemistry, and Composition of Organic Compounds in the Fresh Carbonaceous Chondrite Mukundpura: CM1 or CM2? *Meteoritics & Planetary Science* 55: 1681–96.

Quirico, E., Moroz, L. V., Schmitt, B., Arnold, G., Faure, M., Beck, P., Bonal, L. et al. 2014. Origin of Insoluble Organic Matter in Type 1 and 2 Chondrites: New Clues, New Questions. *Geochimica et Cosmochimica Acta* 136: 80–99.

Rubin, A. E., Trigo-Rodriguez, J. M., Huber, H., and Wasson, J. T. 2007. Progressive Aqueous Alteration of CM Carbonaceous Chondrites. *Geochimica et Cosmochimica Acta* 71: 2361–82.

Salisbury, J. W., D'Aria, D. M., and Jarosewich, E. 1991. Mid Infrared (2.5–13.5 μm) Reflectance Spectra of Powdered Stony Meteorites. *Icarus* 92: 280–97.

Sandt, C., Dionnet, Z., Toplak, M., Fernandez, E., Brunetto, R., and Borondics, F. 2019. Performance Comparison of Aperture-Less and Confocal Infrared Microscopes. *Journal of Spectral Imaging* 8: 1–14.

Suttle, M. D., King, A. J., Schofield, P. F., Bates, H., and Russell, S. S. 2021. The Aqueous Alteration of CM Chondrites, a Review. *Geochimica et Cosmochimica Acta* 299: 219–56.

Takir, D., Howard, K. T., Stockstill-Cahill, K. R., Hibbitts, C. A., Abreu, N., Zolensky, M. E., and Fries, M. 2020.

Spectroscopy and Mineralogy of Aguas Zarca (Abstract #2533). 51st Lunar and Planetary Science Conference. CD-ROM.

Tarantino, S. C., Carpenter, M. A., and Domeneghetti, M. C. 2003. Strain and Local Heterogeneity in the Forsterite-Fayalite Solid Solution. *Physics and Chemistry of Minerals* 30: 495–502.

Tomeoka, K., Kojima, H., and Yanai, K. 1989. Yamato-86720: A CM Carbonaceous Chondrite Having Experienced Extensive Aqueous Alteration and Thermal Metamorphism. *Proceedings of the NIPR Symposium on Antarctic Meteorites* 2: 55–74.

Trigo-Rodriguez, J. M., Rubin, A. E., and Wasson, J. T. 2006. Non-Nebular Origin of Dark Mantles Around Chondrules and Inclusions in CM Chondrites. *Geochimica et Cosmochimica Acta* 70: 1271–90.

Tunney, L. D., Hill, P. J. A., Herd, C. D. K., and Hilts, R. W. 2020. Distinguishing Between Terrestrial and Extraterrestrial Organic Compounds in the CM2 AZ Carbonaceous Chondrite (Abstract #1795). 51st Lunar and Planetary Science Conference. CD-ROM.

Velbel, M. A., Tonui, E. K., and Zolensky, M. E. 2012. Replacement of Olivine by Serpentine in the Carbonaceous Chondrite Nogoya (CM2). *Geochimica et Cosmochimica Acta* 87: 117–35.

Velbel, M. A., Tonui, E. K., and Zolensky, M. E. 2015. Replacement of Olivine by Serpentine in the Queen Alexandra Range 93005 Carbonaceous Chondrite (CM2): Reactant-Product Compositional Relations, and Isovolumetric Constraints on Reaction Stoichiometry and Elemental Mobility During Aqueous Alteration. *Geochimica et Cosmochimica Acta* 148: 402–25.

Villalon, K. L., Heck, P. R., Keating, K., Davis, A. M., and Stephan, T. 2020. GEMS-Like Material in Aguas Zarcas Interchondrule Matrix (Abstract #2757). 51st Lunar and Planetary Science Conference. CD-ROM.

Vinogradoff, V., Le Guillou, C., Bernard, S., Binet, L., Cartigny, P., Brearley, A. J., and Remusat, L. 2017. Paris vs. Murchison: Impact of Hydrothermal Alteration on Organic Matter in CM Chondrites. *Geochimica et Cosmochimica Acta* 212: 234–52.

Walsh, K. J., Ballouz, R. L., Bottke, W. F., Avdellidou, C., Connolly, H. C., Delbo, M., DellaGiustina, D. N., et al. 2020. Likelihood for Rubble-Pile Near-Earth Asteroids to be 1st or nth Generation: Focus on Bennu and Ryugu (Abstract #2253). 51st Lunar and Planetary Science Conference. CD-ROM.

Weisberg, M. K., McCoy, T. J., and Krot, A. N. 2006. Systematics and Evaluation of Meteorite Classification. In *Meteorites and the Early Solar System* II, edited by D. S. Lauretta, and H. Y. McSween Jr., 19–52. Tucson, Arizona: University of Arizona Press.

Weitkamp, T., Scheel, M., Giorgetta, J., Joyet, V., Roux, V. L., Cauchon, G., Moreno, T., Polack, F., Thompson, A., and Samama, J. 2017. The Tomography Beamline ANATOMIX at Synchrotron SOLEIL. *Journal of Physics: Conference Series* 849: 012037.

Wells, M., Pel, J. W., Alistair, G., Wright, G. S., Aitink-Kroes, G., Azzollini, R., Beard, S. et al. 2015. The Mid-Infrared Instrument for the James Webb Space Telescope, VI: The Medium Resolution Spectrometer. *The Astronomical Society of the Pacific* 127: 646–64.

Yada, T., Abe, M., Okada, T., Yogata, K., Miyazaki, A., Hatakeda, K., Kumagai, K. et al. 2021. Preliminary Analysis of the Hayabusa2 Samples Returned from C-Type Asteroid Ryugu. *Nature Astronomy* 6: 214–20.

Yang, X., Hanna, R. D., Davis, A. M., Neander, A. I., and Heck, P. R. 2021. A Possible Record of an Active Asteroid: Discovery of a Compact Lithology in the AZ CM Chondrite (Abstract #6075). 84th Annual Meeting of the Meteoritical Society.

Yesiltas, M., Sedlmair, J., Peale, R. E., and Hirschmugl, C. J. 2016. Synchrotron-Based Three-Dimensional Fourier Transform Infrared Spectro-Microtomography of Murchison Meteorite Grain. *Applied Spectroscopy* 71: 1198–208.

Zanetta, P.-M., Leroux, H., Le Guillou, C., Zanda, B., and Hewins, R. H. 2021. Nebular Thermal Processing of Accretionary Fine-Grained Rims in the Paris CM Chondrite. *Geochimica et Cosmochimica Acta* 295: 135–54.

Zolensky, M. E., Mittlefehldt, D. W., Lipschutz, M. E., Wang, M. S., Clayton, R. N., Mayeda, T. K., Grady, M. M., Pillinger, C., and David, B. 1997. CM Chondrites Exhibit the Complete Petrologic Range from Type 2 to 1. *Geochimica et Cosmochimica Acta* 61: 5099–115.

The Meteoritical Society

Meteoritics & Planetary Science 56, Nr 6, 1151–1172 (2021)
doi: 10.1111/maps.13696

A preparation sequence for multi-analysis of µm-sized extraterrestrial and geological samples

Alice ALÉON-TOPPANI[1]*, Rosario BRUNETTO[1], Jérôme ALÉON[2], Zelia DIONNET[1,3,4], Stefano RUBINO[1], Dan LEVY[1,2], David TROADEC[5], François BRISSET[6], Ferenc BORONDICS[7], and Andrew KING[7]

[1]Institut d'Astrophysique Spatiale, UMR 8617, CNRS, Univ. Paris-Saclay, Bât 120-121, 91405 Orsay Cedex, France
[2]Institut de Minéralogie, de Physique des Matériaux et de Cosmochimie, UMR 7590, Sorbonne Université, Museum National d'Histoire Naturelle, CN RS, IRD, 61 rue Buffon, 75005 Paris, France
[3]INAF-IAPS, Rome, Italy
[4]DIST-Università Parthenope, Naples, Italy
[5]Institut d'électronique de microélectronique et de nanotechnologie, UMR 8520, Laboratoire central, Cité scientifique, Avenue Henri Poincaré, CS, 60069, 59652 Villeneuve d'Ascq Cedex, France
[6]Institut de Chimie Moléculaire et des Matériaux d'Orsay, CNRS, UMR 8182, Univ. Paris-Saclay, Orsay, France
[7]SOLEIL Synchrotron, Gif-sur-Yvette, France
*Corresponding author. E-mail: alice.aleon@universite-paris-saclay.fr

(Received 17 November 2020; revision accepted 05 April 2021)

Abstract–With the recent and ongoing sample return missions and/or the developments of nano- to microscale 3-D and 2-D analytical techniques, it is necessary to develop sample preparation and analysis protocols that allow combination of different nanometer- to micrometer-scale resolution techniques and both maximize scientific outcome and minimize sample loss and contamination. Here, we present novel sample preparation and analytical procedures to extract a maximum of submicrometer structural, mineralogical, chemical, molecular, and isotopic information from micrometric heterogeneous samples. The sample protocol goes from a nondestructive infrared (IR) tomography of ~10 to ~70 µm-sized single grains, which provides the distribution and qualitative abundances of both mineral and organic phases, followed by its cutting in several slices at selected sites of interest for 2-D mineralogical analysis (e.g., transmission electron microscopy), molecular organic and mineral analysis (e.g., Raman and/or IR microspectroscopy), and isotopic/chemical analysis (e.g., NanoSIMS). We also discuss here the importance of the focused ion beam microscopy in the protocol, the problems of sample loss and contamination, and at last the possibility of combining successive different analyses in various orders on the same micrometric sample. Special care was notably taken to establish a protocol allowing correlated NanoSIMS/TEM/IR analyses with NanoSIMS performed first. Finally, we emphasize the interest of 3-D and 2-D IR analyses in studying the organics–minerals relationship in combination with more classical isotopic and mineralogical grain characterizations.

INTRODUCTION

Over the past few decades, analyses of microscopic samples have become increasingly important to extract a wealth of scientific information from rare and precious samples. On the one hand, samples, such as the asteroid dust that will be returned by the Hayabusa2 (Watanabe et al. 2017, 2019; Jaumann et al. 2019) or the OSIRIX-REx (Hamilton et al. 2019; Lauretta et al. 2019) space missions, are expected to be very heterogeneous (close to carbonaceous chondrite mineralogy) and require analyses with techniques having nanometer-scale resolution. On the other hand, to gain information from meteorites and geological or biological samples, processes are now increasingly examined at micro/nanometric scales with the aim of

combining different in situ complementary methods (e.g., transmission electron microscopy [TEM] for mineralogy and chemical composition, infrared [IR] spectroscopy for molecular information on silicate and organic matter, nanometer scale secondary ion mass spectrometry [NanoSIMS] for isotopes).

In this context, it is necessary to perform multiple complementary analyses on micrometer-sized samples, from the least destructive to the most destructive methods to maximize scientific outcomes and minimize sample loss and contamination. Multi-analytical sequences were successfully used in the recent past to analyze (1) samples from comet Wild 2 and asteroid Itokawa returned by the Stardust and Hayabusa space missions, respectively (e.g., Zolensky et al. 2008; Nakamura et al. 2011); and (2) very small and unique meteorites (e.g., Acfer 094, Matsumoto et al. 2019). Those sequences either consisted of successive analyses on the same thin section such as XANES (X-ray absorption near edge structure), TEM, and finally NanoSIMS which, in the end, consumed integrally the section (e.g., Stadermann et al. 2005; Zolensky et al. 2008; De Gregorio et al. 2011), or consisted of 3-D-XCT (X-ray computed tomography), -XRD (X-ray diffraction), or -XRF (X-ray fluorescence) analyses of a grain subsequently sliced in several sections, which were analyzed independently by different techniques (e.g., TEM or NanoSIMS, Nakamura et al. 2011; Matsumoto et al. 2019). Recent approaches to address this issue were to develop specific sample holders allowing multi-analyses (Ito et al. 2020) with limited contamination (Shirai et al. 2020; Uesugi et al. 2020) or to increase the number of prepared samples from a single grain (e.g., Berger and Keller 2015). However, none of these sequences allowed multi-analyses on the same section in variable order or reanalysis after the sequence was completed.

Here, we present a novel sequence to analyze samples of ~10 to 70 µm-sized grains (Aléon-Toppani et al. 2020; Brunetto et al. 2020), which aims at (1) maximizing the scientific output from a single grain, (2) combining different techniques on the same sample preparation step, and (3) using the same technique at successive preparation steps to optimize the scientific information obtained from the sample. This sample analysis sequence begins by an innovative sample preparation of grains welded at the end of a holder needle. Special care is taken during sample preparation to minimize sample loss and sample contamination. Infrared computed microtomography (IR-CT) is performed as a first step for a nondestructive characterization of the 3-D structure and chemistry of the grain (Dionnet et al. 2020). This notably allows the identification of subregions of interest, which can be targeted for further analyses. Subsequently, we follow two different approaches: (1) preparation of sequential focused ion beam (FIB) sections of single ~10 to 65 µm grains, for different 2-D analytical methods (e.g., IR microspectroscopy, TEM, or NanoSIMS), and (2) development of a new FIB section mounting protocol that allows a combination of different analytical methods on the same FIB section starting with NanoSIMS, followed by IR spectroscopy and/or TEM. The second approach can also be used on thick FIB sections extracted from polished sections that were preliminarily characterized by SEM (scanning electron microscope). Here, we focus on (1) IR imaging microspectroscopy because, in addition to being totally nondestructive and comparable to remote sensing observations of small bodies, it allows the possibility to detect and study the spatial distribution of molecular bonds associated with minerals, water, and organic compounds and their co-localization; (2) TEM as it allows the study at the atomic scale of the chemistry and the crystallographic structure of the particle; and (3) NanoSIMS as it provides the distribution of isotopes and trace elements at the 100 nm scale.

MATERIALS AND METHODS

Sample Description

Reference minerals used in this study included San Carlos olivine, calcite, macusanite glass, and two samples widely used for the analysis of water content and D/H ratios (the Bamble Mg-hastingsite amphibole [Engrand et al. 1999] and a mica [CRPG phlogopite, Govindaraju 1994]). In the context of the sample return missions Hayabusa2 and OSIRIS-REx from carbonaceous asteroids, we also focused on carbonaceous chondrite samples. We prepared and analyzed single 10–70 µm-sized grains extracted from the Paris CM chondrite (Hewins et al. 2014) and from the NWA 5515 CK chondrite (Weisberg et al. 2009).

Sample Preparation

As the first step of the preparation chain, the sample was deposited as a single grain on a conductive substrate. Two types of substrates were used: ultraclean silicon wafer and gold plates additionally cleaned with pure analysis-grade ethanol in an ultrasonic bath. Grains with size ranging from $5 \times 40 \times 20$ to $97 \times 53 \times 40$ µm were deposited on those substrates in an ISO 6 clean room. Owing to electrostatic bonds, they usually did not move from the substrate during the transport of the plate from the clean room to the FIB. However, these electrostatic bonds are not strong

enough if the particle size exceeds ~70/100 μm. In this case, particles have to be directly handled in the FIB laboratory and deposited on the conductive substrate just before being inserted into the FIB chamber.

In addition, a few FIB sections extracted from polished sections of grains embedded in epoxy were used for the development of analytical techniques coupling.

Infrared and Raman Microspectroscopy

Both IR and Raman microspectroscopy were performed at the SMIS beamline of synchrotron SOLEIL (France). An Agilent Cary 670 Fourier-transform IR microscope equipped with a focal plane array detector (FPA) was used for the IR characterization of the samples. The spectral resolution was either 4 or 8 cm^{-1}. The spectral range extended from 850 to 3950 cm^{-1}. A 25× objective was used in combination with a high magnification system placed in front of the 128 × 128 pixel FPA detector. The projected pixel size was ~0.66 μm and the field of view was ~84 μm. The spatial resolution was diffraction limited in the whole spectral range. Sections were analyzed in transmission mode. Acquisition time was limited to 128 or 256 scans. Before each analysis, a background spectrum was acquired. In addition, some of the IR analyses presented here were performed with a Thermo Continuum microscope coupled to a Thermo Nicolet 8700 FTIR spectrometer (Thermo Fisher) operating in transmission mode. The source was either the internal globar or the external synchrotron light source, which provides a 100–1000× higher brightness than the globar source.

Raman spectroscopy was also used as a complementary method to study the characteristics on the organic/carbonaceous matter. It was performed using a DXR Raman microspectrometer from Thermo Fisher with a 532 nm exciting laser radiation. Raman maps were recorded with a spectral resolution of 4 cm^{-1} and a spatial resolution of about 1 μm. The laser power was typically in the 0.2–0.5 mW range (conditions similar to that used by Dionnet et al. [2018] on the Paris meteorite to avoid heating of the samples).

Nanoscale Secondary Ion Mass Spectrometry

NanoSIMS is a mass spectrometric method optimized for the scanning imaging of isotopes in μm-sized samples with a sub-μm spatial resolution given by the size of the primary ion beam. For some specific applications requiring efficient detection of trace isotopes (e.g., deuterium), intense primary beams with size on the order of 1 μm can also be used. Isotopic characterization was performed using the NanoSIMS 50 at IMPMC (Paris).

Amphibole and mica samples were studied using the protocol specifically developed to measure D/H ratios in FIB sections (Lévy et al. 2019). All samples were coated with 20 nm Au to ensure conductivity and measured after a storage time of 3 weeks in the vessel chamber of the instrument to ensure minimal residual surface contamination (Lévy et al. 2019). The D/H analysis was performed using a 100 pA Cs^+ beam of ~1.5 μm in size, rastered over an 8 × 8 μm area. The dwell time was fixed to 1000 μs/pixel and images consist of 256 × 256 pixels. A Cs^+ preimplantation was performed during 8 min with a 250 pA beam rastered over 20 × 20 μm to remove Au coating and achieve sputtering equilibrium (hereafter presputtering). These analytical conditions correspond to optimal conditions for the measurement of D/H ratios on FIB sections as determined in Levy et al. (2019) and ensure a large degree of overlap from pixel to pixel, which eliminates isotopic effects due to dynamic contamination during analysis and pitting effects during presputtering. Charging effects were compensated using the normal incidence electron gun. Negative secondary ions H^- and D^- were detected simultaneously using two electron multipliers. Twenty image planes were acquired with typical count rates of ~1.5×10^5 counts per second (c/s) for H^- and ~10 c/s for D^- resulting in typical uncertainties of ~20‰ at the FIB section scale. H isotopic compositions are reported as δD deviations relative to the Standard Mean Ocean Water reference (SMOW, $D/H_{SMOW} = 1.5576 \times 10^{-4}$) given in‰, where $\delta D = (D/H_{sample}/D/H_{SMOW} - 1) \times 1000$.

Transmission Electron Microscopy

Transmission electron microscopy is an electron-based imaging technique with atomic resolution that gives access to the sub-μm structure of the sample, and to information about the crystallography and chemical composition of the minerals/phases constituting the sample. Samples were characterized using a 200 kV FEI field emission transmission microscope (IMPMC, Paris) and a 200 kV 2100+ JEOL microscope (Univ. Paris-Saclay). Both microscopes were equipped with a high angle annular dark field (HAADF) detector and an EDS energy-dispersive spectrometer.

Imaging was carried out in a conventional mode (bright field) as well as in scanning mode using the HAADF detector. A few chemical analyses were obtained in the conventional mode. Imaging and energy dispersive spectroscopy (EDS) were carried out with low-dose conditions to minimize sample damage. Element abundances acquired on a SAMx IDFix system were quantified from EDS spectra by fitting peaks for all

elements detected and applying a Cliff–Lorimer thin-film correction procedure (Cliff and Lorimer 1975). The typical precision is about 10%. Elemental abundances were normalized to 100%.

Scanning Electron Microscopy

Characterization of polished samples or sample topography was performed using a Zeiss Supra 55 VP FEG SEM (Univ. Paris-Saclay) equipped with an EDAX energy-dispersive detector.

Focused Ion Beam Technique

Samples were prepared using a FEI Strata DB 235 SEM-FIB microscope at IEMN (Lille). It was used to (1) weld the single grains at the tip of W needles to perform X-ray and IR microtomography, (2) recover the grains from the W needle and deposit them on a conductive substrate in order to cut them in several slices of different thickness. After extraction, the slices were either welded on TEM grids for 2-D-IR spectroscopy and TEM characterization or mounted on Al disk for NanoSIMS characterization. For NanoSIMS analyses, the sample slices were sometimes directly extracted from samples embedded in epoxy, polished, and carbon or gold coated.

During FIB sample preparation, a focused beam of gallium ions was used either to ablate volumes of solids in precise locations and at carefully controlled rates with tolerances as fine as ~100 nm or to crack the organo-Pt gas to make precise welding. The samples can be imaged at micrometer resolution during preparation using both secondary ions and electrons. Details of preparation are given in the Results section.

RESULTS

Here, we present (1) the nondestructive 3-D tomography of single μm-sized meteoritic grains and the associated preparation, (2) the preparation of sequential FIB sections of the same single grain for different 2-D analytical methods (e.g., IR, TEM, or NanoSIMS), and (3) a new FIB section mounting protocol that allows different analytical methods on the same FIB section starting with NanoSIMS.

3-D Microtomography of Single Grains

Preparation of the Grain: FIB Welding of a Single Grain at the Tip of a Needle

In order to perform 3-D tomography of a micron-sized grain, it is necessary that the grain (1) stays in sight for most of its surface and (2) that it can rotate over 360°. The grain thus needs to be glued at the tip of a needle. In our study, a single grain deposited on a conductive substrate was welded with platinum or with SEM electronic glue (SEMGlue by Kleindiek Nanotechnik GmbH, Kleindiek et al. 2008; Martina et al. 2016) on a tungsten needle holder using the FIB (Fig. 1). An Al-needle was also successfully used. SEMGlue is an electron-beam hardening glue. Both types of welding were tested because each one has its own advantages: using e-glue prevents the deposition of high atomic number elements such as Pt (thus allowing some types of analyses such as XRF) whereas using Pt instead of e-glue or classical epoxy prevents the contamination of the extraterrestrial grain by terrestrial organics. For both types of welding, the FIB micromanipulator needle was used as holder needle. In the case of a platinum welding, the holder needle approaches the grain with a tilt between 30° and 40° and gently touches the grain on a selected side. Pt is then carefully deposited at the contact between the grain and the tip of the W needle on a restricted surface using the ion beam (30 kV, 300 pA). Four welding points are usually made by rotating the needle at 0, 90, 180, and 270° to ensure a strong welding. In the case of the electronic glue welding, the W needle tip is dipped into the glue while it is still liquid and is subsequently approached to the grain. The electron beam is then used to polymerize the e-glue at the precise location of the contact between the grain and the tip of the needle. In both cases, the particle is initially deposited on the conductive substrate and holds only by electrostatic bonds. Once the welding is complete, the particle can thus be lifted using the W needle, which is finally removed from the FIB chamber.

As studied samples could contain extraterrestrial organic matter, it was important to check the carbon/organic contamination due to our preparation. In the case of the Pt welding, as an organo-Pt gas was used, a slight carbon deposition could be expected over the whole grain, or at least concentrated around the welding point. In the case of e-glue, glue could be a source of carbon contamination by itself. Here, we show that the degree of carbon contamination in the welding process is limited in spatial distribution and amount (Figs. 2 and 3). Indeed, as shown in Fig. 1, both glue and Pt are spatially restricted to the welding zone.

In the case of Pt-glue, IR spectroscopy did not reveal the presence of any CH bonds from a carbon-contaminant layer on the grain, which would suggest an upper limit for the thickness of such a layer of a few tens of nm. The presence of an aromatic contaminant was investigated by Raman microspectroscopy (Fig. 2). Figure 2 shows Raman analyses of carbon

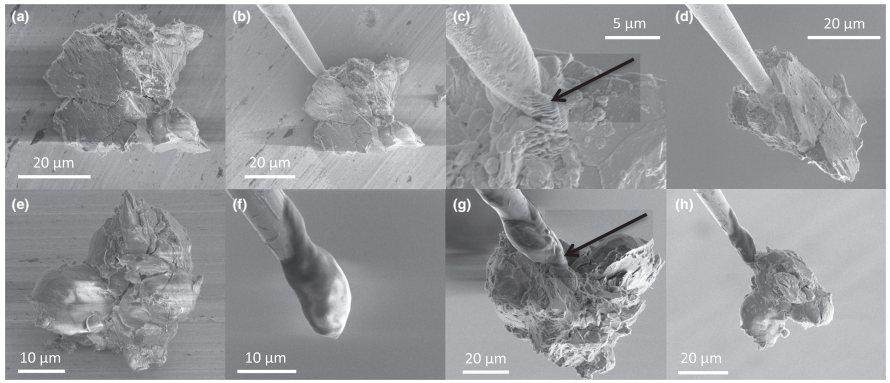

Fig. 1. Secondary electron images illustrating the welding of two grains from NWA5515 chondrite using platinum (a–d) and electronic glue (e–h). a, e) Grains deposited on gold substrate. d, h) Lifting of the grain. b) Contact between the holder needle and the grain. c) Details of the welding between the needle and the grain. f) Tip of the needle with liquid e-glue. g) Contact between the needle and the grain after polymerization of the grain. Arrows in (c) and (g) indicate the contact between the grain and the needle.

contamination for Pt-glue. A very weak dehydrogenated amorphous carbon Raman signature (large band at ~1500–1560 cm^{-1} and a shoulder around 1350 cm^{-1}) was detected around the Pt-welding at the interface between the sample and the needle, clearly distinguishable both spectrally and spatially from the Raman signature of the poly-aromatic carbon of the meteorite (classical D and G bands, with the G band of the Paris meteorite peaking around 1590–1600 cm^{-1}, e.g., Noun et al. 2019). The IR spectrum of the contact between a meteorite grain and the Pt welding confirms the presence of only amorphous dehydrogenated carbon when contamination is present (band around 1600 cm^{-1}). In the case of the Pt-welding, this difference evidences the presence of carbon contamination only near the welding point within about 5 µm (Fig. 2b).

In the case of the e-glue, we have investigated the IR signatures of both the e-glue and the typical organic matter of the CM Paris meteorite. Their IR spectra between 1200 and 1800 cm^{-1} (Fig. 3) carry two distinct signatures: the e-glue presents a maximum around 1711 cm^{-1} (probably due to C = O stretching), while the indigenous organic matter has a maximum around 1603 cm^{-1} (probably -OH bending) with a much weaker band at ~1700 cm^{-1}. The distinct spatial distribution of the intensity of these two bands, plotted in Fig. 3, shows that the e-glue is concentrated around the transition area between the needle and the sample and does not contaminate the sample. In agreement with the IR signature, no clear Raman signature of poly-aromatic carbons was detected in the e-glue, but only a strong fluorescence signal (Fig. 2a). This would allow an easy distinction between indigenous carbon and contamination if present.

For both the e-glue and Pt-welding, contamination is thus spatially restricted to the welding zone and shows a well-characterized spectral signature that could be easily distinguished from extraterrestrial organic matter.

Forty-one grains of minerals or fragments of meteorites were welded following this procedure; 7.3% (three grains) were lost during the welding process (e.g., cracks in the grains, deposition mistakes), 12.2% (five grains) were lost during transport, 9.7% (four grains) due to wrong handling. Twenty-three grains were welded with Pt and 16 grains with e-glue. Over 70% of the grains (29 grains) were analyzed at least once. Among those 29 grains analyzed, 27% were lost after the first analyses and 73% were analyzed several times (e.g., IR or X micro-tomography). Losses after analyses were due to either handling errors or the detachment of the grain from the needle, which could be related to an increase in the fragility of the grains after harsh analysis such as high-energy X-ray micro-tomography at different energies. After two to five campaigns of analyses, 34% of these 29 grains are still available for further analyses. Overall, 51% of the grains were analyzed several times (up to five times) with different methods and 25% are still available for further characterization after one to five analyses. Thus, a

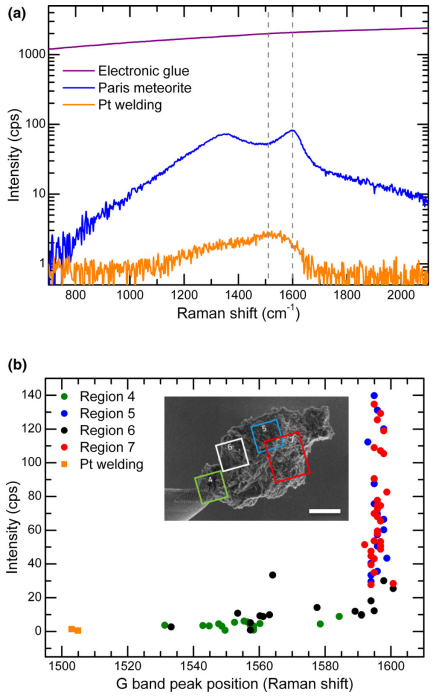

Fig. 2. Raman analysis of the carbon contamination deposited during welding using Pt or electronic glue. a) Raman spectra of the contamination related to the welding with Pt and e-glue compared with the Raman spectrum of the organic matter from the Paris meteorite. The Raman spectrum of the Paris meteorite shows classical D and G bands of poly-aromatic carbons, with the G band peaking around 1590–1600 cm^{-1}, whereas the carbon from the Pt-welding is amorphous and shows a large band around ~1500–1560 cm^{-1} with a shoulder around 1350 cm^{-1}. Finally, in this spectral range, the e-glue does not show any visible signature, but only a strong fluorescence signal. b) Intensity (counts per second) versus G-band position (cm^{-1}) measured from the welding point toward a grain of the Paris meteorite. This graph shows (1) that the surface amorphous carbon contamination is restricted to the surroundings of the welding point (between 2.5 and 5 µm at most) and (2) its intensity is relatively weak. (Color figure can be viewed at wileyonlinelibrary.com.)

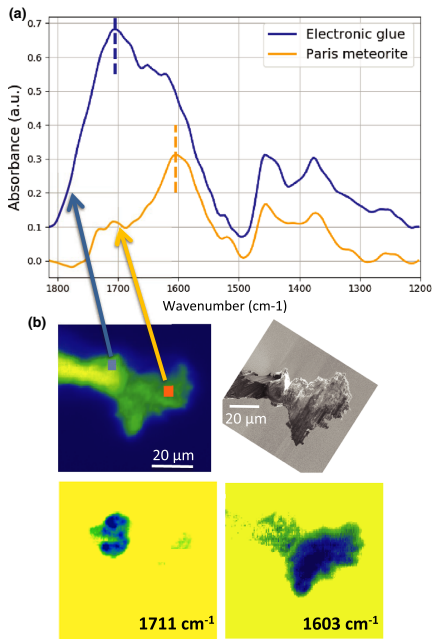

Fig. 3. IR analysis of the carbon contamination deposited during welding using e-glue. a) IR spectra extracted from the hyperspectral mapping of a grain of the Paris meteorite: one is from the e-glue located at the tip of the holder needle and the other one is from a spot of the meteorite rich in organic matter (see location in [b]). b) Secondary electron image (upper right), IR hyper-spectral mapping of the grain (upper left), and distinct distributions of the 1711 (lower left) and 1603 (lower right) cm^{-1} band in the grain and e-glue. (Color figure can be viewed at wileyonlinelibrary.com.)

rather large proportion of grains survived multiple analyses, handling, and transport. It must be emphasized that multiple analyses and handling of the grains induce numerous vibrations and shocks of various origin. For instance, during each campaign of analysis, the needle has to be fixed to a specific holder and can rotate up to 180 times in the case of 3-D analyses, suffering different types of vibration. Between each campaign of analysis, the grain fixed on the tip of the needle has to be placed back in a container to travel from one lab to another, suffering once again different vibrations. The survival of grains after analysis could thus be further increased by minimizing the transport of the grains between each analysis, using a facility-to-facility transport container or developing a universal sample holder that will prevent any handling of the needle (e.g., Ito et al. 2020). For most lost grains, SEM images show that the grains themselves broke rather

than the welding (Fig. S1 in supporting information). To prevent grain loss from the needle, it is thus important to adjust the quantity and localization of Pt welding between the needle and the particle depending on its geometry or structure (e.g., presence of initial fracture, porous/nonporous structure, presence of large welding surface, etc.).

Example of 3-D IR Micro-Tomography

Once a grain is mounted on a needle, it becomes available for 3-D analytical methods, and different types of 3-D characterization can be performed on the same single grain. As IR spectroscopy is a totally nondestructive method, we first performed IR micro-tomography with the Agilent Cary 670 IR microscope equipped with an FPA detector. The needle was connected to a motor to ensure the rotation of the sample under the microscope, around the needle axis. Using the method described by Dionnet et al. (2020), we collected a series of 2-D hyper-spectral maps in transmission for 180 angles, which were later reconstructed to obtain the distribution of the different functional groups in 3-D. The spectral resolution was 16 cm^{-1} for the 3-D-IR tomography. We show here an example of 3-D IR micro-tomography performed on a homogenous grain of calcite (Fig. 4). The continuum at 3550 cm^{-1}, shown in gray, is representative of all the matter (needle and sample). The reconstructed 3-D distribution of the intensity of the 2500 cm^{-1} calcite band is presented in red.

A complementary XCT measurement was performed at the PSICHE beamline of SOLEIL with energy of 17.6 keV and a photon flux of 1.6×10^{11} $phs.s^{-1}.mm^{-2}$. XCT allowed us to study the morphology of the sample at a smaller scale. By combining the two techniques on the same sample, we used the better spatial resolution of the X-ray data to constrain the shape of the IR reconstruction and to partially compensate the scattering/diffraction effects visible on IR data (Dionnet et al. 2020). An example of a whole sequence in 3-D, containing both IR tomography and XCT, has been performed on a fragment of NWA 5515 meteorite and will be presented later in the article.

Sequential FIB Preparation of Single Grains

Preparation of Several Sections from Single Grains

After IR-CT analyses, single grains can be recovered and sliced into several sections for further 2-D mineralogical, chemical, and isotopic analyses (Fig. 5). The holder needle is put back in the FIB chamber in place of the micromanipulator needle (Fig. 5a). Using the Ga beam of the FIB focused at the contact between the grain and the holder needle, the grain is removed from the needle and retrieved on a conductive substrate (Fig. 5b).

Small and very heterogeneous grains are completely covered by platinum in order to be protected from irradiation damages and to improve cohesion (Fig. 5c). The Ga beam is subsequently used to cut the grain into several slices (Figs. 5d and 5e). Then, one after the other, the slices are connected to the W needle using Pt and separated from the substrate using the Ga beam (Fig. 5f). The grains usually have an irregular shape and can be sliced perpendicular to their longest dimension. The width and the height of a grain which can be easily cut are limited to ~20 to ~30 microns as wide cuts would be required to create a cross section of larger particles and FIB sections larger than 20–30 microns would be difficult to manipulate.

In the example provided here, dedicated sections for IR and TEM analyses were welded to a TEM grid using Pt-deposition (Giannuzzi and Stevie 1999; Heaney et al. 2001). Sections for TEM analysis were finally thinned in situ down to ~100 nm for electron beam transparency (Fig. 5i) and sections for IR mapping were thinned down to 1 µm (Fig. 5h). Both sections were cleaned using a low-energy Ga beam at grazing incidence. Finally, one 3 µm thick section was retrieved for NanoSIMS analyses and deposited on an Al substrate. Images of the FIB sections (Figs. 5g–i) show the grain rimmed by a layer of Pt previously deposited over the whole grain. A thin outer layer made of the conductive substrate material that was sputtered by the Ga beam during the cutting of the section from the substrate was sometimes present.

The ion beam current used during the process was chosen to minimize the degradation of the FIB sections. Ion beam voltage was 30 kV except to finish the thinning of the section, which was performed at 5 kV to minimize the damages to the section. Intensities of the ion beam for the deposition of Pt were between 3 and 1 nA with a defocused beam. It was around 20 nA with a large diaphragm to 7 nA to trench the sides and the edges of the section and finally 3–1 nA to thin the section down to 1 µm and 300–500 pA to finish the thinning of the section. Under similar experimental conditions, fragile phases such as phyllosilicates, glass, or even organic material are usually left undamaged, suggesting that our final TEM sections were not damaged during their preparation (Heaney et al. 2001; Lee et al. 2003; Mayer et al. 2007). In addition, (1) using a low voltage during the final thinning, (2) transferring a much thicker liftout section (1–3 microns – Fig. 5) to the TEM grid, (3) minimizing the electron beam imaging during the thinning of the section, (4)

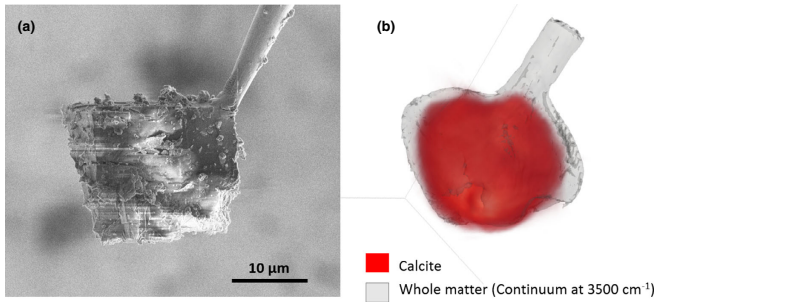

Fig. 4. a) Secondary electron image of a calcite grain Pt-welded at the tip of a W needle. b) IR micro-tomography reconstruction of the calcite grain. Red shows the spatial distribution of the calcite based on its thin 2520 cm^{-1} band whereas gray shows the 3-D reconstruction of the spectral continuum around 3500 cm^{-1}, which includes scattering, diffraction, and absorption of both grain and needle. A filter was applied to the calcite distribution to remove scattering artifacts at the edges of the grains. Note that the orientation of the grain may be slightly different from that of the SE image. (Color figure can be viewed at wileyonlinelibrary.com.)

lowering the ion beam overlap or creating a rigid Pt or natural frame around the thin section (see Fig. 5 or Fig. S4 in supporting information) increase the preservation of organic matter and minimize local specimen heating and mechanical failure (Bassim et al. 2012). If an Ar beam gun is available in the FIB, it could be used to remove the very thin damage layer formed during the Ga ion beam treatment (Kodama et al. 2020).

Thanks to this process, we were able to obtain three slices of about 3 µm thickness from a ~10 × 20 µm grain of olivine and five slices of 1–3 µm thickness from a ~35 × 35 × 15 µm grain of the NWA 5515 chondrite. The loss due to the ablation of the slice is estimated to be around 50%. It is noticeable that after analyses, the two largest slices could be recovered and thinned again to be observed with the TEM. Note that for large FIB section (over ~15 by ~15 microns), the thinning of the section can only be limited to the zones of interest.

Example of IR and Raman Spectra of 2-D Sections

IR transmission microspectroscopy of a 700 nm thick FIB section extracted from a single grain of olivine was performed using the synchrotron beam with an aperture of 8 × 8 µm, a resolution of 8 cm^{-1}, and summing 2048 scans. The Raman mapping was performed in conditions described earlier, with a resolution of 4 cm^{-1}.

The spectra (Fig. 6) show high-quality IR and Raman signatures of olivine within the grain. The IR spectrum shows typical olivine peaks at ~838, ~875, 980 cm^{-1} (Hamilton 2010) and a supplementary peak at 1050 cm^{-1} which could correspond to a weak band of olivine or more probably to amorphous silicate related to a slight re-deposition of oxidized substrate atoms. The Raman spectrum shows the typical olivine peaks at 822 cm^{-1} and 855–856 cm^{-1}. By contrast, the Pt rim shows the presence of a large G band around 1530 cm^{-1} and a shoulder at 1350 cm^{-1} (D band) which can be attributed to the presence of amorphous carbon deposited together with the Pt, similar to what was described above. This amorphous carbon results from the cracking of the organo-metallic gas during Pt deposition. Note that in the absence of Pt deposition, we did not detect any signature of amorphous carbon.

Our different test experiments indicate that a thickness around 1–2 µm is correct for transmission FTIR analysis, either with a synchrotron or globar source. We have calculated that for a 700 nm thick section of macusanite glass, the signal-to-noise ratio is at least four times better with the synchrotron source than the globar source (Fig. S2 in supporting information). When looking at much thinner sections such as TEM sections (~100 nm), the signal/noise ratio is rather low even with the synchrotron, allowing only a first-order analysis of the species present in the section.

As a slight re-deposition of substrate atoms could be expected during FIB preparation, care must be taken in the choice of the substrate. For example, a gold wafer must be used instead of a silicon wafer if the study of silicates is of importance, in order to avoid any deposition of amorphous silicon during FIB preparation.

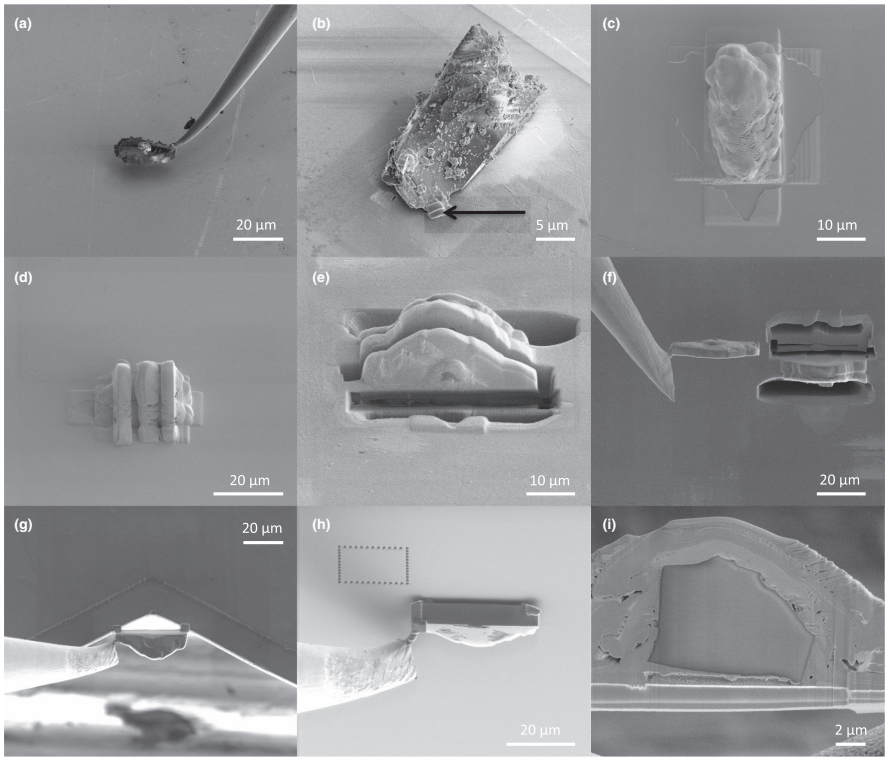

Fig. 5. Secondary electron (a–f, i) and ion (g, h) images of the recovery and slicing of an olivine grain. a) Deposition of the grain on a conductive substrate; (b) olivine grain free of the holder needle, the arrow indicates the remaining Pt welding that was cut in order to recover the grain; (c) deposition of a protective/cohesive layer of Pt over the whole grain; (d, e) cutting of the grain in three slices; (f) lifting of one slice with the needle from the micro-manipulator; (g) welding of the slice on a special TEM M-grid; and (h) deposition of a thick slice on an Al-substrate. Note that the rectangular dotted lines correspond to marks that were previously made on the wafer. i) Detail of one of the slices showing the grain rimmed by the Pt-layer.

NanoSIMS Analyses of 2-D Thick Sections and Following TEM and IR Analyses

Constraints of NanoSIMS Analysis and Preparation of the 2-D Sections

Ever since the development of NanoSIMS analyses, coupling with other microscopies or microspectrometries has been investigated for the analysis of small and precious samples (e.g., Nguyen et al. 2007; Matrajt et al. 2008; De Gregorio et al. 2011; Floss et al. 2014). However, NanoSIMS analyses are usually performed after all other analyses because they are destructive at the 100 nm scale. They can be performed on almost any flat sample surface, provided charge accumulation can be prevented. For instance, NanoSIMS has been done after TEM (e.g., Stadermann et al. 2005; Eswara et al. [2019] and references within) or after TEM + STXM (Le Guillou et al. 2013). Performing NanoSIMS imaging last implies (1) that mineralogical/chemical analysis of the samples must be complete before trace elements/isotopes can be analyzed (e.g., Messenger et al. 2005) and (2) 100 nm thick samples such as TEM

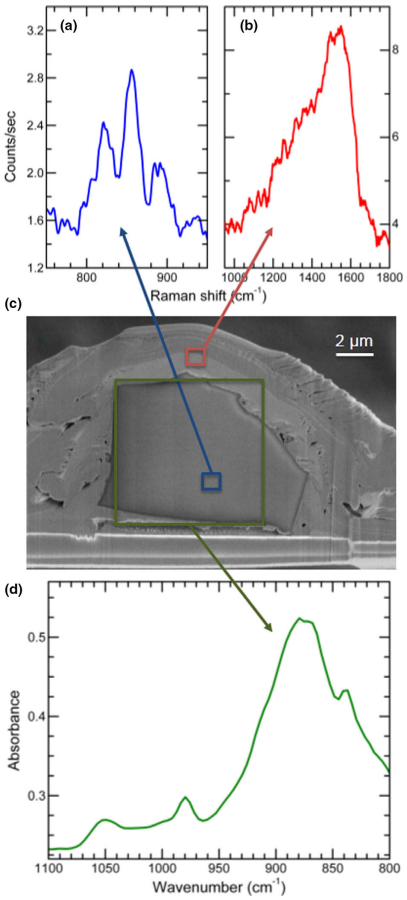

Fig. 6. IR (d) and Raman spectra (a, b) of an ~700 nm thick slice extracted from a 10 × 20 µm grain of olivine (c). IR spectrum was acquired within the grain using an aperture of 8 × 8 µm and a resolution of 8 cm^{-1}. Typical peaks of olivine are observed on the spectra (~838, ~875, 980 cm^{-1}). Raman spectra of the sample were measured both in the grain and in the Pt-layer rimming the grain. Spectral resolution is 4 cm^{-1} and spatial resolution is around 1 µm. Typical Raman shift of San Carlos olivine is observed for the interior of the grain (822 and 855/856 cm^{-1}). The Pt rim shows a large band with a peak centered on ~1530 cm^{-1} and a shoulder on ~1350 cm^{-1} corresponding to the G and D bands of amorphous carbon. (Color figure can be viewed at wileyonlinelibrary.com.)

sections are usually completely sputtered away after analysis or have suffered damages beyond the possibility of further analyses (e.g., Stadermann et al. 2005).

If NanoSIMS analyses are performed first (e.g., to detect isotopically anomalous components in extraterrestrial matter or experimental samples), two approaches have been developed up to now to characterize the phase(s) of interest (e.g., mineralogy of the carrier phase). (1) Sequential ultramicrotome sections have been prepared so that adjacent sections can be analyzed by different techniques (e.g., Matrajt et al. 2008; Simon et al. 2008; De Gregorio et al. 2011; Penen et al. 2016). (2) Alternatively, a second FIB section has been extracted perpendicularly to the NanoSIMS analysis surface of the first FIB section (or the initial polished section or grain, Smith et al. 2005; Floss et al. 2014; Suer et al. 2017), which must be thick enough (Suer et al. 2017). This also has the disadvantage that the area of interest is in direct contact with the protective Pt coating deposited during the second FIB sectioning and may suffer contamination preventing clean EDS chemical analysis or high-resolution imaging.

Our new sample mounting procedure to perform NanoSIMS imaging of FIB sections before subsequent correlated analysis by synchrotron-based microspectroscopies and/or TEM has several requirements. (1) The section of interest must be thicker than the depth of NanoSIMS analysis; (2) distortion of field lines, charging, and topography due to sample preparation must be minimal for NanoSIMS analysis; and (3) the atomic layers damaged by the ion beam must be removed before subsequent mineralogical analyses.

To solve these issues, we prepared 2–3 µm thick FIB sections, which were deposited on flat conductive NanoSIMS sample mounts. We used Si wafers and polished Al or stainless steel disks and found that Al disks were easier to produce, handle, and adapt to the NanoSIMS sample holders so they were used preferentially. The FIB sections should be deposited on top of the Al disk so that the surface to be analyzed is parallel to the extraction lens (EOS) and the topography is restricted to the thickness of the FIB section. However, if the whole surface of the FIB section is in contact with the disk, it is almost impossible to recover the FIB sections. The FIB sections were thus mounted on 1–2 µm bridges made of Pt deposited in the FIB-SEM (Figs. 7a–d). To do so, two parallel Pt stripes are deposited onto the sample mount at a distance of the FIB section length from each other, in the central portion of the Al disk mount for NanoSIMS. Being welded to a W needle, the FIB section is put into contact with the Pt stripes.

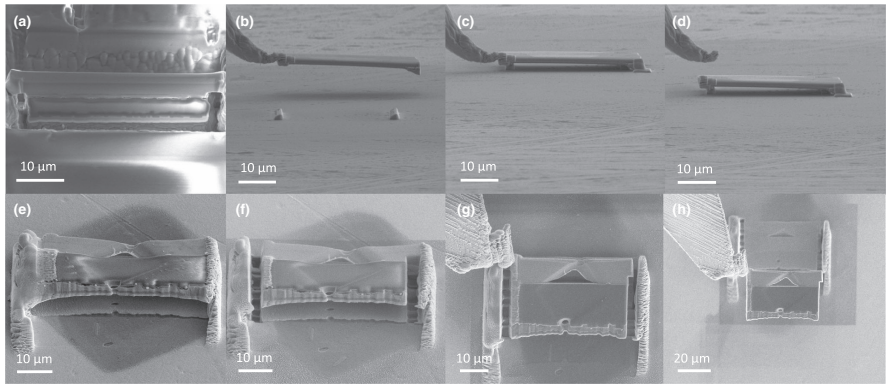

Fig. 7. Electron images of the preparation of the NanoSIMS section on Pt bridge (a-d) and recovery after NanoSIMS analysis for further analyses (e–h). a) Extraction of a thick FIB section from a sample; (b) deposition of the slice on two Pt stripes; (c) welding of the section to the stripes; (d) lifting of the needle after sectioning the needle from the slice; (e) FIB section after NanoSIMS analysis showing the analysis crater; (f) total and partial sectioning of the border of the slice; (g) welding of the needle to one side of the section and final sectioning of the border of the slice; and (h) lifting of the free slice.

Extremities of the FIB sections are then welded to the Pt stripes to form a bridge and maintain the FIB section onto the stripes. The Pt contact between needle and FIB section is finally cut.

Thick FIB sections used here can either be 3 µm thick FIB slices from single grains prepared as described earlier or be directly extracted from bulk sample embedded in epoxy. In the latter case, FIB sections are prepared in a classical way. A 2 µm thick, 3 µm wide Pt-strap is deposited on the surface of the polished section to protect it from ion damage (amorphization or ion implantation). This is followed by ion beam milling of trenches on both sides and cuts at the edges of the section to produce an ~1–2 µm thick section. The FIB section is then extracted from the bulk material by "welding" it using Pt deposition to a tungsten needle controlled by micro-manipulator and severing the final connection to the surrounding material using the ion beam. Compared to ultramicrotomy preparation, where only grains can be prepared for analysis of adjacent slices, the advantage of this method is that both small grains and large polished samples embedded in epoxy can be analyzed, which allows preservation of sample context.

Control of Instrumental Mass Fractionation

In order to ensure that FIB section mounting and preparation did not introduce further isotopic effects (i.e., modify the instrumental mass fractionation), we measured H isotopes in three samples of the Bamble amphibole (Fig. 8). Because of the very large relative mass difference between H and D, hydrogen isotopes are very sensitive to all instrumental effects and can be considered a good sensor of such effects. Three analyses of Bamble samples prepared as (1) polished section, (2) FIB section deposited on an Al disk without Pt bridge, and (3) FIB section deposited on an Al disk with a Pt bridge yielded D/H ratios identical within error, indicating that the preparation of the FIB section and mounting on Pt bridges did not introduce measurable isotopic effects.

Post-NanoSIMS Recovery of FIB Sections

For recovery, the FIB section is severed from the Pt bridge using the Ga beam completely at one end of the section and partially at the other end (Figs. 7e–h) so that the section still holds onto the disk by a small amount of Pt. The needle is then approached to the FIB section and welded to the free extremity of the section. Once the welding is complete, the partially cut side of the section is completely severed, resulting in a section free from the mount. The cut section is slightly smaller than the initial section (Fig. 7f). The needle is subsequently lifted and the section welded to a regular M or finger grid. The top surface of the FIB section is gently cleaned from the NanoSIMS damages using a low-intensity Ga beam from 1 nA to 300 pA (Fig. 9). In order to keep the section's thickness compatible with sensitivity of FTIR, the thinning step is limited to the removal of the layer damaged by ion sputtering during NanoSIMS analysis,

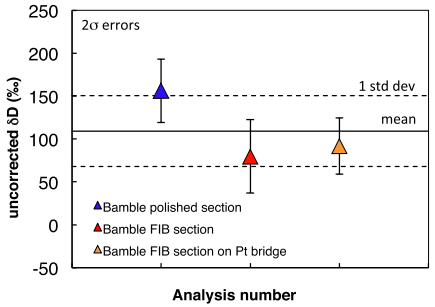

Fig. 8. Hydrogen isotopic composition of the Bamble amphibole analyzed with different sample preparations, uncorrected for instrumental mass fractionation. The similar values obtained for the polished section, the FIB section deposited on Al disk, and the FIB section mounted on Pt bridge indicate the absence of additional instrumental bias due to FIB section preparation and mounting within errors. (Color figure can be viewed at wileyonlinelibrary.com.)

while for subsequent TEM analysis, the section is thinned down to 100 nm. In order to preserve the portion of the section immediately adjacent to the bottom of the NanoSIMS analysis crater, that is, corresponding to the end of the NanoSIMS analysis, it is necessary to remove material on the opposite side of the section that was analyzed by NanoSIMS (Fig. 9).

NanoSIMS-FTIR-TEM Characterization Sequences

The complete analytical sequence has been tested on a sample of CRPG phlogopite (Fig. 10). A 2 µm thick FIB section was extracted from the phlogopite standard included in epoxy and subsequently deposited on Pt bridges in the center of a 1 cm diameter Al-disk for further recovery (Fig. 10a). The H^- distribution map and δD map (Fig. 10b) show distinctly the mica section and its protective Pt coating deposited during FIB section preparation. While the raw δD value of ~−100‰ of the mica (i.e., uncorrected from instrumental mass fraction) is well within typical raw compositions of natural terrestrial hydroxylated minerals measured in these conditions (Lévy et al. 2019), the δD value of organometallic bonded H in Pt is much more negative ($\delta D \sim -500$‰), which can be attributed to matrix effects of instrumental origin between hydroxylated silicates and organics, with organics usually having much more fractionated compositions, that is, much lower D/H ratios, hence δD values (Lévy et al. 2019). A transitional region of width about 1–1.5 µm corresponding to the primary ion beam overlapping on both Pt and phlogopite is visible on both elemental and isotopic

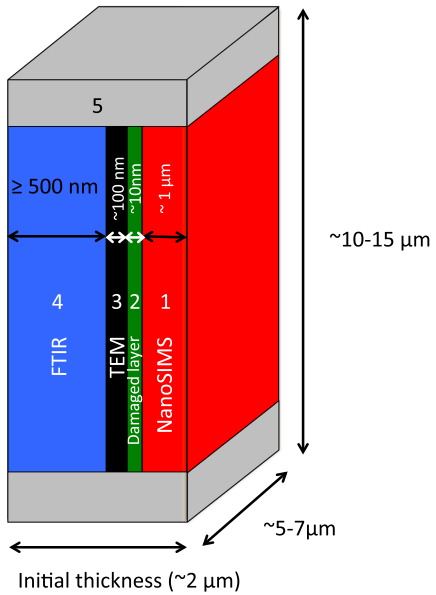

Fig. 9. Cartoon summarizing the cross section of an FIB section prepared for combined NanoSIMS, FTIR, and TEM analyses. The top part exposed to the first NanoSIMS analysis is shown to the right. Once the section is recovered from NanoSIMS analysis, the red 500 nm to 1 µm thick layer (1) has been consumed and the green <10 nm thick layer (2) damaged by the ion beam is removed in the FIB-SEM. After FTIR, the back part of the section (500 nm to 1 µm) (4) is removed in the FIB-SEM, leaving a thin (~100 nm thick) electron transparent section (3). Layer (5) is the border of the FIB section, which is contaminated by Pt from the FIB welding. This procedure allows to analyze by FTIR and TEM a portion of the section immediately adjacent to the bottom of the material analyzed by NanoSIMS, that is, corresponding to the end of the NanoSIMS analysis. (Color figure can be viewed at wileyonlinelibrary.com.)

images. This demonstrates the feasibility of imaging variations of D/H ratios on the order of 100–200‰ at the 1 µm scale using this technique (Lévy et al. 2019). Figure 10c shows the zone analyzed by NanoSIMS on the FIB section. After NanoSIMS analysis, the section was recovered and thinned down to ~1 µm for FTIR imaging using the synchrotron source. The corresponding spectrum obtained on the bulk FIB section is shown in Fig. 10d and is a typical phlogopite spectrum. An OH band is observed around 3650 cm^{-1} and a band corresponding to Si-O vibration is visible at ~1000 cm^{-1}. After FTIR analysis, the section has been

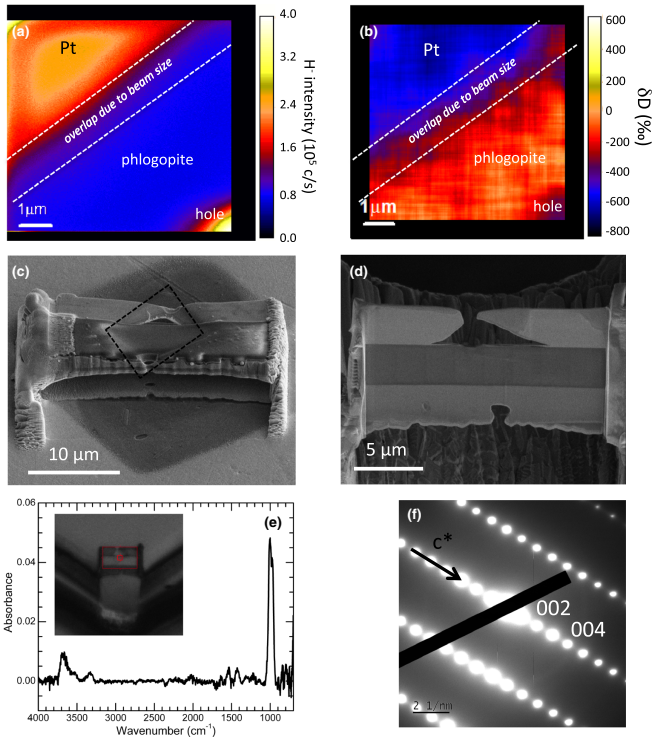

Fig. 10. Complete analytical sequence of a 3 µm thick FIB section from the CRPG phlogopite. a) NanoSIMS ion image of hydrogen. The image overlaps on the phlogopite and the Pt strap, which has higher H^- intensities (given in counts/second) due to the presence of organometallic H. b) Corresponding NanoSIMS image of D/H ratio. c) SE image of the FIB section after NanoSIMS. Notice the presence of a crater corresponding to the analyzed zone and overlapping on phlogopite and the Pt strap (black dotted rectangle). The dark area corresponds to a larger area sputter-cleaned at the beginning of NanoSIMS analysis. d) Section recovered and thinned down to 1 micron for FTIR. e) Baseline corrected FTIR spectrum of the phlogopite spectrum. The optical image of the section in the IR microscope is shown in the corner. f) Diffraction pattern of phlogopite acquired on the section with the TEM after final thinning. (Color figure can be viewed at wileyonlinelibrary.com.)

thinned a second time down to a thickness of ~100 nm for TEM imaging and analysis (Fig. 10e). The acquired diffraction pattern and EDS analysis correspond to the CRPG phlogopite (Fig. 10f).

APPLICATION TO THE NWA 5515 CHONDRITE

Individual sample preparation and analysis steps of our sequence were validated on standard mineral samples. Here, we present an example of application of our new sequence of analysis on a 35 × 35 × 15 µm-sized grain from the NWA 5515 CK chondrite. The full analytical sequence is summarized in Figs. 11 and 12.

As a first step, a 3-D IR micro-tomography of the grain was acquired using our setup. To improve the shape model and the quality of the IR 3-D-reconstruction, X-ray micro-tomography was also performed on the grain (Figs. 11a–e). An average IR spectrum of the whole grain before and after X-ray micro-tomography was acquired and shows that X-ray

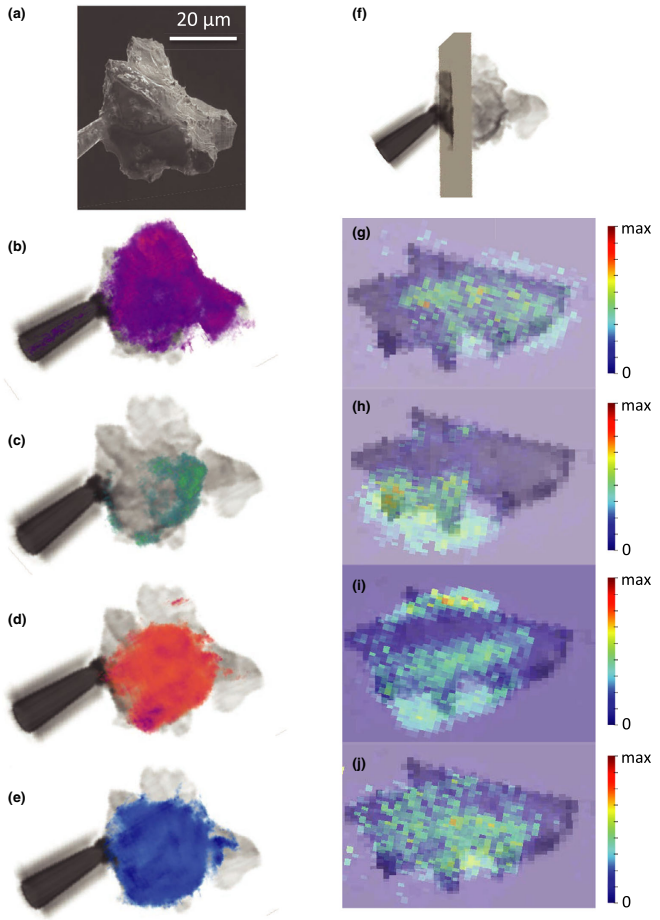

Fig. 11. 3-D reconstruction of a 35 × 35×15 µm-sized grain extracted from the NWA chondrite, and mounted on a tungsten needle. a) Secondary electron image of the grain; (b–e) 3-D-IR data superimposed onto X-ray data, with IR reconstruction of (b) olivine and (c) pyroxene s.l.; (d) organic matter; and (e) water. The 3-D spatial distributions of the silicates were reconstructed using the area of one of the olivine bands around 968 cm^{-1} (in the 930–996 cm^{-1} range) and the area of the Ca-poor pyroxene band around 1118 cm^{-1} (in the 1094–1139 cm^{-1} range). The organic matter and water were reconstructed using the area of the aliphatic (1335–1425 cm^{-1}) and of the OH (1570–1657 cm^{-1}) bending modes, respectively. f) Sectional plan showing the location of the slice that is extracted from the 3-D-IR reconstructed sample (see Dionnet et al. [2020] for details). g–j) 2-D slices virtually extracted from the 3-D reconstruction of the NWA-5515 grain. IR bands are the same as those used to show the 3-D spatial distribution of the silicates, the organic matter, and water. g) IR olivine band, (h) IR Ca-poor pyroxene 1118 cm^{-1} band, (i) IR CH band, and (j) IR OH bending band. Note that, because of the diffraction limited spatial resolution, some artifacts are present at the edges of the 2-D extracted slices. (Color figure can be viewed at wileyonlinelibrary.com.)

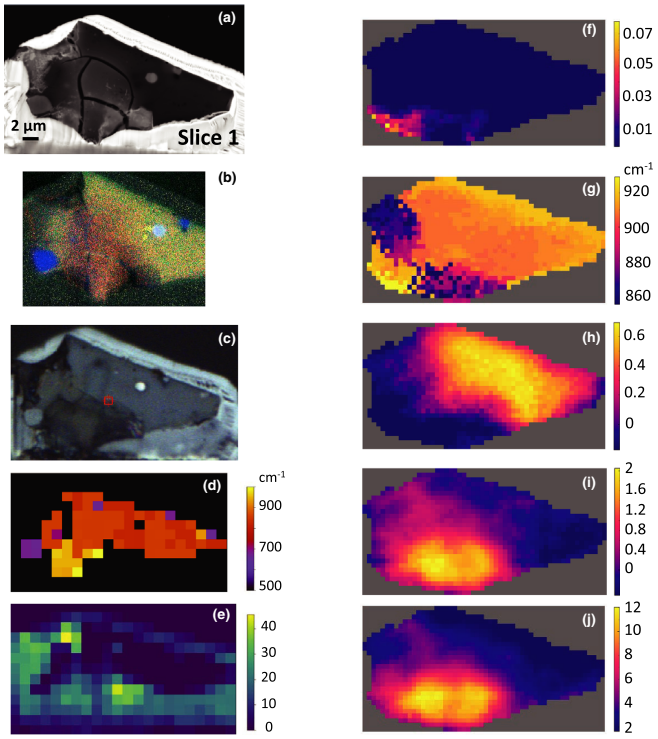

Fig. 12. Scanning electron microscopy, Raman, and IR spectroscopy studies of the slice 1 that was extracted from the NWA5515 grain using FIB (note that the orientation of the slice may slightly vary from one technique to the other, due to a tilt in some geometric configurations). a) Backscattered electron image. b) Composite X-ray map of Si (Red), Mg (green), Fe (blue), S (gray), Ca (yellow) showing the presence of two iron oxides in dark blue, an iron sulfide in light blue, two very small carbonate grains in bright yellow, olivine in yellow, and a more pyroxene-rich zone in red; (c) bright-field optical image; (d) Raman map of band positions of minerals between 500 and 1000 cm^{-1} Raman shift showing the presence of olivine (Fo70) in orange (doublet at 820 and 849 cm^{-1}), pyroxene in yellow (main band at 945 cm^{-1}), and magnetite in purple (main band around 669 cm^{-1}); (e) Raman map of the intensity of the G band located around 1540 cm^{-1}. The Raman maps were acquired with a 1.5 µm spatial sampling. f–j) 2-D-IR hyper-spectral maps (spatial sampling of 0.66 µm) acquired using the FPA detector of (f) the minimum of the second derivative of the spectrum around 1118 cm^{-1} for pyroxene, (g) the main peak position between 868 and 930 cm^{-1} for partially amorphous pyroxene, (h) the area of olivine band around 968 cm^{-1} (947–982 cm^{-1} range), (i) the area of aliphatic CH bending modes between 1335 and 1425 cm^{-1}, (j) the area of OH bending mode between 1570 and 1657 cm^{-1}. Maps show the presence of olivine in a large part of the grain, in addition to pyroxene and partially amorphous pyroxene, whose presence correlates with that of organic matter and water. (Color figure can be viewed at wileyonlinelibrary.com.)

tomography performed under our conditions induced very little modifications of the extraterrestrial grain (Fig. S3 in supporting information). Two types of silicates were identified in the average spectrum of the whole sample: olivine with its spectral features at 908 and 964 cm^{-1} (Hamilton 2010) and a Ca-poor pyroxene with a band at 1118 cm^{-1} (Beck et al. 2014). Figures 11b–e show 3-D-IR data superimposed onto X-ray data with IR reconstruction of silicates, organic matter, and water. The 3-D distributions of the two types of silicates

were reconstructed using the area of one of the olivine band around 968 cm^{-1} (930–996 cm^{-1}) (Fig. 11b) and the area of the orthopyroxene band around 1118 cm^{-1} (Fig. 11c) (1094–1139 cm^{-1}). The organic matter and water 3-D distributions were reconstructed using the CH bending vibration (1335–1425 cm^{-1}) (Fig. 11d) and the OH bending vibration (Fig. 11e) (1570–1657 cm^{-1}), respectively. The 3-D IR micro-tomography distribution of those phases shows that (1) the silicates are distributed heterogeneously with the pyroxene phase near the tungsten needle and (2) organic matter and water are also distributed heterogeneously, but their distribution seems to be correlated. The grain thus shows three parts: a first region with only olivine without any hydration signature or organic matter, a second region with olivine showing alteration signatures with the presence of organic matter and water, and finally a region with a pyroxene associated with organic matter and water.

After 3-D analysis, the grain was recovered and cut in five slices, one of them was thinned down to 100 nm for TEM analysis and the four others were thinned down to two to three microns for other 2-D analysis (Fig. S4). 2-D-IR and Raman maps as well as SEM images of slice 1 are shown in Fig. 12. 2-D-IR maps and SEM images of slices 2 and 4 are shown in Figs. S5 and S6 in supporting information, respectively. 2-D-IR maps, SE image, and TEM images of slice 3 are shown in Fig. S7 in supporting information. As expected by the first analysis in 3-D, 2-D-maps of slice 1 reveal the presence of several types of silicates as well as organic matter and water that are distributed heterogeneously (Figs. 12f–j). Thanks to the better spectral resolution of the 2-D IR spectra (4 cm^{-1}) than that of the 3-D IR spectra (16 cm^{-1}), we were able to distinguish three types of silicates: olivine, a small pyroxene characterized by its 1118 cm^{-1} feature, and partially amorphous silicate that shows a weak pyroxene feature at 1118 cm^{-1} as well as a more large Si-O band between 880 and 1130 cm^{-1}. To better represent their 2-D distribution, we mapped the area of one of the olivine bands around 968 cm^{-1} (947–982); the minimum of the second derivative of the spectrum around 1118 cm^{-1} (Susi and Byler 1983; Dionnet et al. 2018, 2020); and the peak position of the maximum between 868 and 930 cm^{-1}, for olivine (Fig. 12h), pyroxene (Fig. 12f), and the partially amorphous pyroxene (Fig. 12g), respectively. The grain consists predominantly of olivine, except the lower left corner, which consists of both crystalline and partially amorphous pyroxene. Organic matter and water distribution were also mapped using the area of the aliphatic CH bending modes between 1335 and 1425 cm^{-1} (Fig. 12i) and of the area of the OH bending mode between 1570 and 1657 cm^{-1} (Fig. 12j). They show a similar distribution with a concentration of organic matter and hydrated material in the left part of the grain enriched in pyroxene. The Raman map of band positions of mineral matter between 500 and 1000 cm^{-1} (Fig. 12d) confirms the presence of olivine (Fo70) with a doublet at 820 and 849 cm^{-1} and of a Ca-poor pyroxene (band at 945 cm^{-1}; Huang et al. 2000). It also shows the presence of a magnetite grain (main band around 669 cm^{-1}). Finally, the Raman map of the intensity of the G band located around 1540 cm^{-1} (Fig. 12e) confirms the nonuniform distribution of the organic matter in slice 1. Composite X-ray map of Si, Mg, Fe, S, Ca (Fig. 12b) and EDS analyses confirms the presence of olivine (Fo65–70), low Ca-pyroxene (En60), two iron-oxide grains, a small ~2 µm FeNi-sulfide, and two submicron-sized carbonate grains. SE and optical images (Figs. 12a and 12c) show a good correlation between the mineralogical distribution and the morphological aspect of slice 1, notably with more visible cracks in the left part of the grain.

For slices 2, 3, and 4, we also observe a good agreement of the silicates and organic distribution between 3-D IR micro-tomography and 2-D imaging (Figs. S5–S7). Slice 4 shows only olivine without organic matter or water (Fig. S5) whereas slice 2 shows the three types of silicates, as well as correlated organic matter and hydrated matter toward the pyroxene-rich part of the grain (Fig. S6). Slice 3 consists mainly of olivine. TEM images and 2-D-IR maps show that a portion of olivine contains cracks filled with fragile material associated with OH signal (Fig. S7).

The association of water, organics, and cracks with partially amorphous pyroxene indicates that the pyroxene in the lower left part of the grain has suffered some degree of aqueous alteration (Brearley 2006). By contrast, a large part of the grain consists of unaltered olivine. In detail, minor organics and water were also detected in the portion of olivine in contact with pyroxene, indicative of the aqueous alteration inside the grain. Insight on the origin of the aqueous alteration can be gained from the nature of the organics. The position of G band is relatively different from a classical extraterrestrial organic matter which points to terrestrial alteration, in agreement with the mild-weathering stage of NWA 5515 chondrite (Weisberg et al. 2009).

Taken together, these 2-D and 3-D results allow the determination of the mineralogy, state of alteration, and association with organic matter at the two micron scale of a 35 × 35 × 50 µm-sized grain. As a complement of 3-D IR and X-ray analyses, 2-D

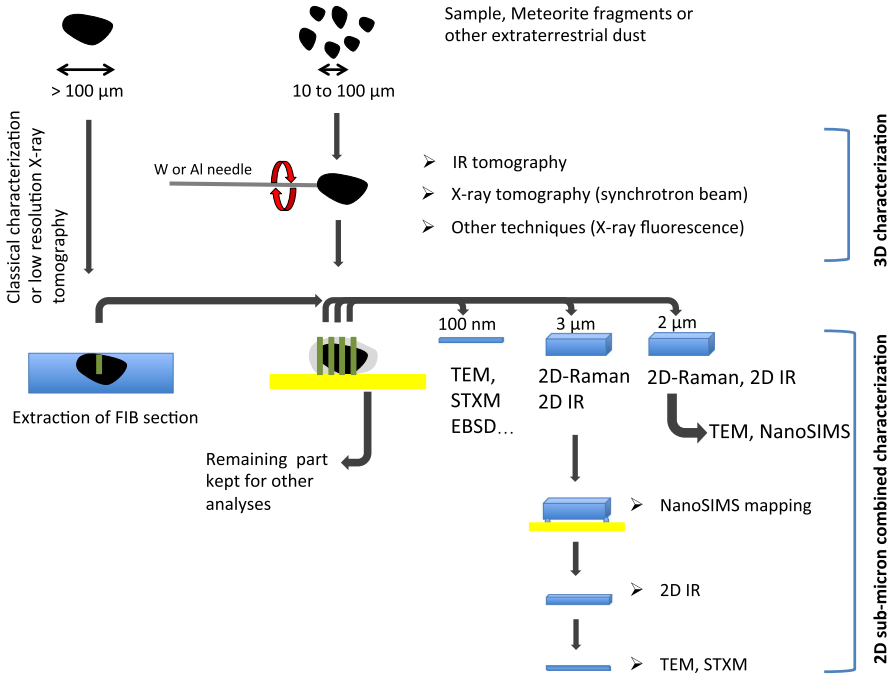

Fig. 13. Cartoon summarizing the new sample preparation and analytical procedures. (Color figure can be viewed at wileyonlinelibrary.com.)

analyses are mandatory because (1) they provide a better lateral and spectral resolution and (2) are necessary to correctly characterize the grain. For example, whereas the mid-IR technique cannot detect the presence of Fe-Ni sulfide contrary to SEM, using only SEM would not allow the detection of water in the pyroxene or to distinguish pyroxene from partially amorphous pyroxene.

In a reverse approach, the 3-D IR distribution could be used to locate precisely the regions of interest to slice the grain for 2-D analysis, provided it is possible to demonstrate a good correlation between the 2-D reconstructed slice extracted from the 3-D reconstruction of the grain and the 2-D-IR hyperspectral map. The 2-D-IR map of slice 1 was thus compared with the 2-D reconstructed slice extracted from the 3-D reconstruction of the grain at the approximate position of slice 1 (Fig. 11f) (see Dionnet et al. [2020] for details). There is a very good agreement between the 2-D IR reconstructed map and the real 2-D IR map as shown by the comparison of Figs. 11g–j and 12f–j. The phases present in the slice (olivine, pyroxene s.l., organic matter, and water) are detected in similar locations in the two maps. This demonstrates that from the 3-D IR images of our grain, we can decide the best location and orientation to slice the grain by FIB in order to optimize the study of interesting spots/phases either in 2-D IR or Raman or with the TEM (with a better spatial and spectral resolution).

DISCUSSION AND CONCLUSIONS

We have developed new sample preparation and analytical procedures to extract a maximum of submicrometer structural, mineralogical, chemical, molecular, and isotopic information from micrometric heterogeneous samples. The full analytical procedure is summarized in Fig. 13.

In this analytical sequence (Fig. 13), a single µm-sized grain welded at the end of a holder needle can be imaged with several 3-D analytical techniques such as IR or X-ray micro-tomography (Tsuchiyama et al. 2009, 2011, 2013, 2014; Yesiltas et al. 2014; Dionnet et al. 2020). IR micro-tomography is performed first, as it is a completely nondestructive technique, differently from XCT (Sears et al. 2016). Other 3-D complementary analyses can also be performed such as X-ray fluorescence spectrometry, Raman, or X-ray micro-diffraction (e.g., Medjoubi et al. 2013; Somogyi et al. 2015; Yesiltas et al. 2018). From this data set, it is possible (1) to get a first quick look at the spatial distribution and abundance at the µm scale of the anhydrous and hydrated mineral phases as well as of the carbonaceous matter and (2) correlate this phase distribution with the 3-D structure of the grain. Using these 3-D data, selected sites could then be chosen and sliced using the FIB to be further explored at a nanometer scale in 2-D.

One of the strengths of our approach is the possibility to combine many different 2-D analytical techniques in almost any possible order according to the requirements of the study. Depending on the chosen combination of techniques, FIB sections of different thicknesses can be prepared for the analysis by 2-D IR and Raman microspectroscopy (Dionnet et al. 2018), NanoSIMS isotopic or trace element mapping, TEM, and nearly any submicron mapping techniques that can handle 100 nm to few microns-thick FIB sections (e.g., STXM, Le Guillou et al. 2013; or EBSD, Kodama et al. 2020). Such combination of submicrometer analytical methods could bring a wealth of combined information including isotopic composition of different minerals, phase relationships, phase abundances, crystallographic structures, distribution of molecular bonds such as OH or CH. Notably, as (1) we have shown that during our sample preparation, organic matter that is mixed with mineral matter is preserved and little contaminated, and (2) as we use different techniques to look at both minerals and organics, it is thus possible to observe spatial relationships between organic and mineral matter. Performing NanoSIMS analysis of H isotopes in organic materials before TEM observations also allows us to avoid isotopic fractionation induced by electron bombardment (De Gregorio et al. 2010; Laurent et al. 2015; Uesugi et al. 2019). Finally, with this sample preparation protocol, it is possible to correlate not only several 3-D analyses or different 2-D characterization but also to place the 2-D nanoscale analyses in the larger framework of the 3-D microstructure (porosity, cracks, voids) and the 3-D assembly of compositional units. This sample preparation protocol can also be applied to biological sample as demonstrated by a companion study on foraminifera focused on the correlative imaging of trace elements by NanoSIMS and nanostructure by TEM.

Overall, the loss of matter along the whole sequence is very small compared to the large amount of information obtained from a very small volume of matter, as small as 10 × 10 × 10 µm and compared to classical sample preparation techniques. Grains larger than 100 micrometer must be handled differently at the beginning of the analytical sequence. Especially, high-resolution 3-D techniques are not always possible but after FIB section extraction, analysis may proceed similar to the protocol described here (Fig. 13).

These analytical developments open thus new perspectives in the multi-technique analysis of small and rare organic/mineral samples. This procedure could be used to analyze precious meteoritic samples such as small desert meteorites (e.g., Newton et al. 1995; Floss et al. 2014), fossil meteorites (e.g., Schmitz et al. 2016), interplanetary dust particles or micrometeorites (e.g., Nakamura et al. 2005; Brunetto et al. 2011; Dobrică et al. 2012) as well as precious extraterrestrial samples returned by ongoing or future space missions such as Hayabusa2 or OSIRIS-REx (Watanabe et al. 2017, 2019; Hamilton et al. 2019; Jaumann et al. 2019; Lauretta et al. 2019). For example, from a single 10 µm CM chondrite-like grain, it is possible to determine the macro-, micro-, and nanostructure; the distribution of -OH and -CH functions; the degree of hydration of minerals associated with the organics; the detection of localized isotopic anomalies; or the isotopic composition of specific regions of interest. Using a similar approach, Matsumoto et al. (2019) evidenced fossil asteroidal ice in the primitive meteorite Acfer 094. Using IR tomography and 2-D mapping, as well as TEM and microspectroscopies after NanoSIMS analysis, our protocol is complementary of previously developed analytical coupling strategies.

In the case of the Hayabusa2 mission, this top-down sequence could also allow the production of spectroscopic data in support of remote sensing astronomical observations and bridge remote sensing and in situ observations of Ryugu at macroscopic scale with the chemical and physical processes operating at the nanoscale. The sequence presented here could be completed for instance by 3-D reflection IR spectroscopy for an accurate comparison with asteroidal surfaces, which is currently under development in our group (Brunetto et al. 2020).

Acknowledgments—We thank Etienne Deloule for providing Bamble amphibole and CRPG phlogopite. We also thank Brigitte Zanda, the Museum National d'Histoire Naturelle, for providing fragments of the

Paris meteorite. We thank Guy Consolmagno for providing NWA 5515 meteorite fragments from the Vatican meteorite collection. We also warmly thank Christophe Sandt, Obadias Mivumbi, Paul Haghi-Ashtiani, Zahia Djouadi, Cateline Lantz, and Donia Baklouti for help, advice, samples, and discussions. We greatly thank the reviewers, Motoo Ito and an anonymous reviewer, and the associate editor Mike Zolensky for constructive comments. This work was partly supported by the French RENATECH network; grants from Ile de France (DIM-ACAV) and SOLEIL (IR microscopic analyses); and grants from Labex CHARMMMAT, LaSIPS, and Region Ile de France (TEM). It was also supported by the CNRS INSU PNP National Planetary Programme and by the Centre National d'Etudes Spatiales (CNES-France, Hayabusa2 mission).

Data Availability Statement—The data that support the findings of this study are available from the corresponding author upon reasonable request.

Editorial Handling—Dr. Michael Zolensky

REFERENCES

Aléon-Toppani A., Brunetto R., Aléon J., Dionnet Z., Rubino S., Levy D., Troadec D., Borondics F., and Brisset F. 2020. A preparation sequence for multi-analysis of micrometer-sized extraterrestrial samples (abstract #2682). 51st Lunar and Planetary Science Conference. CD-ROM

Bassim N. D., De Gregorio B. T., Kilcoyne A. L. D., Scott K., Chou T., Wirick S., Cody G., and Stroud R. M. 2012. Minimizing damage during FIB sample preparation of soft materials. *Journal of Microscopy* 245:288–301.

Beck P., Garenne A., Quirico E., Bonal L., Montes-Hernandez G., Moynier F., and Schmitt B. 2014. Transmission infrared spectra (2–25 lm) of carbonaceous chondrites (CI, CM, CV–CK, CR, C2 ungrouped): Mineralogy, water, and asteroidal processes. *Icarus* 229:263–277.

Berger E. L. and Keller L. P. 2015. A hybrid ultramicrotomy-FIB technique for preparing serial electron transparent thin sections from particulate samples. *Microscopy Today* 23:18–23.

Brearley A. J. 2006. The action of water. In *Meteorites and the early solar system II*, edited by Lauretta D. S. and McSween H. Y. Tucson, Arizona: The University of Arizona Press. pp. 567–586.

Brunetto R., Aléon-Toppani A., Rubino S., Baklouti D., Borondics F., Dionnet Z., Djouadi Z., Lantz C., Nakamura T., Takahashi M., Troadec D., and Tsuchiyama A. 2020. IR micro-spectroscopy and micro-tomography of isolated Murchison grains in preparation of the Hayabusa2 sample return (abstract #1135). 51st Lunar and Planetary Science Conference. CD-ROM.

Brunetto, R., Borg, J., Dartois, E., Rietmeijer, F. J. M., Grossemy, F., Sandt, C., Le Sergeant d'Hendecourt, L., Rotundi, A., Dumas, P., Djouadi, Z., and Jamme, F. 2011. Mid-IR, Far-IR, Raman micro-spectroscopy, and FESEM–EDX study of IDP L2021C5: Clues to its origin. *Icarus* 212:896–910.

Cliff G. and Lorimer G. W. 1975. The quantitative analysis of thin specimens. *Journal of Microscopy* 103:203–207.

De Gregorio B. T., Stroud R. M., Nittler L. R., Alexander C. M. O'D., Kilcoyne A. L. D., and Zega T. J. 2010. Isotopic anomalies in organic nanoglobules from Comet 81P/Wild 2: Comparison to Murchison nanoglobules and isotopic anomalies induced in terrestrial organics by electron irradiation. *Geochimica et Cosmochimica Acta* 74:4454–4470.

De Gregorio B. T., Stroud R. M., Cody G. D., Nittler L. R., Kilcoyne A. L. D., and Wirick S. 2011. Correlated microanalysis of cometary organic grains returned by Stardust. *Meteoritics & Planetary Science* 46:1376–1396.

Dionnet Z., Aleon-Toppani A., Baklouti D., Borondics F., Brisset F., Djouadi Z., Sandt C., and Brunetto R. 2018. Organic and mineralogic heterogeneity of the Paris meteorite followed by FTIR hyperspectral imaging. *Meteoritics & Planetary Science* 53:2608–2623.

Dionnet Z., Brunetto R., Aléon-Toppani A., Rubino S., Baklouti D., Borondics F., Buellet A.-C., Djouadi Z., King A., Nakamura T., Rotundi A., Sandt C., Troadec D., and Tsuchiyama A. 2020. Combining IR and X-ray micro-tomography datasets: Application to Itokawa particles and to Paris meteorite. *Meteoritics & Planetary Science* 55:1645–1664.

Dobričă E., Engrand C., Leroux H., Rouzaud J.-N., and Duprat J. 2012. Transmission electron microscopy of CONCORDIA ultracarbonaceous Antarctic micrometeorites (UCAMMs): Mineralogical properties. *Geochimica et Cosmochimica Acta* 76:68–82.

Engrand, C., Deloule, E., Robert, F., Maurette, M., and Kurat, G. 1999. Extraterrestrial water in micrometeorites and cosmic spherules from Antarctica: An ion microprobe study. *Meteoritics & Planetary Science* 34:773–786.

Eswara S., Pshenova A., Yedra L., Hoang Q. H., Lovric J., Philipp P., and Wirtz T. 2019. Correlative microscopy combining transmission electron microscopy and secondary ion mass spectrometry: A general review on the state-of-the-art, recent developments, and prospects. *Applied Physics Reviews* 6:021312.

Floss C., Le Guillou C., and Brearley A. 2014. Coordinated NanoSIMS and FIB-TEM analyses of organic matter and associated matrix materials in CR3 chondrites. *Geochimica et Cosmochimica Acta* 139:1–25.

Giannuzzi L. A. and Stevie F. A. 1999. A review of focused ion beam milling techniques for TEM specimen preparation. *Micron* 30:197–204.

Govindaraju K. 1994. Compilation of working values and sample description for 383 geostandards. *Geostandards Newsletter* 18:1–158.

Hamilton V. E. 2010. Thermal infrared (vibrational) spectroscopy of Mg–Fe olivines: A review and applications to determining the composition of planetary surfaces. *Chemie der Erde—Geochemistry* 70:7–33.

Hamilton V. E., Simon A. A., Christensen P. R., Reuter D. C., Clark B. E., Barucci M. A., Bowles N. E., Boynton W. V., Brucato J. R., Cloutis E. A., Connolly H. C. Jr., Donaldson H. K. L., Emery J. P., Enos H. L., Fornasier S., Haberle C. W., Hanna R. D., Howell E. S., Kaplan H. H., Keller L. P., Lantz C., Li J.-Y., Lim L. F., McCoy T. J., Merlin F., Nolan M. C., Praet A., Rozitis B., Sandford S. A., Schrader D. L., Thomas C. A., Zou X.-D., Lauretta D. S., and the OSIRIS-REx Team. 2019. Evidence for widespread hydrated minerals on asteroid (101955) Bennu. *Nature Astronomy* 332:332–340.

Heaney P. J., Vicenzi E. P., Giannuzzi L. A., and Livi K. J. T. 2001. Focused ion beam milling: A method of site-specific sample extraction for microanalysis of Earth and planetary materials. *American Mineralogist* 86:1094–1099.

Hewins R., Bourot-Denise M., Zanda B., Leroux H., Barrat J. A., Humayun M., Gopel C., Greenwood R. C., Franchi I. A., Pont S., Lorand J. P., Cournède C., Gattacceca J., Rochette P., Kuga M., Marrocchi Y., and Marty B. 2014. The Paris meteorite, the least altered CM chondrite so far. *Geochimica et Cosmochimica Acta* 124:190–222.

Huang E., Chen C. H., Huang T., Lin E. H., and Xu J. A. 2000. Raman Spectroscopic characteristics of Mg-Fe-Ca pyroxenes. *American Mineralogist* 85:473–479.

Ito M., Tomioka N., Uesugi K., Uesugi M., Kodama Y., Sakurai I., Okada I., Ohigashi T., Yuzawa H., Yamaguchi A., Imae N., Karouji Y., Shirai N., Yada T., and Abe M. 2020. The universal sample holders of microanalytical instruments of FIB, TEM, NanoSIMS, and STXM-NEXAFS for the coordinated analysis of extraterrestrial materials. *Earth, Planets and Space* 72:133.

Jaumann R., Schmitz N., Ho T.-M., Schröder S. E., Otto K. A., Stephan K., Elgner S., Krohn K., Preusker F., Scholten F., Biele J., Ulamec S., Krause C., Sugita S., Matz K.-D., Roatsch T., Parekh R., Mottola S., Grott M., Michel P., Trauthan F., Koncz A., Michaelis H., Lange C., Grundmann J. T., Maibaum M., Sasaki K., Wolff F., Reill J., Moussi-Soffys A., Lorda L., Neumann W., Vincent J.-B., Wagner R., Bibring J.-P., Kameda S., Yano H., Watanabe S., Yoshikawa M., Tsuda Y., Okada T., Yoshimitsu T., Mimasu Y., Saiki T., Yabuta H., Rauer H., Honda R., Morota T., Yokota Y., and Kouyama T. 2019. Images from the surface of asteroid Ryugu show rocks similar to carbonaceous chondrite meteorites. *Science* 365:817–820.

Kleindiek S., Rummel A., and Schock K. 2008. E-beam hardening SEM glue for fixation of small objects in the SEM. In *EMC 2008 14th European Microscopy Congress, Aachen, Germany*, edited by Luysberg M., Tillmann K., and Weirich T. Berlin: Springer. https://doi.org/10.1007/978-3-540-85156-1_283.

Kodama Y., Tomioka N., Ito M., and Imae N. 2020. Developments in microfabrication of mineral samples for simultaneous EBSD–EDS analysis utilizing an FIB–SEM instrument: Study on an S-type cosmic spherule from Antarctica. *Journal of Mineralogical and Petrological Sciences* 115:407–415.

Laurent B., Roskosz M., Remusat L., Robert F., Leroux H., Vezin H., Depecker C., Nuns N., and Lefebvre J.-M. 2015. The deuterium/hydrogen distribution in chondritic organic matter attests to early ionizing irradiation. *Nature Communications* 6:8567.

Lauretta D., DellaGiustina D., Bennett C., Golish D., Becker K., Balram-Knutson S., Barnouin O., Becker T., Bottke W., Boynton W., Campins H., Clark B., Connolly H. Jr., Drouet d' Aubigny C., Dworkin J., Emery J., Enos H., Hamilton V., Hergenrother C., Howell E., Izawa M., Kaplan H., Nolan M., Rizk B., Roper H., Scheeres D., Smith P., Walsh K., Wolner C., and The OSIRIS-REx Team. 2019. The unexpected surface of asteroid (101955) Bennu. *Nature* 568:55–60.

Lee M., Bland P., and Graham G. 2003. Preparation of TEM samples by focused ion beam (FIB) techniques: Applications to the study of clays and phyllosilicates in meteorites. *Mineralogical Magazine* 67:581–592.

Le Guillou C., Remusat L., Bernard S., Brearley A. J., and Leroux H. 2013. Amorphization and D/H fractionation of kerogens during experimental electron irradiation: Comparison with chondritic organic matter. *Icarus* 226:101–110.

Lévy D., Aléon J., Aléon-Toppani A., Troadec D., Duhamel R., Gonzalez-Cano A., Bureau H., and Khodja H. 2019. NanoSIMS imaging of D/H ratios on FIB sections. *Analytical Chemistry* 91:13,763–13,771.

Martina P. G., Griffithsb I., Jonesa C. P., Stitta C. A., Davies-Milnerc M., Mosselmansd J. F. W., Yamashikie Y., Richardsf D. A., and Scotta T. B. 2016. In-situ removal and characterisation of uranium-containing particles from sediments surrounding the Fukushima Daiichi nuclear power plant. *Spectrochimica Acta Part B* 117:1–7.

Matrajt G., Ito M., Wirick S., Messenger S., Brownlee D. E., Joswiak D., Flynn G., Sandford S., Snead C., and Westphal A. 2008. Carbon investigation of two Stardust particles: A TEM, NanoSIMS, and XANES study. *Meteoritics & Planetary Science* 43:315–334.

Matsumoto M., Tsuchiyama A., Nakato A., Matsuno J., Miyake A., Kataoka A., Ito M., Tomioka N., Kodama Y., Uesugi K., Takeuchi A., Nakano T., and Vaccaro E. 2019. Discovery of fossil asteroidal ice in primitive meteorite Acfer 094. *Science Advances* 5:eaax5078.

Mayer J., Giannuzzi L. A., Kamino T., and Michael J. 2007. TEM sample preparation and FIB-induced damage. *MRS Bulletin* 32:400–407.

Medjoubi K., Leclercq N., Langlois F., Buteau A., Lé S., Poirier S., Mercère P., Sforna M.-C., Kewish C. M., and Somogyi A. 2013. Development of fast, simultaneous and multi-technique scanning hard X-ray microscopy at Synchrotron Soleil. *Journal of Synchroton Radiation* 20:293–299.

Messenger S., Keller L. P., and Lauretta D. S. 2005. Supernova olivine from cometary dust. *Science* 309:737–741.

Nakamura T., Noguchi T., Ozono Y., Osawa T., and Nagao K. 2005. Mineralogy of ultracarbonaceous large micrometeorites (abstract #5046). *Meteoritics & Planetary Science* 40 (Suppl).

Nakamura T., Noguchi T., Tanaka M., Zolensky M. E., Kimura M., Tsuchiyama A., Nakato A., Ogami T., Ishida H., Uesugi M., Yada T., Shirai K., Fujimura A., Okazaki R., Sandford S. A., Ishibashi Y., Abe M., Okada T., Ueno M., Mukai T., Yoshikawa M., and Kawaguchi J. 2011. Itokawa dust particles: A direct link between S-type asteroids and ordinary chondrites. *Science* 333:1113–1116.

Newton J., Bischoff A., Arden J. W., Franchi I. A., Geiger T., Greshake A., and Pillinger C. T. 1995. Acfer 094, a uniquely primitive carbonaceous chondrite from the Sahara. *Meteoritics & Planetary Science* 30:47–56.

Nguyen A. N., Stadermann F. J., Zinner E., Stroud R. M., Alexander C. M. O., and Nittler L. R. 2007. Characterization of presolar silicate and oxide grains in primitive carbonaceous chondrites. *The Astrophysical Journal* 656:1223–1240.

Noun M., Baklouti D., Brunetto R., Borondics F., Calligaro T., Dionnet Z., d'Hendecourt L., Nsouli B., Ribaud I.,

Roumie M., and Della-Negra S. 2019. A mineralogical context for the organic matter in the Paris meteorite determined by a multi-technique analysis. *Life* 9:44.

Penen F., Malherbe J., Isaure M.-P., Dobritzsc D., Bertalan I., Gontier E., Le Coustumer P., and Schaumlöffel D. J. 2016. Chemical bioimaging for the subcellular localization of trace elements by high contrast TEM, TEM/X-EDS, and NanoSIMS. *Journal of Trace Elements in Medicine and Biology* 37:62–68.

Sandt C., Dionnet Z., Toplak T., Fernandez E., Brunetto R., and Borondics F. 2019. Performance comparison of aperture-less and confocal infrared microscopes. *Journal of Spectral Imaging* 8:a8.

Schmitz, B., Yin, Q.-Z., Sanborn, M. E., Tassinari, M., Caplan, C. E., and Huss, G. R. 2016. A new type of solar-system material recovered from Ordovician marine limestone. *Nature Communications* 7:11851.

Sears D., Sears H., Ebel D., Wallace S., and Friedrich J. 2016. X-ray computed tomography imaging: A not-so-nondestructive technique. *Meteoritics & Planetary Science* 51:833–838.

Shirai N., Karouji Y., Kumagai K., Uesugi M., Hirahara K., Ito M., Tomioka N., Uesugi K., Yamaguchi A., Imae N., Ohigashi T., Yada T., and Abe M. 2020. The effects of possible contamination by sample holders on samples to be returned by Hayabusa2. *Meteoritics & Planetary Science* 55:1665–1680.

Simon S., Joswiak D., Ishii H., Bradley J., Chi M., Grossman L., Aléon J., Brownlee D., Fallon S., Hutcheon I., Matrajt G., and McKeegan K. 2008. A refractory inclusion returned by Stardust from comet 81P/Wild 2. *Meteoritics & Planetary Science* 43:1861–1877.

Smith J., Dai Z., Weber P., Graham G., Hutcheon I., Bajt S., Ishii H., and Bradley J. 2005. Nitrogen isotopic anomalies in a hydrous interplanetary dust particle (abstract #1003). 36th Lunar and Planetary Science Conference. CD-ROM.

Somogyi A., Medjoubi K., Baranton G., Le Roux V., Ribbens M., Polack F., Philippotb P., and Samamaa J. P. 2015. Optical design and multi-length-scale scanning spectro-microscopy possibilities at the Nanoscopium beamline of Synchrotron Soleil. *Journal of Synchroton Radiation* 22:1118–1129.

Stadermann F. J., Croat T. K., Bernatowicz T. J., Amari S., Messenger S., Walker R. M., and Zinner E. 2005. Supernova graphite in the NanoSIMS: Carbon, oxygen and titanium isotopic compositions of a spherule and its TiC sub-components. *Geochimica et Cosmochimica Acta*. 69:177–188.

Suer T.-A., Siebert J., Remusat L., Menguy N., and Fiquet G. 2017. A sulfur-poor terrestrial core inferred from metal–silicate partitioning experiments. *Earth and Planetary Science Letters* 469:84–97.

Susi H. and Byler D. M. 1983. Protein structure by Fourier transform infrared spectroscopy: Second derivative spectra. *Biochemical and Biophysical Research Communications* 115:391–397.

Tsuchiyama A., Nakamura T., Okazaki T., Uesugi K., Nakano T., Sakamoto K., Akaki T., Iida Y., Kadono T., Jogo K., and Suzuki Y. 2009. Three-dimensional structures and elemental distributions of Stardust impact tracks using synchrotron microtomography and X-ray fluorescence analysis. *Meteoritics & Planetary Science* 44:1203–1224.

Tsuchiyama A., Uesugi M., Matsushima T., Michikami T., Kadono T., Nakamura T., Uesugi K., Nakano T., Sandford S. a., Noguchi R., Matsumoto T., Matsuno J., Nagano T., Imai Y., Takeuchi A., Suzuki Y., Ogami T., Katagiri J., Ebihara M., Ireland T. r., Kitajima F., Nagao K., Naraoka H., Noguchi T., Okazaki R., Yurimoto H., Zolensky M. E., Mukai T., Abe M., Yada T., Fujimura A., Yoshikawa M., and Kawaguchi J. 2011. Three-dimensional structure of Hayabusa samples: Origin and evolution of Itokawa regolith. *Science* 333:1125–1128.

Tsuchiyama A., Nakano T., Uesugi K., Uesugi M., Takeuchi A., Suzuki Y., Noguchi R., Matsumoto T., Matsuno J., Nagano T., Imai Y., Nakamura T., Ogami T., Noguchi T., Abe M., Yada T., and Fujimura A. 2013. Analytical dual-energy microtomography: A new method for obtaining three-dimensional mineral phase images and its application to Hayabusa samples. *Geochimica et Cosmochimica Acta* 116:5–16.

Tsuchiyama A., Uesugi M., Uesugi K., Nakano T., Noguchi R., Matsumoto T., Matsuno J., Nagano T., Imai Y., Shimada A., Takeuchi A., Suzuki Y., Nakamura T., Noguchi T., Abe M., Yada T., and Fujimura A. 2014. Three-dimensional microstructure of samples recovered from asteroid 25143 Itokawa: Comparison with LL5 and LL6 chondrite particles. *Meteoritics & Planetary Science* 49:172–187.

Uesugi M., Ito M., Yabuta H., Naraoka H., Kitajima F., Takano Y., Mita H., Kebukawa Y., Nakato A., and Karouji Y. 2019. Further characterization of carbonaceous materials in Hayabusa-returned samples to understand their origin. *Meteoritics & Planetary Science* 54:638–666.

Uesugi M., Hirahara K., Uesugi K., Takeuchi A., Karouji Y., Shirai N., Ito M., Tomioka N., Ohigashi T., Yamaguchi A., Imae N., Yada T., and Abe M. 2020. Development of a sample holder for synchrotron radiation-based computed tomography and diffraction analysis of extraterrestrial materials. *Review of Scientific Instruments* 91:035107.

Watanabe S., Tsuda Y., Yoshikawa M., Tanaka S., Saiki T., and Nakazawa S. 2017. Hayabusa2 mission overview. *Space Science Reviews* 208:3–16.

Watanabe S., Hirabayashi M., Hirata N., Hirata N., Noguchi R., Shimaki Y., Ikeda H., Tatsumi E., Yoshikawa M., Kikuchi S., Yabuta H., Nakamura T., Tachibana S., Ishihara Y., Morota T., Kitazato K., Sakatani N., Matsumoto K., Wada K., Senshu H., Honda C., Michikami T., Takeuchi H., Kouyama T., Honda R., Kameda S., Fuse T., Miyamoto H., Komatsu G., Sugita S., Okada T., Namiki N., Arakawa M., Ishiguro M., Abe M., Gaskell R., Palmer E., Barnouin O. S., Michel P., French A. S., McMahon J. W., Scheeres D. J., Abell P. A., Yamamoto Y., Tanaka S., Shirai K., Matsuoka M., Yamada M., Yokota Y., Suzuki H., Yoshioka K., Cho Y., Tanaka S., Nishikawa N., Sugiyama T., Kikuchi H., Hemmi R., Yamaguchi T., Ogawa N., Ono G., Mimasu Y., Yoshikawa K., Takahashi T., Takei Y., Fujii A., Hirose C., Iwata T., Hayakawa M., Hosoda S., Mori O., Sawada H., Shimada T., Soldini S., Yano H., Tsukizaki R., Ozaki M., Iijima Y., Ogawa K., Fujimoto M., Ho T.-M., Moussi A., Jaumann R., Bibring J.-p., Krause C., Terui F., Saiki T., Nakazawa S., and Tsuda Y. 2019. Hayabusa2 arrives at the carbonaceous asteroid 162173 Ryugu—A spinning top–shaped rubble pile. *Science* 364:268–272.

Weisberg M. K., Smith C., Benedix G., Herd C. D. K., Righter K., Haack H., Yamaguchi A., Chennaoui A. H., and Grossman J. N. 2009. The Meteoritical Bulletin, No. 96. *Meteoritics & Planetary Science* 44:1355–1397.

Yesiltas M., Kebukawa Y., Peale R. E., Mattson E., Hirschmugl C. J., and Jenniskens P. 2014. Infrared imaging spectroscopy with micron resolution of Sutter's Mill meteorite grains. *Meteoritics & Planetary Science* 49:2027–2037.

Yesiltas M., Jaret S., Young J., Wright S. P., and Glotch T. D. 2018. Three-dimensional raman tomographic microspectroscopy: A novel imaging technique. *Earth and Space Science* 5:380–392.

Zolensky M., Nakamura-Messenger K., Fletcher L., and See L. 2008. Curation, spacecraft recovery, and preliminary examination for the Stardust mission: A perspective from the curatorial facility. *Meteoritics & Planetary Science* 43:5–21.

SUPPORTING INFORMATION

Additional supporting information may be found in the online version of this article.

Fig. S1. Secondary electron images of the holder needle's Pp in experiments in which the welded grain was lost. (a–c) welding with e-glue, (d, e) welding with Pt. The SE images show the systematic presence of remaining fragments of the grains (indicated by arrows) on the Pt or e-glue welding, indicating that in most cases the grain itself broke rather than the welding.

Fig. S2. Secondary electron image (a) and IR spectra extracted of a single pixel from the hyperspectral mapping (b) of a 700 nm thick section of macusanite glass obtained using the Agilent Cary 670 IR microscope equipped with a FPA with c) the synchrotron source and d) a Globar source (128 scan, spectral resolution of 4 cm^{-1}). Signal to noise ratio is at least 4 times better with the synchrotron source than the globar source. The spectral contrast is also better defined with the synchrotron source, in agreement with Sandt et al. (2019).

Fig. S3. Average IR spectra of the whole grain acquired before and after X-ray microtomography (a) in the 2600–3800 cm^{-1} and (b) in the 1200–2900 cm^{-1} range where bands of water and organics are detected. The comparison shows that X-ray micro-tomography performed in our conditions induced very little modifications of the extraterrestrial organics. Notice that some analytical bias may slightly affect the spectra. First, as the two spectra were not acquired with the same spectral resolution (8 and 4 cm^{-1} for the grain before and after X-ray tomography, respectively), we had to decrease the resolution of the second one. Secondly, the spectra were not measured with the same acquisition angle.

Fig. S4. Secondary electron images of (a) the single grain of the NWA5515 chondrite being sliced in the FIB (b, c, e, f) the 4 slices thinned down to 2–3 μm that were recovered from each sides of the grain (S1, S2, S4, and S5) and d) the slice that was recovered from the middle of the grain and thinned down to 100 nm (S3).

Fig. S5. a) Secondary electron image of slice 4, (b, c) 2-D-IR maps acquired using the FPA detector of (b) the spectral continuum at short wavelengths showing absorption of the metal (c) the area of olivine band around 968 cm^{-1} (950–980 cm^{-1}) showing the sole presence of olivine in slice 4 (spurious signal present outside olivine is due to diffraction of IR photons).

Fig. S6. a) Secondary electron image of slice 2, (b–f) 2-D-IR maps acquired using the FPA detector of: (b) the area of olivine band around 968 cm^{-1} (in the 947–982 cm^{-1} range) (c) the minimum of the second derivative of the spectrum around 1118 cm^{-1} for pyroxene, (d) the main peak position between 868 and 930 cm^{-1} for partially amorphous pyroxene, (e) the area of OH bending mode between 1570 and 1657 cm^{-1}, (f) the area of aliphatic CH bending modes between 1335 and 1425 cm^{-1}. Images show the presence of olivine in a large part of the grain, in addition to pyroxene and a partially amorphous pyroxene, whose presence correlates with that of organic matter and water.

Fig. S7. a) The IR average spectrum of slice 3, (b–d) 2-D-IR maps acquired using the FPA detector of: (b) the area of the large IR band around 3 μm, (c) the area of OH bending mode between 1508 and 1705 cm^{-1}, (d) the area of olivine band (906–952 cm^{-1}), e) SE image of slice 3, (f–h) bright field TEM images of different zones of slice 3. Details of unaltered olivine are shown in squares 1 and 3, whereas square 2 shows altered olivine. A zoom of square 2 (g) shows the presence of cracks filled with fragile material in the altered olivine, which is absent in the unaltered area. Altered parts of olivine are always associated with OH signal in the IR map (c) whereas unaltered olivine does not show OH signal.